FINAL REPORT

PROJECT TITLE

Demonstration of Proof of Concept of a Multiphysics Approach for Real-Time Remote Monitoring of Dynamic Changes in Pressure and Salinity in Hydraulically Fractured Networks

REPORTING PERIOD

October 1, 2019–December 31, 2022

SUBMITTED UNDER FUNDING OPPORTUNITY ANNOUNCEMENT (FOA 1990)

WORK PERFORMED UNDER GRANT AGREEMENT DE-FE0031785

SUBMITTED BY

The University of Texas at Austin
Bureau of Economic Geology
3925 W. Braker Lane, Stop A9000
Austin, Texas, 78759-5316

UT AUSTIN DUNS #

170230239

PRINCIPAL INVESTIGATOR

Mohsen Ahmadian, Ph.D.
Ph: 512-471-2999 Fax: 512-471-0140
mohsen.ahmadian@beg.utexas.edu
Signed Electronically

Mohsen ahmadian, Ph.D.

PRIMARY AUTHORS OF FINAL REPORT

Mohsen Ahmadian[*], Mahdi Haddad[*], Alfred Kleinhammes[%], Patrick Doyle[%], Liangze Cui[^], Jun Ge[*], Ben Gremillion[*], William Ambrose[*]

[*]The University of Texas at Austin, [%] University of North Carolina, [^]Duke University

March 31, 2023

SUBMITTED TO

U.S. Department of Energy
National Energy Technology Laboratory

NETL PROJECT MANAGER

Scott Beautz
scott.beautz@netl.doe.gov

Disclaimer

This report was prepared as an account of work sponsored by an agency of the United States Government. Neither the United States Government nor any agency thereof, nor any of their employees, makes any warranty, express or implied, or assumes any legal liability or responsibility for the accuracy, completeness, or usefulness of any information, apparatus, product, or process disclosed or represents that its use would not infringe privately owned rights. Reference herein to any specific commercial product, process, or service by trade name, trademark, manufacturer, or otherwise does not necessarily constitute or imply its endorsement, recommendation, or favoring by the United States Government or any agency thereof. The views and opinions of the authors expressed herein do not necessarily state or reflect those of the United States Government or any

Acknowledgment

This study was supported by the U.S. Department of Energy, Office of Fossil Energy, National Energy Technology Laboratory under Award Number DE-FE0031785, and the State of Texas Advanced Oil and Gas Resource Recovery (STARR) program at the Bureau of Economic Geology (BEG). We express our special gratitude to the entire project team, including primary authors on the cover page as well as our other team members: Jeffrey Chen, Yue Wu, Darwin Mohajeri, Jean-Philippe Nicot, Trevor Pugh, Seyyed Hosseini, Sergey Fomel, Qing Huo Liu, Osareni C. Ogiesoba, and Yongze Jia. for their technical support. We thank the Advanced Energy Consortium (AEC) at the BEG and its members, Exxon-Mobil, Repsol, Shell, and TotalEnergies. We are grateful to the DOE project managers, Mr. Gary L. Covatch and Mr. Scott Beautz, for their technical and administrative assistance throughout this project and the EDX team at the NETL for their assistance to construct the project database. We acknowledge Dassault Systèmes Simulia Corp. and Computer Modelling Group Ltd. for providing the academic Abaqus and CMG licenses and Texas Advanced Computing Center for supporting high-performance computing.

Table of Contents

Section 1: Executive Summary

Hydraulic fracturing has evolved into a multistep process with varying flow rates, carrier fluids (e.g., gel or slickwater), proppant loadings, and proppant grain sizes. As a result, primary recovery from a hydraulically fractured tight-oil reservoir is often a tiny fraction of the original oil in place, ranging between 5 and 10%. As stated in the FOA1990, "part of this problem is due to the inability of current well completion processes to effectively stimulate the entire reservoir volume in contact with the wellbore. Innovative technologies are needed that can help improve the effectiveness of reservoir completion methods, maximize stimulated reservoir volumes, and optimize recovery over the entire producing life span of a well". We first need to enhance the current fracture diagnostic techniques to improve a well-completion design. However, detecting and delineating a subsurface hydraulic fracture is extremely difficult because the induced fracture network is only fractionally propped, and these propped fractures are generally very thin. Microseismic and tiltmeter monitoring techniques can provide information on the fracture extent but provide little or no information on the movement and final distribution of proppant or production fluids. On the other hand, electromagnetic (EM) imaging has shown the capability to monitor proppant distribution throughout the fracture area, especially in the presence of Electrically Active Proppants (EAPs). A previous EM survey of hydraulic fracturing at the Devine Fracture Pilot Site (DFPS) and subsequent EM code developments demonstrated this survey as a robust technique to remotely interrogate the extent of the EAP-filled hydraulic fracture during its propagation.

The objectives of the project were threefold:

(1) to capitalize on the material properties of an EAP to demonstrate remote monitoring of relative changes in pressure, pressure, and flow that are commonly encountered during production from a hydraulically fractured reservoir;

(2) to evaluate EM imaging tools, to achieve Objective 1 in near real-time; and

(3) to develop a multi-physics joint inversion approach to precisely predict flow patterns and physiochemical changes within an EAP-filled fracture network.

This research project was built upon our previous work at the Devine Test Site managed by the Bureau of Economic Geology (BEG) at The University of Texas at Austin (UT-Austin). It also leveraged a significant investment from the Advanced Energy Consortium (AEC) to address the DOE's interest in subsurface flow, containment, and characterization by multiple signals. This three-year and three-month project succeeded in demonstrating the feasibility of a real-time dynamic fluid flow mapping technique at Technology Readiness Level 5 (TRL5) by utilizing a commercially available surface-based Controlled-Source Electromagnetic (CSEM) method (Objectives 1, 2). We demonstrated that injections into an EAP-filled fracture could be successfully coupled with real-time electric field measurements on the surface, leading to remote monitoring of dynamic changes within the EAP-filled fracture. Furthermore, the observed electric field in our study is influenced by bottomhole pressure, flow rate, and salinity, which is demonstrated by comparing these parameters with the electrical field potentials. EM simulations solely based on assumptions of fracture conductivity changes during injection did not reproduce the whole measured electric field magnitudes. Preliminary estimates showed that including Streaming Potential (SP) in our geophysical model is likely needed to reduce the simulation misfit. The observed model misfit was the largest during abrupt flow-rate changes, showing a significant role of SP in the scattered electric field due to an abrupt flow-rate changes in porous media. To the best of our knowledge, our discovery that SP could strongly contribute to the frequency-domain EM

surveys used for monitoring subsurface fluid flow is commonly overlooked in other works and is a significant finding of this project.

Typical EM surveys monitor alterations due to electric-conductivity and magnetic-permeability changes during fluid injections. However, in processes involving fluid flow through porous media, a secondary potential can also be induced due to ionic charge imbalance, introduced as the SP. Typical EM surveys are conducted in frequency domain to improve resolution of detection, and SP surveys have been described only in Direct-Current (DC) mode. The conventional CSEM models neglect the SP physics in subsurface fluid-flow cases, likely leading to a large model misfit which was partly mitigated in our DFPS case by considering an SP analytical solution. Thus, the full accomplishment of Objective 3 in this project requires a numerical code that couples EM and SP in frequency domain. We were unable to develop this code with the allocated budget; however, this code development will be a follow-on goal of this work.

The developed methods in this study have several significant impacts on energy production from hydraulic-fracture networks by deducing the extent of proppant-filled fracture networks, formation stress states, fluid leakoff and invasion, and characterizations of engineered fracture systems. By enabling the optimization of refracturing through monitoring fracture dynamics (e.g., flow, leakoff, pressure evolution, and salinity changes), this work improves production from hydraulically fractured reservoirs. Also, the developed methods in this study offer solutions for subsurface pore flow monitoring in other applications such as subsurface carbon storage, enhanced geothermal systems, mineral solution mining, and saltwater disposal. The dissemination of the collected unique and comprehensive datasets to the public lays the foundation for the advancement of additional geophysical mapping and modeling techniques.

This project has resulted in two peer-reviewed published articles to date (Haddad et al., 2023; Zhang et al., 2022a), three conference manuscripts (Ahmadian et al., 2023; Haddad and Ahmadian 2023; Haddad et al., 2021), and several DOE annual review meeting presentations. These publications and presentations are listed in Section 3. The main themes of these publications are summarized in the following.

To design injection scenarios at the DFPS, Haddad et al. (2023, 2021) constructed hydrogeological and geomechanical models, performed history matching of these models using the data collected during injections into the DFPS hydraulic fracture in 2020, conducted pressure transient analyses to determine overburden stress, and demonstrated the advantages of a poroelastic model to simulate conductivity changes due to fracture reopening. Haddad and Ahmadian (2023) improved the geomechanical model by considering the propped and unpropped fracture conductivities in the model, repeated the history matching of this model, and proposed a simple technique to incorporate the outcomes of this model in a coupled EM-SP model that is targeted to be developed in future studies. Zhang et al. (2022a) proposed a deep transfer learning-based inversion method to accelerate the hydraulic-fracture imaging using a multistep approach composed of constructing simplified- and full-physical models for the generation of approximated training data and true data, respectively. Ahmadian et al. (2023) demonstrated that the real-time surface recorded electric field at the DFPS during injections in 2022 could be induced by a combination of pressure, salinity, and flow-rate changes, inferring the role of SP besides conductivity changes in the electric field.

Due to potential copyright issues with our publications in various journals, we have not copied those papers here. However, we highly recommend the interested readers to refer to these publications to gain a concise picture of major accomplishments of this project. major accomplishments and data are detailed in Section 2 of this document. We have attempted to summarize a high-level excerpt of these work below.

Summary of Major Activities

In the following, we provide a summary of the most important activities and accomplishments related to tasks and subtasks. Detailed results for relevant portions of the accomplishments are shown in Section 2.

In this three-year and three-month research project, we aimed to evaluate the utilization of pressure and salinity responses of an EAP-filled fracture to characterize the hydrogeological behavior of a fracture network in simulated production conditions. We pursued to remotely monitor changes in pressure and salinity within the fracture in real time by recording the surface electric field perturbation due to these pressure and salinity changes. Our main hypothesis was that the EAP could be used as an in-situ sensor for the remote monitoring of changes in pressure, salinity, and flow within an EAP-filled fracture. Our primary laboratory experiments revealed the detectability of large pressure changes within an EAP pack from electrical conductivity changes of the media. Then, we attempted to demonstrate the utility of this novel approach with surface-deployed CSEM surveys at the intermediate pilot scale of the DFPS (Subtasks 6.1 to 6.5). Simultaneously, we measured the following (Subtasks 6.1, 6.4, 6.5):

(1) bottomhole pressure and salinity in five monitoring wells;
(2) injection rate using high-precision flowmeters, recorded on data loggers;
(3) distributed acoustic signal in four observation wells; and
(4) surface tilt on the survey area.

we developed hydrogeological and geomechanical models because of the following reasons:

(1) to evaluate the robustness of these models to estimate the Bottomhole Pressure (BHP), fracture reopening and propped aperture, and fluid transport during water injection;
(2) to design the injection tests (Subtask 5.1); and
(3) to calibrate the hydrogeological and hydromechanical properties of the formation through history matching (Subtask 7.3).

To develop the geomechanical model, we needed the overburden stress over the horizontal hydraulic fracture at the DFPS, which is usually estimated from a density log. However, no density log was available at this test site for the shallow depth of interest. Hence, we estimated the overburden stress using post-shut-in pressure transient analyses (Subtasks 6.1, 7.3).

The presented field data, numerical and analytical models, and data analyses in this report support the correlations between pressure, salinity, and flow with the surface recorded electric field at the DFPS scale (Subtasks 6.4, 6.5). These correlations demonstrate that injections into an EAP-filled fracture could be successfully coupled with real-time electric field measurements on the surface, leading to remote monitoring of dynamic changes within the EAP-filled fracture. Furthermore, by comparing the electrical field traces with the Bottomhole Pressure (BHP), flow rate, and moderate salinity (200 vs. 2500 ppm), we concluded that the observed electric field in our study is influenced by fracture dilation and flow rate. Useful for the EM model developments, the stochastic analysis of the tilt data showed a radially dilated fracture with almost zero central offset with respect to the injection well and zero dip. The salinity effect on the electric field was observed when saltwater was injected. However, EM simulations solely based on assumptions of fracture conductivity changes during injection did not reproduce all of the measured electric field magnitudes. Preliminary estimates showed that including Streaming Potential (SP) in our geophysical model may be needed to reduce the simulation misfit. The later laboratory studies of the impact of fluid flow on the SP further supported the SP contribution to the recorded electric field at the DFPS.

We conducted numerical modeling extensively in this project because of the following reasons:

(1) to discern feasibility of detecting salinity and pressure changes (Subtask 3.1);
(2) to evaluate the layering and fracture depth using seismic data (Subtask 4.1);
(3) to inform design of optimal CSEM survey configurations for successful demonstration of the concept (Subtask 5.2);
(4) to assess the involved physics in the EM field by modeling the collected CSEM data during the field injection tests (Subtasks 7.1); and
(5) to invert these data to obtain subsurface conductivity changes (Subtask 7.1).

We started the EM modeling effort using the existing DFPS electric well logs and improved this model with the collection of the field data using prior AEC data and during the first and second surveys. Once the sensitivity of detection was demonstrated, we conducted the first field survey at the DFPS in Year 1, analyzed the collected data, determined and addressed the field test shortcomings, and conducted the second, more extensive field survey at the DFPS in Year 2, and improved the EM model based on the new datasets.

We first evaluated two approaches for EM inversion: 1.) based on Duke's conventional EM code that was previously validated at multiple scales; and 2.) based on Machine Learning (ML), aiming to speed up the inversion process significantly (Subtasks 4.2, 7.1). We started with the preliminary analysis of the DFPS Time Domain Induced Polarization (TDIP) data which were collected at the DFPS in 2017. We conducted this analysis using a machine-learning method to obtain the optimized location of 16 control points defining the fracture boundary. Through this analysis, we successfully delineated the boundary of the hydraulic fracture filled with EAP, which was in consistence with the outcomes of a primary EM study (Ahmadian et al., 2019).

Then, we performed EM forward modeling to design of the CSEM survey at the test site, we conducted EM models and determined the optimal borehole transmitter configuration. Considering that there is an Electrical-Resistivity-Tomography (ERT) array at the Devine Monitoring Well 1 (DMW 1), we modeled a case including this array (Subtask 5.2). These EM models benefited from a code that has been developed based on the Discontinuous Galerkin Frequency-Domain (DGFD) method by Professor Liu's research team at Duke University in the past two decades. Also, these models adopted the electric properties of the Devine media measured in a laboratory setting at the University of North Carolina by Prof. Kleinhammes and his partners (Subtask 3.1). To ensure the accuracy of the DGFD models, we compared the 1D analytical model with the 3D DGFD case as well as the COMSOL results (Subtask 7.1). The comparison suggested a good match between these solutions. Subsequently, we obtained EM field sensitivities larger than 1% corresponding to 5% change in conductivity of the EAP-filled fracture for the transmitter array centered at 45-m depth and length of 10 m (Subtask 5.2).

Following the collection of the CSEM data in 2020 (Subtask 6.1), we conducted numerical simulations and field data interpretations. We used a pixelwise machine-learning method to invert the real-time fracture conductivity changes during water injections into the EAP-filled fracture (Subtask 7.1). Using this inversion model, we were seemingly able to correlate the conductivity changes to BHP variations in multiple wells despite the presence of some noise in the inversion results. However, we obtained 74% total-field misfit between the simulation results and field data for the scattered EM field (Subtask 7.1). Thereby, we attempted to reduce this misfit by including 3D conductivity distributions in our model due to the presence of the following features at the test site: layered media, injection-well metal casing, surface injection pipe, and observation-well metal posts and surface casings (Subtask 7.1). Including these reduced the total-field misfit to 37%. We

reduced this misfit to 31% by varying the layer-conductivity combination using a machine-learning technique (Subtask 7.1).

To reduce the complexity of these models and consequent interpretations of the 2022 field data, we conducted the following:

(1) removed the surface injection pipe and observation-well metal posts;
(2) precisely logged the surface conductivity (Subtask 7.1);
(3) re-logged the existing wells to evaluate whether previous injections had changed the EAP distribution at the fracture depth (Subtask 6.4); and
(4) drilled a new monitoring well (DMW 9) at the southwest edge of the survey area to assess whether excessively large scattered field in that region, observed during our first deployment, could originate from a subsurface feature or the surface metal casing (Subtask 6.4).

Having developed the hypotheses about the possible causes of the large model misfit, we evaluated these hypotheses during a second field deployment to the DFPS in 2022 and conducted multiple injections during the CSEM survey (Subtask 7.1). Subsequently, we updated the EM model by the surface-conductivity data, new well log data, and the 2022 CSEM survey data, reducing the total-field misfit to 29% (Subtask 7.1). We then proceeded to analyze the scattered field misfit by comparing simulations versus collected field data. The largest scattered field misfit of 228% occurred at early times of injection, simultaneous with large pressure changes at the onset of injection. The smallest scattered field misfit of 59% occurred during maximum fracture dilation when flow rate was not changing. These observations led us to the significant realization about the possible role of SP in the large scattered field misfit, which we had ignored during our 2020 analysis. The contribution of SP in our EM scattered field could be explained by an SP analytical solution (Subtask 7.1).

To further isolate the SP as a critical contributor into the large model misfit, we assessed the effect of the following model input parameters on the misfit: the number of fracture layers, dilated-fracture shape (e.g., circular or elliptical), major axis azimuth, and fracture offset with respect to the injection well. We used the geomechanical model (Subtask 5.1, 7.3), tiltmeter data (Subtask 6.5), and fiber optic data (Subtask 6.5) to guide the dilated fracture dimension in the simulation cases. This sensitivity analysis, optimized by the modified efficient K-Nearest Neighbor (KNN) method, resulted in the minimum misfit of 55% for the fracture state close to shut-in (Subtask 7.1). We further reduced this misfit to 48% by subtraction of the SP-induced field from the measurements. These analyses reconfirmed the significant role of the SP in the recorded electric field at the DFPS. To achieve an accurate inversion of conductivity response during subsurface fluid injections, reducing the misfit to 5% should be targeted. As such, due to the large scattered field misfit, we could not perform a valid inversion of these results (Subtask 7.1).

Meanwhile, we evaluated this mechanism in inducing the electric field with porous flow using laboratory experiments during BP2 (Subtask 3.1). Our investigations about the SP revealed that the SP physics can be generally coupled with the conventional EM response through medium conductivity and active-source frequency. Therefore, a comprehensive assessment of the combined SP and EM responses requires numerical coupling of the SP and conventional EM in a simulator. This is an outstanding research topic that our team would like to pursue. A 3D poroelastic model must be coupled with this simulator to compute the pore pressure gradient, which helps calculate the current density according to the SP theory. To our knowledge, the existing EM community lacks a numerical forward model to simulate the SP and EM together, especially in the frequency domain.

Also, this forward model would be critical for evaluating the causative mechanisms for our EM field observations. Upon the development of this coupled simulation tool, the heavily instrumented DFPS and well-characterized EAP-filled fracture at this test site would provide a unique infrastructure to validate this code and demonstrate its robustness in studying applications related to subsurface porous flow monitoring.

We proposed conducting joint forward and inversion of seismic and CSEM surveys under Subtasks 5.4 and 7.4. To analyze the seismic response of the fracture at the DFPS, we started by developing a series of synthetic numerical experiments with varying velocity models and acquisition parameters (Subtask 5.3). These experiments comprised a thin layer experiment, an effective medium experiment, pore pressure experiment, and a combined effective medium and pore pressure experiment. The latest experiment adopted the velocity model derived from zero- and nonzero-offset DAS VSPs at the east, north, and west wells at the DFPS (Appendix A.3). The seismic numerical experiment did show that PS-wave reflections are more sensitive to the dilated fracture than PP-wave reflections, particularly at long offsets. However, these numerical experiments confirmed our initial findings using the synthetic data that the fracture detection would require SNRs of 50 to 60 dB. The low sensitivity of seismic waves to the fracture is primarily due to the large discrepancy between seismic wavelengths and the fracture aperture. Therefore, we did not conduct a seismic survey during the field tests at the DFPS. Nevertheless, these seismic study lessons would help design future experiments beyond the current project for fracture detection by suggesting to use of high-frequency seismic sources (which we did not have access to) and considering PS-wave reflections. Therefore, instead of the initially proposed seismic survey, during the second field deployment in 2022, we performed the following:

(1) a tiltmeter monitoring survey to record subtle surface uplift during injections that would be useful to infer the dilated fracture geometry (Subtask 6.5; Appendix A.4); and
(2) DAS passive monitoring of strain magnitude in several observation wells (Subtask 6.5).

The outcomes of these substitutive monitoring techniques were useful for the EM-model sensitivity analyses in Subtask 7.1.

Team Members and Their Significant Contribution

The principal performer of this research was the Bureau of Economic Geology (BEG) at The University of Texas at Austin, and the sub-performers were Duke University and the University of North Carolina.

The BEG was responsible for

(1) program leadership, planning, and communication by Mohsen Ahmadian (Task 1);
(2) workforce coordination for technology deployment by Mohsen Ahmadian (Task 2);
(3) geological characterization of the DFPS cores by William Ambrose and Osareni C. Ogiesoba (Subtask 3.2);
(4) developing and implementing plans for injections by Mohsen Ahmadian and Mahdi Haddad (Subtask 5.1);
(5) recruiting pressure-injection, drilling, logging, and geophysical-survey contractors by Mohsen Ahmadian (Subtask 6.1, 6.4, 6.5);
(6) submitting a permit application for saltwater injection tests at the DFPS to the Texas Commission on Environmental Quality (TCEQ) by Mohsen Ahmadian and Mahdi Haddad (Subtask 6.1);

(7) seismic survey feasibility and modeling by Ben Gremillion, Osareni C. Ogiesoba, and Sergey Fomel (Subtask 5.3) and vertical seismic profiling data collection from the DFPS by Mahdi Haddad and Silixa, LLC (Appendix A.3);
(8) developing hydrogeological and geomechanical injection models by Mahdi Haddad, Jun Ge, Mohsen Ahmadian, J.-P. Nicot, and Seyyed Hosseini (Subtasks 5.1, 5.3, 7.3);
(9) developing datasets and disseminating them to the project collaborators by Mahdi Haddad and Mohsen Ahmadian;
(10) coordinating efforts for the data analyses and interpretations by Mohsen Ahmadian and Mahdi Haddad (Subtasks 6.4, 6.5, 7.3).

Duke University was mainly responsible for

(1) developing EM forward and inversion models to help interpret the field data primarily by Liangze Cui and Qing Huo Liu (Subtasks 4.2, 5.2, 7.1).

The University of North Carolina was in charge of

(1) conducting laboratory experiments for characterizing the EM properties of the rock and soil samples collected at the DFPS and EAPs, under pressure, salinity, and flow conditions of the field tests by Patrick Doyle, Alfred Kleinhammes, and Yue Wu (Subtask 3.1).

We contracted ESG Solutions to assist in

(1) the development and implementation of plans for the CSEM surveys at the DFPS (Subtask 5.1);
(2) the development of datasets;
(3) data analyses and interpretations (Subtasks 6.4, 6.5); and
(4) guiding discussions for EM model developments (Subtask 7.1).

Bulleted List of Activities by Task

A list of the accomplishments in major tasks and subtasks with dates is listed below. The details of these accomplishments are discussed in Section 2. The reporting periods of the quarterly reports can be found in Section 4. Finally, the deliverables and milestones are shown in Exhibit A1-1 in Section 8. Although we refer to the quarterly reports in the list of accomplishments, there is no need for the reader to refer to the quarterly reports to follow the details of these accomplishments because most of the technical contents of those quarterly reports are incorporated in this final report for the reader's convenience. Also, the content of this report is easily accessible through the navigation pane which can be viewed by going through View tab, Show/Hide tab, and Navigation Panes tab, and selecting Bookmarks option in the PDF reader software program. Also, references to the figures, tables, and equations in this report contain an embedded hyperlink for the ease of access to them.

1. Project Management and Planning

1.1 Project Coordination and Communication

- Assigned a postdoctoral fellow to the project at UNC. Q1BP1
- Assigned three graduate students to the team at Duke University. Q1BP1
- Interviewed a new student at UT-Austin to work on code optimization for modeling in Subtask 4.1. Q1BP1
- Carried out briefing on project budgeting and reporting. Q1BP1

- Carried out monthly research team meetings to review progress and assign responsibilities for the quarters. Q1BP1-Q3BP2
- Hired a new student at UT-Austin to work on code optimization for modeling in Subtasks 4.1 and 5.3. Q2BP1
- Requested a 6-month extension at 1/30/21. Q1BP2
- Submitted a request for additional work to DOE/NETL project manager and presented this to the DOE team during our midyear report in May. Q2BP2
- Requested a nine-month extension. Q3BP2
- Completed contracting for nine-month extension request. Q5BP2
- Held a two-day in-person meeting with the UNC, Duke, and ESG Solutions Inc. (called ESG in this report for brevity, and formerly known as Deep Imaging Technologies or DIT) teams in Houston, Texas, on September 20-21, 2022, to discuss various topics in this project more in-depth than our weekly virtual meetings. Q8BP2
- Conducted the annual presentation to the DOE/NETL on 10/26/2022. Q9BP2.
- Held weekly joint meetings with a UT-Austin reservoir geomechanics specialist, ESG's geophysicists, UNC physicists, and Duke University modeling staff to discuss the collected data. Q4BP2-Q9BP2
- Submitted 13 quarterly research-performance progress reports to the DOE.

1.2 Coordination of Pilot Test Activities

- Held meetings with several geophysics survey vendors (ESG, MPT, Collier, and Inversion Technologies) and negotiated bids and proposals. Q2BP1-Q4BP1
- Completed the first deployment to the DFPS in September 2020. Q1BP2
- Planed for drilling a new monitoring well in the southwest corner of the previous survey area. Q4BP2
- Completed the drilling of a new monitoring well in the southwest corner of the previous survey area. Conductivity logging showed that EAP proppant was not present at the fracture depth. Q5BP2
- Completed the second deployment to the DFPS in February 2022. Q6BP2

1.3 Reporting

- Held kick-off meeting with DOE on 11/4/19. Q1BP1
- Submitted the BP2 continuation report on 6/30/20. Q3BP1
- Sent the TMP on 10/9/20. Q1BP2
- Presented a midyear oral presentation to the DOE on 6/15/2021. Q3BP2
- Presented a conference paper about hydrogeological and geomechanical modeling of injections in 2020 at the 55th US Rock Mechanics / Geomechanics Symposium, online. Q3BP2
- Conducted a detailed pass-down presentation to the new DOE project manager on 2/5/2021. Q2BP2
- Conducted the annual presentation to the DOE/NETL on 10/14/20 and 8/24/2021. Q1BP1, Q4BP1
- Submitted a no-cost extension request on 6/8/2022. Q7BP2
- Published our journal article about the geomechanical and hydrogeological models of injections in 2020 in the Rock Mechanics and Rock Engineering journal. Q9BP2
- Published two conference manuscripts on the EM interpretations and geomechanical modeling of the injection cycles at the SPE Hydraulic Fracturing Technology Conference 2023. Q9BP2

- Submitted all quarterly research performance progress reports to the DOE. Q1BP1-Q9BP2

2. Workforce Readiness for Technology Deployment

- Completed and sent to DOE. Q1BP2

3. Electromagnetic Response of Laboratory Fracture Models and Incorporation of Mixing Rules

3.1 Electrical Measurements in the Laboratory

- Designed an impedance analysis cell to accommodate a miniaturized fracture-bearing anomaly with fluid injection port. Q1BP1
- Submitted the design drawing to the machine shop at the University of North Carolina (UNC) for fabrication. The necessary components for the benchtop measurements were purchased and assembled for the preliminary tests. Q1BP1
- Conducted electrical measurements in the laboratory and determined that relative conductivity changes induced by either injecting saline solutions into a model fracture, or pressurizing the electrically active proppant (EAP), exceed the go-no-go goal of 1–5% contrast change set in the Project Management Plan (PMP). Q2BP1-Q4BP1
- Constructed an impedance analysis cell to accommodate a miniaturized fracture-bearing anomaly with a fluid injection port. Q2BP1
- Characterized the impedance response of the laboratory fracture model both with and without injection of saline solution. Q2BP1
- Modified a cell to permit simultaneous application of lithostatic and hydrostatic pressure, replicating the configuration encountered at the DFPS. Q4BP1
- Recorded the impedance response due to increasing lithostatic pressure as well as increasing and decreasing hydrostatic pressure. Q4BP1
- Developed a laboratory fracture model that simulates the in-situ impedance response of the Devine fracture when high-pressure water or saline solution is injected into the fracture:
    - Modified a laboratory-testing cell to permit simultaneous application of lithostatic and hydrostatic pressure replicating the exact configuration encountered at Devine.
    - Recorded the impedance response using four electrodes with increase of hydrostatic pressure during injection of fluids into the fracture model, and with hydrostatic pressure decrease during the drainage of the injected fluids from the cell.
    - Injected water and 1 S/m NaCl solution into the cell in separate experiments,
    - Recorded the impedance response to saline injections into a sand column and analyzed the conductivity changes induced by saline injections as function of 1.) salt concentration and 2.) the elapsed time for ion migration and diffusion in the cell. Q2BP2
- Developed a laboratory fracture model that simulates the in-situ impedance response of the Devine fracture when high-pressure water or saline solution is injected into the fracture:
    - Restricted fluid flow within our column.
    - Evaluated EAP response to different fluid salinities.
    - Assessed effects of flow rate on our fracture model.
    - Studied the contribution of volume fraction into salinity effects, and started developing mixing rules. Q3BP2
- Continued the laboratory fracture injection tests with various water saturations, water salinities, and rock matrix types:

    - Investigated impact of the scale of the investigation domain on wet sand and clay systems.
    - Showed that upscaling of the laboratory results to the field through wet sand is not complicated from the perspective of imaginary component of impedance [Im(Z)] in fractured EAP systems.
    - Showed that this upscaling through wet clay is more complicated, but can be managed by reducing the ion content surrounding the EAP fracture. Q4BP2
- Characterized the electrical properties of the DFPS materials and incorporated them in our fracture injection tests:
    - Investigated impact of the pressure and salinity changes on Devine clay material electrical properties.
    - Showed that mixed clay/water system conductivity can be predicted from the injection fluid ion concentration. Q5BP2
- Increased static pressure always reduces the grain contact within water-immersed unconsolidated systems. However, this can lead to different total conductivity changes of the grain pack depending on the conductivity of the grain material. Q8BP2
- Measured SP across an EAP pack and sand pack in other experiments. The EAP response was gradual, and the sand response was almost instantaneous, to changes in the injection rate. Q8BP2
- Identified similarities between the trends of the scattered electric field recorded at the DFPS and the laboratory-recorded SP induced by flow through a proppant pack. Q8BP2

3.2 Rock Characterization

- Completed an extensive description of 249 ft (76 m) of core from the DFPS, including the Standard Oil No. 9 Wilson (Wilson-9), DMW-1, and DMW-3 cores (Appendix A.2 in Section 8). Q1BP1, Q2BP1
- Interpreted facies and depositional-systems for these three cores. Q1BP1
- Slabbed and photographed selected intervals from the DMW-1 and DMW-3 cores to document lithology, stratification, and accessory features such as fractures and microfaults. Q1BP1
- Proposed a tidally influenced deltaic interpretation based on stratification and vertical facies relationships, implying that a significant degree of heterogeneity exists in the section where injection is proposed. Q2BP1

4. Code Optimization for Modeling

4.1 VSP/Seismic RTM Validation

- Assigned a PhD student (Ben Gremillion) to the project. Q1BP1
- Performed RTM (reverse time migration) on synthetic data in layered media to validate its effectiveness and sensitivity in producing images based on seismic data. Q1BP1
- Completed Reverse Time Migration (RTM) modeling of fracture-bearing layered media based on Devine configuration to validate its effectiveness and sensitivity in producing images based on seismic data. Q2BP1-Q4BP1

4.2 Joint VSP/Seismic and Electromagnetic Inversion

- Used the theory of Born iterative method for inversion with the volume integral equation; the forward problem is solved by the stabilized Bi-Conjugate Gradient method combined with the Fast Fourier Transform (BCSG-FFT). The corresponding codes have been

developed previously and validated by Duke with some synthetic and field cases. (Ahmadian, LaBrecque et al. 2018, Fang, Hu et al. 2018, Hu, Fang et al. 2018). Q1BP1

- Explored EM inversion with ML method on the DFPS TDIP data, which had been collected at the DFPS in 2017. We first generated synthetic EM data for the fracture scattering based on the DFPS configuration. A fully connected Neural Network (NN) is then designed and optimized to invert for the shape of the fracture, which is characterized by a B-spline closed curve. This process aims to obtain an NN configuration to invert for changes in fracture shape and parameters in near real time. Q1BP1
- Tested principal component analysis (PCA), input standardization, and filtering for either scaling the input data or reducing the input dimension to accelerate the NN training process from hours to minutes. Q2BP1
- Narrowed the conventional EM inversion domain using VSP/seismic data. Q3BP1
- Reduced time required for the NN training and inversion processes to half an hour by including field data screening. Q3BP1
- Worked on creating an EM inversion approach based on machine learning and made progress in accelerating the training process from hours to minutes. Q4BP1
- Validated the DGFD solver under the new configuration (with steel casing and ground transmitters and receivers) according to the ESG's measurement system. We have started to generate the training data for NN based inversion. Q1BP2
- Improved the DGFD solver by adding a new method to tackle the cases where the transmitter is placed far away from the injection well; it avoids including the transmitter in the computational domain by using the so-called total-field/scattered-field technique, thus making the computation much faster. The improved solver can efficiently generate a large amount of training data. Q2BP2, Q3BP2

5. Design of Field Experiment/Sensitivity Analysis

5.1 Fluid Flow Modeling

- Constructed a hydrogeological layer-cake model in CMG software program to design injections at the DFPS and to improve the interpretation of previous EM surveys. Q1BP1-Q4BP1
- Modeled the reservoir conditions of the injection zone and matched the model to the available fluid injection data from the DFPS and utilized the available core data in this model improvement. Q2BP1
- Modeled several injection scenarios under the reservoir conditions of the injection zone at The University of Texas DFPS and estimated the pore pressure and salinity variations during and after the injection, as well as in the conditions with extraction after injection. The required volume of water was also estimated at different injection scenarios and cases. Q3BP1-Q4BP1
- Updated our hydrogeological model with field data gathered from our first deployment, and started the development of a poroelastic model. Q1BP2
- Updated our hydrogeological model with field data gathered from our first deployment, developed a poroelastic model, and performed history matching of the poroelastic model with field data gathered from the September 2020 field deployment. Q2BP2

5.2 Electromagnetic Sensitivity Analysis

- Conducted a sensitivity analysis of at least 1% contrast and determined several transmitter-and-receiver scenarios that passed the go-no-go decision point for BP1. Q2BP1-Q4BP1

- Conducted EM sensitivity analysis under the Devine configuration with multiple borehole transmitters. The recommended electrode position is given in order to gain maximum signal. Q2BP1-Q4BP1-Q1BP2

5.3 VSP/Seismic Sensitivity Analyses

- Began seismic modeling to examine the seismic response to the fracture. Q2BP1
- Created velocity and density models based on the DFPS cores with fractures at z = 54 m (175 ft) for seismic modeling and migration and performed simulations to examine the seismic response to the fracture. Sensitivity appears too low for detection. Q2BP1-Q4BP1
- Considered changes in seismic velocity and response due to variations in effective confining pressure in the vicinity of the fracture, with the availability of pore pressure simulations and geomechanical data from the Wilson-9 well. Q2BP2
- Performed seismic modeling with a vertical seismic profile (VSP) configuration and a small receiver spacing to mimic potential DAS acquisition using the DAS fibers along three observation wells at the DFPS. Q2BP2
- Detected that the fracture response is 54 dB weaker than that of the fracture model shot gather. Q2BP2
- Concluded that the noise in the background and fracture model shot gathers is negligible but is significant in the fracture response. Q2BP2
- Calculated an SNR of at least 50 dB to be necessary for detecting the horizontal fracture at the DFPS. In other words, we think this improves detectability by 10 dB over our previous effective medium results. Q2BP2
- Analyzed synthetic data from a time-lapse Vertical Seismic Profiling (VSP) using DAS to determine the feasibility of detecting changes in elastic properties of the subsurface that may be caused by fracture dilation at the DFPS. Our results show that P-to-S-wave reflections yield more accurate images of the fracture than P-to-P-wave reflections. Amplitudes in P-to-S-wave images also show a greater relative change due to fracture dilation than amplitudes in P-to-P-wave images. These results suggest that imaging P-to-S-wave reflections would be more suitable for detecting dilation-induced elastic changes than the conventional approach of imaging P-to-P-wave reflections. Unfortunately, site conditions at the DFPS may cause the available equipment source bandwidth to be significantly lower than that used in this experiment, making detection of changes in elastic properties unfeasible. Thus, in our recent deployment, we chose to substitute seismic imaging with passive strain measurements with our existing fibers. Q6BP2

5.4: Multi-Physics Forward Modeling

- Did not proceed with the joint inversion of the VSP/seismic and EM fields, having shown the shortcoming of a seismic survey to detect the fracture changes in our numerical models.

6. Field Construction/Field Survey Studies/Data Gathering

6.1 Formation Well Testing

- Contracted Geoprojects International, Inc. to perform the hydrological operations, and deployed the geophysics survey team from ESG in order to collect the initial sensitivity analysis. Q4BP1

- Deployed to the DFPS for the Phase 1 tests and conducted a series of injections to calibrate our fluid models. Q4BP1
- Deployed In-Situ^{TM} pressure, temperature, depth, and salinity transducers in the injection well, DMWs 1 and 2, and tested these transducers also for online reading of the downhole pressures while connected to the field computer. Q4BP1
- Collected the downhole pressure data and flow rate in injection well, and the downhole pressure data in DMWs 1 and 2 for subsequent history matching studies. Q4BP1
- Used tangent method and *G*-function pressure analysis to estimate fracture closure pressure using the pressure data collected during the 2020 field experiments, in lieu of the absence of the bulk density logs. Q1BP2
- Planned for the second deployment in the sixth quarter of BP2. Q4BP2
- Conducted 10 injection cycles with variations in the injection rate and duration, and the injected fluid ion content for the Phase 2 field test. Q6BP2
- Confirmed the outcomes of our initial pressure transient analyses, based on the 2020 field deployment data, by repeating the *G*-function analyses using data from six injection cycles of the 2022 field deployment. Q8BP2

6.2 Seismic Surveys

- Identified that surface seismic sensitivity to change of preexisting fractures at the DFPS requires very high sensitivity tooling. We proposed to perform VSP with DAS fiber to improve Signal-to-Noise Ratio (SNR) during data gathering. Q2BP2
- Deployed to the DFPS and conducted multiple time-lapse surveys to obtain a velocity model using VSP by actuating a weight-drop seismic source at various locations and recording acoustic waves at three previously installed fiber optic cables in the north, east, and west observation wells. Q4BP2
- Concluded that the current fiber-optic cable configuration may provide adequate SNRs for the discernment of fractures in an active source VSP study. However, several logistical issues including lack of adequate supplemental funding that we had requested from the DOE limited its inclusion in this study. Q4BP2

6.3 Development of Strategies for Real-Time Monitoring

- Contracted ESG and planned to test two different configurations for EM imaging at the DFPS. Q1BP2
- Developed a master plan for the final field deployment to the DFPS, and determined January 11-February 2, 2022 for this field deployment. Q4BP2-Q6BP2
- Finalized and implemented the CSEM survey design to resolve the shortcomings of the previous survey by
    - increasing the receiver spacing to 30 ft,
    - centralizing the transmitter line with respect to the northwest-southeast symmetry axis of the receiver survey area, and
    - replacing the surface injection steel pipe with a heavy-duty polypropylene (poly) pipe. Q6BP2
- Planned and executed bottomhole and surface pressure monitoring, precise flow-rate measurement, surface tiltmeter mapping, and passive wellbore DAS during the final CSEM survey. Q6BP2

6.4 Smart Proppant Test 1: In-Situ Remote Pressure Response Measurements

- Submitted a comprehensive report about the Phase 1 deployment. Q1BP2

- Demonstrated encouraging preliminary EM analyses using a set of surface transmitter and receivers. Borehole transmitter introduced some noise and signal reversal that we believe stems from lack of constant current. Q1BP2
- Drilled a new monitoring well (DMW 9) and performed induction logging and verified that the EM anomaly we had observed in our September 2020 experiment at the southwest corner of our array was not due to the presence of EM proppant at that location. Q5BP2

6.5 Smart Proppant Test 2: In-Situ Remote Salinity Tests

- Planned for in-situ remote salinity tests as part of the second deployment to the DFPS. Q4BP2-Q5BP2
- Conducted the remote salinity tests during the second deployment to the DFPS. Q6BP2
- Submitted a comprehensive report about the Phase 2 deployment, including plots of the y-axis absolute amplitude of the surface electric field potentials for three groups of receivers at a constant distance from the injection well for four injection cycles on January 23, 26, and 27. Q7BP2
- Discovered some shortcomings with how the ESG processed the collected data, although the movies of the contour plots of the surface electric field were very informative. This suggested that the in-house software program at the ESG (i.e., DMAX) requires improvements to generate contours with tight color-bar ranges or to override any assumed spatial significance. Q7BP2
- Demonstrated the temporal correlation of the surface electric potentials with the flow rate and bottomhole pressures by plotting together the bottomhole pressure and salinity profiles for the injection well, DMWs 1 and 2, the injection flow rate, and the electric potentials. Q7BP2
- Showed that the early-time EM field originates mainly from the SP response of the media at high flow rates into a limited space and large pressure gradients using an SP analytical solution. Q8BP2
- Analyzed the collected DAS data of the east and west wells during the second field deployment and showed the preferential fracture dilation slightly toward the west well. Q9BP2
- Analyzed the collected tiltmeter data of the second field deployment using a statistical model by FRx Inc., and determined the most probable dilated fracture characteristics.Q9BP2
- Estimated the fracture radius using the tilt study, consistent with the pressures at DMW 1 and DMW 2. Q9BP2

6.6 Tracing Fluid Breakthrough

- Planned to use salinity as a tracer in the second field tests. Q4BP2-Q5BP2
- Used salinity as a tracer in the second field tests. Q6BP2

7. Data Processing and Interpretation

7.1 Electromagnetic Inversion of Field Data

- Generated more than 18,000 synthetic data for the training process of electromagnetic (EM) inversion. We built two ML models and performed EM inversion with the synthetic data. Q3BP2

- Fed the field data collected by ESG during the first field deployment into our well-trained pixelwise ML model and obtained meaningful inversion results. Q3BP2
- Obtained a large misfit between the discontinuous-Galerkin-frequency-domain (DGFD) simulation results of the ML-based fracture conductivity and the field dataset collected by ESG, probably due to assuming a homogeneous medium in the initial solutions. To reduce this misfit, we replaced the homogenous medium with a layered medium. Q4BP2
- Tried to fit the field data collected by ESG during the 2020 field deployment with our ML model and tuned the conductivity values for different layers. However, the recovered electric field did not agree with ESG's primary field very well. Therefore, we analyzed the electric field at each receiver and tried to remove some of the receivers that contributed the most to the data misfit. Q4BP2
- Obtained an 18.4% data misfit on the E_x component based on the overall recovered electric field. This data misfit is within our expectations. However, considering the E_y component, we still had a combined E_x-E_y data misfit of 30.89%. Part of this misfit likely originated from 3D effects and surface heterogeneities, probably due to the presence of the casing, steel tubing on the ground, and buried mud pits used for drilling of the observation wells. Q4BP2
- Used the DGFD method to simulate different field models with various environmental effects. Specifically, we considered the effects of the ground surface metal injection conduit to the injection well, vertical metal posts, and metal surface casing surrounding the PVC wells. Q5BP2
- Demonstrated that removing the ground metal pipe used for injection and the metal marker posts at various wells could reduce complexity of the EM fracture response during the second field experiments, based on the EM results of the first experiment. Our modeling suggested that to reduce the effects of well surface casing, the receivers should also be deployed at least 4 m away from the corresponding wells. Q5BP2
- Developed a version of our Discontinuous Galerkin Frequency-Domain (DGFD) model with a layered medium, an inhomogeneous surface layer, and considered the January-2022 source and receiver experiment configurations. The inclusion of inhomogeneous surface layer did not improve the data misfit between forward simulation and total electric field data gathered by ESG. Based on our discussions with ESG, there is no calibration factor in the equipment that would contribute into this error. Q6BP2
- Simulated the scattered field for an early injection time, close to shut-in, and several hours after shut-in, and compared the simulated field with the data. The EM signal is maximized at the case close to shut-in due to lower contribution of SP. Q8BP2
- Demonstrated that the early-time misfit can be mainly due to SP as a second mechanism for changing the surface-recorded EM field. Q8BP2
- Estimated the conventional electric field by subtracting the SP electric field from the experiment measurements, which reduced misfit of the DGFD simulations. We used an SP analytical solution to determine this SP electric field because we do not have funds to develop coupled SP-EM numerical model. Q9BP2
- Used the modified K-nearest-neighbor (KNN) method to minimize the misfit between the DGFD simulation with the measured EM data. We evaluated the effect of shape and size of the dilated fracture at 17:26 during injection on January 26, 2022. The large misfit between these simulations and the Devine data may infer the role of streaming potential on the recorded electric field. Q9BP2

7.2: VSP/Seismic Imaging and Migration

- Did not proceed with the joint inversion of the VSP/seismic and EM fields, having shown the shortcoming of a seismic survey to detect the fracture changes in our numerical models.

7.3 History Matching of Fluid Flow Models

- Defined benchmark cases for performing history matching of our hydrogeological model because of high quality of the data collected during field deployment in September 2020.
- Improved the hydrogeological model by adjusting the fracture and formation permeability to match the bottomhole pressure with the field data that was collected during the injection experiments on September 23 and 25, 2020. Q2BP2
- Developed a fully-coupled poroelastic model and adjusted the corresponding parameters to match the bottomhole pressure with the 2020 field data, mainly because of the shortcomings of a hydrogeological model to predict hydraulic-fracture conductivity changes through time. Q2BP2
    - The hydrogeological models can now benefit from the evolution of hydraulic fracture geometry through time obtained from the poroelastic model. This poroelastic model was useful for seismic inversion studies such as our surface seismic sensitivity studies (Subtask 5.3).
- Developed poroelastic models for injections during the field deployment on January 2022 and improved these models by considering the propped and unpropped fracture zones. Q8BP2
- Tuned the poroelastic solutions by minimizing the discrepancy between the injection-well BHP from the field data and simulations, leading to enhanced permeability values for the hydraulic fracture zone. Q8BP2

7.4 Joint VSP/Seismic and EM Inversion

- Did not proceed with the joint inversion of the VSP/seismic and EM fields, having shown the shortcoming of a seismic survey to detect the fracture changes using our numerical models.

Section 2: Accomplishments

A. Major Goals

This three-year and three-month research project aimed to assess the feasibility of a contrast agent–assisted geophysical approach to remotely monitor pressure, flow, or salinity changes in a preexisting hydraulic fracture. Keys to achieving this global objective include the following:

(1) unique access to ongoing Advanced Energy Consortium (AEC) studies of the DFPS which hosts an established and well-characterized hydraulically fractured anomaly propped with Electrically Active Proppants (EAPs); and
(2) access to laboratory studies showing the intrinsic responses of an EAP pack to pressure and salinity changes and fluid invasion.

Previous TRL 4 and 5 studies by our team at the DFPS (Denison et al., 2015; LaBrecque et al., 2016; Ahmadian et al., 2018, 2019) have led to the characterization of the identified fracture anomaly at the DFPS. Using these works, we updated forward and inversion models for the latest EM surveys. We used material properties based on the proposed laboratory studies to characterize the impact of salinity, pressure, and flow rate on the EAP EM properties and the DFPS rock properties as inputs for these solvers to discern the feasibility of detection and design of an optimal DFPS configuration for successful surveys. In BP1, the detection sensitivity of these surveys was demonstrated (BP1 decision point), and field survey work was initiated with freshwater injections. During the Q6BP2, while performing the final CSEM survey, we conducted ten injection cycles of freshwater and saltwater slugs using the central injection well at the DFPS. In addition, we monitored fluid invasion and pressure using five previously screened monitoring wells. Our final interpretation of the collected data is presented in Subtask 6.5. Following this field data interpretation, we analyzed the tiltmeter survey data and confirmed our initial estimates of the fracture dilation area. Also, we attempted to reduce the misfit of our EM simulations compared with the Devine measurements by including the average SP from an analytical solution in the misfit calculations. This latest numerical study confirmed the large contribution of the SP in the initial model misfit, inferring the importance of developing a coupled EM-SP model in the next phases of this study.

1 Project Management and Planning

1.1 Project Coordination and Communication

- See foregoing summary in Section 1.

1.2 Coordination of Pilot Test Activities

- See foregoing summary in Section 1.

1.3 Reporting

- See foregoing summary in Section 1.

2 Workforce Readiness for Technology Deployment

See foregoing summary in Section 1.

3 EM Response of Laboratory Fracture Models and Incorporation of Mixing Rules

3.1 Electrical Measurements in the Laboratory

The primary objective in this subtask was to characterize laboratory-based fracture models that simulate some of the anticipated experiments that we planned to conduct at the UT's Devine Field Pilot Site (DFPS). For this purpose, we designed and constructed a variety of impedance probes, two of which are described in this report. These probes were devised to characterize selected materials and fracture models via impedance spectroscopy. We aimed to emulate the geometry of the DFPS formation and fracture configuration in these probes as much as possible, allowing to vary lithostatic and hydrostatic pressure, flow of liquids through the cell, and exposure to saline liquids that either are injected or saturate the granular material. Varying these parameters in a wide range would allow to quantify composite or system parameters.

The laboratory experiments improved our understanding of the EM response of fractures, determined the effect of pressure and salinity changes on the impedance response under control settings, and developed mixing rules. The resulting data were used as input for Duke's EM forward modeling efforts (Subtasks 5.2, 7.1), to determine the EAP signal detectability, and to serve a decision for the project transition from BP1 into BP2 because of the following outcomes:

(1) verification that 10s of psi change in pressure and/or 1000s of Total-Dissolved-Solid (TDS) change in salinity of the miniaturized fractures containing EAP in the laboratory can yield 1-5% change in electrical conductivity of a 100% EAP pack; and
(2) verification by EM forward modeling that a 1-5% change in electrical conductivity of a propped fracture leads to at least 1% change in SNR in Electrical-Resistive-Tomography (ERT) measurement under the DFPS conditions and configuration (Subtask 5.2).

Our laboratory studies for electrical measurements can be itemized as follows:

(1) characterization of fracture models and materials using four-electrode impedance cells;
(2) measurement of material constants;
(3) investigation of EAP pack conductivity dependence on lithostatic and hydrostatic pressure changes;
(4) investigation of mixed EAP-and-sand pack conductivity dependence on salinity using fracture models;
(5) investigation of salinity effect in combined EAP-and-clay fracture models; and
(6) measurement of SP in sand and EAP columns.

Laboratory experiments captured the intrinsic dependences of pressure and salinity of the conductivity of composite systems. An EAP pack compacted at a lithostatic pressure of 150 psi displayed a high conductivity of approximately 700 S/m. The same pack subjected to moderate hydrostatic pressure showed the conductivity reduction by 10 to 20 %. However, when the hydrostatic pressure overcame the lithostatic pressure and the granular column expanded, equivalent to the reopening of the fracture at the DFPS, the pack conductivity decreased dramatically. Despite the high dependence of the EAP-pack conductivity on pressure, the conductivity of water-saturated clay that was collected from the fracture depth at the DFPS showed negligible pressure dependence. EAP-and-sand fracture models showed an obvious rise in conductivity when saltwater was injected into these samples. EAP-and-clay fracture models under lithostatic pressure showed no change in conductivity during the flow of saline solutions of various salinity through the EAP-filled fracture. Nevertheless, scaling of these findings to formation size is yet an open question – most likely the volume fraction of the EAP layer is the appropriate scaling parameter.

EAP-sand and EAP-clay mixture experiments underline the importance of a multiphysics approach in this project. At the DFPS, the injected liquids flow slowly through the fracture zone conceivably providing sufficient time for the liquid to invade the clay-rich layer adjacent to the EAP layer. Hydrogeological models would be able to specify the fraction of the injected liquids that imbibe into the low-permeability clay and provide, leading to an estimate of the composite conductivity changes of the EAP-filled fracture and clay layers.

Laboratory tests of new hypotheses that evolve during the analysis of measurements in the formation scale can be conducted quickly and provide essential insight on how to go forward. Among these hypotheses, we evaluated the possibility of explaining the results of the Devine field experiments using the Streaming Potential (SP) in a laboratory setting, as discussed at the end of this subtask.

Four-electrode impedance cells for characterizing fracture models and materials

To accomplish the goals outlined above, we designed and built several cells that enable EM characterization of materials and fracture models using 4-electrode impedance spectroscopy. The cells can be pressurized simulating overburden or lithostatic pressure and hold liquids as well as granular material saturated with liquids. Flow ports are incorporated enabling flow through the cell as well as injection ports where hydrostatic pressure can be applied by injecting liquids. The goal is to mimic the geometry of the Devine field experiment where the fracture is subject to overburden pressure of approximately 150 psi and liquids are horizontally injected into the fracture. Here, two representative cells that were extensively used in the laboratory tests are shown.

Multi-electrode cell

We designed and built a multi-electrode probe for studying the effect of injecting saline solutions containing various amounts of TDS into a laboratory-designed fracture. The impedance cell is designed to hold 10-voltage and 2-current electrodes that can be combined in multiple configurations to test a variety of detection volumes. The intent is to achieve a resemblance of the ERT matrix of electrodes that was previously used at the DFPS field study. As designed, the fracture was located at the geometric center of the cell. Two centrally located injection ports were added to accommodate saline injections into the fracture. Overburden pressure can be applied through a screw mechanism. Figure 3-1 shows a photo of the assembled cell filled with sand and a schematic of the cell design. Table 3-1 summarizes the cell properties.

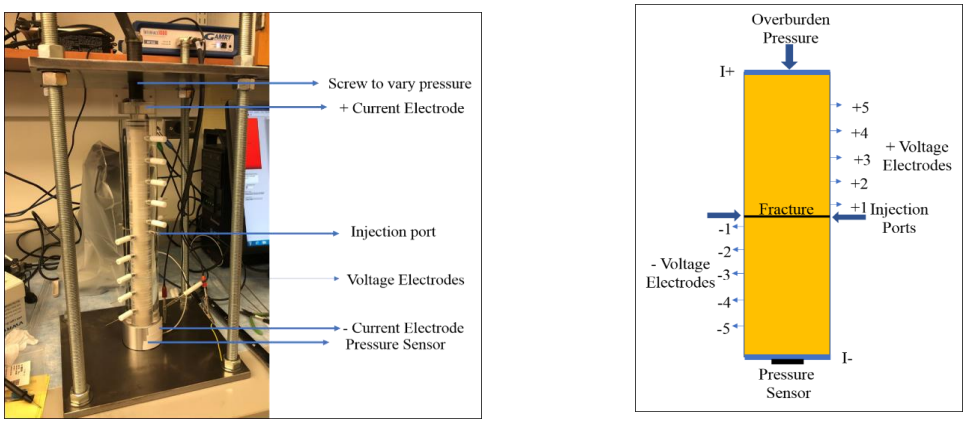

Figure 3-1: Image and schematic of assembled multi-electrode cell filled with sand.

Four-electrode measurements using specific electrode configurations were designated by electrode numbers as given in Figure 3-1 and Table 3-1. Most experiments employed centrally symmetric electrode pairings: (+1,−1); (+5,−5), but sequentially located electrodes, for instance, (−5,−4) and (−4,−3) could also be used.

Experiments showed that pressure applied at the top of this cell would not propagate through the length of the cell (silo effect). When application of pressure was required only the center part of the probe with electrodes (+1,-1) was utilized with pressure applied using steel rods.

Table 3-1: Geometric properties of multi-cell impedance cell.

Electrode Configuration	Electrode Separation (inches)	Electrode Separation (cm)	Detection Volume (cm^3)	Detection Volume (Pore) (cm^3)
(+1,−1)	0.75	1.905	9.6528	3.8611
(+2,−2)	3.75	9.525	48.264	19.306
(+3,−3)	6.75	17.145	86.875	34.75
(+4,−4)	9.75	24.765	125.49	50.194
(+5,−5)	12.75	32.385	164.1	65.639
(−5,−4); (−4,−5); (−3,−2); (−2,−1); (+1,+2); (+2,+3); (+3,+4); (+4,+5)	1.5	3.81	19.306	7.722

This probe was used in most experiments involving fluid flow provided by a peristaltic pump (Figure 3-2).

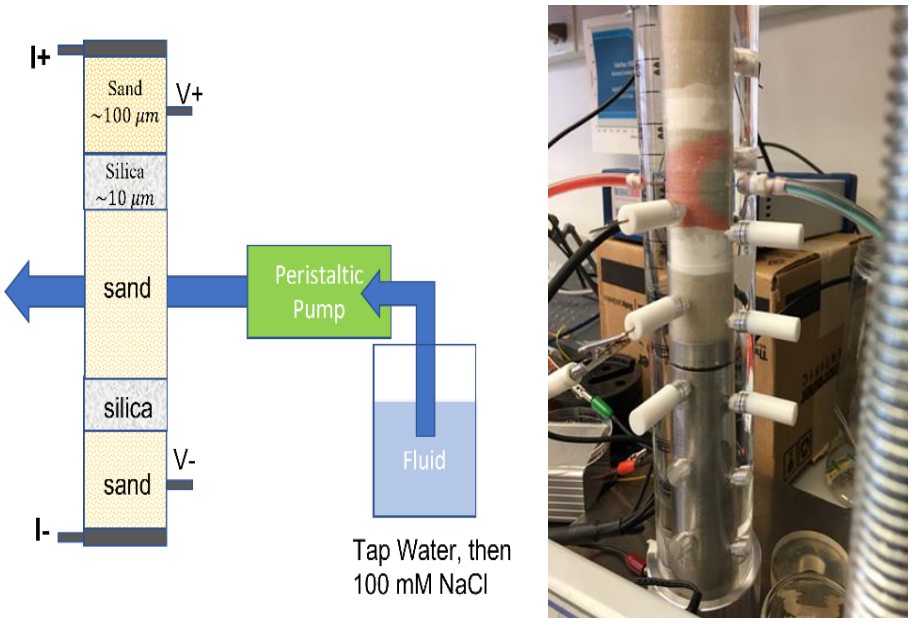

Figure 3-2: Cell with liquid flow through center of probe (in this case, colored liquid was injected to visualize how the plume spreads once liquid enters the probe). Entrance and exit ports are on opposite sides of the probe.

High-pressure probe

Applying high pressures required a leak-proof probe of short height (Figure 3-3). This probe was built in two versions, with and without sideway injection ports and was used widely in this work.

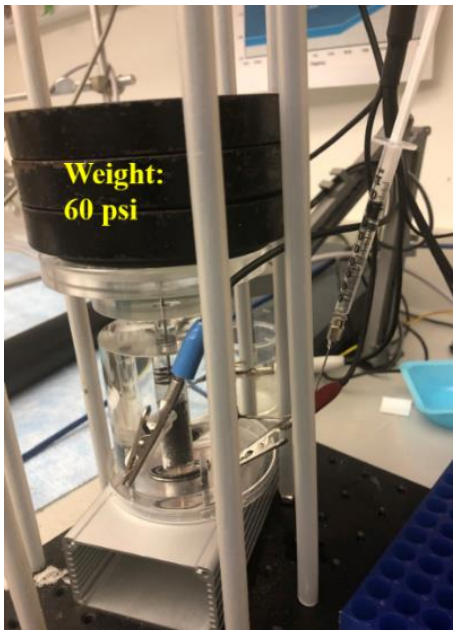

Figure 3-3: High pressure probe.

Measurement of material constants

Material properties change when the parameters under which they are characterized are altered. We determined conductivity and relative permittivity for various materials that were intended as input parameters for EM models. These parameters depend on pressure, temperature, brine saturation, and ionic content among other parameters. Here, we discuss conductivity values for an EAP pack under pressure and conductivity and dielectric constant for clay taken from the DFPS at 54-m depth adjacent to the Devine fracture layer.

We also characterized fracture models by surrounding EAPs with sand or clay. Notably, the conductivity values for such setups represent the whole system: EAP, surrounding material, pressure, brine saturation, and fluid flow. All these parameters contribute to one value of the composite conductivity with the volume percentage of the EAP being a major factor for upscaling the results.

Conductivity of EAP pack as function of pressure

The conductivity of EAP depends strongly on pressure. Using the high-pressure probe, a column of EAP saturated with water was sequentially pressurized up to 200 psi (Figure 3-4).

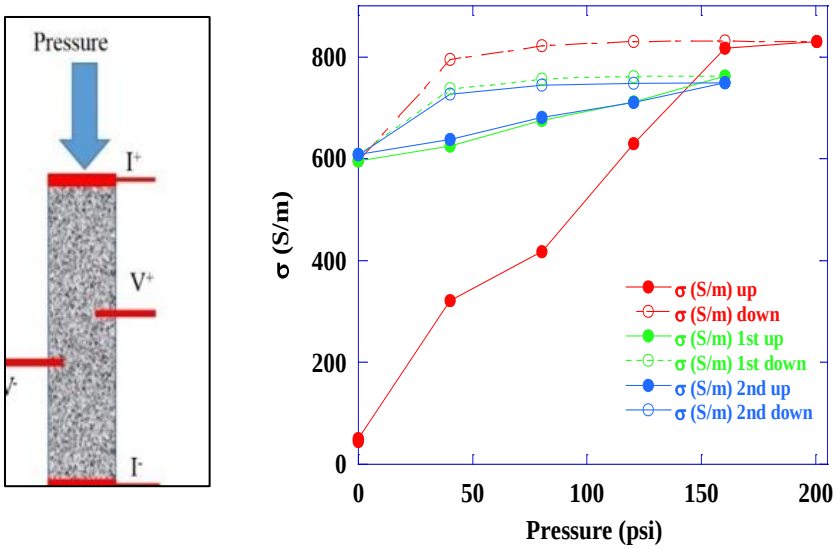

Figure 3-4: (left) Schematic of experiment: a column of EAP saturated with water is incrementally pressurized (the pressure was applied to the top current electrode). (right) Conductivity as a function of applied overburden pressure.

The conductivity of EAP as a function of overburden pressure is shown in Figure 3-4. The conductivity increases with pressure due to a decreasing contact resistance: granules are pressed more tightly together at higher pressures. At an applied pressure of 150 psi (estimated overburden pressure at Devine) the conductivity value is approximately 700 S/m. Because of the high conductivity, the permittivity is negligible. The observed hysteresis is because of the fact that granules being tightly pressed together at high pressure remain stuck to each other and require time to disengage when the pressure is released.

Conductivity and permittivity of Devine clay as function of salinity and pressure

The conductivity of clay depends linearly on the ion content (or total TDS) with a value of 0.11 S/m at 2500 ppm NaCl. The conductivity of clay shows only a weak dependence on pressure changing only by 0.05 % when pressure is increased from zero to 150 psi. The relative permittivity of clay shows little dependence on pressure and salinity with the observed variation at low frequency due to packing issues. The frequency dependence of the relative permittivity is strong with values reaching 10^7 at 0.1 Hz. This value may be large enough to influence the model outcomes at low frequencies.

The measurements were conducted using the high-pressure probe. Materials include Devine clay samples taken from 173-ft depth and mixtures with water extracted directly from the test site. Dielectric and conductivity measurements of homogeneous Devine clay and water mixtures were carried out as a function of pressure and salinity changes. Measurement conditions were guided by the expected Devine test parameters. Results provide some sense of what to expect when the Devine testing was carried out. The experimental datasets could be compared with field test results, and elements of these measurements were incorporated into the EM modeling efforts.

We measured the properties of clay as a packed dry powder and as a packed powder wetted with water. The water salinity varied from approximately 100 ppm (tap water) to 2500 ppm (mostly composed of NaCl). The salinity of the DFPS water used in these measurements was approximately 595 ppm. The applied pressure varied from 0 to 150 psi which is close to the overburden pressure at the fracture depth. The experimental setup is shown in Figure 3-5. We considered a homogeneous

clay-water mixture allowing us to apply a straightforward equivalent circuit model to determine the electrical properties of the clay-and-water mixture.

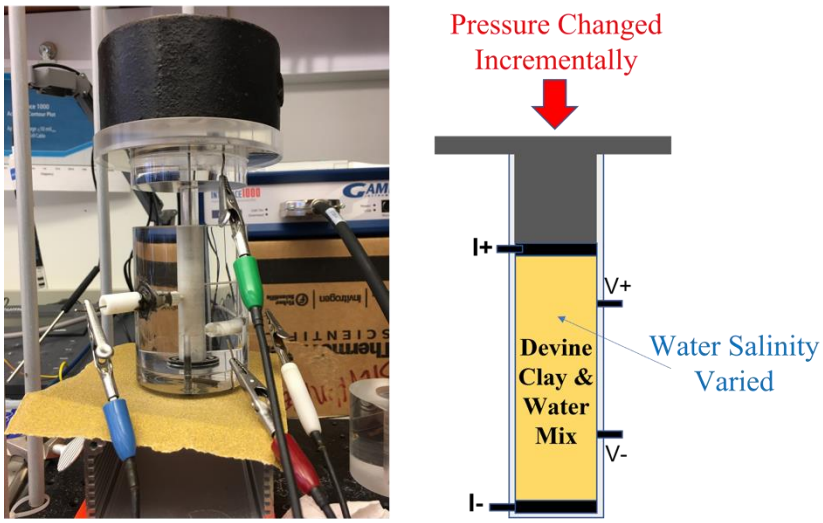

Figure 3-5: Experimental setup for 4-electrode impedance measurements made as a function of pressure and salinity. (left) The measurement apparatus. The measured system is a homogeneous mixture of Devine clay and water. The clay is densely packed, and water occupies the intergranular space. Pressure was applied by stacking 2-kg mass plates on top of the electrode plunger, which rested on the clay and moved freely. For measurements where the salinity is varied, a constant 150 psi was applied, equivalent to the estimated overburden pressure at the fracture depth at Devine. (right) Schematic diagram of the 4-electrode measurement system. Current was applied through electrodes at either of the sample ends. Voltage measurements were made at the electrodes placed within the sample space. The top current electrode moved with the plunger applying pressure to the clay column.

The clay-and-water system is essentially composed of a connected resistive fluid and a dense jammed system of charged clay grains. We modeled such a system as a resistor and a capacitor, arranged in parallel. The conductivity, σ, and dielectric constant, ϵ', of the system can be computed as

$$\sigma = \frac{R}{R^2+X^2}\frac{d}{A}, \tag{3-1}$$

$$\epsilon' = \frac{-X}{R^2+X^2}\frac{d}{A}\frac{1}{\varepsilon_0\omega}, \tag{3-2}$$

where R and X are the measured real and imaginary impedance, d is the voltage electrode separation, A is the cross-section of the sample, ε_0 is the permittivity constant, and ω is the angular frequency.

Effect of lithostatic and hydrostatic pressure changes on EAP pack conductivity

The interplay of lithostatic and hydrostatic pressure variation causes interesting and observable changes in the conductivity of an EAP column. When hydrostatic pressure is introduced at constant overburden pressure, the conductivity decreases slightly but rebounds when the pressure is released. When the applied fluid pressure exceeds the overburden pressure, and the injected fluid lifts the plunger, the conductivity decreases dramatically. When the fluid is withdrawn, the system conductivity is restored to values obtained prior to the initiated changes. The observed conductivity changes as functions of applied water pressure are explained based on further experimental results.

An experimental setup was designed to simulate the field experiment at the DFPS and provided insight to determine the mechanisms that affect the impedance changes during high-pressure injections into the Devine fracture. The experiment utilized the high-pressure probe design with the side-way injection port (Figure 3-6).

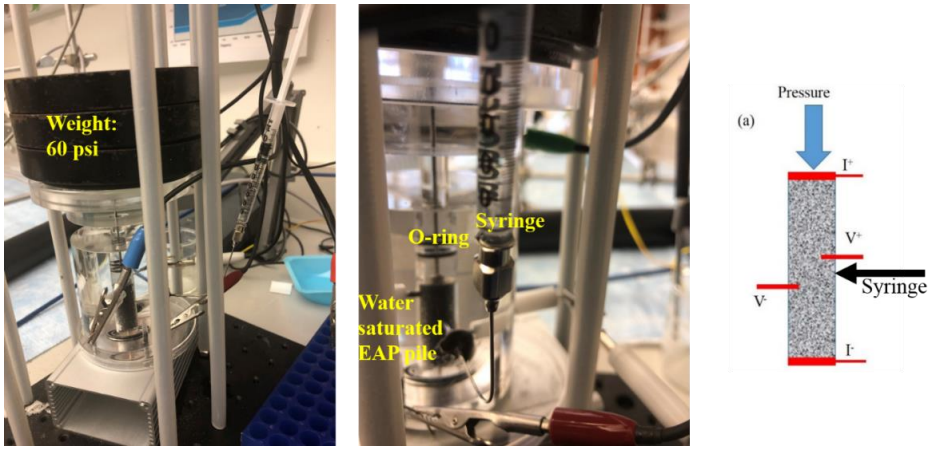

Figure 3-6: (left) Cell used in experiments simulating the Devine geometry: lithostatic pressure of 60 psi is applied by weights stacked on top of the pressure cell. Water is injected at high pressure from the side through a syringe. (right) A schematic diagram of the sample, injection port, and the voltage electrodes. The syringe injection port is located midway between the two voltage electrodes. The impedance measurement employs a four-electrode configuration.

This cell permitted the simultaneous application of lithostatic pressure from above and pore pressure control from the circumferential area (perpendicular to the lithostatic pressure). Weights were placed on top of the cell, simulating large lithostatic pressures up to 60 psi. Water was injected from the side using a syringe, representing the water injection at Devine. Besides the images of the cell, Figure 3-6 schematically shows the location of the voltage electrodes with respect to the sample and injection port.

The external pressures were applied to a water-saturated EAP column. Care was taken to avoid air being incorporated into the column. To reduce friction, a single lubricated O-ring was employed to seal the piston gliding down the shaft onto the EAP column and to ensure that hydrostatic pressure can be applied. All potential leak spots were O-ring sealed or secured using glue.

The experiment employed a 10-Hz waveform to measure impedance and recorded impedance values every 6 s. Thus, changes in impedance could be monitored in-situ, just as they were conducted at the DFPS. The impedance recorded as a function of time is shown in Figure 3-7 through Figure 3-9. Figure 3-7 gives an overview of the executed experimental changes as a function of time, Figure 3-8 shows detailed changes in pressure, and Figure 3-9 plots the percent changes in conductivity induced by various changes in pressure.

Figure 3-7 shows that the overall experiment was divided into four separate phases in which the applied pressure was implemented differently. This figure is duplicated in Figure 3-8 to show more details about pressure changes.

(1) The pressure applied to the EAP column was increased in 3 steps of 20 psi, resulting in an ultimate overall lithostatic pressure of 60 psi. This pressure change caused an increase in conductivity (Figure 3-8, Phase 1).
(2) Water was injected at low pressure using the syringe, filling voids within the cell and within the column. The injected water also would separate granules and increase the porosity of the EAP column. This pressure change caused a reduction in conductivity (Figure 3-8, Phase 2).
(3) Greater pressure was applied, which would create large voids within the column, generating a further decrease in conductivity. When the pressure was released, water flowed back into the syringe. This backflow would reduce contact resistance, leading to an increase in conductivity. The observed relaxation in conductivity was not instantaneous but showed a slight time dependence (Figure 3-8, Phase 3)

When even greater pressure was applied, the O-ring-sealed piston slided up and a volume of water developed above the EAP column. The conductivity dropped precipitously to approximately 1 S/m. When the pressure was suddenly released, the conductivity rebounded to a higher value than was recorded before the increase in hydrostatic pressure: the upper electrode slammed into the EAP column, compacting granules tighter together than they were before the last pressure increase (Figure 3-8, Phase 4).

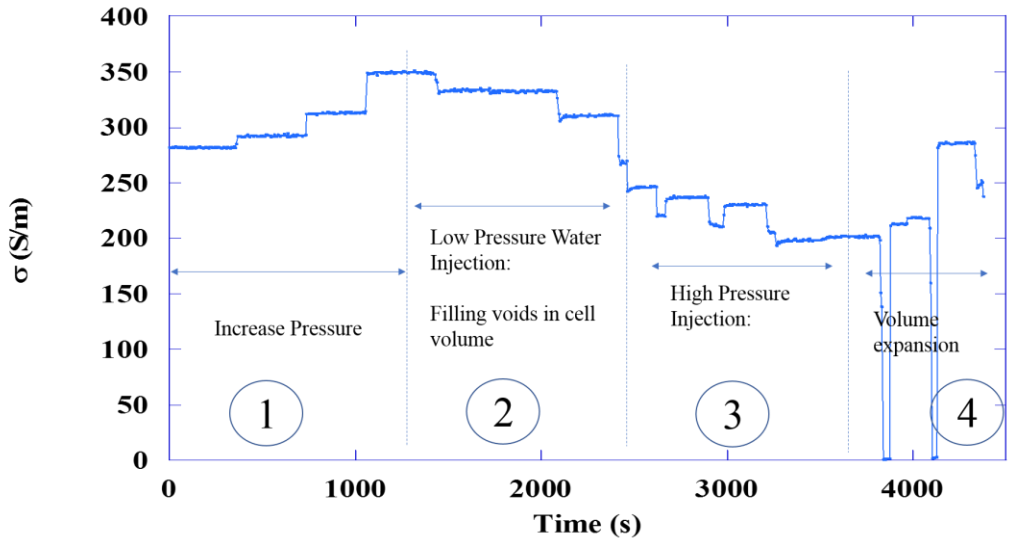

Figure 3-7: Conductivity record as a function of time. Lithostatic and hydrostatic drained-hydraulic pressures were applied to the EAP column in four different ways as described in the text. Circled numbers between dotted vertical lines indicate the experimental phases.

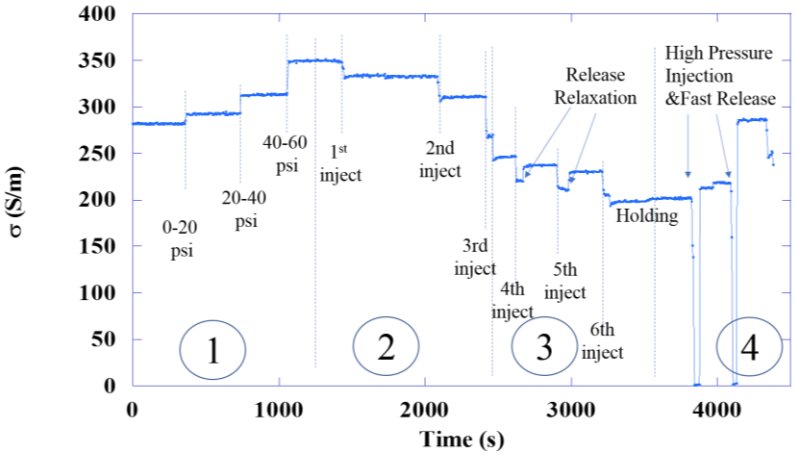

Figure 3-8: Figure 3-7 with further details about pressure changes during the experiment. Circled numbers between dotted vertical lines indicate the experiment phases.

Figure 3-9 details the percent changes in conductivity caused by the change in applied pressure. The percent values were computed with respect to the conductivity recorded before any pressure perturbation. For instance, for the pressure change from 20 psi to 40 psi, the two plateau values are: 293 S/m at 20 psi and 313.5 S/m at 40 psi. The percent change, %*change*, is computed as follows:

$$\%change_{20\rightarrow 40\ \mathrm{psi}} = \frac{\Delta\sigma}{\sigma_{20\ \mathrm{psi}}} * 100 = \frac{20.5}{293} * 100 = 7\%.$$

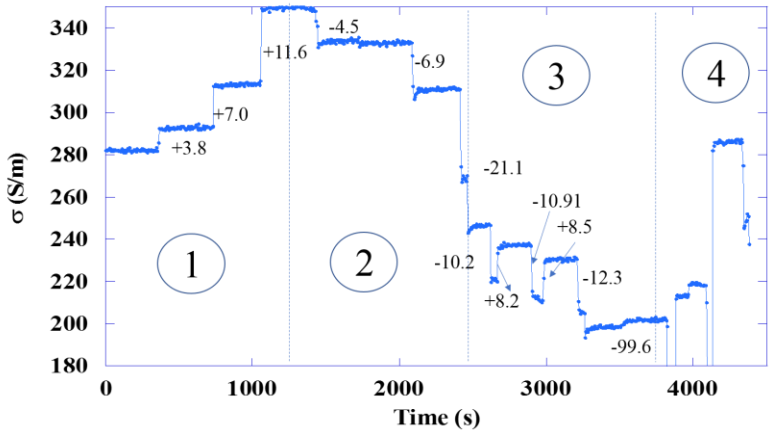

Figure 3-9: Percent changes in conductivity induced by changes in lithostatic and drained-hydraulic pressure. Circled numbers between dotted vertical lines indicate experiment phases.

All percent changes in conductivity induced by stepwise increases in pressure (Figure 3-9) exceeded the go-no-go criteria in the grant proposal. In addition, in the case of high drained-hydraulic pressure that allows a volume of water to form in and above the EAP column, the observed changes in conductivity were as large as 99 percent (Figure 3-9, Phase 4).

The experimental results were interpreted in the context of experiments that investigated the impedance response of an EAP column subject to lithostatic or hydrostatic pressure. In these experiments, the pressure was applied directly to a column of water-soaked EAP (lithostatic pressure) or to the same column with an additional volume of water added above the EAP granules

(pore pressure). The applied pressure did not cause any discernable movement or dislocation of the cell piston. The results are summarized in Figure 3-10.

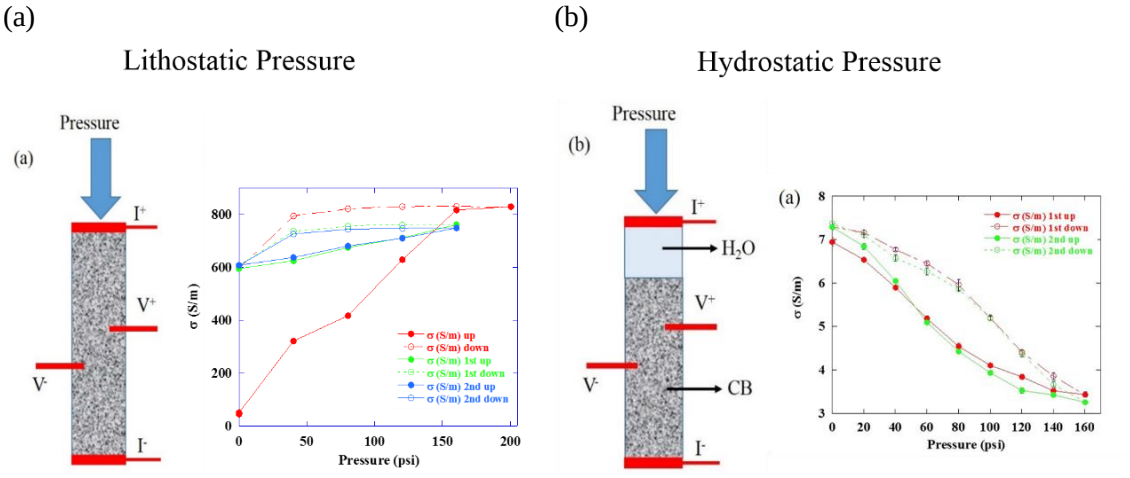

Figure 3-10: Conductivity changes induced in a water-soaked EAP column under (a) lithostatic pressure; (b) hydraulically induced pore pressure.

As seen in Figure 3-10a, increasing lithostatic pressure gives rise to increasing conductivity—the contact resistance between the granular particles that form the EAP column decreases with increasing lithostatic pressure, causing the overall conductance of the column to increase.

In contrast, the pore-pressure increase due to the piston load overlying a layer of water above the EAP column reduces the column conductivity (Figure 3-10b). In other words, increasing pore pressure increases the contact resistance as this change increases porosity within the granular pack and reduces the grain-to-grain contact areas. Note that the conductivity of the water-soaked EAP column is 7 S/m at 0 psi indicating that the conductivity is due to connection of the proppants, not their compaction or the fluid conductivity.

The interpretation of the data shown in Figure 3-10b is supported by an experiment where the EAP column was replaced with sand. Figure 3-10c shows that the conductivity of a sand column under hydrostatic pressure increases with increasing pressure – the opposite trend as observed in an EAP column under the same circumstances. Just as in case of the EAP column, the increased pressure slightly increases the intergranular distance. However, in case of sand where the solution conductivity determines the system conductivity, the slight increase in the amount of solution within the detection volume increases the recorded conductivity.

Based on the temporal evolution shown in Figure 3-7 through Figure 3-9, switching between lithostatic and hydraulic pressures and increasing the applied pressure leads to inclining or declining changes in conductivity, as summarized by the experimental results shown in Figure 3-11. In that case, no hysteresis was observed and expected.

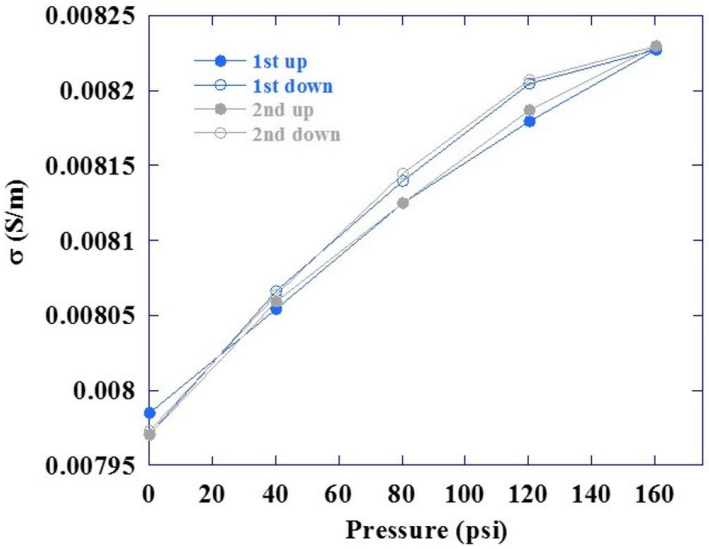

Figure 3-11: A sand column under hydrostatic pressure shows increasing conductivity as a function of applied pressure. A schematic of the experiment setup is shown in Figure 3-10b.

A summary of the important findings is listed as follows:

(1) Increasing lithostatic pressure causes increased conductivity within the EAP column because contact resistance between granules decreases.
(2) Slightly increasing the hydraulic, pore pressure causes voids within the cell and column to be filled and slightly reduces contact resistance.
(3) Higher hydrostatic pressure pushes granules apart, concomitantly decreasing conductivity. When the pressure is released, the water flows back into the syringe and the conductivity returns to a higher value.
(4) Application of very large hydraulic pressure overcomes the lithostatic pressure and separates the EAP filled column from the overlying piston. When the pressure is released, the water rushes back into the syringe and the piston compacts the EAP column, reinstating electrical contact and leading to a jump in conductivity from approximately 1 S/m to 220 S/m.

We expected that the conductivity response of the Devine fracture when subjected to water injection would be similar to that observed in our experiments.

Relative change in conductivity is large when either lithostatic or hydraulic pressure is applied to the EAP pack; Figure 3-9 shows that relative change in conductivity could be as much as ~200% to ~20,000%.

Either case passed the go-no-go criteria for BP1 of 5% change by a significant margin.

Measurement of streaming potentials in sand and EAP columns

Measurement of the SP in sand and EAP columns indicate that the streaming potential can be viable source for an additional electric field in the DFPS experiment and may explain the discrepancies between EM measurements and simulations. The laboratory experiments show that changes in flow cause nearly instantaneous changes in potential across the detection volume for sand columns while the response is more gradual for EAP columns.

The analysis of the recorded electric field data at the DFPS as a function of fluid flow and the electric field data simulated by EM models showed that the model data were too low by approximately a factor of 2. It was hypothesized that a SP induced by the flow of the injected liquids through the granular proppant layer could account for the missing electric field strength.

In the SP theory, large spatiotemporal fluid pressure changes and fluid injections into a medium can induce detectable electric currents (De Groot and Tolhoek, 1951; Fitterman, 1979; Sill, 1983; Ishido et al., 1983). Assuming no active transmission source of electric current, the SP, ϕ, can be formulated through conservation of the volumetric current density (Sheffer and Oldenburg, 2007), leading to a Poisson's equation as Equation (3-3):

$$\nabla.\sigma\nabla\ \phi = -\nabla.L\nabla h, \tag{3-3}$$

where σ denotes the electrical conductivity, L is cross-coupling coefficient, and ∇h is the gradient of the hydraulic head. ∇h can be obtained by solving the diffusivity Equation (3-4):

$$\nabla.K\nabla h = S_s\frac{\partial h}{\partial t} - Q_h, \tag{3-4}$$

where K denotes the formation permeability, S_s represents specific storage, and Q_h is the injection rate. The temporal flow-rate profile is the input to Equation (3-4), and ∇h is retrieved from this equation to be used in Equation (3-3) to calculate the SP.

We conducted preliminary SP measurements in the laboratory using gravity-induced water flow through EAP and sand packs to further evaluate the SP as a mechanism that may have led to the electric potential-difference changes during injection at the DFPS (Figure 3-12). Flow rates were controlled by maintaining the hydraulic head above the grain pack and estimated as 0.13 mL/s throughout the flow interval. These experiments were carried out using water with a conductivity of 0.00017 S/m, and sand and EAP packs stacked in the same column. The electrodes were recessed, and therefore, there was no EAP contact with electrodes and moto-electric effects were eliminated.

An immediate SP response was recorded with a single-step flow-rate change. We observe similar maximum SP magnitudes in both sand and EAP; however, the sand interval reached a steady potential-difference value almost immediately while the EAP interval took about 30 minutes to reach the steady state. When the flow ceased, the sand pack returned to its original potential difference again almost immediately, and the EAP pack took a much longer time (about 1.5 hours) to return to the pre-injection state.

The laboratory measurements showed that the steady flow of liquids through an EAP layer at a very modest flow rate led to observable SP. Further experiments and models are needed to clarify if spatially varying flow rates, as encountered at the DFPS, would lead to the desired electric field distribution that may bring EM measurements and models into agreement.

(a)

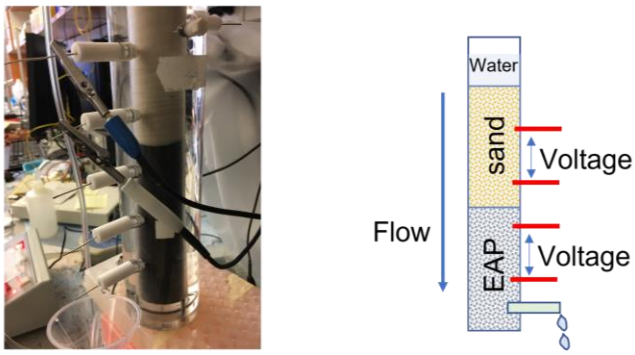

(b)

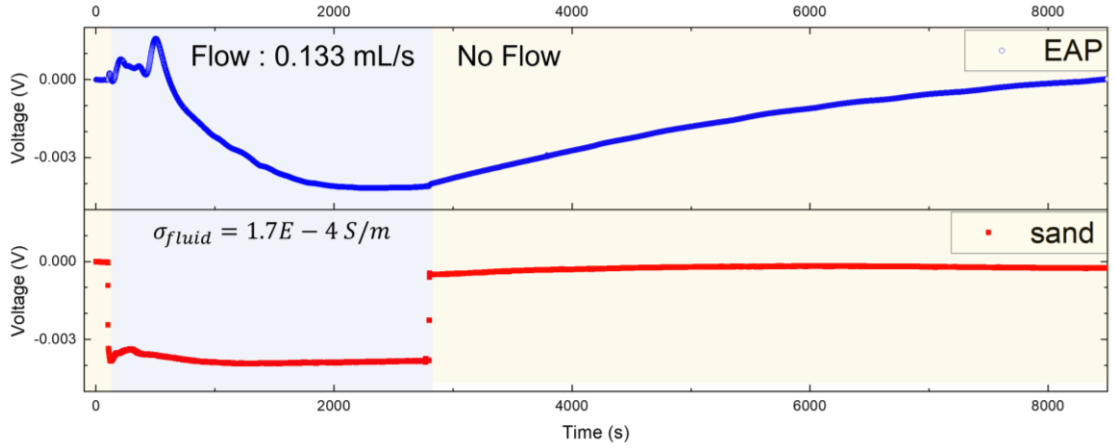

Figure 3-12: (a) Image of the experimental setup and a schematic diagram, in the absence of a transmitter, to measure the SP. (b) Temporal change of the recorded voltage along EAP and sand granular material intervals, induced by the fluid flow at rates between 0.13 and 0 ml/s.

Summary and discussion of experimental results

(1) The conductivity of the EAP increases with increasing lithostatic pressure (Figure 3-4 , Figure 3-10a). At an overburden pressure of 150 psi, conductivity of approximately 700 S/m was obtained (700 psi in Figure 3-4). When the hydrostatic pressure was slightly increased at constant lithostatic pressure, the conductivity decreased by 5 to 20% as shown in Figure 3-10b. When the hydrostatic pressure overcame the lithostatic pressure (corresponding to a fracture opening at Devine), the conductivity decreased dramatically by 99% (Figure 3-7 through Figure 3-9). Confirmation and explanation of the observed conductivity changes were provided by separate experiments using either lithostatic or hydrostatic pressure (Figure 3-10, Figure 3-11). The observed conductivity changes as function of the fluid injection pressure passed the go-no-go criteria for BP1 of 5% change by a significant margin.

(2) SP is a viable source for electric fields that might contribute to the measured fields at the DFPS. Even low steady-state fluid flow generates easily measurable potentials across the detection volume (Figure 3-12).

(3) UNC performed all tests that were proposed in the original proposal. In addition, UNC explored the possibility that SP could contribute to the electric fields recorded at the sensor location at the DFPS.

Comparing laboratory experiments with measurements at the DFPS need to be done carefully as the conditions under which results are obtained are very different. Regarding this, the following points are of critical importance.

(1) Laboratory models are under complete control of the experimenter and experiments can be checked, rechecked, and repeated. Initiated changes are controlled and lead in most cases to well defined outcomes.
(2) Excitation and detection volumes are well defined in laboratory models. Conversion from impedance values to conductivity and relative permittivity is straightforward.
(3) Material constants and even properties of mixed system can be determined in a laboratory setting.
(4) At Devine, the excitation volume and the detection volume are not well defined. Excitation by the dipolar electric field occurs far from the fracture zone and even the detection volume might be orders of magnitudes larger than the volume of the fracture. In the laboratory, the fracture is a dominant part of the detection volume, possibly over-accentuating its influence on a measurement. It would be hard to associate a volume percentage to the fracture if the detection volume is ill defined.
(5) Scaling results, especially combined conductivity and relative permittivity, to field dimensions is still uncertain.
(6) State of EAP consolidation is well defined in laboratory model: either unconsolidated, weakly connected, or well compacted.
(7) Even the state of the EAP layer at Devine is unknown and must be deduced from the electric field changes observed when fluid is injected at different pressures.

While laboratory measurements show repeatedly that the conductivity of a highly compressed EAP column at 150 psi is approximately 700 S/m, measurements at Devine produced a value of 60 S/m for the fracture layer. This discrepancy can only be explained if the proppant layer does not represent a fully connected and compressed unit.

In the laboratory setting, the interplay between lithostatic and hydrostatic pressure showed that liquid injections that do not overcome the overburden pressure lead to small, but noticeable decreases in EAP conductivity while injections that overcome the lithostatic pressure cause dramatic changes in conductivity. When the overburden pressure was overcome by the injected fluid at Devine, no dramatic changes in electric field values were observed by the sensors. As elaborated in Subtask 7.3, a geomechanical model of the pressure evolution at the fracture zone indeed showed that only a small fraction of the fracture opened when the overburden pressure was overcome. Laboratory experiments may produce ideal responses to initiated changes (here the complete opening of the fracture) while field experiments are constrained by forces not included in the laboratory setting leading to an only partially opened fracture.

The geomechanical model indeed predicts that while most of the liquid flows through the fracture layer with its large permeability, some of the injected liquid leaks into the clay. However, this model needs to be extended to the cases where the EAP pack is not completely connected.

Laboratory settings are ideal for quick tests of novel ideas arising from the analysis of field data. Here, the viability of the SP could be assessed quickly. The laboratory experiments confirm that SP should be included in the EM models as an independent source term for electric fields. The results displayed in Figure 3-12 show clearly that the cross-coupling constant L [Equation (3-3)] that links fluid and ionic flow depends on the material through which the fluid flows: identical fluid flow through sand and EAP packs shows SP of similar amplitude; however, decay and rise of SP display vastly different time constants when flow is changed. L also depends on permeability and

liquid saturation. Therefore, *L* must be determined in laboratory experiments as a function of these parameters which should match the characteristics of the formation strata.

The EM-based tomography of the fracture site uses dipolar electric fields that interrogate the site and monitor changes caused by external agents (i.e., fluid injection). It is unknown whether the active-source electric fields interact with the electric fields induced by the SP. This interaction needs to be studied in laboratory experiments. If this interaction is frequency dependent, it must be included in the computer model as well.

SP is a viable source of an electric field that could explain the discrepancy between observed fields and those generated by computer models. Moreover, understanding the interplay between active-source EM fields and the flow-generated SP field can lead to new and exciting applications in probing fluid flow. CO_2 flow in carbon sequestration applications is only one possible system in which SP measurements can be used to monitor flow.

3.2 Rock Characterization

To inform fluid flow modeling (Subtask 5.1) and verify the electrical and elastic property stratification at the DFPS (Subtasks 4.1, 4.2, 5.3), we conducted a detailed rock characterization of 249-ft (76-m) long core that was previously collected at the DFPS. The bed lithology and rock types in the DFPS area was identified by comparing DMW 3, DMW 1, and the Standard Oil No. 9 Wilson well (Figure 3-13 and Figure 3-14). For brevity, we refer to the Standard Oil No. 9 Wilson well as Wilson-9 well in the following. A detailed description of these cores was completed (Figure 3-15). Preliminary interpretation is that most of the cores are representative of tidal-flat, tidally influenced embayment, crevasse-splay and splay-channel in a deltaic setting. Appendix A.2 elaborates extensively on this rock characterization effort.

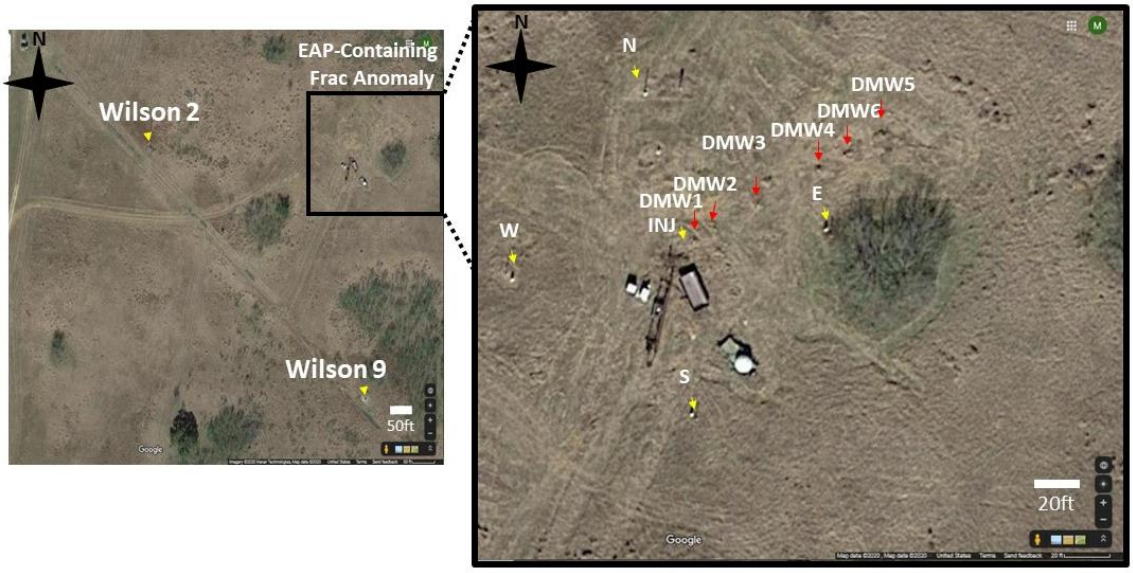

Figure 3-13: Existing DFPS layout and well positions are shown in these areal images. The injection well, (marked INJ) in the right panel is approximately 400 ft away from Wilson-9 well, which is shown on the left panel. DMWs 1, 2, 3, 4, 6, and 5 are 10, 20, 45, 75, 91, and 107 ft away from the injection well, respectively. The position of fracture anomaly containing EAP is shown in Figure 5-1. The observation wells that are marked with W, N, E, and S on the right panel are approximately 75 ft from the injection well.

Figure 3-14: Representative cores from the DFPS Wilson-9 well (left two panels) and DMW 3 (right panel) are shown. Based on the predominance of cyclic mudstone beds and mud-draped ripples, we interpret this zone as tidal-flat facies. The two cores on the left had been used for prior geomechanical studies during the design phase of hydraulic fracturing at the DFPS with EAPs. Due to similarity between Wilson-9 well and DMW 3, the porosity/permeability and velocity data from Wilson-9 well were used for various modeling studies that were conducted as part of this project. White arrow in the center panel shows the location from which core plugs were extracted for geomechanical studies. The black arrow on the right panel indicates the position of the EAP containing fracture at ~ 175 ft. Core tags are 1 by 2 inches across.

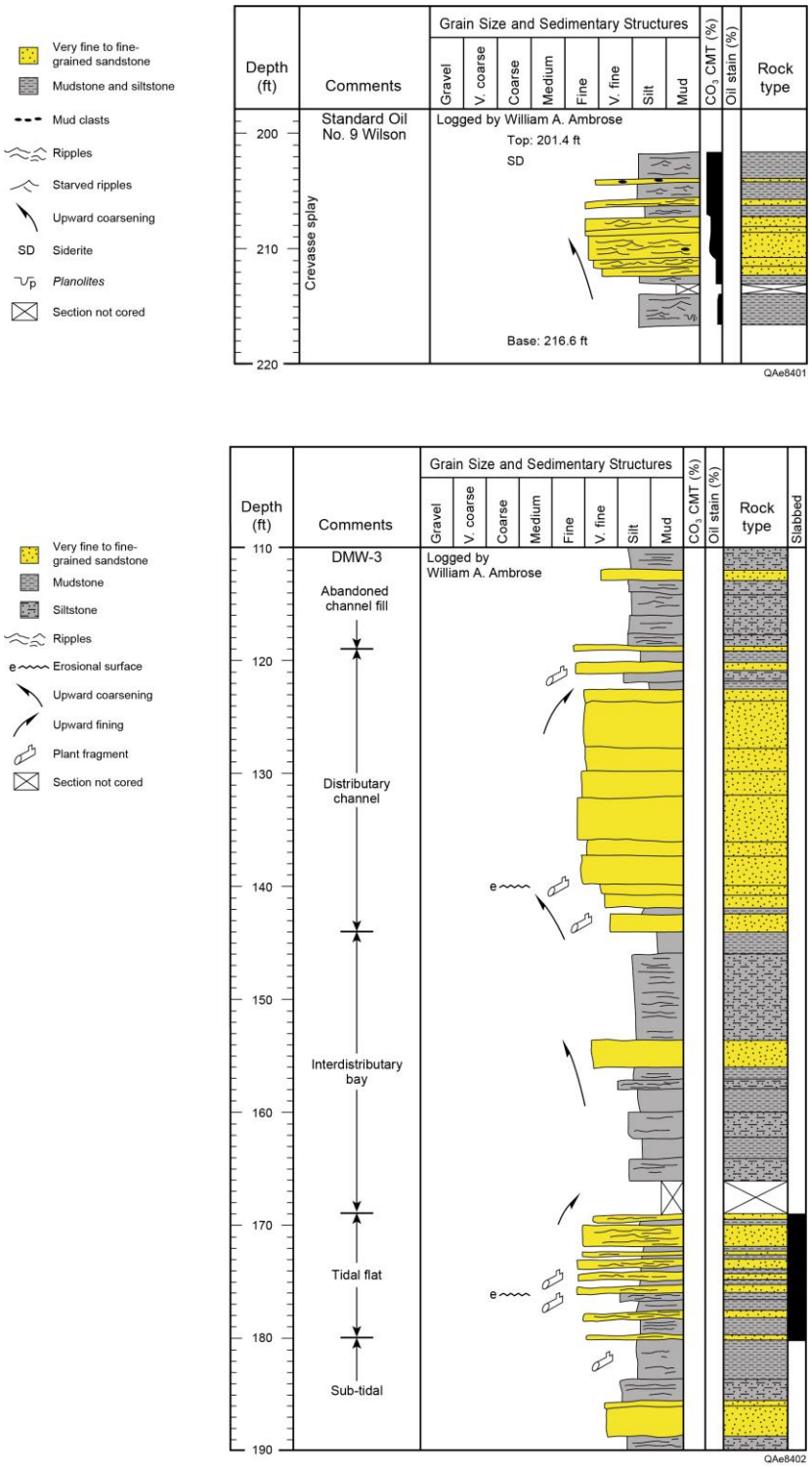

Figure 3-15: Description and interpretation of the Wilson-9 well from 200 to 220 ft (top) and DMW-3 core from 110 to 190 ft (bottom). Selected core photographs in the zone of interest are shown in Figure 3-14.

4 Code Optimization for Modeling

4.1 VSP/Seismic RTM Validation

Before running new tests at the DFPS, we validated a 3D Reverse Time Migration (RTM) imaging code based on synthetic data to detect fractures embedded in targeted geological layers. The RTM code is for elastic full-wave imaging based on the Finite-Difference Time-Domain (FDTD) method and was developed previously by Zeng and Liu (2001). The numerical experiments for this validation are designed to mimic the steps used for imaging after a real geophysical exploration is conducted. This work is elaborated in the following.

First, a ground truth model including velocity profiles based on a hypothetical four-layered earth scenario was constructed (Figure 4-1). Simulated "field" data were "measured" by a line of receivers and dipole sources at the ground surface. In our numerical experiment, this mock "field test" was completed by the forward simulations. The source time function was a Ricker wavelet with a central frequency of 200 Hz. There were 10 sources being excited sequentially, with the source locations given by x=20(n-1) m (n = 1, 2, …, 10) and y=0, z=-5 m. Thus, there are 10×48 = 480 recorded signals, which served as the measurement data for the next imaging step. As an example, Figure 4-2 shows the recorded signal at one of the receivers. The simulation time window for the wavefield is 400 ms.

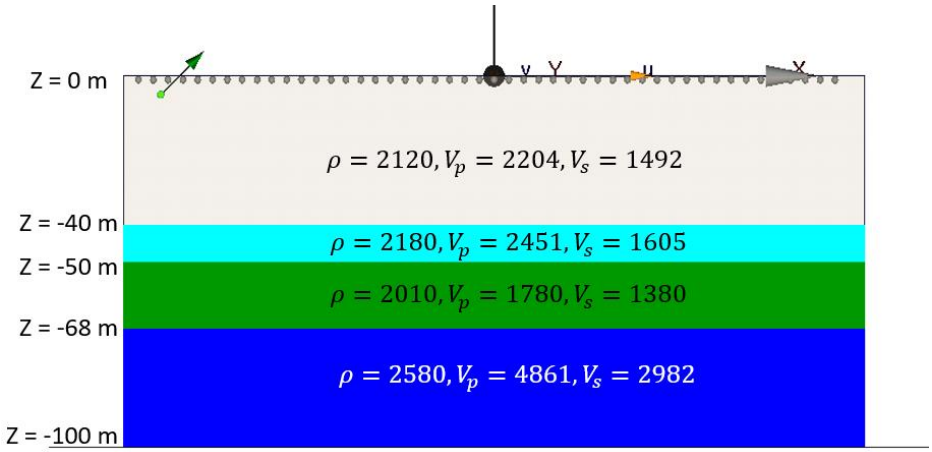

Figure 4-1: The ground truth model with four layers used for the forward simulation of a surface seismic experiment. For this simulation, 48 receivers were uniformly spaced on the ground. The source was a dipole indicated by the green arrow. Density, ρ, P-wave velocity, V_p, and S-wave velocity, V_s, are in kg/m^3, m/s, and m/s, respectively.

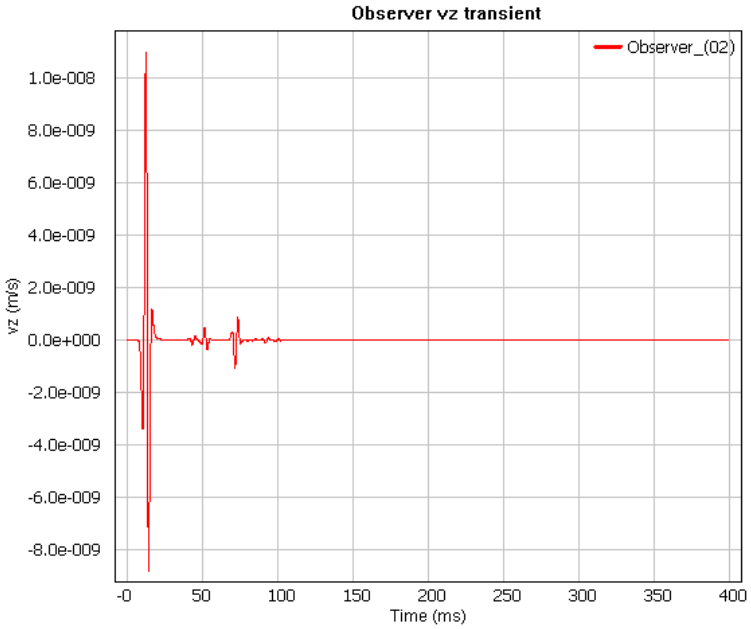

Figure 4-2: The signal recorded at the receiver (-92, 0, -1) m, when the source was at (-90, 0, -5) m. The direct wave and waves reflected at each interface can be identified.

The RTM imaging process began with an initial simple half-space model as a starting point (Figure 4-3). The signal traces obtained in this step were then compared to the experimental synthetic field data from the previous step to deduce which layer interfaces may be missing in this starting model. The recorded signals at the receivers were used as the source time functions of these virtual sources at the original receiver locations and excited backpropagation (i.e., time reversal). Next, the original Ricker wavelet was used as the source time function for the original sources and excited a forward propagation. Then, a cross-correlation of the "back propagation" and "forward propagation" signals in time was calculated at each location to obtain the final image. Figure 4-4 gives the imaging result, where the missing interfaces at z = -50 m and z = -68 m are revealed clearly. As a result of this basic exercise, we concluded that in our starting model (Figure 4-3), there should be two additional layer interfaces at those locations. Hence, the RTM approach is valid.

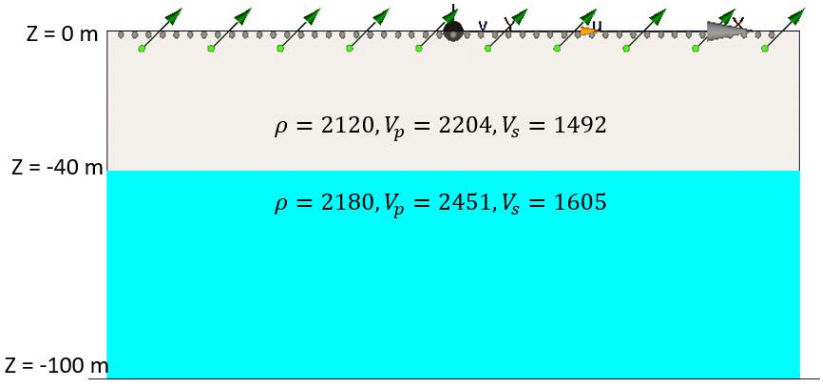

Figure 4-3: The starting model used as a basis for inversions during the RTM imaging. This model only contains the first layer interface of the ground truth and the lower 3 layers were combined in the second layer. The 48 receivers were the same as in Figure 4-1. The 10 dipole sources were existing at the same time, meaning they were stimulated at the same time.

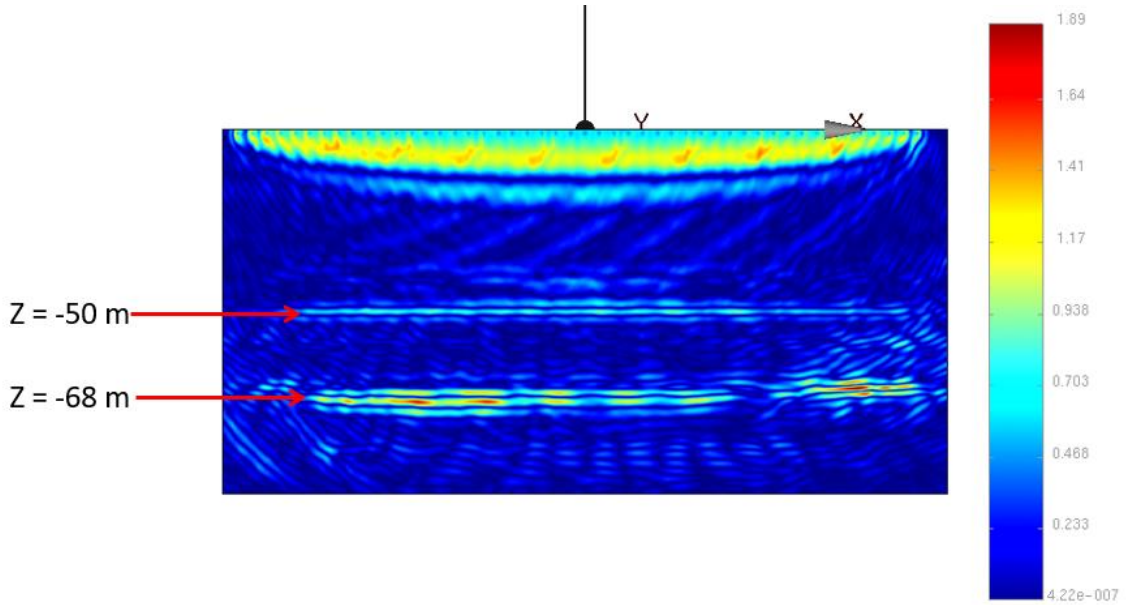

Figure 4-4: The final imaging result. The color bar shows relative energy and thus is unit-less. The large values indicate a scattering or reflective object. Because the layer interfaces at z = -50 m and z = -68 m do not exist in the starting model in Figure 4-3, they are revealed by the imaging process.

4.2 Code Optimization for Joint VSP/Seismic and Electromagnetic Inversion

We evaluated two approaches for EM inversion: 1.) based on Duke's conventional EM code that was previously validated at multiple scales; and 2.) based on Machine Learning (ML), aiming to speed up the inversion process significantly. The first method was adopted to obtain the fracture depth using 2017 experiment data (Ahmadian et al., 2018). The second method was targeted to optimize the fracture boundary defined by 16 control points (Zhang et al., 2022a). For this purpose, we analyzed the DFPS Time Domain Induced Polarization (TDIP) data collected in 2017. This analysis resulted in the boundary of the EAP-filled hydraulic fracture consistent with the outcomes of a primary EM study (Ahmadian et al., 2019). To ensure the accuracy of the DGFD models, we compared the 1D analytical model with the 3D DGFD case and the COMSOL results. The comparison suggested a good match between these solutions. Due to the limited SNR of a seismic survey to detect fracture dilation (as elaborated in Subtask 5.3), we did not conduct joint seismic-and-EM inversion. Although we did not conduct the joint inversion, we believe the developed machine-learning-based EM inversion methodology suggests good novelty to the EM modeling literature and, therefore, is discussed in the following. We evaluate this inversion methodology using synthetic data and apply the same inversion model to the 2020 field data in Subtask 7.1.

2017 experiment data interpretation and EM simulation

Two approaches for EM inversion have been developed in Professor Liu's laboratory at Duke University. One approach is based on Duke's conventional EM code, which we had developed and validated previously at multiple scales: the DFPS intermediate scale test and Clemson small scale studies, and various synthetic inversion studies at Duke (Denison, Murdoch et al., 2015; LaBrecque, Brigham et al., 2016; Fang, Dai et al., 2017; Fang, Hu et al., 2018; Hu, Fang et al., 2018; Fang, Dai et al., 2019; Fang, Hu et al., 2019). The second approach is based on ML approach (Puzyrev, 2019), which aims to speed up the inversion process significantly. The theory for each of these approaches are described briefly below.

Conventional EM inversion

We applied the Born iterative method (BIM) as our inverse scattering solver. In this forward solver, the volume integral equation is solved with the stabilized bi-conjugate gradient combined with the Fast Fourier Transform (BCGS-FFT). In BIM, the Green's function for the background medium is fixed and the scattered field is written as

$$\phi_{sct}(\mathbf{r}_R,\mathbf{r}_T) = k_h^2 \int d\mathbf{r}' g_b(\mathbf{r}_R,\mathbf{r}')\chi(\mathbf{r}')\phi(\mathbf{r}',\mathbf{r}_T)\,. \tag{4-1}$$

The BIM is an iterative method of solving the above nonlinear inverse problem with iterations. It starts with an initial guess of χ_0, then the total field $\phi^{(n)}$ can be found by a forward solver. This total field is used to approximate the real total field ϕ at the $(n+1)^{th}$ iteration using Equation (4-2):

$$\phi_{sct}(\mathbf{r}_R,\mathbf{r}_T) = k_h^2 \Delta V \sum_{p=1}^{N} g_b(\mathbf{r}_R,\mathbf{r}_p)\chi^{(n+1)}(\mathbf{r}_p)\phi^{(n)}(\mathbf{r}_p,\mathbf{r}_T)\,. \tag{4-2}$$

Then, $\chi^{(n+1)}$, representing the model parameter vector, can be obtained by solving this linear equation. This iteration ends when predefined criteria are satisfied. The system of equations can be written in general form as Equation (4-3):

$$\mathbf{b} = \mathbf{J}\mathbf{x}, \tag{4-3}$$

where ***b*** is the scattered field $\phi_{sct}(\mathbf{r}_R,\mathbf{r}_T)$, ***x*** is the model parameter to be updated, and ***J*** is Jacobian matrix with the entries as

$$J_{ij} = k_h^2 \Delta V g_b(\mathbf{r}_i,\mathbf{r}'_j)\phi^{(n)}(\mathbf{r}'_j,\mathbf{r}_T)\,. \tag{4-4}$$

Because Equation (4-3) is usually underdetermined, the solution of Equation (4-3) is transformed to an optimization problem using the following objective function:

$$F(\mathbf{x}) = \frac{1}{2}\frac{\left\|\mathbf{W}_d(\mathbf{b}-\mathbf{J}\mathbf{x})\right\|^2}{\left\|\mathbf{b}\right\|^2} + \gamma^2\frac{1}{2}\frac{\left\|\mathbf{W}_m(\mathbf{x}-\mathbf{x}_p)\right\|^2}{\left\|\mathbf{x}_p\right\|^2}, \tag{4-5}$$

where $\boldsymbol{W}_d$ is the weight describing the estimated uncertainties in the available dataset, $\boldsymbol{W}_m$ is the weight describing the degree of confidence in the prescribed model. γ is the regularization parameter applied to determine the relative importance of the two terms. $\mathbf{x}_p$ is the a priori information of the parameters. Taking the gradient of the left-hand side of Equation (4-5) and making it to be zero yields

$$\left(\frac{\mathbf{J}^T\mathbf{W}_d^T\mathbf{W}_d\mathbf{J}}{\left\|\mathbf{b}\right\|^2} + \gamma^2\frac{\mathbf{W}_m^T\mathbf{W}_m}{\left\|\mathbf{x}_p\right\|^2}\right)\mathbf{x} = \frac{\mathbf{J}^T\mathbf{W}_d^T\mathbf{W}_d}{\left\|\mathbf{b}\right\|^2}\mathbf{b} + \gamma^2\frac{\mathbf{W}_m^T\mathbf{W}_m}{\left\|\mathbf{x}_p\right\|^2}\mathbf{x}_p\,, \tag{4-6}$$

where T denotes the complex conjugate transpose.

A forward model in which a ground-truth model was constructed is shown in Figure 4-5. The ground-truth model had a homogenous half space with a conductivity of 0.01 S/m and a 30×25×0.2-m-scale horizontal fracture of 12.5 S/m conductivity, centered at (0,0,−54). The operation

frequency was 1.667 Hz. The earth conductivity was chosen to be 0.01 S/m. The transmitters and receivers were located in four boreholes located at (−50.443, −6.7252, −100~0), (−6.8725, 50.162, −100~0), (50.231, 6.8307, −100~0), and (6.2975, −49.920, −100~0) m.

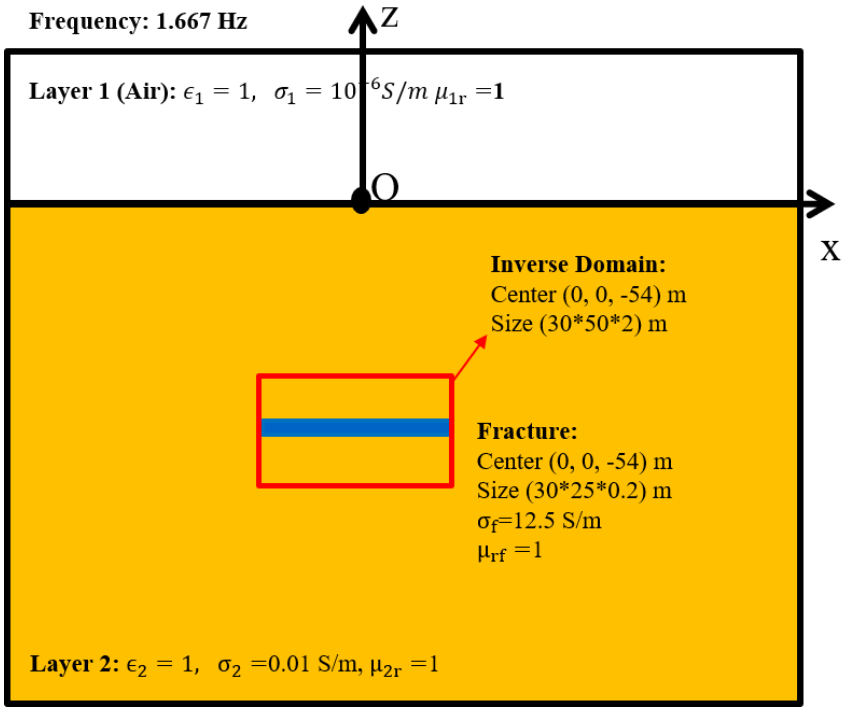

Figure 4-5: Modeled EM parameters. The ground-truth model is a homogenous half space with a conductivity of 0.01 S/m and a 30×25×0.2-m-scale horizontal fracture of 12.5 S/m conductivity, centered at (0, 0, −54). The operation frequency was 1.667 Hz. σ is electric conductivity, ε is permittivity, and μ is magnetic permeability.

The RTM model, in which a ground-truth model with a homogeneous half space and a 20-cm-thick horizontal fracture was constructed, is shown in Figure 4-6. The background is unconsolidated sand. Figure 4-7 shows the RTM results under this configuration. The rough shape (red box) of the fracture at the x-z plane was reconstructed. We used this result as the reference for our inversion domain selection. From the RTM results, the thickness of the fracture can be approximated to ~2 m and the size in the x direction to ~30 m. Therefore, the calculation domains in the x and z directions were chosen as 30 m and 2 m, respectively. The inversion calculation domain in the y direction was chosen as 50 m.

Figure 4-8 shows the inversion results using the RTM results as the inversion domain reference, in which the inversion domain was 30×50×2 m with its center at (0, 0, −54). The inverted results show that the shape and size of the fracture in the x and y directions can be reconstructed well with the help of the RTM information. However, the thickness and the location of the fracture in the z direction is not accurate enough. We also observed some artifacts close to the transmitters and receivers. Because of these reasons and the reasons elaborated in Subtask 5.3, we decided not to conduct seismic surveys during the DFPS field tests. Instead, we conducted distributed acoustic sensing of strain magnitude at several observation wells and tiltmeter mapping on the ground surface to guide the EM models with the estimates of the dilated fracture area.

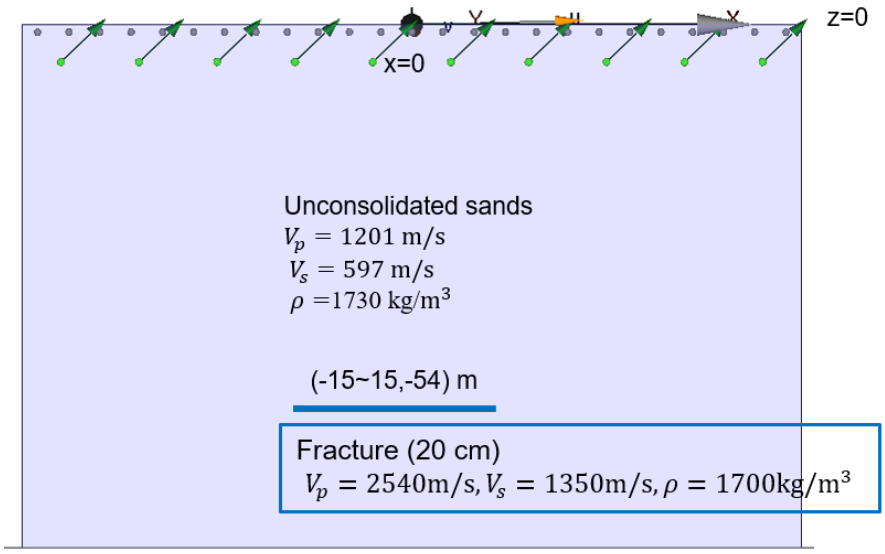

Figure 4-6: RTM model based on the forward model.

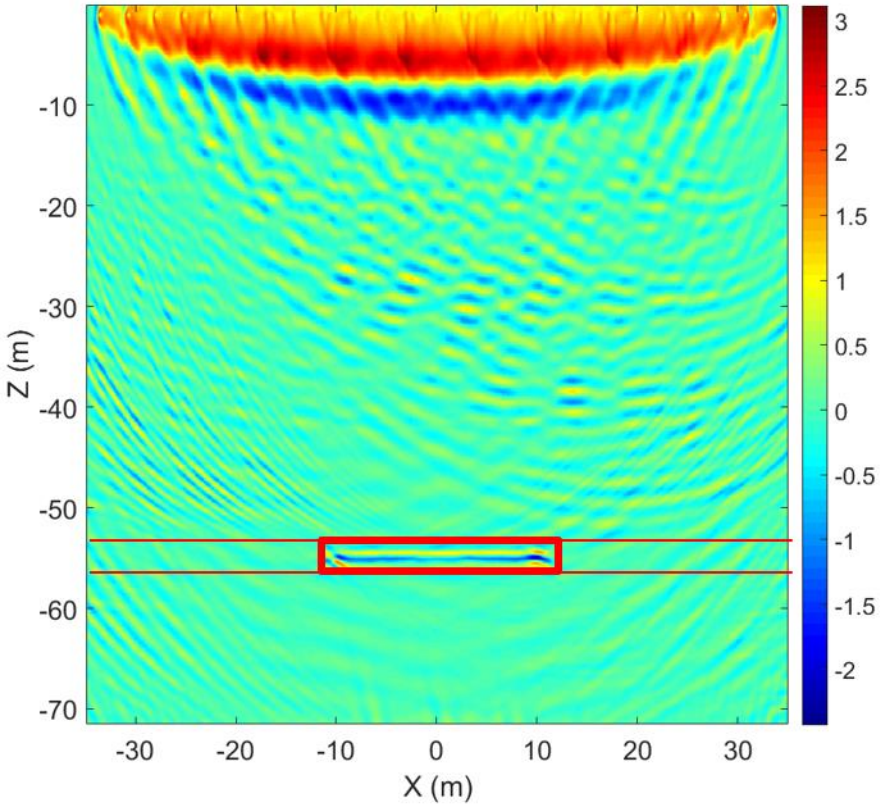

Figure 4-7: RTM results.

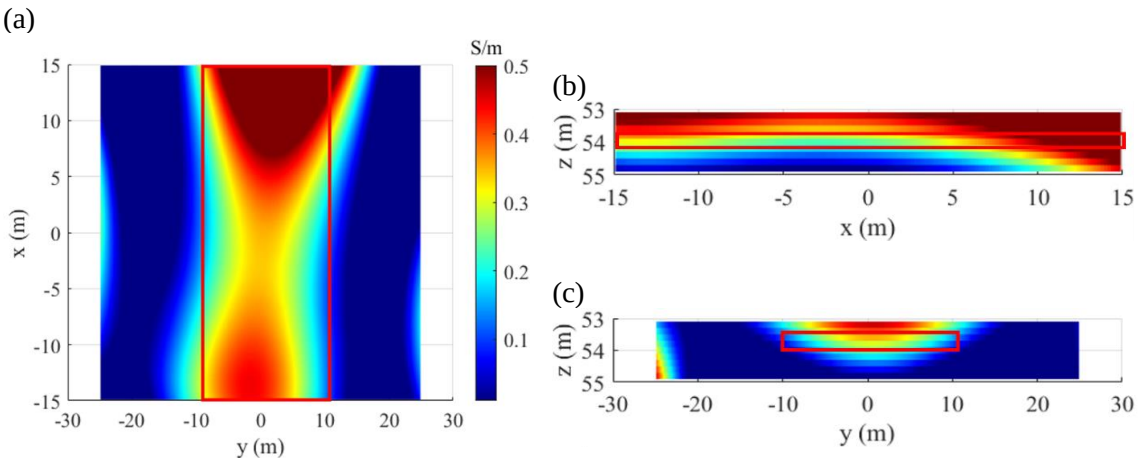

Figure 4-8: Reconstructed EM image at the first step. Red boxes show the size and location of the original model. (a) The x-y plane at z = −54 m. (b) The x-z plane at y = 0 m. (c) The y-z plane at x = 0 m.

EM inversion with machine learning method using the Devine 2017 data

Machine-learning-based inversion aims to speed up the inversion process. By optimizing the neural network configuration and training data size, we should be able to train a neural network to obtain an approach with high validation/testing accuracy. The routine can be used to process the EM measurement data and deliver changes in the EM signal distribution within the fractures in near real-time.

Previous voxel-based inversion showed that the hydraulic fracture at Devine is almost horizontal and is located at a depth of ~54 m (Ahmadian, LaBrecque et al., 2018; Ahmadian, LaBrecque et al., 2019). Consequently, to speed up the inversion modeling, we opt to restrict the fracture within a 2D horizontal plane. Furthermore, since the fracture can be thought of as a connected region instead of a cluster of isolated regions, instead of treating the fracture as independent pixels, we characterize the fracture with a closed curve and try to invert the curve parameters to previous math results. This approach reduces the number of unknowns tremendously. According to the estimations from the previous tiltmeter survey, which was conducted during the hydraulic fracturing exercise at the DFPS (Ahmadian, LaBrecque et al., 2018), we can constrain the fracture inside a 30-m-radius circle with the injection well as the center and model this circle with 16 equally distributed control points using the 4th-order B-spline function. By shrinking the distances between the control points and the center, we can fit the closed curve to the fracture shape.

Consequently, we have 16 scaling factors (with lower and upper bound values between 0.2 and 1) to invert. The lower bound 0.2 is set empirically by realizing that there is no direction where the fracture doesn't grow at all. The current training process uses 5,000 data points, including 1,000 fracture shapes of 5 conductivities (1, 2, 5, 10, 20 S/m). The best inversion case is shown in Figure 4-9. While good agreements to prior the DFPS results are observed, this inversion is not stable yet and needs further fine tuning. We evaluated the accuracy of the method and then performed a grid-search to optimize the hyperparameters of the neural networks and training process. Examples of parameters that we studied include neural network depth, width, dropout rate, learning rate, and early stopping criteria.

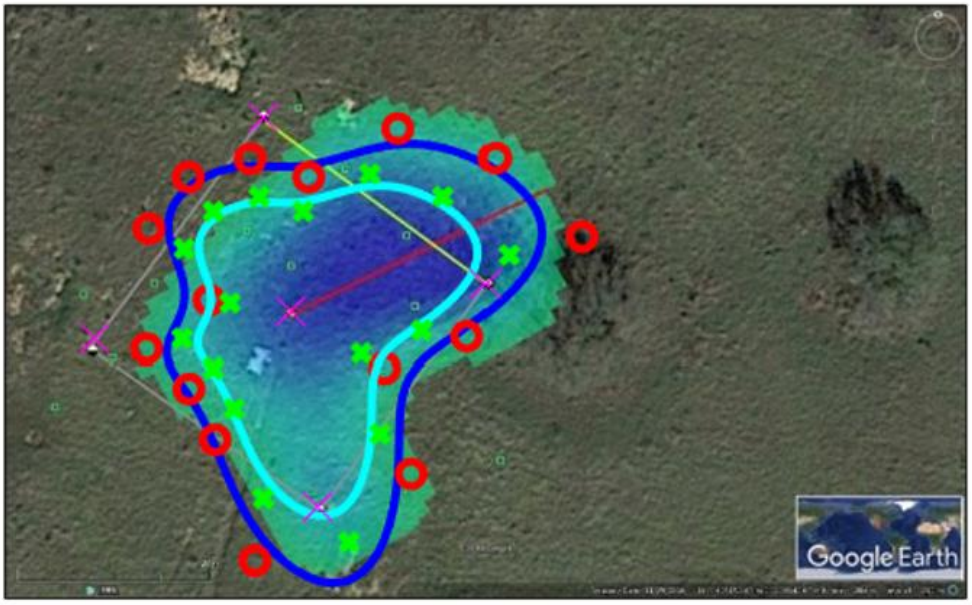

Figure 4-9: The current best inversion result is shown, where the red dots are the inverted 16 governing points and the blue curve is the interpolated B-spline closed curve. The reference shown represents result from previous DFPS inversion results.

Subsequently, using the available TDIP data previously obtained from the DFPS (Ahmadian, LaBrecque et al., 2018), we continued to optimize the ML approach for EM inversion. As shown so far, the best result obtained by this method was based on a training set with 5,000 synthetic data points. Although some of those results showed good correlation with the previous DFPS inversion results, they face two nontrivial problems:

(1) The inversion results were not stable enough and were sensitive to the choice of the training subset and network hyperparameters, where the hyperparameters include the depth and width of the Neural Network (NN), dropout rate (noise robustness of the NN), learning rate (training speed), batch size (training speed), and others.

(2) The training time was around 10 hours, which indicates that we need to exclude the training process from the real-time inversion.

One potential method to improve these aspects is to train the NN in advance so that the fracture can still be reconstructed in real time. However, one tradeoff is that the flexibility of excluding certain measurements in inversion would be lost. In other words, if we find multiple very noisy data points in the process of collecting post-fracturing data, we cannot directly abandon them because the pre-trained NN cannot be dynamically adjusted to the new set of input data.

Therefore, we proceeded with improving the training process. The candidate methods used included principal component analysis (PCA), standardizing the input data, and filtering out the input data based on the background field accuracy. PCA is a dimension reduction technique to filter the data points with small variance indicating that the measured voltage is insensitive to different fracture shapes. Therefore, the large-variance data points can be deleted for simplifying the NN architecture and accelerating the training process. The input data standardization is to order different data points independently by assuming that they conform to the normal distribution with zero mean and unit standard deviation. The tradeoff is loss of accuracy if the data is far away from normal distribution.

Our numerical experiments show that:

(1) PCA and filtering can both accelerate training speed significantly by reducing the dimension of the input data; and

(2) although standardization can scale all data features to the same scale, its acceleration effect is not obvious.

The reconstructed results from a 60-feature PCA and a 293-feature filtering are shown in Figure 4-10 and Figure 4-11, both of which took less than 1 hr to train. The reconstructed result from the 60-feature PCA captures some details at the bottom part of the fracture but loses the top right region, which should have large conductivity. Whereas the 293-feature filtering result gets the overall shape, it loses many details, especially at the bottom.

Hence, we conclude that the PCA and filtering method can be employed when training is needed in a limited time after obtaining and selecting the high-fidelity data points, and comes with a potential loss of accuracy. The next step is to quantitatively study the performance of PCA and filtering and try to speed up the training process to about 20 min and improve the inversion results.

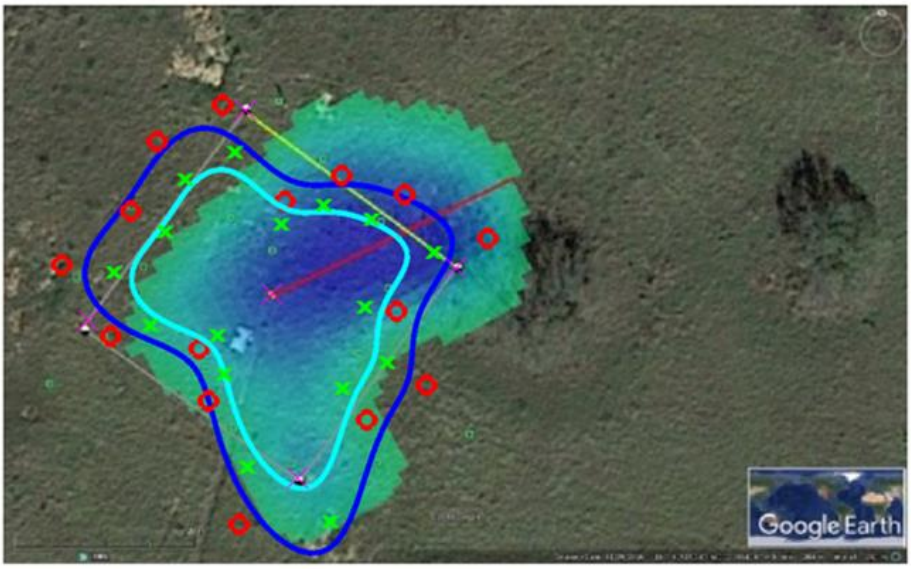

Figure 4-10: The 60-feature PCA results, which capture details of the bottom part of the fracture but miss the top right part. The red dots are the inverted 16 governing points and the blue curve is the interpolated B-spline closed curve. The background reference shown represents the validated DFPS EAP inversion footprint obtained in 2018.

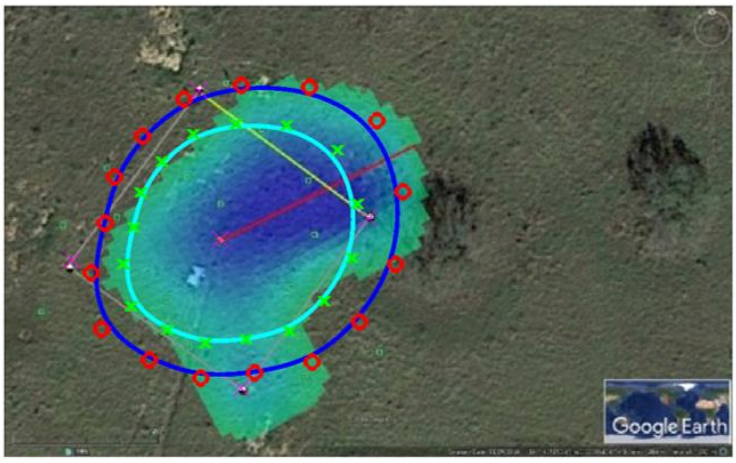

Figure 4-11: The 293-feature filtering results, which capture the whole picture of the fracture but miss some details.

So far, we compared several methods to reduce the input dimension of the NN to expedite its training process. Although both principal component analysis (PCA) and a primary field-based filtering technique can reduce training time, their reconstruction is not accurate for the Devine field data because of the large shape discrepancy between the validated DFPS EAP inversion footprint and the core tests. Then, we applied a secondary field-based filtering technique to NN design, which was successful to reduce the training time and guarantee the reconstruction accuracy.

The secondary field-based filtering technique is as follows:

(1) Use the synthetic scattered data to calculate the data range per transmitter–receiver pair.
(2) Use these ranges to filter out the corresponding field data outliers.
(3) Use the remainder field data as input for the NN.

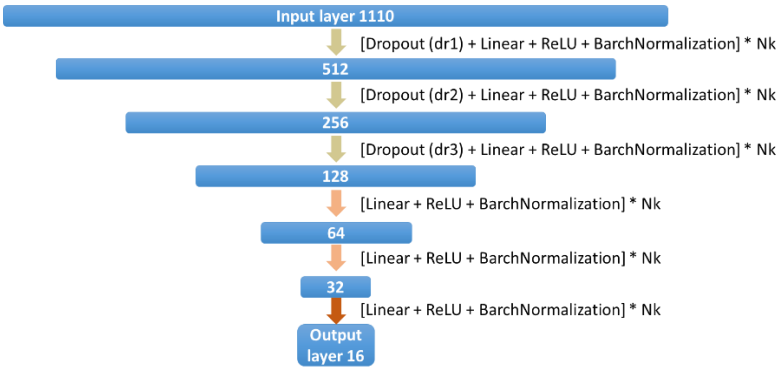

Figure 4-12: The architecture of the neural network (NN), in which the number of neurons at each layer are shown in boxes. Each layer of the NN includes N_k-cascaded kernels, namely a dropout layer (for the top three layers), linear mapping layer, ReLU nonlinear layer, and batch normalization layer.

In our numerical experiments, the input dimension (number of field data) can be reduced from 1643 to 1110 if we only remove the field data outside of the corresponding synthetic range. By using these input data, we can train a NN as shown in Figure 4-12. To guarantee that the training process can be finished within 30 min, we selected the kernel number per layer (N_k) to be 2 and the dropout rates for the top three layers as 0.3, 0.1, and 0.0.

To estimate the confidence level of different parts of the fracture and increase the robustness of the reconstruction, we first divided all synthetic data (7500 sets of fractures) into 10 groups (750 cases each). Next, we selected one group as the validation group and other nine as the training groups. With this method, we can form one training-validation pair, and by selecting different validation groups, we can arrive at 10-fold training-validation pairs, each of which can independently train one NN. Subsequently, 10 NNs can reconstruct 10 fractures, as shown in Figure 4-13 from the same filtered field data. Finally, we can take the mean value of these 10 fracture shapes as the blue curve plotted in Figure 4-14 to estimate the fracture shape. The standard deviation of the 10 fracture shapes is proportional to the length of the black lines in Figure 4-14, which can then be used to estimate the confidence level of the fracture boundaries.

The reconstructed shape has high confidence level and agrees well with the reference (validated DFPS EAP inversion footprint) at the right top region; however, both the bottom region and left top region have low confidence levels and some discrepancies with the reference.

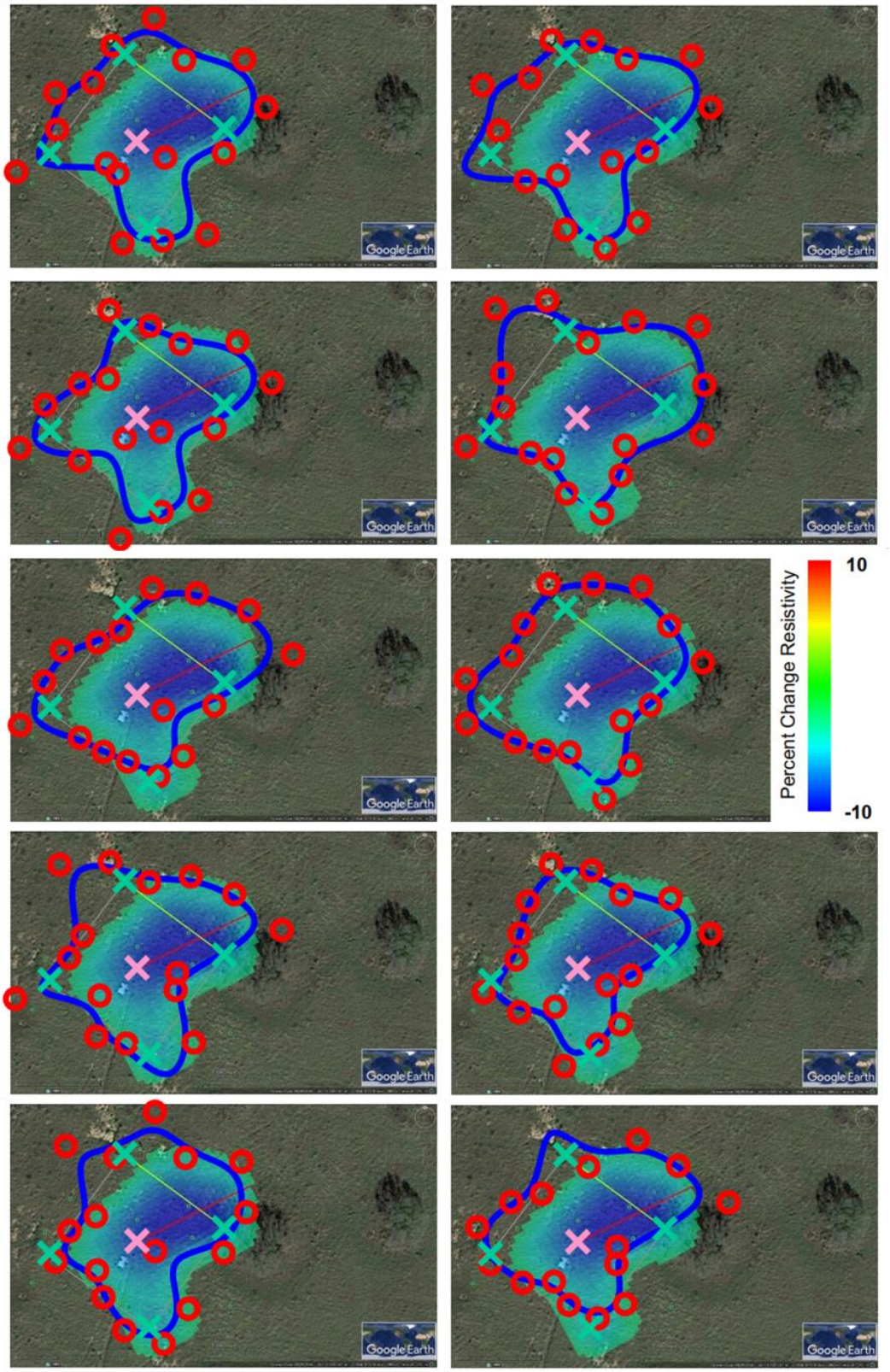

Figure 4-13: The 10 reconstructed fracture shapes from different subsets of the same synthetic data pool. The red dots are the inverted 16 governing points, and the blue curve is the interpolated B-spline closed curve. The crosses are the injection well (pink) and observation wells (green). The background reference shown represents the validated DFPS EAP inversion footprint obtained in 2018.

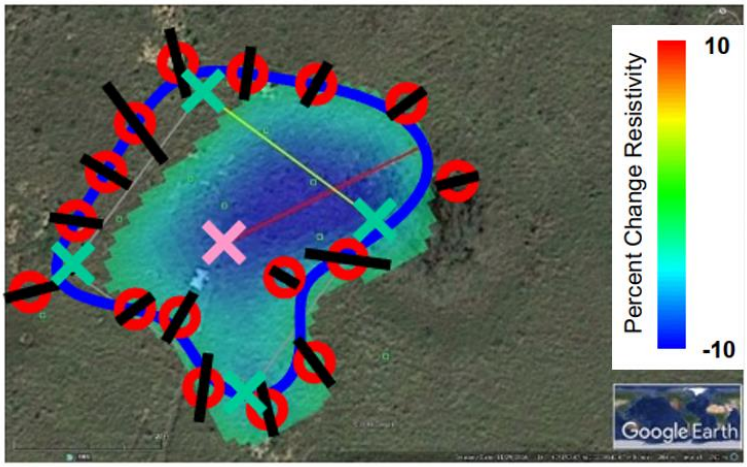

Figure 4-14: The final reconstructed fracture shape averaged from the 10 fracture candidates. The red dots are the 16 governing points, each of which is the mean value of corresponding points in the 10 fracture candidates. The black lines' lengths are proportional to the standard deviation of corresponding governing points. The blue curve is the interpolated B-spline closed curve. The crosses are the injection well (pink) and observation wells (green). The background reference shown represents the validated DFPS EAP inversion footprint obtained in 2018.

The entire workflow of our current inversion model is shown in Figure 4-15, including preprocessing and filtering, forward modeling, training and validation, and estimation. The two filters filter out the data with large standard deviations and reduce the dimensions of the training data, thus they can both improve the inversion accuracy and speed up the training process.

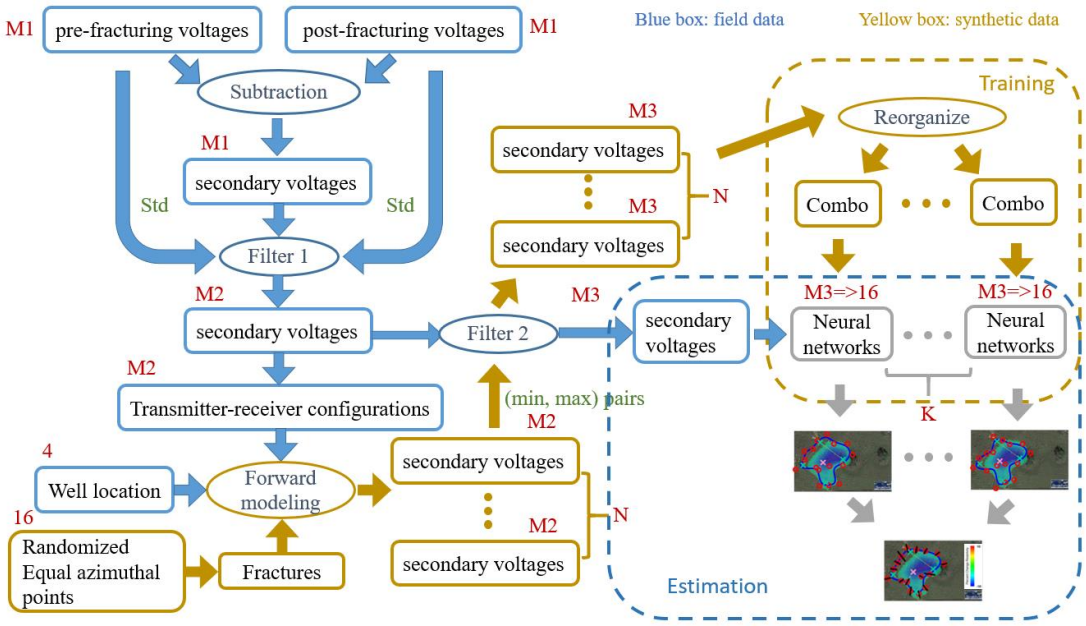

Figure 4-15: Workflow of the whole inversion process. The rectangular boxes represent data or models, elliptical boxes represent operators, and red letters or numbers represent the dimension of corresponding data or objects. Filter 1 deletes secondary voltages smaller than the standard deviation (std) of either the pre or post-fracturing voltages, and filter 2 deletes the secondary voltages outside of the corresponding (min, max) pairs.

Afterwards, we continued improving the accuracy of the reconstruction by tuning the bandwidth of the secondary field-based filtering technique. The parameter "offset" we used in tuning is defined as follows:

$$\min(\text{sythetic data}) - \Delta * \text{offset} < \text{measured data} < \max(\text{sythetic data}) + \Delta * \text{offset},$$

where Δ means half of the difference between the maximum and minimum of the synthetic data. Compared to a negative offset, a positive offset means looser constraints, thus more training data are included. To evaluate the similarity between the inversion result and the reference, we use the Intersection over Union (IoU, also known as the Jaccard similarity coefficient), which is widely used in computer vision for comparing the similarity of two sample sets. IoU is defined as the intersection area divided by the union area of the comparison pair A and B:

$$IoU = \frac{A \cap B}{A \cup B}.$$

The inversion results with positive values of offset (larger dataset) and negative values of offset (smaller dataset) are shown in Figure 4-16 and Figure 4-17, respectively.

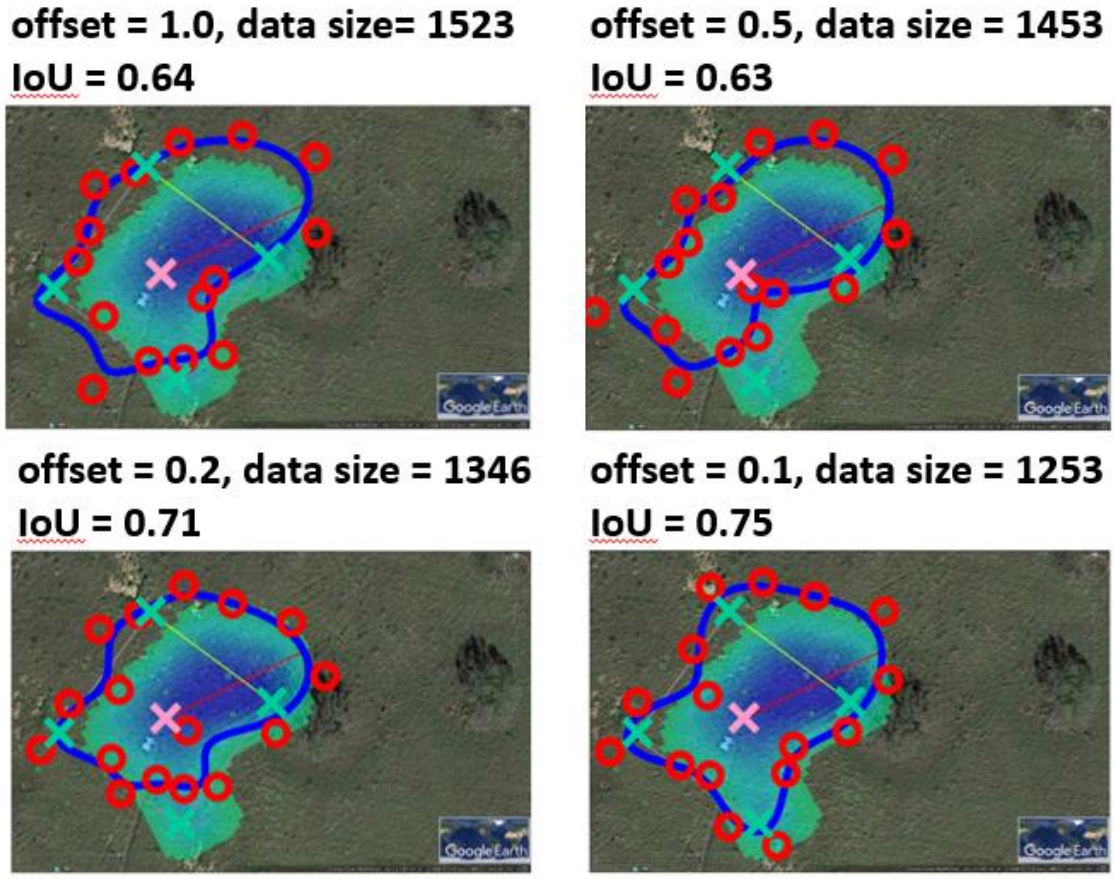

Figure 4-16: The reconstructed fracture shape with different positive values of offset.

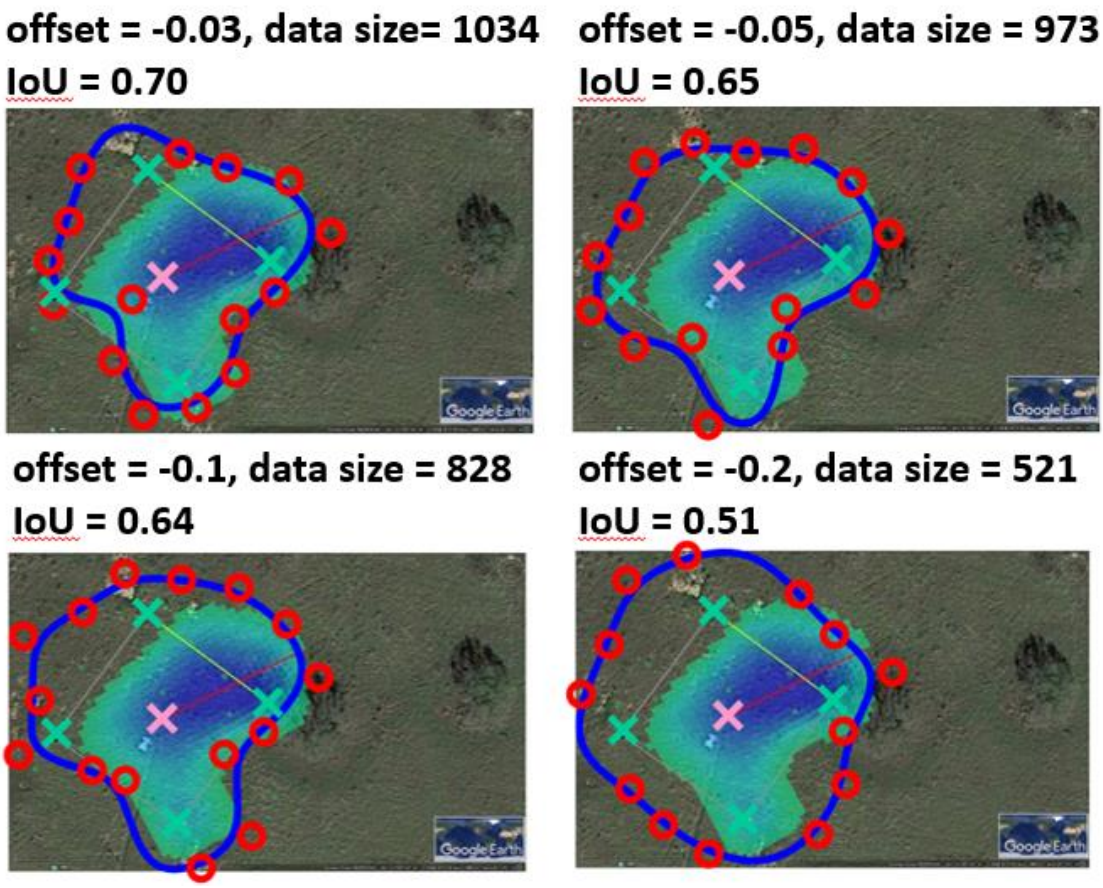

Figure 4-17: The reconstructed fracture shape with different negative values of offset.

In Figure 4-16 and Figure 4-17, we can find relatively good agreement at the south and east side of the fracture image between NN results and the reference. The discrepancy of these solutions on the west side may originate from the significant effect of the conductivity distribution on the NN inversion, which needs further investigation in other studies beyond the current project.

5 Design of Field Experiment /Sensitivity Analysis

5.1 Fluid Flow Modeling

To prepare for the 2020 field tests, we constructed a hydrogeological layer-cake model using the Builder™ and STARS™ packages in the commercial software program CMG developed by the Computer Modelling Group Ltd. We completed multiple simulations for different field injection scenarios. Then, we tuned this model using prior coring and fluid injection history at the DFPS. This hydrogeological model is capable of predicting the initial injection volumes, species transport, and saline water transport. However, to compensate for the shortcomings of a hydrogeological model to predict hydraulic-fracture conductivity changes over the fracture area and through time, we developed a poroelastic model using the commercial software program Abaqus (Dassault Systèmes, 2017). These modeling efforts are elaborated by Haddad et al. (2021, 2023) and summarized in the following.

The hydrogeological model area is 1383 ft × 1383 ft extending from the ground surface to a depth of 350 ft. The Tartan gridding system used in the current model contains 658,845 grid cells centering on the injection well and at the injection depth of 175 ft, as shown in Figure 5-1. This figure also shows the monitoring and observation wells relative to the injection well and the propped hydraulic fracture geometry. Considering that injections at the DFPS induce only single-phase flow (water injection into the water table), this degree of mesh refinement seemed reasonable for providing solutions with adequate resolution, especially around the injection well and fracture zone. Also, this degree of refinement allowed to obtain solutions during the subsequent parameter tuning processes without adding too much computational burden to the whole system. Aligned with the goals of this study, this model was constructed based on the following assumptions:

(1) layer-cake strata over the modeled area of interest, without consideration of any natural structures in the formation, which seems a reasonable assumption considering the scale of the model;
(2) uniform reservoir conditions and properties within each layer at the same depth;
(3) an open reservoir boundary to account for an infinite reservoir relative to the small modeled area; and
(4) water-saturated formation below the water level.

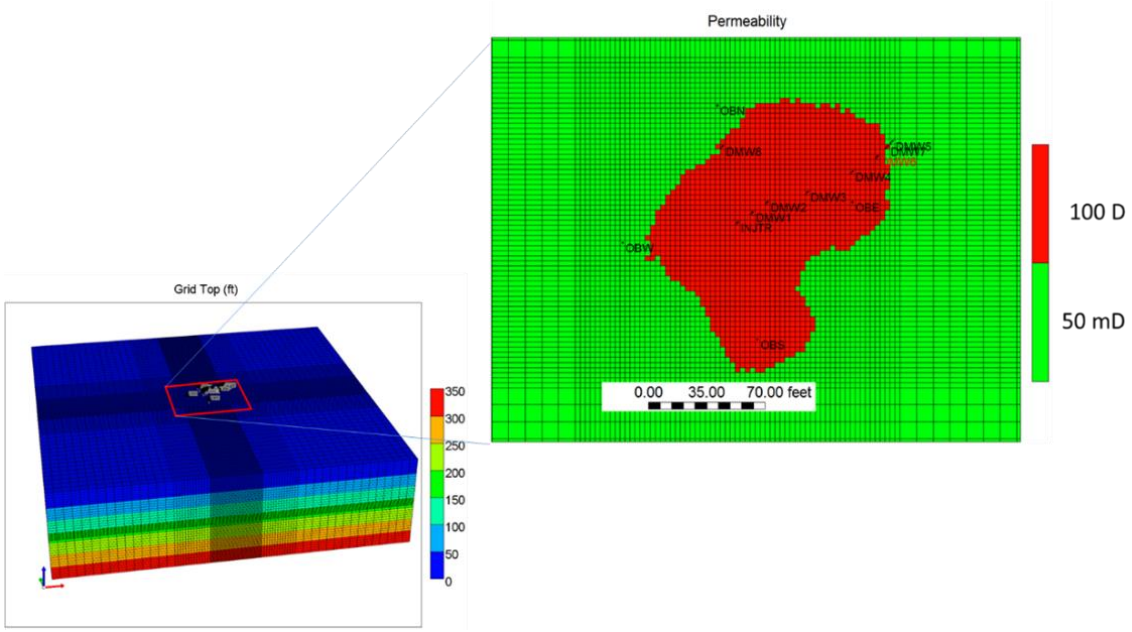

Figure 5-1: (left) Tartan 3D gridding system of the preliminary CMG model covering an area of 1383 ft × 1383 ft with a depth of 350 ft. (right) Plan view of the fracture and locations of wells at injection depth (175 ft) zoomed on the area of interest. The grid refinement around the injection zone (0.02 ft for the fractured zone) allowed us to capture the fluid flow behavior with high resolution. The position of fracture anomaly containing EAP is shown schematically in the right panel.

The initial reservoir properties are listed in Table 5-1.

Table 5-1: Initial reservoir properties in the model.

Reservoir Property	Average
Permeability (md)	50
Porosity	0.19
Initial pressure gradient (psi/ft)	0.433
Total depth (ft)	353
Water level (ft)	100
Water saturation	1
Temperature (°F)	80
Model dimensions (ft^2)	1355 by 1355
Gridding system	Tartan gridding
Boundary	Open
Wells	Injection active

During drilling of validation wells in 2018, several of those wells were screened for future use. DMWs 1 and 2 were lined with 2-inch ID PVC casing and were screened at depth of 170-180 ft. At that time, while drilling DMW 3, which is 15 ft and 35 ft away from DMWs 2 and 1, respectively (Figure 3-13), a set of level loggers were deployed in the screened wells, and the resulting pressure and temperature data in each well was recorded. The current fluid flow model is set up with assumed initial hydrostatic pressure and temperature from those studies. In addition, porosity and permeability values are from UT/BEG's Wilson-9 core collection, which were subjected to laboratory geomechanical tests during design phase of hydraulic fracturing of the DFPS in 2017 (Ahmadian, LaBrecque et al., 2018). Because Wilson-9 well is very close to the injection well (Figure 3-13), and indeed demonstrates a very similar stratigraphy at the depth of interest (Figure 3-14), we assumed that the geomechanical properties of the injection site are similar to those at Wilson-9 well. The permeability of the hydraulic fracture zone in the model is estimated using the cubic law.

We then calibrated the model parameters (e.g., reservoir permeability, wellbore tubing roughness, and gridblock size) using the collected level logger data and the other DFPS historical data that were available to us. One calibration dataset was the pressure pumping data measured by the level logger during the hydraulic-fracturing injection in 2017 (Figure 5-2). The goal of the simulation was to match the initial portion of the curve (i.e., pad injection) before proppant placement.

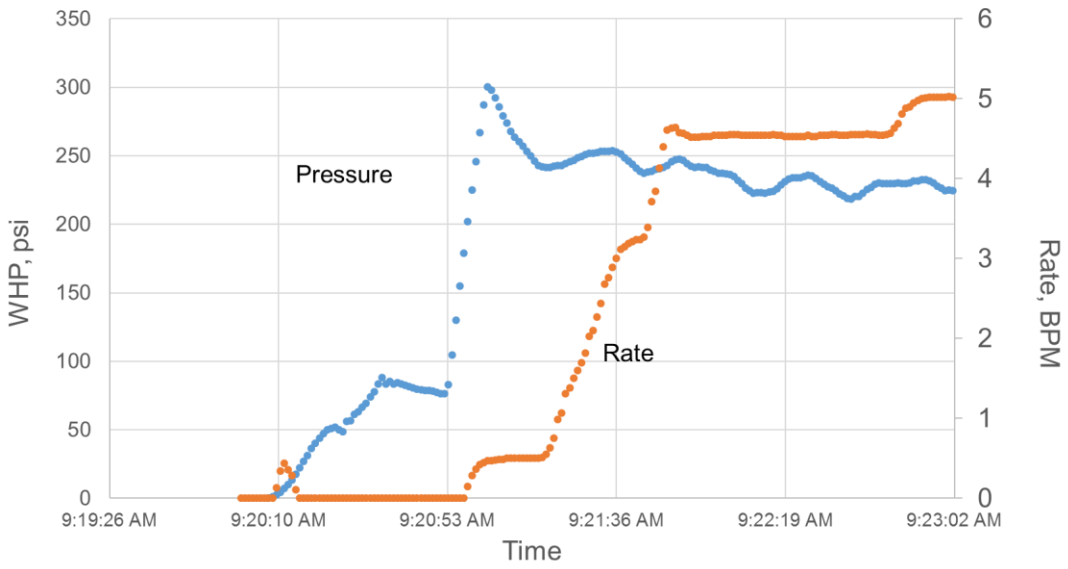

Figure 5-2: Historical data from the injection well for hydraulic fracturing conducted in 2017. "WHP" and "BPM" stand for wellhead pressure and barrel per minute, respectively.

The history matching process used the injection rate (actual history data) as constraint for the injection well, and simulated the wellhead pressure (WHP) variations at different rates. In this process, the reservoir properties (especially the formation permeability), the size of the gridblocks at the injection interval, and the wellbore roughness were the main variables that were used to match the data. To match the WHPs (Figure 5-3), the following major changes were made:

(1) the gridblock size at the injection intervals was changed from 0.02 ft to 1.0 ft to avoid the numerical convergence problem;
(2) the reservoir permeability was increased from 50 mD to 150 mD to obtain bottomhole pressures (BHP) in the reasonable range; and
(3) the wellbore tubing roughness was adjusted from 0.0004 to 0.00006 to capture accurate roughness effects from the bottom of the well to the wellhead.

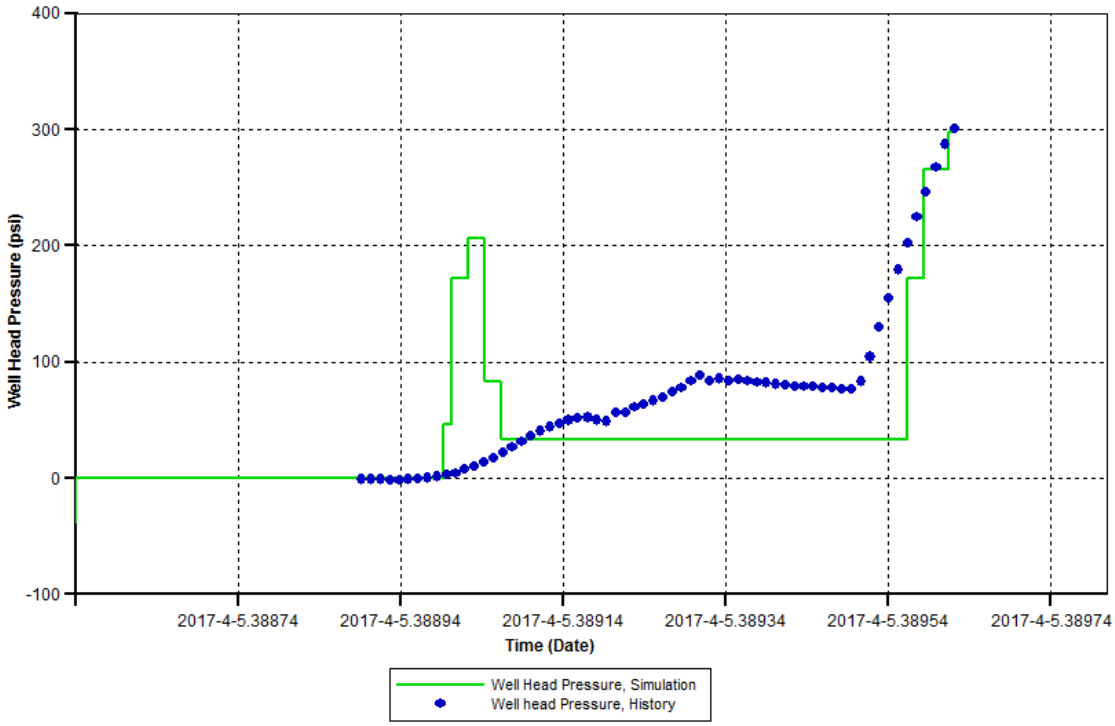

Figure 5-3: History-matching results from the simulation for the pre-fracturing portion of Figure 5-2. The simulated wellhead pressure curve (green line) reaches closer and closer to the historical wellhead pressure (blue dots) after reservoir permeability was increased from 50 mD to 150 mD.

Because the permeability of the existing proppant-filled hydraulic fracture was expected to be much higher than the permeability of the protolith rock, the proppant-packed fracture permeability was calculated based on the Carmen-Kozeny equation (Barree, Duenckel et al., 2019):

$$k = \frac{d_m^2}{180} \frac{\Phi^3}{(1-\Phi)^2}, \quad (5\text{-}1)$$

where d_m is the diameter of a proppant grain, equal to 105 microns for the US mesh 140, Φ represents porosity and is generally between 0.26 and 0.47 and equal to 0.36 on average for a proppant pack with disorganized particle configurations. With the above parameters, the calculated permeability is between 2 and 23 Darcy and the average value of 7.07 Darcy.

To further calibrate the model parameters, we used additional DFPS historical data that were available to us. During the drilling of the monitoring wells in 2018, DMW 2 was lined with 2-inch internal-diameter PVC casing and was screened at depth of 170 to 180 ft. At that time, while the drilling of DMW 3, a set of level-loggers were deployed in DMW 2 and the resulting pressure variations were used to further refine the model parameters. By tuning fracture permeability to 10 Darcy, a reasonable history matching results were achieved (Figure 5-4).

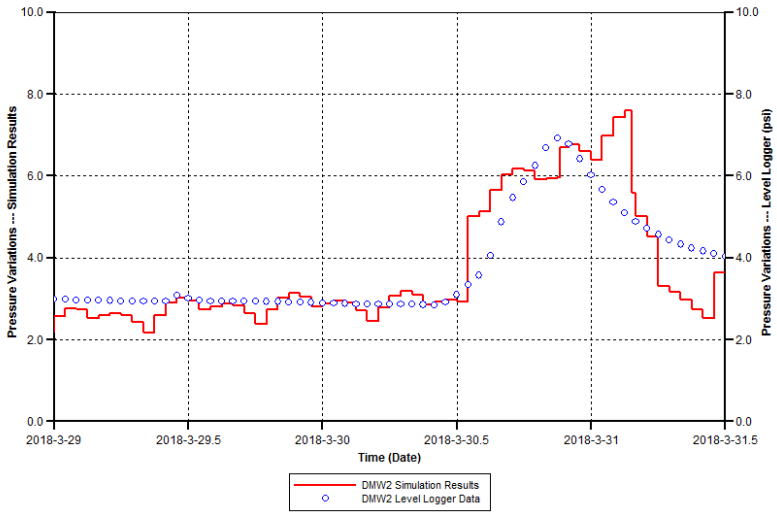

Figure 5-4: History matching on pressure variations in DMW 2 while drilling DMW 3.

The calibrated model was used to further estimate the pore pressure variations during and after the injection activities under different injection scenarios (Table 5-2).

Table 5-2: Some modeled injection scenarios.

Case	Description
110_S2	Injection with rate 110 bbl/day for 4 hours, resting time for 12 hours, and then extraction at the same site.
180_S2	Injection with rate 180 bbl/day for 4 hours, resting time for 12 hours, and then extraction at the same site.
250_S2	Injection with rate 250 bbl/day for 4 hours, resting time for 12 hours, and then extraction at the same site.

The injected volume of water for the three proposed cases are 18.33 bbl, 30 bbl, and 41.67 bbl, respectively. The simulation results from case 180_S2 are shown in Figure 5-5 through Figure 5-8.

Figure 5-5: Pressure plume for case 180_S2 at 4 hours, 16 hours, and 20 hours.

The pressure evolution around the injection site during and after injection, resting, and extraction are shown in Figure 5-5. The injection pressure reaches as high as 400 psi after 4 hours of injection with the injection rate of 180 BPD (bbl/day). Pressure is quickly released after 12 hours of resting time. Pressure is further decreased during extraction at the same site. The pressure evolution is substantially different from the evolution of salinity at the injection site (Figure 5-6 and Figure 5-7). The salinity plume represents the occupied space by the injected saltwater at 20,000 ppm salinity, which is markedly larger than the initial 900 ppm salinity in the formation. This is especially important for the determination of the injected fluid flow pathways. A planar view of salinity migration is shown Figure 5-7; the upper left plot shows the salinity plume after 4 hours of injection. The radius of this plume covers the site of DMWs 1 and 2, and reaches to the location of DMW 3. In the upper right plot, the salinity plume slightly diffuses outward after 12 hours of resting. This means that most of the injected saline water is still reserved around the injection site even after a long resting period. The lower left plot shows the salinity plume after 4 hours of extraction at the injection site. Because the fracturing layer is very thin in the model, at the center point of extraction, the high salinity water mixes with the low salinity water diffusing from the upper and lower layers resulting in a lower salinity at the center compared to the advancing maximum-salinity front (lower left panel in Figure 5-7). Even after 6 days (128 hours extraction), there is still a little saltwater left near the injection well (lower right panel in Figure 5-7). This could be seen more clearly in Figure 5-6.

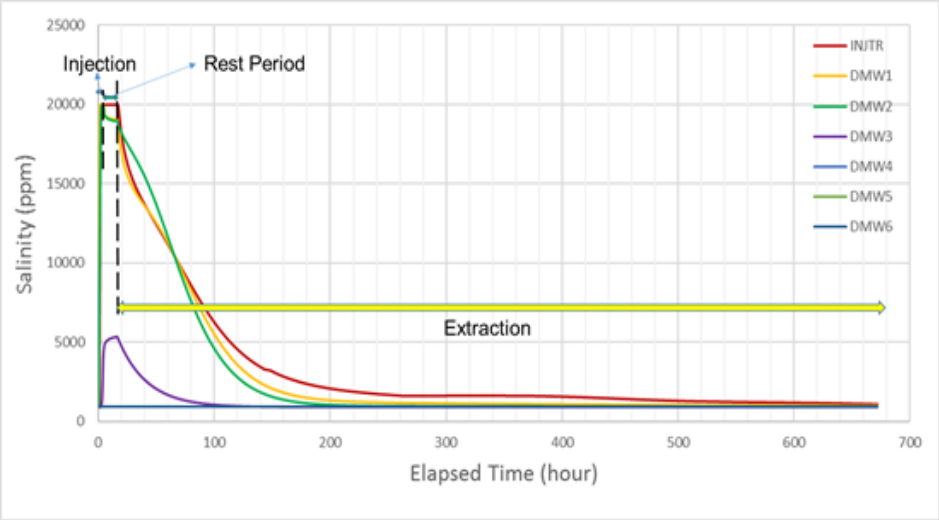

Figure 5-6: Salinity plume for the case 180_S2 at 4 hours, 16 hours, 20 hours and 6 days.

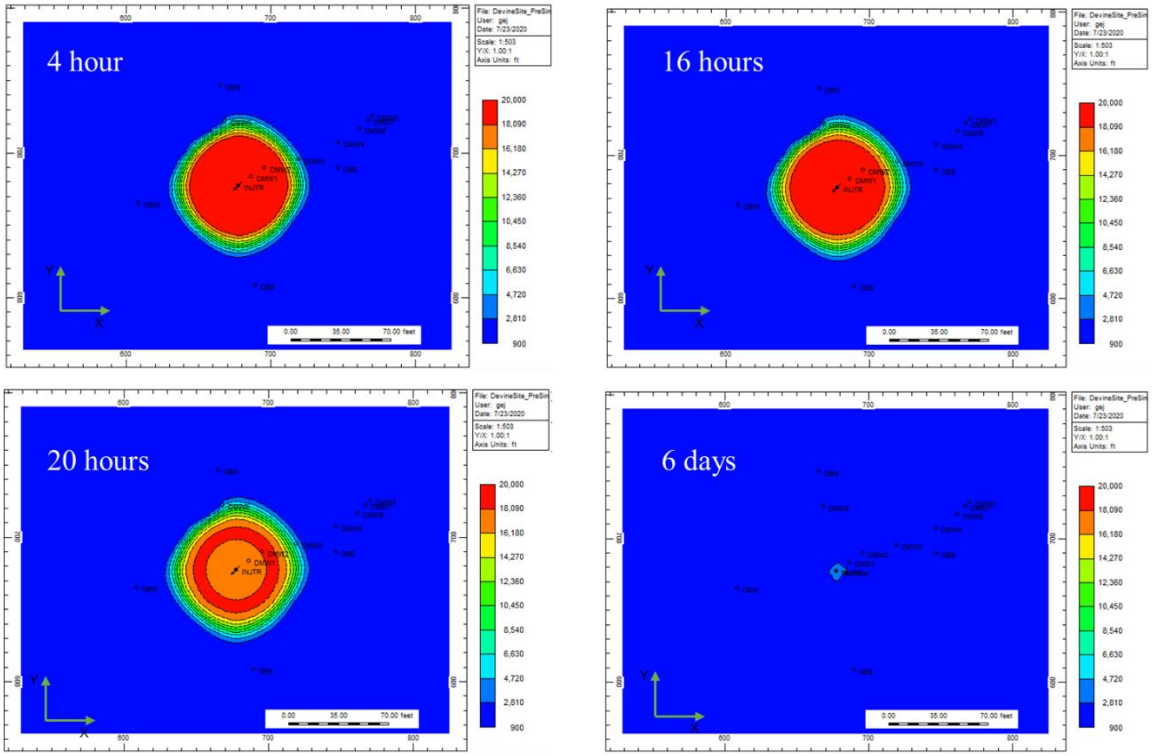

Figure 5-7: Planar view of salinity plume for the case 180_S2 at 4 hours, 16 hours, 20 hours and 6 days.

The lower left panel in

Figure 5-7 clearly shows that salinity at the DMW 2 became larger than that at the injection site and DMW 1 in a certain time interval. From this figure, salinity at the injection site keeps decreasing after the start of extraction and decreases to around 2000 ppm after 200 elapsed hours (more than 7 days). The salinity of injection site decreases to around 1000 ppm after 600 hours. Further extraction is needed to reach 900 ppm original formation salinity. Figure 5-8 gives an idea on the total volume of water extracted at different elapsed times.

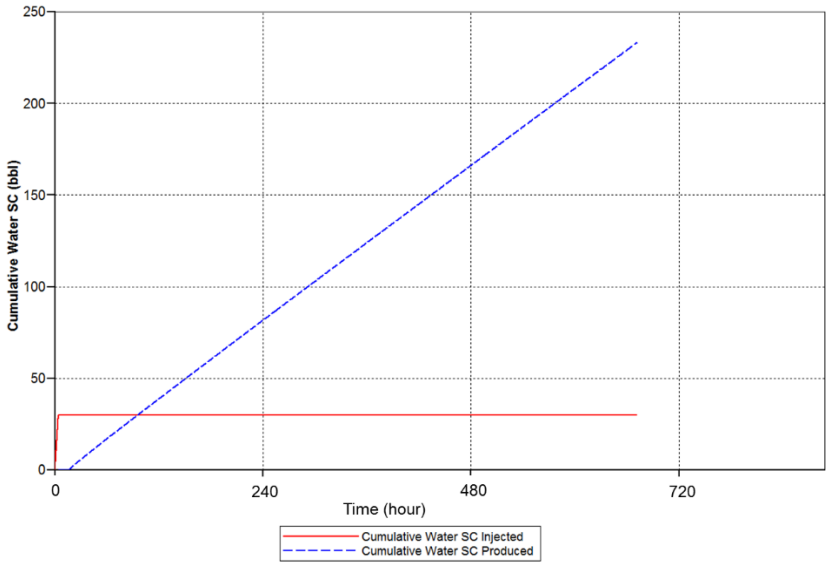

Figure 5-8: Cumulative water injected and produced with time.

This tuned model was used for the design of the field injection scenarios as elaborated in Subtask 6.1.

Then, we updated the model parameters through history matching process with the latest injection-rate and pressure data that were collected in September 2020. This was done by adjusting the fracture and formation permeability to match the BHP with the field data (Figure 5-9), as elaborated in Subtask 7.3. These models are essential because of their capabilities in predicting the initial injection volumes, species transport, and saline water transport.

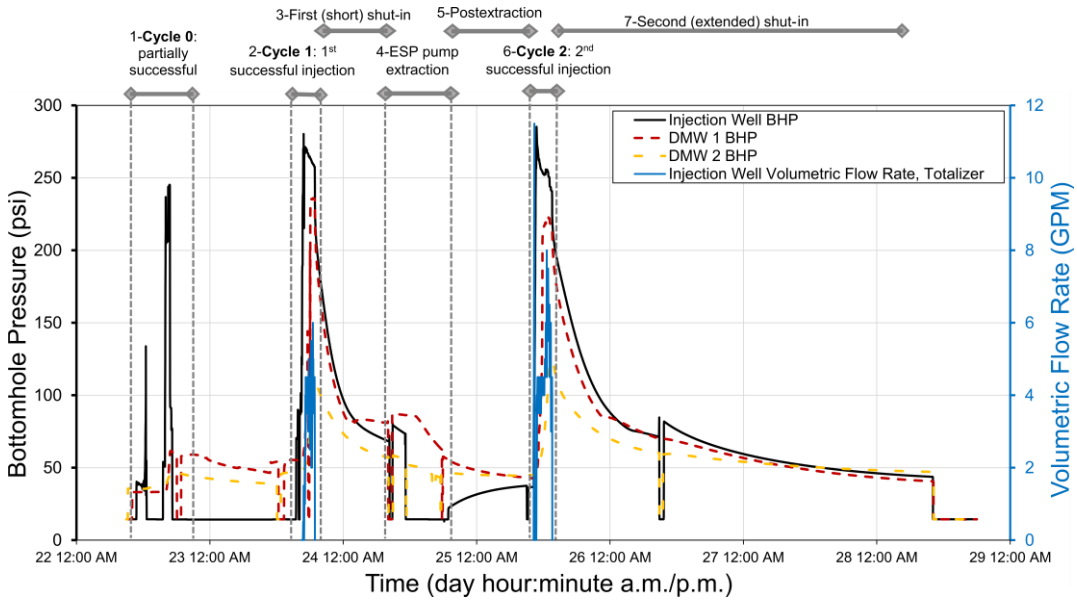

Figure 5-9: (left ordinate) Bottomhole pressure recordings for the injection well, monitoring well 1 (i.e., DMW 1), and monitoring well 2 (i.e., DMW 2); (right ordinate) friction-based volumetric flow rate at the injection well, through one week of injection and shut-in. The time interval on the abscissa is from September 22 to September 29, 2020, represented by numbers 22 through 29 for brevity, and time is recorded based on the U.S./Texas central daylight time zone. BHP in legends stands for bottomhole pressure at depth 175 ft, right at the fracture mouth in the injection well or expected fracture opening in the monitoring wells. During two time periods where the recorded pressure stays level at 14.2 psi (97.95 kPa), the injection well pressure transducer was removed from the well and kept at the surface.

Because of in-situ stresses, the hydraulic fracture conductivity can change over the fracture area and through time. These changes are hard to predict with hydrogeological models. To overcome this limitation, we also developed a fully-coupled poroelastic model in the commercial software program Abaqus (Dassault Systèmes, 2017). This model solves for change of poroelastic stresses as well as fracture reopening and formation pressure at the DFPS (Subtask 7.3). In addition to the petrophysical properties (e.g., porosity, permeability, and density), this model requires estimates of the rock mechanical properties (e.g., Young's modulus, Poisson's ratio, water bulk modulus, fracture initiation stress, and fracture toughness), leakoff coefficient, and in-situ stresses. We obtained primary estimates of porosity, permeability, density, Young's modulus, and Poisson's ratio from an unpublished, internal report (Gonzalez et al., 2016).

Our poroelastic model is based on cohesive zone model which simplifies a complex and microscopic process of fracture nucleation, coalescence, and propagation. This simplification has become possible by incorporating a macroscale cohesive law consisting of an elastic linear response prior to fracture initiation, followed by the assessment of a progressive damage response after satisfaction of a fracture initiation criterion (Haddad et al., 2017). To model reopening of a

horizontal hydraulic fracture in this site, we assumed a horizontal cohesive layer with zero thickness, between a 175-ft thick upper rock layer and 175-ft thick lower rock layer (Figure 5-10). We modeled a triaxial stress state by directly loading the lateral boundaries by the minimum and maximum horizontal stresses and the overburden stress in the depth direction through gravity. Because the model is extended up to the ground surface, the upper-boundary normal stress is zero.

We used maximum principal stress criterion for fracture initiation and Benzeggagh-Kenane energy model for fracture propagation (Haddad and Sepehrnoori, 2015). The optimal overburden stress to match the BHP data was obtained from an upper bound of the rock density (Gonzalez et al., 2016), and the horizontal stresses were obtained based on the friction coefficient of 0.3 and the generalized Angelier's shape parameter (Simpson, 1997) of 2.5, the average value of this parameter in reverse faulting stress regime.

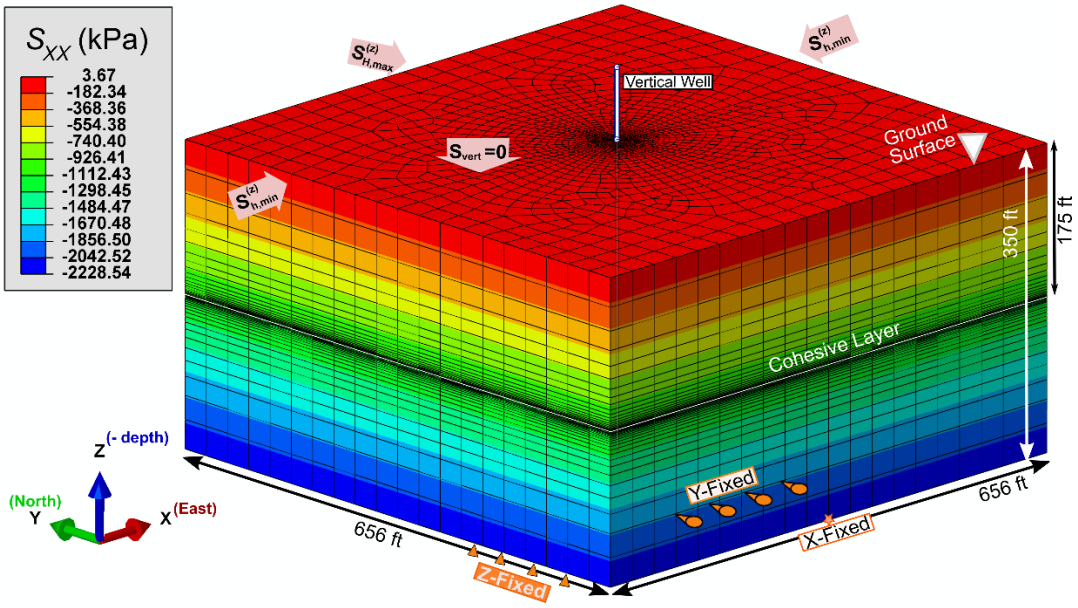

Figure 5-10: Poroelastic model geometry with the details of the boundary conditions and a vertical injection well. The contours show the normal stress component in x-direction (east-west direction), aligned with S_{hmin} azimuth. A horizontal hydraulic fracture reopens over the horizontal cohesive layer, initiating from the intersection of the vertical well and the cohesive layer.

Then, we proceeded with history matching of the poroelastic model parameters after we collected the injection data in 2020 and 2022 at the DFPS, as elaborated in Subtask 7.3.

5.2 Electromagnetic Sensitivity Analysis

For the design of the CSEM survey at the DFPS, we conducted EM models using Discontinuous Galerkin Frequency-Domain (DGFD) method and determined the optimal borehole transmitter configuration. Considering that there is an Electrical-Resistivity-Tomography (ERT) array at DMW 1, we modeled a case including this array. These models adopted the electric properties of the Devine media measured in a laboratory setting at the University of North Carolina (Subtask 3.1). Using 2017 experiment data, we obtained EM field sensitivities greater than 1% corresponding to 5% change in conductivity of the EAP-filled fracture for the transmitter array centered at 45-m depth and length of 10 m. We re-evaluated this configuration using the 2020

injection data and obtained current transmission at 71-m (233-ft) depth in DMW 1 as the optimal case for the maximum fracture contrast during injections. However, using a borehole transmitter was not pursued in the 2022 field deployment mainly because of the interference of the transmitted current with the nearby receivers.

As discussed in Subtask 6.4, the 2020 field experiment results suggested the influence of the surface conductivity and metal injection pipe on the simulation misfit versus gathered EM field data. To reduce the complexity of the EM models and consequent interpretations of the 2022 field data, we logged the surface conductivity, re-logged all wells at the test site, and removed the surface injection pipe and observation-well metal posts. Updating the EM model according to these changes at the test site and using the 2022 CSEM survey data reduced the total-field misfit to 29%. The largest and smallest scattered field misfits of 228% and 59% occurred at an early time of injection and maximum fracture dilation, respectively. The occurrence of the largest misfit simultaneous with large pressure changes at the onset of injection and the smallest misfit at minimal flow-rate changes supported the possible role of SP in the large scattered field misfit. Also, this SP contribution in our EM scattered field could be explained by an SP analytical solution.

In the following, we further elaborate these modeling efforts and findings separately for the experiment data collected in 2017, 2020, and 2022.

2017 experiment data interpretation and EM simulation

We analyzed the EM-detection sensitivity under the Devine configuration for the 2017 experiment data to optimize the location of the transmitters and receivers. Our stated goal is 1% sensitivity when the fracture conductivity changes by 5% (e.g., EAP conductivity change of 500 S/m vs. 525 S/m).

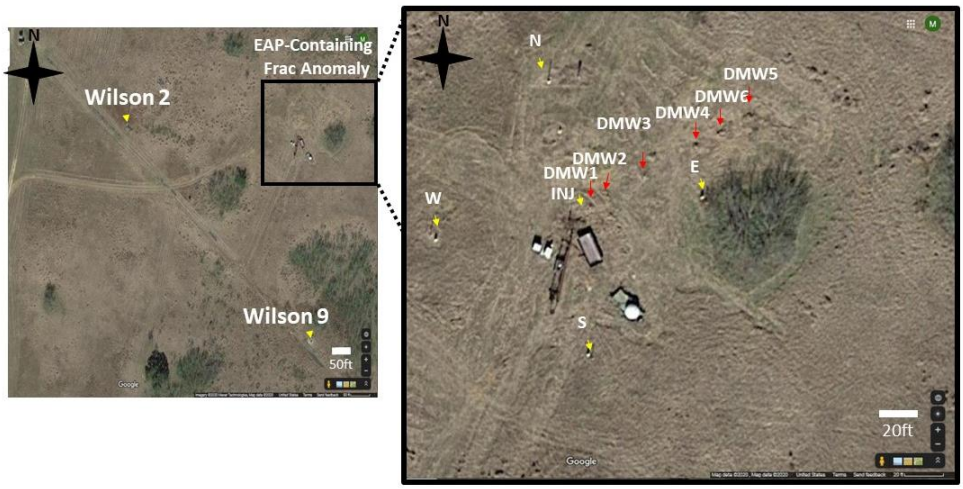

Figure 5-11: Areal images showing the existing DFPS layout and well positions. The injection well (INJ) in the right panel is approximately 400 ft away from Wilson 9, which is shown in the left panel. DMWs 1, 2, 3, 4, 6, and 5 are 10, 20, 45, 75, 91, and 107 ft away from INJ, respectively. The position of the fracture anomaly containing EAP is shown in Figure 4-9 through Figure 4-11. The observation wells utilized for CSEM survey are marked with N, S, E, W in the right panel and at approximately 75-ft distance from the injection well and together with DMW 1 have been previously instrumented with ERT arrays.

We calculated the electric field by using the existing ERT transmitter electrodes in DMW 1 (Figure 5-11). Receivers were positioned on the ground surface in a 100-m-by-100-m area or on any of the

four receiver arrays located in the four preexisting ERT-instrumented observation boreholes (N, W, S, E wells). The sensitivity, when fracture conductivity changes, is defined as,

$$Sens.(\alpha) = |\Delta E_\alpha|/|E_{\sigma_0}| \times 100\%, \tag{5-2}$$

$$\Delta E_\alpha = \Delta E_{\alpha,\sigma_1} - \Delta E_{\alpha,\sigma_0}, \tag{5-3}$$

$$E_\sigma = \sqrt{|E_{x,\sigma}|^2 + |E_{y,\sigma}|^2 + |E_{y,\sigma}|^2}, \tag{5-4}$$

where α refers to x, y, or z components of the E field and σ refers to the fracture conductivity. Furthermore, we considered four positions for transmitter electrodes in DMW 1: at z of Tx1 = −71 m, Tx2 = −54 m, Tx3 = −45 m, and Tx4 = −25 m (Figure 5-12). The frequency and the current of the transmitter were set to 1 Hz and 1 A. The results of this test are shown in Figure 5-13 and Figure 5-14.

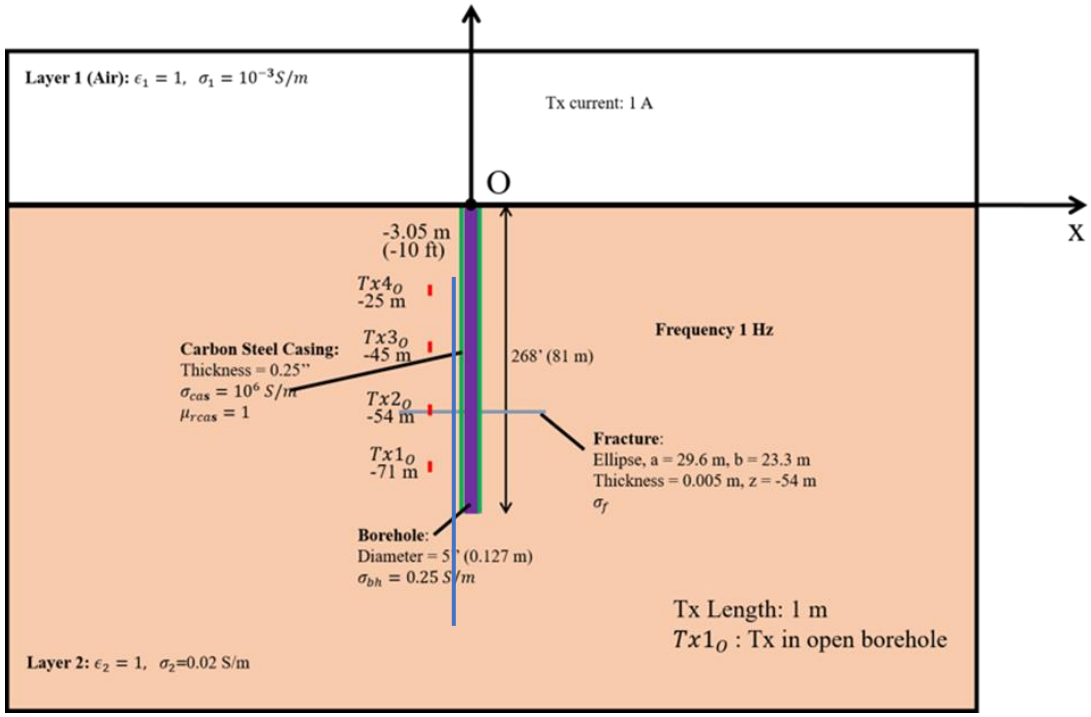

Figure 5-12: Devine configuration used for EM sensitivity analysis, with the position of transmitters (10 ft away from the injection borehole) shown in DMW 1.

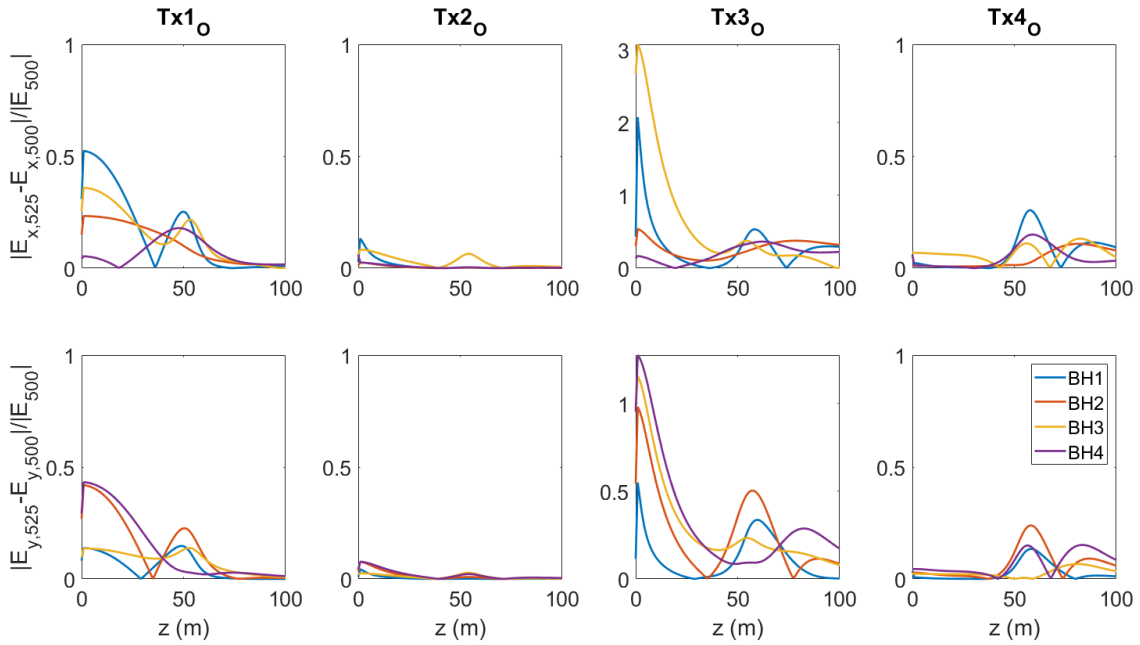

Figure 5-13: Sensitivity results of receivers in four observation boreholes with the transmitter dipoles set on DMW 1. The $Tx3_O$ configuration produced largest results of the three configurations of transmitters. Results in BH3 and BH4 are greater than 1%.

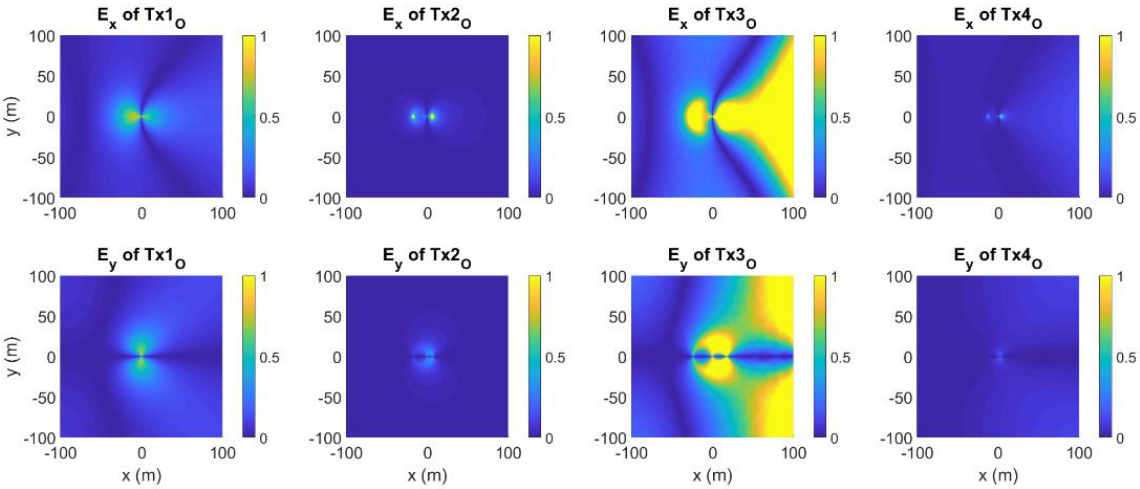

Figure 5-14: Sensitivity results of the surface receiver when the transmitters are set in the DMW 1, which is 10 ft away from the injection borehole. Similar to Figure 5-13, the configuration with $Tx3_O$ produced the largest results of the three configurations of transmitters. A large area of contrast on the surface is >1%.

Based on the results above, we can conclude that the configuration of $Tx3_O$ at z = −45 m has the highest EM sensitivity. In the next simulations, we studied the influence of transmitter length on EM sensitivity when each transmitter pair was centered at z = −45 m. The lengths of $Tx1_O$, $Tx2_O$, and $Tx3_O$ are 1 m, 10 m, and 30 m, respectively. The results of this test are shown in Figure 5-15 and Figure 5-16.

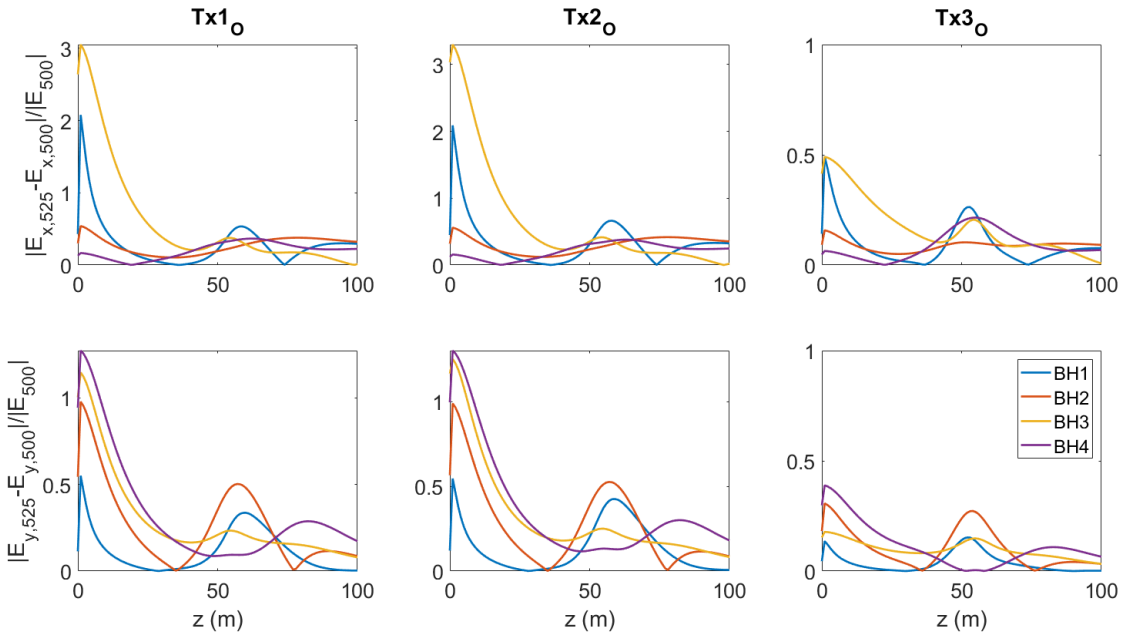

Figure 5-15: Sensitivity results of receivers in four observation boreholes in which different length transmitters are set in DMW 1, 10 ft away from the injection well and centered at z = −45 m. The configuration with $Tx1_O$ (1 m) and $Tx2_O$ (10 m) produced similar results, which are larger than those with $Tx3_O$ (30 m). Sensitivities in BH3 and BH4 are >1%.

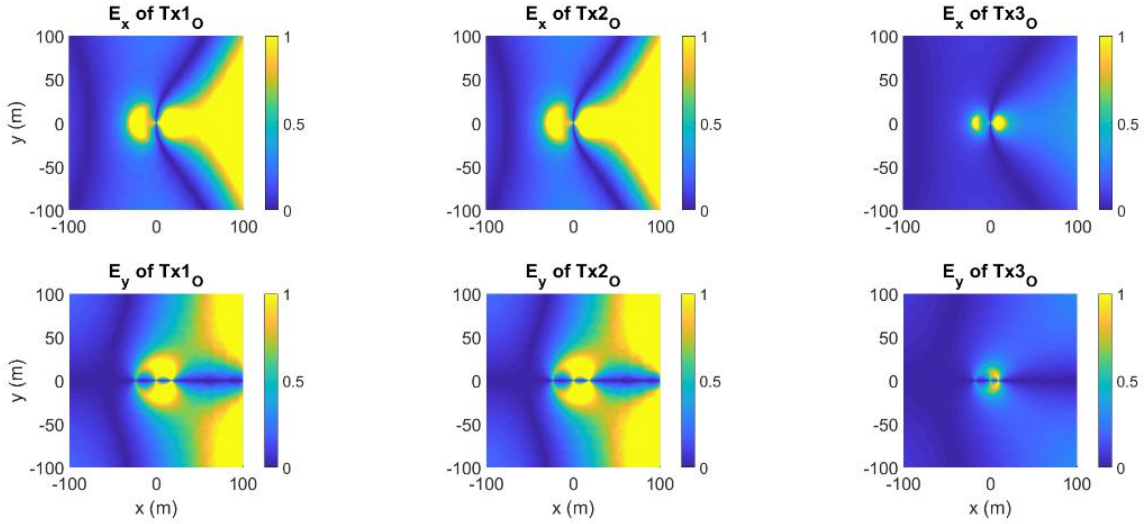

Figure 5-16: Sensitivity results of receivers in four observation boreholes in which the transmitters are set in DMW 1, 10 ft away from the injection well and centered at z = −45 m. The configuration with $Tx1_O$ and $Tx2_O$ produced similar results, which are larger than those with $Tx3_O$. As with Figure 5-15, a large area of surface results revealed a contrast >1%.

Based on the two studies above, we can conclude that when the transmitter is centered at z = −45 m, with the length between 1 m and 10 m, the EM results could produce sensitivities greater than 1%. Thus, through these simulations, we have shown that even a 5% change in conductivity of the EAP-filled fracture can result in a contrast in the signal greater than 1%.

The laboratory results at UNC and EM forward modeling results at Duke University suggested that we successfully met go-no-go criteria for BP1. Based on these results, in Q3BP1, we began engaging CSEM survey contractors and prepared preliminary efforts for field activities.

2020 experiment data interpretation and EM simulation

In the 2017 experiment, we performed EM sensitivity analysis under various surface and borehole electrode configurations. Here, we considered the borehole transmitter (BH-TXC) configuration that ESG used in the September 2020 deployment. Five of the existing electrical resistivity tomography (ERT) transmitter electrodes in DMW 1 were considered as transmitters (Tx1, Tx2, Tx3, Tx4 and Tx5) in our models. The depths of these transmitters are shown in Figure 5-17. We used the frequency of 2 Hz and the electric current of 1 A in the transmitters. Receivers were positioned on the ground surface (in a 200 m × 200 m grid).

The sensitivity to the fracture conductivity changes is defined as Equations (5-2), (5-3), and (5-4).

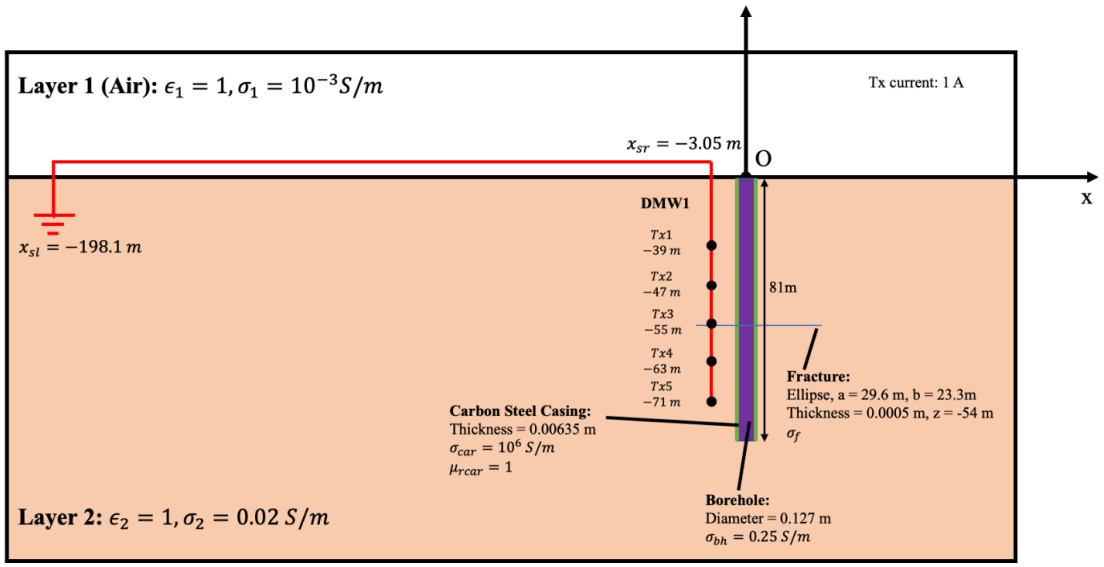

Figure 5-17: Devine configuration used for EM sensitivity analysis, with the position of transmitters (Tx), 3.05 m away from the injection borehole, shown in DMW 1.

The results of the test are shown in Figure 5-18 through Figure 5-23. The absolute amplitude of the primary field (total field at time zero, with $\sigma = 500\ S/m$), the absolute amplitude of the secondary field or scattered field (difference between the fields of $\sigma = 525\ S/m$ and $\sigma = 500\ S/m$), and the sensitivity are given based on different transmitter settings.

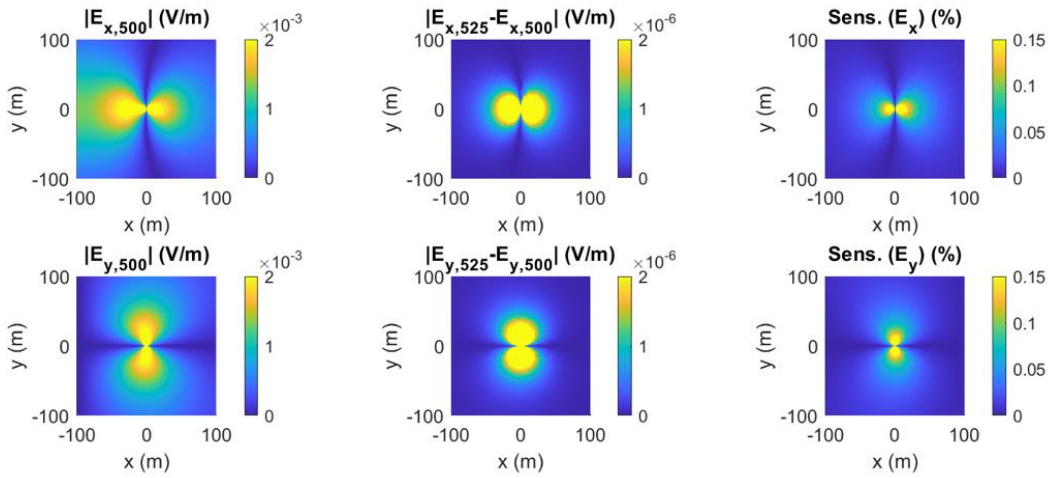

Figure 5-18: Sensitivity results of the surface receiver when only Tx1 is activated.

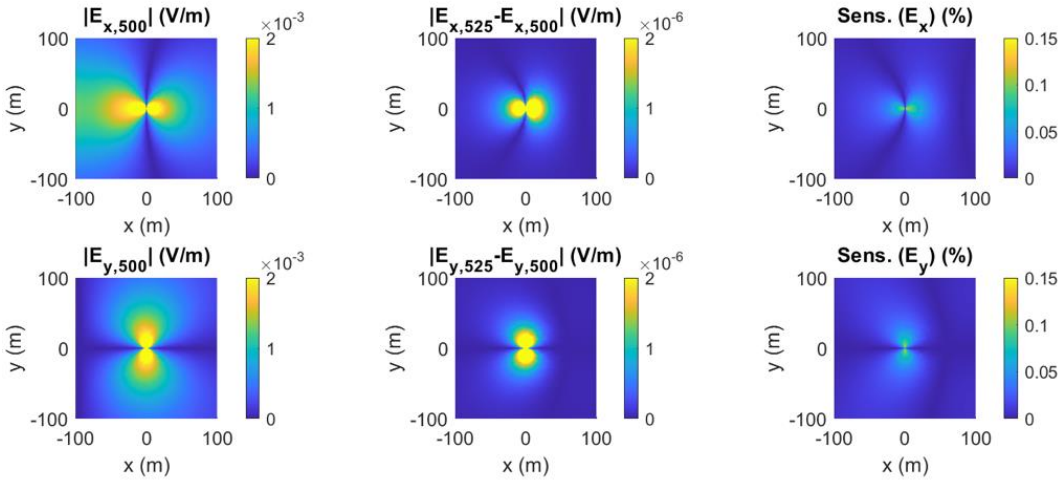

Figure 5-19: Sensitivity results of the surface receiver when only Tx2 is activated.

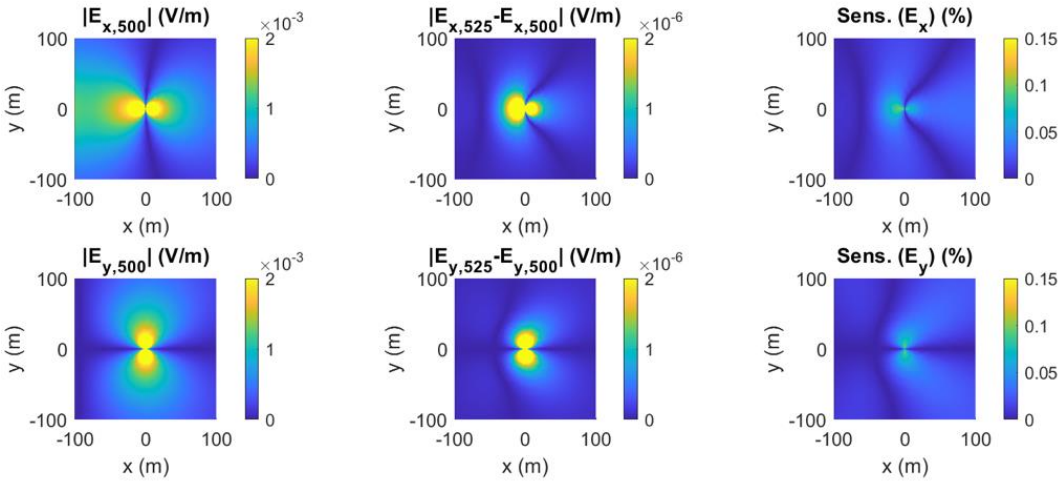

Figure 5-20: Sensitivity results of the surface receiver when only Tx3 is activated.

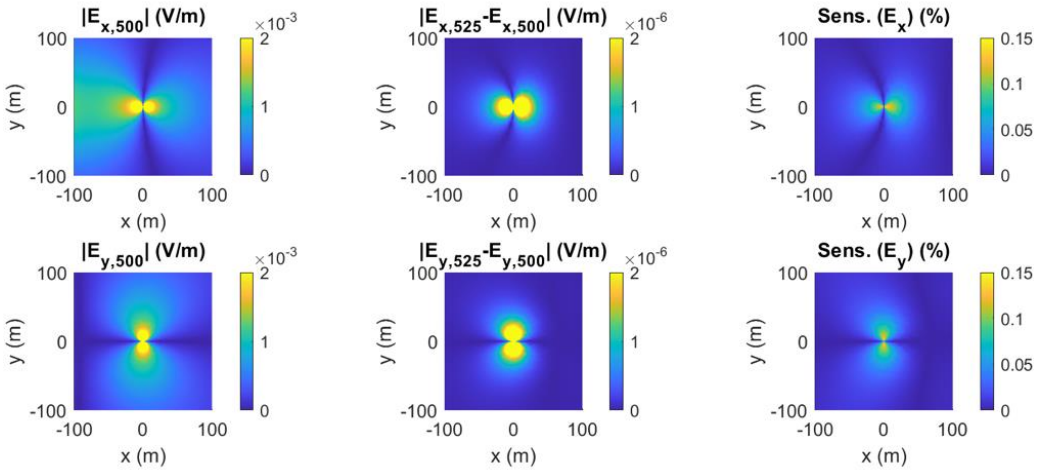

Figure 5-21: Sensitivity results of the surface receiver when only Tx4 is activated.

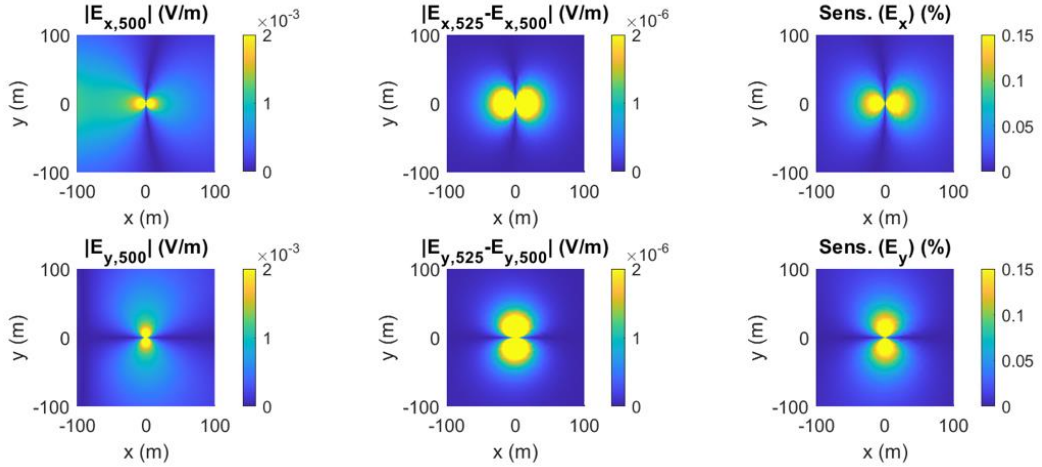

Figure 5-22: Sensitivity results of the surface receiver when only Tx5 is activated.

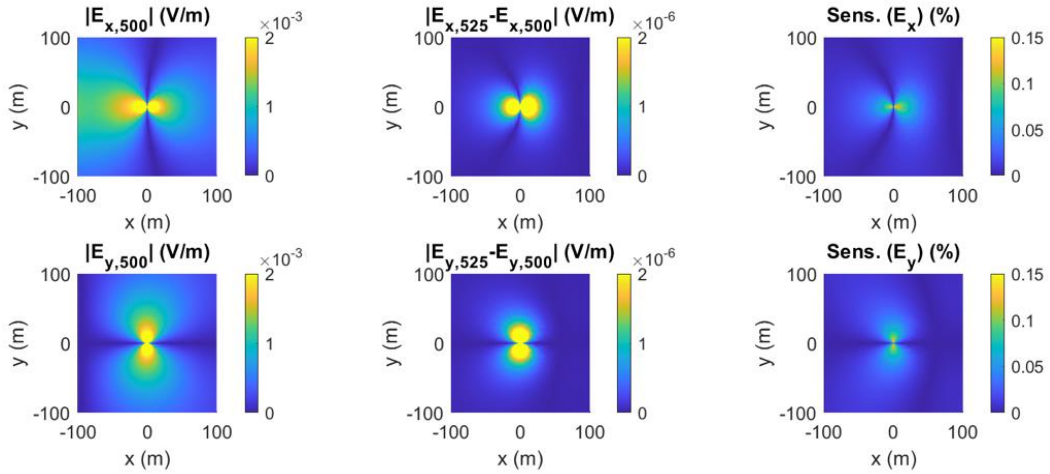

Figure 5-23: Sensitivity results of the surface receiver when 5 transmitters are activated together. Each transmitter current is 0.2 A in this case.

The activation of transmitter Tx5 only, located at z = −71 m in DMW 1, led to the most considerable sensitivity according to Equation (5-2). The actual experimental field data collected at the DFPS in 2020 indicated that smaller contrast values could be detected by the ESG's system. However, using a borehole transmitter was not pursued in the 2022 field deployment mainly because of interference of the transmitted current with the nearby receivers.

5.3 VSP/Seismic Sensitivity Analyses

To determine the feasibility of imaging a hydraulic fracture at the DFPS using seismic methods, synthetic modeling is necessary to investigate the sensitivity of field experiments. We performed a series of synthetic experiments with varying velocity models and acquisition parameters to analyze the seismic response of the fracture. For each experiment, we constructed two elastic velocity models. The first is called the background or baseline model, and corresponds to the subsurface before fluid is injected into the fracture. The second is called the fracture or monitor model, and corresponds to the subsurface after fluid injection when the fracture is maximally dilated. Seismic data simulated from both models were subtracted from each other to isolate the seismic response of the fracture, which was then analyzed for its sensitivity to fracture properties. These experiments using the synthetic velocity models showed that the seismic response of the fracture is significantly less than that of conventional reflectors, requiring SNRs of 50 to 60 dB for detection. To re-evaluate the seismic response of the fracture using field data, we conducted zero- and nonzero-offset VSPs at the DFPS (Appendix A.3) and simulated and imaged the acquired VSP data. In addition to re-confirming the required SNR of 50 dB for the fracture detection, these later results showed that the PS-wave reflections are more sensitive to the dilated fracture than PP-wave reflections, particularly at long offsets, which is useful in designing future experiments beyond the current project. The details of these modeling efforts and the outcomes are discussed in the following.

Thin Layer Experiment

Seismic velocities and densities in the model were determined from the Wilson-9 core measurements, and the values of these parameters are given in Table 5-3. We treated the fracture as a horizontal 1-cm-thick, graphite-filled region at 54-m depth (Zhernokletov et al., 2007). However, due to the small time step required and instability of seismic modeling on a 1-cm depth grid, we averaged the fracture properties over 25 cm in the depth direction. The fracture geometry is based on the actual footprint of an EAP-filled fracture at the DFPS. The resulting elastic models are 100 m wide by 70 m deep, with lateral sampling at 1 m and vertical sampling at 0.25 m, respectively. These velocity and density models yielded a laterally extensive horizontal reflector at a 44-m depth and a localized horizontal fracture at a 54-m depth, respectively. To reduce artifacts in the modeled seismic data, we applied a 0.25-m-radius smoothing filter in the vertical direction and 3-m-radius smoothing filter in the horizontal direction to the 2D velocity model. The resulting 2D velocity and density models are plotted in Figure 5-24. For clarity, Figure 5-25 shows the plan view of the seismic velocities and density at the fracture depth.

Table 5-3: Seismic velocities and densities used for modeling in the thin layer experiment.

Depth Interval	P Velocity (m/s)	S Velocity (m/s)	Density (kg/m^3)
0–44 m	1201	597	1730
>44 m	1936	1331	1990
1-cm fracture at 54 m	2540	1350	1700
25-cm fracture at 54 m	1959	1331	1978

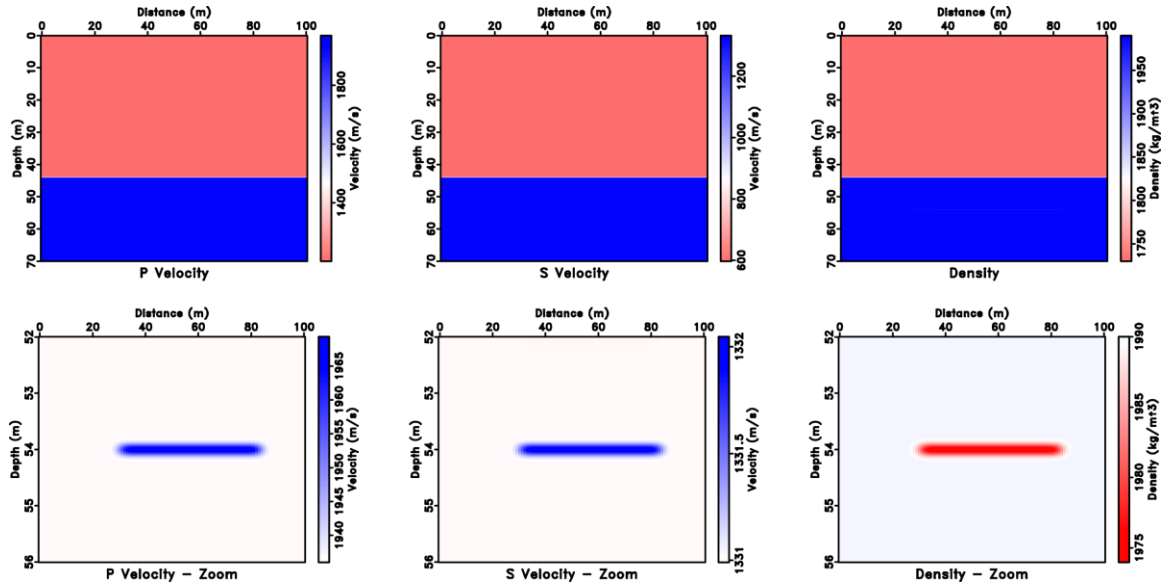

Figure 5-24: 2D seismic velocity and density models used for seismic modeling in the thin-layer experiment. The top row is the model vertical cross section (in the depth direction), and the bottom row shows the 25-cm-thick fracture over the vertical cross section of the model shown in Figure 5-25, at x=65 m, where x is the axis in east-west direction.

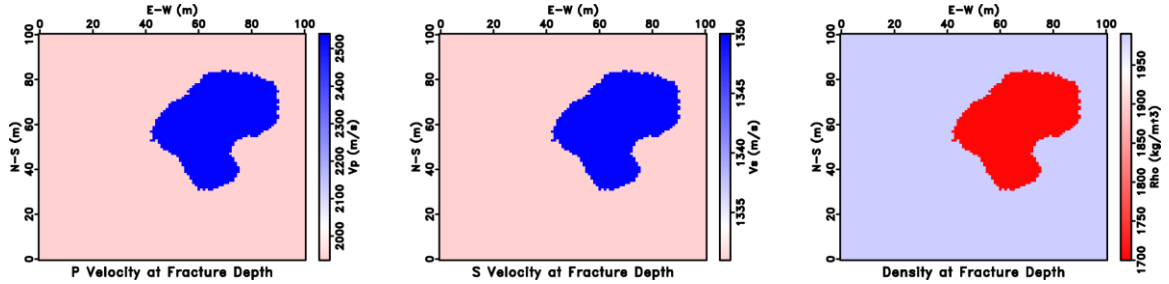

Figure 5-25: Seismic velocities and densities at the fracture depth, illustrating the fracture geometry.

We performed modeling using a vertical-component only Ricker wavelet with peak frequencies at 50, 100, and 200 Hz. Our experiment setup includes 101 receivers at 1-m spacing and a sampling rate of 10,000 Hz. Shot gathers are recorded for 0.2 s. To test the effects of noise contaminating the data, we first normalized the shot gathers, and then added mean-zero random noise with range of 0.05 and variance of 0.01. We tested the ability of stacking to increase the Signal-to-Noise Ratio (SNR) of the noisy data by simulating multiple shot gathers with differently-seeded random noise and summing the data across the shot axis. The number of shots stacked together, called the source stacking fold, were tested for 10-fold and 100-fold experiments.

Our results with the 50, 100, and 200 Hz source are plotted in Figure 5-26, Figure 5-27, and Figure 5-28, respectively. The reflection from the fracture can be seen clearly in the difference panel (top right plot) in all 3 figures. The amplitude response of the fracture is weakest for the 50 Hz source, and is subsequently stronger for the 100 and 200 Hz sources. In the noise-contaminated data, source stacking has significantly reduced the amplitude of the noise relative to the observed data. However, the difference panel of the noisy data shows that the noise conceals the fracture reflection for all 3 source peak frequency cases. Table 5-4 displays the SNR of the fracture response for varying source frequencies and source stacking fold. Given the current seismic velocity and density model parameters, this shows that the fracture may not be detectable if the noise amplitude is up to

5% the strength of the strongest reflector. However, this experiment is limited by the fact that we treated the fracture as a graphite layer averaged over a 25-cm grid cell instead of a ~1-cm thick fluid-filled fracture. We address this limitation in the next experiment with effective medium modeling.

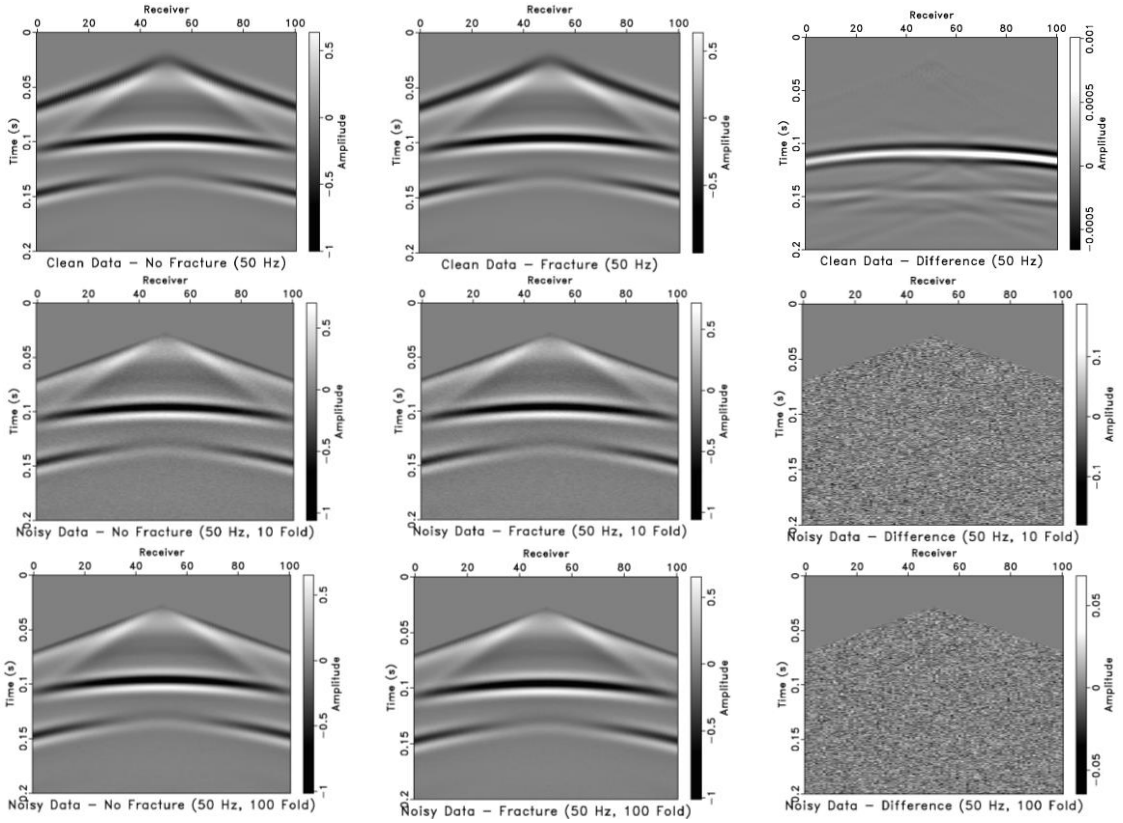

Figure 5-26: Seismic modeling results with 50-Hz source. (top row) Clean data; (middle row) noisy data with 10-fold stack; (bottom row) noisy data with 100-fold source stack.

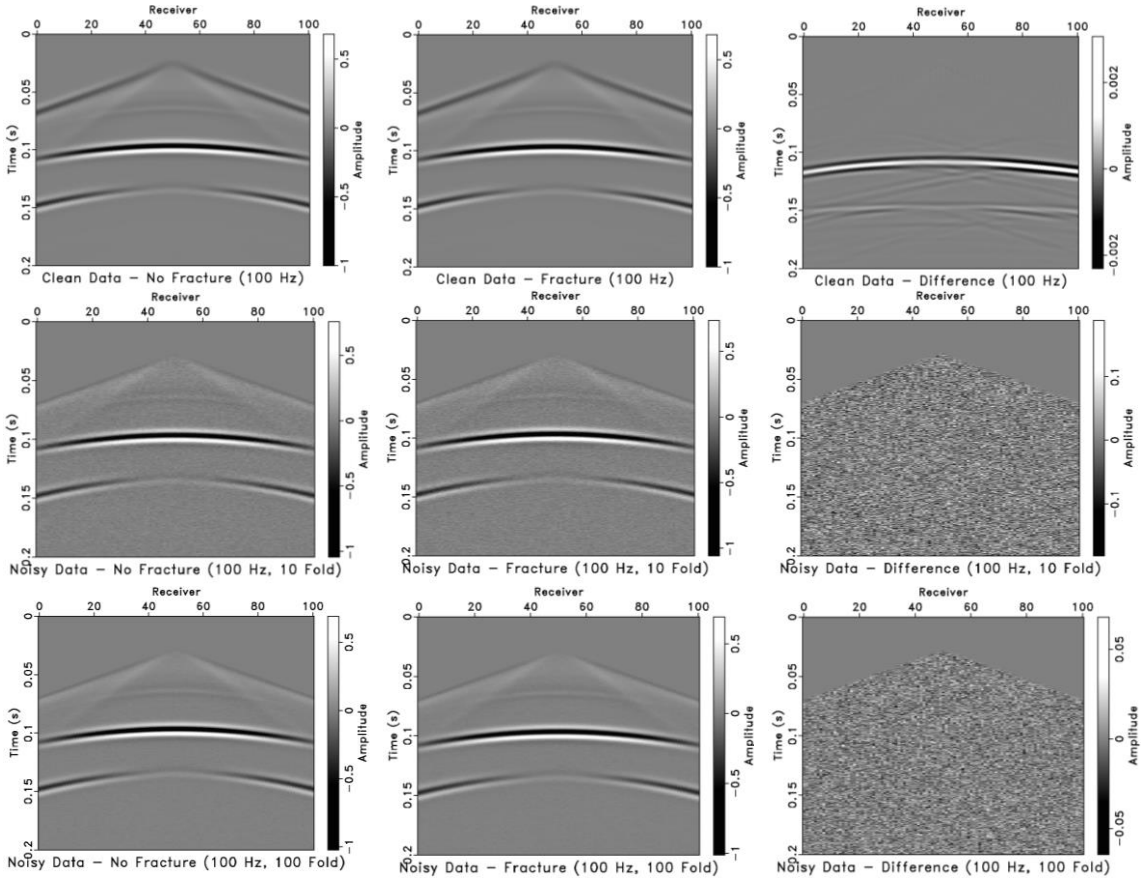

Figure 5-27: Seismic modeling results with 100-Hz source. (top row) Clean data; (middle row) noisy data with 10-fold stack; (bottom row) noisy data with 100-fold source stack.

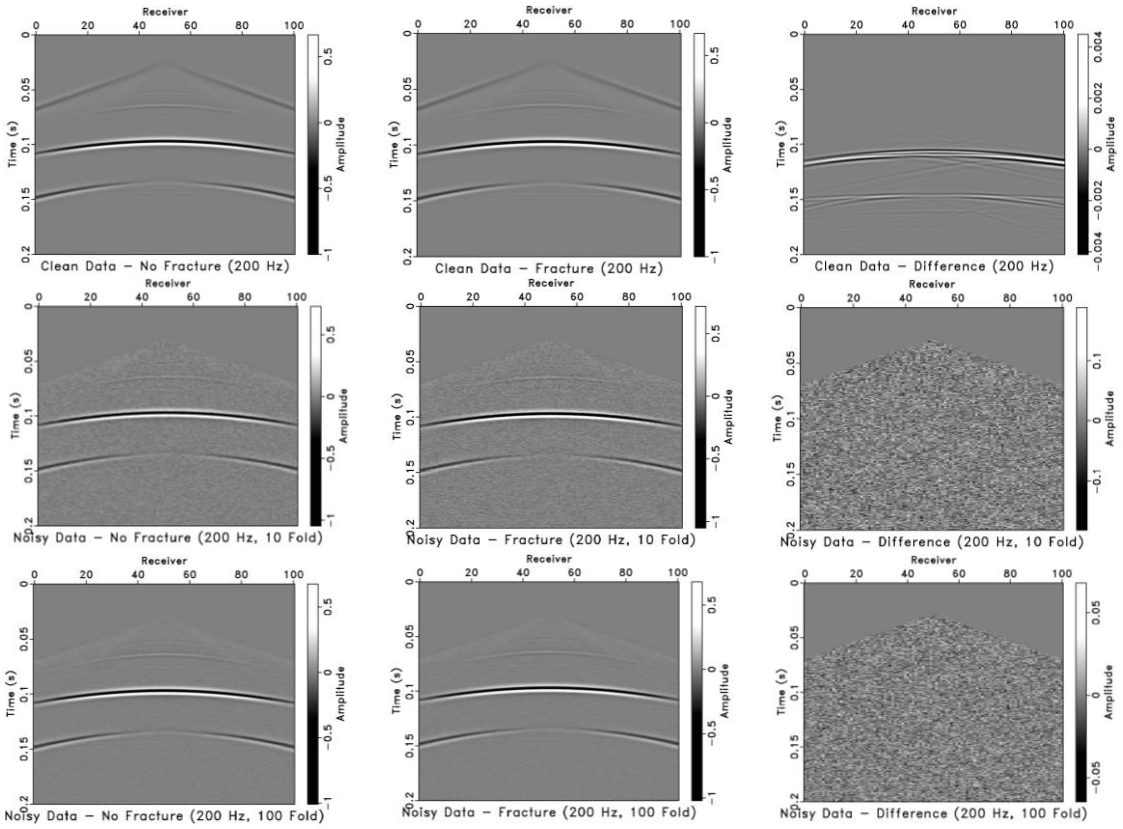

Figure 5-28: Seismic modeling results with 200-Hz source. (top row) Clean data; (middle row) noisy data with 10-fold stack; (bottom row) noisy data with 100-fold source stack.

Table 5-4: Signal-to-Noise Ratio (SNR) of thin layer modeling results.

Frequency (Hz)	Stacking Fold	SNR (dB)
50	10	-49.52
100	10	-44.35
200	10	-41.47
50	100	-39.53
100	100	-34.36
200	100	-31.48

Effective Medium Experiment

Effective medium theory enables modeling of the response of features smaller than the computational grid. We followed the additional compliance approach of Coates and Schoenberg (1995) in treating the fracture as an effective medium. The elastic stiffness tensor of an isotropic medium is given by

$$\boldsymbol{C}_b = \begin{bmatrix} M & \lambda & \lambda & 0 & 0 & 0 \\ \lambda & M & \lambda & 0 & 0 & 0 \\ \lambda & \lambda & M & 0 & 0 & 0 \\ 0 & 0 & 0 & \mu & 0 & 0 \\ 0 & 0 & 0 & 0 & \mu & 0 \\ 0 & 0 & 0 & 0 & 0 & \mu \end{bmatrix}, \tag{5-5}$$

where λ and μ are the Lamé parameters and M is equal to $\lambda+2\mu$. Equation (5-5) is the elastic stiffness of the background medium without the fracture. The fracture increases the compliance perpendicular to the fracture by the normal fracture compliance, Z_N, and parallel to the fracture by the tangential fracture compliance, Z_T. The elastic stiffness of the model cells intersected by the fracture are given by

$$\boldsymbol{C}_f = \begin{bmatrix} M(1-r^2\delta_N) & \lambda(1-r\delta_N) & \lambda(1-\delta_N) & 0 & 0 & 0 \\ \lambda(1-r\delta_N) & M(1-r^2\delta_N) & \lambda(1-\delta_N) & 0 & 0 & 0 \\ \lambda(1-\delta_N) & \lambda(1-\delta_N) & M(1-\delta_N) & 0 & 0 & 0 \\ 0 & 0 & 0 & \mu(1-\delta_T) & 0 & 0 \\ 0 & 0 & 0 & 0 & \mu(1-\delta_T) & 0 \\ 0 & 0 & 0 & 0 & 0 & \mu \end{bmatrix}, \tag{5-6}$$

where

$$r = \frac{\lambda}{M}, \tag{5-7}$$

$$\delta_N = \frac{Z_N M}{L + Z_N M}, \tag{5-8}$$

and

$$\delta_T = \frac{Z_T \mu}{L + Z_T \mu}. \tag{5-9}$$

Here, L is the length of the fracture inside a given cell. Equations (5-5) and (5-6) allow us to perform effective medium modeling with a thin (millimeter-scale) fracture.

To evaluate the seismic response of the fracture with different inputs, we vary three parameters in our experiments: fracture width, Z_N/Z_T ratio, and source peak frequency. The values used in our experiments are given in Table 5-5.

Table 5-5: Parameters varied in seismic modeling for effective medium experiment.

Parameter	Value
Fracture width (mm)	1, 2, 5, 10, 20
Z_N/Z_T	0, 0.1, 0.2, 0.3, 0.4, 0.5
Source peak frequency (Hz)	20, 30, 40, 50, 60, 70, 80, 90, 100

For a given fracture width, Z_N is equal to f_w/K_{fluid}, where f_w is the fracture width, and K_{fluid} is the bulk modulus of the fluid inside the fracture (Wu et al., 2005; Titov et al., 2019). We assumed K_{fluid} of 2.25 GPa, and the bulk modulus of water. We can assign values to Z_T using the Z_N/Z_T ratio. For a dry, gas-filled fracture, Z_N/Z_T is equal to $1-\nu/2 \approx 1$, where ν is the Poisson's ratio of the medium

surrounding the fracture (Binder et al., 2020). For a fluid-filled fracture with no traction along the interface, Z_N/Z_T converges to 0. While an open, fluid-filled fracture is expected to have a low value of Z_N/Z_T (Verdon and Wüstefeld, 2013), Z_N/Z_T ratios can vary widely, which is why we test the values given in Table 5-5. The grid spacing of the model, L, is equal to 25 cm, for all cells in the presence of the fracture.

We used the same background velocities and densities from two-layer model in the thin-layer experiment (Table 5-3). One component of the elastic stiffness tensor is plotted for the background model and a fractured model in Figure 5-29. The grid spacing of the velocity and density models is 25 cm. 101 receivers are assumed on the ground surface at 1-m intervals starting at x=0. Total recording time is 0.25 s and the time step is 5×10^{-5} s. Our source is a Ricker wavelet located at x = 50 with the varying peak frequency between 20 and 100 Hz (Table 5-5). Field tests suggest that the simulated source, a Betsy seisgun, can generate reflections in the 20 to 70 Hz frequency range (Varsek and Lawton, 1985a,b).

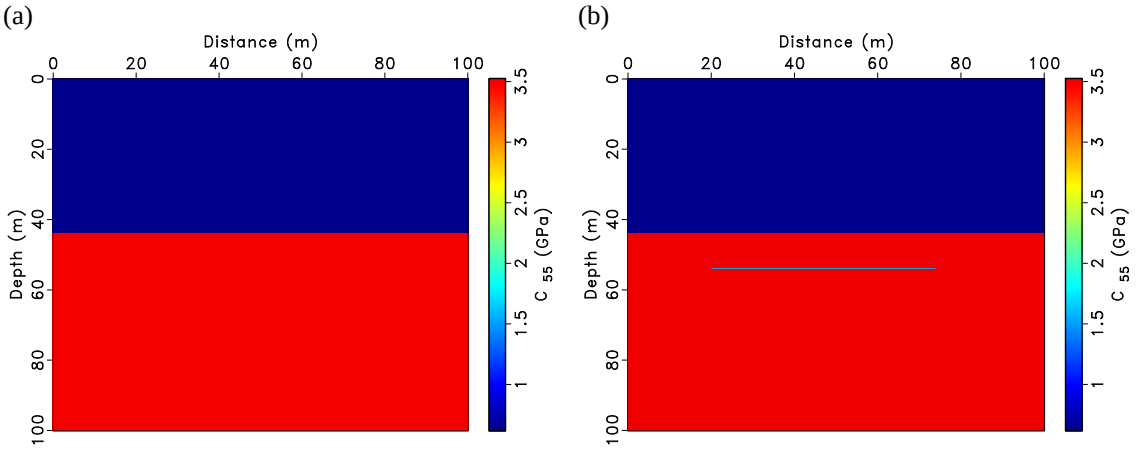

Figure 5-29: Values of the C_{55} component of the elastic stiffness tensor for (a) the background model and (b) a model in the presence of a fluid-filled fracture. The fracture is 20 mm wide and Z_N/Z_T is equal to 0.1.

To evaluate the strength of the fracture seismic response, we treated the scattered field from the fracture as signal and the scattered field from the reflector at z=44 m as noise and calculated the corresponding SNR. The resulting SNRs are plotted in Figure 5-30 as functions of fracture width, Z_N/Z_T ratio, and source peak frequency. Figure 5-30 shows that the fracture response is greatest for larger fracture widths, lower Z_N/Z_T ratios, and higher peak frequencies. In the idealized case of Z_N/Z_T of 0 (Figure 5-30a), the fracture response is independent of fracture width and SNR is relatively high; however, in all other cases, the fracture response is at least 30 dB weaker than that of the reflector at z=44 m.

We plotted the seismic data of one experiment in Figure 5-31. The chosen experiment has parameters that could be reasonably expected in the field resulting in one of the strongest modeled fracture responses. Figure 5-31 shows that the fracture contribution to the total scattered field is negligible.

To examine the fracture response in the presence of noise, we added Gaussian noise such that the recorded data have an SNR of 60 dB. The scattered field and its components are plotted in Figure 5-32. The noise level is very low relative to the reflection, but has a significant imprint on the fracture response.

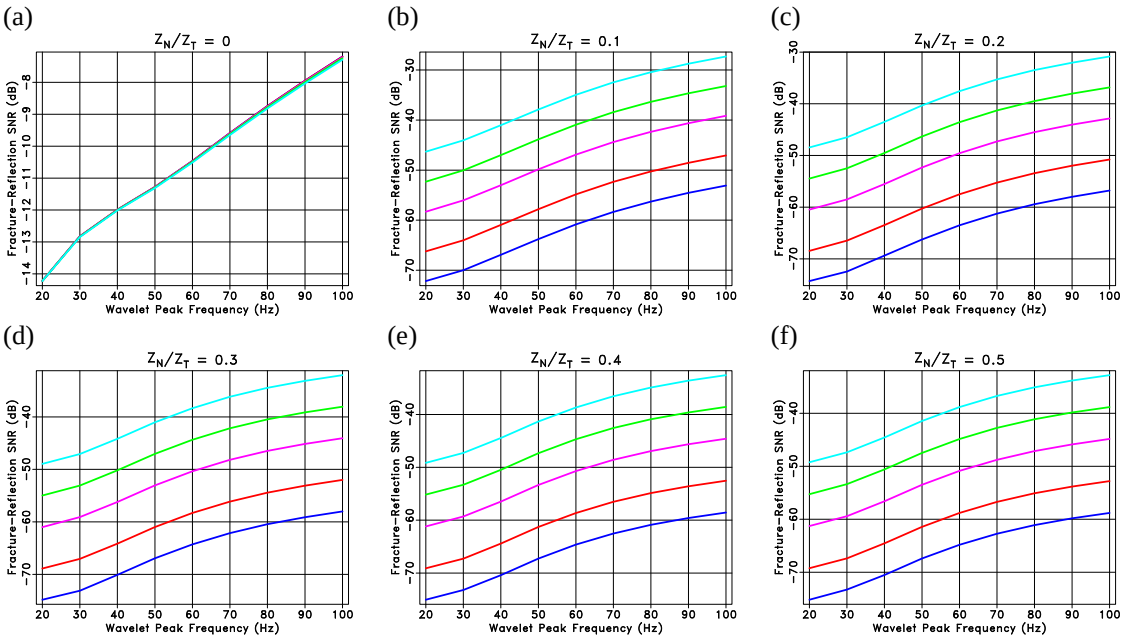

Figure 5-30: Fracture response strength relative to response of the reflector at z=44 m as a function of source peak frequency for various ratios of ZN and ZT. Results are for fracture widths of 1 mm (blue), 2 mm (red), 5 mm (magenta), 10 mm (green), and 20 mm (cyan).

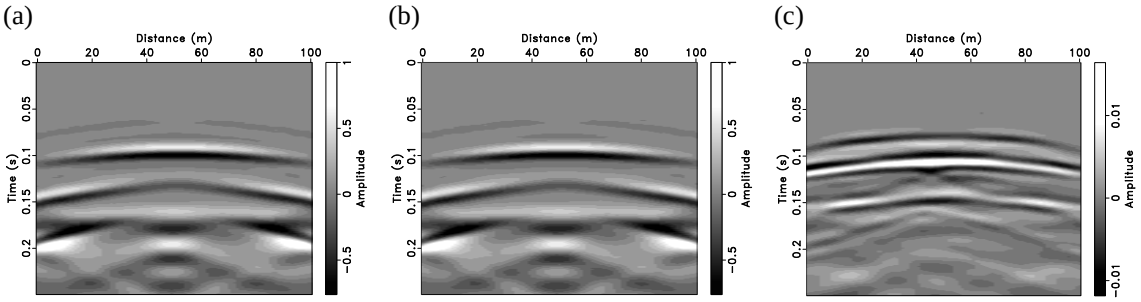

Figure 5-31: Seismic modeling results for a fracture width of 20 mm, ZN /ZT = 0.1, and a source peak frequency of 50 Hz. (a) Total scattered field. (b) Scattered field from reflector. (c) Scattered field from fracture.

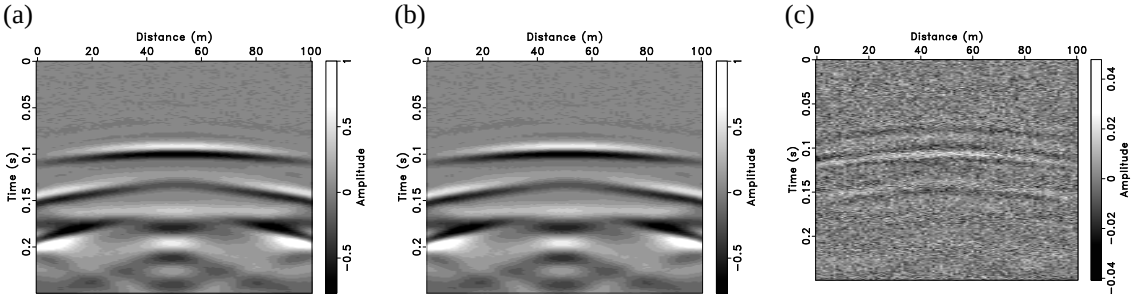

Figure 5-32: Same as Figure 5-31 but with the added Gaussian noise. The noise level is set such that the total recorded shot gather (not shown here) has an SNR of 60 dB.

The results of the effective medium experiment suggest that the fracture response is at least 30 dB weaker than that of the reflector at z=44 m, and an SNR of at least 60 dB is likely necessary to image the fracture.

Pore Pressure Experiment

In the previous experiment, we treated the fracture as an effective medium to overcome the difficulties of seismic modeling with a millimeter-scale feature; however, the seismic response of the fracture in this regime was too small to be reliably detectable. With the availability of pore pressure simulations and geomechanical data from the Wilson-9 well (Gonzalez et al., 2016), we evaluated the effect of variations in effective confining pressure in the vicinity of the fracture on the seismic velocities and seismic responses.

We first established a relationship between seismic velocity and effective confining pressure based on core plug measurements from the Wilson-9 well. We averaged the P- and S-wave velocities of the Wilson-9-7V and Wilson-9-13V core plugs and fit a quadratic polynomial to the data, as shown in Figure 5-33. The corresponding P- and S-wave velocities as functions of effective confining pressure, P_{eff}, are given by

$$V_P(P_{eff}) = 1898 + 0.554P_{eff} - 0.0001399P_{eff}^2, \quad (5\text{-}10)$$

$$V_S(P_{eff}) = 1312 + 0.33P_{eff} - 0.0000909P_{eff}^2 \quad (5\text{-}11)$$

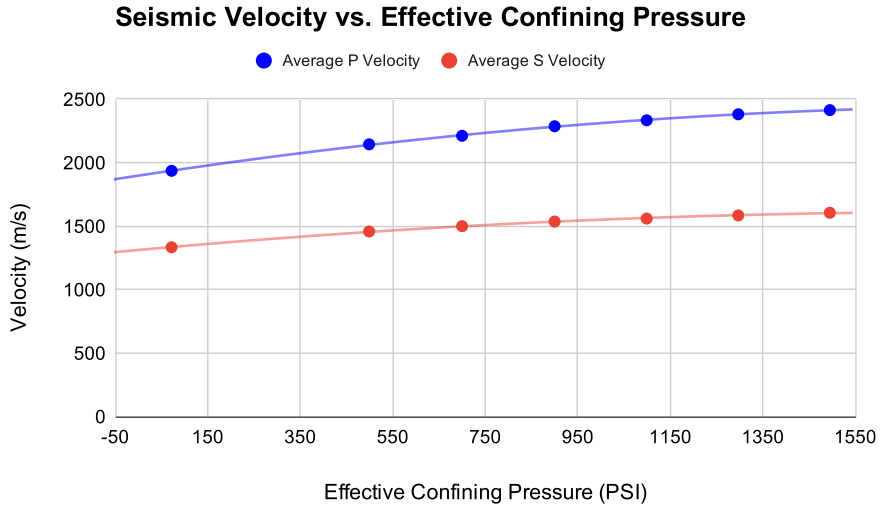

Figure 5-33: Average seismic velocities of Wilson-9-7V and Wilson-9-13V core plugs with respect to effective confining pressure with quadratic polynomial fit.

Given that the in-situ effective confining pressure at the fracture interval is 157.5 psi, we used these equations to calculate the P- and S-wave velocities of the consolidated sand below 44-m depth. The seismic velocities of the interval shallower than 44-m depth are based on the unconsolidated sand model used in previous experiments (Table 5-3). Figure 5-34 displays the two-layer background model used for seismic modeling (i.e., the model in the absence of the fracture).

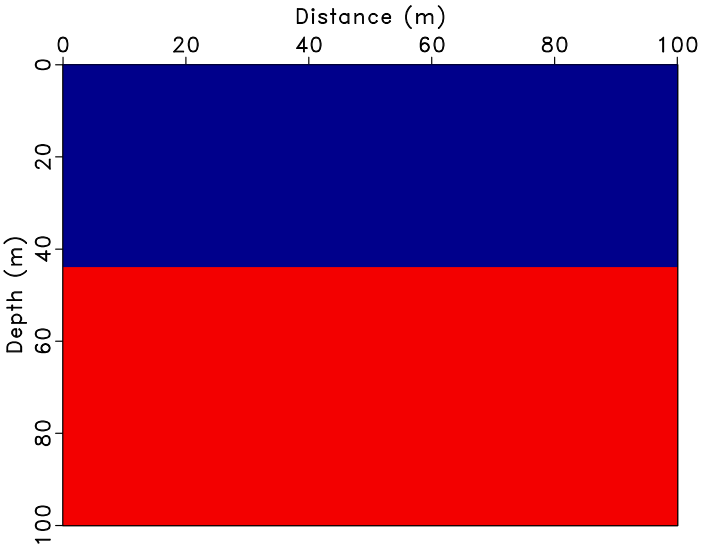

Figure 5-34: Seismic velocities and densities for the background model.

We assumed that the excess pore pressure in the background model is zero, which results in the total confining pressure equal to the effective confining pressure. Since the effective confining pressure is equal to the total confining pressure minus pore pressure, P_{pore}, the change in seismic velocity in the vicinity of the fracture as a function of pore pressure is given by

$$\Delta V_P\left(P_{pore}\right) = -83.78 + 0.554\left(157.5 - P_{pore}\right) - 0.0001399\left(157.5 - P_{pore}\right)^2, \quad (5\text{-}12)$$

$$\Delta V_S\left(P_{pore}\right) = -49.72 + 0.33\left(157.5 - P_{pore}\right) - 0.0000909\left(157.5 - P_{pore}\right)^2. \quad (5\text{-}13)$$

Then, we utilized pore pressure simulation data to calculate changes in seismic velocity at the fracture. Figure 5-35 gives our calculated values of P- and S-wave velocities, and Figure 5-36 shows a velocity and reflectivity profile at x=50 m. The increase in pore pressure in the vicinity of the fracture creates a drop-in velocity in a 2-m thick rock volume centered at the fracture depth.

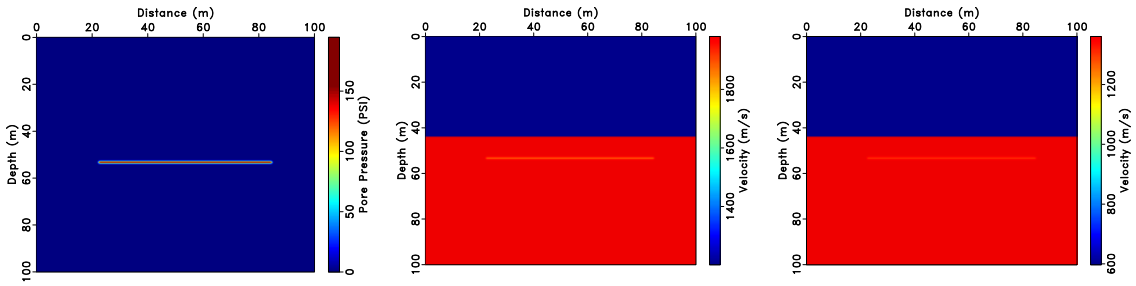

Figure 5-35: Pore pressure (left) and corresponding P- and S-wave velocities (center, right) for the fracture model.

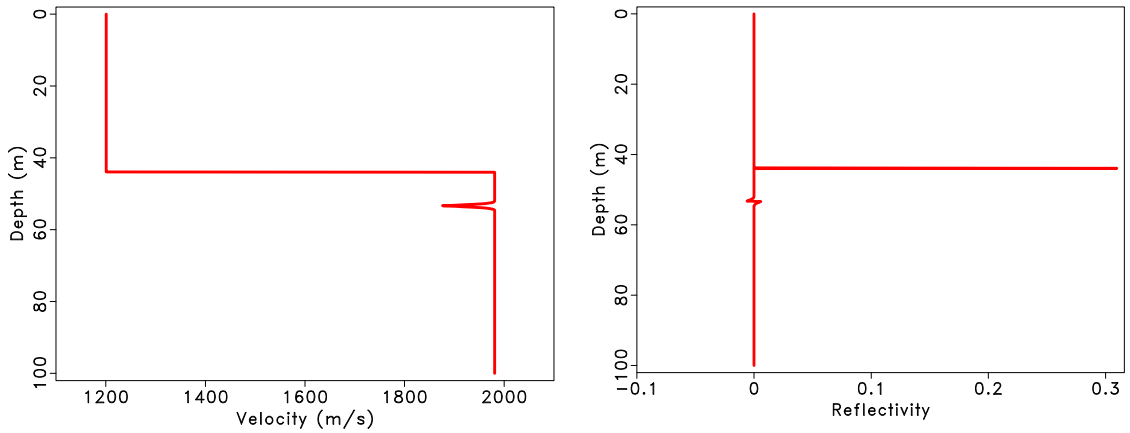

Figure 5-36: (left) P-wave velocity profile; (right) zero-offset P-wave reflectivity profile; both at x=50 m.

Because three of the existing observations wells at the DFPS are equipped with a functioning DAS fiber, we next performed seismic modeling with a Vertical-Seismic-Profile (VSP) configuration and a small receiver spacing to mimic a potential DAS acquisition. The source is a Ricker wavelet with 50 Hz peak frequency and is located at (x,z) = (25,0) m. 1001 receivers are located at x=50 m with 0.1-m depth spacing from 0 to 100 m. We generated a shot gather for both the background model and the fracture model and took the difference between them to isolate the fracture response. Figure 5-37 displays our modeling results. The layer interface at 44-m depth is clearly visible with P-wave and S-wave reflections, transmissions, and mode conversions present in the left and center panels. Subtracting the background model shot gather from the fracture model shot gather yields the fracture response in the right panel of Figure 5-37. While reflections, transmissions, and mode conversions due to the fracture are present, their seismic response is considerably weaker than that of the reflector at z=44 m. Overall, the fracture response is 54 dB weaker than that of the fracture model shot gather. Figure 5-38 is the same as Figure 5-37 with the exception that Gaussian noise has been added such that the fracture model shot gather has an SNR of 50 dB. The noise in the background and in the fracture-model shot gathers is negligible but is significant in the fracture response. Based on these findings, it appears that an SNR of at least 50 dB is necessary to detect the fracture.

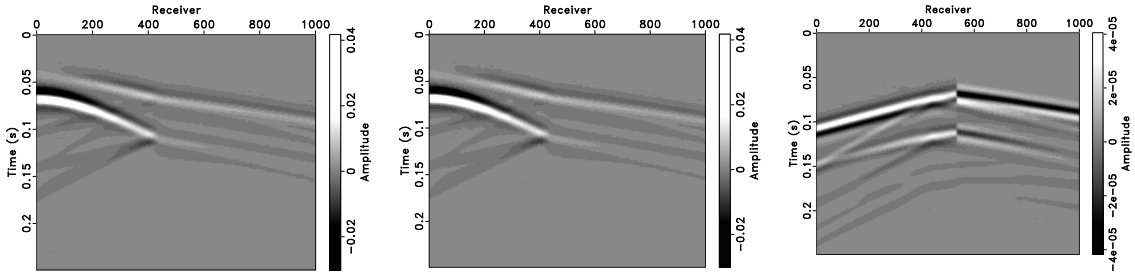

Figure 5-37: Vertical component of VSP shot gather of background model (left), fracture model (center), and the difference between them (right).

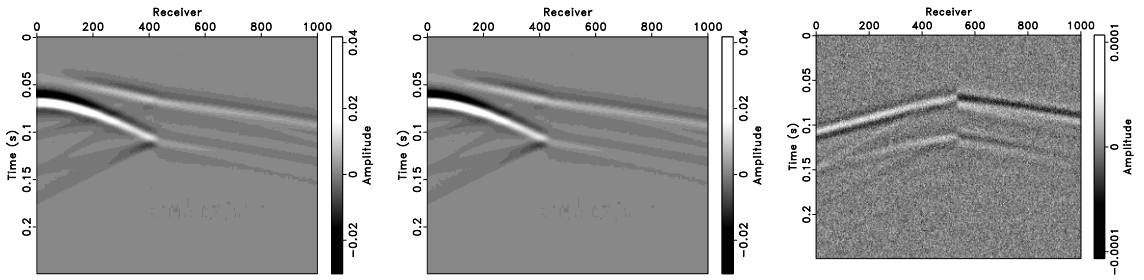

Figure 5-38: Vertical component of VSP shot gather of background model (left), fracture model (center), and the difference between them (right) with added noise. Noise level is set such that the fracture model has 50 dB SNR.

Combined Effective Medium and Pore Pressure Experiment

In the previous seismic experiments, we utilized a simple two-layer model to generate synthetic seismic data. For our final seismic experiment, we acquired three zero-offset VSPs at the DFPS using fiber optic cables and estimated a 1D velocity profile based on first arrival picks. We then modeled the elastic effects of fracture dilation on this new velocity model using both the additional compliance and increased pore pressure approaches from the previous two experiments. Finally, we imaged synthetic elastic walkaway VSP data from two acquisition layouts to evaluate the effect of the acquisition parameters on the image quality.

In May 2021, we contracted Silixa for a deployment to the DFPS to acquire zero-offset DAS VSPs at the east, north, and west wells instrumented with fiber optic cables. These VSPs and the velocity profiles corresponding to their picked first P-wave arrivals are plotted in Figure A3-9, Figure A3-10, and Figure A3-11. From the first arrival picks, Silixa estimated a single 1D velocity model that minimized travel-time misfit for the east, north, and west wells. This optimized velocity model is plotted in Figure A3-12.

To simulate acquiring and imaging data from a time-lapse VSP at the DFPS, we generated three different datasets based on changes in the elastic properties of the fracture before and after fluid injection. The datasets are:

(1) baseline dataset, which simulates a seismic dataset acquired prior to fluid injection;
(2) monitor dataset, which simulates a seismic dataset acquired after fluid injection and when the fracture is at maximum dilation; and
(3) monitor dataset minus baseline dataset, which isolates the scattered field caused by the fracture at maximum dilation.

The third dataset is the primary dataset used as input for imaging. Fracture dilation changes the elastic properties of the subsurface, which in turn creates the differences between the baseline and monitor datasets. Therefore, two elastic parameter models (P-wave velocity, S-wave velocity, and density) are necessary for generating the baseline and monitor data. The P-wave velocity of the baseline model was taken from the velocity profile obtained in Figure A3-12. We used a P-to-S-wave velocity ratio of 1.5, based on measurements on core plugs at the DFPS (Gonzalez et al., 2016), to construct the baseline S-wave velocities. Baseline density was constructed using Gardner's relation (Gardner et al., 1974).

The elastic parameters for the monitor model are the same as those of the baseline model except at the fracture location. Here, we combined the additional compliance approach in the effective medium experiment and the effective stress-velocity relation in the pore-pressure experiment to model elastic changes caused by fluid injection into the fracture. The parameters are the same as

those in the previous experiments. The elastic parameter models used to generate the baseline and monitor datasets are plotted in Figure 5-39 and Figure 5-40, respectively.

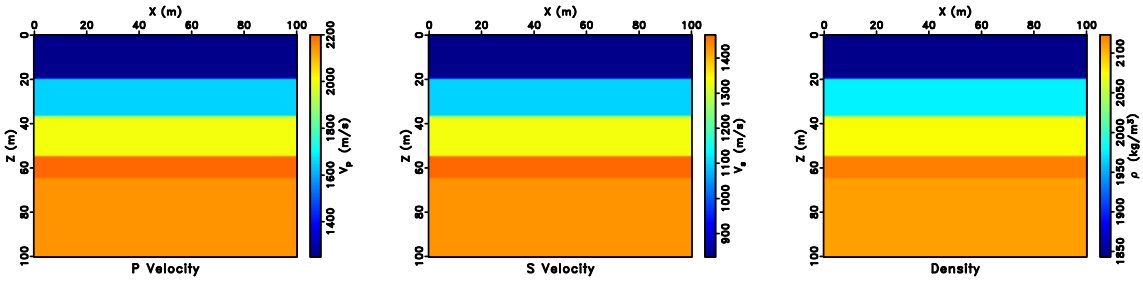

Figure 5-39: The elastic parameter model, used to generate the baseline dataset.

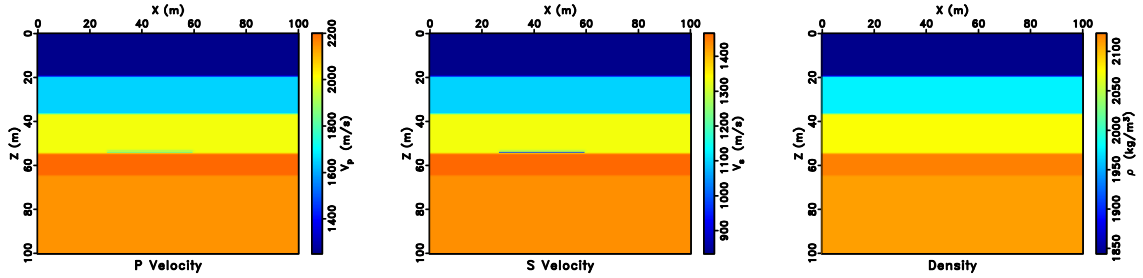

Figure 5-40: The elastic parameter model, used to generate the monitor dataset. Note the decrease in P- and S-wave velocities at Z=54 m caused by the dilated fracture.

We also tested the effect of varying source coverage to compare seismic acquisition under ideal conditions and seismic acquisition constrained by concurrent EM acquisition. Additionally, the limited time that the fracture remains dilated may further constrain the number of sources we could acquire in the monitor survey. The acquisition layouts are plotted in Figure 5-41. In the full coverage experiment, 56 sources are placed at 2-m intervals from X=0 to X=110 m. In the limited coverage experiment, 13 sources are placed at 2-m intervals from X=0 to X=24 m, meaning short-offset sources are not present in these data. We simulated DAS acquisition by recording the vertical component of the wavefield at the east-well approximate location at 1-m intervals from Z=0 to Z=100 m. To approximate acquisition with a small vibroseis capable of generating high frequencies, we used a vertical acceleration Ricker wavelet with a peak frequency of 180 Hz for seismic modeling.

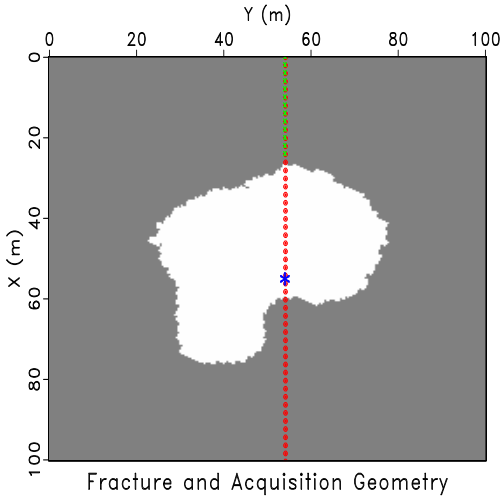

Figure 5-41: Source and receiver locations overlying the fracture footprint in map view. Red dots and green x's indicate source locations for the full- and limited-coverage experiments, respectively. The blue star is the approximate location of the east well, where the wavefield is recorded at 1-m depth intervals.

Once the data were generated, data processing prior to imaging consisted of an amplitude gain to correct for geometric spreading and filtering in the frequency-wave-number domain to isolate the upgoing component of the wavefield. Shot gathers before and after processing are plotted in Figure 5-42.

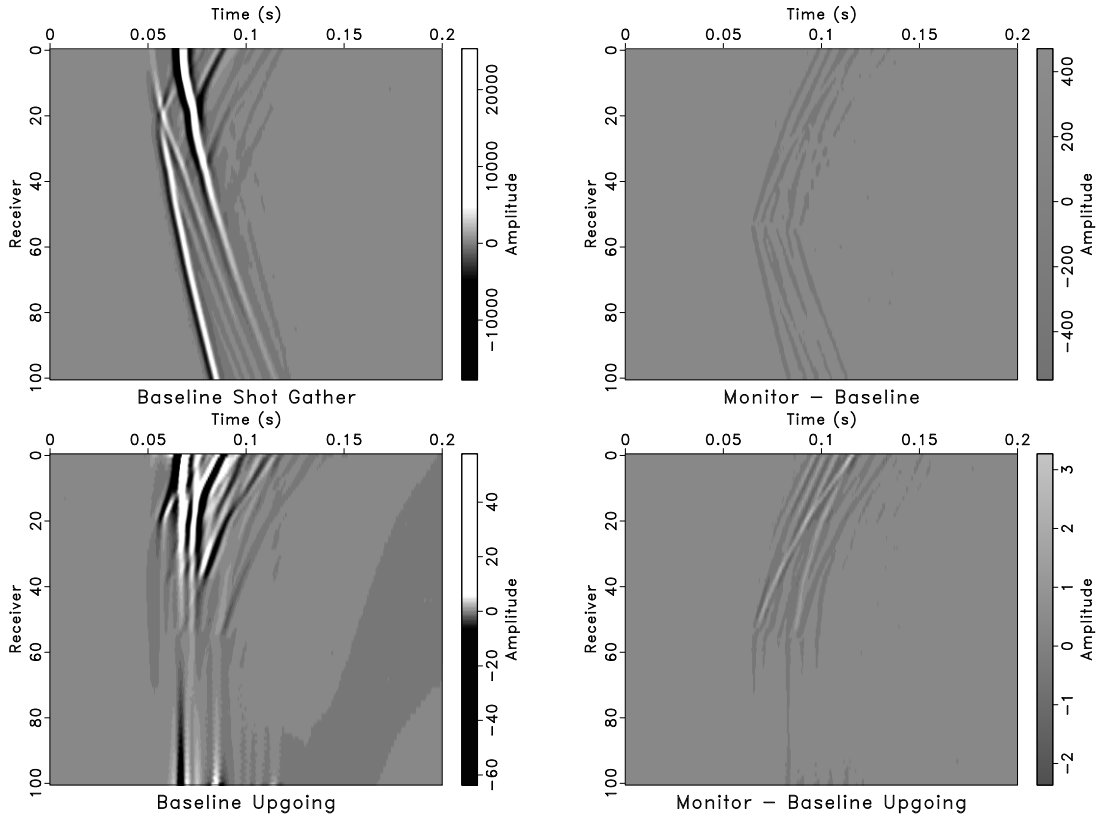

Figure 5-42: Selected shot gathers from a source at X=20 m before (top row) and after (bottom row) data processing. The left column is from the baseline dataset and the right column is from the monitor dataset minus the baseline dataset.

To image the processed data using elastic Reverse Time Migration (RTM), the source and reflected wavefields must be decomposed into P- and S-wave modes. We used the Helmholtz decomposition to separate an input wavefield into its corresponding curl-free P- or divergence-free S-wave mode (Yan and Sava, 2008). The image output by the elastic RTM is then given by

$$I_{ij}(x,z) = \sum_t D_i(x,z,t) U_j(x,z,t), \tag{5-14}$$

where D is the source wavefield, U is the reflected wavefield, and $i,j = P,S$ indicate the wave mode being imaged. In this manner, we imaged the P-to-P (PP) reflections, I_{PP}, and the P-to-S (PS) reflections, I_{PS}, for each dataset.

We first qualitatively analyzed the images obtained from the monitor data minus the baseline data. We focused on this dataset because it recorded the scattered field created by the dilated fracture, and therefore contained the portion of the wavefield we were most interested in. The PP and PS images for the full- and limited-source coverage experiments are given in Figure 5-43 and Figure 5-44, respectively.

In the full-coverage PP image (left side of Figure 5-43), a positive amplitude (white) sub-horizontal event coincides with the fracture location, suggesting that the fracture is well imaged in this experiment. Conversely, in the limited-coverage PP image (right side of Figure 5-43), amplitudes are smeared about an elliptic shape and the fracture location intersects both positive and negative (black) amplitudes. The misplacement of the fracture reflection in the limited coverage experiment suggests that accurate imaging of PP reflections depends upon recording data from short-offset sources. A possible explanation for this is the fact that P-wave particle motion is parallel to the direction of wave propagation and DAS only records strain in the direction of the fiber optic cable, which is vertical in this case. At short offsets, reflected P-waves travel nearly vertical, and so are well recorded by the DAS receivers. At longer offsets, reflected P-waves deviate from the vertical direction, making the DAS receivers less sensitive to their presence.

The PS images from both experiments (Figure 5-44) appear quite similar, with a positive amplitude horizontal event coinciding with the fracture location to the left of the fiber optic cable. The primary difference between the image of the fracture from the full and limited coverage PS experiments appears to be migration artifacts in the full coverage image introduced by sources on the right side of the fiber optic cable. The similarity between the PS images in Figure 5-44 suggests that imaging PS reflections from the fracture is robust in the absence of short-offset sources. This may make PS imaging more suited to imaging the fracture than PP imaging when field constraints may limit the number of sources and prohibit short-offset data.

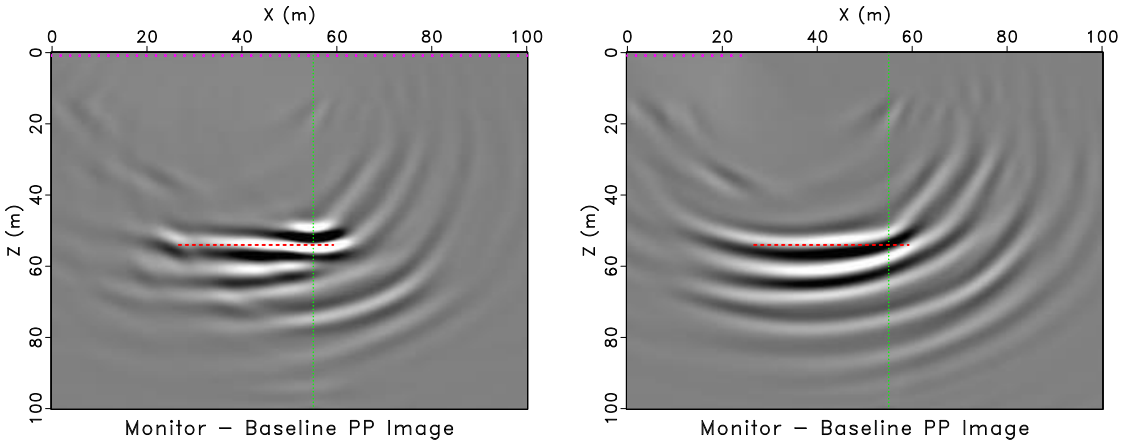

Figure 5-43: PP images of the monitor dataset minus the baseline dataset for the full coverage (left) and limited coverage (right) experiments. The horizontal red dashed line indicates the fracture location, the vertical green dotted line indicates the DAS receiver line, and magenta x's at the ground surface indicate source locations.

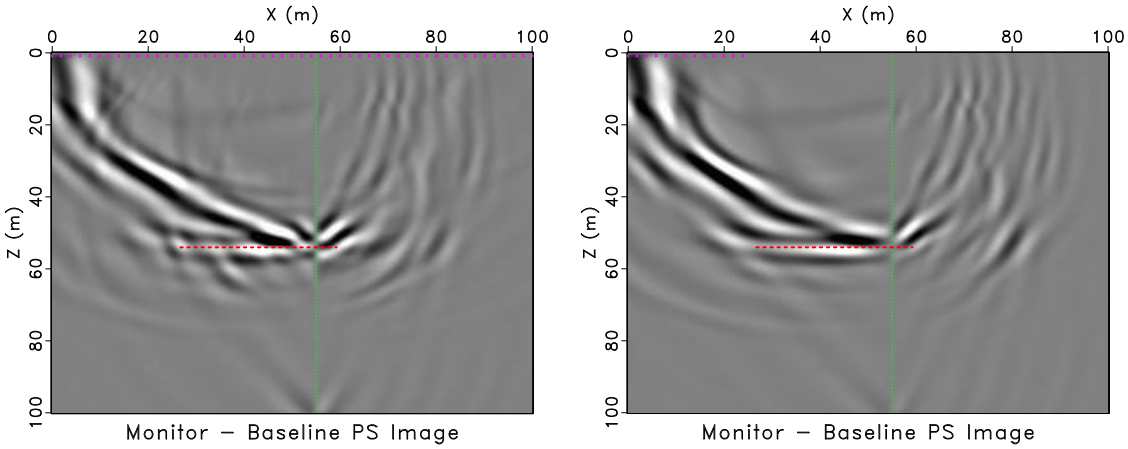

Figure 5-44: PS images of the monitor dataset minus baseline dataset for the full coverage (left) and limited coverage (right) experiments. The horizontal red dashed line indicates the fracture location, the vertical green dotted line indicates the DAS receiver line, and magenta x's at the ground surface indicate source locations.

For a more quantitative analysis of our results, we compared the Root Mean Square (RMS) amplitudes between the baseline and monitor-minus-baseline images in the vicinity of the fracture. Here, we considered a different approach for the computation of the SNR in seismic data for the fracture detection from that in the previous experiments. Adopting this new approach was because we worked with seismic images in the current numerical experiment. The imaging operator distributes amplitudes about ellipses, meaning random noise in the seismic data does not translate to random noise in a seismic image. This prevented us from simply adding noise to our images to compute the SNR. Seismic images also provide an advantage in that the amplitudes of interest are localized to their scattering location (in this case, the fracture). This means we could compare amplitudes exclusively in the fracture proximity before and after dilation, which is generally not possible in seismic data because the location of the scattering energy due to the fracture is different in each shot gather.

Figure 5-45 demonstrates where the RMS amplitudes are calculated in each image and Table 5-6 shows our results. The amplitude ratio in Table 5-6 is the ratio of the monitor minus baseline RMS amplitude to the baseline RMS amplitude, and provides a quantitative comparison of the dilated fracture reflectivity compared to that of the background medium. We observe that the amplitude ratio for the PP images in both the full- and limited-coverage case are about 0.5, meaning the change in amplitudes caused by fracture dilation is about half that of the amplitudes created by the background medium. The amplitude ratios from the PS images are higher, ranging from ~0.7 to ~0.9, meaning that the fracture dilation has a greater relative effect on the PS amplitudes than the PP amplitudes. This further suggests that PS imaging is more appropriate for detecting fracture dilation effects than PP imaging.

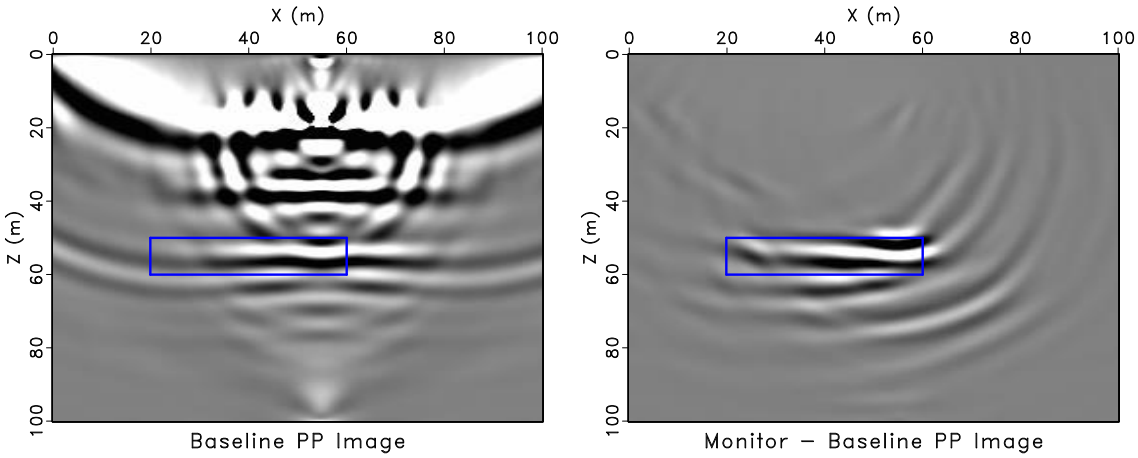

Figure 5-45: Baseline and monitor-minus-baseline PP images from the full-coverage experiment, where the RMS amplitudes are calculated from the region bounded by the blue box. The RMS amplitudes are similarly computed for other PP and PS images.

Table 5-6: The RMS amplitudes and their ratios from the baseline and monitor-minus-baseline images. The amplitudes from the full-coverage experiments are less than those of the limited coverage experiments because the image amplitudes are normalized by the number of sources, and sources to the right of the fiber optic cable do not contribute reflection energy to the RMS calculation area.

Reflection Mode	Source Coverage	Baseline RMS Amplitude A_B	Monitor – Baseline RMS Amplitude A_{M-B}	Amplitude Ratio A_{M-B}/A_B
PP	Full	16.62	7.72	0.46
	Limited	30.18	15.11	0.50
PS	Full	7.80	5.34	0.68
	Limited	17.66	16.33	0.92

In this final experiment, we used a 180 Hz peak frequency Ricker wavelet to approximate the potential bandwidth of a small vibroseis, called Thumper, available at the UT-Austin NHERI experimental facility. However, after contacting the operations manager at NHERI, it appears that Thumper only operates at high frequencies (up to 400 Hz) in environments with ground surface composed of bedrock rather than soil. At soil-covered sites, Thumper is generally only shaken up to 80 Hz due to the attenuation of high frequencies in the near surface. Given that the DFPS is soil-covered, we likely would not be able to achieve the same sensitivity as the synthetic experiments in this experiment, and thus would not be able to image the dilated shallow fracture. Mechanical and explosive sources show similar attenuating characteristics, with peak frequencies in the range

of 20-30 Hz and little signal above 100 Hz (Kaip et al., 2017). Therefore, we decided not to conduct a seismic survey in the 2022 field deployment, and substituted the effort with gathering passive distributed strain measurements during injection, using our pre-installed fiber cables in east, west, and north observation wells.

Our results show that the seismic response of the fracture is significantly less than that of conventional reflectors, requiring SNRs of 50 to 60 dB for detection. The low sensitivity of seismic waves to the fracture is largely due to the large discrepancy between seismic wavelengths and the fracture aperture. Notably, seismic wavelengths are on the order of meters to tens of meters for active sources on land, while the fracture aperture is on the order of millimeters to centimeters. Seismic waves are generally sensitive to features of wavelength scale, leading to a small effect of the dilated fracture on the wavefield. Our final experiment did show, however, that PS-wave reflections are more sensitive to the dilated fracture than PP-wave reflections, particularly at long offsets. Such information could be useful in designing future experiments beyond the current project for fracture detection using active source seismic data.

5.4: Multi-Physics Forward Modeling

- See foregoing summary in section 1.

6 Field Construction/Field Survey Studies/Data Gathering

6.1 Formation Well Testing

In September 2020, we mobilized to the DFPS to perform a preliminary hydrogeological and fracture characterization test at this site. The major objectives of this deployment were:

(1) to invite the major service partners to the DFPS and de-risk the larger deployment in 2022;
(2) to perform a series of high-pressure injections with freshwater into the existing fracture, in order to calibrate our hydrogeological models and develop a calibrated geomechanical model that is capable of capturing the dynamic fracture behavior during reopening; and
(3) to test the sensitivity of geophysical equipment with the vendors' proposed layout.

To address the anomaly in this first CSEM survey at the southwest edge of the survey area, in October 2021, we drilled a new observation well, called DMW 9, near the south well. To evaluate the hydraulic conductivity of this well and the effect of drilling this new well on the injectivity of the injection well, we conducted a 10-hr injection test. This test resulted in the injection-well and DMW-1 BHPs close to those during the 2020 injection test.

In January 2022, we were deployed to the DFPS again and performed the final CSEM survey during 10 injection cycles consisting of freshwater and saltwater slugs. These experiments were targeted to study the feasibility of detecting flow using a surface-based EM equipment. Our setup was featured by a tank-switch system at the upstream of the injection manifold to seamlessly switch between freshwater and saltwater. Also, we deployed many bottomhole autonomous transducers in the monitoring wells to track pressure and salinity changes at fracture depth during injections. The accurate estimation of the flow rate during the 2022 injection tests helped us establish a correlation between the injection rate and surface recorded electric potential, as elaborated in Subtask 6.5. Because we did not conduct any seismic surveys during the latest field deployment due to the simulated low SNR of fracture dilation (Subtask 5.3), we substituted seismic survey with surface tiltmeter mapping as a remote-sensing technique of the fracture dilation.

The field data interpretations show that comparing the EM field potential across various injection cycles can provide a first clue on assessment of the contribution of salinity changes, the EAP-filled fracture dilation, and flow-induced SP to the total observed EM field variations.

The details about the injection tests in 2020 and 2022 are discussed in the following, as well as in our publications (Ahmadian et al., 2023; Haddad and Ahmadian, 2023; Haddad et al., 2021, 2023).

2020 field deployment and data analyses

Survey implementation

Throughout the injection experiments in 2020, a frequency-domain surface CSEM survey was conducted. We deployed three transmitter locations as shown in Figure 6-1.

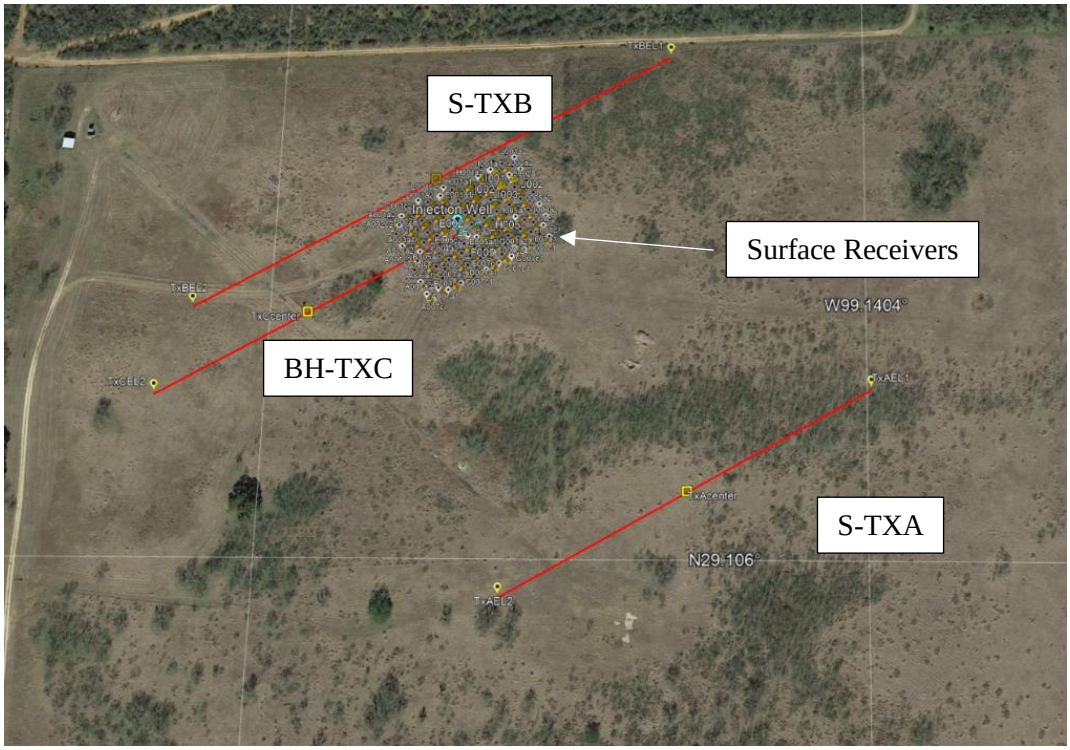

Figure 6-1: Transmitter locations shown by red lines in the survey area. The S-TXA and S-TXB transmitters were installed on the ground surface, whereas the BH-TXC transmitter injected current into a previously installed ERT electrodes inside DMW 1.

The S-TXA transmitter was located south easterly of the receiver array at a distance of 200 m to lead to the strongest signal response, according to the models developed by ESG for several possible surface transmitter locations. The use of surface transmitter is consistent with the way that ESG performs all their commercial surveys. This ensures a significant reduction in airwave sensitivity. This transmitter setup is typically thought of as a grounded dipole. Datasets using this setup were collected on 9/22, 9/23, and 9/24.

The purpose of the S-TXB transmitter, located at 20-m distance from the north westerly edge of the receiver array setup, was to use a cross-correlation method that has been pioneered by ESG for shallow structure detections. However, due to the lack of time, no significant effort was made to run injection experiments with this setup during this deployment.

The purpose of the BH-TXC transmitter, which was centrally placed in the borehole, was to attempt a direct coupling with the formation, near the fracture depth, using the borehole electrode arrays that had been previously installed at the annular space of the DMW-1 borehole. EM models developed at Duke University had shown (Subtask 5.2) that a significant signal improvement could be expected in this setup compared to the surface transmitter deployment. A dataset using this setup was collected on 9/25 and 9/26. As predicted by these models, the signal strength using the BH-TXC transmitter was 2 orders of magnitude greater than that using the S-TXA transmitter. However, all signal strengths with the surface transmitter were clearly within the detection limits of the ESG's measurement system.

We contracted Geoprojects International, Inc. (referred to as Geoprojects for brevity) to operate pumps, water truck, packer setup, and the electric submersible pump for the injection tests in September 2020. At the same time, we deployed the geophysics survey team from ESG in order to collect data for the initial sensitivity analysis. The entire deployment to the DFPS was 15 days with the daily activity outline as follows:

(1) prepared the DFPS and cleared the brush on September 14;
(2) laid out the ESG survey grid on September 15-20;
(3) mobilized Geoprojects and prepared for injections on September 21;
(4) conducted three cycles of pressure injection into the preexisting fracture, and collected the electric field data by the ESG equipment on September 22-25;
(5) demobilized Geoprojects on September 26;
(6) continued pressure monitoring on September 21-28; and
(7) demobilized ESG on September 29.

A few areal and drone images from the test area are shown in Figure 6-2 and Figure 6-3. A side view of the survey area is shown in Figure 6-4.

Figure 6-2: (top) Injection pumps and water truck, 300 ft away from the survey area. (bottom) The rig for setting straddle packers and electric submersible pumps at the wellhead.

Figure 6-3: (top) The ESG setup of a grid of 70 receivers over the fractured zone. (bottom) The ESG crew.

Figure 6-4: (left) Mohsen Ahmadian, the project principal investigator who planned and coordinated the field deployment. (middle) Mahdi Haddad and (right) Bharadwaj Muralidharan, research fellows from the BEG who helped Mohsen in conducting this field deployment.

Geoprojects conducted a series of isolated water injections into the previously characterized horizontal hydraulic fracture at 175-ft (53.34-m) depth based on a 110 BPD modeled injection scenario. Simultaneously, ESG's staff performed a CSEM survey, using a grid of 70 surface receivers which were centered over the injection well. To minimize the introduction of environmental noise for the EM geophysical surveys, the injection pumps and water truck were placed 300 ft away from the injection wellhead (Figure 6-5). The water injection was conveyed to the wellhead through a 300-ft long, 2-inch diameter, steel surface pipe.

(a) (b)

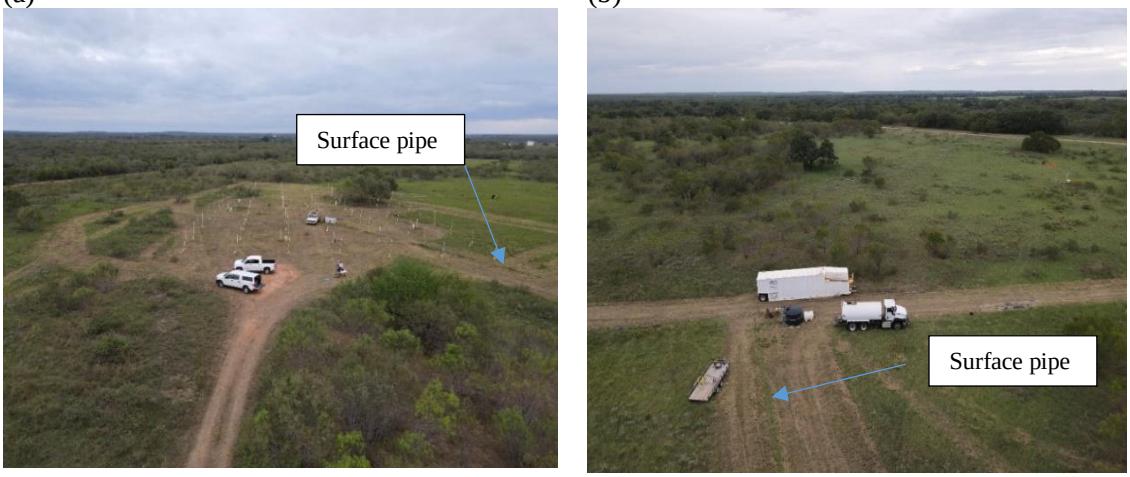

Figure 6-5: (a) A grid of 70 receivers, set up by ESG crew over the fractured zone at the DFPS. (b) Pump station 300 ft away from the injection well, set up by Geoprojects. Water was conveyed through a 300-ft long surface pipe to the injection well to reduce pump noise at the survey area.

Injection was conducted in two separate days, September 23 and 25, spaced by a flowback exercise on September 24. These injections were preceded by an initial injection test during September 22 that only partially succeeded due to an injection packer failure (Figure 6-6), which we later remedied by the installation of a bridge plug at the depth of 192 ft in the injection well. In all cases, analogue wellhead pressure gauges (Figure 6-7) and digital In-Situ™ pressure transducers were used to measure the resulting pressure profiles at either the perforation zone in the injection well, or adjacent to the previously screened and gravel-packed regions in DMWs 1 and 2 at the fracture depth.

Figure 6-6: Puncture in the upper packer, which was encountered during the 9/22 injection. This was remedied by the placement of a bridge plug in the injection well below the perforation zone on 9/23.

Figure 6-7: Wellhead assembly, consisting of an analog pressure gauge, connections to the injection well casing, and the shutoff valve (the yellow valve on the horizontal segment of the wellhead assembly), which was connected to the 300-ft long surface pipe. The In-Situ™ bottomhole digital pressure and salinity transducer was suspended by a 177-ft long rope hanging from the end cap above the analog gauge.

The resulting pressure profiles from the injection well and DMWs 1 and 2 are shown in Figure 6-8.

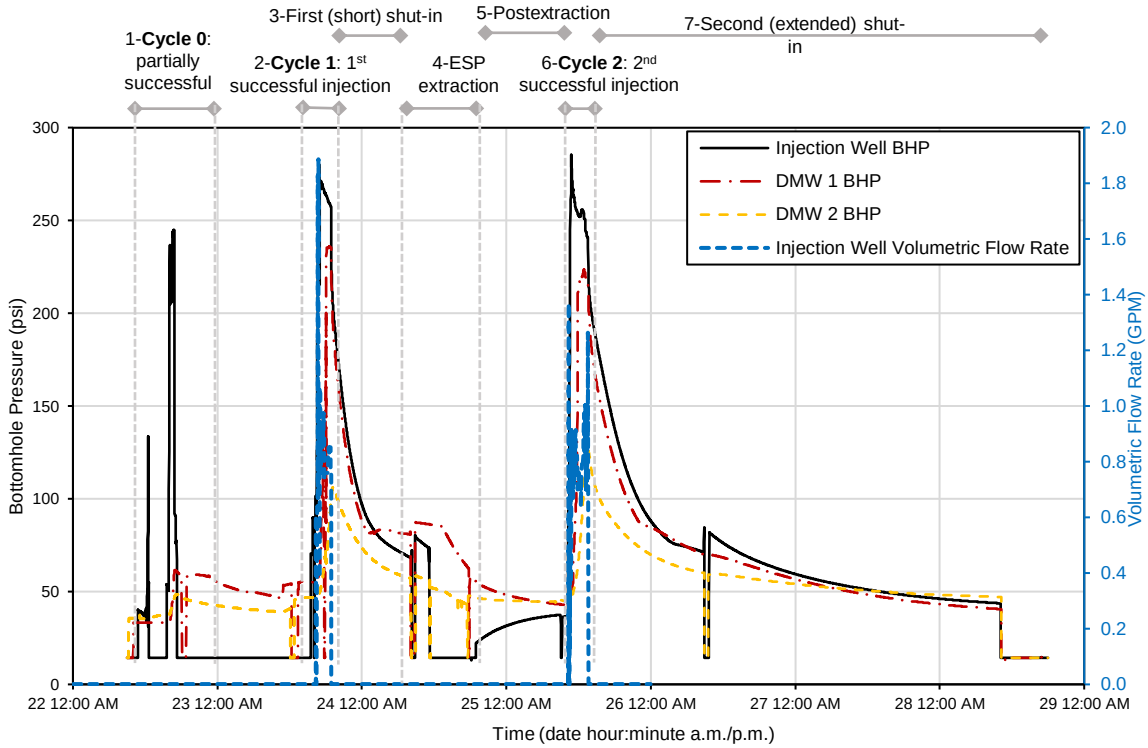

Figure 6-8: (left ordinate) Bottomhole pressure for the injection well, DMWs 1 and 2; (right ordinate) friction-based volumetric flow rate at the injection well, through one week of injection and shut-in. The time interval on the abscissa is from September 22 to September 29, 2020, represented by numbers 22 through 29 for brevity, and time is recorded based on the U.S./Texas central daylight time zone. BHP in legends stands for bottomhole pressure at depth of 175 ft, right at the fracture mouth in the injection well or expected fracture opening in the monitoring wells. During two time periods where the recorded pressure stays level at 14.2 psi (97.95 kPa), the injection well pressure transducer was removed from the well and kept at the surface.

As noted in Figure 6-8, We can specify seven exclusive time intervals in our field experiments: 1.) partially successful pump attempts on September 22; 2.) first successful injection with surface geophysics on September 23; 3.) first shut-in for a short time period beginning on September 23 and ending on September 24; 4.) water extraction using an Electric Submersible Pump (ESP) on September 24; 5.) post-extraction period; 6.) second successful injection with borehole geophysics on September 25; and 7.) extended shut-in from September 25 through September 28. The fluid pressure changes at the injection and monitoring wells at the fracture depth agree with the event logs and wellhead pressure gauges. The retrieval and deployment of the pressure transducers, as conducted several times during the experiment, are reflected in Figure 6-8 by step-wise pressure changes (e.g., on September 24 at 8 a.m. and September 26 at 9 a.m.) to the barometric pressure of ~14 psi.

We separated the injection Periods 2 and 6 by a short shut-in, flowback, and post-extraction time periods corresponding to time Intervals 3, 4, and 5, respectively (Figure 6-8). The purpose of the intermediate time Periods 3 through 5 was to evaluate the feasibility of the reservoir-pressure return to the in-situ conditions after the first injection period. The results can be illustrated by the comparison of the original BHP with the BHP after 3 days of shut-in without extraction on September 28 and BHP prior to the second successful injection on September 25. The original BHP

interpreted by the water level at 127 ft below the ground surface in the injection well, which was measured on September 16, 2020, was 35.5 psi. This was calculated as the summation of the atmospheric pressure (14.69 psi) and the hydrostatic pressure from a water column of 48 ft, equal to fracture depth at 175 ft subtracted by the water level depth at 127 ft. After 3 days of shut-in on September 28, the BHP plateaued at 42.4 psi (Figure 6-24), which is 7 psi higher than the original BHP. In addition, water extraction in September 24 led to a BHP of 36.5 (Figure 6-24), which is only 1 psi above the original BHP.

During flowback time (Interval 4), an ESP was installed below the fracture depth within the injection well, and water was extracted from the wellbore space (Figure 6-8). However, the reservoir flowback rate was small, and the pumping operation required to extract the entire volume from the injection well was very quick and frequently interrupted due to pump overheating. As a result, the BHP evolution for the injection well during the post-extraction period was incremental. Ultimately, the slow-rate formation flowback led to the gradual increase of the water level in the injection well during the time that ESP was turned off, and led to registration of a decreased pressure head over the pressure transducer in the adjacent monitoring wells (Figure 6-29). Thus, this exercise was only partially successful due to insufficient water circulation over the ESP to cool down the pump during the extraction.

Although we did not have a very precise flowmeter that could measure flow rates below 1 gpm, the data suggest that appreciable nonzero flow rates were recorded only after the wellhead pressure exceeded 170 psi (1.172 MPa). We believe the fluid flow was mainly received by the horizontal fracture because 1.) the In-Situ^{TM} pressure transducers in DMWs 3 and 4 (which are open to the formation only at 130- to 140-ft depth range) did not register any pressure spikes and 2.) the high-pressure front was detected at the DMW-1 and DMW-2 wellheads in less than one hour. The delay in the peak of pressure for DMWs 1 and 2 compared to the injection well is attributable to the time lag of pore-pressure diffusion from the injection well toward the monitoring wells through fluid flow in the packed and reopened horizontal fracture.

Pressure transient analysis

The hydraulic fracture at the DFPS is horizontal, and the minimum principal stress is the stress component normal to the fracture plane; in this case, this stress is the overburden (lithostatic) stress, S_{vert}, at 175-ft (53.34-m) depth. This principal stress is of utmost importance for fracture growth, reopening, and closure, and the integration of a density log through depth would lead to a direct measurement of this principal stress. Unfortunately, no density log was available for this site. To indirectly estimate this principal stress, we used two methods that analyze the collected bottomhole injection pressure data during the shut-in periods. Both these methods assume that the water pressure within the fracture is at equilibrium with the principal stress normal to the fracture plane. These methods are 1.) tangent method; and 2.) *G*-function method, which are based on the developed concepts for a diagnostic fracture injection test. For the hydraulic fracture reopening, the BHP should exceed S_{vert}. During the shut-in period, S_{vert} can be reached again through the BHP right at the fracture closure. We call this pressure the Fracture Closure Pressure (FCP).

The first analysis consists of drawing two lines tangential to the post-shut-in BHP data, one tangent to the pressure profile right after shut-in and the second tangent to the pressure profile once the pressure profile deviates from this sharp decline (Figure 6-9). The fluid pressure associated with the intersection point of these two lines represents the instantaneous shut-in pressure (ISIP) corresponding to the point where the friction drag is eliminated after the closure of the wellhead shutoff valve. This analysis resulted in ISIP equal to 210 psi (1.448 MPa) and may denote an upper bound for the FCP. As expected, the identical pressure values obtained by this tangent method during the first and second shut-in periods show the independence of ISIP from operational

conditions. Provided that we assume a negligible difference between ISIP and FCP, the overburden stress gradient can be estimated as 1.2 psi/ft (27.156 kPa/m), obtained by dividing 210 psi (1.448 MPa) by the fracture depth of 175 ft (53.34 m).

The second method is *G*-function analysis which helps identify the fracture-closure time right when $G \cdot \partial P/\partial G$ deviates downward from a linear trend. *G* is a dimensionless time (i.e., *G*-time) and is calculated by

$$G = (4/\pi)\big(g(\Delta t_D) - g(0)\big), \tag{6-1}$$

where

$$g(\Delta t_D) = (4/3)\big((1 + \Delta t_D)^{1.5} - \Delta t_D{}^{1.5}\big), \tag{6-2}$$

$$\Delta t_D = \big(t - t_p\big)/t_p, \tag{6-3}$$

t = current time,
t_p = total pumping time,
P = BHP, and
$\partial P/\partial G$ = *G*-time derivative of the BHP (Castillo, 1987; Fekete Inc., 2014).

We calculated $G.\partial P/\partial G$ at point *i* numerically using a central discretization scheme as

$$G_i\,(P_{i+1} - P_{i-1})/(G_{i+1} - G_{i-1}), \tag{6-4}$$

where the indices *i*+1 and *i*-1 correspond to a time step after or before the current time step *i*, respectively. In this analysis, $G \cdot \partial P/\partial G$ is plotted versus *G*-time and a line passing through the origin is drawn tangential to the $G \cdot \partial P/\partial G$ plot to obtain the deviation of $G \cdot \partial P/\partial G$ from a linear trend (Figure 6-10). Accordingly, the fracture closure pressure occurred at 4:50 p.m. on September 25 and is equal to 154.536 psi. This time is almost 3 hr after recording ISIP during this shut-in period showing that 1.) compared to ISIP, the BHP needed to drop for an extra 50 psi to lead to fracture closure; and 2.) fracture closure does not occur instantaneously after shut-in and is a relatively slow process. The slow fracture-closure process can be caused by the small fluid-leakoff rate or small rock permeability.

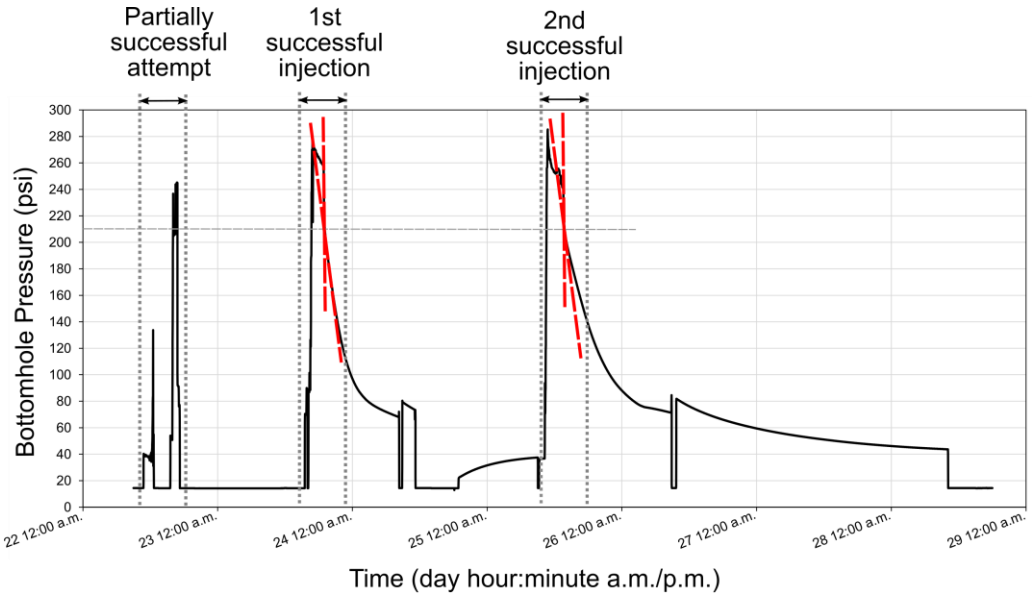

Figure 6-9: Injection well bottomhole pressure versus time. Time is recorded based on the U.S./Texas central daylight time zone. The intersection of the lines tangential to the post-shut-in bottomhole pressure evolution show the instantaneous shut-in pressure, which can be interpreted as the fracture closure pressure or the overburden stress over the horizontal hydraulic fracture.

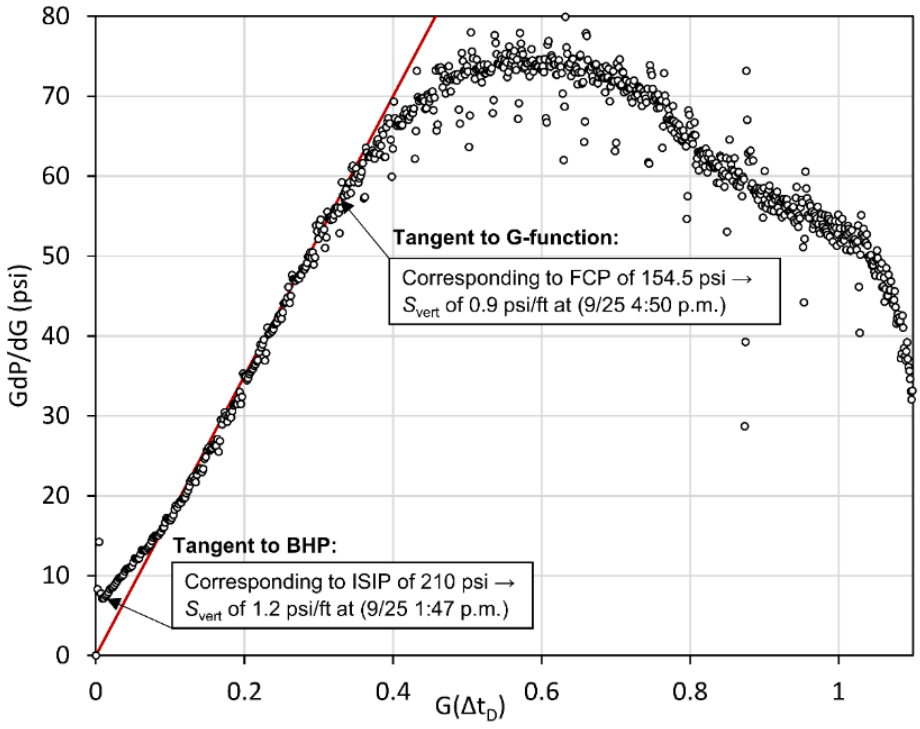

Figure 6-10: G-function pressure analysis. The black circles are $G \cdot \partial P/\partial G$ based on the field data collected on 9/25/20, and the red line is a straight line drawn from the origin and tangent to the trend followed by the black circles. The point where the black-circles trend deviates from the linear red line denotes the Fracture Closure Pressure (FCP). The instantaneous shut-in pressure (ISIP), obtained from Figure 6-9, corresponds to a much earlier data point compared to that for the FCP.

2022 field deployment and data analyses

Survey implementation

On January 2022, we deployed to the DFPS and performed the final CSEM survey during 10 injection cycles consisting of freshwater and saltwater slugs. We used the central injection well at the DFPS for these injections and several monitoring wells for the downhole monitoring of pressure and salinity. Figure 6-11 and Figure 6-12 show the areal and close-up views of the pump station and the survey area. We located the pump station around 400 ft far from the survey area to minimize noise due to the pump operation and the generator in the CSEM survey recordings. To eliminate the possible interference caused by the old surface metal pipe, we replaced it with a 400-ft long polypropylene pipe between the injection wellhead and the pump station. Moreover, to eliminate the possible interference of an induced EM field due to electric current in a domestic power line with the CSEM survey, we did not use the electric power line at the test site to energize the pumps. Instead, we rented and used an isolated diesel-fueled portable generator and designed and implemented a fuse box to energize two pumps independent from each other.

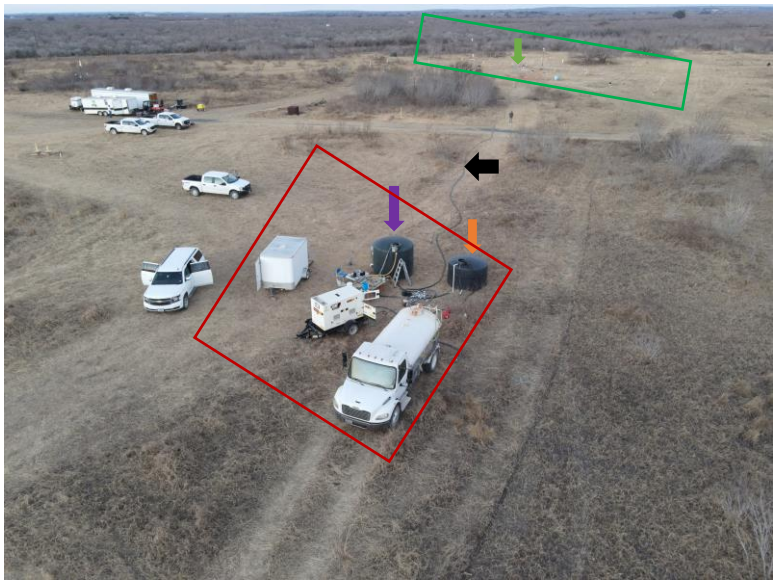

Figure 6-11: Areal view of the pump station (red box) and the survey area (green box), during the field deployment on January 2022. The equipment in this picture are as follows: a tank truck, a portable diesel-fueled electric generator, a workstation trailer, freshwater tank pointed by a purple arrow, a saltwater tank pointed by an orange arrow, a polypropylene pipe pointed by a black arrow, and an injection manifold connecting the pumps to the polypropylene pipe. The polypropylene pipe connected the pump station to the injection wellhead that is marked by a green arrow. The portable diesel-fueled generator provided the electric power to the electric submersible pumps that were immersed inside the surface water tanks, and the water truck transported Yancey municipality water to the test site.

Figure 6-12: (upper) A panoramic view of the pump station; (lower) a close view of the survey area. (lower) Injection well and DMW 1 through 4 are pointed by blue, red, green, black, and purple arrow. 3-ft long receiver rods, shown for instance by the white arrow, were hammered to the ground for the CSEM survey and were wired to a receiver hub, shown by the yellow arrow, for data communication to the wireless antenna, shown by the pink arrow.

Our hydrogeological and poroelastic modeling attempts require robust measurement of the injection flow rate. An accurate estimation of the flow rate helped us establish a correlation between the injection rate and surface recorded electric potential. During the 2020 injection tests, we diagnosed shortcomings in the accuracy and the range of operation of the utilized flowmeter. To improve these, we evaluated the alternative flowmeter manufacturers and decided to use MX series oval gear flowmeters manufactured by MacNaughts Americas. To extend the range of flow-rate measurement below 1 gallon per minute (gpm), we designed an injection manifold consisting of two flowmeters at low and high flow-rate ranges, as shown in Figure 6-13. Flowmeters MX09 and MX19 are suitable for flow-rate ranges of 0.1-2.2 gpm and 2-18.5 gpm, respectively. In addition, we incorporated two VantageView totalizers from Precision Digital™ in this design to log the flow rates through the injection time. Because of the sensitivity of the gears inside the flowmeters, we added two strainers at the inputs of the flowmeters to remove fine particles in the injection water before entering the flowmeters. Furthermore, we placed two ball valves at the inlets of these

flowmeters to control flow through these flowmeters. Generally, at the start of injection, due to the small flow rates, we opened flow through MX09 flowmeter, and at later time when the flow rate increased, we switched the main flow line toward MX19 flowmeter. The CirrusSense™ digital pressure transducers before and after this manifold would inform us about the pump outlet pressure and any pressure-drop anomalies through this manifold (e.g., through the strainers due to the accumulation of debris).

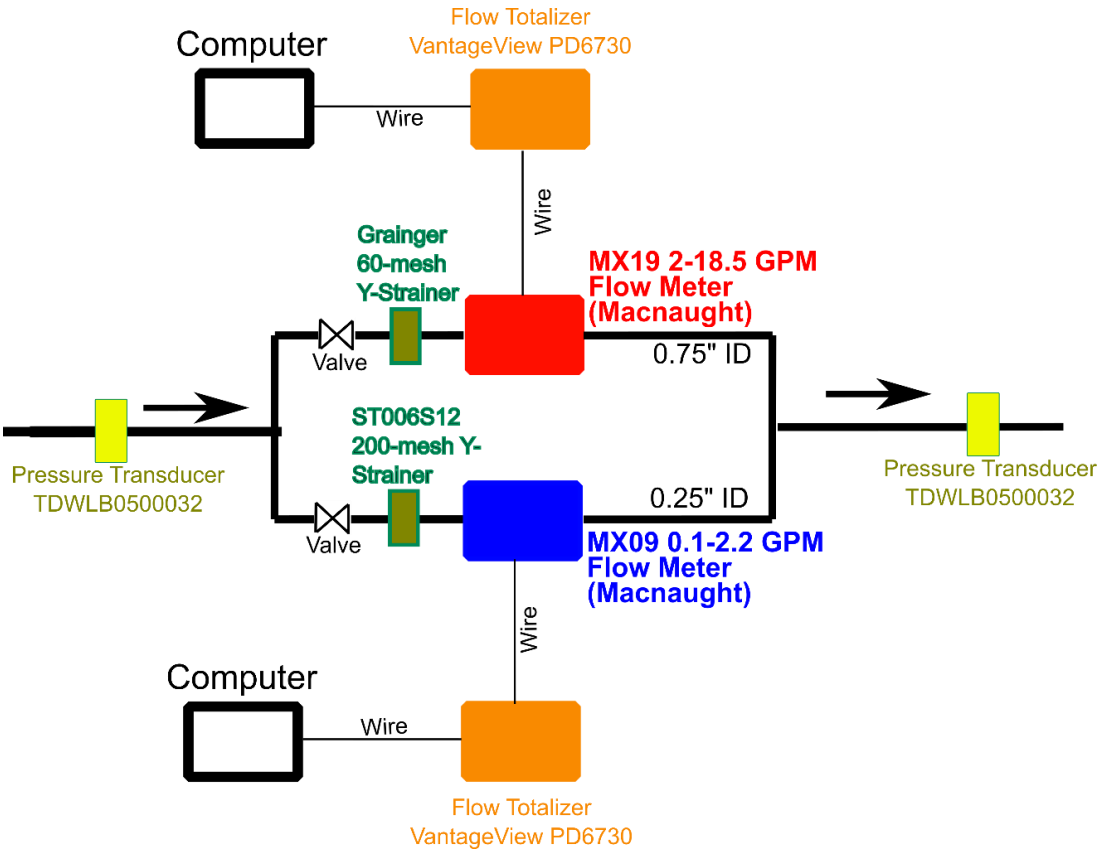

Figure 6-13: The designed flowmeter manifold and logging system, installed at the injection line. Two low and high flow-rate flowmeters provide a wide range of flow rate measurement from 0.1 up to 18.5 gpm. Strainers filter water before entering the sensitive flowmeters, and ball valves control flow through these flowmeters, depending on the flow rate. Flow rates are logged in the memory of two totalizers and downloaded to a field computer.

We implemented the injection manifold shown in Figure 6-13 in the 2022 field test. The image of this implementation at the test site is shown in Figure 6-14. We installed this section downstream of the tank-switch section shown in Figure 6-15. We added a bypass line to this design to avoid damage to the flowmeter during unexpected surge in the flow rate throughout the injection experiments. We controlled flow through either the bypass line, the low flow-rate meter line, or the high flow-rate meter line using three ball valves in these lines. Once the injection experiments were complete, we opened the strainers from the injection manifold and inspected them. Figure 6-16 shows the importance of installing these strainers at the inlet of the flowmeters in saving the flowmeters, as a substantial amount of solid debris was accumulated in the strainers throughout the experiments.

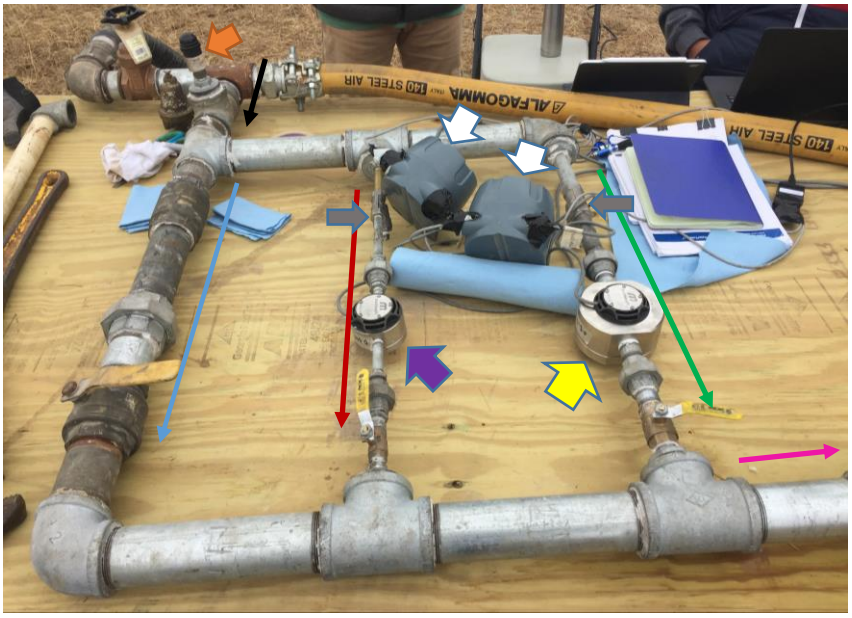

Figure 6-14: Flowmeter lines in the injection manifold for the precise measurement of flow rate at various intervals: 0.1-2.2 gallons per minute (gpm) with the low flow-rate meter, marked by the purple arrow; and 2-18.5 gpm with the high flow-rate meter, marked by the yellow arrow. Two digital totalizers, marked by the white arrows, logged the flow rates of these flowmeters per minute. The black and pink arrows show the flow direction into the injection manifold and out of the manifold toward the injection wellhead. The blue, red, and green arrows show the flow direction through a bypass line in parallel to the flowmeters, the flow direction through the low flow-rate meter, and the flow direction through the high flow-rate meter, respectively. The gray arrows point toward two strainers that were installed at the inlet of the flowmeters to protect these flowmeters from solid debris in the injected water. The orange arrow points to a CirrusSense™ pressure transducer that is installed at the outlet of the injection manifold.

We also monitored surface pressure at the injection wellhead, and at the DMW-1 and DMW-2 wellheads using three additional CirrusSense™ digital pressure transducers. The reason for this surface pressure monitoring was to collect data as backup for the bottomhole pressure measurement using In-Situ™ transducers. Figure 6-14 shows one of these transducers installed at the outlet of the injection manifold.

A tank-switch system was installed at the upstream of the injection manifold as shown in Figure 6-15 for a seamless switch between freshwater and saltwater tanks. This tank-switch system included ball valves in the high-pressure and bypass lines for each of the saltwater and freshwater tanks. These valves would control water flow from either of these tanks to the injection manifold. This afforded us a method to obtain a sharp, piston-wise displacement of one slug of freshwater or saltwater by another. For this purpose, we used one surface storage tank and an ESP for the freshwater and one surface storage tank and an ESP for the saltwater (Figure 6-11, Figure 6-12top). We used a gate valve (pointed to by the purple arrow in Figure 6-15) to adjust the injection flow rate.

(a) (b)

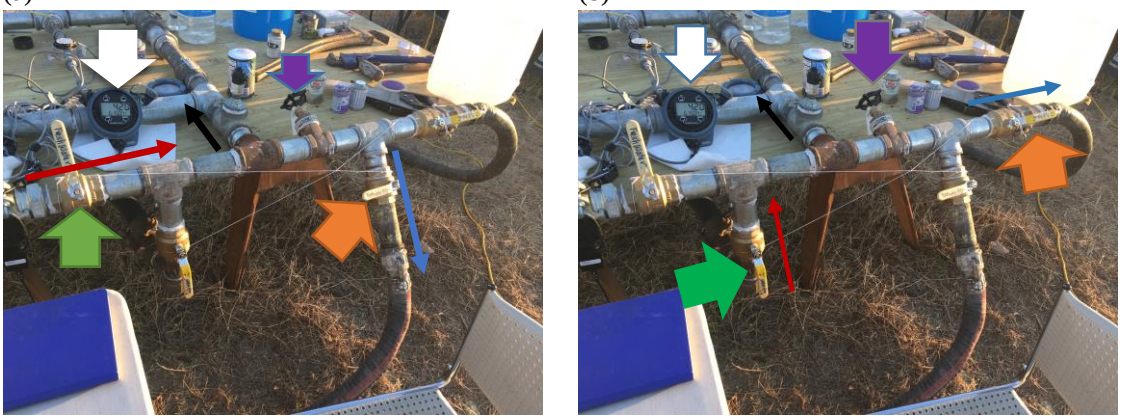

Figure 6-15: The tank-switch section of the injection manifold. This manifold allowed us to switch between the freshwater and saltwater tanks seamlessly, by opening only two ball valves marked by green and orange arrows. (a) Configuration for freshwater injection and (b) configuration for saltwater injection. The valves direction marked by red and blue arrows open flow from the pump to the manifold through the high-pressure line, and from the manifold to the storage tank through a bypass line, respectively. The gate valve marked by the purple arrow allowed the flow-rate control by diverting some of the pumped volume to the bypass line. The black arrow shows the main flow direction toward the wellhead. Flow rate and volumes injected were digitally measured using VantageView totalizers (white arrow).

Figure 6-16: Two images of a strainer at different viewing angles, exposed at the end of all injection cycles. The orange/brown materials inside the strainer mesh are the solid debris separated from the injection water and accumulated behind the mesh in the strainer. The accumulation of this debris was confirmed during the experiments by a relatively large pressure drop through the injection manifold.

We deployed 9 bottomhole pressure/salinity transducers (i.e., AquaTroll 200) in the injection well, DMWs 1, 2, 3, 4, and 9, the south well, the north well, and the west well. Moreover, we deployed a pressure transducer (i.e., AquaTroll 700) in the east well and a barometer transducer (i.e., BaroTroll) in the west well. These transducers are shown in Figure 6-17a. We also checked the calibration of all transducers for conductivity measurement using the saltwater samples that we received from In-Situ Inc. (Figure 6-17b). With the exception of DMW 9, all the transducers were positioned next to the perforation or screened zone in these wells. Because of an obstruction in DMW 9, the transducer could only be lowered down to 141 ft below ground. Because DMWs 5, 6, 7, and 8 contain no screened zone and DMW 7 is decommissioned, we did not deploy bottomhole transducers in these wells. After completing the injection experiments, we realized that four out of nine AquaTroll 200 transducers, which had been positioned in the north, south, west and east wells,

failed to record pressure and conductivity properly. We contacted In-Situ Inc. for the recovery of these data from the failed transducers. Unfortunately, the manufacturer was unable to recover these data, and we permanently lost these data.

(a) (b)

Figure 6-17: (a) Bottomhole pressure/salinity transducers used during the field deployment in January 2022. (b) An image of the WinSitu™ software program during calibration of conductivity measured by the injection well transducer. We conducted this calibration using the water samples received from In-Situ Inc.

Because we did not conduct any seismic surveys during the latest field deployment, we added surface tiltmeter mapping as a remote-sensing technique for fracture dilation. We divided fifteen tiltmeters into three groups and connected each group to a data logger, as shown in Figure 6-18a. We used preexisting vaults at the DFPS for the installation of the tiltmeters (Figure 6-18b). The implementation of the tiltmeter survey is elaborated in Appendix A.4, and the tiltmeter mapping results are discussed in Subtask 6.5.

(a) (b)

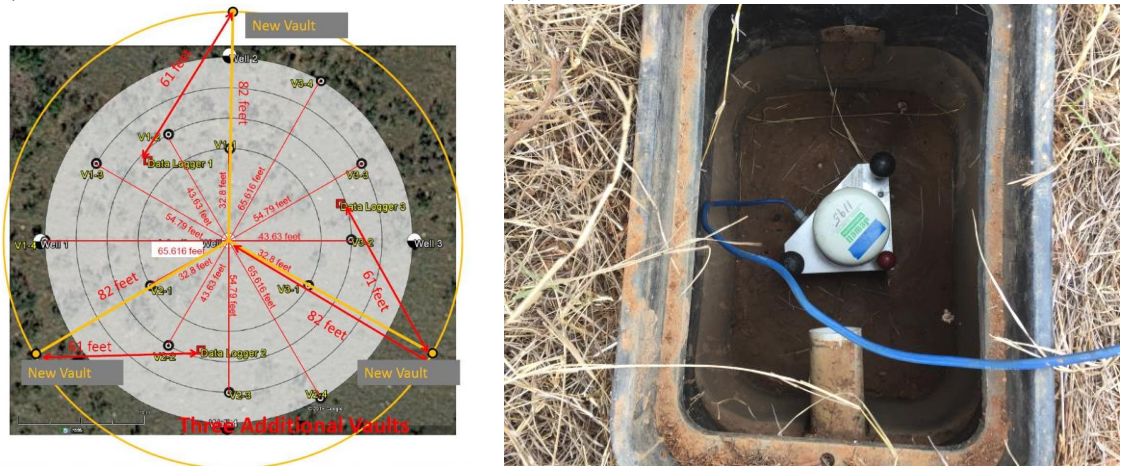

Figure 6-18: (a) Tiltmeter vault station map; (b) an image of a tiltmeter inside a preexisting vault in the ground. Five tiltmeters were connected to each of three data loggers through underground wires, and these data loggers were wired on the surface to one central computer for data collection. The data loggers and the central computer were energized by 20-volt, rechargeable, lead-acid batteries.

We conducted 10 injection cycles using freshwater and saltwater slugs at various volumes at the DFPS, representative five of which are listed in Table 6-1. We designed the experiments to study the feasibility of detecting flow using a surface-based EM equipment. In addition, we compared the EM field in the presence or absence of saltwater in the formation during flow experiments. During this deployment, ESG experimented with a new set of receivers, which promised to enable

wireless communication of the surface receivers with their command center. This scheme was tested to enable real-time data imaging during our study. Although ESG ultimately succeeded in demonstrating this communication method, we experienced a few equipment failures on multiple receivers during the initial injection cycles, and the collected data included multiple dropout points, deeming the collected data during those injection cycles mostly unusable. Thus, for the data analysis, we only focused on representative days when ESG confirmed that the equipment functioned as expected and all data were quality-controlled without significant data-loss intervals. These representative days are January 23, 26, and 27.

Table 6-1: Summary of five injection cycles during the injection campaign in January 2022 at the DFPS. Injections before 1/27 included only injection of freshwater at different volumes. The injections on 1/27 included injection of freshwater and saltwater. Each injection cycle is preceded by a surface-line and injection-well refilling interval before pressuring the formation. We used military time style for reporting daily time, starting from 00:00 at midnight, moving to 12:00 at noon, and finishing the daily time at 23:59.

Injection Cycle No.	Date (day/month/year)	Injection Scenario	Injection Slug	Refilling start time (hour: minute)	Refilling finish time (hour: minute)	Shut-in time (hour: minute)	Injected Volume (US Gallons)
1	1/21/2022	Repeating 9/20/2020	Freshwater	9:28	10:48	15:14	1126.02
2	1/23/2022	Flow-rate Test	Freshwater	11:31	11:41	16:50	603.38
3	1/24/2022	Repeating 9/20/2020	Freshwater	12:00		16:35	952.1
4	1/26/2022	Freshwater + Chase Freshwater Injection	Freshwater	12:00	12:03	17:56	1200.2 (freshwater)
5	1/27/2022	Saltwater + Chase Freshwater Injection	Small Saltwater Slug + Large Freshwater Slug	12:00	12:06	18:06	215.6 (saltwater); 990 (freshwater)

The representative injection cycles during January 23, 26, and 27 encompass the variation of all parameters that we planned on testing during the injection campaign, as follows:

(1) on January 23, we injected freshwater at variable flow rates;
(2) the January-26 injection was analogous to the injection experiments during our 2020 field campaign; and
(3) on January 27, we repeated the January-26 injection with the change of the injected fluid from freshwater to saltwater.

Although we focused on these three days, it is essential to note that our observations of total field measurements may be influenced to some extent by the cumulative injection volumes and leakoff before each cycle.

The first four experiments included freshwater injection of 1126, 603, 952 and 1200 US gallons on January 21, 23, 24, and 26, respectively. Then, we proceeded with saltwater injections. Because the calculated volume of the surface pipe and injection wellbore volume were approximately 200 US gallons, we decided to use multiples of 200 US gallons as our standard injection volumes. Thus, on January 27, 2022, we injected 216 gallons of a 2400 ppm solution and chased the saltwater slug with 990 gallons of freshwater, with the approximate one-to-five ratio of saltwater to freshwater slug volume. The injected water salinity was limited to 2400 ppm to remain below the permitted salinity of 2500 ppm.

Having completed the targeted experiments, we conducted multiple rounds of freshwater injections of 2150, 729, 3485, and 1262 US gallons to reduce the formation salinity back to its initial state. The total dissolved solid (TDS) of the freshwater was 266 ppm and the water was sourced from Yancey municipal water sale. Considering that the injected freshwater salinity of 266 ppm was

below the average DFPS water salinity of 702 ppm, we succeeded to reduce the in-situ salinity below the initial TDS values by injecting Yancey-sourced freshwater after the saltwater injections (Table 6-2).

Table 6-2: Measured TDS obtained from a hand-held PmoYoKo digital salinity meter, for samples obtained before and after the injection experiments, on January 13, 2022 and February 2, 2022.

Well	Total Dissolved Solid (ppm) before injection experiments	Total Dissolved Solid (ppm) after injection experiments
Injection	182	274
DMW 1	263	160
DMW 2	726	334
DMW 3	583	561
DMW4	1690	1706
DMW 5	330	315
DMW 6	775	752
DMW 9	1070	270

Because the injection well is perforated at the depth of 175 ft below ground, and DMWs 1, 2, and 9 are screened at a depth of 170-180 ft below ground, the monotonic BHP evolution in these wells during the injections proved that these are hydraulically connected (Figure 6-19). On the other hand, DMWs 3 and 4, which are screened at a depth of 130-140 ft, did not experience any change in the BHP, suggesting that the injected fluid did not migrate up to the screen depth of these wells. In addition, for the hydraulically connected wells, the pressure spike magnitudes were inversely proportional to the distance of a well from the injection well: 10, 20, and 99 ft for DMWs 1, 2, and 9, respectively.

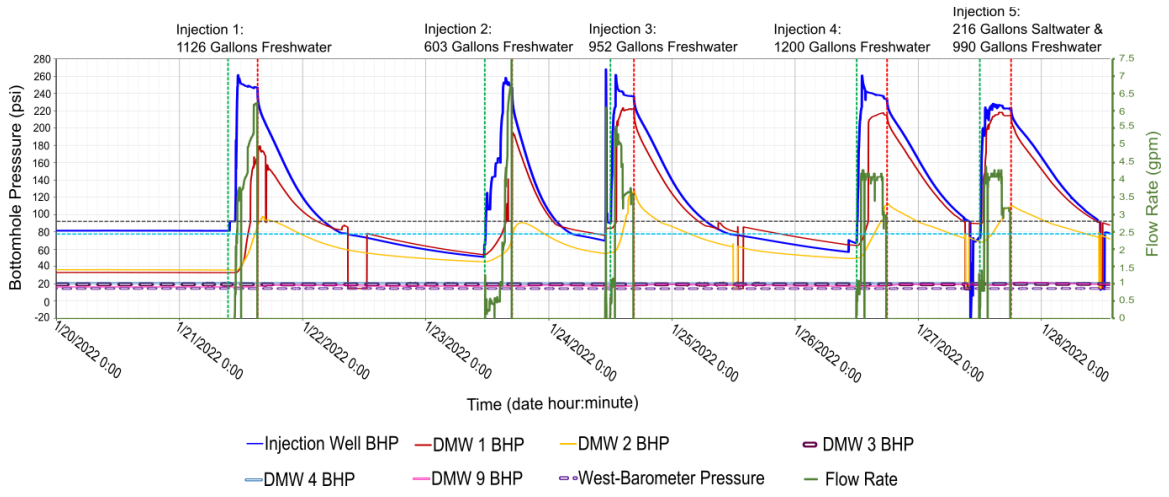

Figure 6-19: Bottomhole pressure at the injection well, DMWs 1-4, and 9, ambient pressure, and flow rate during January 21-27 injection cycles. DMW-4 bottomhole pressure remains constant at the initial pressure while the injection well and DMW-1 bottomhole pressures rise during the injection tests. The initial bottomhole pressures are different because the transducers were deployed to various depths: 175 ft at the injection well; 170 ft at DMW 1; 148 ft at DMW 3; 135 ft at DMW 4, and 141 ft at DMW 9. Also, the initial water table was at different depths: 17 ft at the injection well; 130 ft at DMW 1; 138 ft at DMW 3; 125 ft at

DMW 4; and 136 ft at DMW 9. The vertical green and red dash lines mark the starting time and shut-in time of each injection experiment, respectively. The horizontal blue dashed line = the hydrostatic pressure of 77.33 psi for a 175-ft long water column in the injection well. The bottomhole pressure drop below 77.33 psi during shut-in shows the development of vacuum pressure in the corresponding well.

Figure 6-20 compares the relative change of TDS with respect to the initial TDS for each well. These data show that the bottomhole TDS either remained at the initial state (e.g., in DMWs 3 and 4) or dropped below the initial state (e.g., in DMWs 1, 2, and 9) during the freshwater injections prior to 1/27/22. The TDS drop during these freshwater injections in these connected wells is because the salinity of freshwater (266 ppm) was below the average salinity of the formation (703 ppm). Likewise, the lack of drop in TDS in DMWs 3 and 4 during this period suggested that the freshwater did not break through to the zone at 130 to 140 ft below ground.

During the 1/27/2022 injection period, when we first introduced a small quantity of saltwater in the injection well, the injection well salinity rose quickly by 2200 ppm, presumably because the small saltwater slug was diluted by the remaining freshwater within the surface pipes. The relatively small TDS change in DMWs 1 and 2, less than 200 and 100 ppm, suggests that the saltwater quickly diffused in the proppant-filled fracture in radial direction from the injection well **(**Figure 6-20).

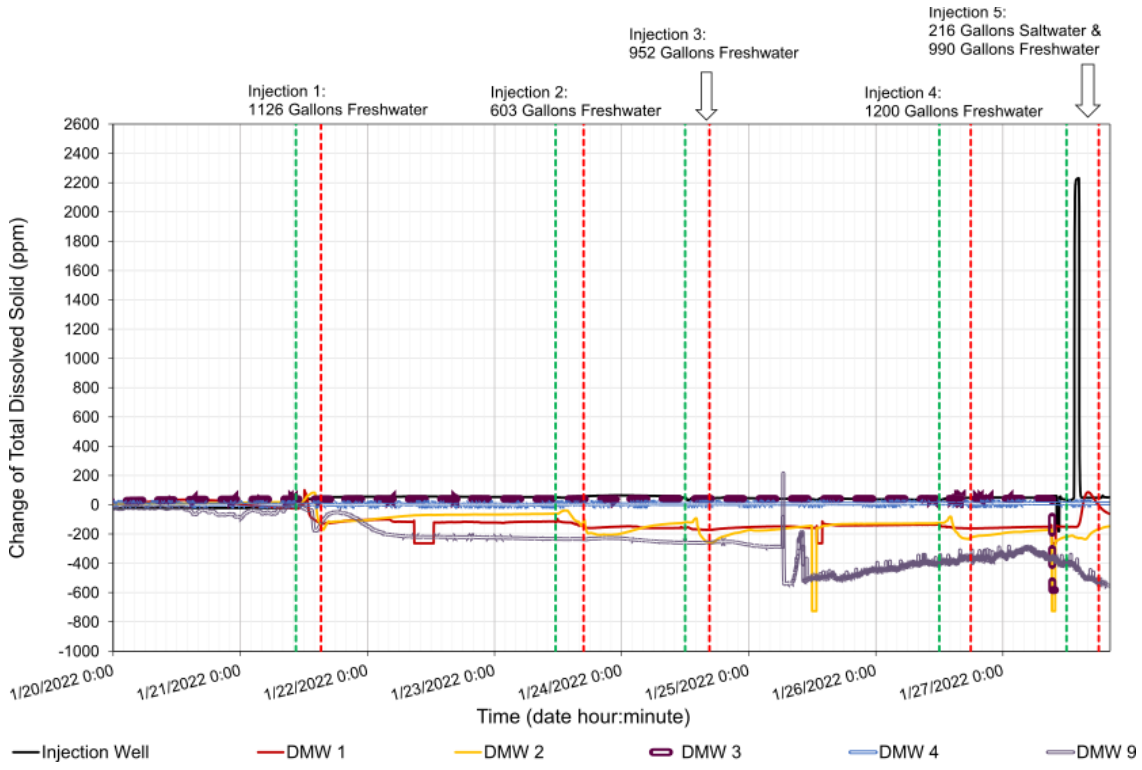

Figure 6-20: Change of bottomhole total dissolved solid (TDS) at the injection well and DMWs 1-4 and 9. We calculated relative change of TDS at a given time compared to the initial TDS value obtained before the first injection. Refer to Table 6-2 for the initial TDS values in each monitoring well. The vertical green and red dash lines mark the starting time and shut-in time of each injection experiment, respectively.

Pressure transient analyses

To confirm the finding of the *G*-function pressure transient analysis of the 2020 post-injection data, we repeated this analysis for multiple shut-in periods after injections on January 23, 24, 26, 27, 28, and 31. The recorded BHP during these days was of adequate quality to result in the FCP at an expected range from our previous experience (Haddad et al., 2021, 2023). These analyses are based on Equations (6-1), (6-2), and (6-3). As an improvement in conducting these analyses, we first fitted a 6th order polynomial into the (*G*-time, $G \cdot \partial P/\partial G$) points and then drew a line from the origin and tangential to the fitted polynomial to obtain the downward deviation of $G \cdot \partial P/\partial G$ from this tangent. Figure 6-21, Figure 6-22, and Figure 6-23 show these plots for January (23, 24), (26, 27), and (28, 31), respectively. These analyses led to the FCP of 163.99, 155.64, 154.79, 144.43, 138.86, and 151.58 psi for January 23, 24, 26, 27, 28, and 31, respectively. Due to the widely scattered *G*-function data points during the other injection days, we could not derive the FCP in these days. The average and standard deviation of the obtained FCPs are 151.55 and 8.10 psi, respectively. If we eliminate 138.86 psi from this list due to the lower quality of the post-shut-in data on January 28 compared to the other days, the average and standard deviation change to 154.09 and 6.33 psi. This later average value is consistent with our previously published FCP of 154.5 psi based on the BHP data collected during an injection campaign in 2020 (Haddad et al., 2021, 2023).

The fracture closure was estimated to occur 2 hours and 57 minutes (2:57) after shut-in on January 23. The fracture closure occurred at 5:59, 6:57, 8:26, 9:05, and 4:56 on January 24, 26, 27, 28, and 31, respectively. Except for January 31, with the progress of the injection cycles, the required time for the fracture closure increased, likely due to the increased effect of the previously injected volumes at later injection days. Slow fluid leakoff rates or micro-scale rock permeability may explain the elongated leakoff time until the fracture closure at the later injection days.

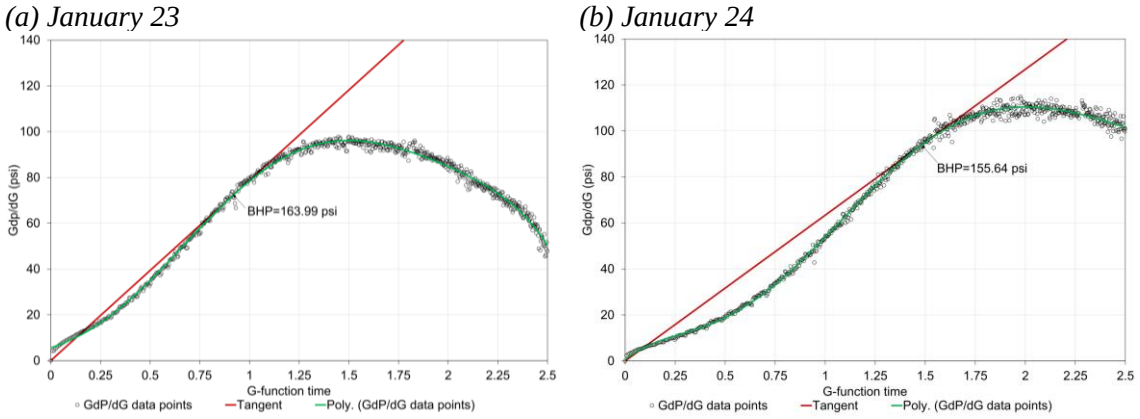

Figure 6-21: G-function pressure analyses for (a) January 23 and (b) January 24. Black circles = $G \cdot \partial P/\partial G$, derived from field data, green line = 6th order polynomial fitting into the black circles, and red line = a straight line drawn from origin and tangent to the fitted line. FCP = point where the fitted line deviates downward from the linear red line. The G-function time interval corresponds to the data from (a) 1/23/2022 16:50 until 1/24/2022 4:18 and (b) 1/24/2022 16:35 until 1/25/2022 5:00. The FCP time is (a) 1/23/2022 19:47 and (b) 1/24/2022 22:34.

(a) January 26 *(b) January 27*

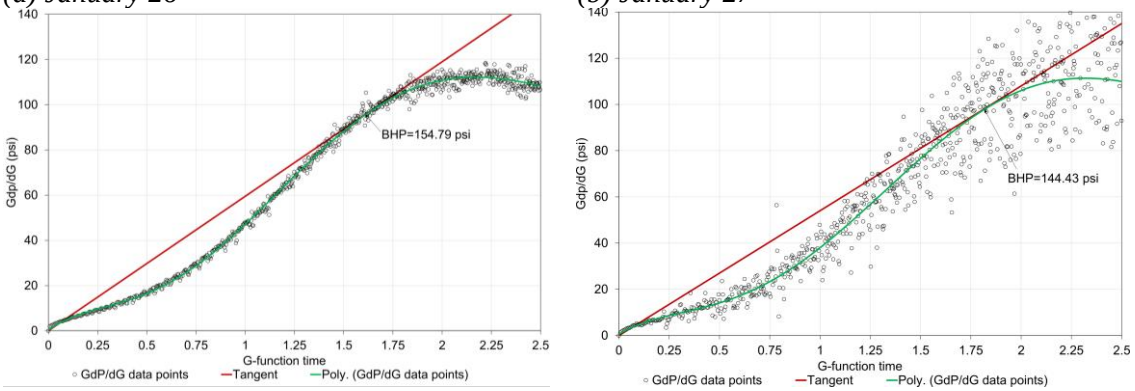

Figure 6-22: G-function pressure analyses for (a) January 26 and (b) January 27. Black circles = $G.\partial P/\partial G$, derived from field data, green line = 6th order polynomial fitting into the black circles, and red line = a straight line drawn from origin and tangent to the fitted line. FCP = point where the fitted line deviates downward from the linear red line. The G-function time interval corresponds to the data from (a) 1/26/2022 17:56 until 1/27/2022 6:55 and (b) 1/27/2022 18:06 until 1/28/2022 7:23. The FCP time is (a) 1/27/2022 00:53 and (b) 1/28/2022 2:32.

(a) January 28 *(b) January 31*

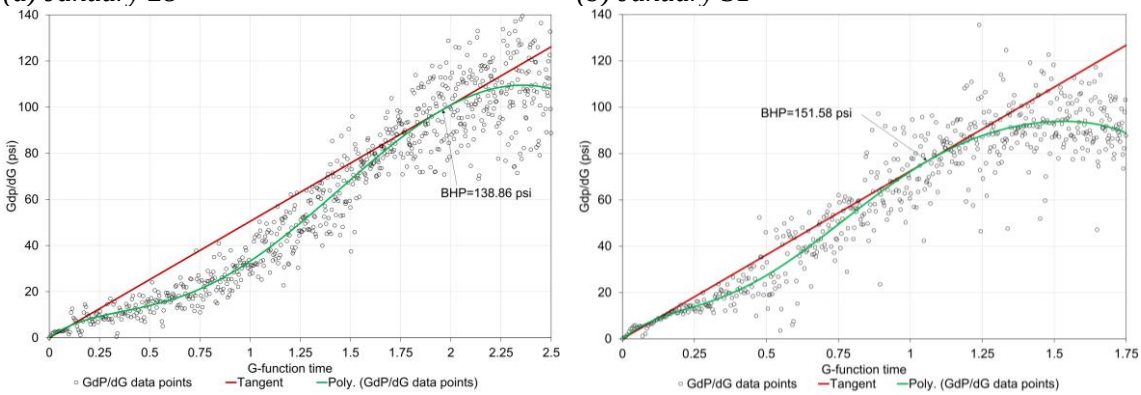

Figure 6-23: G-function pressure analyses for (a) January 28 and (b) January 31. Black circles = $G.\partial P/\partial G$, derived from field data, green line = 6th order polynomial fitting into the black circles, and red line = a straight line drawn from origin and tangent to the fitted line. FCP = point where the fitted line deviates downward from the linear red line. The G-function time interval corresponds to the data from (a) 1/28/2022 20:09 until 1/29/2022 8:54 and (b) 1/31/2022 18:33 until 2/1/2022 4:01. The FCP time is (a) 1/29/2022 5:14 and (b) 1/31/2022 23:29.

From these post-shut-in pressure transient analyses, we confirmed the S_{vert} gradient of 1.08 psi/ft to be used in our poroelastic models.

6.2 Seismic Surveys

As discussed in Subtask 5.3, our effective medium model results showed that 50 dB of SNR is necessary to detect a fracture in a seismic survey using a Ricker wavelet source with a 50 Hz peak frequency. Seismic modeling in Subtask 5.3 relied on a simplified two-layer velocity model. To

obtain an accurate velocity model for this modeling effort and to re-assess whether we can achieve 50 dB of SNR due to fracture dilation during water injection into the EAP-filled hydraulic fracture at the DFPS, we were deployed to the DFPS on May 2021. We performed zero- and nonzero-offset VSP seismic surveys using existing downhole fiber optic cables. This field test resulted in a velocity model optimized from VSP measurements in several wells at the DFPS (Appendix A.3). The incorporation of these results into seismic models, as discussed in Subtask 5.3, further confirmed that active VSP with the available weight drop equipment could not result in 50 dB of SNR. Therefore, additional seismic surveys beyond the VSP were not conducted in this project.

6.3 Development of Strategies for Real-Time Monitoring

We chose to contract ESG because they were able to offer commercially available CSEM equipment with the following specifications:

- transmitters installation on the ground surface and electrical current transmission into the ground creating an EM field;
- layout of receivers on the surface with 20- to 100-ft cables connecting to rods in the ground measuring electrical potential;
- simultaneous electric field recording by a swath of receivers over the area being monitored and recorded before and after the injection commencement;
- voltage measurement at the rate of 50,000 samples per second during the injection;
- signal processing for data quality;
- the baseline signal subtraction from the recorded signal at each time step (normally 1-2 minutes); and
- the capability to image the differences.

6.4 Smart Proppant Test 1 in 2020: In-Situ Remote Pressure Response Measurements

During the 2020 field deployment, we injected high-pressure water into the EAP-filled fracture, and the pressure breakthrough curves are discussed here as part of the data analysis. During this deployment, we mainly investigated the impact of pressure buildup and leakoff on CSEM recordings using freshwater injection. As a reminder from Subtask 6.1, the surface S-TXA transmitter setup was used on 9/22, 9/23, and 9/24, and the borehole BH-TXC transmitter setup was used on 9/25 and 9/26. The results of this field deployment are discussed in the following.

EM field interpretation

We attempted to understand the behavior of the EM field in response to the BHP changes during 2020 field experiments as shown in Figure 6-8. Because the movies representing the time-series of the EM field data subtractions, provided to us by ESG, are massive in size, in Figure 6-24, Figure 6-25, Figure 6-27, Figure 6-28, and Figure 6-29, we attempt to demonstrate the surface potential changes as snapshots corresponding to the major event logs. As postulated in this project, the expected EM contrast response is a signal decrease during fracture opening or flow of water in propped fractures (i.e., increase of contact resistance resulting from water invasion between the EAPs, or by separation of EAPs during fracture dilation) and a signal increase as a result of fluid leakoff into the formation during the shut-in periods (i.e., a decrease of contact resistance between the EAPs as a result of water leakoff, and EAP compaction). The concept is that the doped proppant pack that has already been placed, is more electrically conductive when the fracture is closed than when it is open or contains appreciable amounts of water.

For the September-22 operation, the most distinct observation was noted when the BHP in the injection well nears or exceeds our calculated FCP of 154 psi at approximately 15:59 (Figure 6-24). At this time, a decrease in surface potential appears over the injection well and DMWs 1 and 2,

suggesting a fracture dilation near the injection well. However, this signature is mirrored by an increase in surface potential on the west and southwest sides of the injection well, which persisted throughout the recordings. This signature needed further investigation by drilling a new monitoring well. As noted earlier, there was a lot of field personnel activity during the 9/22 operations because of the packer assembly and pipe fitting failure near the surface receivers that exhibited positive or negative potential values (Figure 6-24). Although we did not register an appreciable flow in our flowmeter, the increase in water levels in DMWs 1 and 2 suggests that indeed a small amount of fluid flow took place during this injection. The injection flow rate was recorded as zero throughout this test mainly because the flow rates were below 1 gpm, the minimum measurable value by the totalizer used by Geoprojects.

On September 23, having installed a bridge plug to replace the failed straddle packer, we resumed injection at 4:19 p.m.; however, in response to the surface pipeline connection failure, the injection was shut off after 8 minutes (Figure 6-25). Having fixed the leakage, we restarted injection at 4:29 p.m. Going through a stepwise increase of flow rate and pressure, the wellhead injection pressure rose to 165 psi (1.138 MPa) in 1 hr and 15 min to lead to the maximum flow rate of approximately 3.5 gpm (2.208×10^{-4} m^3/s). After almost 2.5 hr of injection, the reservoir was shut in at 6:53 p.m., and the wellhead shutoff valve was closed (Figure 6-25).

During the time interval of 16:37 until 20:47, the hydraulic fracture was expected to remain dilated at the injection well, leading to an increase in the electrical impedance of the electrically conductive proppant pack inside the fracture. In fact, with the exception of the southwest tip of the survey area, the electric potential data appear to corroborate this expectation over much of the survey area (Figure 6-25). On the southwest of the array, outside the propped zone, the electric signal increase repeated. One possible explanation for this observation is that because of clay rich lithology of injection zone, the introduced fluids leached salt from the host rock and increased the observed electric conductivity. This could also be an artifact caused by the 300-ft long surface pipe that was used for delivering water to the injection well, which was placed over this region. To rule out the coupling of the surface pipe with the transmitter signal, prior to the 2022 deployment, we replaced the injection pipe by a poly pipe and drilled a new monitoring well (DMW 9) at the southwest edge of the array location to measure the water level and salinity as well as to collect an ERT log for the evaluation of the presence of EAPs at this location. These are elaborated further at the end of the current subtask.

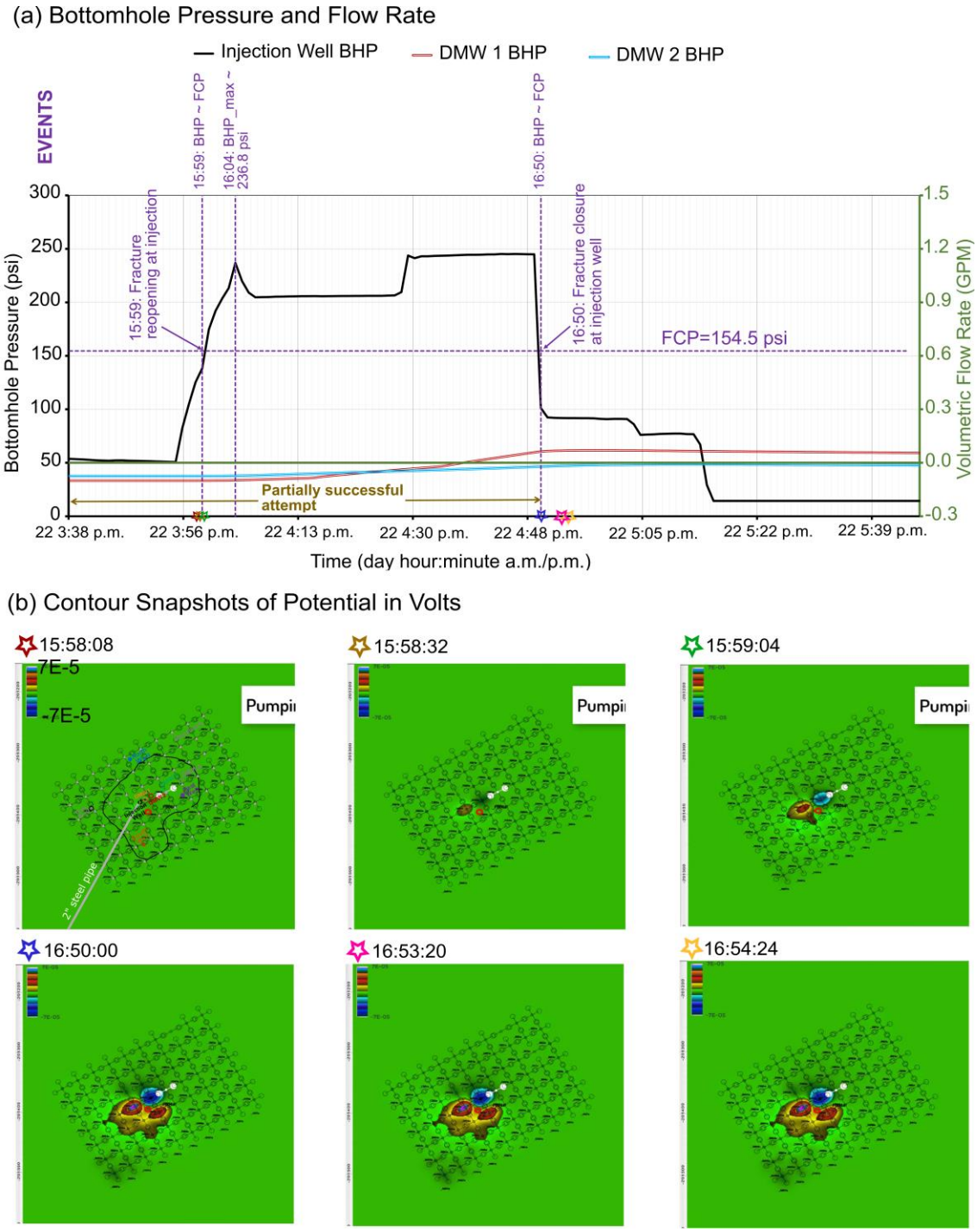

Figure 6-24: (upper plot, left ordinate) Bottomhole pressure (BHP); (upper plot, right ordinate) totalizer-based volumetric flow rate in the injection well; (contours) snapshots of relative change in surface potential at six distinct times; focused on the partially successful attempts for injection on September 22. The injection flow rate is zero throughout this test mainly because the flow rates were below 1 gpm, the minimum measurable value by the totalizer used by Geoprojects.

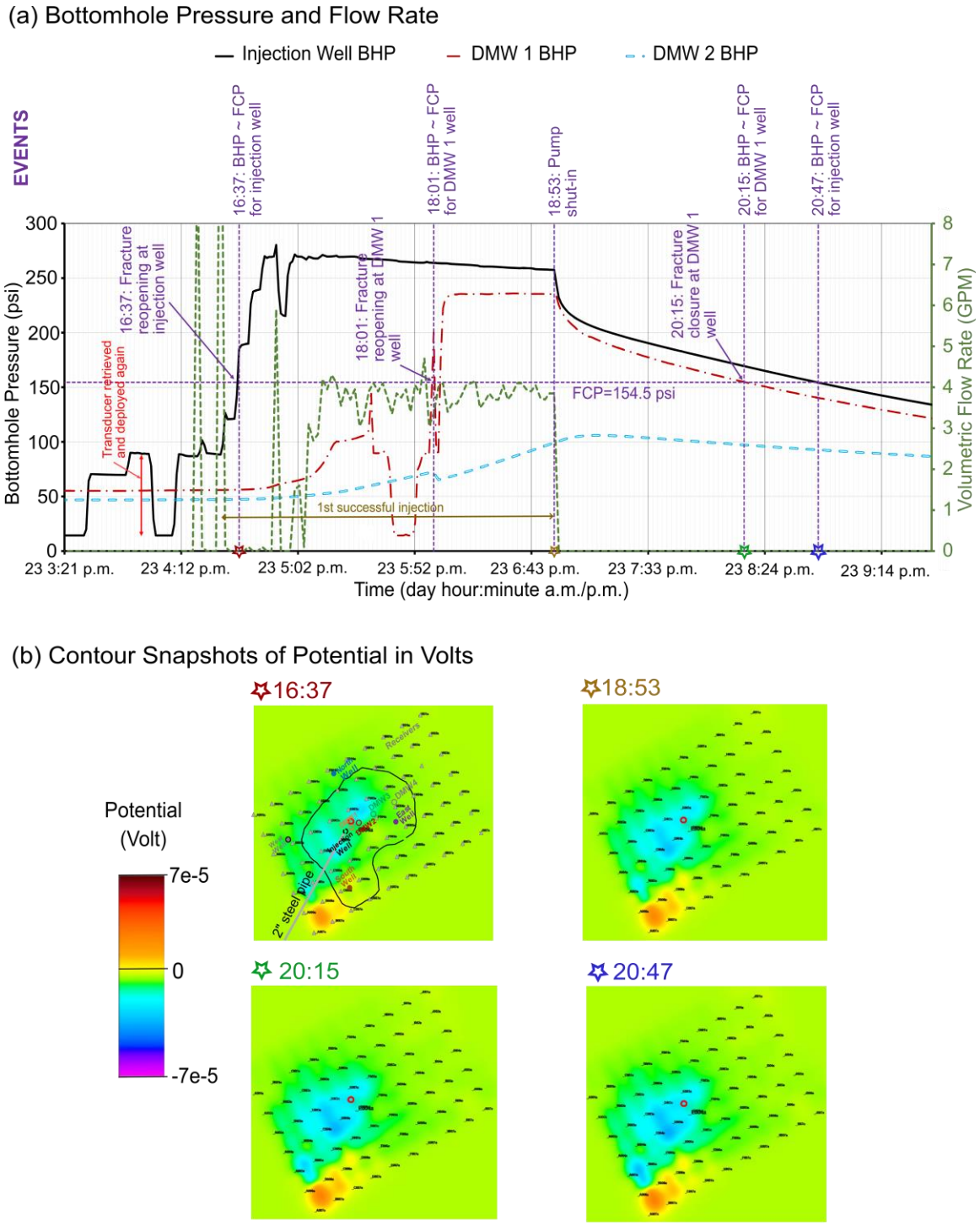

Figure 6-25: (upper plot, left ordinate) Bottomhole pressure (BHP); (upper plot, right ordinate) totalizer-based volumetric flow rate in the injection well; (contours) snapshots of the relative change in surface potential at four distinct times; focused on the first successful injection attempt on September 23.

On September 24, no injection was conducted. Instead, an ESP was installed at the bottom of the injection well, and water extraction from the wellbore space was conducted. As noted in Subtask 6.1, the process was frequently interrupted by the pump overheating, because the reservoir

deliverability was too low to fill in the wellbore space for the continued water extraction. During the several interruptions to allow water from the fracture to enter the well, we deployed a level meter in the injection well and noted that the water level had dropped below the fracture depth. Then we waited for the water level in the well to rise to about 150-160 ft below ground and resumed extraction and repeated this cycle. We stopped the intermittent water extraction after about 3 hours (Figure 6-27). The CSEM survey using the S-TXA transmitter revealed that 1.) there was discontinuous flow in the vicinity of the injection well during the extraction time; and 2.) the southwest edge of the survey area again showed the same positive electric potential. We hypothesize that although the BHP decreases during the water extraction, the decrease in the electric conductivity is a result of continued flow of water within the EM proppant pack in the vicinity of the injection/extraction well from surrounding areas (e.g., see BHP in DMWs 1 and 2 during extraction in Figure 6-27). Because we operated below the FCP, we expected the fracture aperture to remain propped during extraction, and the contribution of the fracture aperture change on the change of electric conductivity to be negligible; however, the intermittent fluid flow of water due to high extraction rates can still reduce the electric conductivity significantly. This is supported by our previous laboratory studies (Subtask 3.1), when the introduction of water in a column filled with EAPs led to a much more significant change in electrical conductivity, than the confining pressure over a column of the EAPs, dropping conductivity from ~600 S/m to ~7 S/m (Figure 6-26).

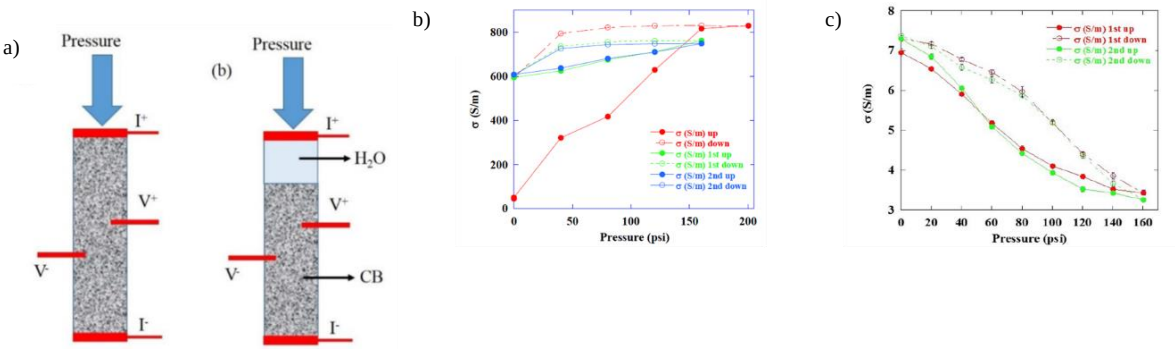

Figure 6-26: (a) Schematic of column setups showing the experiments when we applied external pressure directly over a water-saturated EAP column (lithostatic case) or within a water column above the EAP column (hydrostatic case). (b) Conductivity-pressure hysteresis loops, recorded for external pressure directly applied to the EAP column. Closed circles: increasing pressure. Open circles: decreasing pressure. Red circles: original loop starting from 44 S/m at 0 psi and ending at 830 S/m at 200 psi. On reducing the pressure (open red circles), the conductivity barely changes until zero pressure, when a residual conductivity of 600 S/m is recorded. Subsequent hysteresis loops (green and blue circles) nearly retrace each other. (c) Conductivity of the EAP column shown in (a) as a function of applied hydrostatic pressure. While the conductivity of the EAP column in (b) increases with the applied pressure, the conductivity of the EAP pack decreases substantially when fluid is introduced to the system.

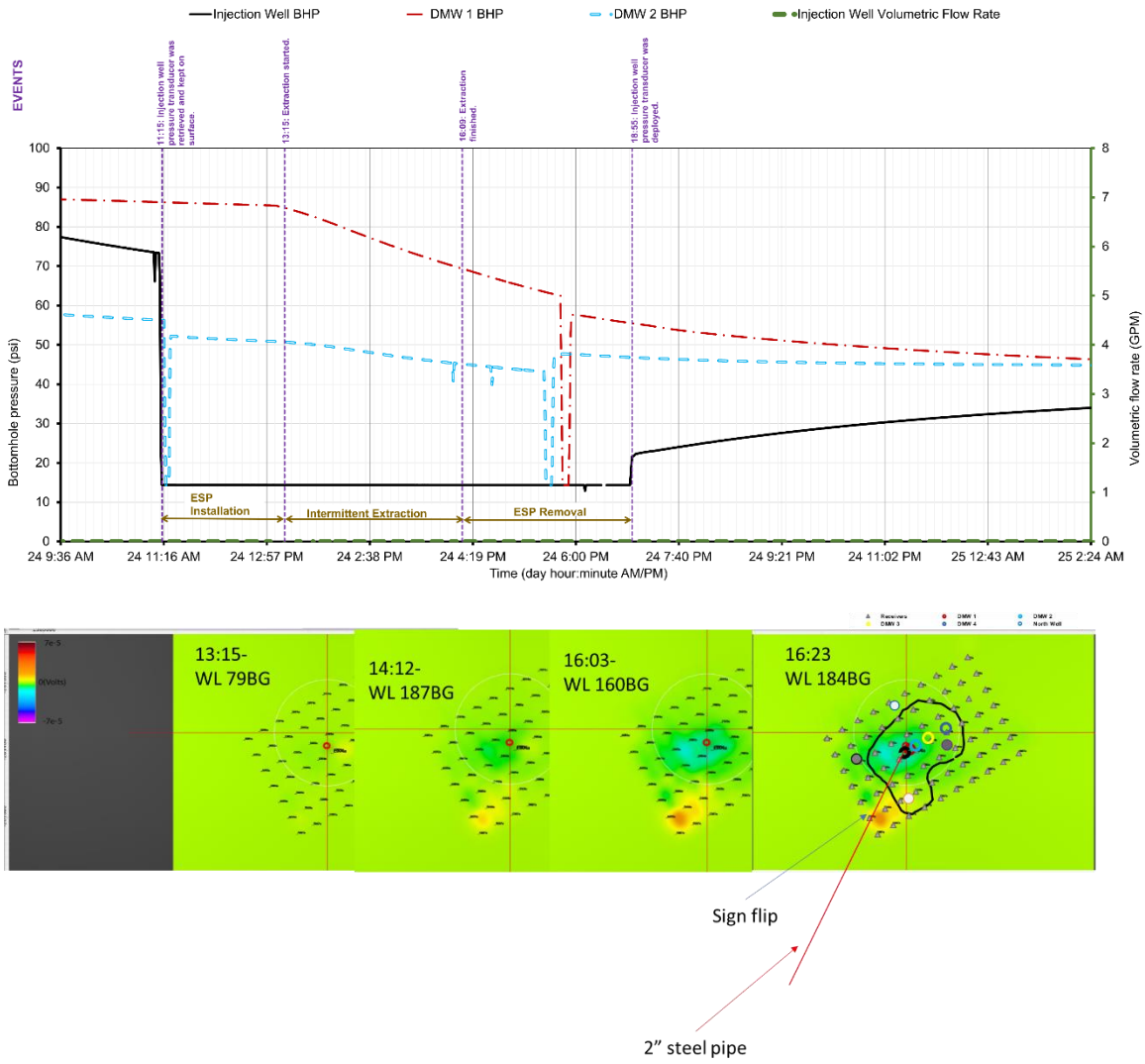

Figure 6-27: (upper) Bottomhole pressure in the injection well and DMWs 1 and 2, and the injection/extraction well flow rate; (lower) contour snapshots of surface potential at four distinct times; during water extraction on September 24, 2020. WL stands for water level in the injection/extraction well, and BG stands for feet below ground surface.

Starting on September 25, all collected EM data are based on using the BH-TXC transmitter. In these studies, we used the previously emplaced ERT terminals in the annular space of the DMW-1 borehole to transmit electric current into the formation (Figure 5-12 and Figure 6-28). The pressure pumping events and EM time series data during injection on September 25 are shown in Figure 6-28. During this injection, we repeated the water injection process as we did on September 23 except for a larger maximum flow rate compared to that on September 23. Having filled the wellbore space first, we started injection at 10:23 a.m., increased the flow rate up to 4.2 gpm (2.650×10^{-4} m^3/s) and maintained it for almost 2 hr, and gradually increased the flow rate up to 7 gpm (4.416×10^{-4} m^3/s) in 42 min starting at 12:11, and gradually reduced the flow rate to zero in 42 min, starting at 12:53. The total injection period was 3 hr and 12 min (Figure 6-28). This was followed by the shutoff valve closure and monitoring of the BHP until September 28.

As was predicted from forward modeling, the use of the BH-TXC transmitter led to a significant enhancement in EM contrast, which was about two orders of magnitude stronger than what was

recorded using the S-TXA surface transmitter (Figure 6-25). This anomaly appeared as early as when the injection well was filling with water, even with the well cap off, and before any pressure pumping had started (see the electric potential contours between 10:15 in Figure 6-28b). The BHP exceeded the FCP at 10:30 a.m. and the pressure at DMW 1 exceeded the FCP at 10:48. Unlike the results obtained during the 9/23 injection with S-TXA, the EM signal gradually increased with the BH-TXC transmitter on 9/25. However, the contrast signals on both days were spread over an almost identical area.

We postulated that several constraining factors that were not envisioned initially may have contributed to these results: recall that the use of borehole transmitters is not a standard practice for ESG. The technical advisors at ESG informed us that because DMW 1 (i.e., the location of BH-TXC) is only 10 ft away from the injection well, there is an inherent problem with this setup; i.e., the transmitted electric current stability is no longer independent of the formation coupling to the fluid and the EM proppant. Thus, as more fluid was being pumped, the coupling changes (signal sign could flip). These observations were also confounded by the fact that the applied field current fluctuated significantly during the 9/25 exercise. Although ESG made significant efforts to keep the current as stable as possible, this resulted in periods when the transmitter was off in order to add or subtract coupling rods in the dipole grounding location. Under normal circumstances, with the surface deployed transmitter (i.e., with small current changes that are not as large percentage of the current), ESG can compensate this issue effectively, because the receiver data are normalized to the transmitter current in the frequency domain. However, the changes observed with the BH-TXC transmitter were as much as 6 to 12 dB of the total current transmitter and as such without further investigation, we cannot be certain that the data are unaffected by current changes. Beyond the current project, we would like to target a future study on using one of the other existing ERT arrays at the DFPS (in either of the four corner observation wells) to conduct the borehole transmission to minimize fluid coupling with the source. Further, this future study should benefit from an improved source generator with the capability to transmit steady current and additional modeling to confirm the reliability of the BH-TXC transmitter data.

We also conducted an extended shut-in period after the second successful injection period to observe the BHP decline at zero flow rate. The EM data on 9/26 is supportive of fluid leakoff from the fracture to the surrounding media and rock, leading to fracture compaction, with a concomitant increase in conductivity (Figure 6-29). However, to overcome the potential issue with fluid coupling with BH-TXC, we only show the results for a fluid leakoff period during which ESG reported a steady current through the BH-TXC transmitter (Figure 6-29). As expected, the steady water leakoff from the fracture into the formation coincided with an increase in the electrical conductivity signature which can be interpreted as further EAP compaction. However, at the end of this time, we again observed an area on the southwest edge of the survey array with relatively low conductivity. Again, this could be a result of electric coupling with the 300-ft long steel surface pipe that was sitting near this anomalous zone.

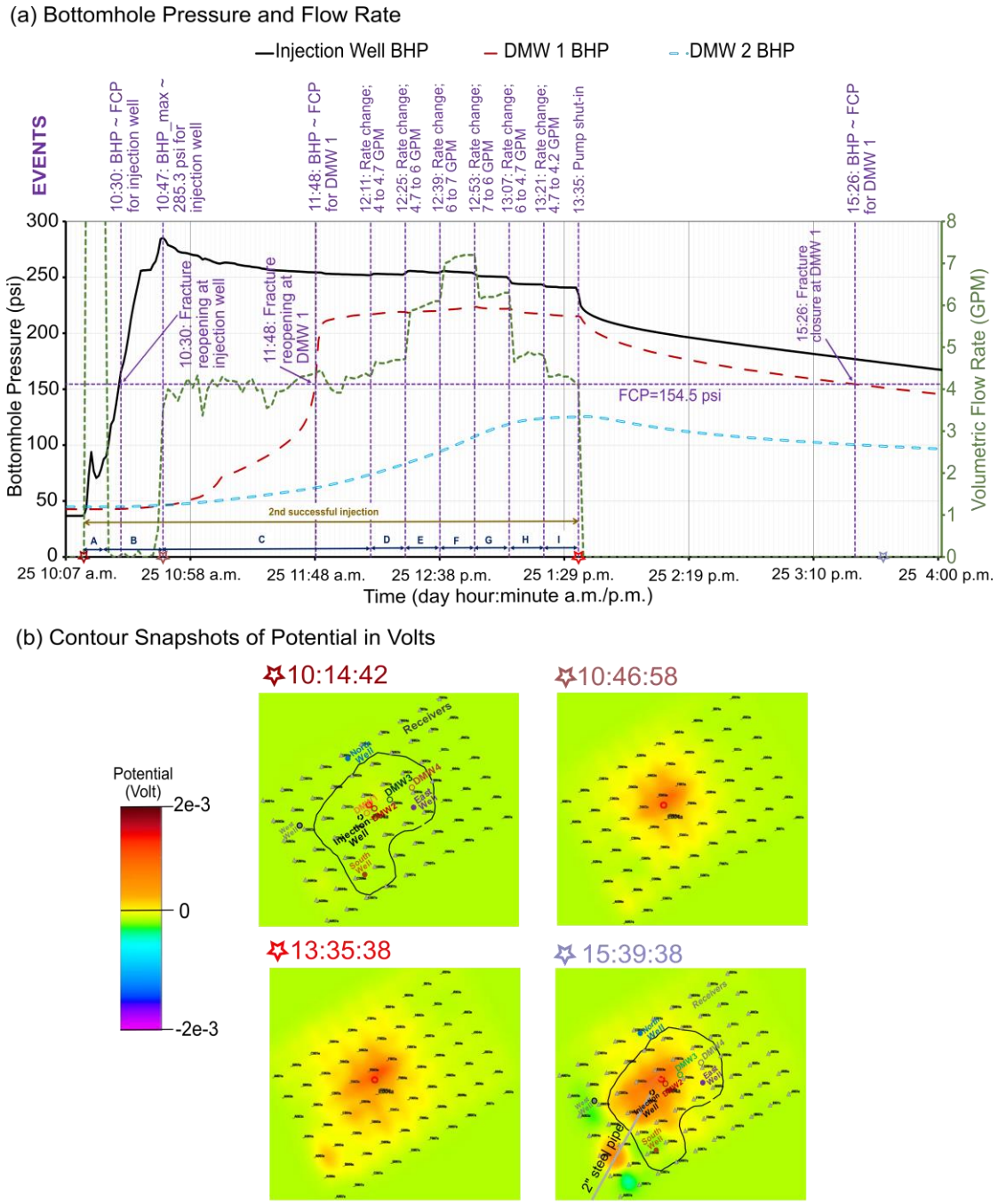

Figure 6-28: (a; left ordinate) Bottomhole pressure (BHP) and (a; right ordinate) totalizer-based volumetric flow rate in the injection well; (b) contour snapshots of the surface electric potential at different times; for the second successful injection time period during September 25. The time intervals A through I for the totalizer-based flow rates correspond to wellbore filling, increase of the flow rate from zero to 4.0 gpm, constant flow rate at 4.0 gpm, step-up of flow rate to 4.7 gpm, step-up of flow rate to 6.0 gpm, step-up of flow rate to 7 gpm, step-down of flow rate to 6 gpm, step-down of flow rate to 4.7 gpm, and step-down of flow rate to 4.2 gpm, respectively. At 1:35 p.m., the injection pump was shut down and the flow rate reduced from 4.2 gpm to zero. The exact timings of these step-up and step-down rates are listed in Table 6-3. (b). As was predicted from forward modeling, using the BH-TXC transmitter led to a significant enhancement in the EM anomaly, which was about 2 orders of magnitude stronger than the anomaly recorded using the S-TXA surface transmitter. However, significant noise was encountered as a result of the proximity of the BH-TXC transmitter to the injection well.

Table 6-3: Averaged flow-rate data within various time intervals on September 25, used for hydrogeological and geomechanical studies. Time periods A through I are marked in Figure 6-28. The volumetric flow rates in the last column are derived from equation $Q = \pi D^4 \Delta P / 128 \mu L$, where $D, \Delta P$, and L denote the surface line internal diameter, friction pressure drop, and length, and μ is the water viscosity, 1cp in this study.

Time period	Initial time (date hour:minute a.m./p.m.)	End time (date hour:minute a.m./p.m.)	Time duration (minute)	Totalizer flow rate (gpm)	Friction-based flow rate (gpm)
A	25 10:15 a.m.	25 10:23 a.m.	8	0	0
B	25 10:23 a.m.	25 10:47 a.m.	24	Linear 0-4	Linear 0-0.8
C	25 10:47 a.m.	25 12:11 p.m.	24	4	0.8
D	25 12:11 p.m.	25 12:25 p.m.	14	4.7	0.8
E	25 12:25 p.m.	25 12:39 p.m.	14	6	0.8
F	25 12:39 p.m.	25 12:53 p.m.	14	7	0.8
G	25 12:53 p.m.	25 13:07 p.m.	14	6	0.8
H	25 13:07 p.m.	25 13:21 p.m.	14	4.7	0.8
I	25 13:21 p.m.	25 13:35 p.m.	14	4.2	0.8
Postinjection	25 13:35 p.m.	28 9:35 a.m.	4,080	0	0

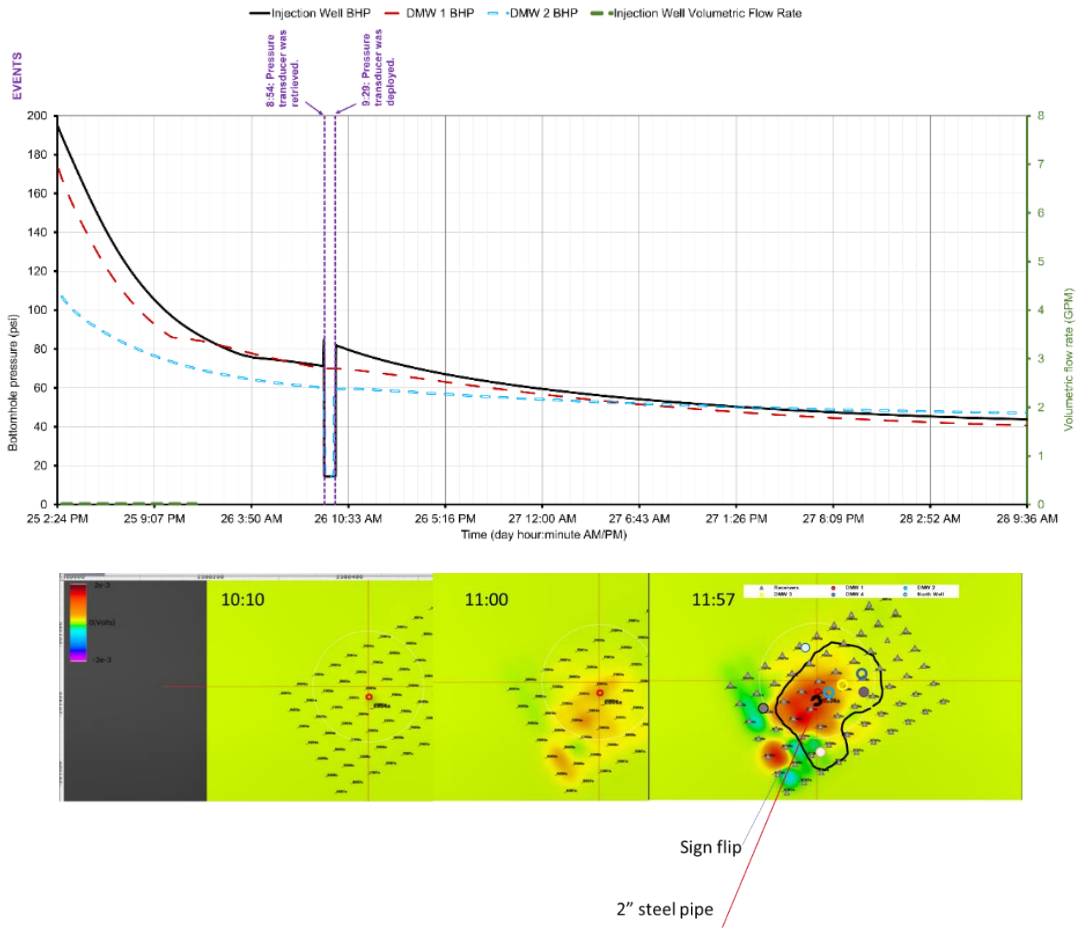

Figure 6-29: (upper) Bottomhole pressure in the injection well and DMWs 1 and 2, and the injection well flow rate; (lower) contour snapshots of surface potential at four distinct times; during the extended shut-in period on September 25 through 28.

Overall, during the 2020 field deployment, we succeeded in obtaining the expected EM signal decrease during fracture reopening or flow of water in propped fractures and the expected signal increase as a result of fluid leakoff into the formation during the shut-in periods. Most of the observations on 9/23 (dilation), 9/24 (extraction), and 9/26 (compaction) are consistent with our expectations.

These field data, however, revealed the need to determine the cause of sign flip when using a borehole transmitter. However, because of 1) lack of sufficient funds and 2) surface tooling was already sensitive in detecting the EM signature at the DFPS (and ultimately is much less intrusive in a production setting), we chose this approach over the borehole transmitter approach for the 2022 field test. Also, before the 2022 field deployment, we replaced the metal injection pipe with a poly pipe to eliminate its potential interference with the signal on the southwest side of the array. In addition, as elaborated in the following, we emplaced one monitoring well (DMW 9) on the southwest edge of the array to further investigate the source of this signal anomaly. Beyond the current project, a complementary research can address the possible fluid coupling with the source by using 1.) one of the other existing ERT arrays at the DFPS (in either of the four corner observation wells) to conduct the borehole transmission; and 2.) an improved transmitter with the capability to output steady current.

Drilling a new monitoring well and re-logging all wells

In October 2021, we drilled a new monitoring well, called DMW 9, near the south well (Figure 6-30), to address one anomaly in the first CSEM survey at the drilled location. We completed this well by screened casing and sand pack at the depth interval of 170 to 180 ft. Then, we attempted to evaluate the hydraulic conductivity of this new well and the effect of drilling that on the injectivity of the injection well during a 10-hr injection test in December 2021. As shown in Figure 6-31, the general trends of the injection well and DMW-1 BHP during this injection test are close to those during the injection test in September 2020. In addition, increasing the BHP of the injection well is proceeded by the mild increase of the DMW-9 BHP, which shows that DMW-9 sand pack and casing screen are hydraulically conductive and that DMW 9 can be used as a monitoring well.

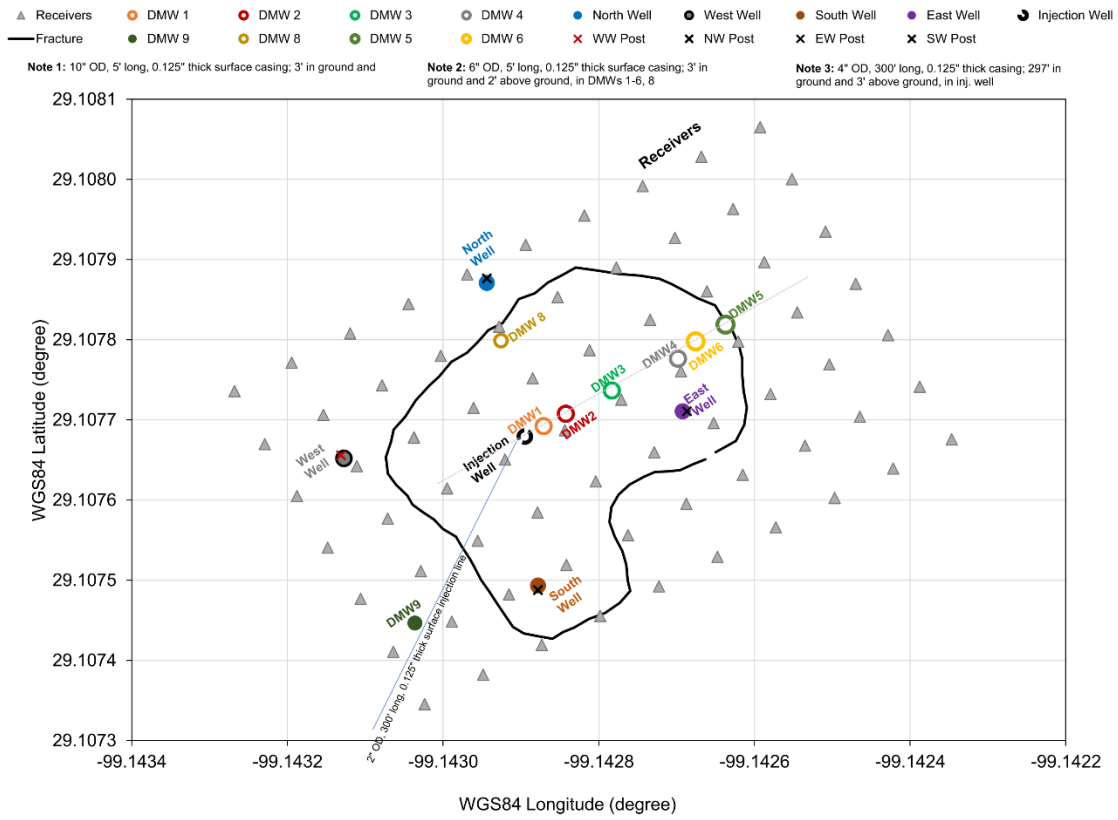

Figure 6-30: The DFPS wells, the boundary of the interpreted horizontal fracture, the EM antenna during September 2020 survey, and the surface injection pipe. The recently drilled well in the southwest of the south wells is DMW 9.

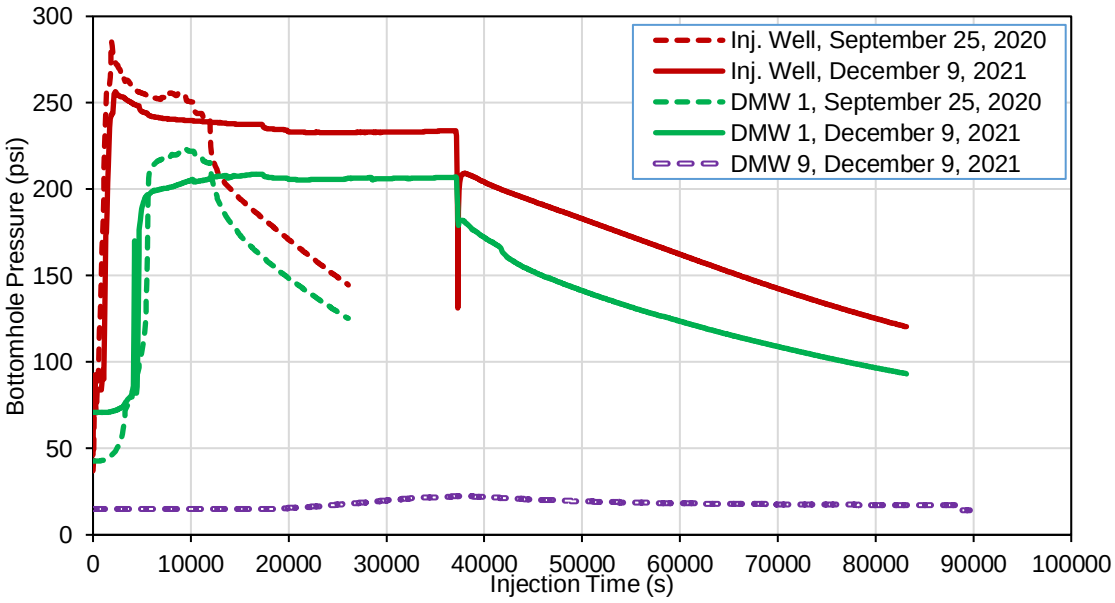

Figure 6-31: Comparison of the bottomhole pressure of the injection well and DMW 1 during a 10-hr injection test in December 2021 and one injection test in September 2020; and comparison of the bottomhole pressure of DMW 9 and the injection well during the injection test in December 2021.

We also obtained conductivity logs in various monitoring wells at the DFPS to evaluate the effect of previous injection tests on proppant displacement and the hosting rock conductivity. A possibly substantial displacement of electrically conductive proppants would be inferred from significant changes in a conductivity well log as evaluated by comparing the recently obtained logs with those acquired in 2018. Figure 6-32 shows the comparison of the new conductivity logs with the logs in 2018 for DMWs 1, 2, 3, 5, 6, and 9. In this figure, we labeled the conductivity logs after the tool frequency: 100 kHz for Tool HMI453, and 35 kHz for Tool EM-2PIA. Because of its higher frequency, Tool HMI453 surveys shallower rock volumes compared to Tool EM-2PIA. Thereby, EM-2PIA is more favorable for reducing borehole effects and increasing the rock signal in the data acquisition. Neglecting the possible depth shifts, all logs follow an identical trend through various layers. We observe a large jump in conductivity at 175 ft of depth in all wells except for DMWs 5 and 9, possibly because these wells do not intersect the propped fracture area. These results are consistent with our previous estimation of the extent of EAP fracture at the DFPS (Ahmadian et al., 2018, 2019).

The advantage of using Tool EM-2PIA in logging deep rock volumes and reducing the wellbore effect is clearly demonstrated also by the comparison of

(1) the DMW-2 logs using various tools in Figure 6-32b;
(2) the DMW-3 logs using various tools in Figure 6-33a; and
(3) the DMW-5 logs using various tools in Figure 6-33b.

Figure 6-34a shows that the proppant pack at DMW 6 was undisturbed during the past injections because the logs obtained in 2018 and 2021 match with each other. Figure 6-34b shows that

(1) the DMW-5 log can still be used as the background log because of the overlapping logs obtained in 2018 and 2021, and
(2) DMW 9 does not cross the EAP-filled fracture because no conductivity picks are observed in the associated log at 175-ft depth.

Figure 6-35 shows that the DMW-1 induction log obtained in 2018 is very close to the DMW-2 induction logs in 2018 and 2021 above 170-ft depth. Because of the slight deviation of DMW 1 at 170 ft, we were not able to log this well below 170 ft and therefore, we could not evaluate the possible proppant displacement in the vicinity of this well due to the past injections.

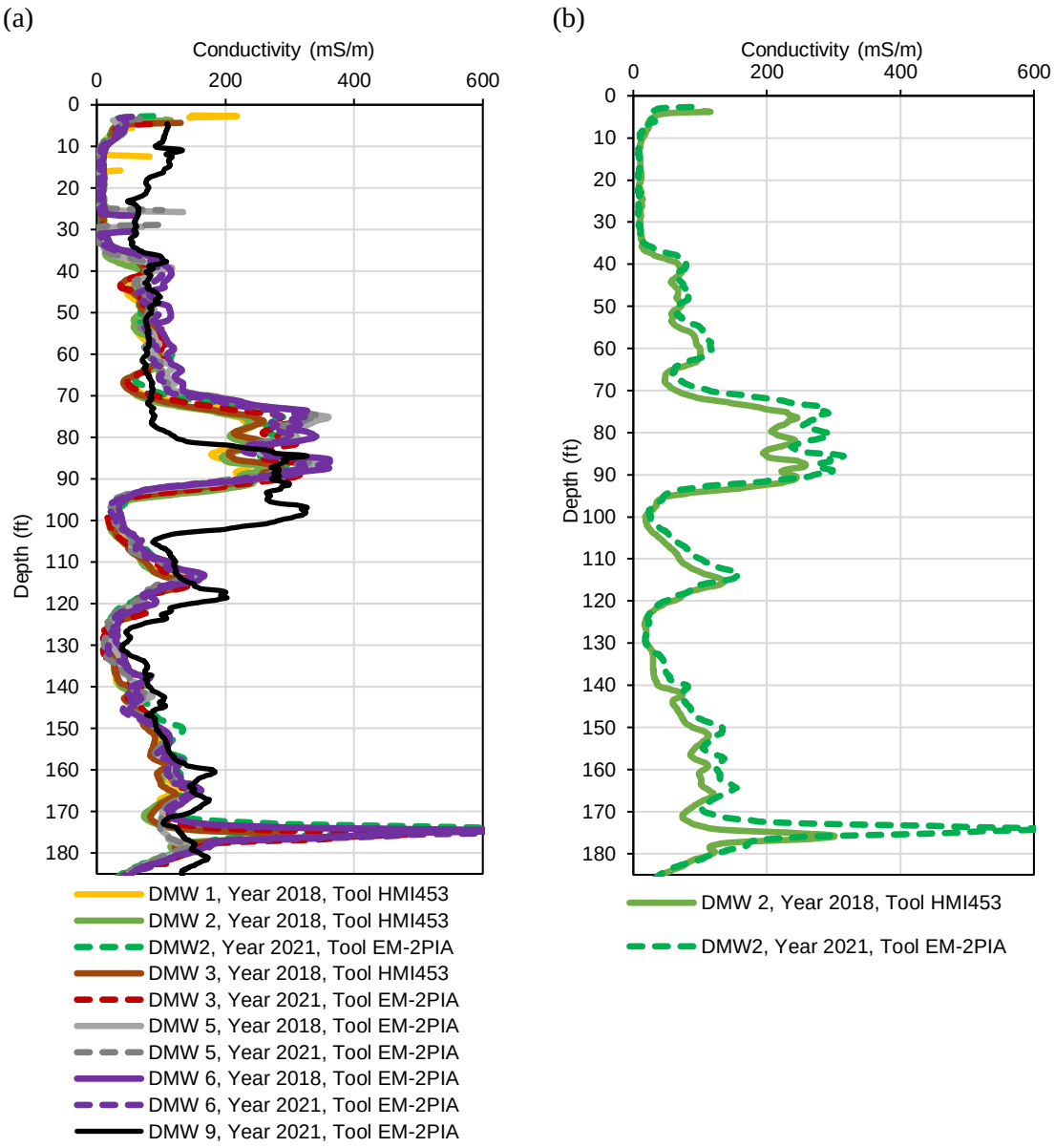

Figure 6-32: (a) Induction logs in DMWs 1, 2, 3, 5, 6, and 9, obtained using Tools HMI453 and EM-2PIA in 2018 and 2021. (b) Comparison of DMW-2 logs, obtained in 2018 and 2021, using HMI453 and EM-2PIA, respectively. EM-2PIA is more favorable than the other tool because of reducing borehole effects and increasing the rock signal, as EM-2PIA acquires data at lower frequencies than the other tool.

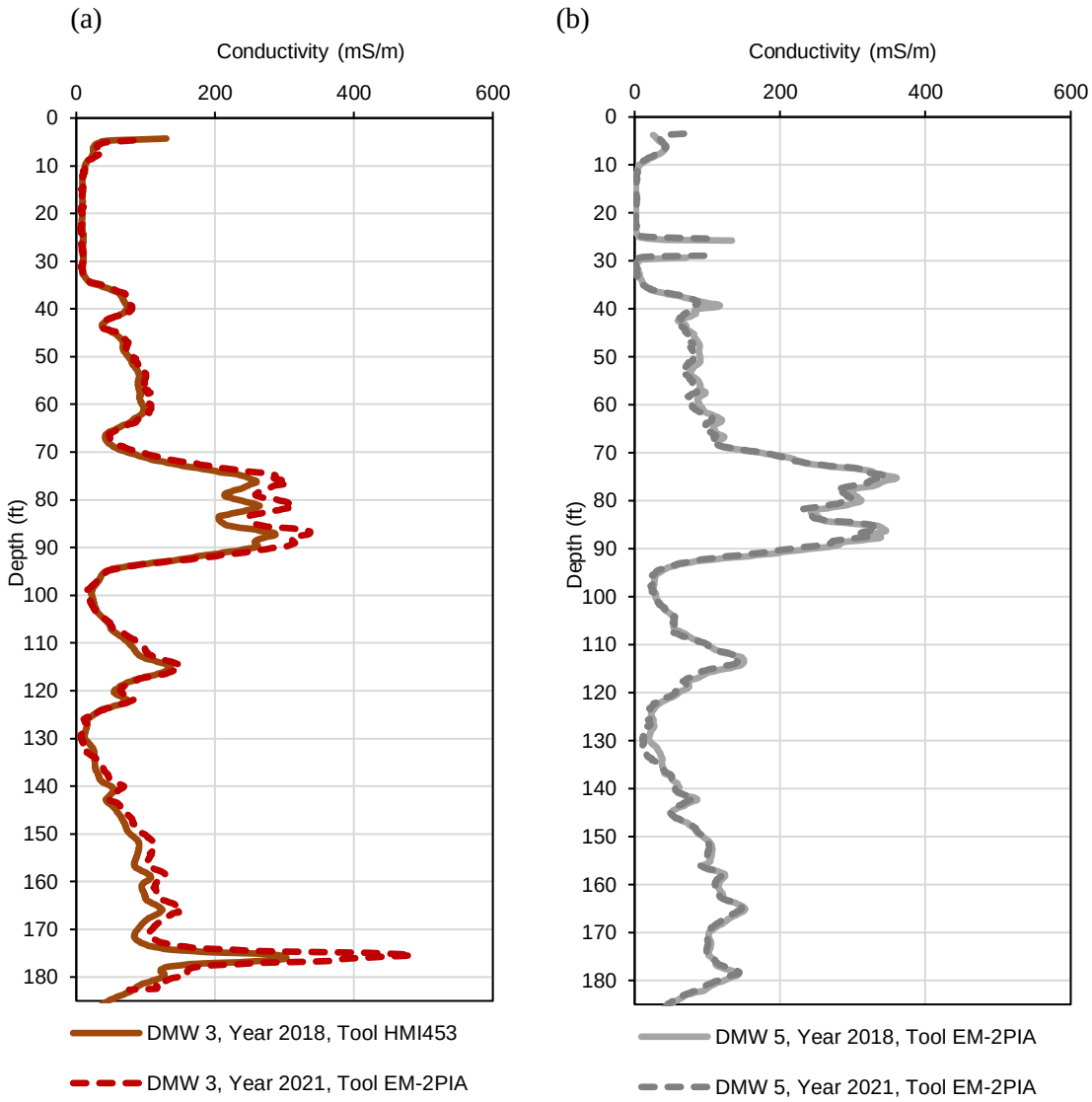

Figure 6-33: Comparison of induction logs for (a) DMW 3, and (b) DMW 5. These logs were obtained in 2018 and 2021, using HMI453 and EM-2PIA. EM-2PIA is more favorable than the other tool because of reducing borehole effects and increasing the rock signal, as EM-2PIA acquires data at lower frequencies than the other tool. No difference is observed in DMW-5 logs, obtained with the same tool but at different times; however, a large jump in conductivity is observed in DMW 3 at 175-ft depth from the HMI453 log to the EM-2PIA log, as the later log increases the rock signal at lower acquisition frequencies compared to the other tool.

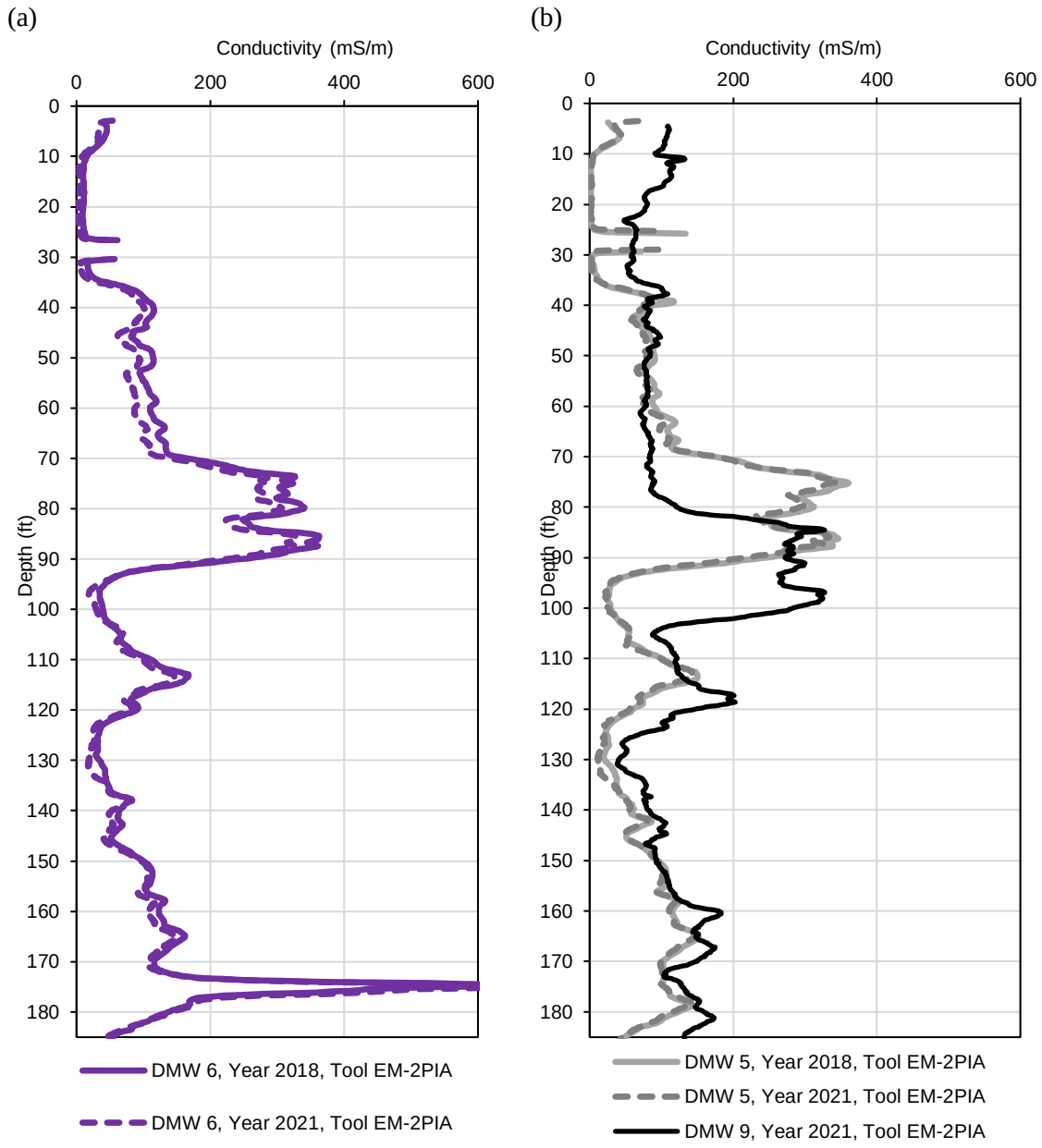

Figure 6-34: Comparison of induction logs for (a) DMW 6, and (b) DMWs 5 and 9. These logs were obtained in 2018 and 2021, using Tool EM-2PIA. Neglecting the possible depth shift in DMW-5 logs, no significant difference is observed between logs obtained in 2018 and 2021. DMW 5 is located outside the EAP-filled fracture and the associated log can be used as the background log. Comparison of DMW-9 log with the background log in DMW 5 shows no signs of electrically active proppants at 175-ft depth. Therefore, DMW 9 is located outside the propped fracture area.

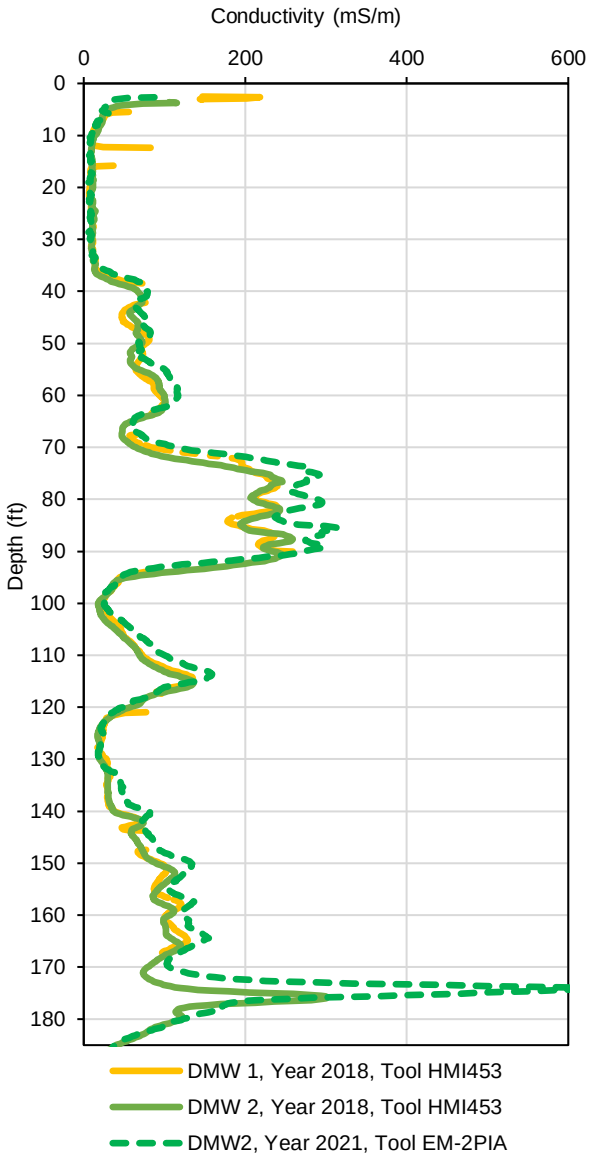

Figure 6-35: Comparison of induction logs for DMWs 1 and 2. These logs were obtained in 2018 and 2021, using HMI453 and EM-2PIA. EM-2PIA is more favorable than the other tool because of reducing borehole effects and increasing the rock signal, as EM-2PIA acquires data at lower frequencies than the other tool. A large jump in the conductivity log is observed in DMW 2 at 175-ft depth from the HMI453 log to the EM-2PIA log, as the later log increases the rock signal at lower acquisition frequencies compared to the other tool. Logging DMW 1 below 170-ft depth was not possible due to the well deviation at 170-ft depth.

Collectively, these results suggest that the unexpected signal observed near the location of DMW 9 in the September-2020 data are consistent with our other hypothesis that the surface metal pipe used during the injections was the source of the noise at that location.

6.5 Smart Proppant Test 2 in 2022: In-Situ Remote Salinity Tests

During the 2022 field deployment, we used salt as tracer, and the breakthrough curves are discussed below.

EM field interpretation

Our 2022 EM field interpretation relied on the movies that ESG provided us, which compared the change of the EM field with respect to a reference starting time, T_0. Table 6-4 shows an exemplary set of movie clips for the evolution of the electric field on January 26, along with additional coinciding recorded events, flow rate, cumulative injected volume, and pressure. The second row in Table 6-4 represents clips from pseudo-amplitude of the scattered field, defined as the total field amplitude at a specific time subtracted by the total field amplitude before the injection time. The third row is the absolute value of pseudo-amplitude. The equations for the scattered field pseudo-amplitude and pseudo-amplitude absolute are as follows:

$$\text{Pseudo-amplitude} = |\vec{E}(\text{t})|-|\vec{E}(0)|, \tag{6-5}$$

$$\text{Pseudo-amplitude Absolute} = ||\vec{E}(t)|-|\vec{E}(0)||, \tag{6-6}$$

where $\vec{E}(0)$ and $\vec{E}(t)$ denote the electric field vectors at time *0* and time *t*, respectively. Time *0* is selected arbitrarily, which was commonly chosen as a few minutes before the start of injection. In these formulations, the scattered electric field pseudo-amplitude is calculated as the amplitude of the total electric field in time *t* subtracted by the amplitude of the total electric field in time *0*. Because this subtraction can lead to positive and negative numbers and because amplitude is fundamentally always positive, Equation (6-5) does not express amplitude, and it is rather called "pseudo" amplitude. To reflect only the magnitude of this subtraction rather than its sign, the pseudo-amplitude absolute was introduced. However, these parameter definitions by ESG led to an inconsistency between the contours of pseudo-amplitude and pseudo-amplitude absolute. To demonstrate this inconsistency between contours of pseudo-amplitude and the pseudo-amplitude absolute, a representative set of movie frames corresponding to contours at 12:25 is shown in Figure 6-36 and Figure 6-37. As shown in Figure 6-36, there is a receiver on the west of the injection well that is grayed, and the pseudo-amplitude is supposedly between -8×10^{-7} and 8×10^{-7} V/m. Based on this, the absolute value of pseudo-amplitude should be between 0 and 8×10^{-7} V/m. However, the same receiver pseudo-amplitude absolute is at least 1×10^{-6} V/m from ESG video frame, as shown in Figure 6-37. ESG believes that the internal calculations in the graphics software program DMAX smooth out the colored contours and has caused this issue. As such, we suggested the use of the conventional scattered field formulations to ESG for the calculation of the amplitude as follows:

$$\text{Amplitude} = |\vec{E}(t)- \vec{E}(0)|. \tag{6-7}$$

The difference between the amplitude formulation in Equation (6-7) and Equation (6-5) is that the latter equation subtracts two vectors $\vec{E}(\text{t})$ and $\vec{E}(0)$ first to obtain the scattered field vector and then calculates the amplitude of this vector, and the former equation calculates the amplitude of each vector $\vec{E}(t)$ and $\vec{E}(0)$ first and then subtracts these amplitudes from each other. Because the scattered electric field is still a vector, we prefer Equation (6-7) for the calculation of the scattered field amplitude.

We recognize the difference in the two representations of amplitude in Equations (6-5) and (6-7). While the ESG's pseudo-amplitude method does have its own advantages when dealing with much deeper EM targets, in the Devine case, the scattered field formulation in Equation (6-7) is more plausible.

Table 6-4: Evolution of the scattered field pseudo-amplitude, pseudo-amplitude absolute, and phase absolute, from 11:55 until 12:25 on January 26. The events, flow rate, cumulative injected volume, and bottomhole pressure (BHP) are listed. The color contours for all these parameters start to grow from the central injection well. The largest expansion of the color contours occurs for the phase absolute, showing the largest sensitivity of this parameter to injection. The largest change of the snapshots occurs during the surface line refilling, which is likely related to the release of the trapped water inside the injection well into the proppant pack once the wellhead valve was opened at the beginning of the refilling.

Time	11:55	12:00	12:05	12:10	12:25	Legend
Pseudo-amplitude; |E(t)|-|E(0)|	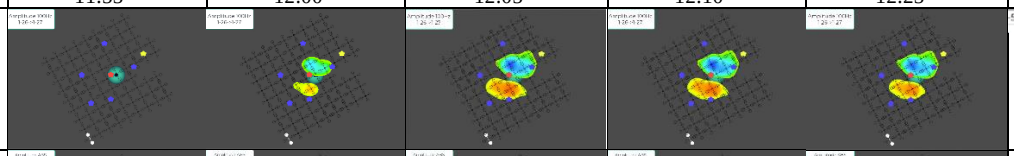					
Pseudo-amplitude Absolute; ||E(t)|-|E(0)||	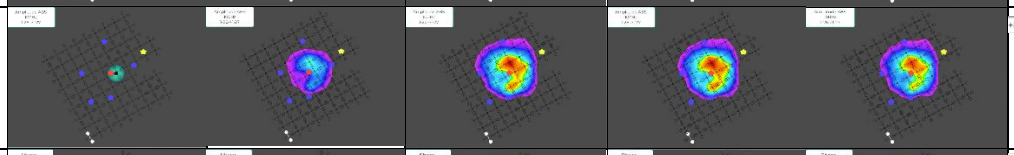					
Phase Absolute; |phi(t)-phi(0)|	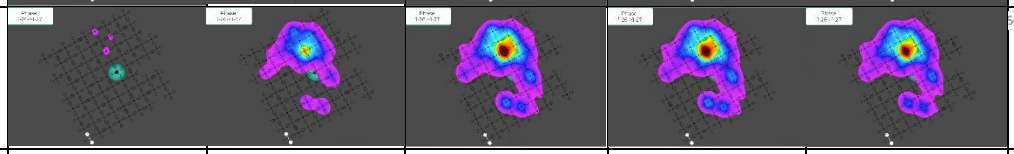					
Event	-	Started refilling	Started injection	-	-	
Flow rate (gpm)	0	0	0.6	0.6	0.9	
Cumulative Volume (Gal.)	Cumulative Injection so far: 2713 gallons	0	0.6	2.9	13.5	
BHP (psi)	67	67.4	92	98	176	

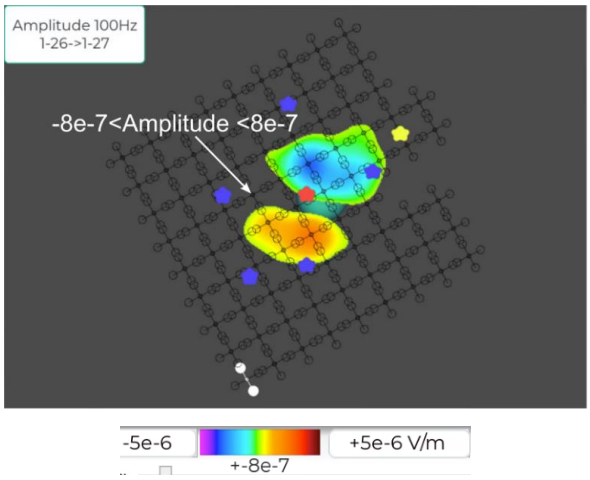

Figure 6-36: Scattered field contours of pseudo-amplitude at 12:25 on January 26. The red star marks the injection well, the blue stars mark the east, west, north, and south wells, and DMW 9, and the yellow star marks DMW 5. The hollow black circles show the receiver rods, and the receivers are located at the centers of the crosses. The color bar ranges from -5×10^{-6} to $+5\times10^{-6}$ V/m, excluding the noise floor range of -8×10^{-7} to $+8\times10^{-7}$ V/m.

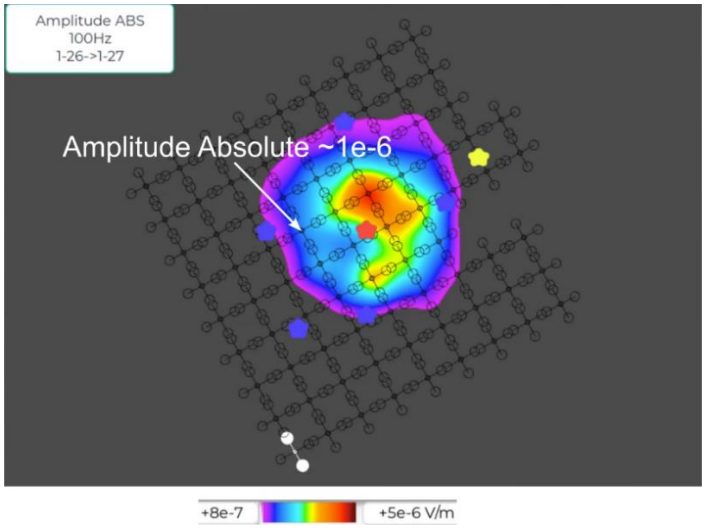

Figure 6-37: Scattered field contours of the pseudo-amplitude absolute at 12:25 on January 26. The red star marks the injection well, the blue stars mark the east, west, north, and south wells, and DMW 9, and the yellow star marks DMW 5. The hollow black circles show the receiver rods, and the receivers are located at the centers of the crosses.

We devised a simplified routine to try to understand the data. This routine is based on plotting the individual receiver electric potentials of the surface electric field combined with the flow rate and bottomhole pressure through time. Having plotted these electric potentials for the x- and y-component of the electric field for various receivers, ESG suggested that the diurnal effects are coupled with the x-component of the electric field due to the large swings in the daily temperature during one of the injection cycles. However, the Y-component of the electric field was decoupled from these diurnal effects. Thus, to unify the interpretation of the results, we decided to limit the initial interpretation to Y-component of the pseudo-amplitude absolute only, as follows:

$$\text{Y-component of Pseudo-amplitude Absolute} = ||E_y(t)|-|E_y(0)||, \tag{6-8}$$

where E_y is the Y-component of the electric field in the complex domain, and $E_y(0)$ and $E_y(t)$ denote this complex number in time *0* and time *t*. We plotted the electric field using the Y-component of the pseudo-amplitude absolute of the surface electric field, based on Equation (6-8), through time obtained from individual receivers. To assess the possibility of a correlation between the electric field changes and flow rate or bottomhole pressure (BHP), we combined these plots with the injection flow rate and BHPs at the injection well and DMWs 1 and 2. This combination of plots helped us to quickly compare the governing parameters of the fracture behavior with the electric potential changes.

Figure 6-38 through Figure 6-46 plot the Y-component of pseudo-amplitude absolute electric potentials for a group of individual receivers at almost a constant distance from the injection well for January 23 (Figure 6-38 through Figure 6-40), January 26 (Figure 6-41 through Figure 6-43), and January 27 (Figure 6-44 through Figure 6-46). To ensure that a unified method is used for the comparison of the electric potentials, and to evaluate the preferential azimuth of the electric field distribution, we only considered the signal from equidistant receivers from the injection well in each of these plots. Figure 6-38, Figure 6-41, and Figure 6-44 plot the electric potentials for the receivers at the closest distance of 22 ft from the injection well. Figure 6-39, Figure 6-42, and Figure 6-45 plot the electric potentials at receivers that are at 47 ft of distance from the injection

well. The electric potentials for the receivers at an equidistance of 87 ft from the injection well are shown in Figure 6-40, Figure 6-43, and Figure 6-46.

To test the possibility that an EAP pack can be used as a sensor for determining the in-situ flow rate, on January 23, we injected almost 600 US gallons of freshwater at variable flow rates in nearly five hours. Figure 6-38 plots four electric potentials for receivers located at 22 ft from the injection well during this injection cycle. Three important intervals can be observed in these electric potentials.

Interval 1 in Figure 6-38 spans the time interval when the surface line and injection well were being refilled with freshwater after opening the injection wellhead valve, coinciding with an abrupt increase of the electric potential. We believe this sharp increase of the electric potential is because of releasing the trapped water in the injection well into the formation by opening the wellhead valve. Thus, reducing the conductivity of the EAP-filled fracture. We believe even in the presence of the continuous overnight leakoff associated with the previous injection cycle, the water in the well was trapped inside the injection well because the wellhead valve was tightly closed during this leakoff. This is analogous to the trapped water in a straw placed in a cup of water, while one holds their thumb on the straw's opening; when the thumb is removed, the water trapped in the straw rushes into the cup. We observed a similar early-time jump of the electric potential signal during refilling on January 26 (Figure 6-41) due to the release of the trapped water in the injection well after opening the wellhead valve. However, we did not observe this behavior on January 27. We believe this is because the injection cycles before these two later days had loaded the formation with thousands of gallons of water. This likely slowed down the injected water leakoff into the formation in January 27, leading to less vacuum effect at the fracture depth and negligible well water flow into the formation after opening the injection wellhead valve.

Interval 2 in Figure 6-38 spans the time interval of injection at low flow rates (equal or below 1 gpm), characterized also by the gradual decline of the electric potential signal. One possible explanation of this slow decline can be attributed to the gradual, gravitational resettlement of the EAPs, very close to the injection well, that had been disturbed by the sudden flow of stored water inside the injection well into the proppant pack by opening the wellhead valve during Interval 1. As we have shown previously, when the EAP pack is tightly packed, its conductivity increases. We believe, the flow rates smaller than 0.5 gpm throughout this interval were inadequate to provide enough fluid volumes to cause an increase in the electric potential signal by reopening the fracture.

Interval 3 in Figure 6-38 spans the time interval of injection at high flow rates (above 1 gpm), when a strong correlation is observed between the electric potential signal, the flow rate, and the injection-well BHP. This correlation is based on the significant, monotonous increase of the electric potential signal simultaneous with the rise of the flow rate and BHP. The injection-well BHP exceeds the FCP of 154 psi at the beginning of Interval 3, leading to the fracture reopening, near the injection well. Consequently, we observe the change in the trends of the electric potential of all receivers from declining to plateau at the beginning of Interval 3, followed by a small bump in the electric potential signal. This small bump was proceeded by a large increase of the electric potential signal likely due to the increase of the EAP pack resistivity during the further extension of the reopened fracture area. In other words, we believe that the signal increase here is because the elevated fluid pressure reopened the fracture and separated the EAP grains from one another.

Collectively, these results suggest a strong correlation between flow rate, fracture dilation, EAP pack compaction, and electric potential signal. In addition, because the pseudo-amplitude of the signal among the four receivers is different, this novel method we have developed can identify the preferential fluid movement direction.

(a)

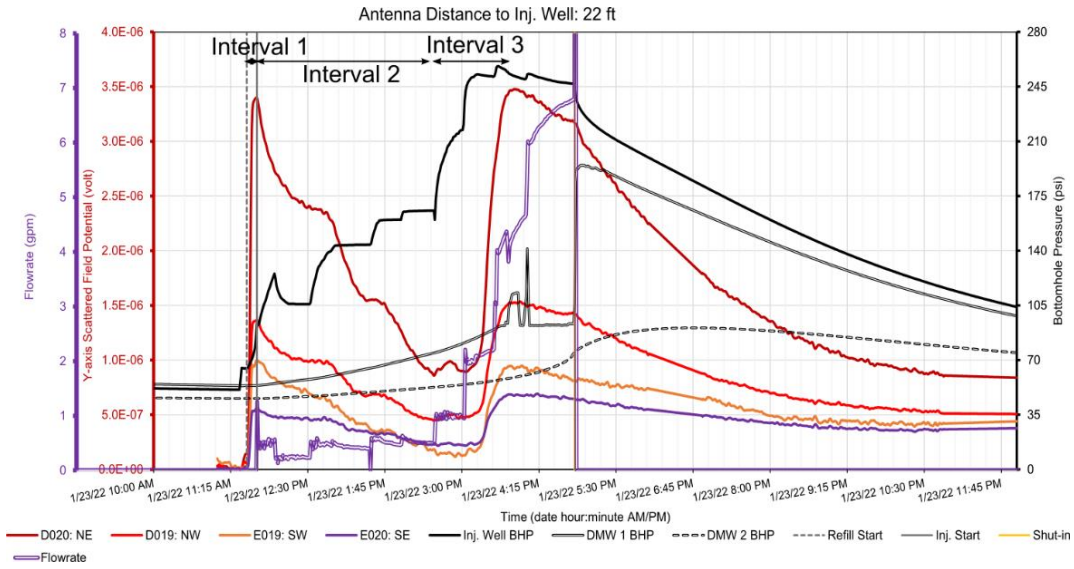

(b)

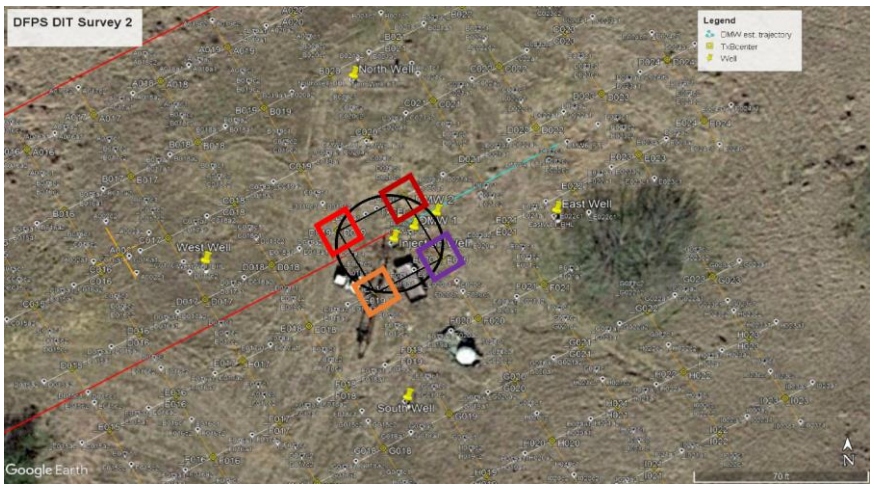

Figure 6-38: (a) Temporal change of the scattered field potential in receivers at 22 ft of distance from the injection well, flow rate, and the bottomhole pressure (BHP) at the injection well and DMWs 1 and 2, on January 23. The step-wise change of the DMW-1 BHP at 100 psi after Interval 3 is because of our special setup at the DMW-1 wellhead where we installed a flowmeter to measure the flow rate out of DMW 1. We noticed that the flow rate was very small, and measuring these flow rates required pinching a valve at the DMW-1 wellhead to regulate pressure and flow. We closed this valve around 17:00, which was followed by an expected sharp rise of the DMW-1 BHP. (b) Plan view of the survey area and the colored squares that mark the location of the receivers with electric potentials plotted in (a). The vertical black lines in (a) indicate the starting and finishing times of refilling the surface line and the injection well with water during Interval 1.

(a)

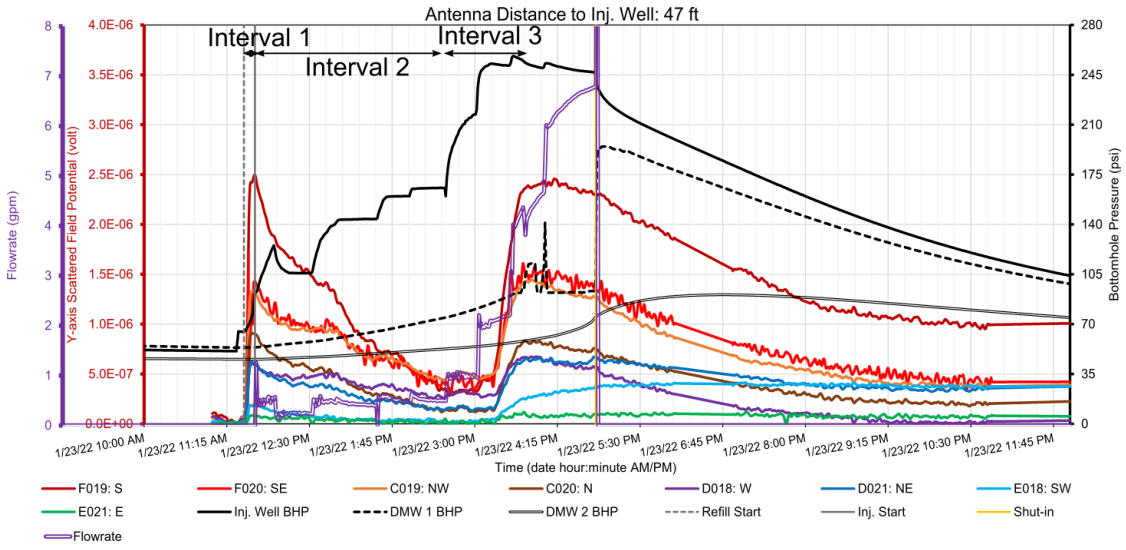

(b)

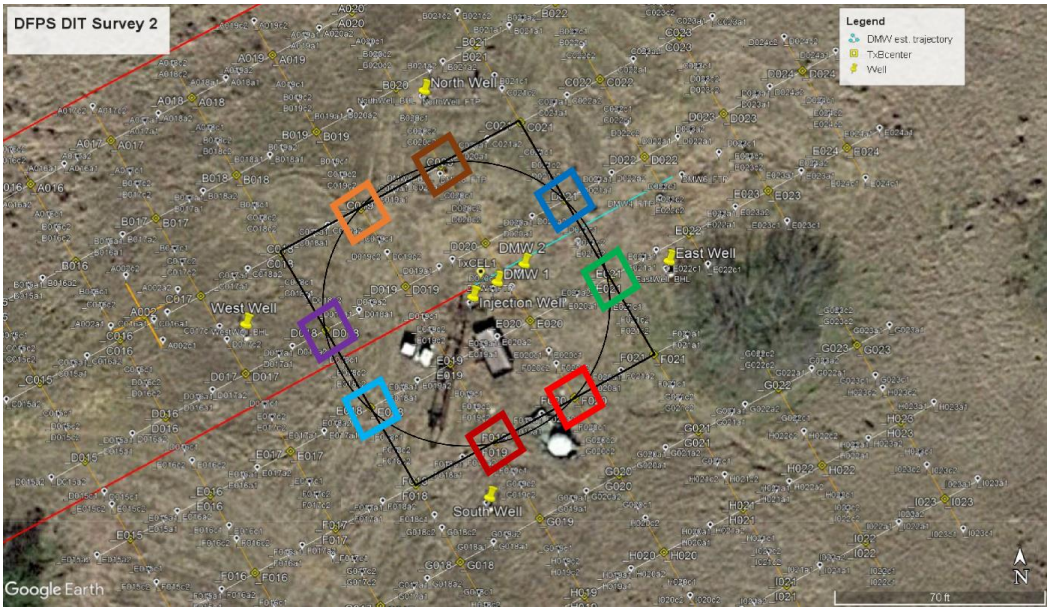

Figure 6-39: (a) Temporal change of the scattered field potential in receivers at 47 ft of distance from the injection well, flow rate, and the BHP at the injection well and DMWs 1 and 2, on January 23. (b) Plan view of the survey area and the colored squares that mark the location of the receivers with electric potentials plotted in (a). The vertical black lines in (a) indicate the starting and finishing times of refilling the surface line and the injection well with water during Interval 1.

(a)

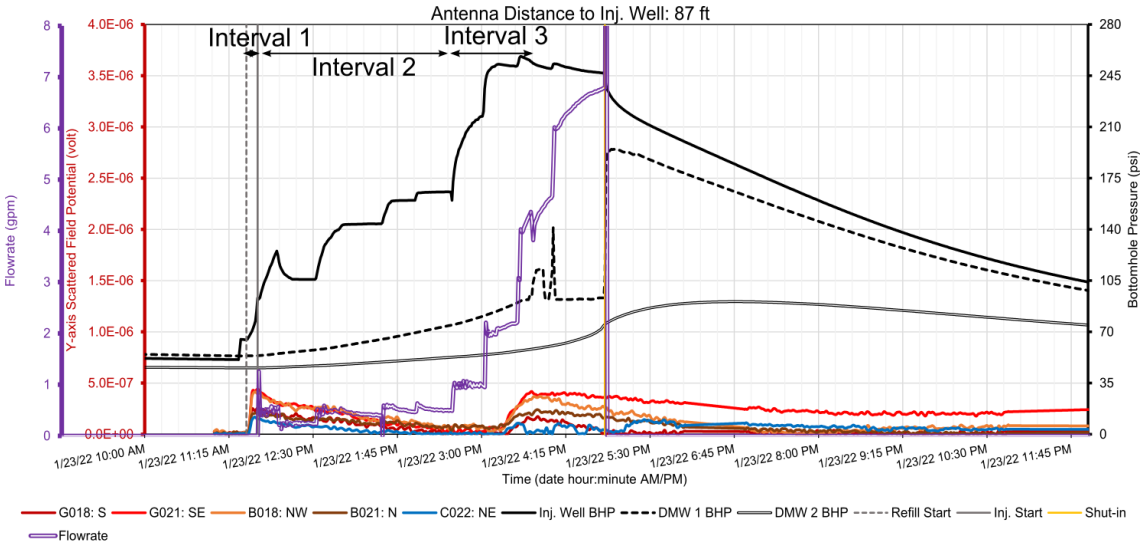

(b)

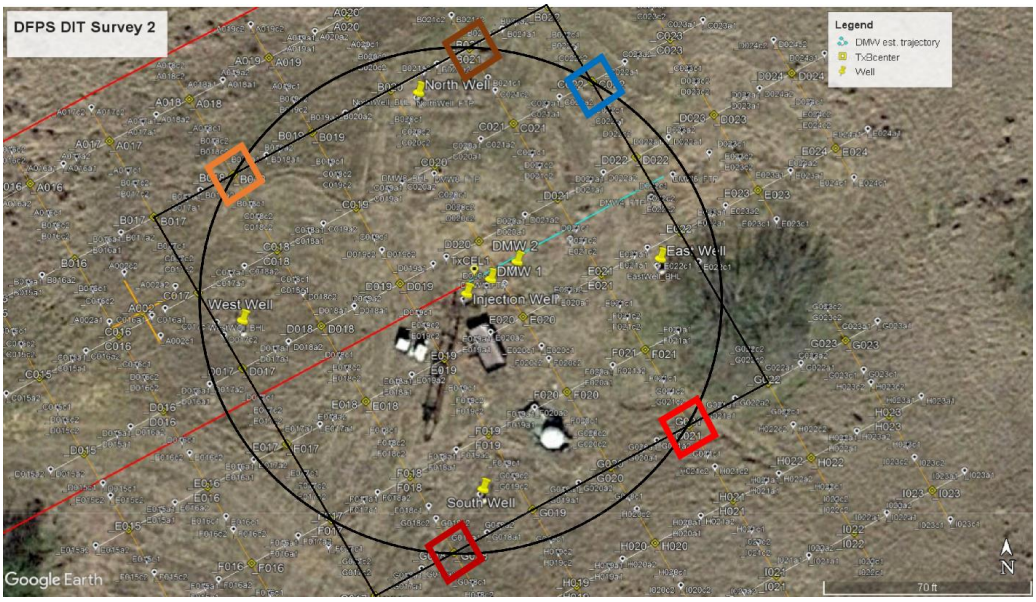

Figure 6-40: (a) Temporal change of the scattered field potential in receivers at 87 ft of distance from the injection well, flow rate, and the BHP at the injection well and DMWs 1 and 2, on January 23. (b) Plan view of the survey area and the colored squares that mark the location of the receivers with electric potentials plotted in (a). The vertical black lines in (a) indicate the starting and finishing times of refilling the surface line and the injection well with water during Interval 1. Only five electric potentials out of eight are shown because of the data dropout for the remaining three receivers.

The January-26 injection was analogous to the injection experiments we had conducted during our injection campaign in September 2020. It involved injecting almost 1200 US gallons of freshwater in six hours. Figure 6-41 shows the electric potentials associated with the closest receivers to the injection well, combined with the plots of flow rate and BHPs for the injection well and DMWs 1 and 2. Similar to January 23 (Figure 6-40), three important intervals can be identified in the electric potentials: Interval 1, concurrent with the sudden flow of the trapped water inside the injection well

into the EAP pack; Interval 2, coincident with the gradual drop of the signal due to the EAP resettlement; and Interval 3, coincident with the signal increase due to the sharp increase of the flow rate and significant fracture reopening. The difference between these electric potentials and those in January 23, as shown in Figure 6-40, is as follows. On January 23, we observed a transition between a declining trend to an inclining trend of the electric potentials from Interval 2 to Interval 3, when the injection-well BHP exceeds the FCP (Figure 6-40). However, we observe this transition on January 26, almost 45 minutes after the exceedance of the injection-well BHP from the FCP. This transition from a declining trend to an inclining trend occurs again when the flow rate increases to 4 gpm (Figure 6-41a through Figure 6-43a). We believe this is because of the gradual increase of the flow rate on January 23 and a much more abrupt increase of the flow rate during January 26. For instance, increasing the flow rate to 4 gpm during Intervals 1 and 2 took almost four hours on January 23 and only one hour on January 26.

(a)

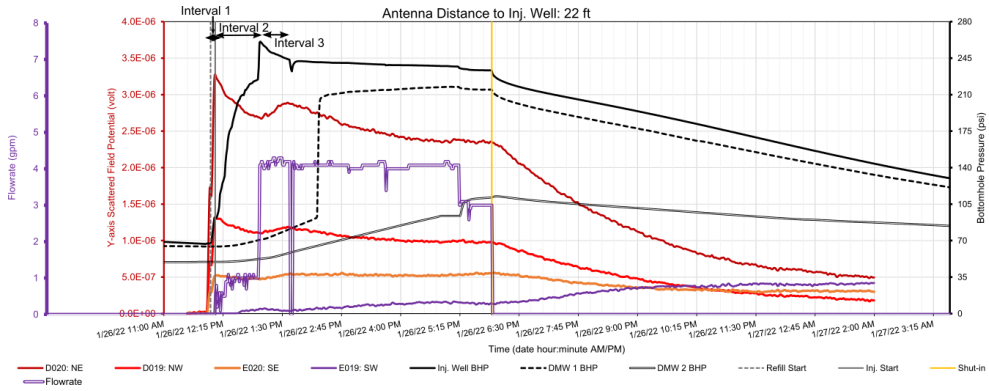

(b)

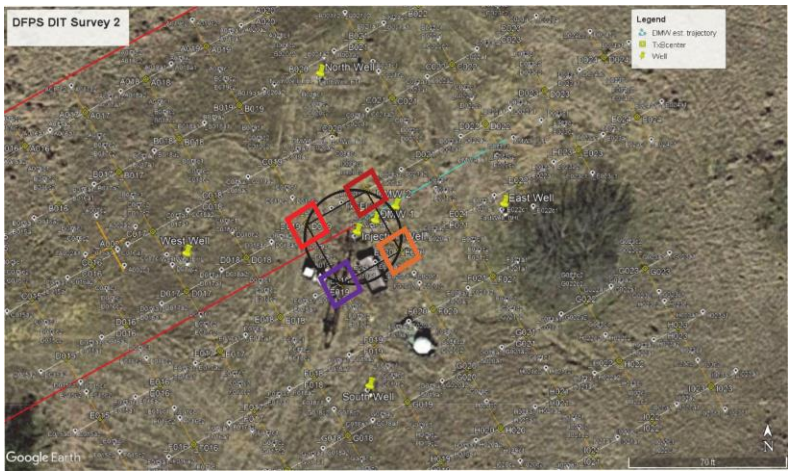

Figure 6-41: (a) Temporal change of the scattered field potential in receivers at 22 ft of distance from the injection well, flow rate, and the BHP at the injection well and DMWs 1 and 2, on January 26. The vertical black lines indicate the starting and finishing times of refilling the surface line and the injection well with water during Interval 1. Intervals 2 and 3 correspond to the declining and inclining trends of the electric potentials and are shown with horizontal arrows. Solid yellow vertical line represents the start of shut-in period when EAP compaction dominates and electric potentials dropped. (b) Plan view of the survey area and the colored squares that mark the location of the receivers with electric potentials plotted in (a).

(a)

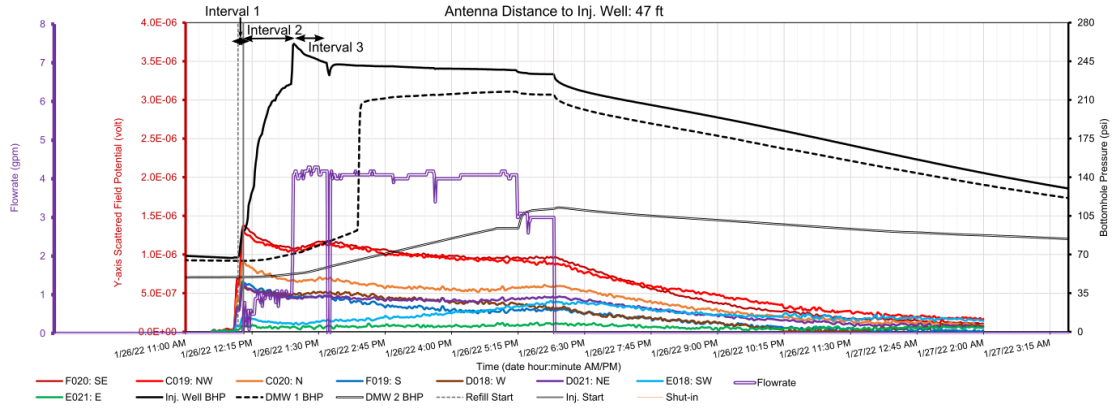

(b)

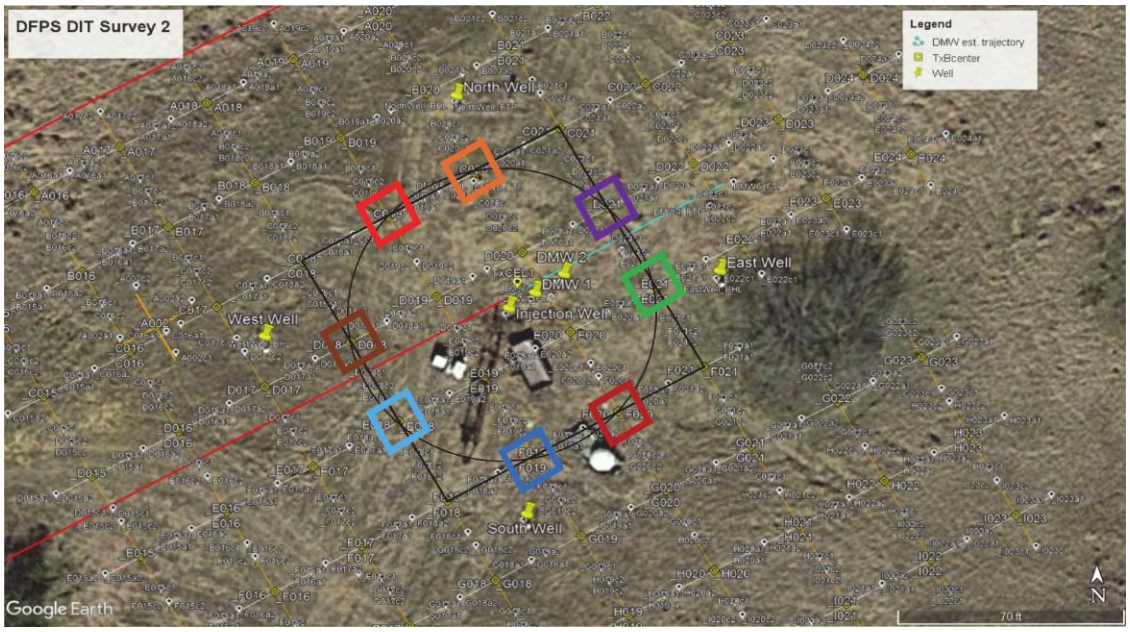

Figure 6-42: (a) Temporal change of the scattered field potential in receivers at 47 ft of distance from the injection well, flow rate, and the BHP at the injection well and DMWs 1 and 2, on January 26. Interval 1 corresponds to the surface-line refilling period, and Intervals 2 and 3 correspond to the declining and inclining trends of the electric potentials. Solid yellow vertical line represents the start of shut-in period when EAP compaction dominates and electric potentials dropped. (b) Plan view of the survey area and the colored squares that mark the location of the receivers with electric potentials plotted in (a).

(a)

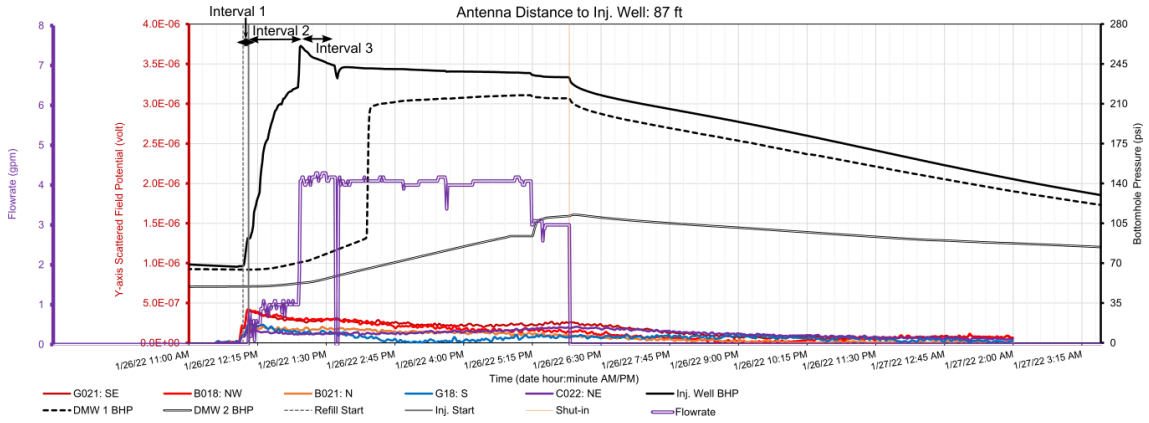

(b)

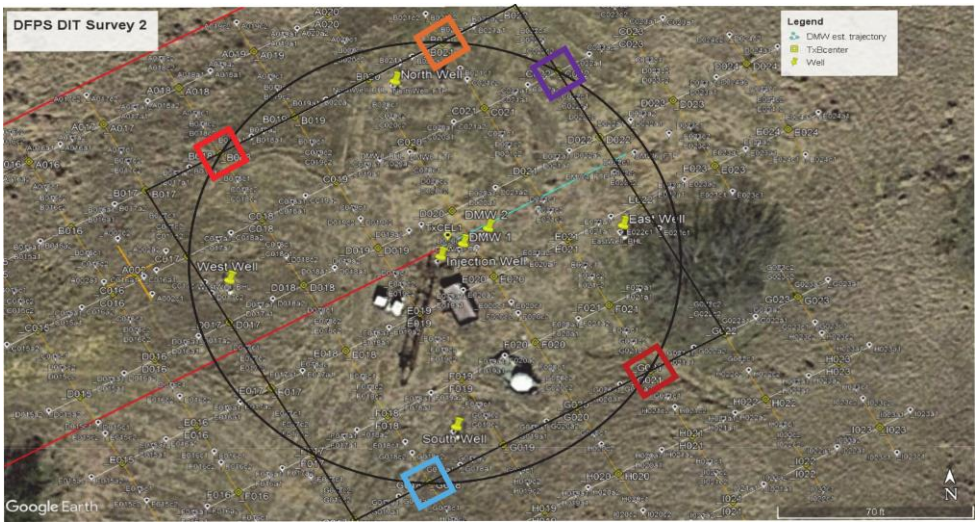

Figure 6-43: (a) Temporal change of the scattered field potential in receivers at 87 ft of distance from the injection well, flow rate, and the BHP at the injection well and DMWs 1 and 2, on January 26. Interval 1 corresponds to the surface-line refilling period, and Intervals 2 and 3 correspond to the declining and inclining trends of the electric potentials. Solid yellow vertical line represents the start of shut-in period when EAP compaction dominates and electric potentials dropped. (b) Plan view of the survey area and the colored squares that mark the location of the receivers with electric potentials plotted in (a).

Figure 6-44, Figure 6-45, and Figure 6-46 show the electric potentials recorded on January 27 at groups of receivers 22, 47, and 87 ft away from the injection well, respectively. These plots are combined with the flow-rate profile, and bottomhole pressure and salinity at the injection well and DMWs 1 and 2. The injection cycle on January 27 started by refilling the surface line and the injection well at noon, followed by pressurizing the injected fluid at 12:08 (Interval 1 in Figure 6-44 through Figure 6-46). Two injection slugs were used in this cycle. The first injection slug was 200 gallons of saltwater at 2500 ppm, followed by the injection of a freshwater slug of 990 gallons. Considering that there were approximately 200 gallons of freshwater on the surface line and the injection well cumulatively before we started injection on this day, it took 1 hour and 15 minutes (until ~13:25) for the saltwater slug to arrive at the injection well perforations. Comparing the electric potentials at the closest receivers to the injection well in Figure 6-41a through Figure 6-46a for January 26 and 27 reveals the following differences:

(1) an absence of an inclining trend during Interval 1 on January 27;
(2) the presence of only a declining trend during Interval 2 on January 23 and 26 (Figure 6-38a through Figure 6-43a), and the presence of both inclining and declining trends during Intervals 2a and 2b (see below for explanation of Intervals 2a and 2b) on January 27, prior to the increase of the flow rate to 4 gpm;
(3) a significant drop of the electric potentials during Interval 2b on January 27 down to 2.5×10^{-7} volt (Figure 6-44a), and the absence of this drop on January 26 (Figure 6-41a); and
(4) a one-hour delay for the transition of the electric potential trends to inclining trend within Interval 3, with respect to the exceedance of the injection-well BHP from the FCP, or a 22-minute delay with respect to the flow-rate increase to 4 gpm, on January 27 (Figure 6-44a), whereas this transition occurred 40 minutes after the injection-well exceedance of the FCP on January 26 (Figure 6-41a).

The only difference between injections on January 26 and 27 is the increase of salinity to 2500 ppm for the initial 200 gallons of injection on January 27 in contrast to the complete freshwater water injection on January 26. The causative mechanism to explain the above-listed difference in the electric potentials is not clear to us yet. However, we can hypothesize two mechanisms for these differences:

(1) this can be due to the loading of the formation and fracture with 3900 US gallons of injected water from January 21 to 26, versus 2700 gallons before January 26 and 1126 gallons before January 23, making a temporally more extensive water pocket inside the proppant pack. Adding extra water to this large water pocket at low flow rates during a later cycle can temporarily increase the scattered field (Interval 2a); however, this scattered field quickly returns to the previous state (Interval 2b), because the additional water volume during the new injection dissipates quickly inside this water pocket; and
(2) as elaborated in Subtasks 3.1 and 7.1, the SP may explain these differences based on the following observations: 1.) the first peak in the electric potentials, that falls in Interval 2, on January 27 coincides with the maximum injection-well bottomhole pressure temporal derivative; and 2.) the second peak in the electric potentials, that falls in Interval 3, follows the abrupt increase of the flow rate to 4 gpm that occurred several minutes before this peak.

Evaluating the possible mechanisms for the change of the electric potentials may require further investigation by developing new poroelastic and EM models. For instance, the SP cannot yet clearly explain the decline of the electric potentials when a step-wise increase in the bottomhole pressure and flow rate is observed at 13:00 on January 27.

Another observed feature in the electric potentials of January 27 is that the abrupt increase of electric potentials at 13:22 coincides almost with the sudden increase of the injection-well downhole salinity (Figure 6-44). However, this correlation contradicts Ohms' law which predicts a decrease of potential with an increase of conductivity at a constant electric current. Since the salinity just arrives to the injection perforation at roughly 13:25, it is unlikely this effect is due to salinity. We believe that fracture dilation as a result of an abrupt flow-rate change dominates any possible effects of salinity changes up to 2500 ppm. In other words, the sharp increase of the electric potentials at 13:22 can be a response to the significant, step-wise increase of the injection flow rate at 13:00, 22 minutes before the sharp increase of the electric potentials, and consequently, to the gradual fracture dilation that extends to a larger fracture area. This delay is also observed during the other days, and we believe it is related to fluid invasion, fracture dilation, and an increase in the fracture fluid flux resulting from grain separation in the EAP pack.

(a)

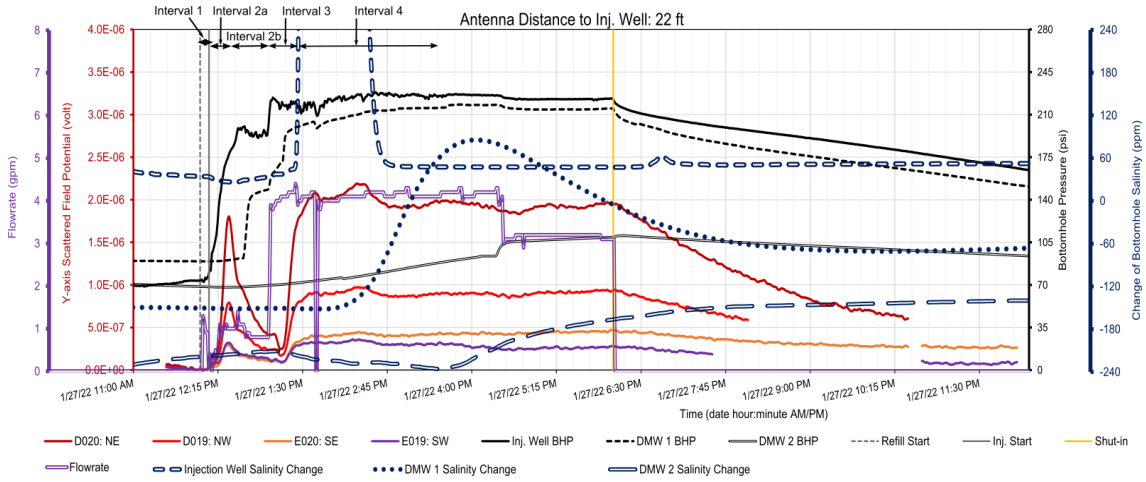

(b)

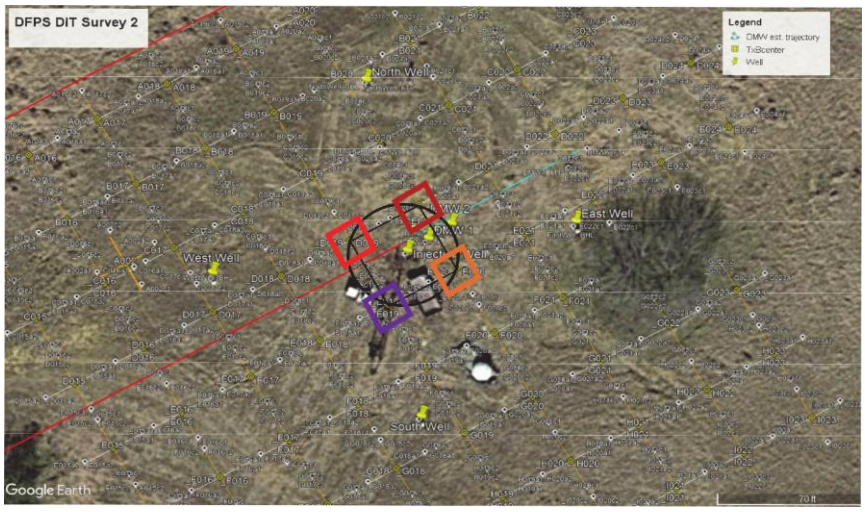

Figure 6-44: (a) Temporal change of the scattered field potential in receivers at 22 ft of distance from the injection well, flow rate, salinity, and the BHP at the injection well and DMWs 1 and 2, on January 27. The vertical black lines indicate the starting and finishing times of refilling the surface line and the injection well with water during Interval 1. Solid yellow vertical line represents the start of shut-in period when EAP compaction dominates and electric potentials dropped. Salinity increased at the injection well and DMWs 1 and 2 at 13:25, 14:15 and 15:35, respectively. Salinity in the injection well reached to 2500 ppm which is clipped in order to zoom into the salinity ranges for the other wells more clearly. Intervals 2a and 2b respectively contain inclining and declining trends that were not observed in the previous days. Interval 3 corresponds to the electric potentials' major inclining trend related to the flow-rate increase to 4 gpm. Interval 4 corresponds to the period of time at 4 gpm before salinity slug reached to DMW 2. (b) Plan view of the survey area and the colored squares that mark the location of the receivers with electric potentials plotted in (a).

The injection well bottomhole salinity decreased from 2500 ppm to freshwater salinity right before 14:45 (Figure 6-44), while saltwater continued to diffuse toward DMWs 1 and 2 and arrive at these wells at 14:15 and 15:35, respectively (see the salinity curves in Figure 6-44 through Figure 6-46). In contrast to the electric potential curves for January 23 and 26, when the electric potentials were generally decreasing after Interval 3, the period of time on January 27 after Interval 3 contains

multiple smaller peaks and troughs that may correspond to the changes in salinity between the injection well and DMW 2 (compare Figure 6-41 and Figure 6-44). Nonetheless, the fracture dilation and compaction seem to be playing a much more dominant role in the electric potential than the effect of salinity changes on January 27.

(a)

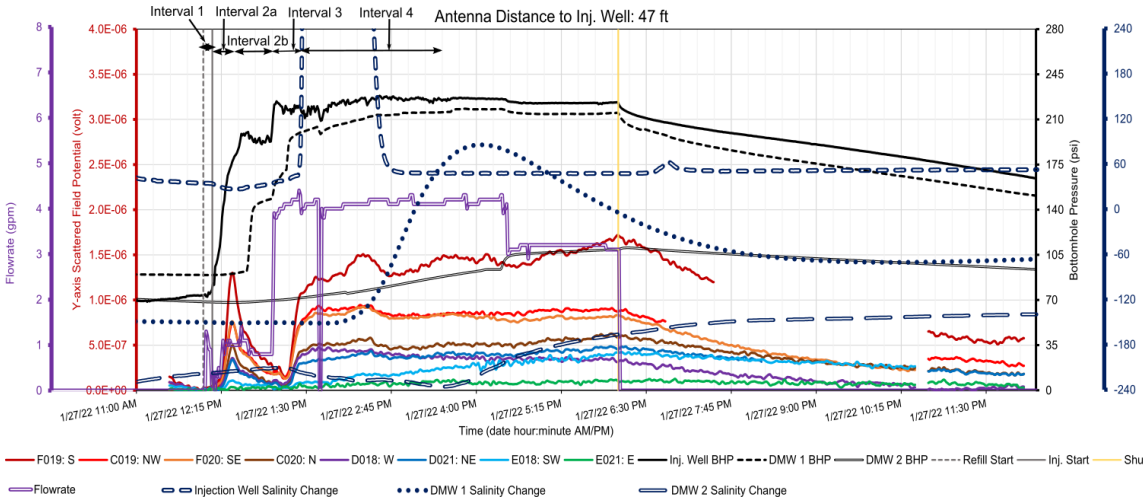

(b)

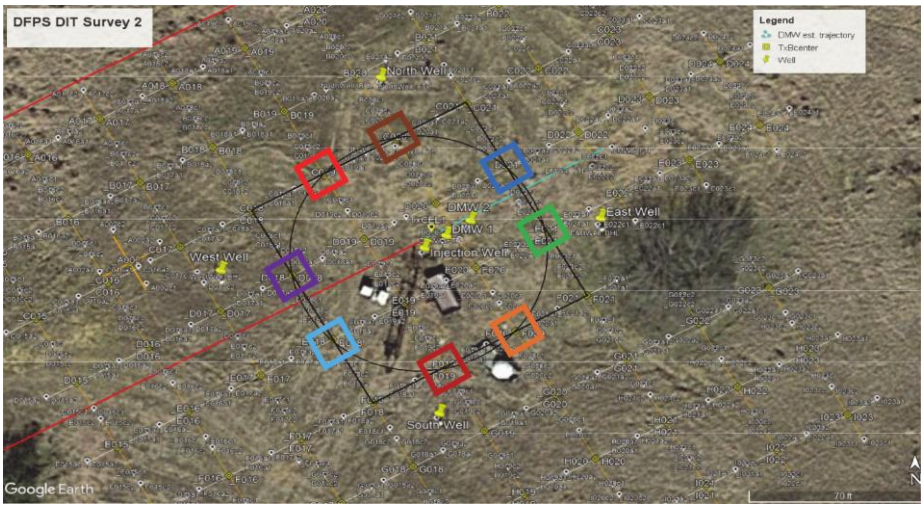

Figure 6-45: (a) Temporal change of the scattered field potential in receivers at 47 ft of distance from the injection well, flow rate, salinity, and the BHP at the injection well and DMWs 1 and 2, on January 27. The vertical black lines indicate the starting and finishing times of refilling the surface line and the injection well with water during Interval 1. Solid yellow vertical line represents the start of shut-in period when EAP compaction dominates and electric potentials dropped. Salinity increased at the injection well and DMWs 1 and 2 at 13:25, 14:15 and 15:35, respectively. Salinity in the injection well reached to 2500 ppm which is clipped in order to zoom into the salinity ranges for the other wells more clearly. Intervals 2a and 2b respectively contain inclining and declining trends that were not observed in the previous days. Interval 3 corresponds to the electric potentials' major inclining trend related to the flow-rate increase to 4 gpm. Interval 4 corresponds to the period of time at 4 gpm before salinity slug reached to DMW 2. (b) Plan view of the survey area and the colored squares that mark the location of the receivers with electric potentials plotted in (a).

(a)

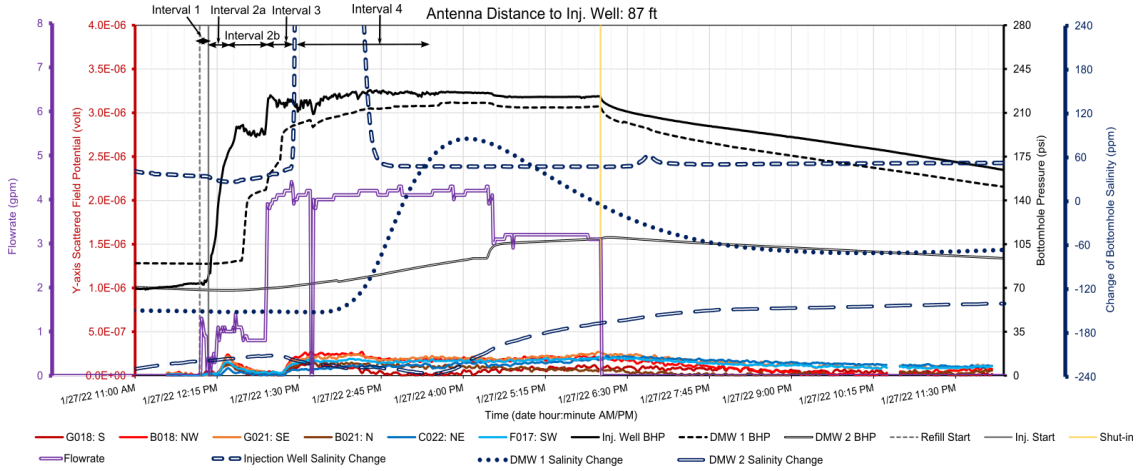

(b)

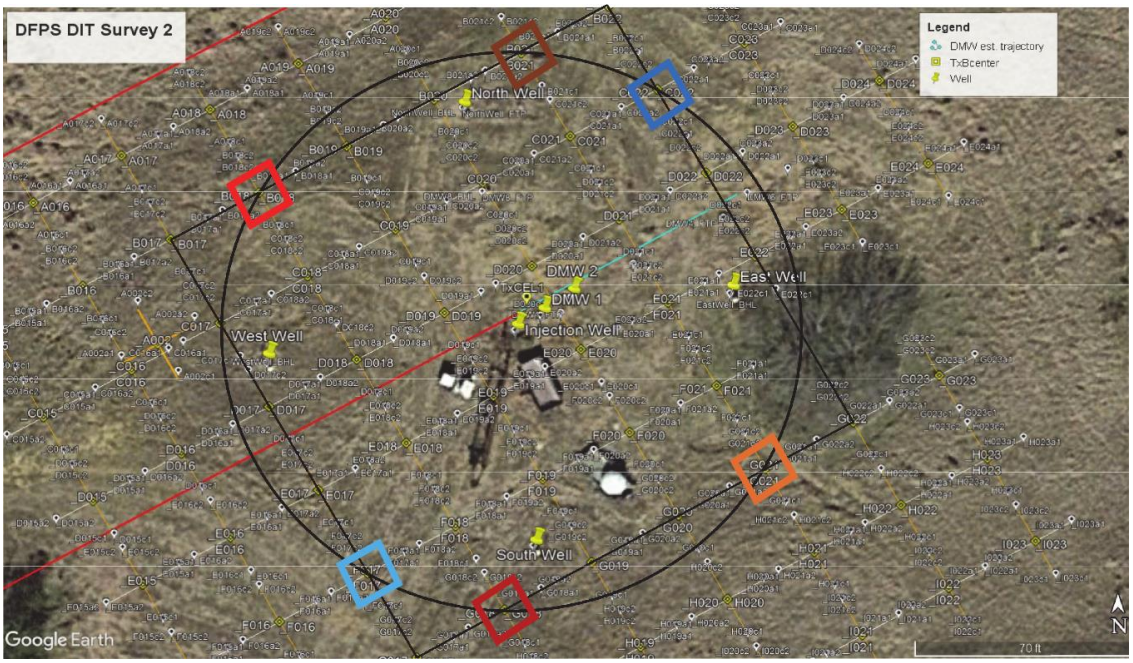

Figure 6-46: (a) Temporal change of the scattered field potential in receivers at 87 ft of distance from the injection well, flow rate, salinity, and the BHP at the injection well and DMWs 1 and 2, on January 27. The vertical black lines indicate the starting and finishing times of refilling the surface line and the injection well with water during Interval 1. Solid yellow vertical line represents the start of shut-in period when EAP compaction dominates and electric potentials dropped. Salinity increased at the injection well and DMWs 1 and 2 at 13:25, 14:15 and 15:35, respectively. Salinity in the injection well reached to 2500 ppm which is clipped in order to zoom into the salinity ranges for the other wells more clearly. Intervals 2a and 2b respectively contain inclining and declining trends that were not observed in the previous days. Interval 3 corresponds to the electric potentials' major inclining trend related to the flow-rate increase to 4 gpm. Interval 4 corresponds to the period of time at 4 gpm before salinity slug reached to DMW 2. (b) Plan view of the survey area and the colored squares that mark the location of the receivers with electric potentials plotted in (a).

The first peak of the electric potentials on January 27 coincides with the exceedance of the injection-well BHP from the FCP (Figure 6-44 through Figure 6-46). We can attribute this peak to the temporary fracture reopening and the reduction of the proppant pack conductivity due to freshwater injection, followed by fracture closure due to too low injection flow rate to keep the fracture open. Thus, fracture dilation and closure can obviously be measured by surface EM geophysics. Also, as elaborated in Subtasks 3.1, the SP theory could likely present a second causative mechanism for this peak because of the coincidence of this first peak with the maximum gradient of the injection-well BHP. Using additional laboratory experiments as discussed in Subtask 3.1, we showed that SP likely contributed significantly into the electric potential changes during injection at the DFPS. These experiments in the presence or absence of the EAP pack showed the impact of EAPs on this potential.

Tiltmeter mapping

During the field deployment in January 2022, FRx Inc. deployed fifteen surface-mounted tiltmeters in shallow subsurface vaults distributed around the injection well at the DFPS. The tiltmeters were operated, and data were recorded from 19 January through 2 February 2022. These devices monitored the surface deformation in terms of angular deviation relative to gravity resulting from the injection. During injections performed between 22 January and 1 February, the tiltmeter system provided a nearly continuous data stream.

The signal response for most of the injection cycles was of the same order of magnitude as long-term noise, much of which seemed to have a diurnal nature. Nevertheless, we were able to estimate the tilt response and prepare temporal trends and tilt vector plots. Further interpretations estimated probability distributions of the coefficients describing a discrete, planar fracture of uniform aperture and almost circular extent embedded in a homogeneous matrix; even though injection pressure and rates may have affected only infiltration and flow through porous media, which would be better interpreted using concepts of poroelasticity.

FRx harnessed non-parametric statistics to characterize the statistical distribution of the estimated parameters. This approach involves considering the projections of subsets of only a few tiltmeters. Because four tiltmeters generate eight signals which are tilts in x- and y-directions per tiltmeter, each quadruplet of tiltmeters can describe the eight fracture parameters needed for the fracture characterization (Appendix A.4). There are 1365 unique subsets that can be formed from fifteen tiltmeters (i.e., the combination of four out of 15 tiltmeters at a time). The 1365 sets of estimated fits define eight probability distributions for the eight fracture parameters, which can be examined to determine what values are most probable to occur. This is similar to a Theil-Sen estimator or Kendall-Theil Robust Line Analysis.

The estimated fracture radius from this tilt study is consistent with the bottomhole pressure data at DMWs 1 and 2, showing the exceedance of the fracture closure pressure at DMW 1 and not at DMW 2. The graphical display of the inversion results and the details of the tiltmeter setup are elaborated in Appendix A.4.

6.6 Tracing Fluid Breakthrough

In these studies, we used salt as tracer and the breakthrough curves are discussed as part of data analysis in Subtasks 6.4 and 6.5.

7 Data Processing and Interpretation

7.1 Electromagnetic Inversion of Field Data

Following the collection of the CSEM data in 2020 (Subtask 6.1), we conducted numerical simulations and compared them to the observed EM data from the equipment and analyzed the misfit. We obtained 74% total-field misfit between the simulation results and field data. Next, we made several attempts to deduce the possible sources of this misfit by including the following features at the test site in the models: layered media, injection-well metal casing, surface injection pipe, and observation-well metal posts and surface casings. Including these modifications reduced the total-field misfit to 37%. Therefore, we removed most of those objects before the 2022 field tests to resolve the EM modeling complexities due to the presence of these objects. We reduced this misfit further to 31% by varying the layer-conductivity combinations using a machine-learning technique. The total-field misfit for 2022 deployment was 29%.

Next, we calculated the scattered-field misfit for the 2022 CSEM data. However, the scattered-field misfit results were very large between 59% and 228% for various injection times. We attempted to reduce the EM model misfit by varying the following input parameters: the number of fracture layers, dilated-fracture shape (e.g., circular or elliptical), major axis azimuth, and fracture offset with respect to the injection well. We used the geomechanical model (Subtask 5.1, 7.3), tiltmeter data (Subtask 6.5, Appendix A.4), and fiber optic data (Subtask 6.5) to guide the dilated fracture dimension in the simulation cases. This analysis, optimized by the modified efficient K-Nearest Neighbor (KNN) method, resulted in the minimum misfit of 55%. As elaborated in the current subtask, the 2022 field data showed the possible effect of the SP on the model misfit. We further reduced this misfit to 48% by the subtraction of an estimate for SP-induced field from the measurements.

To achieve an accurate inversion of conductivity response during subsurface fluid injections, reducing the scattered-field misfit down to at least 5% should be targeted. As such, due to the large scattered field misfit, we could not perform an accurate inversion of the field data in this subtask. However, for the sake of completeness, we will discuss the application of the inversion workflow proposed in Subtask 4.2 to obtain an initial image of the 2020 EM field data. This is informational only, and we realize that we need to improve these substantially once we develop a numerical code that couples EM and SP, as will be targeted in our future proposal submissions.

Attempts to invert 2020 experiment EM data

In Subtask 4.2, we demonstrated our NN-based ML method and performed EM inversion with the 2017 field data provided by MPT. Below, we show our attempts to obtain a fracture conductivity solution for the CSEM survey data collected using the CSEM survey configuration that was used in the 2020 field experiment. First, we generated the training data with the DGFD solver. The most challenging part in making this synthetic dataset was to include the steel casing in the DGFD model, which we resolved using a highly conductive thin layer. As discussed below, we first validated the DGFD solution in comparison with the COMSOL solution for this case. Next, we used this validated model to test inversion solutions using pixelwise and contour-based ML models using synthetic data. As presented in the following, both of these inversions were successful in generating reasonable fracture conductivity solutions. For the 2020 field data, however, the contour-based ML model did not produce a reasonable solution, and we do not present that here. On the other hand, the pixelwise ML model was slightly better at producing meaningful results, as presented here, suggesting this approach may be more reliable than the contour-based ML model in our application. Nevertheless, because the electric field magnitude range obtained from the field data was significantly larger than that obtained from the synthetic model (obtained from forward EM models

of synthetic cases), we were not able to generate physical inversion solutions using either of these methods. As discussed below, we attribute this challenge to the missing physics of the SP in the EM model.

DGFD solver validation in the presence of the injection well casing

Figure 7-1 shows the locations of transmitters and receivers on the ground surface (xy plane located at z = 0). The area is 200 m × 200 m. The numbers in the figure are coordinates of endpoints of transmitter or receiver in meter. The green circle denotes the centered borehole, which is steel cased.

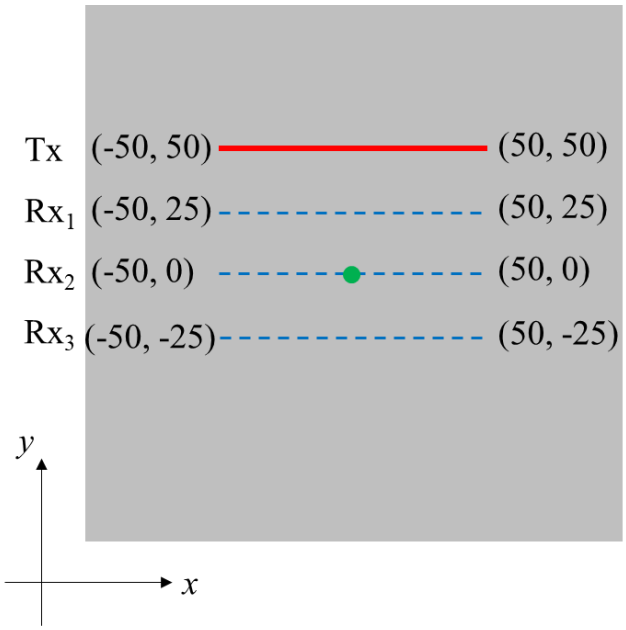

Figure 7-1: Locations of the surface transmitters and receivers used in the DGFD solver validation. The red solid line is the transmitter, and the blue dashed lines are three lines of receivers.

The comparisons of the forward modeling results between the DGFD solver and COMSOL software program are shown in Figure 7-2 through Figure 7-4. Most results agree very well with each other. Note that the disagreement in the imaginary part of E_x can be neglected because the values of the imaginary parts are much smaller than the values of real parts; thus, the real parts are dominant.

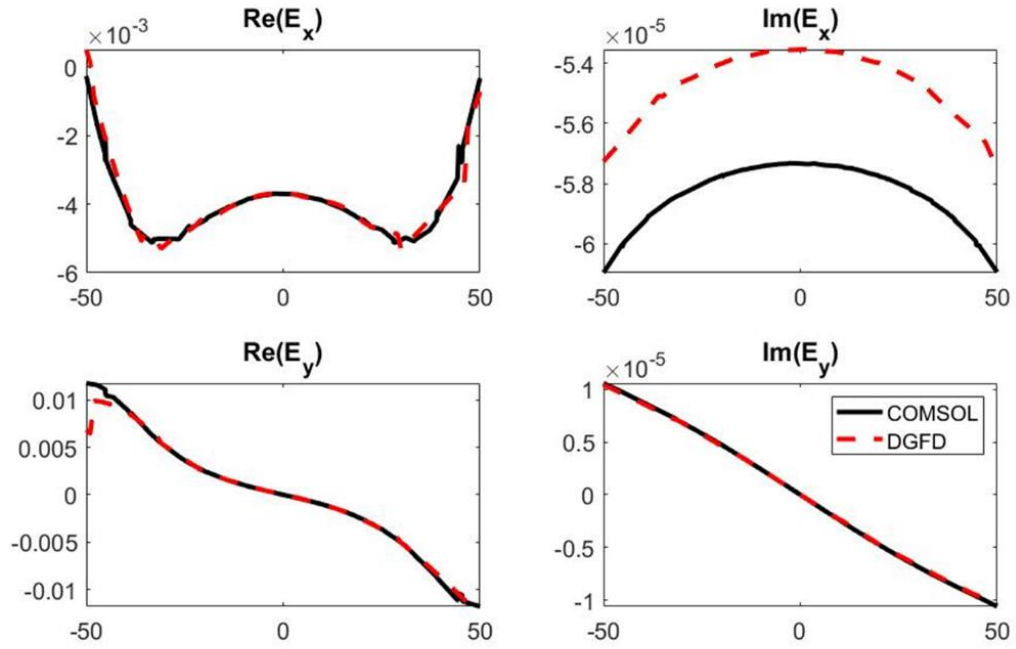

Figure 7-2: Comparison of simulation results for Rx1 between DGFD and COMSOL. x-axis denotes location of receiver while y-axis denotes electric field.

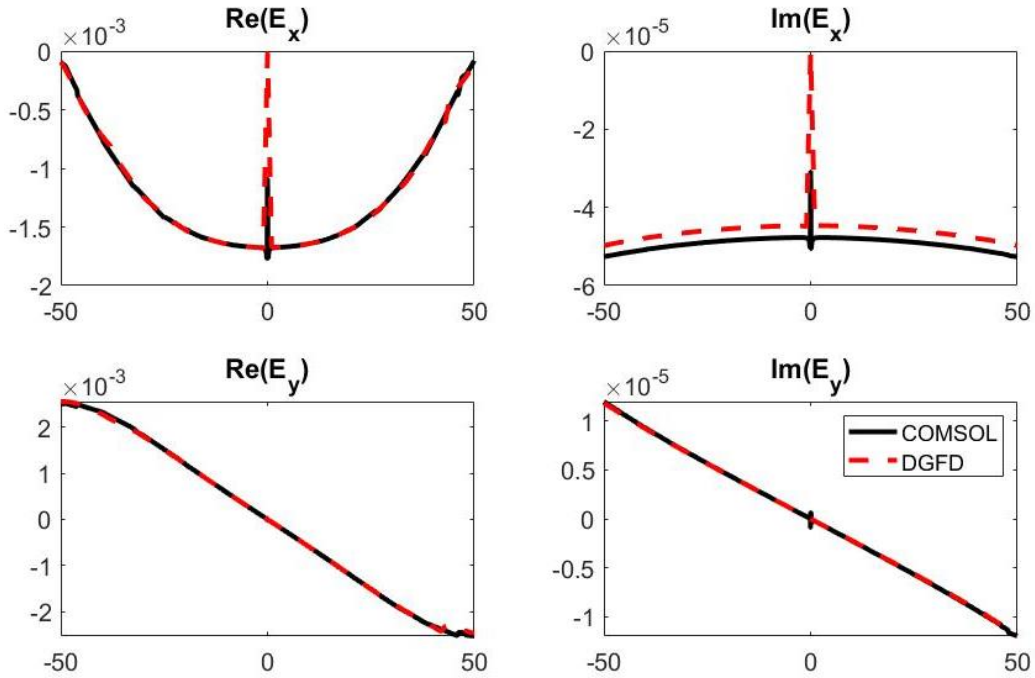

Figure 7-3: Comparison of simulation results for Rx2 between DGFD and COMSOL. x-axis denotes location of receiver while y-axis denotes electric field. The jump around the origin is because of the steel casing.

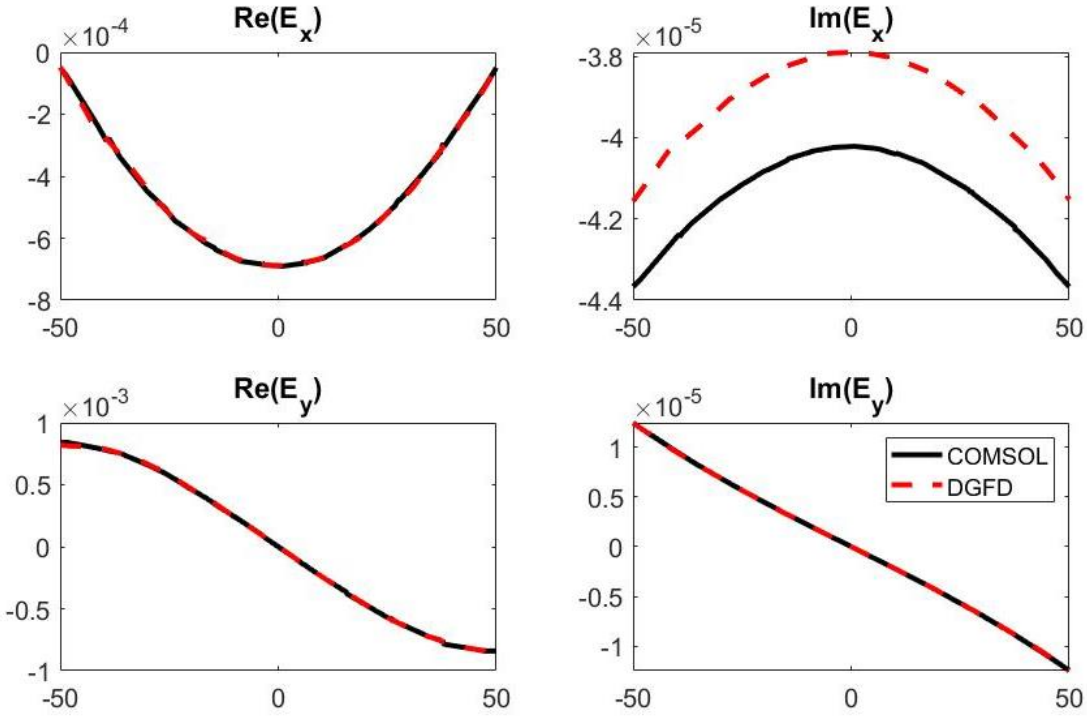

Figure 7-4: Comparison of simulation results for Rx3 between DGFD and COMSOL. x-axis denotes location of receiver while y-axis denotes electric field.

After the validation of the DGFD solver under the new configuration, we started generating the training data. The initial inversion results of the 2020 data are shown in the following.

Figure 7-5 shows the ESG's 2020 EM measurement configuration at the DFPS, as was elaborated in Subtask 6.1. This utilized the south transmitter, located about 200 m to the south of the injection well. This far-away transmitter presents a significant challenge for the training data generation process for the EM inversion because the transmitter needs to be included in the computational domain using conventional methods. This domain is shown by the large dashed rectangle marked with "A" in Figure 7-5 with the scattering boundary condition. A large computational domain means that we have to solve a very large linear system which requires very large computer memory and very long CPU time. Therefore, this method is not efficient for generating a large amount of training data in a short time for inversion.

To overcome this challenge, we adopted a special treatment for the transmitter by using the so-called "total-field/scattered-field formulation". In this way, the transmitter can be placed outside the simulation domain, leading to a smaller simulation domain to model. To accomplish this, we need to add an equivalent source to the outer boundary. This method is shown as the small dashed rectangle, marked with "B" in Figure 7-5.

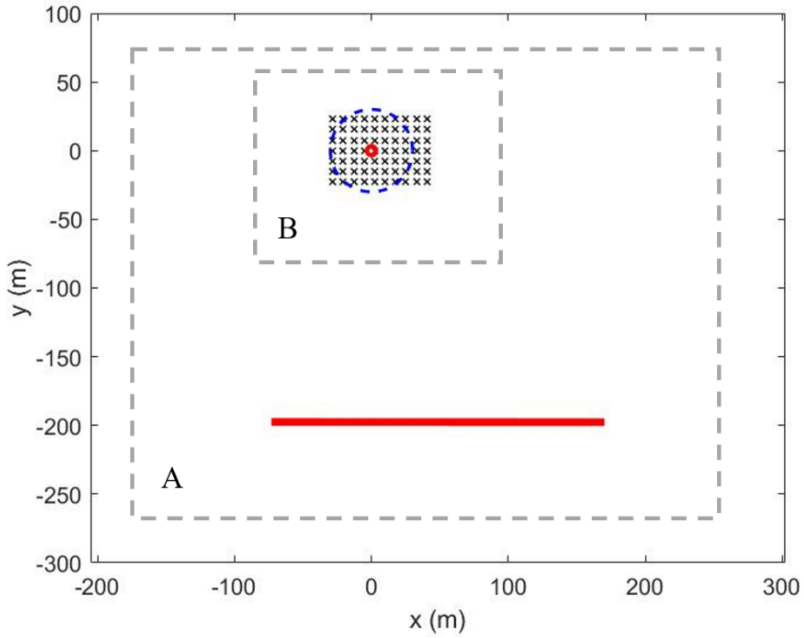

Figure 7-5: Plan view of the DFPS with ESG's EM measurement configuration. The red circle is the location of the injection well with a steel casing, which is 81-m long in depth direction. The black crosses around the injection well represent 70 receivers on the ground. The red line is the south electric current transmitter located about 200 m to the south of the injection well, also on the ground. Here, we use a circular shaped fracture, which is marked with blue dashed line and located at -54 m below ground.

The comparison of results obtained by including the transmitter in the computational domain (Method A) and excluding that (Method B) is shown in Figure 7-6 and Figure 7-7 which confirm a very good agreement between the two methods. The implemented Method B has a significant advantage in generating training data for inversion. For each randomized fracture, it only takes less than 3 minutes for the DGFD solver to finish the simulation or 5 times faster than the other method. Using this method, we could efficiently generate a large amount of training data for the DFPS with the south transmitter. Then, the CSEM survey data collected by ESG could be fed into the trained Neural Network to finish the inversion process.

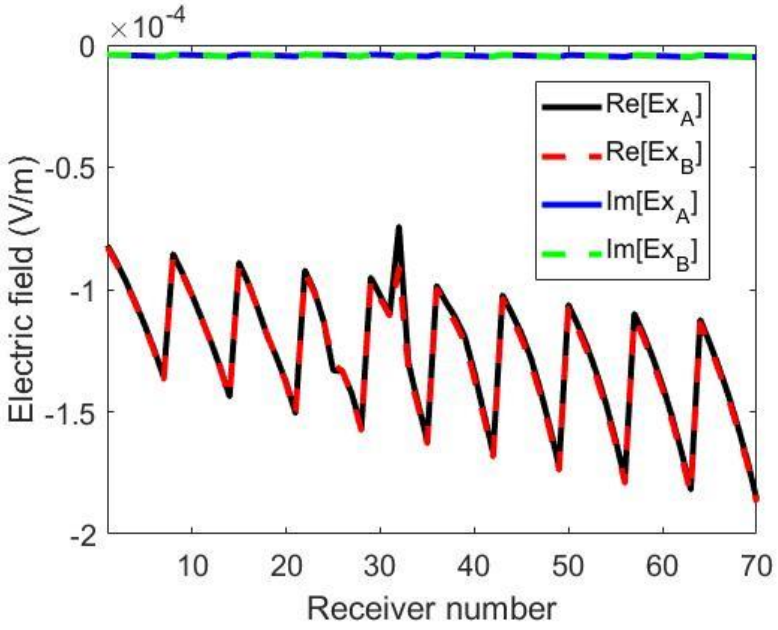

Figure 7-6: Comparison of x-component of electric fields at 70 receivers with the transmitter included inside (Method A) and outside (Method B) of the computational domain.

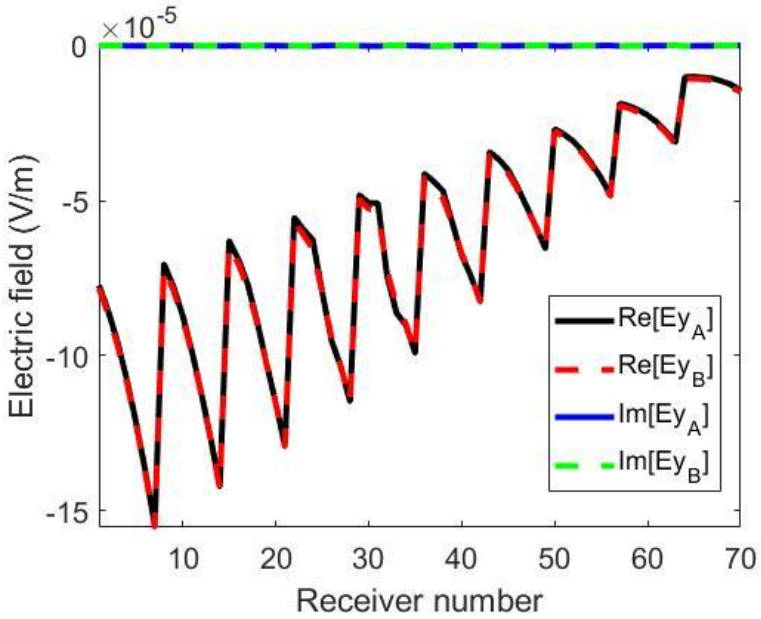

Figure 7-7: Comparison of y-component of electric fields at 70 receivers with the transmitter included inside (Method A) and outside (Method B) of the computational domain.

Machine learning for the EM field inversion

We implemented two ML methods to perform EM inversion for real-time hydraulic fracture imaging during the injection process. The flowchart in Figure 7-8 shows these methods. The entire inversion solver consists of three parts: training-data generation, training, and estimation.

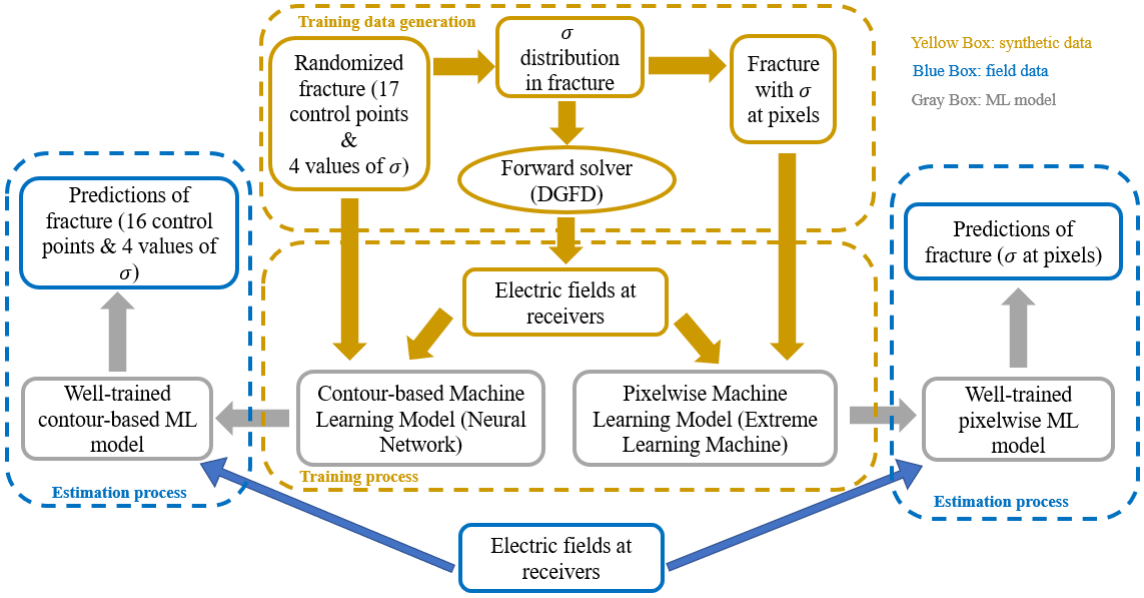

Figure 7-8: Flowchart of methodology used for the EM inversion. The yellow boxes represent the considered synthetic data. The blue boxes represent the field data. The gray boxes are machine-learning models.

In the training-data generation process, we started from generating contour-based randomized fractures defined with four zones, each of which has a boundary and a value of conductivity. Figure 7-9 shows one example of the randomized fractures. According to the results from the inversion results we had obtained in 2017 when mapping the original EAP anomaly at the DFPS (Ahmadian et al., 2018, 2019), we fixed the outmost boundary to the pea-shaped black boundary in Figure 7-9. The numbers of control points for the yellow, red, and blue zones are 1, 4, and 12, respectively; thus, there are 17 control points in total. We then assigned four random numbers representing the fracture conductivities to each zone.

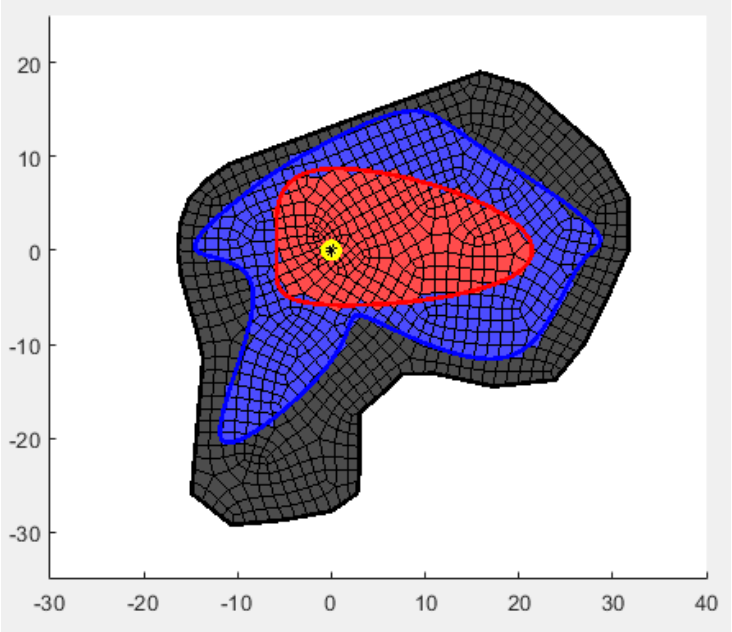

Figure 7-9: One example of randomized fractures. It has four zones of conductivity values, shown by different colors.

The generated contour-based fractures were then transformed into pixelwise fractures with different conductivities at different pixels to describe the conductivity distribution. Then the fracture information was fed into the previously validated forward solver to obtain the synthetic electric-field data at predefined receivers.

For the contour-based ML model, we used a NN-based ML process which we described in Subtask 4.2. The fracture information, including 17 control points, 4 values of conductivity, and the synthetic electric-field data, were used for training. The measured electric-field data were then fed into the well-trained NN to predict the control-point locations and conductivities. For the pixelwise ML model, we used the extreme learning machine (ELM). The pixelwise synthetic fracture information and synthetic electric-field data (obtained from the forward DGFD model) were used for training. The measured electric-field data were then fed into the well-trained ELM model to predict conductivity at each pixel.

We successfully generated more than 18,000 different fractures (i.e., synthetic data points), which were first used to train both ML models. In the following, we first present a test of both pixelwise and contour-based inversion model results by considering a synthetic dataset and then present a subset of field results with the measured data collected by our team in September 2020 to the inversion model to obtain an estimate for fracture conductivity changes.

Inversion of synthetic data using the pixelwise ML model

We randomly chose 90% of the synthetic data to train our pixelwise ML model and used the rest of the data for testing. The inversion results from the testing dataset are shown in Figure 7-10. We used the model and data misfits to evaluate the accuracy of inversion. The model misfit is the relative error between the prediction from the model and the ground truth of the conductivity distribution. We can feed the predicted conductivity distribution back into the forward model to calculate the corresponding electric field. The data misfit is the relative error between this regenerated electric field and ground true electric field, as follows:

$$Model\ misfit = \frac{|\sigma_{Predict} - \sigma_{true}|}{|\sigma_{true}|}, \tag{7-1}$$

$$Data\ misfit = \frac{|E_{regenerated} - E_{true}|}{|E_{true}|}, \tag{7-2}$$

where σ and E denote the electrical conductivity and electric field, respectively, and subscript *predict* or *true* refers to the associated parameter that is predicted by the ML model or is assumed as ground truth. In Equation (7-1) or (7-2), the ground truth represents either the assumed fracture conductivity or the modeled electric-field for the fracture conductivity in the testing dataset, respectively.

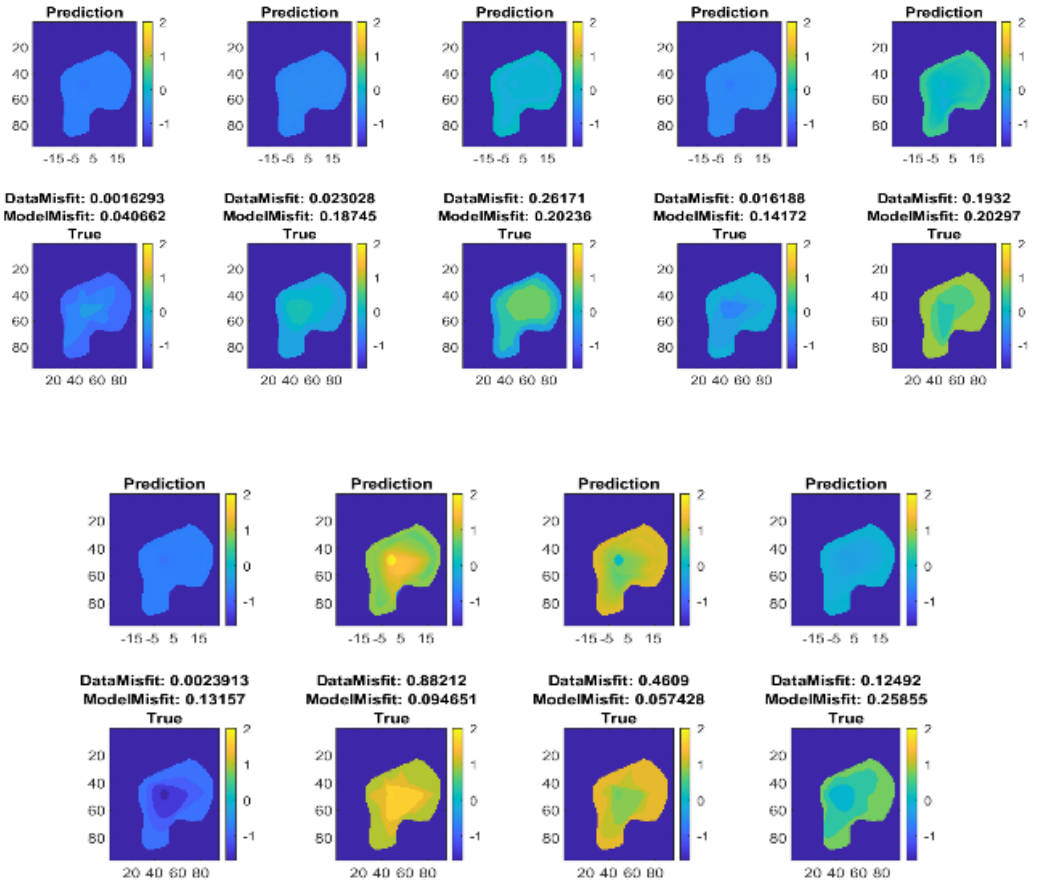

Figure 7-10: Nine inversion results from the testing dataset with the pixelwise ML model and their corresponding data and model misfits. Each result consists of an upper and lower contour plot corresponding to the predicted fracture conductivity obtained from an inversion solution and ground-truth synthetic model, respectively. These conductivity contours are shown in a logarithmic scale. The average model and data misfits of the data above are 14.85% and 40.95%, respectively.

The model misfit is relatively large, which mainly originates from overfitting.

Inversion of synthetic data using the contour-based ML model

We randomly chose 80% of the synthetic data to train our contour-based ML model and used the rest of the data for testing. The inversion results from the testing dataset are shown in Figure 7-11. The definitions of the model and data misfits are similar to those provided by Equations (7-1) and

(7-2). The only difference is that the model misfit here is the relative error between the prediction from the model and the ground truth of the 17 control points and 4 conductivities. The average model and data misfits of the data are 13.82% and 2.51%, respectively.

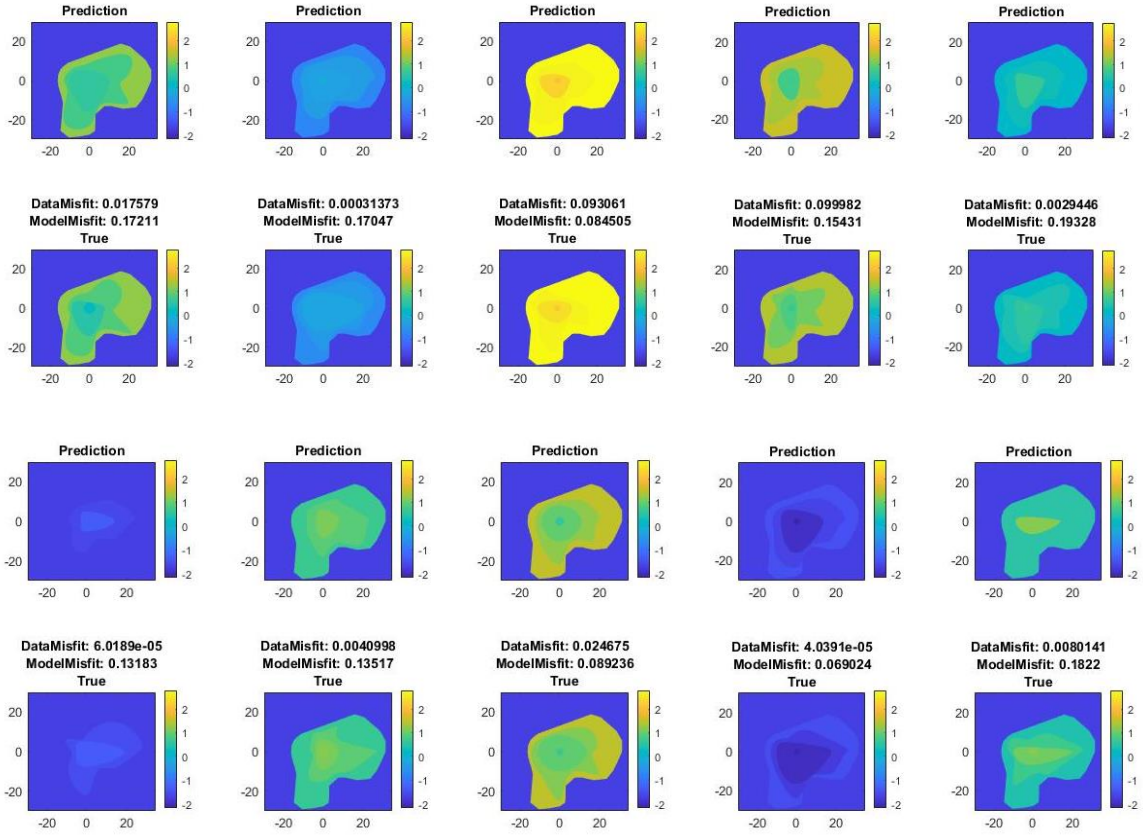

Figure 7-11: 10 inversion results from the testing dataset with the contour-based ML model and their corresponding model and data misfits. Each result consists of an upper and lower contour. The upper contour shows the ML-model prediction of the conductivity changes, and the lower contour is the synthetic ground-truth conductivity distribution that was assumed as input to the forward model. These conductivity contours are shown in a logarithmic scale.

Inversion of field data using the pixelwise ML model

After obtaining the well-trained pixelwise ML model, we fed the field data collected during September 2020 into the ML model to obtain the inversion results. Specifically, the field data from Stage 1c on the afternoon of September 22 were used for this inversion.

Because injection started at 15:52, we used the experiment electric field at 15:52 as the primary field. Then, we subtracted the primary field from the electric field at the later time stamps to determine the secondary field, which was directly fed into our ML model. The output is the pixelwise conductivities. We selected several time stamps on the afternoon of September 22 to perform the inversion. These time stamps were obtained from the bottomhole pressure (BHP) profile in the injection well, and DMWs 1 and 2 as shown in Figure 7-12. The inversion results are shown in Figure 7-13. It is notable that the fracture opened at 15:58 and reclosed at around 17:00 according to Figure 7-12. The inversion results show a corresponding pattern of the fracture reopening and closure (Figure 7-13). Before 15:58, conductivity was high because the fracture was

packed with compacted EAPs. When the fracture opened at 15:58, the contact resistance among the EAPs at the central part of the fracture increased, leading to a rapid conductivity decrease within this area. Between 16:00 and 17:00, conductivity at the boundary of the fracture oscillated, which may originate from noise and low sensitivity of the measurements. Nevertheless, conductivity at the center of the fracture remained low, at nearly zero, until the fracture reclosed at 17:00. Then, the fracture conductivity increased because the injection stopped, and water leaked out of the fracture leading to the proppant pack compaction.

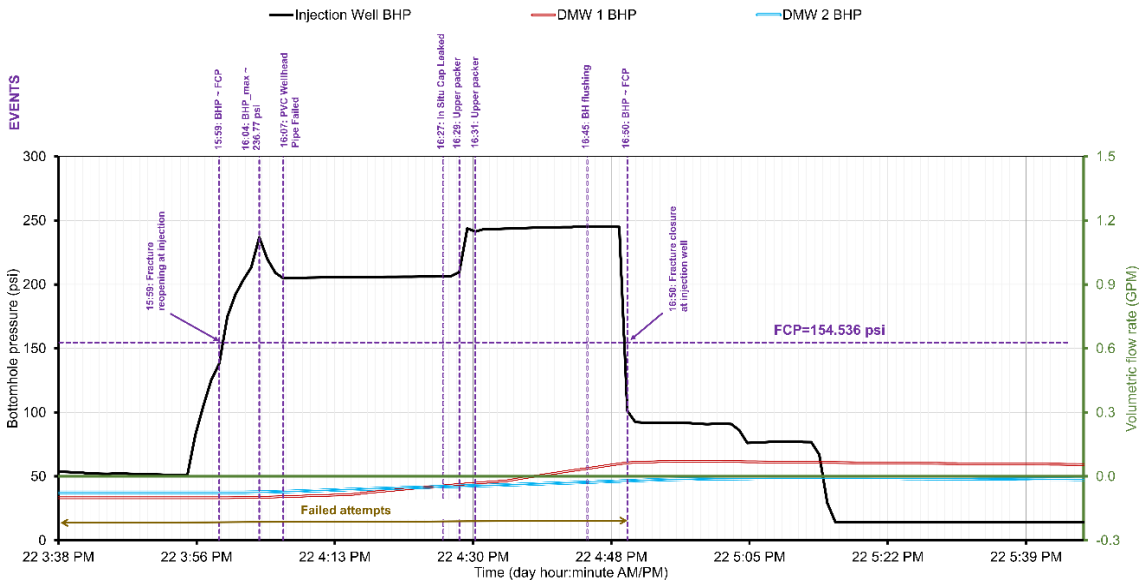

Figure 7-12: Bottomhole pressure of different wells on the afternoon of September 22, 2020.

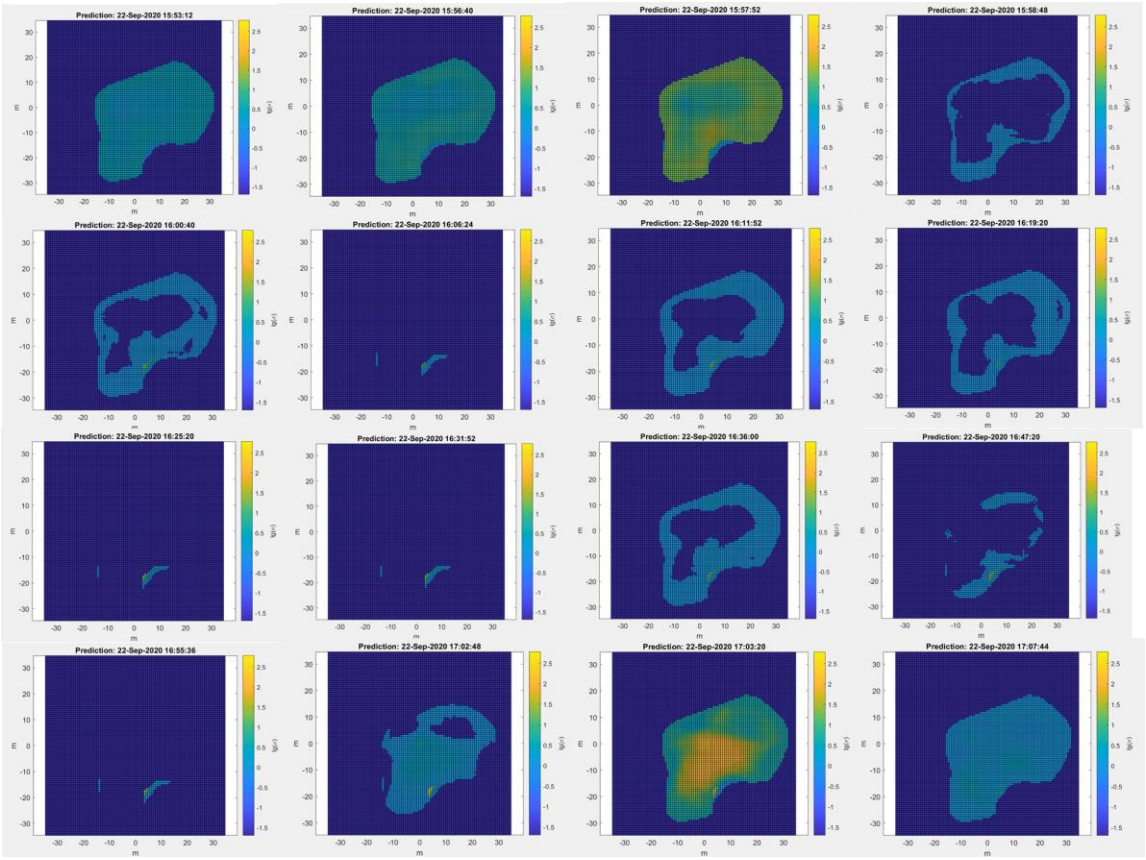

Figure 7-13: Inversion results at different injection times using the pixelwise ML model.

In summary, although there was some noise in the inversion results, we were still able to correlate the inversion results to the BHP changes. This correlation, however, does not mean that this inversion solution would provide the fracture conductivity map. The regenerated electric field, obtained by plugging in the change of fracture conductivity, which had resulted from the ML inversion, into DGFD forward model led to a larger than 200% difference in electric field from the observed field data. The experiment data need to be denoised first, and then, the pixelwise inversion model should improve after including the SP in the EM forward model to generate the training dataset.

In addition to our attempt to invert the 2020 field results, in the following section, we present another application of neural network routine to deduce the subsurface layer conductivities. Then, to justify the large data misfits, we demonstrate the large effect of metal objects (e.g., injection pipe and observation well posts) in the survey area on these EM data misfits.

Layer conductivity optimization using a ML model

Up to this point, the presented forward models for the Devine case were built by simply assuming that the lower half space is a homogenous medium with uniform conductivity of 0.02 S/m (Figure 7-14). However, we realized that this assumption is not supported by the collected field data as it led to a 74.45% data misfit between our simulated electric field and the ESG's total field obtained on September 22, 2020. In fact, the surface EM field does not change monotonously, thus indicating potential 3D effects, probably due to the presence of the casing, steel tubing on the ground, and buried mud pits used for drilling the observation wells. To investigate the effects of these objects on the data misfit, we first constructed a layered medium model to fit the total field better than the

homogenous model case. Using this multilayer model assumption, we were able to reduce the total field misfit down to 31%.

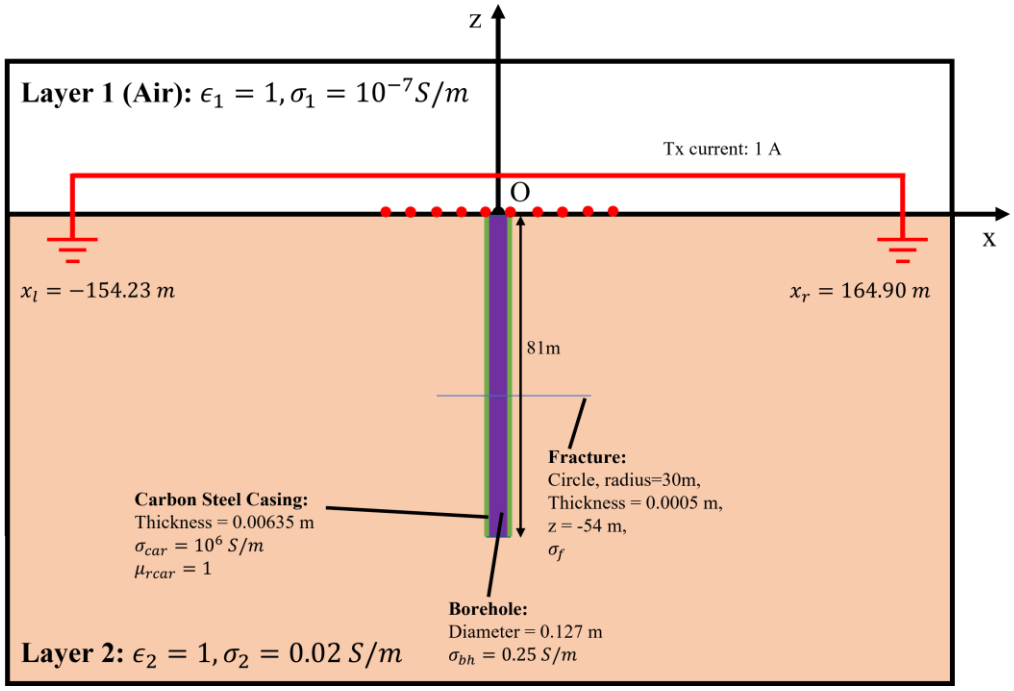

Figure 7-14: *Homogenous Devine model with the assumed background conductivity of 0.02 S/m.*

To design the layered medium, we started with the log data collected in 2017 at the DFPS (Ahmadian et al., 2018, 2019). According to the conductivity values at different depths, we divided the original homogeneous space into five layers with the boundaries at depth-direction coordinates of 0, -10, -20, -30, and -90 m (Figure 7-15).

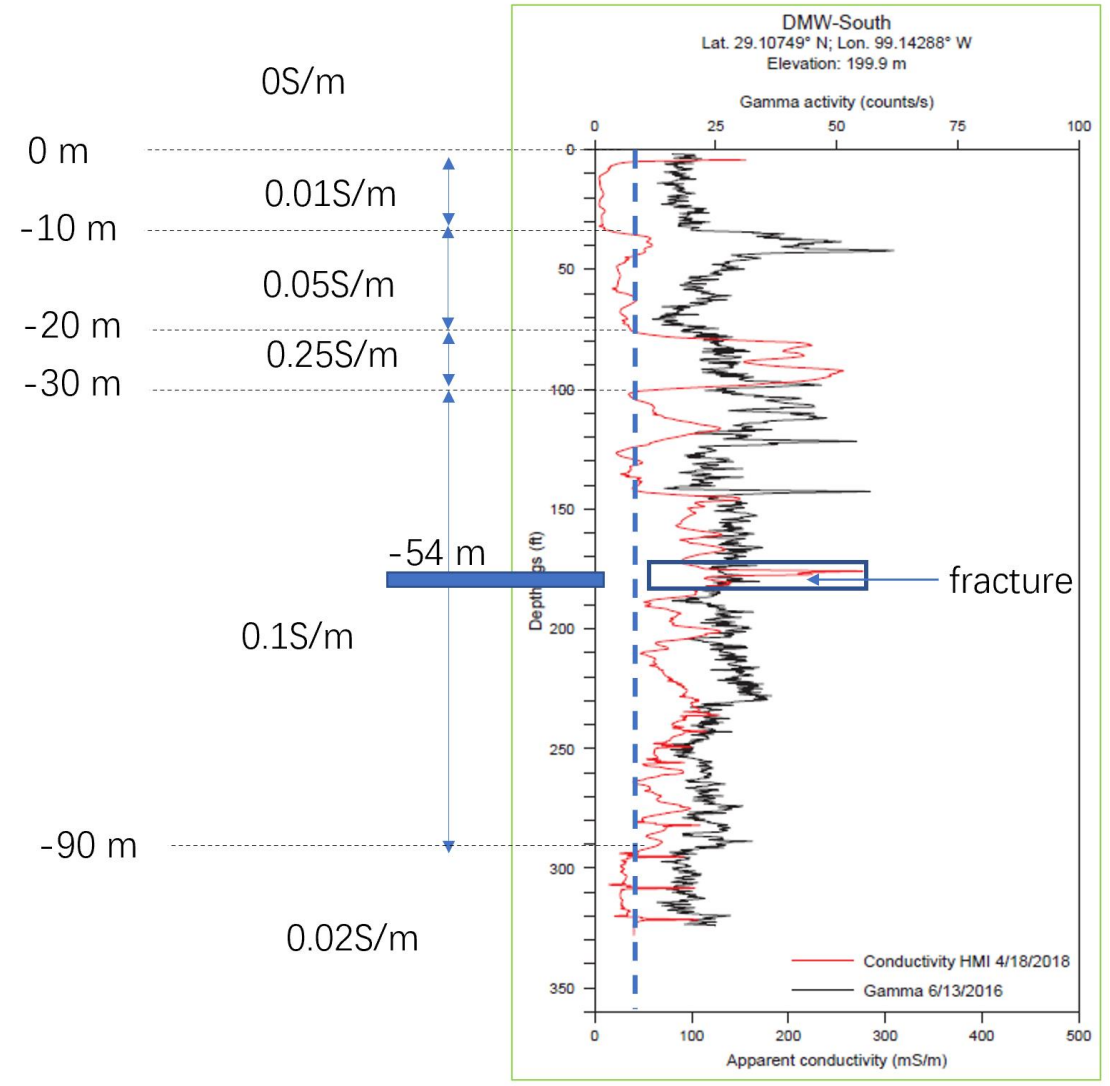

Figure 7-15: The log data and divided layers. The conductivity of each layer is obtained by averaging the conductivity log, shown by the red line in the right plot, for the associated depth interval.

To optimize the conductivity values of these layers, we built an NN and trained it by synthetic data. To generate the synthetic dataset, we used an analytical method based on the layered-medium Green's functions to calculate the electric field. The five layers were assigned conductivity ranges, from top to bottom, of [0.0005, 0.5] S/m, [0.01, 0.5] S/m, [0.02, 0.5] S/m, [0.005, 0.5] S/m, and [0.005, 1] S/m, respectively, as shown in Figure 7-16.

We generated 400,000 random synthetic datasets using these conductivity ranges, and then used 80% of them as training dataset, 19% of them as validation dataset, and 1% of them as testing dataset.

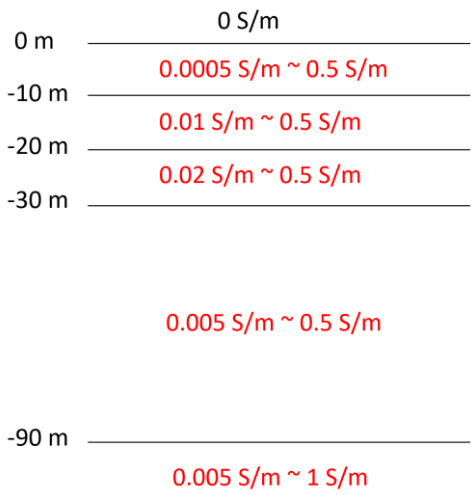

Figure 7-16: Conductivity value range of the layered medium model.

The NN structure consists of an input layer, four hidden layers, and an output layer (Figure 7-17). Based on the analysis that is described below, we deleted 20 "noisy" antennas from the original 70 antennas. The dimension of our input layer is 200, which consists of the real and imaginary parts of the E_x and E_y components [Real(E_x), Real(E_y), Imag(E_x), Imag(E_y)] for the remaining 50 antennas. The dimension of our output layer is five, which is the resulting conductivity values of the five layers in the layered medium.

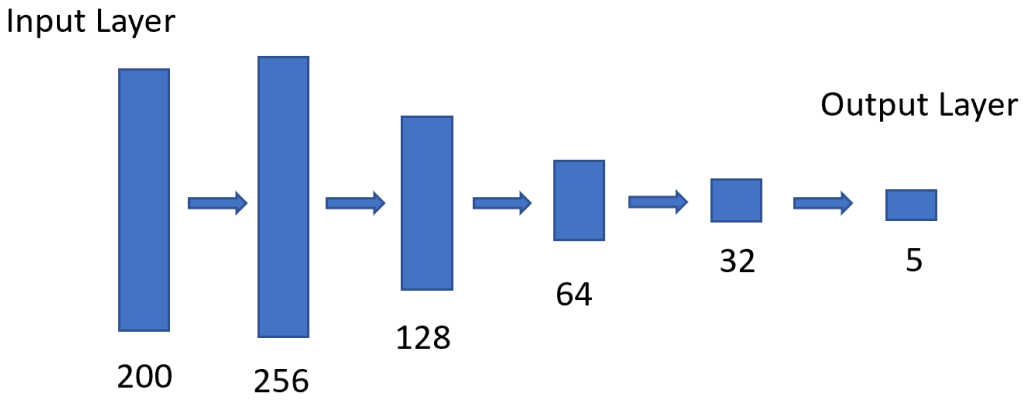

Figure 7-17: Structure of the neural network.

In the following, we first present the ML model testing results with the synthetic data and then, feed the field-test data from ESG into the ML model to obtain an inversion solution for the layered medium conductivity values.

ML model testing using synthetic data

We used the model and data misfits to evaluate the precision of this inversion. The model misfit is the relative error between the conductivity prediction from the ML model and the ground truth (1% testing data) of the conductivity distribution, as expressed in Equation (7-1). We fed the predicted conductivity distribution back into the forward model to calculate the corresponding electric field. The data misfit is the relative error between this recovered electric field and the ground-truth electric field, as expressed in Equation (7-2). For this specific problem, the ground truth in Equation

(7-1) or (7-2) represents either the assumed layered conductivity values or the modeled electric field for the layered conductivity in the testing dataset, respectively.

Figure 7-18 and Figure 7-19 show the model and data misfits of the 4000 testing cases, and Figure 7-20 and Figure 7-21 show the model and data misfits for an exemplary modeled test case. The horizontal axis of Figure 7-20 is the index of the five-dimension output layer of the ML model, which is the conductivity of the five layers from the shallowest to the deepest layer (Figure 7-16). The horizontal axis of Figure 7-21 is the index of the 200-dimension input layer of the ML model consisting of the real part and imaginary part of the E_x and E_y components [Real(E_x), Real(E_y), Imag(E_x), Imag(E_y)] for 50 antennas. The average model and data misfits of the 4000 testing data are 15.96% and 4%, respectively.

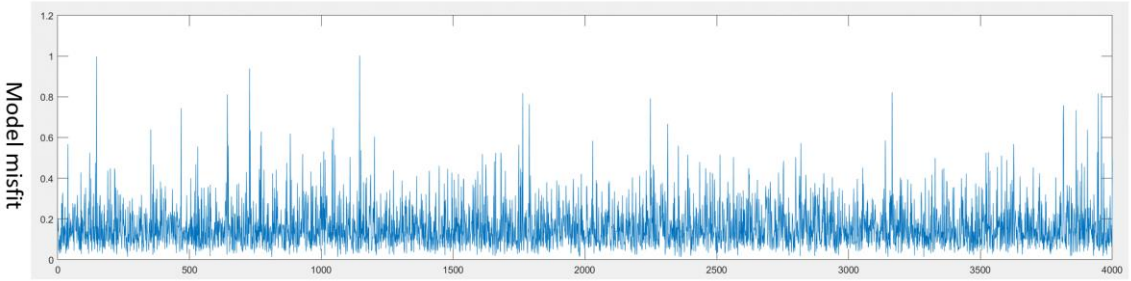

Figure 7-18: Model misfit of testing data, in the range of 0 to 1.2, corresponding to 0% to 120%. The horizontal axis refers to the label of a modeling dataset.

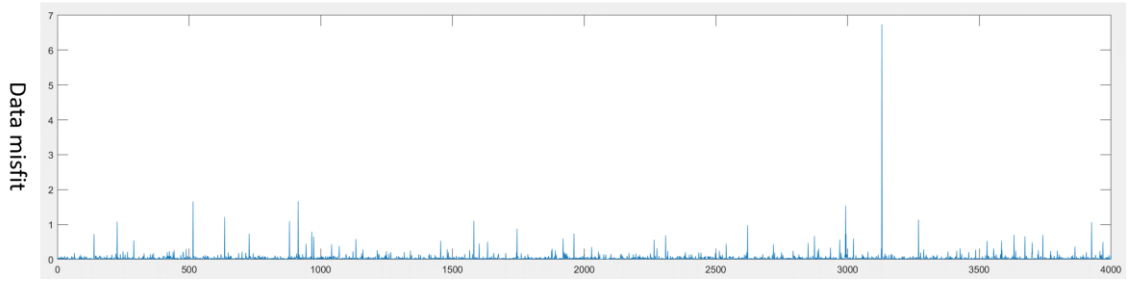

Figure 7-19: Data misfit of testing data, in the range of 0 to 7, corresponding to 0% to 700%. The horizontal axis refers to the label of a modeling dataset.

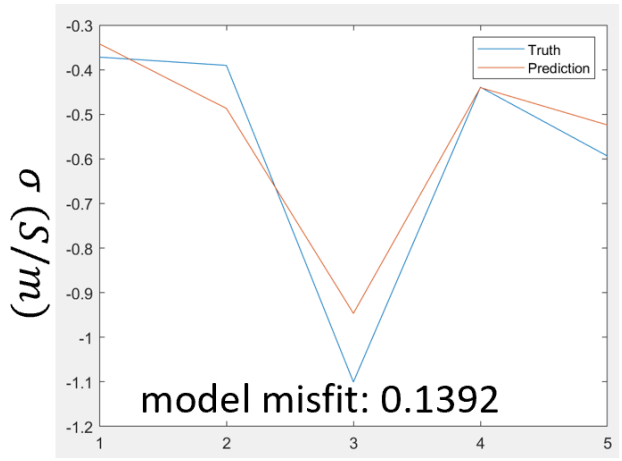

Figure 7-20: Model misfit of an example testing case. The horizontal axis is the layer index from 1 to 5 corresponding to the shallowest through deepest layers, respectively.

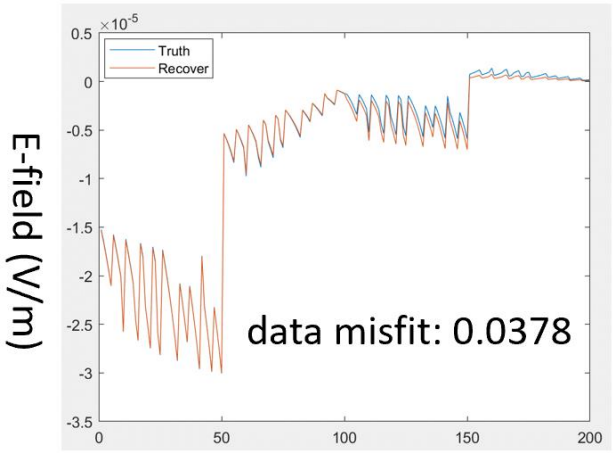

Figure 7-21: Data misfit of an example of test cases. The horizontal axis refers to the input parameter index corresponding to the real or imaginary part of the E_x or E_y component [Real(E_x), Real(E_y), Imag(E_x), Imag(E_y)] for 50 antennas. Then, the horizontal axis dimension is 200 = (50 antennas × 2 electric field axes × 2 complex-number components).

ML testing results with field data

Our ultimate goal was to match the simulated electric field with the collected (ground-truth) data from ESG and obtain the corresponding layered conductivity distribution. Therefore, after obtaining the well-trained ML model based on synthetic test cases, we fed the field-test data from ESG into the ML model to obtain an inversion solution for the layered medium conductivity values. We used the field data from the afternoon of September 22, 2020 for this inversion.

Because injection started at 15:52, we used the experiment electric field at 15:52 as the primary field. We considered the electric current frequency of 5 Hz here. However, we also tested frequencies of 50 Hz and 100 Hz. The final output for different frequencies were very similar to each other.

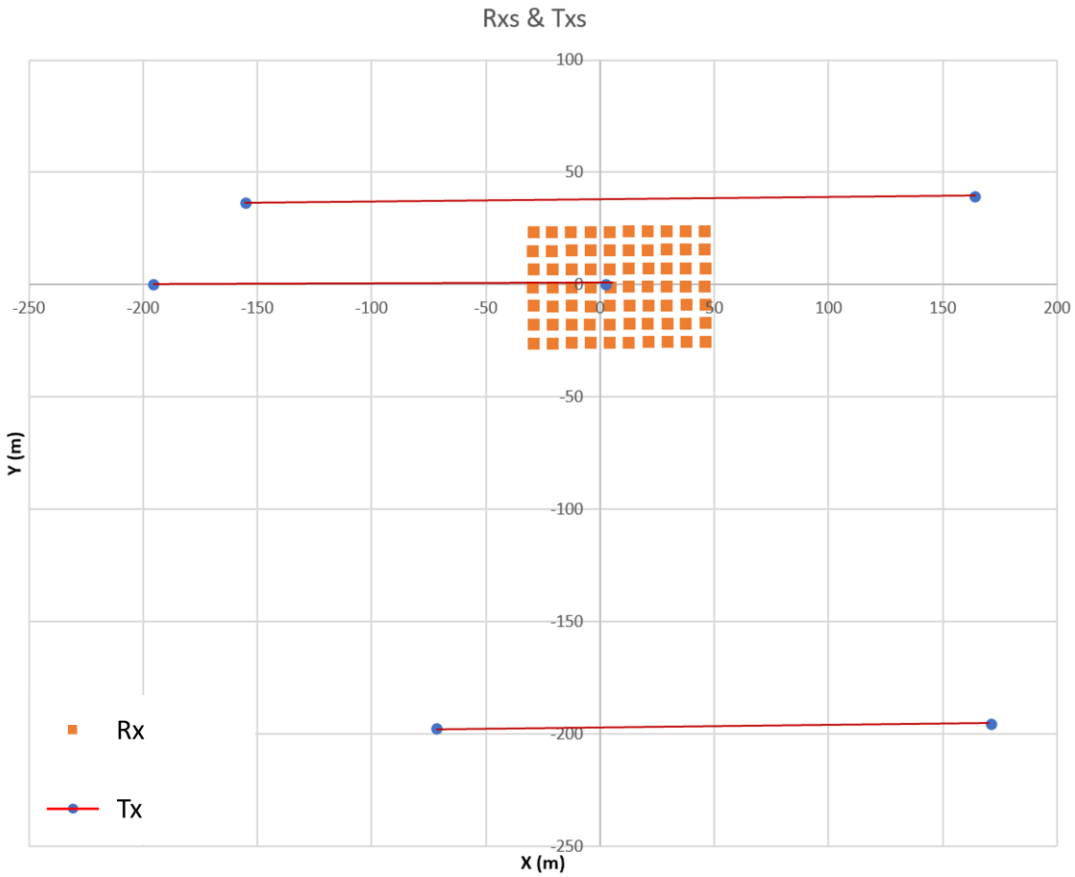

Figure 7-22: Receiver (RX) and transmitter (TX) locations, shown by orange rectangles and red lines, respectively.

The receiver and transmitter configuration are shown in Figure 7-22. We started by considering the conductivity of the five layers to be 0.05, 0.02, 0.2, 0.01, 0.08 S/m from the shallowest to the deepest layer according to the conductivity logs. Then, we calculated the electric field of this distribution by our BCGSFFT analytical model and compared it with the Devine experiment primary field in Figure 7-23. The orange line shows the data misfit between the two datasets. Initially we used the data from all the 70 receivers for this analysis. However, we were notified by the ESG that 4 receivers (RXs) were too noisy and should be eliminated from this analysis. The E_x-E_y combined data misfit with the remaining 66 recievers was 37.17% (Figure 7-23).

Subsequently, we found that three additional RXs near the injection well were also noisy (i.e., RXs 24, 30, and 31). Because of the suspected abnormal signal near the surface pipe, in the southwest corner of the receiver array, we also removed the RXs near the surface steel pipe (i.e., RXs 6, 7, 12, 13, and 19). The deleted RXs are shown by vertical lines in Figure 7-23. The vertical blue lines mark the RXs near surface pipe, the red lines mark the RXs near the injection well, and cyan lines mark the other abnormal RXs. The location of the bad receivers is also highlighted by colored stars in Figure 7-24.

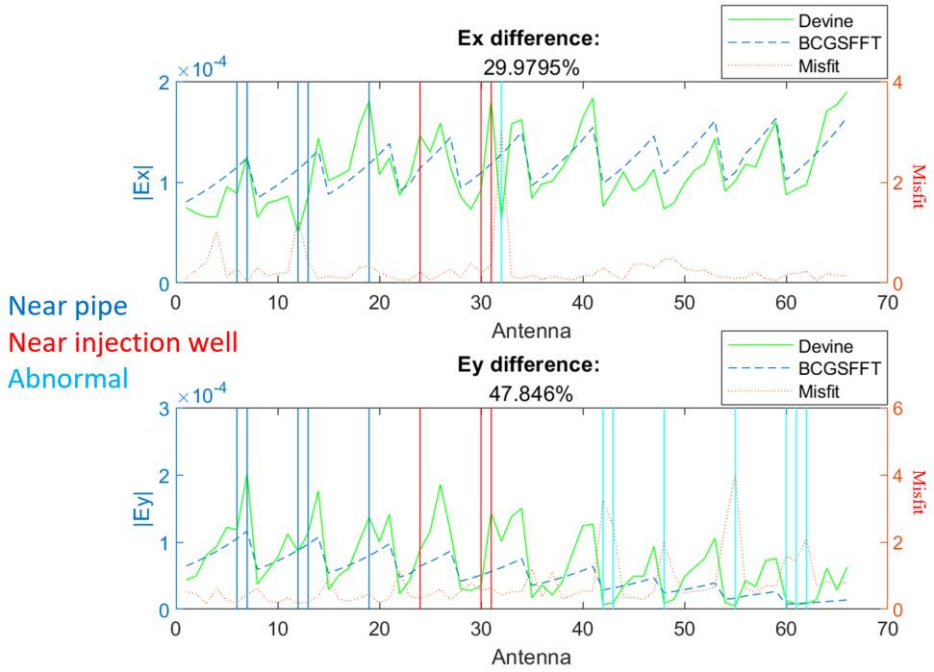

Figure 7-23: Comparison between our analytical model output and the electric field data, quantified by: (upper) E_x data misfit, and (lower) E_y data misfit. This resulted in a combined E_x-E_y data misfit of 37.17%.

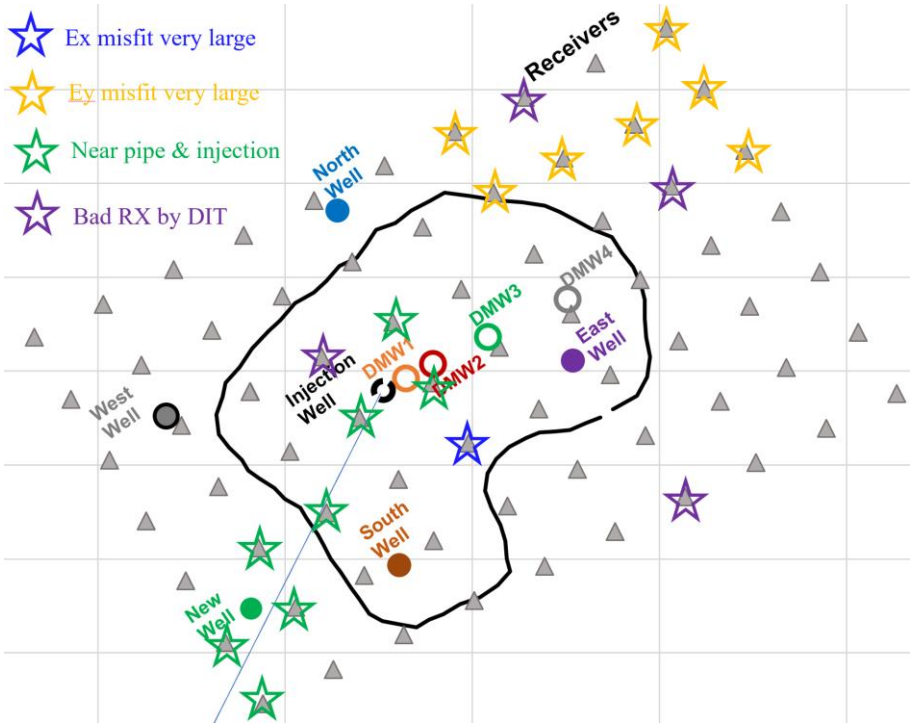

Figure 7-24: Receiver (RX) map and the deleted RXs marked by colored stars.

By only considering the remaining 50 receivers, the optimal conductivity of the layers from the shallowest to the deepest layer were determined to be as follows: 0.2631, 0.0826, 0.0720, 0.0067, and 0.6790 S/m by the ML model. These led to the best match for the E_x component with the misfit

of 18.46% and the combined E_x-E_y misfit of 34.46% (Figure 7-25). We also considered the ML outcome that resulted in the best match for the E_y component (0.0198, 0.0245, 0.0450, 0.0128, and 0.8863 S/m), but the data misfit for the combined E_x-E_y (37.21%) was worse than the previous case (Figure 7-26). When we solved for the best match for the combined E_x-E_y components (Figure 7-27), the corresponding conductivity for the five layers were calculated to be 0.0903, 0.0229, 0.0906, 0.0104, and 0.9426 S/m from the shallowest to the deepest layer. For this case, the E_x-E_y combined misfit was 30.89%.

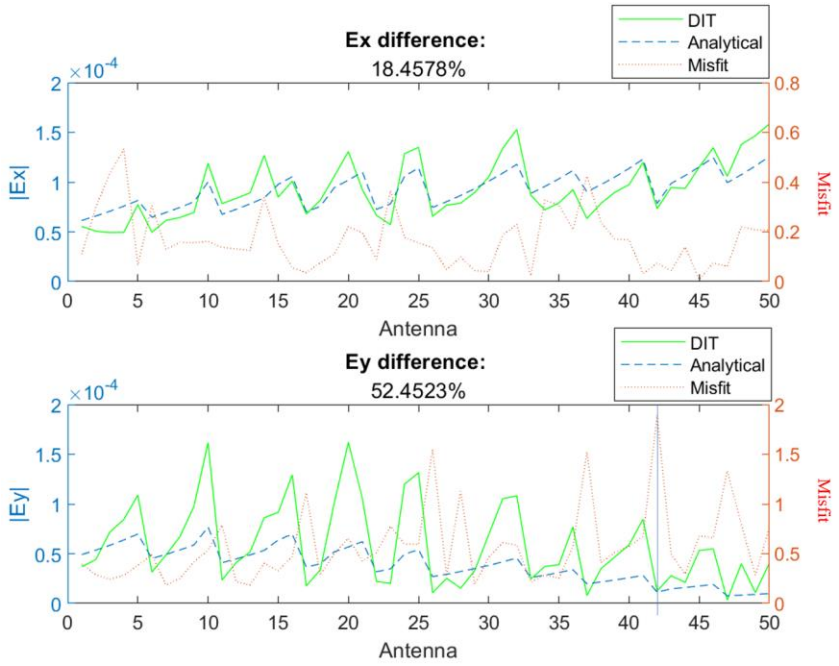

Figure 7-25: The best match for E_x component.

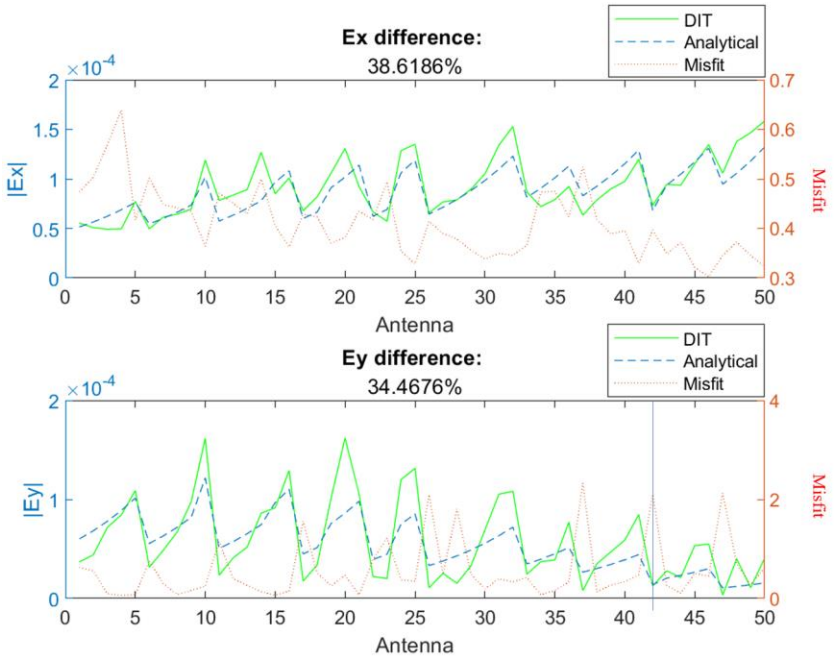

Figure 7-26: The best match for E_y component.

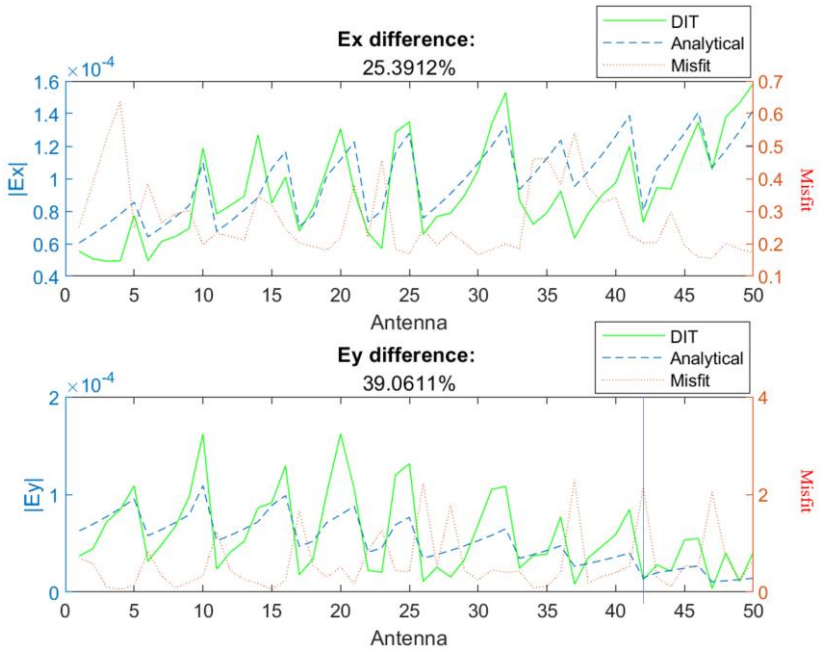

Figure 7-27: The best match for E_x-E_y combination.

The data misfits that we obtained above show that the E_y misfit is larger than E_x misfit by 13% (Figure 7-27). We suspect the accuracy of E_y data. Therefore, we relied on E_x component more than E_y component, which had led to the five-layer conductivity values of 0.2631, 0.0826, 0.0720, 0.0067, and 0.6790 S/m, from the shallowest to the deepest layer.

As shown in Figure 7-23 through Figure 7-27, a layered model for conductivity distribution is more reasonable than a homogeneous model. However, this analysis led to conductivities largely different from the values estimated by the conductivity logs in five layers (Figure 7-15). This large discrepancy could be explained by

(1) non-uniqueness of an inversion solution, as a relatively wide conductivity range was considered for each layer;
(2) the effect of 3D metal objects in the survey area; and
(3) removing 20 receivers due to noisy field data.

Reason 2 above is supported by the fact that the electric field along any single receiver line was not a monotonic function, probably due to the presence of 3D metal and nonmetal objects in the survey area, such as the metal posts used as markers for the corner wells, the metal ground injection pipe, the surface casings, metal injection pipe on the ground, and buried mud pits used for drilling of the observation wells. Thereby, we attempted to address the possible influence of these factors below.

Effect of surface metal objects on EM data misfit

Here, we show the work we conducted to perform numerical studies to evaluate the effect of the metal posts, injection pipe, and surface casing on the electric field.

The input parameter used for our modeling included a five-layer medium with the conductivity values driven from resistivity logs that were collected in 2018 at the DFPS (Ahmadian et al., 2018, 2019). We set the boundaries of these five layers at depths of 0, -10, -20, -30, and -90 m, as shown in Figure 7-28.

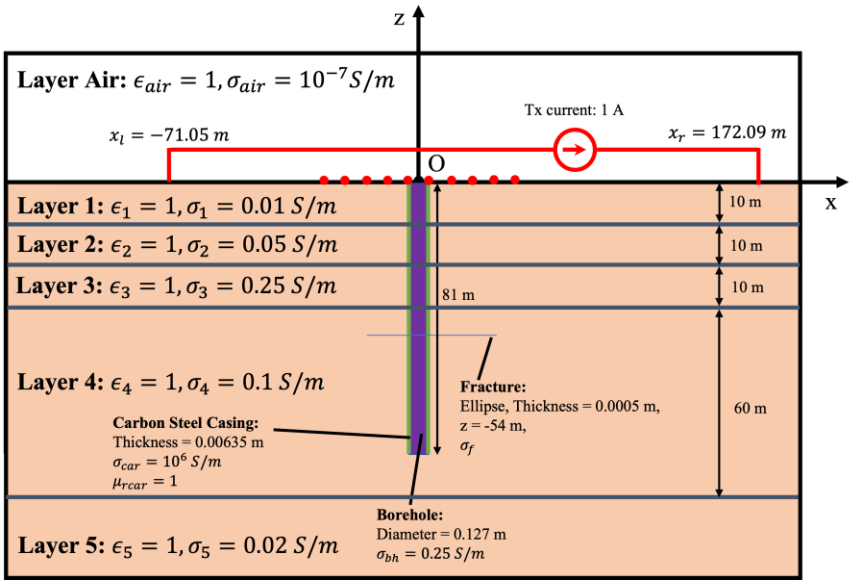

Figure 7-28: Layered model parameters used for forward modeling to calculate the electric fields. The conductivity of each layer is obtained by averaging the conductivity logs of various wells, which were obtained in 2018. The center of the coordinate is at the injection well, the x-direction is the line from injection well towards DMWs 1-4, the z-direction is the opposite direction of depth. The x-y-z axis system follows the right-hand rule.

The position of the ground injection pipe, surface casings, and marker posts are schematically shown in Figure 7-29.

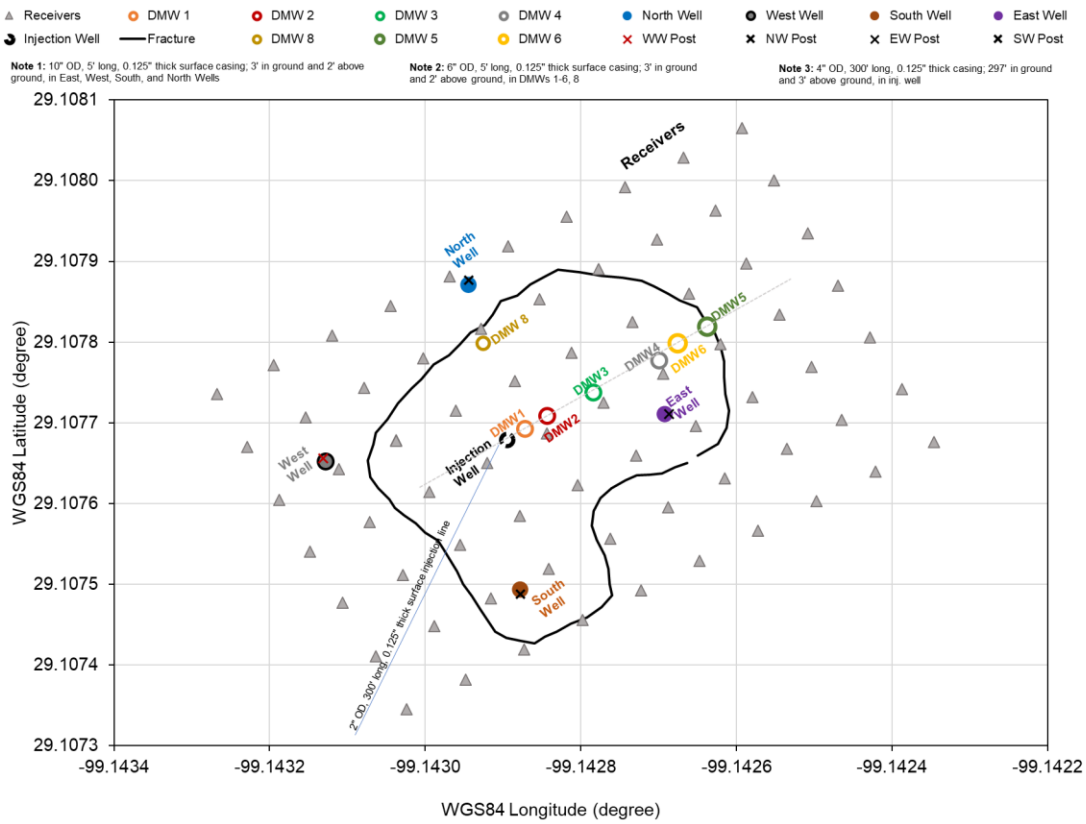

Figure 7-29: The receivers, wells, and horizontal ground metal pipe locations and sizes in the experiment. The ground injection pipe runs across the field from southwest to the center injection well, and is 2 inches in diameters and 300 ft in length. In our models, the conductivity of all metal pipes is assumed to be 10^6 S/m.

First, we studied the impact of the ground surface steel pipe used for injection by comparing the misfit of the electric field between the models with and without this pipe using a 3D DGFD case (Figure 7-30). Also, to ensure the accuracy of the DGFD models, we compared the 1D analytical model with the 3D DGFD case without the pipe. These comparisons as well as the differences between the simulated electric field with and without the metal pipe (called misfit, here) are shown in Figure 7-30.

The comparison of the simulated and analytical electric field in the absence of the metal pipe suggests a very good match between these two solutions. The large misfit of the simulated electric field between cases in the presence or absence of the metal pipe at all receivers, especially close to the pipe, show that the metal pipe can substantially influence the electric field. This difference is 20%-500% across various receivers near the metal pipe. The receivers with large misfit are RXs 5, 9, 10, 14, 15, and 19 (Figure 7-31). This difference is more pronounced for E_y component. The case with the pipe follows the ESG data trend better than the case without the pipe. Collectively this analysis led us to remove the ground pipe before the 2022 CSEM survey to reduce such a large contribution to the misfit.

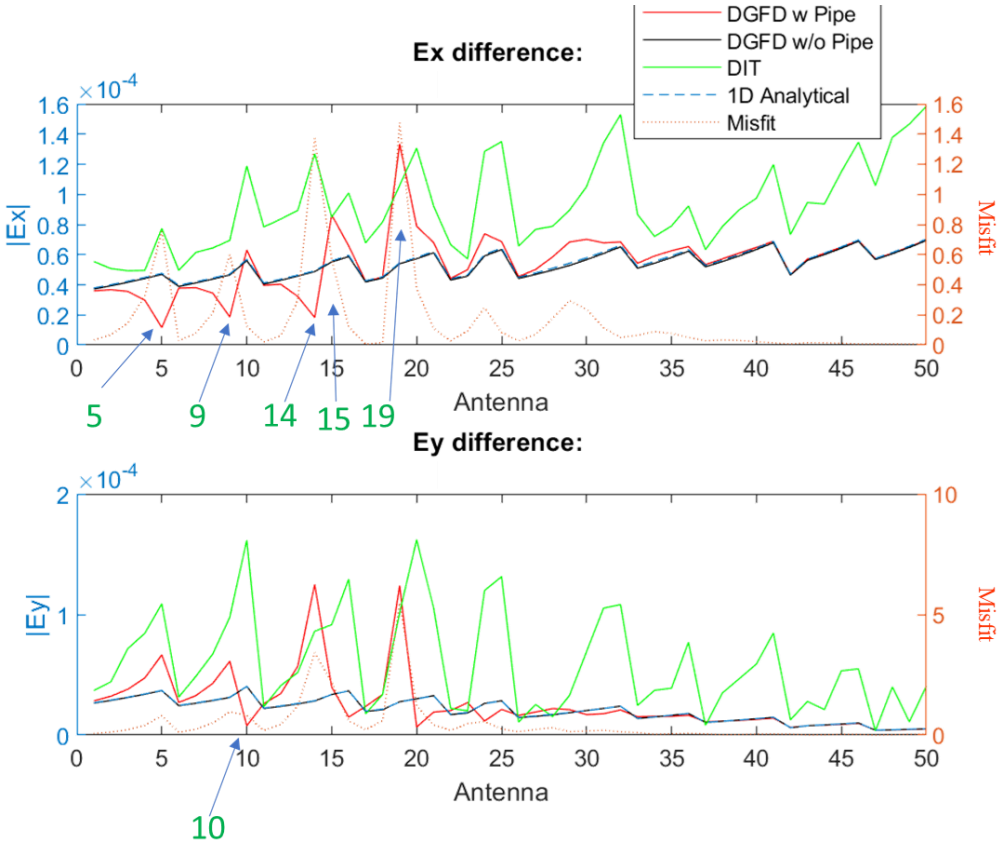

Figure 7-30: Comparison of the total electric fields obtained from the DGFD forward models that include or exclude the ground metal pipe. The 1D analytical solution and field data obtained by ESG (formerly called DIT) are compared with the DGFD results. "Misfit" here represents the difference between the DGFD results in the presence of the ground pipe and the DGFD results without this pipe, NOT the difference between the simulation and field data. Large misfits are observed for receivers 5, 9, 10, 14, 15, and 19 next to the pipe, as shown in Figure 7-31.

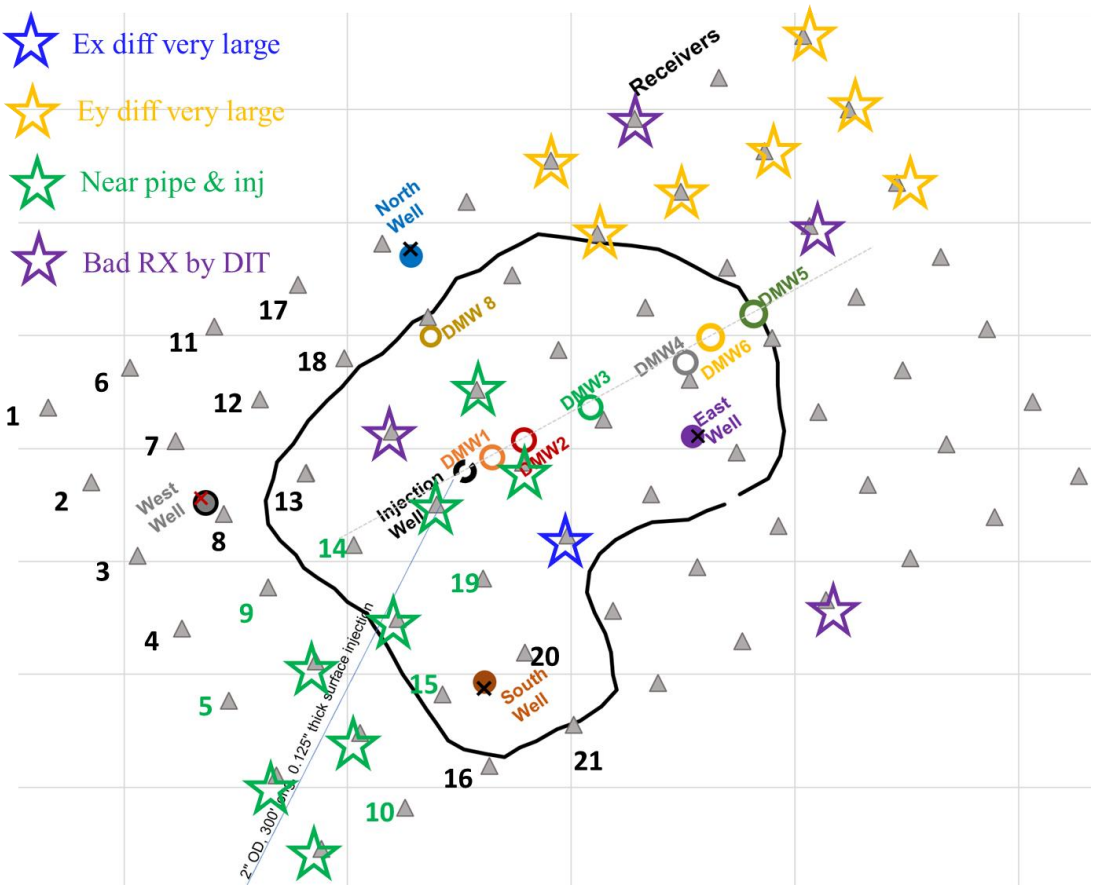

Figure 7-31: Schematics of wells, receivers, and the ground surface steel pipe at the DFPS. The contour of the EAP-filled fracture boundary is shown by the black line. The receivers that are marked with the green stars are the ones at the closest distance to the ground surface injection pipe.

Next, we looked at the contribution of the steel posts next to the observation wells and surface casings on our data misfit. To simplify the problem, we only considered these features associated with the west well. The west well and the associated post are located at $(-20.83, 7.84)$ and $(-20.96, 8.40)$ m in the coordinate system shown in Figure 7-29. The model included the EAP-filled fracture, the steel injection-well casing, the layered medium, the steel ground pipe, and the west-well surface casing and the associated metal post. We compared the data misfit of the electric field between the models with and without the west-well surface casing and post (Figure 7-32). We obtained a large data misfit at receiver RX 8 only, which is at the close distance of 0.5 m to the west well (Figure 7-31). The west-well post and surface casing associated with the west well do not influence the other receivers. However, the 40% misfit at the x-component of the electric field at receiver RX 8 is still too large to neglect. Therefore, in the 2022 field survey, we removed all the steel marker posts from the DFPS.

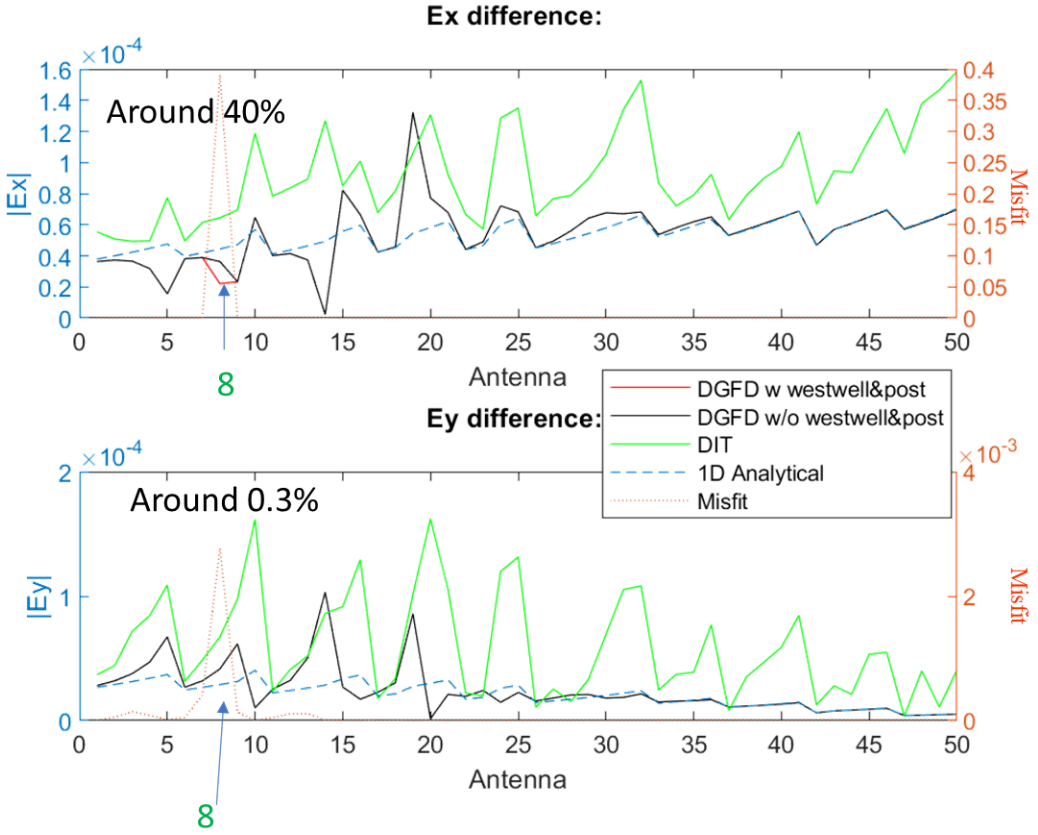

Figure 7-32: Comparison of the total electric fields obtained from the DGFD forward models that include or exclude the west-well surface casing and post. The 1D analytical solution and field data obtained by ESG are compared with the DGFD results. "Misfit" here represents the difference between the DGFD results in the presence of the west-well surface casing and post and the DGFD results without these, NOT the difference between the simulation and field data. A large misfit is observed only for receiver 8 next to the west well.

In a follow-on sensitivity analysis to assess the exclusive impact of an observation-well surface casing, we considered two simulation cases, with and without the well-well surface casing. Here, the misfit represents the relative difference between the electric fields obtained from the models with and without the west-well surface casing, as plotted in Figure 7-33. We observed 3% and 9% misfits in E_x and E_y components, respectively, at receiver RX 8 close to the west well. However, the remaining receivers were influenced minimally by the west-well surface casing. As we were not able to remove the surface casing of the wells before the 2022 field tests, to avoid the adverse influence of the surface casing of a well on the electric field, installing the receivers at the largest possible distance from all wells would be a rational solution to minimize the surface casing effect on the recorded electric field.

Ultimately, to refine our evaluation of the effect of the receiver distance to a well surface casing on the recorded EM field, we modeled a dense receiver mesh by placing a receiver in between two receivers in the previous 7×10 array, leading to a 13×19 receiver array. Similar to the previous evaluations, we measured the misfit of the electric fields with and without the west-well surface casing as shown in Figure 7-34. The closest and second closest receivers to the west well are RXs 31 and 30, respectively (Figure 7-35). The presence of the west-well surface casing led to 9% and 1% misfits of the y-component of the electric field at the first and second closest receivers to the west well, respectively. The 1% misfit was achieved for receiver RX 30 at a 3.28-m distance from

the west-well surface casing (Figure 7-35). Therefore, if a receiver is more than 3.28 m (11 ft) away from a well with the surface casing, this misfit can be reduced to less than 1%, which is experimentally acceptable. As such, this work helped us to plan for the 2022 field deployment by suggesting to install the receivers at least 4 m away from all surface casings. This 4-m spacing was calculated as the product of 3.28 m and 120%, which is the safety factor assumed in a general engineering design of instruments. However, because of the field-test implementation complexities (e.g., as uniform receiver grid spacing versus irregular well spacing), we were not able to exactly honor this distance for all receivers in the 2022 field deployment.

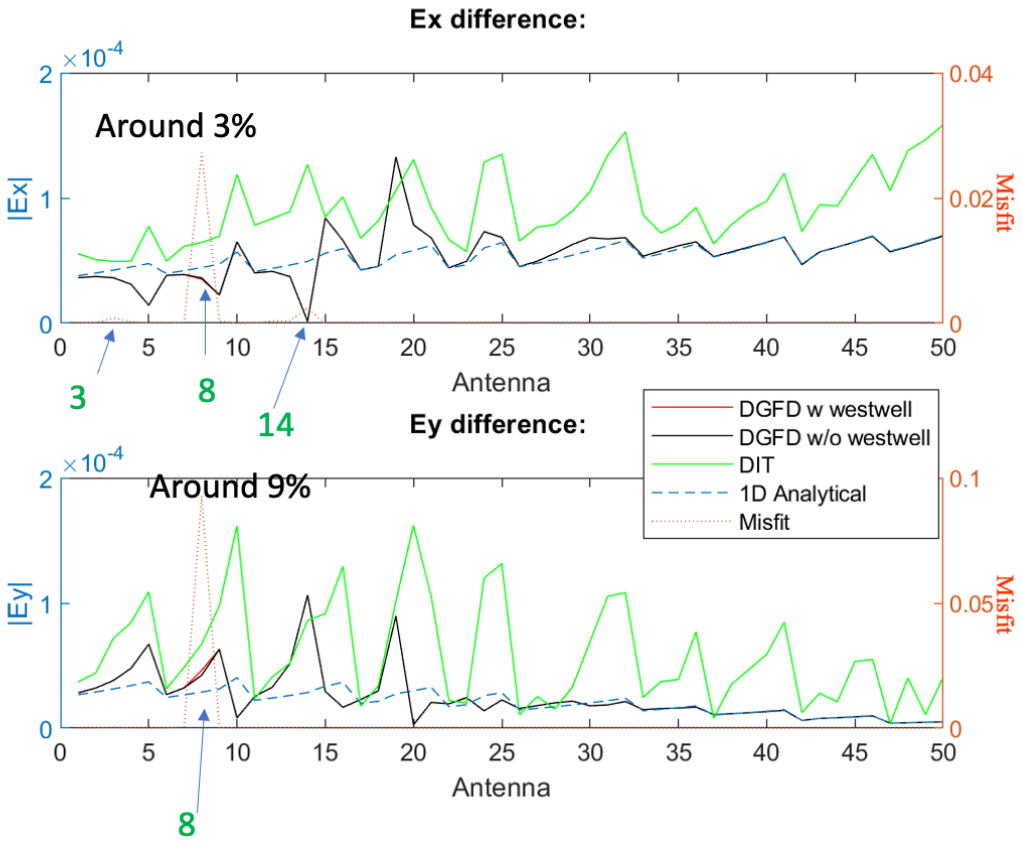

Figure 7-33: Comparison of the total electric fields obtained from the DGFD forward models that include or exclude the west-well surface casing. The 1D analytical solution and field data obtained by the ESG (formerly called DIT) are compared with the DGFD results. Here, "misfit" represents the difference between the DGFD results with and without the west-well surface casing, NOT the difference between the simulation and field data. A large misfit is observed for receiver RX 8 at the closest distance to the west well (Figure 7-31).

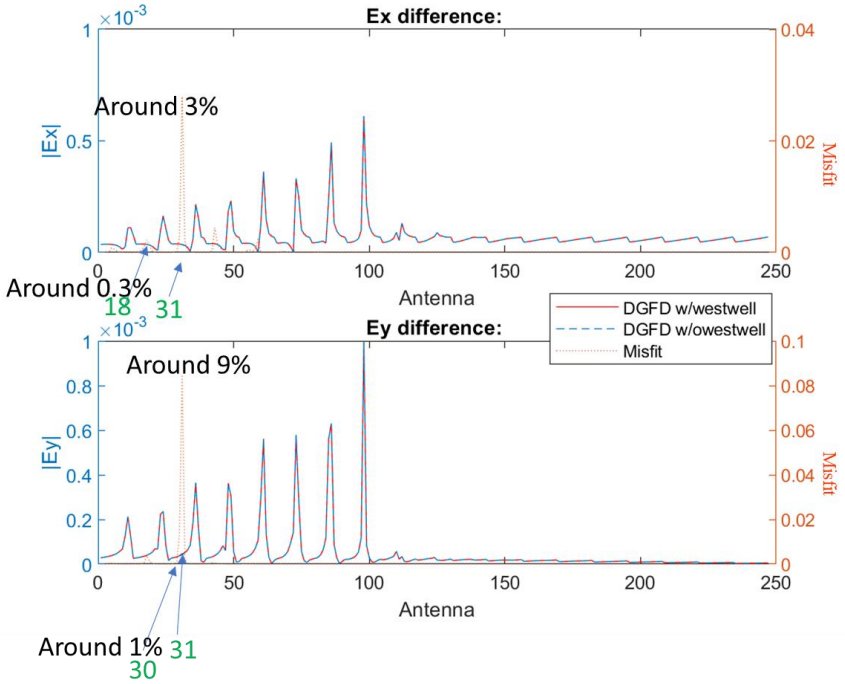

Figure 7-34: Comparison of the total electric fields obtained from the DGFD forward models of the dense receiver (13×19) array that include or exclude the west-well surface casing. Here, "misfit" represents the difference between the DGFD simulation results with and without the west-well surface casing, NOT between the simulation and field data. A large misfit of 9% is observed for receiver RX 31 at the closest distance to the west well. A misfit of approximately 1% is observed for receiver RX 30 (Figure 7-35), which is 3.28 m away from the west well.

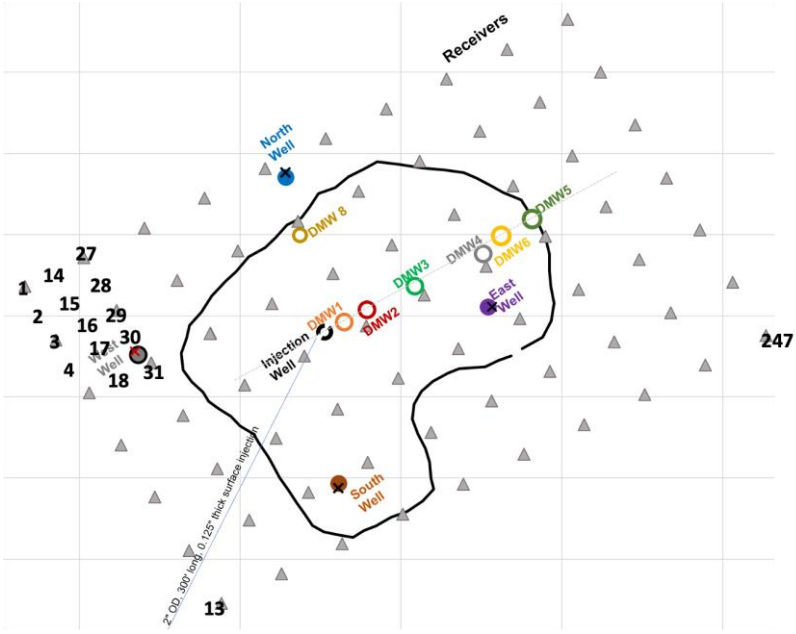

Figure 7-35: Schematic representation of the dense receiver array overlapping with the wells and surface metal pipe at the DFPS. The contour of the EAP-filled fracture boundary is shown by the black line. To demonstrate the dense array, a few receivers of this array are shown by the black index numbers on the left-hand side.

Considering an inhomogeneous surface layer to reduce misfit

The 2020 field experiments suggested that the surface conductivity and metal pipe on the ground potentially influenced the simulation total field misfit versus gathered EM field data. Before the 2022 field experiments, we replaced the long metal surface pipe, which had previously been used for injection, with a 500-ft long polypropylene pipe. We also surveyed the entire field surface conductivity before the injection experiment. As suspected, these data revealed the presence of inhomogeneities in the surface layer at the DFPS. Subsequently, we updated our DGFD forward solver by including this inhomogeneous surface layer, and calculated our model misfit again. This work is described below.

Figure 7-36 shows a cross-sectional view of our multilayered model based on conductivity values for all layers. The subsurface layers in this model are distinguished from one another by the contrast in their electrical conductivity as obtained by running induction well logs at the DFPS in 2018 (Ahmadian et al., 2019). The center of the coordinate system is at the injection well, the x-direction is the line from the injection well toward DMWs 1-4, and the z-direction is the opposite direction of depth. This coordinate system follows the right-hand rule, meaning that the y-axis points toward northwest.

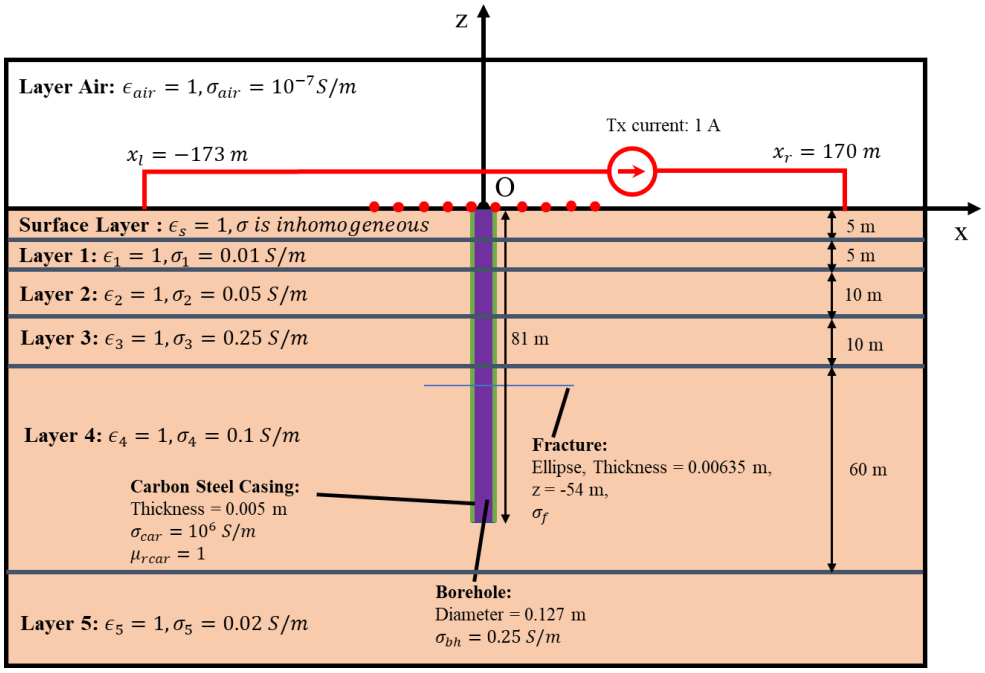

Figure 7-36: The x-z cross section of the DGFD layered model including seven layers the top of which being the inhomogeneous surface layer with embedded permittivity and conductivity values. We assumed that all layers are homogeneous except for the surface layer which is inhomogeneous. The red TX line and red RX dots represent the transmitter and a line of receivers. Fracture was assumed to be a thin sheet with an initial conductivity value of 50 S/m.

The division of the surface layer area in x-y view is shown in Figure 7-37. Initially, we measured conductivities for each of these areas using a conventional Schlumberger's array, and the measured values are shown in Figure 7-37.

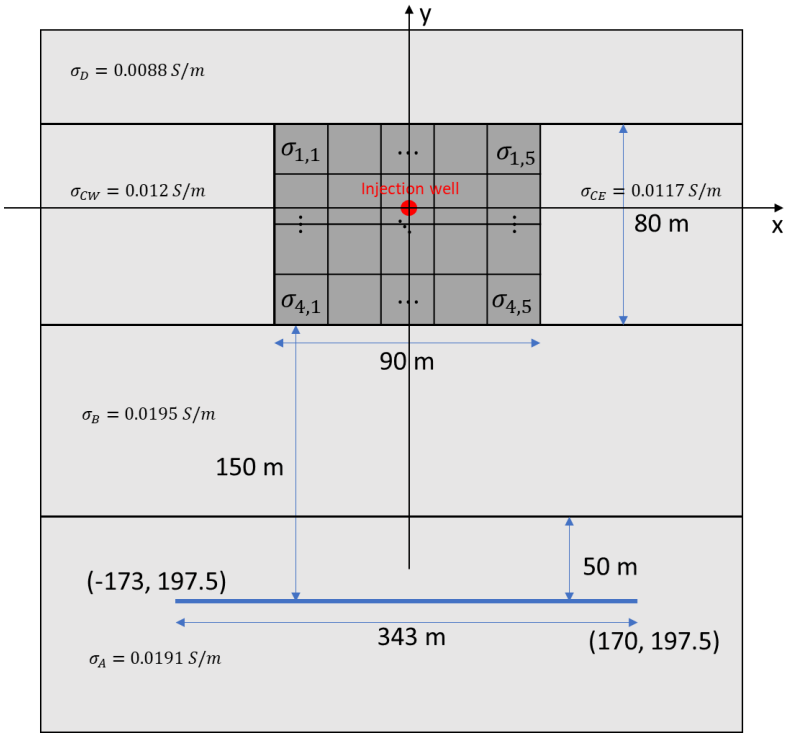

Figure 7-37: The plan view of the inhomogeneous surface layer in the layered medium DGFD model for the DFPS field deployment in January 2022. The surface is divided into four different areas from south to north: area A, area B, area C, and area D. Area C contains a central area as filled by dark-gray color where the electrical receivers were installed. Because this central area is the most important area of the experiment, we decided to run a dense electrical survey over this central area using a CMD-Explorer EM conductivity meter (GF Instruments, S.R.O.). The dimensions and measured conductivities are marked in the figure except for the central area that is shown in Figure 7-38. To use the conductivity measurements in the central area in the DGFD model, we averaged these measurements within each block of a 4-by-5 block array.

Because the center of the survey area, which is overlying the EAP-filled fractured zone, is the most important area of the experiment, we conducted a dense survey on this area. This area is marked by the dark-gray color in Figure 7-37. For this dense survey, we used a CMD-Explorer EM conductivity meter (GF Instruments, S.R.O.). Figure 7-38 shows the measurement points along the walking path over this central area. To utilize this data in the model, we divided the dense survey area into a 4×5 block array. Next, we calculated the average value of the electrical conductivity within each block after multiple measurements. These average values are listed in Table 7-1.

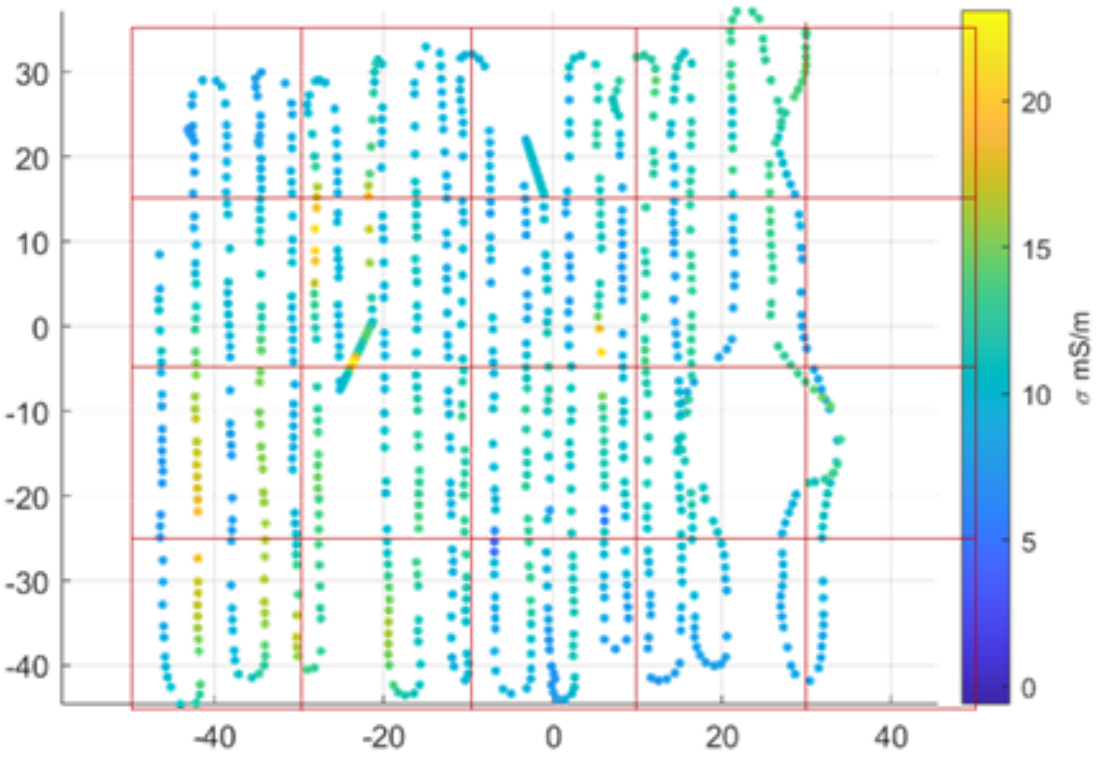

Figure 7-38: The measurement points and apparent conductivity values on the central area in Figure 7-37, and the 4×5 block array for averaging the measurements.

Table 7-1: Conductivity for each block in the central area, as shown in Figure 7-37. The indices 1 through 5 on the first row denote the block number from left to right in Figure 7-38, and the indices 1 through 4 on the first column represent the block number from top to bottom in Figure 7-38.

$\sigma_{i,j}$ (mS/m)	1	2	3	4	5
1	9.9096	11.1925	11.3283	13.0994	13.8024
2	12.5196	12.6377	10.5567	11.8084	9.8662
3	13.7670	12.5017	11.8137	12.0472	11.9304
4	14.5261	12.5387	10.2288	9.5621	9.5639

The simulation models for the 2022 field data are based on the layout of the surface receivers, transmitter line, injection and monitoring wells, and the fracture boundary, as shown in Figure 7-39. The triangles on this figure form a 10×9 grid of receivers laid out uniformly, 30-ft (9.14-m) apart from one another and almost centered at the injection well. Due to the presence of a tree at the test site, we skipped installing 9 receivers out of 90 in this 10×9 grid. In addition, we installed a transmitter line at almost 645 ft (197 m) of distance from the injection well. Each receiver in this survey area was associated with four 6-ft long copper electrode rods hammered into the ground, shown by the white balloons in Figure 7-40a and pointed to by red arrows in Figure 7-40b. This receiver configuration allowed to obtain the electric field on the ground surface in two lateral directions parallel to the alignment of the receivers in northeast-southwest and northwest-southeast directions. Each couple of rods associated with a receiver was installed in a lateral direction with a spacing of 25 ft (7.62 m) from one another. The difference between voltage that was received in two rods in x-direction divided by the rod distance led to the E_x component of the electric field that

was assigned to the respective receiver. Similarly, the voltage difference of the two rods in y-direction divided by the rod distance provide the E_y component of the electric field. Consistent with the receiver deployment map, we simulated 10 columns by 9 rows of receivers spread in east-west and north-south directions, respectively.

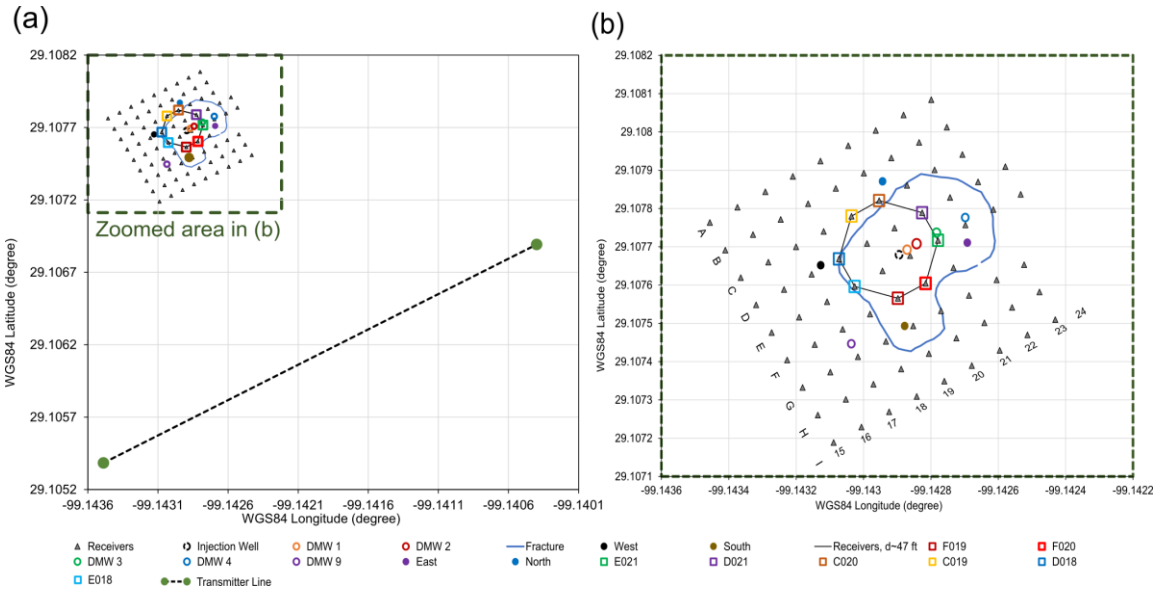

Figure 7-39: *Controlled-Source Electromagnetic (CSEM) Survey area in plan view at the DFPS in January 2022: (a) a zoom-out view including the transmitter line, receivers, wells, and the fracture shape; (b) a zoom-in view of the receivers, wells, and fracture boundary. The propped fracture boundary was derived from a previous survey during the primary hydraulic fracturing in 2017 (Ahmadian et al., 2019). Bottomhole pressure and salinity were recorded at the injection well and DMWs 1, 2, and 9 at 10, 20, and 107 ft of distance from the injection well. The receivers at 47 ft of distance from the injection well are highlighted for reference throughout electric potential-difference analyses later on.*

(a)

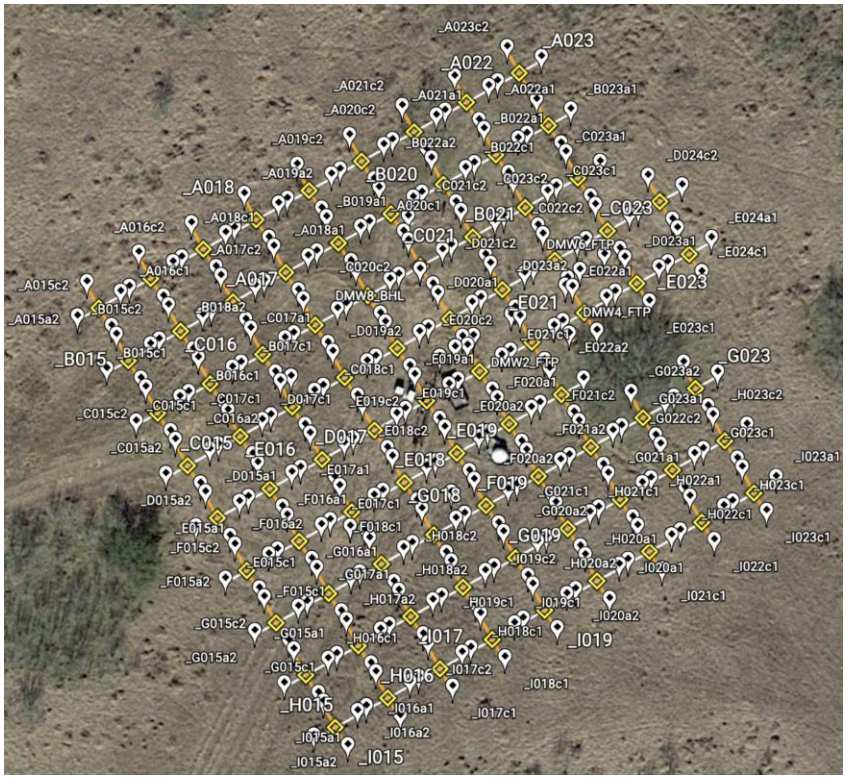

(b)

Figure 7-40: (a) Receiver deployment map. (b) An image of a set of four receiver rods, shown by four red arrows, and the associated wireless receiver, shown by a blue arrow, near DMW 4. The black lines show the wires that connected these receivers to the receiver rods. The wireless receiver communicated the data with the wireless tower, shown by the black arrow.

We then added the acquired inhomogeneous surface conductivity to our DGFD forward model, and proceeded to simulate the total field that was collected by ESG when no injection was being conducted.

We assumed the transmission frequency of 100 Hz and the presence of a circular fracture with 30-m radius with conductivity of 50 S/m. Figure 7-41 shows that the simulated amplitude of the E_x or E_y component of the total electric field using either the homogenous or inhomogeneous surface layer matches with each other for different receivers. This figure also compares these simulated amplitudes with the one acquired by the ESG's equipment. Although the trend line (the manually drawn black line) through the ESG data is similar to the simulated electric field results, there is still a significant misfit between the simulated and measured data.

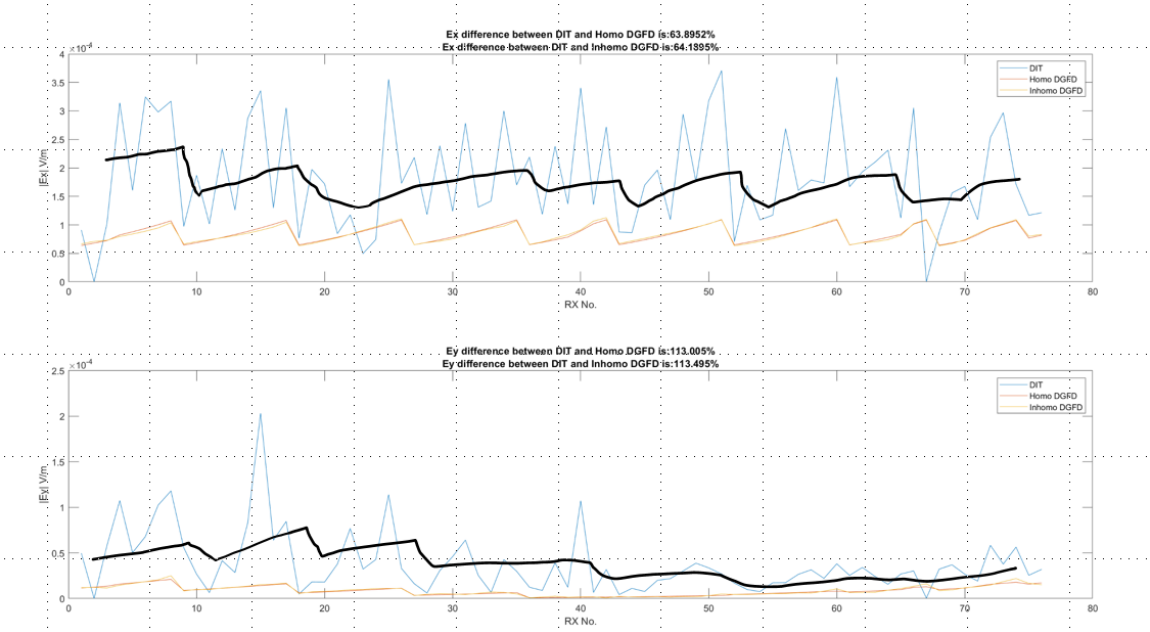

Figure 7-41: Comparison of the simulated E_x (top) and E_y (bottom) total electric field using either the homogenous or inhomogeneous surface layer compared with the ESG (DIT) measurements. Models assumed a 50 S/m circular fracture and a transmission frequency of 100 Hz. Although the trend line (black line) of simulated results follows the same trend as ESG measurements, a misfit of greater than 60% and 100% for the E_x and E_y components are observed. Inclusion of the measured inhomogeneous surface conductivity in the model did not improve this misfit.

As discussed above, considering the inhomogeneous surface layer did not reduce the total field misfit compared to the homogeneous case. Because we did not know about the calibration factor of the CMD-Explorer equipment, we adjusted the surface conductivity distribution using a multiplying factor per survey block, which led to the reduction of the misfit to 29%.

Evaluation of the scattered field magnitudes

Although the total field misfit was large, the difference between the total field, commonly called scattered field, could result in a small misfit, leading to a useful dataset for the EM field inversions. Thereby, in the following, we focus more on the scattered field misfit rather than the total field misfit. To represent changes of the electric field, the scattered electric field is defined as total electric field at a given time minus total field before injection, as formulated by Equations (7-3), (7-4), and (7-5):

$$\vec{E} = E_x\hat{x} + E_y\hat{y}, \tag{7-3}$$

where E_x and E_y denote the two components of the total electric field. Then, by selection of a zero-time t_0, the scattered field at time t can be calculated as the difference in the total field at time t and time t_0, as follows:

$$\vec{E}^{sct}(t) = \vec{E}(t) - \vec{E}(t_0) = \big(E_x(t) - E_x(t_0)\big)\hat{x} + \Big(E_y(t) - E_y(t_0)\Big)\hat{y}. \tag{7-4}$$

Then, the amplitude of the scattered field can be calculated as

$$\left|\vec{E}^{sct}(t)\right| = \sqrt{(|E_x(t) - E_x(t_0)|)^2 + \left(\left|E_y(t) - E_y(t_0)\right|\right)^2}. \tag{7-5}$$

We used Equation (7-5) to plot the contours of the scattered field. The routine for drawing the scattered electric field contours is described below:

Figure 7-42a shows a cross-sectional view of our multilayered model, showing the assumed conductivity values for all layers, which were obtained by running induction well logs at the DFPS in 2018 (Ahmadian et al., 2019). The center of the coordinate system is at the injection well, the x-direction is the line from injection well toward DMWs 1-4, and the z-direction is the opposite direction of depth. This coordinate system follows the right-hand rule, meaning that the y-axis points toward northwest, as the x-axis (the axis crossing through DMWs 1-4) is toward northeast. As shown in Figure 7-38, the surface layer of the model was divided into multiple zones to use the measured surface conductivity. Compared to this figure, here, we divided the survey zone into a denser 8×10 grid. The resulting values per gridblock within the dark-gray zone in Figure 7-42b are listed in Table 7-2. Note that Figure 7-42a may seem the same as Figure 7-36, however, the number of assumed layers and their thicknesses are different in these two figures. In our latest work, we used seven conductivity layers, as shown in Figure 7-42a, obtained from the induction logs, in contrast to five layers in Figure 7-36. Also, Figure 7-37 and Figure 7-42b may look identical; however, the size of the grid representing the inhomogeneous surface-layer conductivity is 4×5 in Figure 7-37 which is refined to 8×10 in Figure 7-42b to generate a more precise model.

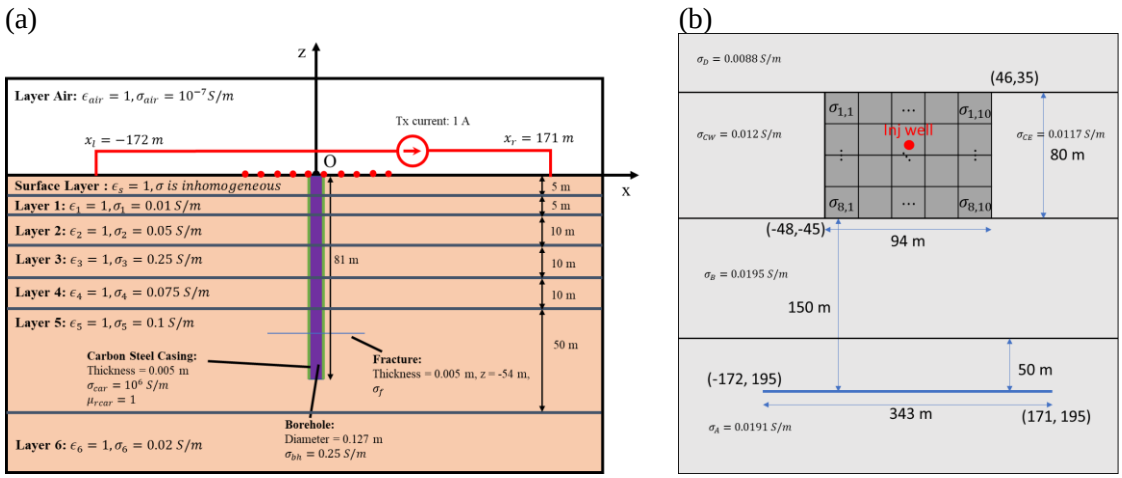

Figure 7-42: (a) The x-z cross section of the DGFD layered model including seven layers in the model with embedded permittivity and conductivity values. (b) Plan view of the model, including the schematics of an inhomogeneous surface layer shown by dark-gray meshed area overlying the propped fracture and where receivers are installed. All layers assumed homogeneous except for the surface layer. The red TX line in (a) = the transmitter. The red RX dots in (a) = a line of receivers. Fracture assumed to be a thin sheet with an initial conductivity value of 60 S/m. The surface layer in (b) divided into areas A through D from south to north. Area A, B, and D conductivities marked in (b). Area C conductivity surveyed by a CMD-Explorer EM conductivity meter (GF Instruments, S.R.O.), and gridblock conductivity calculated by averaging the CMD-Explorer measurements within each gridblock of an 8×10 mesh.

Table 7-2: $\sigma_{i,j}$ conductivity in mS/m for each gridblock within the dark-gray area in Figure 7-42b. The indices 1 through 10 on the first row = the gridblock number from left to right in Figure 7-42b. The indices 1 through 8 on the first column = the gridblock number from top to bottom in Figure 7-42b.

		x-index									
		1	2	3	4	5	6	7	8	9	10
y-index	1	9.9	10	11	5	5	10	10	13.8	10	13.8
	2	9	12.5	5	11	8	10.6	20	9.9	13.8	13.8
	3	13.8	10	15	20	7	9	20	11.9	30	30
	4	5	12.5	10	10	10	30	11.8	9.6	10	20
	5	20	12.5	20	20	0.4	10	9	9.6	10	11.9
	6	13	0.2	20	20	20	8	8	9.6	5	11.9
	7	5	15	0.4	12.5	30	5	5	9	9	9.6
	8	14	10	12.5	12.5	10	10	9.5	9.5	9.5	9.6

We used the surface conductivity distribution in an EM forward model and compared the resulting contours for the total electric field at 10 a.m. on January 26 with those from the field data (Figure 7-43). To quantify this comparison, we defined the misfit between these contours as the average of the difference between the amplitude of the total electric field obtained from the simulation and the field data in 81 discrete data points at receivers.

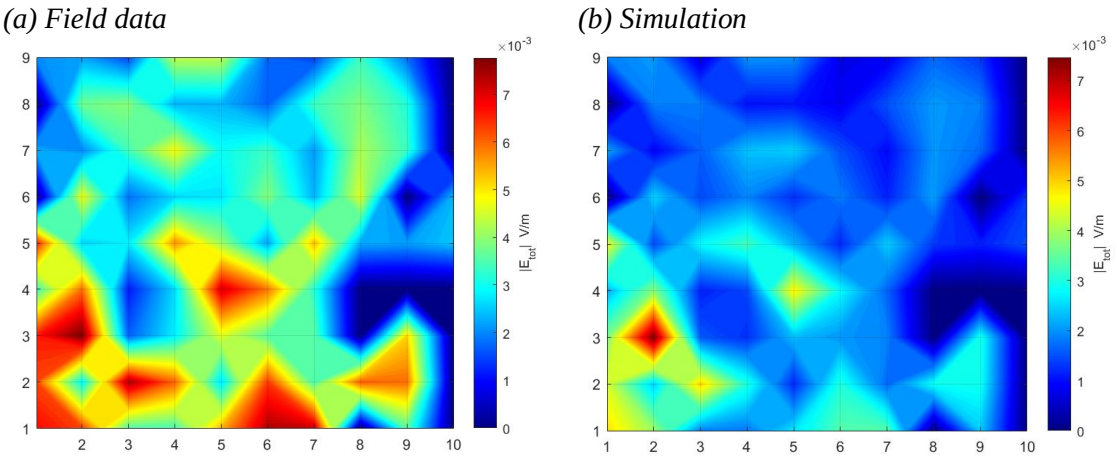

Figure 7-43: Total electric field in the plan view, on January 26 at 10:00 a.m., obtained from (a) the field data, and (b) simulation. The total field misfit was 29%.

Based on the significant variation of electric field trace values observed during the injection times (see Subtask 6.5), we considered three states of the dilated fracture on January 26, 2022, to simulate the change of the total field (i.e., scattered field) due to conductivity changes (Figure 7-43):

- State 1, at 12:18 (T_1), with a change of the electrical conductivity from the background 60 S/m to 40 S/m in a circular area of the propped fracture, around the injection well, with a radius of 1.34 m;
- State 2, at 17:33 (T_2), with a change of the electrical conductivity from the background 60 S/m to 10 S/m in a circular area of the propped fracture, around the injection well, with a radius of 4.6 m; and
- State 3, at 22:26 (T_3), with a change of the electrical conductivity from the background 60 S/m to 40 S/m in a circular area of the propped fracture, around the injection well, with radius of 3 m.

States 1 through 3 correspond to 12 minutes after the start of injection, 5 hours and 26 minutes after the start of injection, and 4 hours and 30 minutes after shut-in, respectively. The background conductivity of 60 S/m was obtained from the conductance of 300 mS divided by 0.5 cm propped fracture aperture from our previous logging at the DFPS (Ahmadian et al., 2019). The 40 S/m conductivity in state 1 was estimated during the first 12 minutes of injection, as fracture closure pressure was not exceeded during this time. However, we assumed that further injection until T_2 led to the drop of conductivity in the circular area down to 10 S/m due to further dilation of the fracture. These assumed trends are supported by our laboratory observations (Subtask 3.1). At state 3, we assumed that leakoff led to the drop of conductivity to that in State 1. The dilated fracture dimensions were determined using the conservation of mass. The scattered field was calculated by the subtraction of the total field at the initial time before start of injection from the total field at a specific state.

As shown in Table 7-3, the average misfits of the simulated scattered electric field amplitude from the field data are 228%, 59%, and 83% for States 1, 2, and 3, respectively. These misfits were calculated from the difference between the scattered field amplitude obtained from the simulations and field data at individual receivers as plotted in Figure 7-43, according to misfit definition:

$$\text{Misfit}(|E_f^{sct}|, |E_s^{sct}|) = \sqrt{\sum_{i=1}^{N}\left[\left(|E_{f,i}^{sct}| - |E_{s,i}^{sct}|\right)^2\right]} \Big/ \sqrt{\sum_{i=1}^{N}\left[|E_{s,i}^{sct}|^2\right]}, \quad (7\text{-}6)$$

where $|E_{f,i}^{sct}|$ and $|E_{s,i}^{sct}|$ are the scattered field amplitude from the field data and simulation at receiver *i*, and *N* denotes the number of receivers, which is 81 in this work.

The maximum misfit at State 1 shows that the EM model fails to simulate conductivity changes early and may be more suitable for the simulation of conductivity changes at later stages of injection and leakoff. Given that the scattered field values for early times are expected to be low, it is reasonable that a low value of the denominator in Equation (7-6) would result in a large misfit in State 1. However, as described in Subtask 6.5, the analysis of receivers' potential at State 1 also showed an unexpected rise in the electric field potential. Together, these results suggest that fracture conductivity changes alone cannot justify the observed large potential differences at the receivers at an early time. Instead, this large gap can likely be explained by the SP at early times of injection. These results are further substantiated by an analytical solution for the SP, as elaborated later on in this subsection.

Table 7-3: Three states of the dilated fracture on January 26, 2022, for the calculation of the scattered field. The misfit column refers to the difference in the scattered field amplitude obtained from the simulation and the field data. The misfit is obtained from averaging the actual difference between the simulation and field data for all receivers (Figure 7-44).

State	Time	From Simulation		From Field Data		Misfit (Average of all receivers)
		Scattered Field Amplitude Maximum (V/m)	20× Scattered Field Amplitude Maximum (V/m)	Scattered Field Amplitude Maximum (V/m)	20× Scattered Field Amplitude Maximum (V/m)	
S_1, 1.3 m, 40 S/m	T_1, 12:18	1.2×10^{-7}	2.4×10^{-6}	4.8×10^{-7}	9.6×10^{-6}	228%
S_2, 7.65 m, 10 S/m	T_2, 17:33	3.4×10^{-7}	6.8×10^{-6}	3.4×10^{-7}	6.8×10^{-6}	59%
S_3, 3.0 m, 40 S/m	T_3, 22:26	1.2×10^{-7}	2.4×10^{-6}	1.4×10^{-7}	2.8×10^{-6}	83%

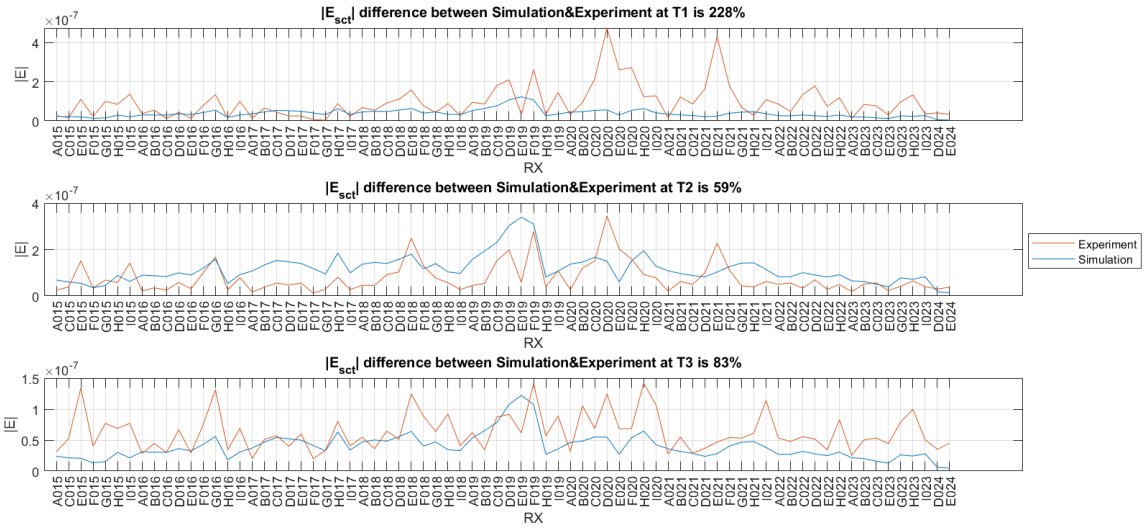

Figure 7-44: Comparison of the scattered field amplitude (|E(t)-E(0)|) from the simulations (blue line) and field data (orange line) at all receivers, at specific times: (upper) T_1 or 12:18; (middle) T_2 or 17:33; (lower) T_3 or 22:26.

KNN method as a minimization technique

Through the above EM modeling efforts, we showed that a single-layer circular fracture model would lead to the misfit of 59% for the scattered field close to shut-in on January 26, 2022. Here, we attempted to reduce this misfit by providing the model with more degrees of freedom. For this purpose, first we designed a three-layer circular fracture model and improved the misfit of the scattered electric field between the DGFD simulation and the experiment data. We used the modified efficient KNN method (Cui et al., 2020) as briefly introduced in the following. In these cases, we assumed that the simulated scattered electric field should agree with the measured scattered electric field at the DFPS regardless of the SP contribution. Then, we proceeded with comparing the EM field simulation results and an SP analytical solution. Subsequently, we considered the effect of SP on the misfit by subtracting the average SP across the survey receivers from the DFPS measurements and attempted to minimize this misfit using the KNN method. Afterwards, we investigated the effect of the dilated fracture shape and orientation on the misfit by conducting further numerical simulations and comparing the resulting misfits. As elaborated about the larger EM signal compared to the SP at time T_2 (0.5 hr before shut-in) in Table 7-3, we conducted this EM simulation study based on the survey data collected at 17:32 on January 26, 2022.

KNN method is an optimization algorithm which can extract more features from the datasets than the conventional optimization methods through the advanced workflow and simulation techniques (Cui et al., 2020). The purpose of this method is to find the size and conductivity of the fracture leading to the minimum scattered electric field misfit. Figure 7-45 shows the flowchart of the modified efficient KNN method. The implementation of the method is demonstrated in the following steps:

(1) Construct a dataset to start. This is the most important step and does not need too many samples as usually needed in the conventional ML methods. Empirically, only 10 to 100 samples are required in this step for most situations. Additionally, the samples should be chosen uniformly in the range of the variables.

(2) Randomly divide the original dataset into two parts: 90% for training and 10% for testing. The preprocessing Python StandardScaler tool is used to standardize the dataset, and the Python KNeighborsRegressor tool is employed to train and test the KNN model. In this step, we obtain model Ω that projects the input parameter vector $\boldsymbol{x}$ into an output scalar function $f(\boldsymbol{x})$ to be used in the subsequent steps.

(3) Generate a matrix for input vector x comprising all target parameters. The matrix should represent adequate divisions of the input variables (e.g., 1% division of the variable interval). The matrix should not offer point groups with the same K-nearest neighbors to avoid an ambiguous output. The variable intervals should also be set at the beginning. If the loop of the algorithm stops too fast to obtain a satisfactory result, a matrix size increase is suggested.

(4) Input the matrix from Step 3 to model Ω from Step 2 and use the KNN regression to predict $\hat{f}(\boldsymbol{x})$ from each set of $\boldsymbol{x}$ input variables in the matrix. Obtain the maximum or minimum of $\hat{f}(\boldsymbol{x})$ among the predictions based on the requirement for the extreme value. Record the corresponding value of vector $\boldsymbol{x}$ and then export its value to the solver for its exact solution (either analytically or numerically through solvers such as DGFD). Record the vector $\boldsymbol{x}$ and the exact solution into the initial dataset to update it.

(5) If the exact solution is equal to the last record within the allowed error in the n^{th} iteration, as $|f(\boldsymbol{x}_n) - f(\boldsymbol{x}_{n-1})| < |\varepsilon f(\boldsymbol{x}_n)|$, stop the loop, because the algorithm cannot further improve the outcome. If the exact solution is not equal to the last record or if it is the first iteration, repeat Steps 1 to 4. In case of an infinite loop, we set a counter to stop the loop after 500 iterations.

It is noteworthy that the most time-consuming step in this algorithm is Step 4 because of the expensive numerical simulation process. In other words, the efficiency of the optimization algorithm usually depends on the time needed to run the numerical simulations. This is also the reason to reduce the number of samples in this work.

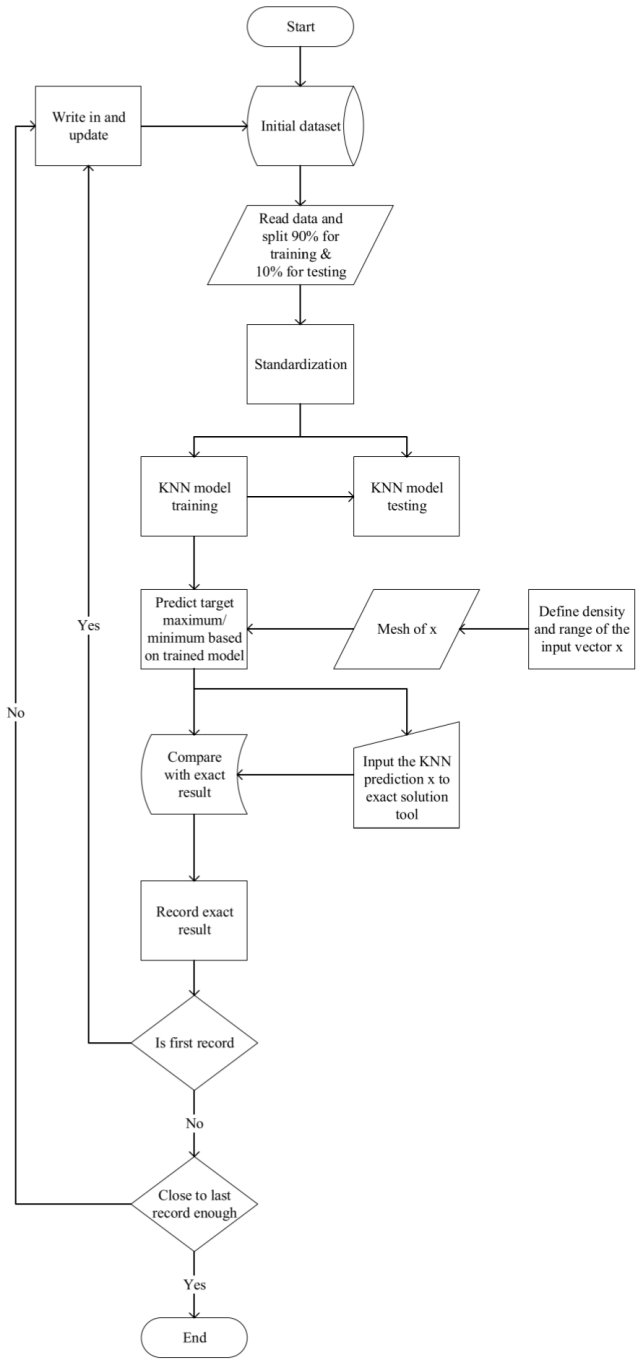

Figure 7-45: Flowchart of the modified efficient KNN method (courtesy of Cui et al., 2020).

Application of KNN method on misfit minimization of three-layer circular fracture case without streaming potential

To simulate the fracture size and conductivity at 17:32 on January 26, 2022 (T_2 in Table 7-3), we designed a fracture model which has three circular layers centered at the injection well. The inner to outer layer radius and conductivity are indexed with subscripts 1 to 3 as r_1, r_2 and r_3 in meter and σ_1, σ_2 and σ_3 in S/m (Figure 7-46).

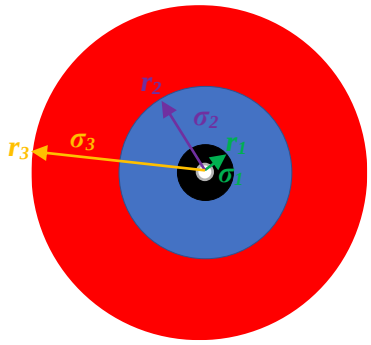

Figure 7-46: Schematics of a three-layer circular fracture case. r_1, r_2 and r_3, and σ_1, σ_2 and σ_3 refer to the radius and conductivity of circular layers at the fracture depth, centered at the injection well (the most internal gray circle). These radii and conductivities vary at different simulation cases.

The range of each parameter is as follows: r_1, 5-10 m; r_2, 10-20 m; r_3, 20-30 m; σ_1, 0.02-10 S/m; σ_2, 20-30 S/m; and σ_3, 30-60 S/m. We used the inhomogeneous surface layer DGFD model and settings presented in Figure 7-42 and Table 7-2 for the 2022 experiment data. We considered 60 S/m for the background conductivity of the EAP-filled fracture and randomly chose 90 different permutations of the parameters in the above ranges and built the initial dataset for the simulated scattered electric field. The measured scattered electric field is the field difference between the initial time T_0 at 10:00 and time T_2 at 17:32 on January 26. Therefore, the Ω: $\boldsymbol{x} \rightarrow f(\boldsymbol{x})$ in KNN method can be defined by $\boldsymbol{x}$ as the fracture parameter vector and $f(\boldsymbol{x})$ as the misfit of the scattered electric field obtained from the simulation compared to that from the recorded data:

$$\boldsymbol{x} = [r_1, r_2, r_3, \sigma_1, \sigma_2, \sigma_3], \tag{7-7}$$

$$f(\boldsymbol{x}) = \frac{\left|E_{Simu}^{sct} - E_{Exp}^{sct}\right|}{\left|E_{Simu}^{sct}\right|}. \tag{7-8}$$

Then, we used the modified KNN method to minimize the misfit. After nine iterations, the misfit was reduced from starting 64.8% to a minimum misfit of 55.1%, and the corresponding fracture parameter vector is [7.08, 19.58, 28.95, 0.02, 20, 49.09]. Notably, the initial misfit of 64.8% is larger than the smallest misfit of 59% in Table 7-3. This discrepancy is due to random selection of a combination of six fracture parameters at the first iteration here, whereas we had chosen a single combination of radius and conductivity for a single-layer fracture case in Table 7-3. The iteration process is shown in Figure 7-47 by plotting the misfit versus iteration number.

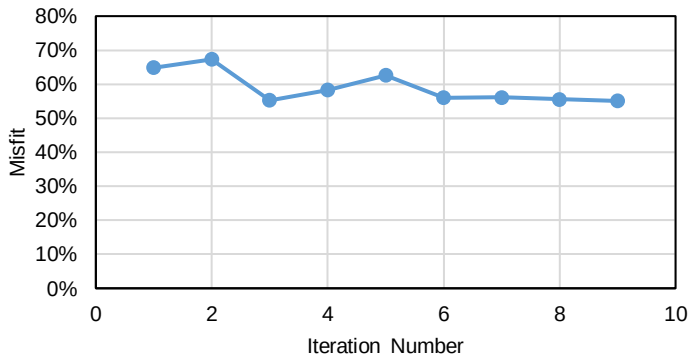

Figure 7-47: Modified KNN method minimization process. The misfit reduced from 64.8% to 55.1%.

Table 7-4 shows some example cases of the three-layer circular fracture design. The least misfit is for Case 5.

Table 7-4: Example cases for three-layer circular fracture design. $\boldsymbol{x} = [r_1, r_2, r_3, \sigma_1, \sigma_2, \sigma_3]$ *in a three-layer circular fracture case.*

Case #	$\boldsymbol{x}$	$\boldsymbol{f(x)}$
1	[5,16.32,25.26,0.02,20, 50]	64.8%
2	[7.92,16.25,28.75,0.02,20, 53.33]	62.6%
3	[7.5,20,30,10,10,50]	56.2%
4	[5.26,20, 30, 0.36, 20, 46.67]	55.3%
5	[7.08, 19.58, 28.95, 0.02, 20, 49.09]	55.1%

Figure 7-48 compares the scattered field amplitude obtained from the simulation and experiment data at each receiver for the case with the smallest misfit that is determined by the modified efficient KNN method.

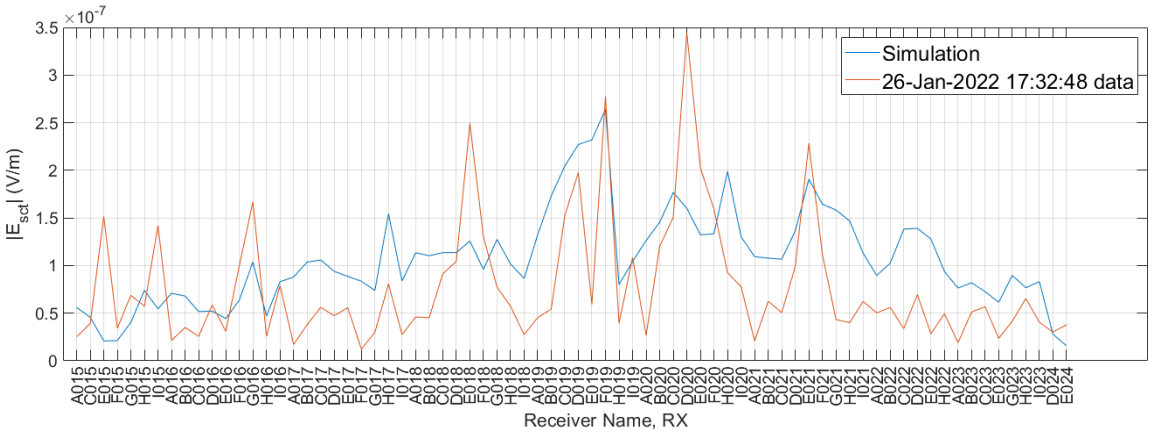

Figure 7-48: Comparison of the scattered electric field obtained from the simulation and experiment. The numerical simulation using the suggested input parameters r_1, r_2, r_3, σ_1, σ_2, *and* σ_3 *of 7.08 m, 19.58 m, 28.95 m, 0.02 S/m, 20 S/m, and 49.09 S/m by the modified efficient KNN method led to the minimum misfit of 55.1%.*

The calculated scattered field misfits so far are too large, and the corresponding cases may not be useful for developing a reliable inversion dataset. From another viewpoint, this implies that considering only the conventional EM response may not seem adequately rigorous to simulate the Devine injection experiments because of excluding the other possible phenomena for the electric field disturbance. One possible phenomenon could be the induced electric current by flow through porous media, namely the SP, supported by 1.) laboratory experiments as discussed in Subtask 3.1; and 2.) the possibility to fill the gap between the EM model and field data by an SP analytical solution. The latter support for the significant contribution of the SP to the EM field is discussed in the following. Then, we attempt to engage the KNN method to minimize the model misfit while considering the SP in the minimization process.

Streaming potential analytical solution versus EM field data and simulation

To evaluate whether the calculated scattered field and DGFD calculations follow the expected trend of conductivity reduction when fluid flows through EAPs, we performed a comparison of the modeled scattered electric field amplitude versus that from the field data at State 1 on January 26, 2022 (Table 7-3). The similar centrally rising trend of the scattered electric field obtained from the simulation (Figure 7-49b) and field data (Figure 7-49a) supports our laboratory observation that freshwater injection into electrically conductive media can increase contact resistance of the EAP pack and lead to a discernable electric field change. The scattered electric field amplitude from the field data and simulation (Figure 7-49a, b) are also placed together with Figure 7-49d for the estimated SP electric field using an analytical solution (Sheffer and Oldenburg, 2007), with corresponding values for State 1. To generate the SP solution, we assumed a steady-state flow and a uniform half-space model. The injection rate, Q, hydraulic conductivity, K, the cross-coupling coefficient, L, and the conductivity of the uniform half-space, σ, the injection source depth, h, and the source volume, v_s, are listed in Figure 7-49c. We assumed v_s as unit volume. The computed SP electric field amplitude rises to a maximum of 8.5×10^{-6} V/m. Despite the convention of reporting scattered field amplitude per unit electric current, we normalized the scattered field amplitudes at a current of 20 A, which is the current applied during the CSEM survey at the DFPS. This multiplication was essential to make the active-source scattered electric field comparable to a passive-source SP.

Figure 7-49a and Figure 7-49b show that the maximum scattered field amplitude from the field data at State 1 was 9.5×10^{-6} V/m, and was computed to be only 2.4×10^{-6} V/m from the EM simulation. However, the maximum SP electric field amplitude is 8.5×10^{-6} V/m. This comparison reveals a previously unnoticed but quite significant phenomenon: SP may dominate the observed field responses a State 1 of the January-26 injection.

(a) Scattered field obtained from field survey data × 20

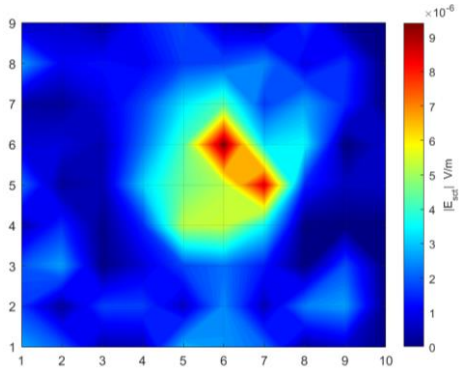

(b) Scattered field from DGFD model simulation × 20

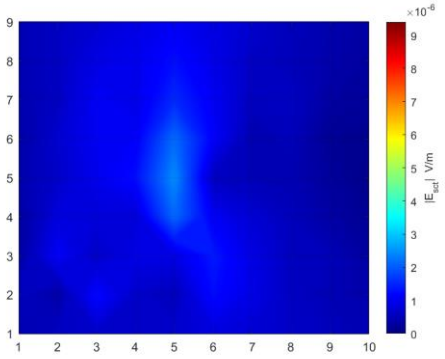

(c) Half space for SP solution

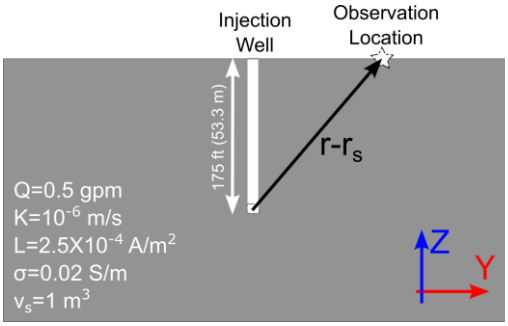

(d) SP analytical solution

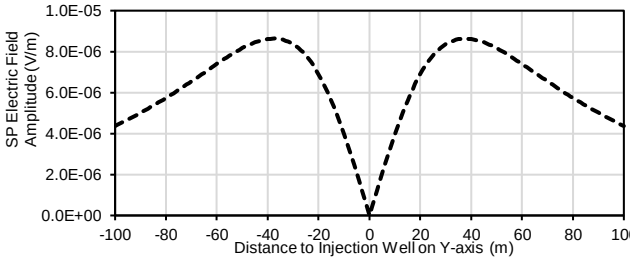

Figure 7-49: (a) Scattered field magnitude from the field data. (b) Scattered field magnitude from the simulation. (c) Cross section of a half-space, homogeneous model including a well to calculate SP due to injection into the media through a single-point perforation at 53.3 m (175 ft) of depth. (d) Total SP electric-field amplitude along y-axis. The scattered fields in (a) and (b) at 12:18 pm, 12 minutes after the start of injection on January 26, 2022. See Figure 7-42 for DGFD model assumptions (including surface conductivity inhomogeneity and layered media).

These results were encouraging to evaluate the SP contribution to the misfit, as we pursued in the following. Notably, from a geophysical perspective, the ultimate target of these model improvements should be to reduce the scattered field misfit between the simulation and true field data down to 5%. Provided that we add the SP term to the denominator of Equation (7-6) in future works, we expect that the misfit will be drastically reduced, especially when flow rate is suddenly changed, as in State 1.

Application of KNN method on misfit minimization of three-layer circular fracture case with streaming potential

To include the effect of the SP in our misfit calculations, we assumed that the DFPS measurements are the summation of the SP and the conventional EM field. Because we did not have funding to develop a numerical code for calculating the SP, we used an analytical solution suggested by Sheffer and Oldenburg (2007) for a point-source injection into a homogenous half-space medium, as expressed by:

$$\phi(\boldsymbol{r}) = \frac{LQ(\boldsymbol{r_s})v_s}{2\pi\sigma K|\boldsymbol{r} - \boldsymbol{r_s}|}, \tag{7-9}$$

where v_s represents the source volume, $\boldsymbol{r}$ and $\boldsymbol{r_s}$ denote the observation and source locations, $|\boldsymbol{r} - \boldsymbol{r_s}|$ denotes the distance between the source and observation locations, K is the hydraulic conductivity in m/s of the volume under study, L is the streaming-current cross-coupling conductivity coefficient in A/m^2, Q is an additional term used to represent any external point sources of fluid flow imposed on the volume in m^3/s, and σ is the electrical conductivity in S/m.

The differentiation of SP with respect to *x* or *y* led to the electric field induced by the SP along the *x*- or *y*-axis for the Devine case at 17:32 on January 26 (T_2 in Table 7-3), as shown in Figure 7-49d. The parameters that we used in this case are as follows: $Q = 1.89 \times 10^{-4}\ m^3/s$, $K = 7.50 \times 10^{-5} m/s$, $L = 5 \times 10^{-7} A/m^2$, $\sigma = 0.6\ S/m$, and $v_s = 1$.

The SP electric field at each receiver is shown in Figure 7-50 based on the receiver location as input to the analytical solution.

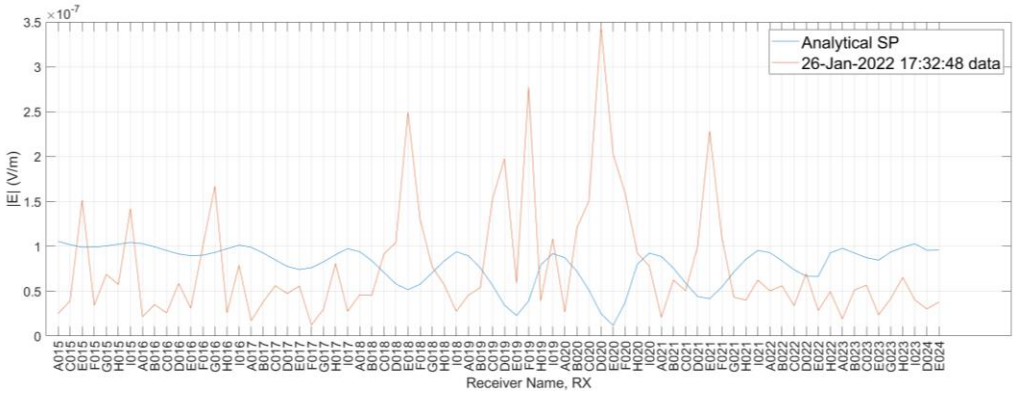

Figure 7-50: Comparison of the analytical SP with the measured electric field amplitude.

As Figure 7-50 shows, the scattered electric field from the data and SP are largely different, especially at four receiver intervals of C018-F018, C019-F019, C020-F020, and C021-F021. To explain these large differences, one way is to develop a reliable coupled SP-EM calculator and compute the SP contribution accurately; however, this does not fit into the current project objectives and budget. Therefore, we chose to subtract the average of the SP electric field across various receivers from the scattered field measurements. This resulted in a smaller misfit value of 47.6% compared to a value of 55.1% in the cases without considering the SP. This suggests another corroborating evidence that the SP may significantly contribute into our field measurements. This analysis is further detailed below.

The average analytical SP electric field in all receivers along the *x*- and y-directions (Figure 7-51) are 5.31×10^{-8} and $4.86 \times 10^{-8}\ V/m$, respectively. We subtracted these SP electric field values from the measured scattered electric field in the *x*- and *y*-directions to obtain the difference. Afterwards, we recalculated the misfit of the new difference from the simulated scattered electric field as we had included in the previous electric field dataset to build a new KNN mapping model.

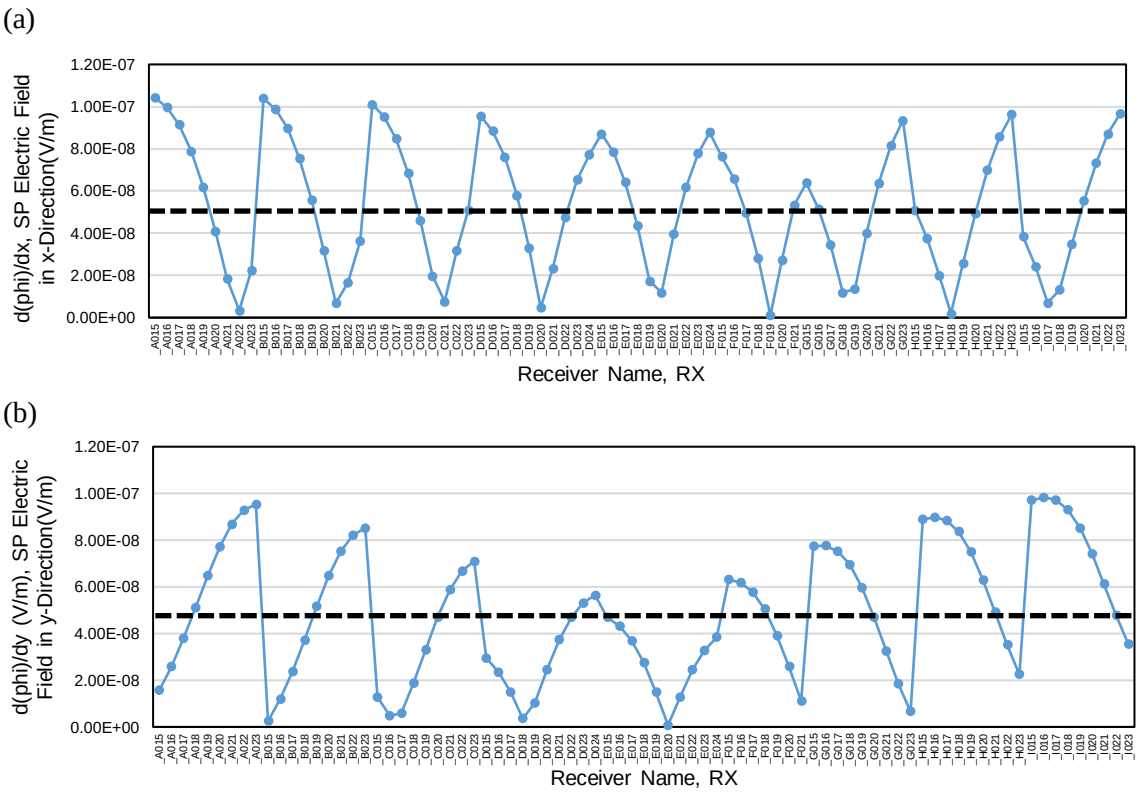

Figure 7-51: The SP electric field in (a) x-direction and (b) y-direction, at each receiver, derived from the analytical SP solution. The average electric fields of 5.31×10^{-8} *and* $4.86 \times 10^{-8}\ V/m$ *in x- and y-directions are shown by the black dash lines.*

The updated misfit formulation is according to Equation (7-10):

$$f(x) = \frac{\left|E_{Simu}^{sct} + E_{SP}^{AVG} - E_{Exp}^{sct}\right|}{\left|E_{Simu}^{sct}\right|}. \tag{7-10}$$

Then, we repeated the modified efficient KNN method steps and minimized the misfit again. After 18 modified efficient KNN iterations, the minimal misfit is 47.6%, and the corresponding fracture parameter vector is [10 m, 20 m, 30 m, 0.02 S/m, 20 S/m, 50 S/m]. The minimization results are shown in Figure 7-52.

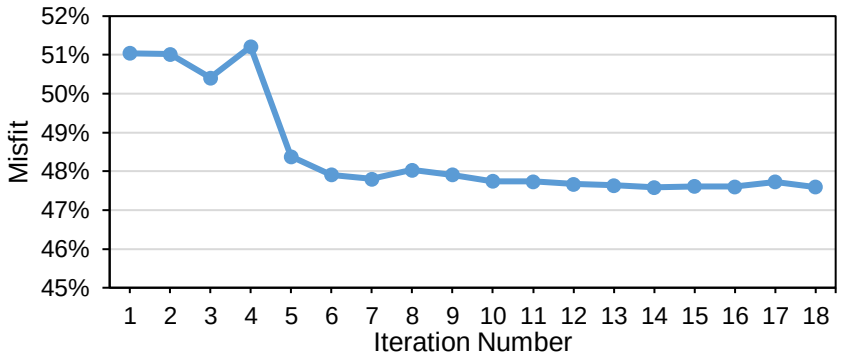

Figure 7-52: Modified KNN method minimization process. The misfit reduces from 51.0% to 47.6%.

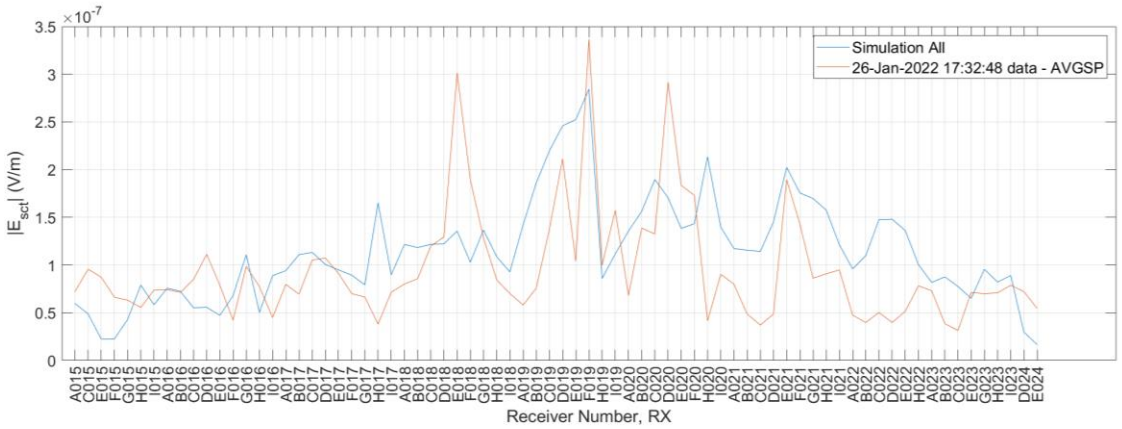

Figure 7-53: Comparison between the simulation and experiment scattered electric field for the case with the minimum misfit of 47.6% obtained from the modified efficient KNN method. This case corresponds to the fracture parameters r_1, r_2, r_3, σ_1, σ_2, and σ_3 of 10 m, 20 m, 30 m, 0.02 S/m, 20 S/m, and 50 S/m.

Figure 7-53 compares the scattered electric field amplitude in each receiver location from the data and a simulation case with the smallest misfit determined from the modified efficient KNN method. The minimum misfit decreased from 55.1% in Figure 7-47 to 47.6% in Figure 7-53, implying that the SP can significantly influence the misfit.

Table 7-5 shows examples of three-layer circular fracture cases and corresponding misfits ***f(x)***, after subtraction of the average SP electric field from the scattered field measurements. The minimum-misfit is for Case 5.

*Table 7-5: Example three-layer circular fracture cases, defined by parameter vectors **x**, and corresponding misfits **f(x)**, after subtraction of the average SP electric field from the scattered field measurements. **x** is defined as $[r_1, r_2, r_3, \sigma_1, \sigma_2, \sigma_3]$ in a three-layer circular fracture case.*

Case #	***x***	***f*(*x*)**
1	$[9.58, 16.67, 28.95, 0.44, 20, 49.09]$	51.0%
2	$[9.6,\ 18.5,\ 29.5,\ 0.02,\ 20, 50]$	48.4%
3	$[7.5,\ 20,\ 30,\ 10,\ 10,\ 50]$	48.0%
4	$[9.6,\ 19,\ 28.125, 0.02, 20, 48]$	47.9%
5	$[10,\ 20,\ 30,\ 0.02,\ 20, 50]$	47.6%

The misfit of 47.6% is still too large, and the corresponding case may not represent a case with adequate accuracy to be added to an inversion dataset. Further, the fracture-size parameters r_1, r_2, and r_3 are not realistic because they violate the mass conservation. Therefore, we need to improve our fracture design and the SP calculation to reduce the misfit further.

Misfit reduction considering rotated elliptical three-layer fracture cases with streaming potential

To improve the fracture shape in our simulation cases, we referred to ESG scattered electric field distribution, as shown in Figure 7-54a. This figure infers an elliptical fracture disturbance by the injected fluid or dilation with a rotated axis azimuth of N45°E. Thus, we used ellipses for layers 2 and 3. Besides, we rotated these ellipses for 45° clockwise from the north and used the EAP-filled

fracture contour relative to our previous surveys. This rotated elliptical fracture design with the fixed EAP-filled anomaly are shown in Figure 7-54b. The fracture parameter vector, in this case is

$$x = [r_1,\ a_2,\ a_3, \sigma_1,\ \sigma_2,\ \sigma_3],$$

where r_1 denotes the internal circular zone, and a_2 and a_3 are the major axis of the ellipse zones, shown respectively by the yellow, red, and blue regions in Figure 7-54b. σ_1, σ_2, and σ_3 are the corresponding fracture conductivities in these zones. The radius and semi-major axes are reported in meter and conductivity in S/m. We considered a fixed eccentricity of $e = \sqrt{3}/2$ (equivalent with the major-to-minor axis ratio of 2). We assumed the background conductivity of 0.1 and 60 S/m for the nonfractured zone and EAP-filled fracture at 175-ft depth, respectively (outer red region and gray region in Figure 7-54b. To minimize misfit, we conducted various simulation cases for different radius and semi-major axes and corresponding conductivities. We calculated the misfit after subtracting the average SP electric field from the measured scattered field.

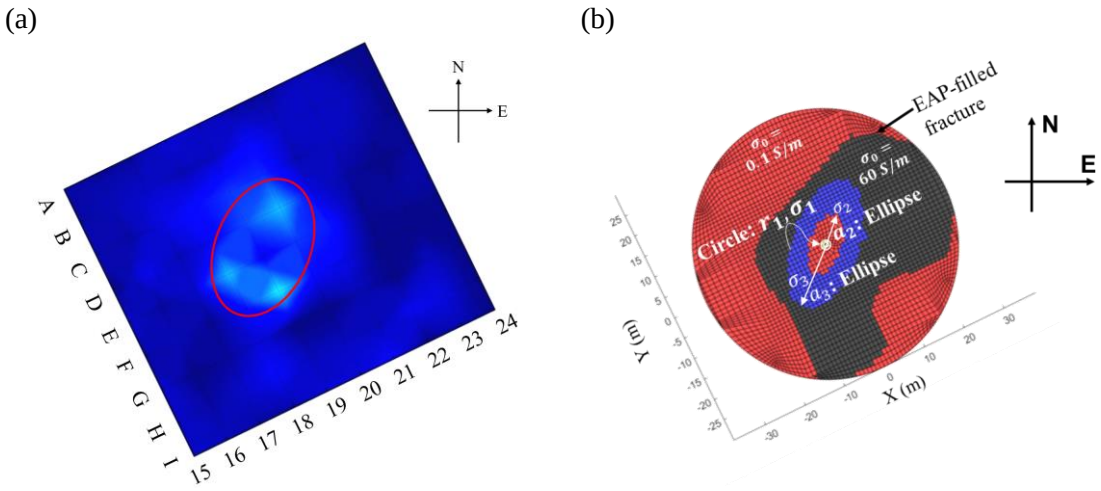

Figure 7-54: (a) ESG scattered electric field distribution. (b) Rotated elliptical fracture design (central red and blue regions) within the fixed EAP-filled anomaly (gray region) obtained from the MPT EM survey during hydraulic fracturing in 2017. The coordinate system origin is at the injection well. Figure (b) is intentionally shown in a smaller size than Figure (a) because (b) represents a suggested fracture change at 175-ft depth that would likely induce the electric field in an extended area on the ground surface as shown in (a).

The smallest misfit is 47.8%, corresponding to the fracture parameter vector of *x*=[1 m, 5 m, 7 m, 8 S/m, 10 S/m, 10 S/m]. The comparison of the scattered electric field amplitude at each receiver from this simulation case and the measurements is shown in Figure 7-55.

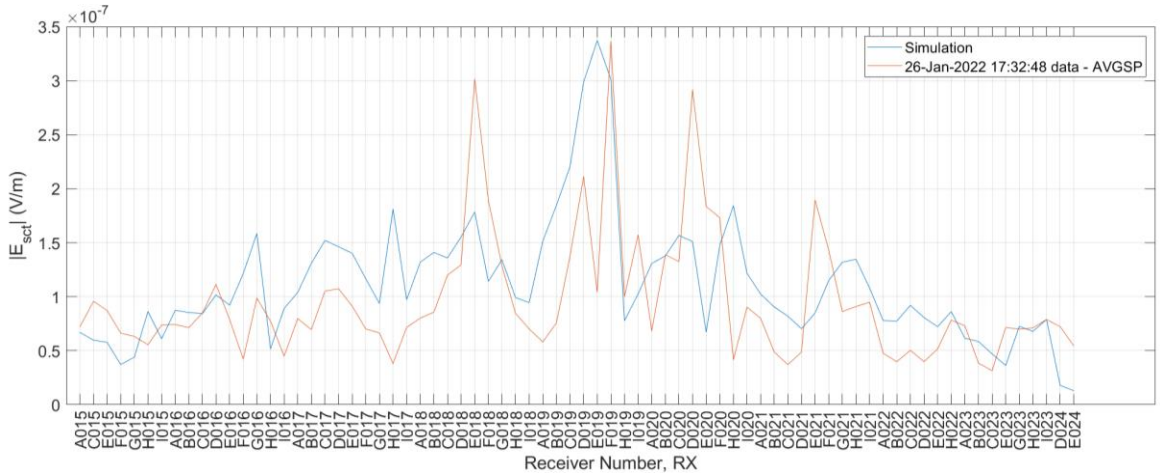

Figure 7-55: Comparison between the simulation and experiment scattered electric field, leading to the minimal misfit of 47.8%. The corresponding fracture parameter vector is [1, 5, 7, 8, 10, 10].

Compared to the previous three-layer *circular* case with the SP, this new design results in an almost similar misfit. However, the fracture size is supported by mass conservation, and we considered the pea-shape EAP-filled fracture anomaly in this new design. In contrast, these were not considered in the previous circular case.

Table 7-6 lists the misfit of the scattered electric field amplitude obtained from the corresponding simulation cases and the DFPS measurements subtracted by the average SP electric field. The minimum misfit belongs to Case 5.

Table 7-6: Example cases for the rotated elliptical fracture and the misfit of these case from the DFPS measurements subtracted by the average SP electric field.

Case #	***x***	***f*(*x*)**
1	[5,13, 17, 0.02, 20,50]	51.5%
2	[1, 7, 15, 0.02, 20,50]	49.5%
3	[1, 5, 10, 10, 20, 30]	47.9%
4	[1, 5, 10,10,10,15]	47.9%
5	[1, 5, 7, 8, 10,10]	47.8%

In Table 7-3, we showed that the conventional EM simulation led to a 59% misfit in comparison with the scattered field measurements without SP subtraction. In the above, we showed that this misfit could reduce to 47.8% with average SP subtraction, considering elliptical fracture geometries in the DGFD simulations. The 12% misfit reduction likely infers the significance of including the SP as a favorable additional degree of freedom in matching the simulations with the data. Nevertheless, 47.8% misfit is still too large for the corresponding case to be added to the inverse-model training dataset. Part of this large misfit can result from the shortcomings of the adopted analytical solution to simulate the following: 1.) formation heterogeneity, 2.) dynamic fracture dilation, and 3.) the central metal casing. Considering that the SP analytical solution is developed for a point injection into a homogeneous half-space, these three effects cannot be included in an analytical solution due to their complexities related to material characteristics in 3D and involved physics. Hence, a rigorous assessment of their effects requires numerical coupling of the SP and conventional EM in a simulator, as we plan to develop in our future studies (see Plans for the Next

Proposal). The development of this new simulation tool is targeted to reduce the misfit to 5% for the inclusion of the corresponding cases to the inverse-model training dataset.

Therefore, in a continuation proposal, we plan to develop and perform accurate numerical modeling of the SP and EM responses by coupling 3D poroelastic, SP, and EM models. To the best of our knowledge, current EM community lacks a numerical forward model to simulate the SP and EM together, especially in the frequency domain. Developing this forward model would be critical not only for the evaluation of the causative mechanisms for the EM field observations but also for the formulation of an inverse model to achieve an accurate visualization of conductivity response during subsurface fluid injection studies. Given the extensive infrastructure, well-characterized EAP-filled fracture, and various datasets available to our team, our unique test bed at the DFPS is an ideal location to validate the next set of codes and use them to demonstrate the robustness of a coupled EM-and-SP numerical tool for the above applications.

7.2 VSP/Seismic Imaging and Migration

Because the seismic survey numerical studies showed low SNRs for the detection of the fracture dilation during injections, we did not proceed with the seismic surveys. See subtask 5.3 for details.

7.3 History Matching of Fluid Flow Models

To prepare for the field tests, we built hydrogeological models in CMG software program (Computer Modelling Group Ltd., 2020) (Subtask 5.1). These models are essential because of their capabilities in predicting the initial injection volumes, species transport, and saline water transport. In the current subtask, we improved this model by adjusting the fracture and formation permeability to match the bottomhole pressure with the field data that was collected during the injection experiments on September 23 and 25, 2020. Because of in-situ stresses, the hydraulic fracture conductivity can change over the fracture area and through time. These changes are hard to predict with hydrological models. To overcome this limitation, we also developed a fully-coupled poroelastic model in Abaqus (Dassault Systèmes, 2017) (Subtask 5.1). This model predicts the fracture aperture and formation pressure at the DFPS. In the current subtask, we proceeded with history matching of this poroelastic model by adjusting a wider range of input parameters than those used to match the hydrogeological models. This subtask also discusses the improvement of the history matching of this poroelastic model by 1.) 2022 injection data; 2.) considering the preexisting proppant pack conductivity by including a high-permeability thin layer adjacent to the hydraulic fracture; and 3.) new estimates of the overburden stress based on post-shut-in pressure transient analyses. Further, as a substitute to a seismic survey, we performed tiltmeter mapping during the 2022 injection tests, and the results were useful for defining EM simulation cases (Subtask 6.5).

The hydrogeological models can benefit from the evolution of hydraulic fracture geometry through time obtained from the poroelastic model. This poroelastic model can also be useful for 1.) the seismic inversion studies such as in our surface seismic sensitivity studies; and 2.) determining 3D pore-pressure spatiotemporal gradients to be imported to a prospective SP analysis, based on SP theory as elaborated in Subtask 3.1. The details of these modeling efforts are presented in the following.

History Matching of Hydrogeological Models Using 2020 Injection Data

The main purpose of this modeling effort was to history match our preliminary models (Subtask 5.1) with the field injection pressure and rates. This modeling effort compares the injection

simulations scenarios with the injection history, and improves the formation properties assumed in our model, so that we were able to plan our 2022 injection campaign more precisely.

During the fracture reopening process, the fracture permeability changes substantially. As shown in Figure 7-56, if we assume three stages for the fracture reopening process, Stages 1 and 3 resemble a closed fracture filled with proppants, while Stage 2 represents a reopening fracture process with the dramatic changes of the fracture permeability through time.

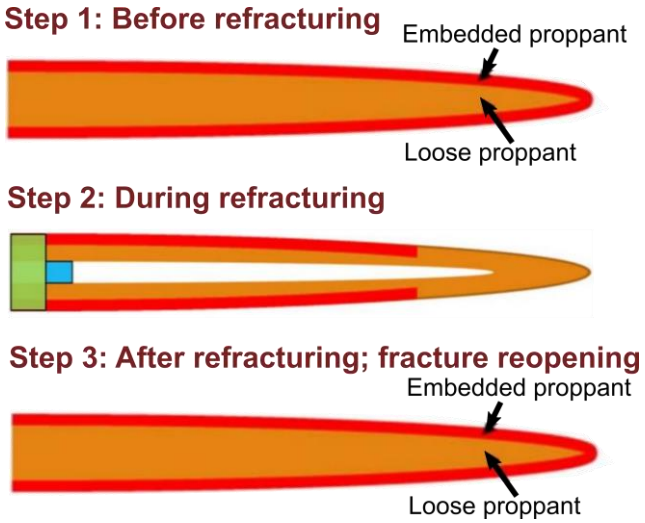

Figure 7-56: Three stages during one cycle of refracturing process.

The permeability of a propped hydraulic fracture is much higher than the permeability of the host rock, but still much lower than an open, proppant-free fracture conduit. We estimated the propped fracture permeability after Barree et al. (2019):

$$k = \frac{d_m^2}{180}\frac{\varphi^3}{(1-\varphi)^2}, \tag{7-11}$$

where d_m is the proppant diameter, and φ denotes the proppant pack porosity. For the US mesh 140, d_m is about 105 microns (0.105 mm) and φ is in the range of 0.26 to 0.47 for a proppant pack. The expected value of φ for a proppant pack with disorganized particles is 0.36. With these parameters, the calculated permeability is between 2 and 23 Darcy. During the history matching process, the proppant pack permeability, matrix permeability, and the open fracture permeability were varied to match the field data. We obtained the propped fracture boundary in plan-view from previous EM studies (Ahmadian et al. 2018, 2019).

The history-matching simulations use the injection rate profile from the field data (Figure 5-1) and output the bottomhole pressure (BHP) variations through time. During this process, we adjusted the formation and fracture permeability to match the BHP from the simulations with the BHP from the field data. We used the injection data during September 25, 2020 to match the simulation results for the injection well and DMWs 1 and 2. Because there is more than one parameter to adjust, to obtain a history-matched BHP, the history matching was conducted using the following procedure: First, one parameter is fixed and the other parameter is varied to match the BHP in one well. Second, the other parameter is varied to match the BHP in the other wells. Hundreds of simulations were performed to match all field data. On the basis of core permeability measurements from prior

laboratory studies, we started by using a matrix permeability value of 10 mD (Gonzalez et al., 2016) and proceeded to change it slightly to match the new field results in Cycle 2.

We first used the Cycle 2 injection data (9/25/20 data in Figure 5-1) to match the simulation results for the injection well and DMWs 1 and 2. Then, to validate the matched parameters, the updated model was used to solve for the BHP data, which was obtained during Cycle 1 for these wells (9/23/20 data in Figure 5-1). Because there is more than one parameter to adjust, to obtain a history-matched BHP, the history matching was conducted with the following procedure: first, one parameter is fixed and the other parameter is varied to match the BHP in one well; and second, the other parameter is varied to match the BHP in the other wells. Hundreds of simulations were performed to match all field data. Based on core permeability measurements from prior laboratory studies, we started by using a matrix permeability value of 10 mD (Gonzalez et al., 2016) and proceeded to change it slightly to match the new field results in Cycle 2. To better match the field data, 1.) the closed-propped fracture permeability was varied between 7 and 9 Darcy, and the opened fracture permeability was varied between 20 and 80 Darcy spatiotemporally during the fracturing process.

The Cycle 2 history matching of the BHP in the injection well and DMWs 1 and 2 are shown in Figure 7-57 through Figure 7-59, respectively.

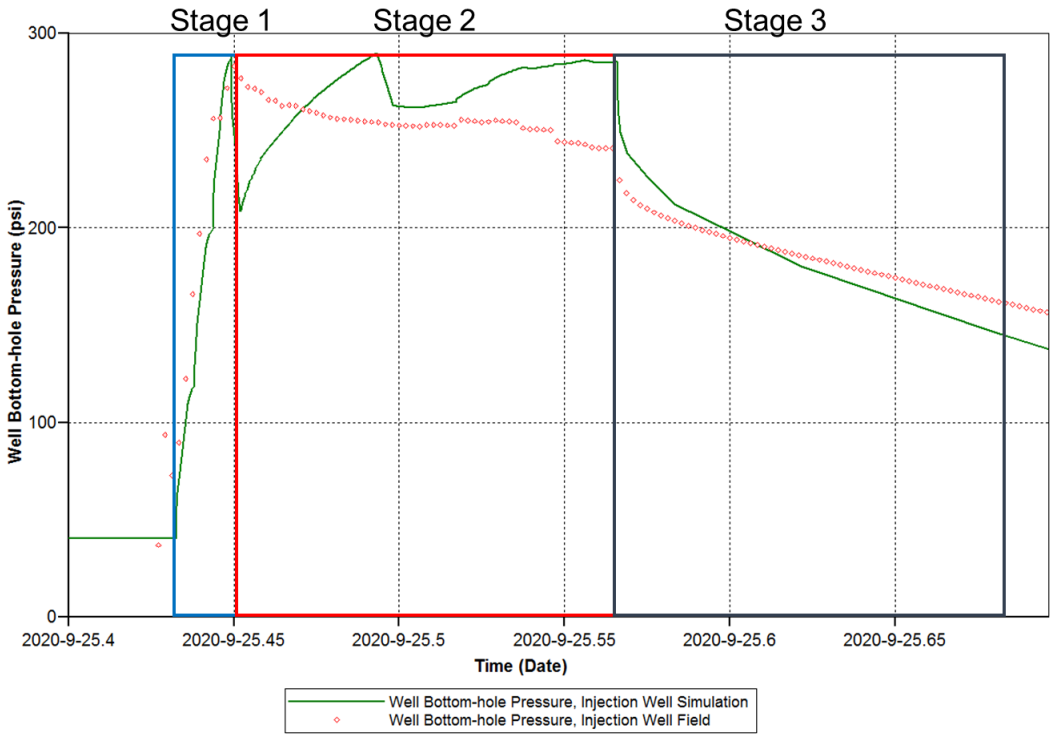

Figure 7-57: History matching of the BHP in the injection well during Cycle 2 in September 25, 2020. The main parameter to adjust for history matching is the fracture permeability. The propped fracture permeability of 7-9 Darcy was used for Stages 1 and 3, and the opened fracture permeability was used for Stage 2 when the area of the opening fracture changes linearly. This fracture permeability variation between stages was validated by comparison of the bottomhole pressure from the field data and simulation in DMWs 1 and 2 during both Cycles 1 and 2, as shown in Figure 7-58 through Figure 7-61.

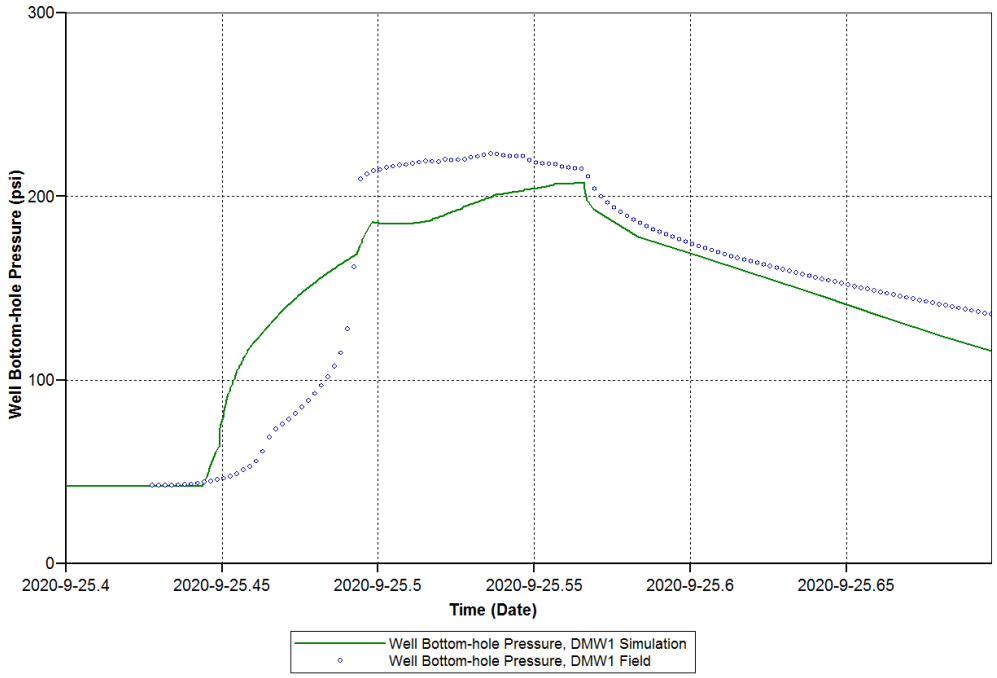

Figure 7-58: History matching of the BHP in DMW 1 during Cycle 2 in September 25, 2020.

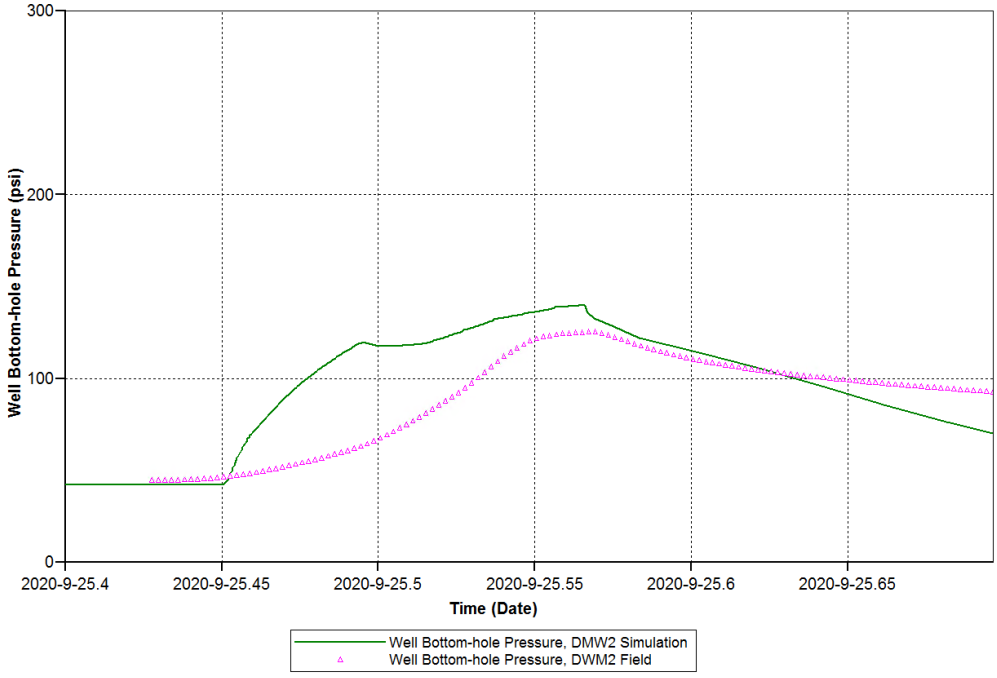

Figure 7-59: History matching of the BHP in DMW 2 during Cycle 2 in September 25, 2020.

Subsequently, the input data of the history-matched model were changed to those in Cycle 1 to validate the accuracy of theses parameter adjustments. The verification results are shown in Figure 7-60 through Figure 7-62. This result verified the updated model parameters are suitable for the formation conditions.

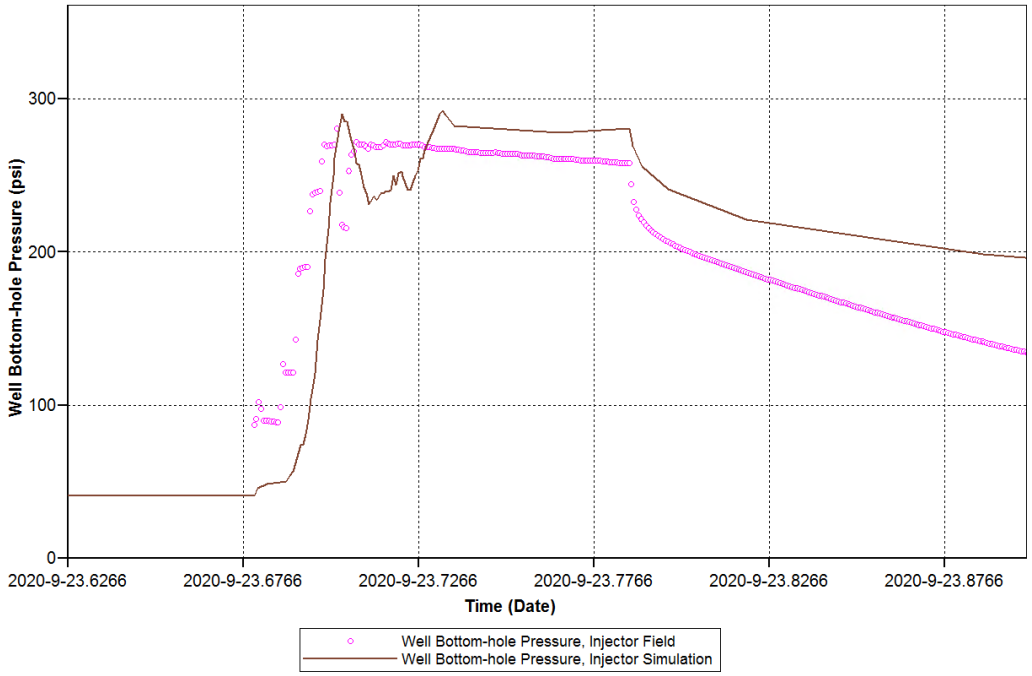

Figure 7-60: History matching of the BHP in the injection well during Cycle 1 in September 23, 2020.

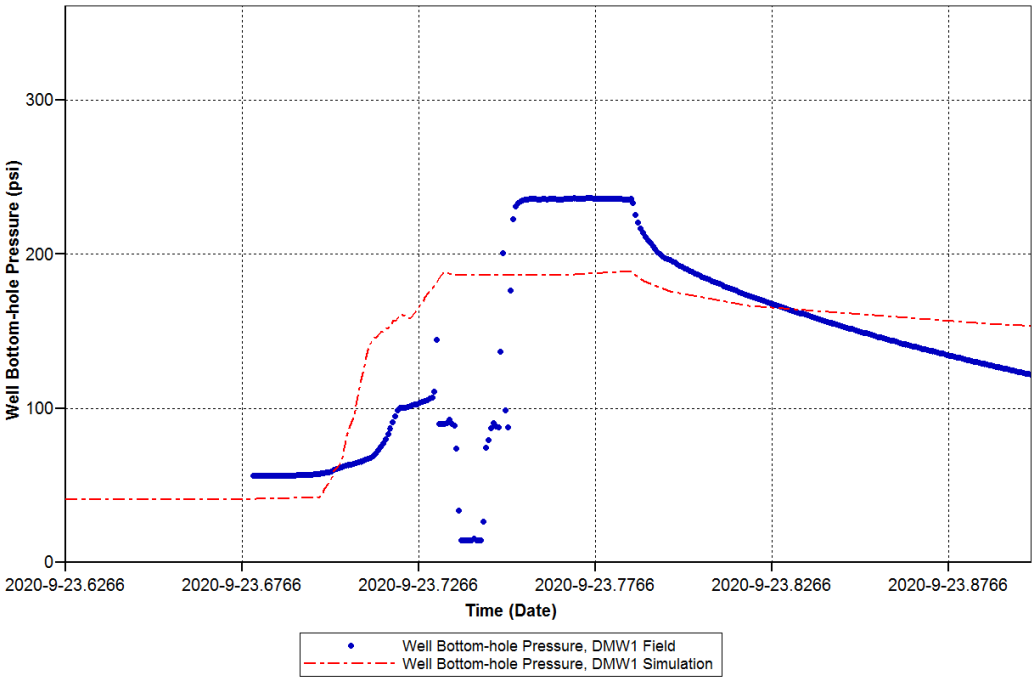

Figure 7-61: History matching of the BHP in DMW 1 during Cycle 1 in September 23, 2020.

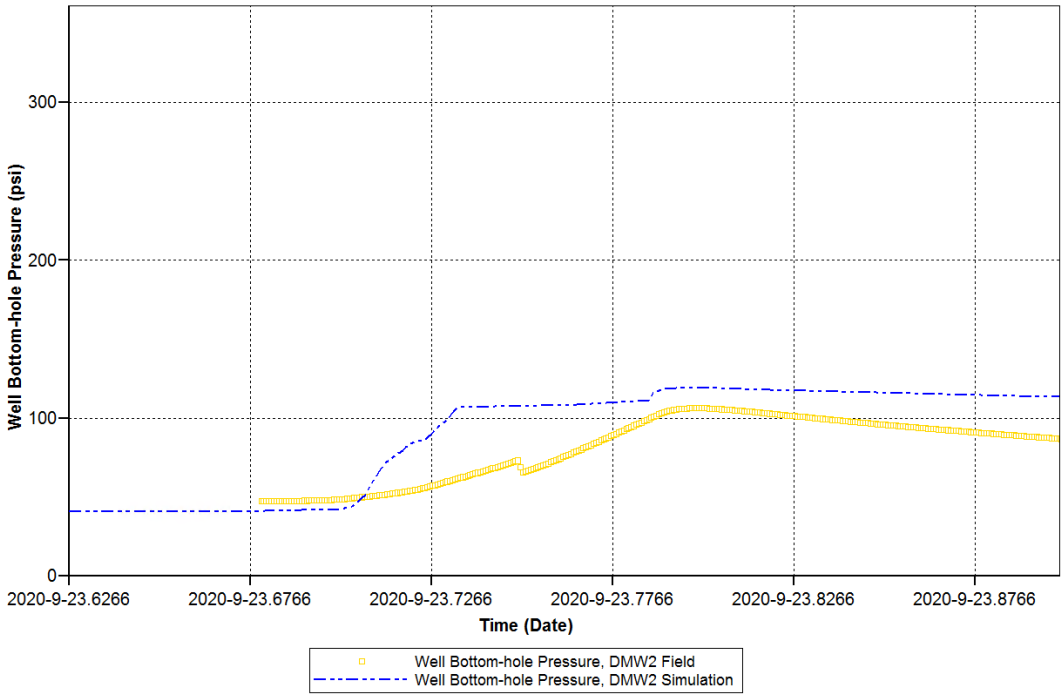

Figure 7-62: History matching of the BHP in DMW 2 during Cycle 1 in September 23, 2020.

Because of the discrepancy between the field and simulation BHP data during injection shut-in, we continued this history matching effort to improve our hydrogeological model. To better match the field data, the closed-propped fracture permeability was varied between 7 and 9 D, and the opened fracture permeability was varied between 20 and 80 D spatiotemporally during the fracturing process. This new effort led to a matching BHP from the simulations and field data during Cycle 2, as shown in Figure 7-63 for the injection well and DMWs 1 and 2.

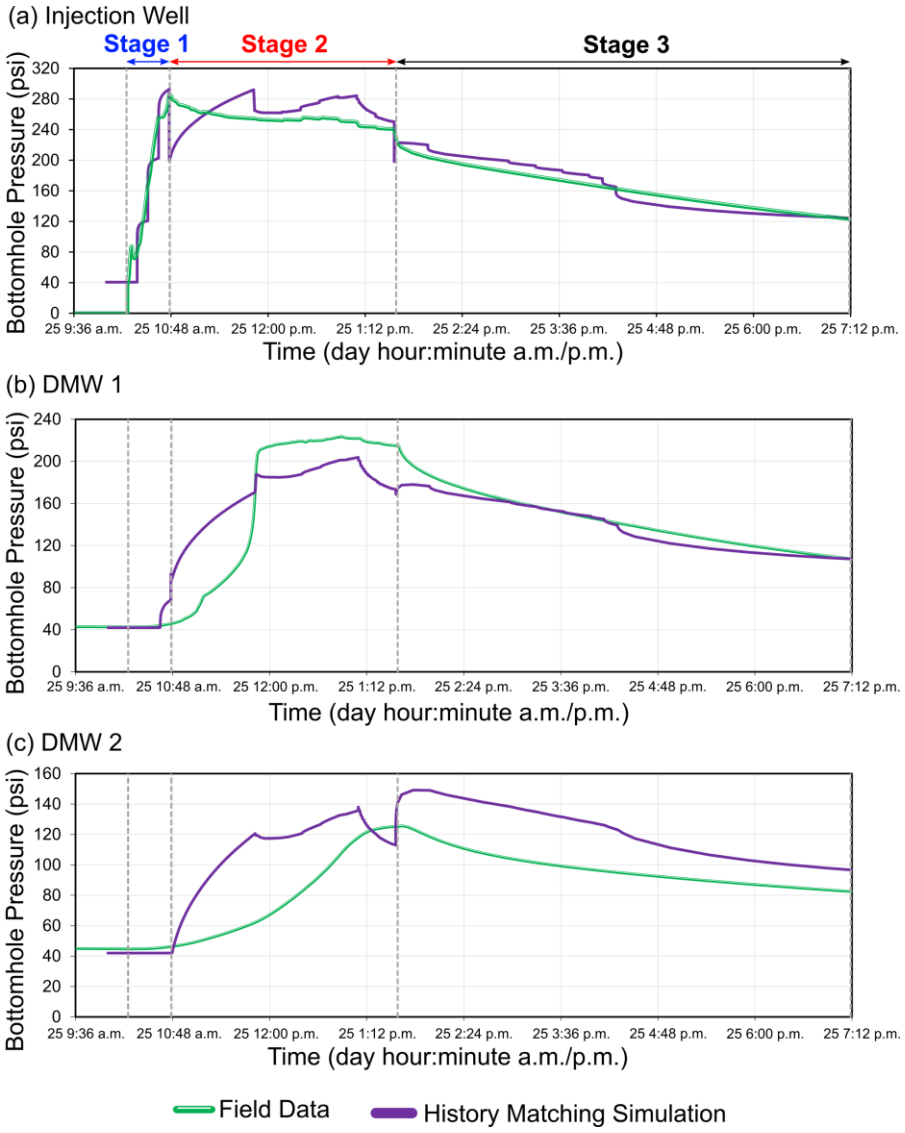

Figure 7-63: (a) Improved history matching of the BHP in the injection well during Cycle 2 on September 25, 2020. The main parameter to adjust for history matching is the fracture permeability. The propped-fracture permeability of 7 D was used for Stage 1, and the opened fracture permeability was used for Stage 2, when the area of the opening fracture changes in three steps. The propped-fracture permeability of less than 7 D was used for Stage 3 after fracture closure, with variations along the fracture. (b, c) Comparison of the BHP from the field data and simulation in DMWs 1 and 2 to validate the fracture-permeability variation between stages during Cycle 2.

History Matching of Poroelastic Models Using 2020 Injection Data

We also conducted history matching of the poroelastic model by adjusting a wider range of input parameters than those used to match the hydrogeological models. The hydrogeological models can now benefit from the evolution of hydraulic fracture geometry through time obtained from the poroelastic model. This poroelastic model was useful for the seismic inversion studies such as in our surface seismic sensitivity studies (Subtask 5.3).

We attempted a comprehensive study on the sensitivity of the bottomhole pressure to rock permeability, initially open hydraulic fracture area, Young's modulus, and Poisson's ratio. Then,

we obtained the optimal combination of these parameters to reduce the overall discrepancy of the bottomhole pressure from the field data and the geomechanical simulation. To reduce the computational expenses, we did not model the pressure drop within perforations; however, we calculated the pressure drop based on an equation proposed by McClain (1963):

$$\Delta P_{perf} = 0.2369 Q^2 \rho / C_d^2 N^2 D^4, \quad (7\text{-}12)$$

where Q denotes flow rate, ρ is density, C_d represents discharge coefficient, N is number of perforations, D is perforation hole diameter. C_d is assumed as 0.63 according to the perforation geometry in this project (Grose, 1985), one perforation hole is assumed, and the perforation diameter is 0.4 in. Although we assumed only one perforation hole with a relatively small hole diameter, the maximum pressure drop through the perforation in none of the simulation cases exceeded 6 psi, which is almost 4% of the minimum principal stress at 175-ft depth. In fact, this calculation showed that the perforation pressure drop could be neglected for this modeling study.

As a sample set of result out of 50 simulations, Figure 7-64 shows the comparison of the bottomhole pressure from the field data and three simulation cases, different only by the initially open area of the hydraulic fracture: (Case 46) 100 m^2; (Case 47) 28 m^2; and (Case 48) 400 m^2. The closest simulation result to the BHP data belongs to Case 46 with 100 m^2 initial fracture area. The other tuned input parameters to history match the BHP are as follows: porosity of 0.23; rock permeability of 150 μD; Young's modulus of 100,000 psi; Poisson's ratio of 0.1; Biot-Willis coefficient of 0.9; fracture initiation stress of 60 psi; fracture toughness of 930 psi.$\sqrt{in}$; water viscosity of 1 cp; leakoff coefficient of 0.2 m^3/kPa.s; S_{vert} gradient of 24.53 psi/ft; S_{hmin} and S_{Hmax} gradients of 32.2 and 39.9 kPa/m. The offered formation permeability value of 150 μD by these models is substantially lower than that by the hydrogeological models, but consistent with the sub-mD permeability measurements of the regional cores by Gonzalez et al. (2016). To obtain a history match during the extended shut-in period, we had to substantially lower the formation permeability. This model improvement is important for the interpretation of EM data during shut-in (e.g., on September 26 through 28). This study also offers two feedbacks to the hydrogeological model: 1.) to evaluate the possibility to history match with micro-scale formation permeability values; and 2.) to widen the history matching time interval to the extended shut-in period.

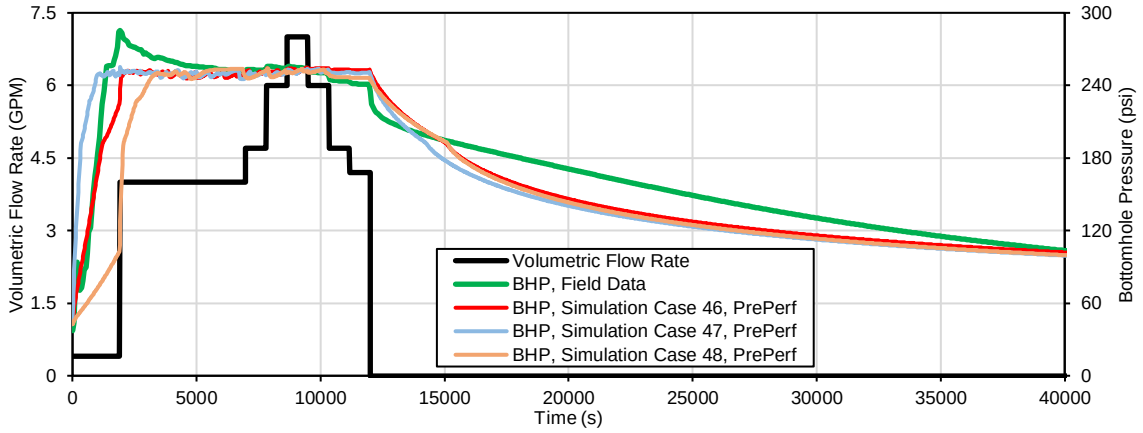

Figure 7-64: (left ordinate) Volumetric flow rate and (right ordinate) bottomhole pressure from field data and three poroelastic simulation cases. The time interval is equivalent with 10:15 a.m. until 1:35 p.m. on September 25, 2020. The simulation cases are different only by the area of the initially open hydraulic fracture: (Case 46) 100 m^2; (Case 47) 28 m^2; and (Case 48) 400 m^2. PrePerf in the legend refers to the bottomhole pressure within the wellbore, obtained by adding the calculated perforation pressure drop to the fracture mouth pressure (Haddad et al., 2021).

The injection pressure is highly sensitive to the rock permeability and Young's modulus. A low rock permeability of 0.15 mD and Young's modulus of 100,000 psi lead to the closest bottomhole pressure to the field data. The case at 100 m^2 initially open hydraulic fracture leads to the closest match to the field data for the bottomhole pressure at early times. The early-time pressure response, however, needs further numerical study with improved volumetric rate measurements because the totalizer measurements below 1 gpm were unreliable.

The quality of the data collected during field deployment in September 2020 allowed us to define benchmark cases for performing history matching of our hydrogeological and geomechanical models. Repeatability of injection experiments and fracture dilation were demonstrated through matching of ISIP during the first and second successful injection cycles. This reproducibility was also shown by the small observed difference between maximum injection pressures as a fracture characteristic during these cycles. With access to field and petrophysical and geomechanical laboratory data, we were able to tune hydromechanical reservoir parameters of the models to result in a history-matched BHP. Discrepancy between estimated permeability by hydrogeological and geomechanical models originated from 1.) their different methods of modeling fracture reopening; 2.) possible poroelastic rock behavior, which was neglected in the hydrogeological model; and 3.) difference in the time intervals in which history-matching analyses of these models were conducted.

The computational models that were developed are essential for designing future injections at the DFPS and for the interpretation of various CSEM surveys at this test site.

History Matching of Poroelastic Models Using 2022 Injection data

As shown in Subtask 6.5, the surface recorded electric field during the second injection campaign in 2022 follows the flow-rate and bottomhole pressure changes. These flow and pressure changes influence the proppant pack's electrical conductivity and likely induce a secondary electric field due to the SP. As elaborated in Subtask 3.1 and also by Ishido et al. (1983), this potential is governed by the spatial pore pressure gradients and temporal flow-rate changes.

To obtain the spatial pore pressure gradients, we improved our DFPS poroelastic model, including a fracture propagation model, to simulate the cyclic fracture reopening during the 2022 multiple injection tests. This model addresses the effect of flow-rate changes on the pore-pressure gradient by receiving the flow-rate profile and the preexisting proppant pack conductivity by including a high-permeability thin layer adjacent to the hydraulic fracture. We used the hydromechanical rock properties obtained in a rock mechanics laboratory to develop this model. However, we used post-shut-in pressure transient analyses for six injection cycles to determine the overburden stress gradient because of the lack of a density log to determine this parameter (Subtask 6.1). These pressure transient analyses were also conducted using the bottomhole pressure data collected in 2020 (Subtask 6.1; Haddad et al., 2021, 2023). Also, the multiple shut-in periods during the latest injection campaign in 2022 provided a unique dataset to validate the previous estimates of the overburden stress and properly calibrate hydrogeological properties at this test site. This modeling effort is useful to determine the 3D pore-pressure spatiotemporal gradients to be imported to a prospective SP analysis.

Poroelastic models for fracture reopening

To assess the multicyclic reopening of the propped fracture during the injection campaign on January 2022 at the DFPS, we developed 3D, finite-element, poroelastic models in Abaqus (Dassault Systèmes, 2017). In these models, pore pressure and stress are monolithically coupled,

leading to the solution for fluid flow in a fracture and porous media without any time lags or leads with respect to the solution for matrix and fracture mechanical deformations. Here, we pursue stress and pore pressure solutions in the porous matrix due to a perforation injection leading to the consequent preexisting fracture reopening upon satisfaction of fracture reopening initiation and propagation criteria. We formulated these criteria using the commonly applied macroscopic traction-separation response (i.e., cohesive-zone crack-tip constitutive model) in hydraulic fracturing simulations adopted after Dugdale (1960) and Barenblatt (1962). Numerous works have demonstrated the viability of this approach for the design and evaluation of multi-stage hydraulic fracturing or the evaluation of fracture interactions (Haddad and Sepehrnoori, 2015, 2016; Haddad et al., 2017).

A schematic diagram of this response is shown in Figure 7-65a. The fracture initiation and propagation models are quadratic nominal stress and Benzeggagh-Kenane (1996) models, respectively. The fracture initiation model defines the initial, linear elastic response of the medium that terminates at a peak fracture initiation stress of σ_i and fracture aperture of δ_i. At larger fracture apertures than δ_i, the fracture propagation model is engaged to define the extended progressive damage where the medium is macroscopically altered by the coalescence of the microscopic weak interfaces between the grains and intergranular cement. This gradual damage is described by a scalar damage factor, D, equal to zero at fracture initiation and unity at full failure where fracture aperture increases to δ_f. At larger fracture apertures than δ_f, the fracture dilation continues to increase at zero tensile strength. Figure 7-65b shows two traction-separation responses used either in the current poroelastic modeling or the hydraulic-fracturing numerical study by Haddad et al. (2023).

In the finite-element model, we defined a dedicated thin layer as a cohesive layer with a traction-separation response. The load-carrying capacity of this cohesive layer is controlled by the elastic-response stiffness, E_l, which is assumed to be 120 times Young's modulus of the host rock, based on previous numerical experiences. σ_i can be generally expressed as the tensile strength of the intact rock. Considering that injections occur into a preexisting, propped hydraulic fracture in the current case, we downscaled the fracture initiation stress to a fraction of the tensile strength of the intact rock. This thin cohesive layer is enhanced by pore-pressure degree of freedom not only on the corner nodes, but also the middle-edge nodes to model flow along the fracture (i.e., slot flow), and normal to the fracture wall (i.e., leakoff). Water injection into this cohesive layer is conducted using a concentrated volumetric flow boundary condition at a middle-edge node at the injection-well location. A few cohesive elements must be initially failed (D=1) to accept the injected fluid and avoid the likely numerical divergence at early times of injection.

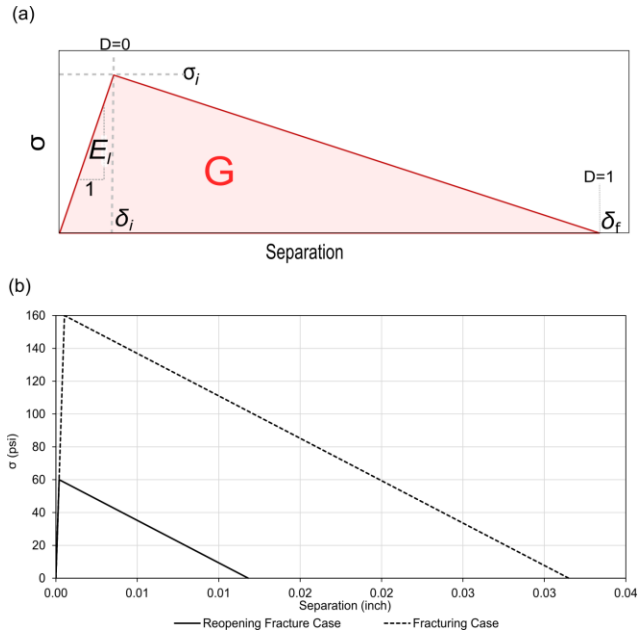

Figure 7-65: (a) Traction-separation response for fracture reopening. El=stiffness during elastic response; σ_i=fracture initiation stress; δ_i=separation at fracture initiation; δ_f=separation at full failure; G=critical energy release rate, equal to area under the traction-separation response; D=damage factor. (b) Two traction-separation responses with different σ_i: 160 psi in the initial fracturing case, based on data in Haddad et al. (2023); 60 psi in all cases in the current work.

The parameters in the traction-separation response can be related to the classic fracture mechanics parameters because the area under the traction-separation response is equal to the critical energy release rate, *G*, that can be calculated from the fracture toughness, *K*, according the Irwin's (1957) work as Equation (7-13):

$$G = K^2(1-\nu^2)/E, \tag{7-13}$$

where ν and E are the host rock Poisson's ratio and Young's modulus. Assuming a linear progressive-damage response, we can derive the ratio of δ_f/δ_i as Equation (7-14):

$$\delta_f/\delta_i = G \cdot E_l/\left(\frac{1}{2}\sigma_i^2\right). \tag{7-14}$$

δ_f/δ_i must be larger than 1 for the progressive-damage response to end at δ_f larger than δ_i, and to avoid the numerical convergence difficulties. To assure that δ_f/δ_i remains larger than 1, we assumed this ratio and back-calculated the critical energy release rate as Equation (7-15):

$$G = \frac{1}{2}\sigma_i^2\left(\delta_f/\delta_i\right)/E_l. \tag{7-15}$$

The 3D poroelastic model, including a horizontal cohesive layer at 175 ft of depth, is shown in Figure 7-66. Injection occurs in the center of the model at a single point, and the lateral boundaries are 656 ft away from this injection point to eliminate the effect of the model size on the solution. Because of the same reason, we extended the model 175 ft above the fracture depth (to the ground surface) and 175 ft below that. All lateral boundaries are under stress boundary conditions: S_{hmin} gradient on the boundaries normal to x-axis, and S_{Hmax} gradient on the boundaries normal to y-axis. The bottom boundary nodes are fixed for z-displacements, and a subset of these nodes on the xz or

yz symmetry planes are fixed for y- or x-displacements. This finite-element model has 85,731 nodes as the corner points of 76,800 continuum, hexahedral, pore-pressure elements (i.e., C3D8P) and 1,600 pore-pressure cohesive elements (COH3D8P). The maximum and minimum element sizes in x- and y-directions are 130 and 2 ft, and these numbers in z-directions are 50 and 0.07 ft, with the minimum sizes close to the injection point or the fracture. All lateral boundaries are under hydrostatic pore-pressure gradient, and the upper and lower boundaries are under constant pore-pressure boundary condition. To include the effect of the propped fracture conductivity on the solution, we defined a thin layer of poroelastic elements with a thickness of 1 cm above and below the horizontal cohesive layer and at a radius of 65 ft and permeability of k_p (blue region in Figure 7-66b). The propped fracture thickness and area were obtained from the fractured core and EM surveys (Ahmadian et al., 2019). For the model simplicity, we considered a circular area of the propped fracture instead of a pea-shaped propped fracture. We determined the radius of this circle by honoring the propped fracture area. Further, based on our previous modeling efforts of the initial fracturing stimulation in 2017 (Haddad et al., 2023), we defined an outer rim around the EAP-filled fracture for the unpropped zone of the hydraulic fracture at the radius of 169 ft and permeability of k_{up} (red region in Figure 7-66b). Including these high-permeability zones for the propped and unpropped fracture zones in the current model is an enhancement of our previously developed poroelastic model for the DFPS (Haddad et al., 2021, 2023).

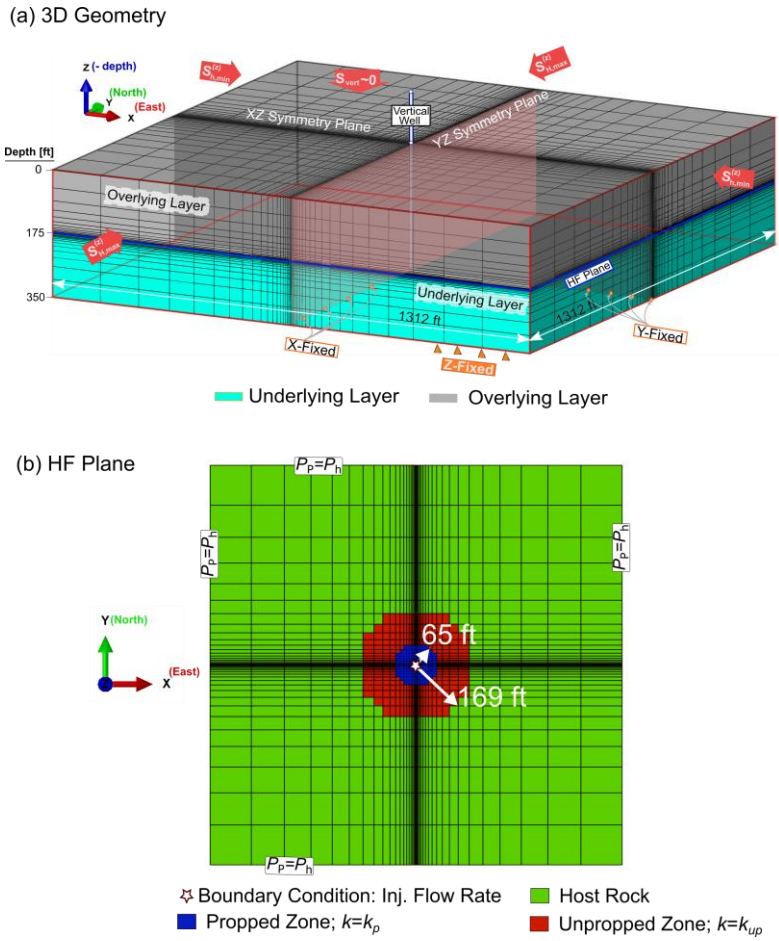

Figure 7-66: Schematics of the poroelastic model in Abaqus. (a) The 3D poroelastic model from the ground surface down to 350 ft of depth. (b) The thin layer of poroelastic elements, adjacent to the cohesive layer, to model: (blue region) the propped fracture zone, centered at the injection well, with an average radius of 65 ft; and (red region) the unpropped fracture zone, with the average radius of 169 ft.

The input parameters for the poroelastic models are listed in Table 7-7. Most of these parameters are adopted from previous geomechanical simulation studies of the DFPS (Haddad et al., 2021, 2023). In addition, we updated the in-situ stresses using the latest bottomhole pressure recordings. Considering that the water-table depth was at 132 ft and the poroelastic model is assumed fully saturated up to the ground surface, we assigned the pore pressure gradient of 0.11 psi/ft in the current models to match the initial bottomhole pressure at the fracture depth in the model with the field data. This pore pressure gradient led to the adjustment of the S_{hmin} and S_{Hmax} gradients based on the stress-controlling fault stability method, as elaborated by Haddad and Eichhubl (2020, 2023). Five simulation cases are considered here at various Viscous Regularization (V.R.) parameters and matrix, propped fracture, and unpropped fracture permeabilities, denoted as k_m, k_p, and k_{up} in this work.

Table 7-7: Poroelastic model parameters.

Parameter	Value
Matrix permeability, k_m [μD]	150 (Cases 1-3); 300 (Cases 4-5)
Unpropped-fracture permeability, k_{up} [mD]	15 (Cases 1-3); 30 (Case 4); 0.3 (Case 5)
Propped-fracture permeability, k_p [mD]	150 (Cases 1-3); 300 (Case 4); 0.3 (Case 5)
Porosity, ϕ (dimensionless)	0.23
Pore-pressure gradient, $\partial P_p/\partial z$ [psi/ft]	0.11
Water viscosity, μ_f [cp]	1
Young's modulus+, E [psi]	10^5
Poisson's ratio, ν (dimensionless)	0.1
Water-bulk modulus, K_w [psi]	311,705
Biot-Willis coefficient, α_{B-W} (dimensionless)	0.9
Dry-rock-bulk modulus, K_d [psi]	41,667
Grain-bulk modulus, K_g [psi]	416,667

Parameter	Value
Fracture toughness, K_I [psi.$\sqrt{in}$]	929.4
Fracture-initiation stress, σ_i [psi]	60
Energy-release rate, G_I [lbf/in]	0.354
Initially open fracture area, A_{init} [ft^2]	81
Leakoff coefficient, α_l [Gal/psi-s]	364.4
Viscous regularization parameter, V.R. (dimensionless)	0.025 (Case 1); 0.03 (Case 2); 0.01 (Cases 3-5)
Friction coefficient, μ_s (dimensionless)	0.3
Generalized Angelier's shape parameter, A_φ (dimensionless)	2.5
S_{vert} gradient, $\partial S_{vert}/\partial z$ [psi/ft]	1.08
S_{hmin} gradient, $\partial S_{hmin}/\partial z$ [psi/ft]	1.48
S_{Hmax} gradient, $\partial S_{Hmax}/\partial z$ [psi/ft]	1.87
Gravitational acceleration, g [ft/s^2]	32.18

Spatial pressure gradients for streaming potential

Conventionally, it is believed that subsurface conductivity changes induce the scattered field during an EM survey. In other words, zero scattered field would be expected based on well-known Maxwell's equations if there is no change in subsurface conductivity. However, from the datasets collected during the second Devine field deployment in 2022, we hypothesize that the SP may have caused changes in the surface recorded electric field. This is because clear correlations are observed between the electric potentials and flow-rate profiles, as elaborated in Subtask 6.5 (Figure 6-38a through Figure 6-46a). The pressure changes may not be related to any conductivity changes at all; however, these pressure changes can influence the electric field through the SP as formulated by the coupled flow theory (De Groot and Tolhoek, 1951) which is expressed by Equations (3-3) and (3-4).

Our poroelastic model can solve Equation (3-4) monolithically coupled with stress equilibrium equations. Evaluating the SP induced by changes in the hydraulic head needs postprocessing of pore-fluid pressure distribution obtained from this poroelastic model at each time increment to calculate the spatial changes in the hydraulic head. This poroelastic model can determine the spatiotemporal pore pressure gradient as a function of the dilated fracture area, rock deformation, fluid leakoff, and gap flow through the proppant pack (Haddad and Ahmadian, 2023). Knowing

that $P/\rho g$ is known as the hydraulic head, h, we obtained the spatial hydraulic-head gradients throughout the model using Darcy's law in x-, y-, and z-directions using Equations (7-16), (7-17), and (7-18):

$$\partial h/\partial x = -\mu v_x/\rho g k_x, \quad (7\text{-}16)$$
$$\partial h/\partial y = -\mu v_y/\rho g k_y, \quad (7\text{-}17)$$
$$\partial h/\partial z = -\mu v_z/\rho g k_z, \quad (7\text{-}18)$$

where v_i is provided in all integration points through time in a poroelastic model developed in Abaqus software program. We developed a user-defined subroutine (i.e., UVARM) to calculate and output the hydraulic-head gradients from v_i. For clarity, we do not present the SP solution in this work and rather provide these spatial hydraulic-head gradients to an SP model after future numerical-solution developments of the Poisson's equation.

Poroelastic model results

We evaluated the effect of V.R. on the injection-well BHP. Notably, V.R. is essential for stabilizing the numerical solution during the progressive damage of gradually degrading cohesive elements (Dassault Systèmes, 2017); however, its effect on the solution should be minimized, which otherwise could lead to large elastic energy dissipation in the model. The V.R. parameter is not known a priori for a specific case and should be determined through a sensitivity study. Thereby, we simulated Cases 1 through 3 at V.R. of 0.025, 0.03, and 0.01, and compared the resulting injection-well BHP from these cases with the field data (Figure 7-67). As expected, this comparison demonstrates that increasing the V.R. leads to a downward shift of the injection-well BHP, likely resulting from further energy dissipation in the model. Hence, we picked the V.R. of 0.01 in the subsequent simulation Cases 4 and 5 which are designed to evaluate the effect of matrix and fracture permeability combinations on the injection-well BHP. Case 4 is defined with permeabilities twice those in Cases 1-3, and Case 5 with the homogeneous permeability equal to the matrix permeability in Cases 1-3. The best match of the BHP to the field data is achieved in Case 4 with k_m of 300 μD, k_p of 300 mD, and k_{up} of 30 mD, demonstrating the advantage of assigning enhanced permeability values to the propped and unpropped fracture zones in reproducing the injection well BHP. The matrix permeability in Case 4 is twice that in the best-fitting case suggested by Haddad et al. (2021, 2023), mainly because the current simulations consider fitting of the models into several injection cycles whereas the previously published case was tuned for fitting the BHP in the first injection cycle.

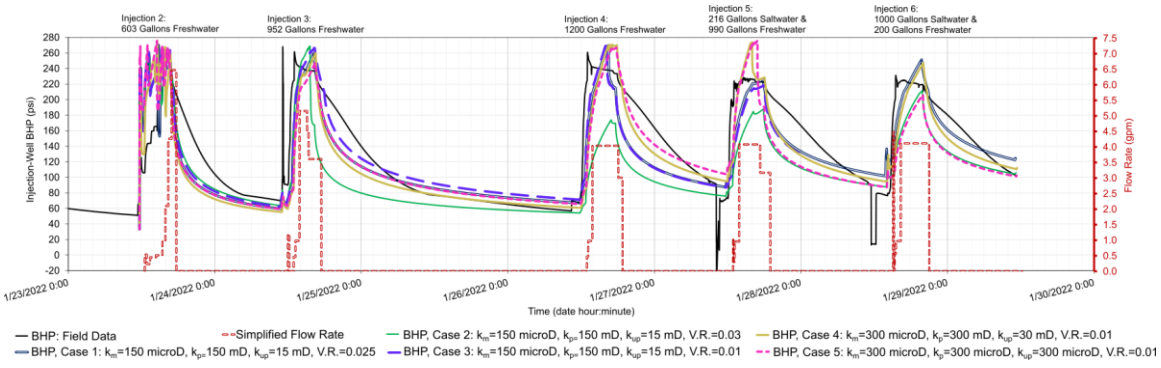

Figure 7-67: Comparison of the injection-well BHP from the field data and the simulations. BHP = Bottomhole Pressure. V.R. = Viscous Regularization parameter. k_m = matrix permeability. k_p = propped-fracture permeability. k_{up} = unpropped fracture permeability. First six injection cycles included in the simulations (Table 6-1).

7.4 Joint VSP/Seismic and EM Inversion

Because the seismic survey numerical studies showed low SNRs for the detection of the fracture dilation during injections, we did not proceed with the seismic inversion and the joint inversion of seismic and CSEM surveys. See section 5.3 for details.

Section 3: Products

A. Training and Professional Development Opportunities

Yiqian Mao from Duke University had a full-time internship at Cadence working on signal integrity and software development from May to August 2020.

Runren Zhang from Duke University had a full-time internship at Apple working on EM signal integrity from January to July 2020.

Duke student Liangze Cui did a summer internship at Schlumberger in 2022.

UT postdoctoral fellow, Mahdi Haddad, who started working on this project in 2021, was promoted to research associate in October 2021.

B. Publications, Conference Papers, and Presentations

Ahmadian, M. (2020) BP1 Continuation Meeting with DOE/NETL.

Ahmadian, M. (2020) Demonstration of Proof of Concept of a Multi-Physics Approach for Real-Time Remote Monitoring of Dynamic Changes in Pressure and Salinity in Hydraulically Fracture Networks. DOE-NETL's 2020 Integrated Project Review Meeting – Oil & Natural Gas. https://netl.doe.gov/sites/default/files/netl-file/20VPRONG_14_Ahmadian.pdf.

Ahmadian, M. (2020) Demonstration of Proof of Concept of a Multi-Physics Approach for Real-Time Remote Monitoring of Dynamic Changes in Pressure and Salinity in Hydraulically Fracture Networks. BEG Friday Seminar Series. 11 December.

Ahmadian, M. (2021) Monitoring Fracture Dynamics with Electromagnetic Geophysics. Carbon Management and Oil and Gas Research Project Review Meeting – Oil & Gas. 24 August. https://netl.doe.gov/21CMOG_OG-proceedings.

Ahmadian, M. (2022) Demonstration of Hydromechanical Fracture Changes Using Electromagnetic Surveys. Resource Sustainability Project Review Meeting. 26 October. https://netl.doe.gov/sites/default/files/netl-file/22RS-26_Ahmadian.pdf.

Ahmadian, M., M. Haddad, L. Cui, P. Doyle, A. Kleinhammes, J. Chen, T. Pugh, Y. Wu, and Q.H. Liu (2023) Real-time Monitoring of Fracture Dynamics with A Contrast Agent-assisted Electromagnetic Method. Presented at the 2023 SPE Hydraulic Fracturing Technology Conference and Exhibition, 31 January-2 February 2023, The Woodlands, Texas, USA. DOI: 10.2118/212376-MS.

Haddad, M., M. Ahmadian, J. Ge, S.A. Hosseini, J.-P. Nicot, and W. Ambrose (2021) Hydrogeological and Geomechanical Evaluation of a Shallow Hydraulic Fracture at the Devine Fracture Pilot Site, Medina County, Texas. Presented at the 55th US Rock Mechanics / Geomechanics Symposium, 20–23 June. ARMA-21-1958. Online.

Haddad, M. and M. Ahmadian (2023) Pressure Transient Analyses and Poroelastic Modeling of Hydraulic Fracture Dilation for Multiple Injection Cycles at the Devine Fracture Pilot Site. Presented at the 2023 SPE Hydraulic Fracturing Technology Conference and Exhibition, 31 January-2 February 2023, The Woodlands, Texas, USA. DOI: 10.2118/212362-MS.

Haddad, M., M. Ahmadian, J. Ge, J.-P. Nicot, and W. Ambrose (2023) Geomechanical and Hydrogeological Evaluation of a Shallow Hydraulic Fracture at the Devine Fracture Pilot Site, Medina County, Texas. Journal of Rock Mechanics and Rock Engineering.
DOI: 10.1007/s00603-022-03115-z.

Zhang, R., Q. Sun, Y. Mao, L. Cui, Y. Jia, W. Huang, M. Ahmadian, Q.H. Liu (2022a) Accelerating Full Wave Inversion by Deep Transfer Learning: A Case Study on Hydraulic Fracture Imaging. IEEE Transactions on Antennas and Propagation **70**(7): 6,117-6,121.
DOI: 10.1109/TAP.2022.3161325.

Section 4: Special Reporting Requirements

- Revised PMP was submitted to Mr. Gary Covatch on 11/20/19.
- Revised DMP was submitted to FITS.NETL.GOV on 12/16/19.
- Submitted DMP, PMP, TMP, BP1 continuation report, and multiple presentations to NETL and DOE
- Submitted supplementary request reports to the NETL program manager and FITS.NETL.GOV.
- Uploaded Haddad et al. (2021) conference paper on EDX at https://edx.netl.doe.gov/dataset/hydrogeological-and-geomechanical-evaluation-of-a-shallow-hydraulic-fracture-at-the-dfps-texas
- Registered Haddad et al. (2021) conference paper in OSTI at https://www.osti.gov/biblio/1898889
- Uploaded Zhang et al. (2022a) article on EDX at https://edx.netl.doe.gov/dataset/accelerating-hydraulic-fracture-imaging-by-deep-transfer-learning.
- Registered Zhang et al. (2022a) article in OSTI at https://www.osti.gov/biblio/1898644.
- Uploaded Haddad and Ahmadian (2023) conference paper on EDX at https://edx.netl.doe.gov/dataset/pressure-transient-analyses-and-poroelastic-modeling-of-hf-reopening-for-injections-at-the-dfps
- Registered Haddad and Ahmadian (2023) conference paper in OSTI at https://www.osti.gov/biblio/1958188
- Uploaded Ahmadian et al. (2023) conference paper on EDX at https://edx.netl.doe.gov/dataset/real-time-monitoring-of-fracture-dynamics-with-a-contrast-agent-assisted-electromagnetic-method
- Registered Ahmadian et al. (2023) conference paper in OSTI at https://www.osti.gov/biblio/1958193
  Registered Haddad et al. (2023) article on EDX and OSTI. The article is accessible at https://doi.org/10.1007/s00603-022-03115-z
- Submitted thirteen quarterly (Q) reports in two Business Periods (BPs) according to the following reporting periods:
  - Q1BP1, October 1 – December 31, 2019;
  - Q2BP1, January 1 – March 31, 2020;
  - Q3BP1, April 1 – June 30, 2020;
  - Q4BP1, July 1 – September 30, 2020;
  - Q1BP2, October 1 – December 31, 2020;
  - Q2BP2, January 1 – March 31, 2021;
  - Q3BP2, April 1 – June 30, 2021;
  - Q4BP2, July 1 – September 30, 2021;
  - Q5BP2, October 1 – December 31, 2021;
  - Q6BP2, January 1 – March 31, 2022;
  - Q7BP2, April 1 – June 30, 2022;
  - Q8BP2, July 1 – September 30, 2022; and
  - Q9BP2, October 1 – December 31, 2022.

Section 5. Changes/Problems

A. Delays

Due to economic impact of COVID19, ESG had a substantial cut-back on workforce and UT-Austin had mandated a partial furlough for all researchers at the Bureau of Economic Geology for 3 months. DOE mandate for verifying all foreign nationals working at Duke University slowed down their progress substantially, starting at March 2021. As such, we were granted 15 months extension to catch up with the delays.

B. Personnel Change

On May 2021, Alfred Kleinhammes of UNC retired. However, he agreed to participate and consult on the project through its conclusion and to assist Patrick Doyle who took his place.

Professor Qing Huo Liu of Duke University retired on 6/30/2022. However, he agreed to participate and consult on the project through its conclusion and to assist Professor David Smith, who took his place.

Section 6: Budgetary Information

Baseline Reporting Quarter	Budget Period 1							
	10/1/19-12/31/19		1/1/20-3/31/20		4/1/20-6/30/20		7/1/20-9/30/20	
	Q1	Cummulative Total	Q2	Cummulative Total	Q3	Cummulative Total	Q4	Cummulative Total
Baseline Cost Plan								
Federal Share	$171,831	$171,831	$171,831	$343,662	$171,831	$515,493	$171,831	$687,324
Non-Federal Share	$42,057	$42,057	$42,057	$84,114	$42,057	$126,171	$42,057	$168,228
Total Planned	$213,888	$213,888	$213,888	$427,776	$213,888	$641,664	$213,888	$855,552
Actual Incurred Costs								
Actual Federal Share	$0	$0	$117,539	$117,539	$157,205	$274,744	$225,404	$500,148
Actual non-Federal Share	$33,165	$33,165	$95,343	$128,508	$27,362	$155,870	$12,356	$168,226
Total Incurred Costs	$33,165	$33,165	$212,882	$246,047	$184,567	$430,614	$237,760	$668,374
Variance								
Variance Federal Share	$171,831	$171,831	$54,292	$226,123	$14,626	$240,749	($53,573)	$187,176
Variance non-Federal Share	$8,892	$8,892	($53,286)	($44,394)	$14,695	($29,699)	$29,701	$2
Total Variance Cumulative	$180,723	$180,723	$1,006	$181,729	$29,321	$211,050	($23,872)	$187,178

Baseline Reporting Quarter	Budget Period 2							
	10/1/20-12/31/20		1/1/21-3/31/21		4/1/21-6/30/21		7/1/21-9/30/21	
	Q1	Cummulative Total	Q2	Cummulative Total	Q3	Cummulative Total	Q4	Cummulative Total
Baseline Cost Plan								
Federal Share	$203,168	$890,492	$203,168	$1,093,660	$203,168	$1,296,828	$203,168	$1,499,996
Non-Federal Share	$53,496	$221,724	$53,496	$275,220	$53,496	$328,716	$53,496	$382,212
Total Planned	$256,664	$1,112,216	$256,664	$1,368,880	$256,664	$1,625,544	$256,664	$1,882,208
Actual Incurred Costs								
Actual Federal Share	$211,455	$711,603	$64,795	$776,398	$90,080	$866,479	$63,151	$929,629
Actual non-Federal Share	$106,923	$275,149	$30,731	$305,880	$36,179	$342,058	$35,622	$377,680
Total Incurred Costs	$318,378	$986,752	$95,526	$1,082,278	$126,259	$1,208,537	$98,773	$1,307,309
Variance								
Variance Federal Share	($8,287)	$178,889	$138,373	$317,262	$113,088	$430,349	$140,017	$570,367
Variance non-Federal Share	($53,427)	($53,425)	$22,765	($30,660)	$17,317	($13,342)	$17,874	$4,532
Total Variance Cumulative	($61,714)	$125,464	$161,138	$286,602	$130,405	$417,007	$157,891	$574,899

Baseline Reporting Quarter	Budget Period 2 - Extension									
	10/1/21-12/31/21		1/1/22-3/31/22		4/1/22-6/30/22		7/1/22-9/30/22		10/1/22-12/31/22	
	Q5	Cummulative Total	Q6	Cummulative Total	Q7	Cummulative Total	Q8	Cummulative Total	Q9	Cummulative Total
Baseline Cost Plan										
Federal Share	$73,728	$1,573,724	$73,728	$1,647,452	$73,728	$1,721,180	$0	$1,721,180	$0	$1,721,180
Non-Federal Share	$16,027	$398,239	$16,025	$414,264	$16,025	$430,288	$0	$430,288	$0	$430,288
Total Planned	$89,755	$1,971,963	$89,753	$2,061,716	$89,753	$2,151,468	$0	$2,151,468	$0	$2,151,468
Actual Incurred Costs										
Actual Federal Share	$124,455	$1,054,085	$249,783	$1,303,868	$194,176	$1,498,044	$139,695	$1,637,739	$83,132	$1,720,871
Actual non-Federal Share	$13,125	$390,805	$0	$390,805	$73,033	$463,838	$0	$463,838	$0	$463,838
Total Incurred Costs	$137,580	$1,444,889	$249,783	$1,694,673	$267,209	$1,961,882	$139,695	$2,101,577	$83,132	$2,184,709
Variance										
Variance Federal Share	($50,728)	$519,639	($176,055)	$343,584	($120,448)	$223,136	($65,967)	$83,441	($83,132)	$309
Variance non-Federal Share	$2,903	$7,434	$16,025	$23,459	($57,008)	($33,550)	$16,025	($33,550)	$0	($33,550)
Total Variance Cumulative	($47,825)	$527,074	($160,030)	$367,043	($177,456)	$189,586	($49,942)	$49,891		

Section 7: Bibliography

Ahmadian, M., M. Haddad, L. Cui, P. Doyle, A. Kleinhammes, J. Chen, T. Pugh, Y. Wu, and Q. H. Liu (2023) Real-time Monitoring of Fracture Dynamics with A Contrast Agent-assisted Electromagnetic Method. Presented at the 2023 SPE Hydraulic Fracturing Technology Conference and Exhibition, 31 January-2 February 2023, The Woodlands, Texas, USA.
DOI: 10.2118/212376-MS.

Ahmadian, M., D. LaBrecque, Q.H. Liu, A. Kleinhammes, P. Doyle, Y. Fang, G. Jeffrey, and C. Lucie (2019) Validation of the Utility of the Contrast-Agent-Assisted Electromagnetic Tomography Method for Precise Imaging of a Hydraulically Induced Fracture Network. Presented at the SPE Annual Technical Conference and Exhibition, Society of Petroleum Engineers.
DOI: 10.2118/196140-MS.

Ahmadian, M., D. LaBrecque, Q.H. Liu, W. Slack, R. Brigham, Y. Fang, K. Banks, Y. Hu, D. Wang, and R. Zhang (2018) Demonstration of Proof of Concept of Electromagnetic Geophysical Methods for High Resolution Illumination of Induced Fracture Networks. Presented at the SPE Hydraulic Fracturing Technology Conference and Exhibition, Society of Petroleum Engineers. DOI: 10.2118/189858-MS.

Allen, G.P., D. Laurier, and J. Thouvenin (1979) Étude Sédimentologique de Delta de la Mahakam: Compagnie Française des Petroles. Notes et Memoires **15**: 1-156.

Ambrose, W.A. (1983) Tide-Dominated Deltaic Deposits of the Spoon Formation (Pennsylvanian) in a Narrow, Subsiding Trough, Southern Illinois (abs.): Geological Society of America. Abstracts with Programs **15**(6).

Ambrose, W.A., E.R. Ferrer, S.P. Dutton, F.P. Wang, A. Padron, W. Carrasquel, J.S. Yeh, and N. Tyler (1995) Production Optimization of Tide-Dominated Deltaic Reservoirs of the Lower Misoa Formation (lower Eocene), LL-652 Area, Lagunillas Field, Lake Maracaibo, Venezuela. The University of Texas at Austin, Bureau of Economic Geology Report of Investigations **226**: 1-46.

Ambrose, W.A., T.F. and Hentz (2010) Depositional Systems and Facies Variability in Highstand Fluvial-Dominated Deltaic and Lowstand Valley-Fill Systems in the Upper Cretaceous (Cenomanian) Woodbine Group, East Texas Field, in T. F. Hentz, ed., The University of Texas at Austin, Bureau of Economic Geology Report of Investigations **274**: 17-81.

Ambrose, W.A., T.F. Hentz, and L.B. Tussey (2015) Pennsylvanian Tidal Depositional Systems in the Anadarko Basin, Northeast Texas Panhandle and Northwest Oklahoma. The University of Texas at Austin, Bureau of Economic Geology Report of Investigations **280**: 1-35.

Ambrose, W.A. and H. Zeng (2016) Wave-Dominated Shoreface Systems in the Lower Luling Sand, Northern Bee County, South Texas. South Texas Geological Society Bulletin **57**: 32–44.

Ambrose, W.A., and Zhang, J. (2018) Letco MV 9696.02 TOH-2A Settlemyre core (Leon County), in M.I. Olariu, W.A. Ambrose, C. Olariu, R. Steel, and J. Zhang eds., Depositional History and Architectural Variability of the Wilcox Group in Texas: The University of Texas at Austin, Bureau of Economic Geology and Austin Geological Society. Core Workshop Guidebook **SW0024**: 25–46.

Barree, R., R. Duenckel, and B. Hlidek (2019) Proppant Sieve Distribution-What Really Matters? SPE Hydraulic Fracturing Technology Conference and Exhibition, Society of Petroleum Engineers. DOI: 10.2118/194382-MS.

Barenblatt, G. (1962) The Mathematical Theory of Equilibrium Cracks in Brittle Fracture. Advances in Applied Mechanics **7**: 55-129. DOI: 10.1016/S0065-2156(08)70121-2.

Bellile, T. (2003) Pennsylvanian of Kentucky Tidal Deposits. http://www4.uwm.edu/course/geosci697/tidal/tidal-deposits.html (last accessed December 19, 2019).

Benzeggagh, M.L. and M. Kenane (1996) Measurement of Mixed-Mode Delamination Fracture Toughness of Unidirectional Glass/Epoxy Composites with Mixed-Mode Bending Apparatus. Composites Science and Technology **56**(4): 439-449. DOI: 10.1016/0266-3538(96)00005-X.

Binder, G., A. Titov, Y. Liu, J. Simmons, A. Tura, G. Byerley, and D. Monk (2020) Modeling the Seismic Response of Individual Hydraulic Fracturing Stages Observed in a Time-Lapse Distributed Acoustic Sensing Vertical Seismic Profiling Survey. Geophysics **85**(4): T225–T235. DOI: 10.1190/geo2019-0819.1.

Breyer, J.A. and P.J. McCabe (1986) Coals Associated with Tidal Sediments in the Wilcox Group (Paleogene), South Texas. Journal of Sedimentary Petrology **56**(4): 510–519. DOI: 10.1306/212F8972-2B24-11D7-8648000102C1865D.

Castillo, J.L. (1987) Modified Fracture Pressure Decline Analysis, Including Pressure-Dependent Leakoff. Presented at the SPE/DOE Low Permeability Reservoirs Symposium, Denver, Colorado, 18-19 May 1987. SPE-16417. DOI: 10.2118/16417-MS.

Coates, R.T. and M. Schoenberg (1995) Finite-Difference Modeling of Faults and Fractures. Geophysics **60**(5): 1514–1526. DOI: 10.1190/1.1443884.

Coleman, J.M. and S.M. Gagliano (1964) Cyclic Sedimentation in the Mississippi River Delta Plain: Gulf Coast Association of Geological Societies Transactions **14**: 67–80.

Computer Modelling Group Ltd. (2020) GEM Compositional & Unconventional Simulator User Guide, Vol. 2010.10. Calgary, Canada: Computer Modelling Group Ltd.

Cui, L., Y. Zhang, R. Zhang, and Q.H. Liu. (2020) A Modified Efficient KNN Method for Antenna Optimization and Design. IEEE Transactions on Antennas and Propagation **68**(10): 6858-6866. DOI: 10.1109/TAP.2020.3001743.

Dalrymple, R.W. (1992) Tidal Depositional Systems, in R.G. Walker and N.P. James, eds., Facies Models: Response to Sea Level Change. Geological Association of Canada: 195–218.

Dassault Systèmes (2017) Abaqus Analysis User's Guide, volume 2017. Waltham, Massachusetts.

Davies, J.L. (1964) A morphogenic Approach to World Shorelines: Zeitschrift für Geomorphologie **8**(5): 127–142. DOI: 10.1127/zfg/mortensen/8/1964/127.

Denison, C.N., T.D. Demchuk, and J.M.K. O'Keefe (2017) Tidal Depositional Systems in the Wilcox/Carrizo of Bastrop County, Texas: Sedimentology, Ichnology, and Palynology. Gulf Coast Association of Geological Societies Transactions **67**: 417–423.

Denison, J., L. Murdoch, D. LaBrecque, and W. Slack (2015) Electrical and Magnetic Imaging of Proppants in Shallow Hydraulic Fractures. American Geophysical Union Fall Meeting

de Groot, S.R. and H.A. Tolhoek (1951) On the Electrochemical Potential. Recueil des Travaux Chimiques des Pays-Bas, **70**(5): 419-420. DOI: 10.1002/recl.19510700506.

de Raaf, J.F.M. and J.R. Boersma (1971) Tidal Deposits and Their Sedimentary Structures. Geologie en Minnow **50**: 479–504.

Dugdale, D. (1960) Yielding of Steel Sheets Containing Slits. Journal of the Mechanics and Physics of Solids **8**: 100-104. DOI: 10.1016/0022-5096(60)90013-2.

Edwards, M.B. (1981) Upper Wilcox Rosita Delta System of South Texas: Growth-Faulted Shelf-Edge Deltas. American Association of Petroleum Geologists Bulletin **65**(1): 54–73.

Evans, G. (1965) Intertidal Flat Sediments and Their Environments of Deposition in the Wash. Geological Society of London Quarterly Journal **121**: 209–245. DOI: 10.1144/gsjgs.121.1.0209.

Evans, G. (1970) Coastal and Nearshore Sedimentation: A Comparison of Clastic and Carbonate Deposition. Geological Association of Canada Proceedings **81**: 493–508.
DOI: 10.1016/S0016-7878(70)80010-4.

Fang, Y., J. Dai, Z. Yu, J. Zhou, and Q.H. Liu (2017) Through-Casing Hydraulic Fracture Evaluation by Induction Logging I: An Efficient EM Solver for Fracture Detection. IEEE Transactions on Geoscience and Remote Sensing **55**(2): 1179–1188.
DOI: 10.1109/TGRS.2016.2620482.

Fang, Y., J. Dai, Q. Zhan, Y. Hu, M. Zhuang, and Q.H. Liu (2019a) A Hybrid 3-D Electromagnetic Method for Induction Detection of Hydraulic Fractures Through a Tilted Cased Borehole in Planar Stratified Media. IEEE Transactions on Geoscience and Remote Sensing **57** (7): 4,568-4,576.
DOI: 10.1109/TGRS.2019.2891674.

Fang, Y., Y. Hu, Q. Zhan, and Q.H. Liu (2018) Electromagnetic Forward and Inverse Algorithms for 3-D Through-Casing Induction Mapping of Arbitrary Fractures. IEEE Geoscience and Remote Sensing Letters **15**(7): 996–1000. DOI: 10.1109/LGRS.2018.2818112.

Fang, Y., Y. Hu, Q. Zhan, D. Wang, R. Zhang, and Q.H. Liu. (2020) A Fast Numerical Method for the Galvanic Measurement in Hydraulic Fracture Detection. IEEE Transactions on Antennas and Propagation **68**(2): 947-957. DOI: 10.1109/TAP.2019.2940591.

Fang, Y., J. Zhou, Z. Yu, Y. Hu, and Q.H. Liu (2015) Application of BCGS-FFT and Distorted Born Approximation for Hydraulic Fracturing Detection and Imaging. Radio Science Meeting [Joint with Antennas and Propagation Symposium (AP-S)], 2015 U.S. National Committee for the International Union of Radio Science (USNC-URSI), IEEE.

Fekete Inc. (2014). Minifrac Pre-Closure Analysis. Available at:
http://www.fekete.com/san/webhelp/welltest/webhelp/Content/HTML_Files/Analysis_Types/Minifrac_Test_Analyses/Minifrac-Pre-Closure_Analysis.htm (accessed at December 22, 2020).

Fisher, W.L. and J.H. McGowen (1967) Depositional Systems in the Wilcox Group of Texas and Their Relationship to Occurrence of Oil and Gas. The University of Texas at Austin, Bureau of Economic Geology. Geologic Circular **67-4**: 1-20.

Fisher, W.L., L.F. Brown Jr., A.J. Scott, and J.H. McGowen (1969) Delta Systems in the Exploration for Oil and Gas: The University of Texas at Austin, Bureau of Economic Geology Research Colloquium: variously paginated.

Fitterman, D.V. (1979) Calculations of Self-Potential Anomalies Near Vertical Contacts. Geophysics **44**(2): 195-205. DOI: 10.1190/1.1440961.

Frey, R.W. and R.G. Bromley (1985) Ichnology of American Chalks: the Selma Group (Upper Cretaceous), Western Alabama. Canadian Journal of Earth Science **22**: 801–828. DOI: 10.1139/e85-087.

Galloway, W.E., T.E. Ewing, C.M. Garrett Jr., N. Tyler, and D.G. Bebout (1983) Atlas of Major Texas Oil Reservoirs. The University of Texas at Austin, Bureau of Economic Geology: 1-139.

Galloway, W.E., T.L. Whiteaker, and P.E. Ganey-Curry (2011) History of Cenozoic North American Drainage Basin Evolution, Sediment Yield, and Accumulation in the Gulf of Mexico Basin. Geosphere **7**: 938–973. DOI: 10.1130/GES00647.1.

Gardner, G.H.F., L.W. Gardner, and A.R. Gregory (1974) Formation Velocity and Density—The Diagnostic Basics for Stratigraphic Traps. Geophysics **39**(6): 770-780. DOI: 10.1190/1.1440465.

Gonzalez, H., J. Canal, P. Fernandez, M.A. Ruano, and T. Workut (2016) Geomechanical and Petrophysical Characterization for Wilson-9 Plugs. Repsol Technology Centre, G.D. Strategy and Control.

Grose, R.D. (1985) Orifice Contraction Coefficient for Inviscid Incompressible Flow. Journal of Fluids Engineering **107**(1): 36–43. DOI: 10.1115/1.3242437.

Haddad, M., M. Ahmadian, J. Ge, S.A. Hosseini, J.-P. Nicot, and W. Ambrose (2021) Hydrogeological and Geomechanical Evaluation of a Shallow Hydraulic Fracture at the Devine Fracture Pilot Site, Medina County, Texas. Presented at the 55th U.S. Rock Mechanics / Geomechanics Symposium, online, 20-23 June. ARMA-21-1958.

Haddad, M. and M. Ahmadian (2023) Pressure Transient Analyses and Poroelastic Modeling of Hydraulic Fracture Dilation for Multiple Injection Cycles at the Devine Fracture Pilot Site. Presented at the 2023 SPE Hydraulic Fracturing Technology Conference and Exhibition, 31 January-2 February 2023, The Woodlands, Texas, USA. DOI: 10.2118/212362-MS.

Haddad, M., M. Ahmadian, J. Ge, J.-P. Nicot, and W. Ambrose (2023) Geomechanical and Hydrogeological Evaluation of a Shallow Hydraulic Fracture at the Devine Fracture Pilot Site, Medina County, Texas. Rock Mechanics and Rock Engineering, online. DOI: 10.1007/s00603-022-03115-z.

Haddad, M., J. Du, and S. Vidal-Gilbert (2017) Integration of Dynamic Microseismic Data with a True 3D Modeling of Hydraulic-Fracture Propagation in the Vaca Muerta Shale. SPE J. **22**(6): 1,714-1,738. SPE-179164-PA. DOI: 10.2118/179164-PA.

Haddad, M. and P. Eichhubl (2020) Poroelastic Modeling of Basement Fault Reactivation Caused by Saltwater Disposal Near Venus, Johnson County, Texas. Presented at the 54th U.S. Rock Mechanics / Geomechanics Symposium, Golden, Colorado, USA, 28 June–1 July 2020. ARMA-20-2006.

Haddad, M. and P. Eichhubl (2023) Fault Reactivation in Response to Saltwater Disposal and Hydrocarbon Production for the Venus, TX, M_w 4.0 Earthquake Sequence. Rock Mechanics and Rock Engineering **56**: 2,103-2,135. DOI: 10.1007/s00603-022-03083-4.

Haddad, M. and K. Sepehrnoori (2015) Simulation of Hydraulic Fracturing in Quasi-Brittle Shale Formations Using Characterized Cohesive Layer: Stimulation Controlling Factors. J. Unconventional Oil Gas Resources **9**: 65-83. DOI: 10.1016/j.juogr.2014.10.001.

Haddad, M. and K. Sepehrnoori (2016). XFEM-Based CZM for the Simulation of 3D Multiple-Cluster Hydraulic Fracturing in Quasi-Brittle Shale Formations. Journal of Rock Mechanics and Rock Engineering **49**(12): 4,731-4,748. DOI: 10.1007/s00603-016-1057-2.

Hentz, T.F., W.A. Ambrose, and D.C. Smith (2014) Eaglebine Play of the Southwestern East Texas Basin: Stratigraphic and Depositional Framework of the Upper Cretaceous (Cenomanian–Turonian) Woodbine and Eagle Ford Group. American Association of Petroleum Geologists Bulletin **98**(12): 2,551–2,580. DOI: 10.1306/07071413232.

Hu, Y., Y. Fang, D. LaBrecque, M. Ahmadian and Q.H. Liu (2017) Reconstruction of High-Contrast Proppant in Hydraulic Fractures with Galvanic Measurements. IEEE Transactions on Geoscience and Remote Sensing **56**(4): 2066–2073. DOI: 10.1109/TGRS.2017.2773080.

Hu, Y., Z. Yu, W. Zhang, Q. Sun, and Q.H. Liu (2016) Multiphysics Coupling of Dynamic Fluid Flow and Electromagnetic Fields for Subsurface Sensing. IEEE Journal on Multiscale and Multiphysics Computational Techniques **1**: 14–25. DOI: 10.1109/JMMCT.2016.2559509.

Ishido, T., H. Mizutani, and K. Baba (1983). Streaming Potential Observations, Using Geothermal Wells and In Situ Electrokinetic Coupling Coefficients Under High Temperature. Tectonophysics **91**: 89-104. DOI: 10.1016/0040-1951(83)90059-8.

Kaip, G., S.H. Harder, and M.S. Karplus (2017) Comparison of Seismic Sources and Frequencies in West Texas. AGU Fall Meeting Abstracts (Vol. 2017): S13C-0679.

Kaiser, W.R., J.E. Johnston, and W.N. Bach (1978) Sand-Body Geometry and the Occurrence of Lignite in the Eocene of Texas. The University of Texas at Austin, Bureau of Economic Geology. Geological Circular **7804**: 1-19.

Klein, G. de V. (1971) A Sedimentary Model for Determining Paleotidal Range. Geological Society of America Bulletin **82**(9): 2,585–2,592.
DOI: 10.1130/0016-7606(1971)82[2585:ASMFDP]2.0.CO;2

Kvale, E.P., A.W. Archer, and H.R. Johnson (1989) Daily, Monthly and Yearly Tidal Cycles Within Laminated Siltstones of the Mansfield Formation (Pennsylvanian) of Indiana. Geology **17**: 365–368. DOI: 10.1130/0091-7613(1989)017<0365:DMAYTC>2.3.CO;2.

Kvale, E.P. and A.W. Archer (1990) Tidal Deposits Associated with Low-Sulfur Coals. Brazil Fm. (Lower Pennsylvanian), Indiana. Journal of Sedimentary Petrology **60**(4): 563–574.
DOI: 10.1306/212F91E7-2B24-11D7-8648000102C1865D.

LaBrecque, D., R. Brigham, J. Denison, L. Murdoch, W. Slack, Q.H. Liu, Y. Fang, J. Dai, Y. Hu, and Z. Yu (2016) Remote Imaging of Proppants in Hydraulic Fracture Networks Using Electromagnetic Methods: Results of Small-Scale Field Experiments. SPE Hydraulic Fracturing Technology Conference, Society of Petroleum Engineers. DOI: 10.2118/179170-MS.

Li, S., C. Olariu, and R.J. Steel (2018) Lower Wilcox Facies Associations in a 700 m Long Core Vogelsang Freida #1, Colorado County, Texas, in M.I. Olariu, W.A. Ambrose, C. Olariu, R. Steel, and J. Zhang, eds. Depositional History and Architectural Variability of the Wilcox Group in Texas. The University of Texas at Austin, Bureau of Economic Geology and Austin Geological Society. Core Workshop Guidebook **SW0024**: 55–79.

Maguregui, J.A. and N. Tyler (1991) Evolution of Middle Eocene Tide-Dominated Deltaic Sandstones, Lagunillas Field, Maracaibo Basin, Western Venezuela, in A.D. Miall and N. Tyler, eds. The Three-Dimensional Facies Architecture of Terrigenous Clastic Sediments and its

Implications for Hydrocarbon Discovery and Recovery. SEPM (Society for Sedimentary Geology). Concepts in Sedimentology and Paleontology **3**: 233–244. DOI: 10.2110/csp.91.03.0233.

McClain, C.H. (1963) Fluid Flow in Pipes: A Clear-Cut Summary of Modern Theory in the Flow of Liquids and Gases Through Piping and Ducts, with Practical Applications and Detailed Worked-out Examples. New York: The Industrial Press. 128 p. https://hdl.handle.net/2027/mdp.39015000477268.

Mutti, E., J. Rossell, G.P. Allen, F. Fonnesu, and M. Sgavetti (1985) The Eocene Baronia Tide Dominated Delta-Shelf System in the Ager Basin, in M.D. Mila and J. Rossell, eds. Excursion Guidebook. 6th European Regional Meeting, International Association of Sedimentologists, Lleida, Spain: 579–600.

Pemberton, S.G., and R.W. Frey (1982) Trace Fossil Nomenclature and the Planolites-Palaeophycus Dilemma. Journal of Paleontology **56**(4): 843–881.

Pemberton, S.G., J.A. MacEachern, and R.W. Frey (1992) Trace Fossil Facies Models: Environmental and Allostratigraphic Significance, in R.G. Walker and N.P. James, eds. Facies Models: Response to Sea Level Change. Geological Association of Canada, St. John's, Newfoundland: 47–72.

Puzyrev, V. (2019) Deep Learning Electromagnetic Inversion with Convolutional Neural Networks. Geophysical Journal International **218**(2): 817–832. DOI: 10.48550/arXiv.1812.10247.

Reineck, H.E. (1967) Layered Sediments of Tidal Flats, Beaches and Shelf Bottoms, in G.H. Lauff, ed. Estuaries. American Association for the Advancement of Science Publication **83**: 191–206.

Reineck, H.E. and F. Wunderlich (1968) Classification and Origin of Flaser and Lenticular Bedding. Sedimentology **11**: 99–104.

Reineck, H.E. and I.B. Singh (1973) Depositional Sedimentary Environments: With Reference to Terrigenous Clastics. Berlin, Springer-Verlag: 1-439.

Roep, T.B. (1991) Neap-Spring Cycles in a Subrecent Tidal Channel Fill (3665 BP) at Schoorldam, NW Netherlands. Sedimentary Geology **71**: 213–230. DOI: 10.1016/0037-0738(91)90103-K.

Sheffer, M.R. and D.W. Oldenburg (2007). Three-Dimensional Modelling of Streaming Potential. Geophys. J. Int. **169**: 839-848. DOI: 10.1111/j.1365-246X.2007.03397.x.

Schoenberg, M. and C.M. Sayers (1995) Seismic Anisotropy of Fractured Rock. Geophysics, **60**(1): 204-211. DOI: 10.1190/1.1443748

Sill, W.R. (1983) Self-Potential Modeling from Primary Flows. Geophysics **48**: 76-86. DOI: 10.1190/1.1441409. DOI: 10.1190/1.1441409.

Simpson, R.W. (1997) Quantifying Anderson's Fault Types. Journal of Geophysical Research **102**(B8): 17,909–17,919. DOI: 10.1029/97JB01274.

Sun, Q., R. Zhang, and Y. Hu (2021) Domain Decomposition-Based Discontinuous Galerkin Time-Domain Method with Weighted Laguerre Polynomials. IEEE Transactions on Antennas and Propagation **69**(11): 7999-8002. DOI: 10.1109/TAP.2021.3076566.

Ta, T.K.O., V.L. Nguyen, M. Tateishi, I. Kobayashi, S. Tanabe, and Y. Saito (2002) Holocene Delta Evolution and Sediment Discharge of the Mekong River, Southern Vietnam. Quaternary Science Reviews **21**(16-17): 1,807-1,819. DOI: 10.1016/S0277-3791(02)00007-0.

Terwindt, J.H.J. (1971) Lithofacies of Inshore Estuarine and Tidal Inlet Deposits. Geologie en Mijnbouw **50**: 515–526.

Titov, A., G. Binder, Y. Liu, G. Jin, J. Simmons, A. Tura, and M. Yates (2021) Modeling and Interpretation of Scattered Waves in Interstage Distributed Acoustic Sensing Vertical Seismic Profiling Survey. Geophysics **86**(2): D93-D102. DOI: 10.1190/geo2020-0293.1.

Van Straaten, L.M.J.U. and Ph.H. Kuenen (1958) Tidal Action as a Cause of Clay Accumulation. Journal of Sedimentary Petrology **28**: 406–413.
DOI: 10.1306/74D70826-2B21-11D7-8648000102C1865D.

Varsek, J. and D. Lawton (1985a) The Seisgun-Part I-Field Tests. Journal of the Canadian Society of Exploration Geophysicists **21**(1): 64–76.

Varsek, J. and D. Lawton (1985b) The Seisgun-Part II-Data Acquisition from a Study of Stacked Sections. J. Can. Soc. Expl. Geophys **21**: 77-88.

Verdon, J.P. and A. Wüstefeld (2013) Measurement of the Normal/Tangential Fracture Compliance Ratio (ZN/ZT) during Hydraulic Fracture Stimulation Using S-Wave Splitting Data. Geophysical Prospecting **61**: 461–475. DOI: 10.1111/j.1365-2478.2012.01132.x.

Visser, M.J. (1980) Neap–Spring Cycles Reflected in Holocene Subtidal Large-Scale Bedform Deposits: A Preliminary Note. Geology **8**: 543–546.
DOI:10.1130/0091-7613(1980)8<543:NCRIHS>2.0.CO;2.

von Brunn, V. and D.K. Hobday (1976) Early Precambrian Tidal Sedimentation in the Pongola Supergroup of South Africa. Journal of Sedimentary Petrology **46**(3): 670–679.
DOI: 10.1306/212F7022-2B24-11D7-8648000102C1865D.

Weimer, R.J., J.D. Howard, and D.R. Lindsay (1982) Tidal Flats and Associated Tidal Channels, in P.A. Scholle and D. Spearing, eds. Sandstone Depositional Environments. American Association of Petroleum Geologists. Memoir **31**: 191–245. DOI: 10.1306/M31424C9.

Wright, L.D., J.M. Coleman, and B.G. Thom (1973) Processes of Channel Development in a High Tide Environment: Cambridge Gulf, Ord River Delta, Western Australia. Journal of Geology **81**: 15–41. https://www.jstor.org/stable/30060692.

Wu, C., J.M. Harris, K.T. Nihei, and S. Nakagawa (2005) Two-Dimensional Finite-Difference Seismic Modeling of an Open Fluid-Filled Fracture: Comparison of Thin-Layer and Linear-Slip Models. Geophysics **70**(4): T57. DOI: 10.1190/1.1988187.

Wunderlich, F. (1970) Genesis and Environment of the "Nellenkopfschenschichten" (Lower Emsian, Rheinian Devonian) at Locus Typicus in Comparison with Modern Coastal Environments of the German Bay. Journal of Sedimentary Petrology **40**: 102–130.

Yan, J., and P. Sava (2008). Isotropic Angle-Domain Elastic Reverse-Time Migration. Geophysics **73**(6): S229-S239. DOI: 10.1190/1.2981241.

Zeng, Y.Q. and Q.H. Liu (2001) Acoustic detection of buried objects in 3-D fluid saturated porous media: Numerical modeling. IEEE Transactions on Geoscience and Remote Sensing **39**(6): 1165-1173. DOI: 10.1109/36.927434.

Zhang, J., R. Steel, and W.A. Ambrose (2016) Greenhouse Shoreline Migration: Wilcox Deltas. American Association of Petroleum Geologists Bulletin **100**: 1,803–1,831.

DOI:10.1306/04151615190.

Zhang, R., Q. Sun, Y. Mao, L. Cui, Y. Jia, W.-F. Huang, M. Ahmadian, and Q. H. Liu (2022a) Accelerating Hydraulic Fracture Imaging by Deep Transfer Learning. IEEE Transactions on Antennas and Propagation **70**(7): 6,117-6,121. DOI: 10.1109/TAP.2022.3161325.

Zhang, R., Q. Sun, X. Zhang, L. Cui, Z. Wu, K. Chen, D. Wang, and Q.H. Liu (2022b) Imaging Hydraulic Fractures Under Energized Steel Casing by Convolutional Neural Networks. IEEE Transactions on Geoscience and Remote Sensing **58**(12): 8,831-8,839.
DOI: 10.1109/TGRS.2020.2991011.

Zhernokletov, D.M., V.V. Milyavskiy, K.V. Khishchenko, A.A. Charakhchyan, T.I. Borodina, G.E. Val'yano, and A.Z. Zhuk (2007) Shock-Wave Loading of Graphite in Steel Targets with Conic Cavities. AIP Conference Proceedings **955**(1): 216-219. American Institute of Physics.
DOI: 10.1063/1.2833014.

Section 8: Appendix

A.1 Milestone Tracking

Exhibit A1-1: Milestone status report and proposed and actual completion dates on major goals of the project.

Task	Subtask/Milestone Description	Planned Completion Date	Percent Complete as of 3/31/2022	Verification Method/ Deliverables	Comments
1.0	Project Coordination, Communication, and Reporting	12/31/22	100%	Email to DOE project managers and FITS@netl.doe.gov	(1) PMP and DMP were updated. (2) TMP was submitted on 10/09/2020. (3) Q1–Q4BP1 and Q1-Q9BP2 reports were submitted to DOE. (4) Continuation presentation and annual review were completed.
2.0	Workforce Readiness for Technology Deployment	10/31/2020	100%, completed 10/31/2020	Presentation file BP2 deliverable	(1) Completed.
3.0	1. Initial Laboratory Studies for HP/HS Responsive EAP 2. Lithology and Cores Studies	09/30/2021 07/30/2020	100% 100%	Q1–Q4 BP1 Reports Q1–Q4 BP1 Reports	(1) Laboratory studies demonstrated that both pressure and salinity cause a marked impact on electric response. (2) We completed an extensive core characterization report describing 249 ft (76 m) of core from the DFPS. See Appendix A.2.
4.0	1. VSP/Seismic RTM Validation 2. Joint VSP/Seismic and EM Inversion	06/30/2020 09/30/2020	100%, completed 6/30/2020 100%	Year 1 Topical Report	(1) RTM code was validated. (2) We successfully built two ML models to conduct EM inversion. We tuned the parameters of the ML models to improve inversion results. Due to the limited SNR of a seismic survey to detect fracture dilation, we did not conduct joint seismic-and-EM inversion.

5.0	1. Field Design: Fluid Flow Modeling 2. EM Sensitivity Analysis 3. VSP or Seismic Sensitivity Analysis	09/30/2020	100% 100% 100%	Q4BP1 Report	(1) We built a fluid flow model and refined using the prior fluid-injection history from the DFPS. We completed multiple simulations for different field injection scenarios. To obtain fracture conductivity changes over the fracture area and through time, we built a poroelastic model. (2) EM sensitivity analysis passed go-no-go criterion. (3) We performed elastic modeling and imaging of seismic data to further evaluate vertical seismic sensitivity to fracture dilation. Results showed that the dilated fracture cannot be imaged using a seismic survey with the current seismic sources and at the DFPS conditions.
6.1	N. Work Plan for Field Studies	12/31/2021	100%	Q6BP2	(1) We drilled a new monitoring well at the southwest corner of the previous survey area to find out if there is any EAP at that location. (2) We removed the surface 2” pipe and replaced it with a poly pipe. We were deployed to the DFPS in Q6BP2 and injected freshwater or 2500-ppm saltwater at various rates into the EAP-filled fracture
6.2–6.6	O. Smart Proppant Field Survey	3/31/2022	100%	Q6BP2 Report	(1) We performed the first set of injections at the DFPS in September 2020 and collected the CSEM, pressure, and flow-rate data. (2) We performed zero- and nonzero-offset iDAS™ VSP seismic surveys at the DFPS in May 2021. (3) We performed the second set of injections at the DFPS in January 2022 and collected the CSEM, pressure, salinity, tiltmeter, DAS, and flow-rate data. (4) We analyzed tiltmeter data to provide input for EM modeling. (5) We used salt as tracer and the breakthrough curves.

7.1	P. EM Inversion of Field Data	12/31/22	100%	Final Report	(1) We developed an inhomogeneous surface layered medium DGFD model for January 2022 experiment configurations and analyzed the scattered field misfit. We showed the misfit was the largest during maximum flow-rate change periods. By comparing the simulation results and an analytical solution for Streaming Potential (SP), we deduced a possible role of SP at various times of injection cycles. (2) Due to the large scattered field misfit and missing physics of SP in the EM model, we could not perform an accurate inversion of the field data.
7.2	Q. VSP/Seismic Imaging	12/31/22	100%	Final Report	(3) We performed elastic modeling and imaging of the seismic data to further evaluate vertical seismic sensitivity to fracture dilation. Results showed that the dilated fracture cannot likely be imaged using the available seismic sources and at the DFPS conditions.
7.3	R. Fluid Flow History Matching	12/31/22	100%	Final Report	(1) We conducted history matching of hydrogeological and geomechanical models based on the data collected from the DFPS in September 2020 and January 2022. (2) We incorporated the injection flow-rate profile in our poroelastic model to assess the dilated fracture area in each injection cycle.
3.1 BP2	F2. Laboratory Studies for HP/HS Responsive EAP and Cores-Mixing Rules	12/31/22	100%	Final Report	(1) Using sand column tests, we showed that flow through the proppant pack could induce SP, inferring a mechanism to explain large misfits of the EM models for the injection tests at the DFPS.

A.2 Depositional Systems and Facies in The Shallow Wilcox Group at The Devine Test Site, Medina County, Texas

Introduction and study area: Depositional systems and facies interpretations in the Wilcox Group in the Texas Gulf Coast are well-documented (Fisher and McGowen, 1967; Edwards, 1981; Galloway et al., 1983; 2011). The Wilcox Group has classically been interpreted to be a succession of fluvially dominated, wave-modified deltas in several depocenters (Fisher et al., 1969). A system of rivers defined by narrow (less than 4-mile or 6.4-kilometer wide), anastomosing percent-sandstone trends provided sediments to these deltaic complexes (Kaiser et al., 1978). However, Breyer and McCabe (1986), followed by recent studies including Ambrose and Zeng (2016), Zhang et al. (2016), Denison et al. (2017), Li et al. (2018), and Ambrose and Zhang (2018) also document tidal systems in the Wilcox Group. This appendix presents and summarizes tidal deposits and their implications for stratigraphic heterogeneity in shallow cores, less than 300-ft or 91.5-m deep, in the Wilcox Group at the Devine Test Site in Medina County, Texas.

Objectives, database, and methods: The two objectives of this study of the shallow Wilcox section at the DFPS were to 1.) describe and interpret facies and depositional systems for three cores at DFPS and 2.) characterize stratigraphic heterogeneity in these cores. This study used data from three cored wells: the Standard Oil No. 9 Wilson (Wilson-9) well, DMW 1, and DMW 3 (Figure A2-1). An open-hole wireline log (Figure A2-2) was acquired from an injection well located 10 ft (3 m) west-southwest of DMW 1 (inset map in Figure A2-1). This wireline log was used to relate the spontaneous potential (SP; different from streaming potential that is discussed in Subtask 3.1), gamma ray (GR), and resistivity (RES) curves to lithology in cores.

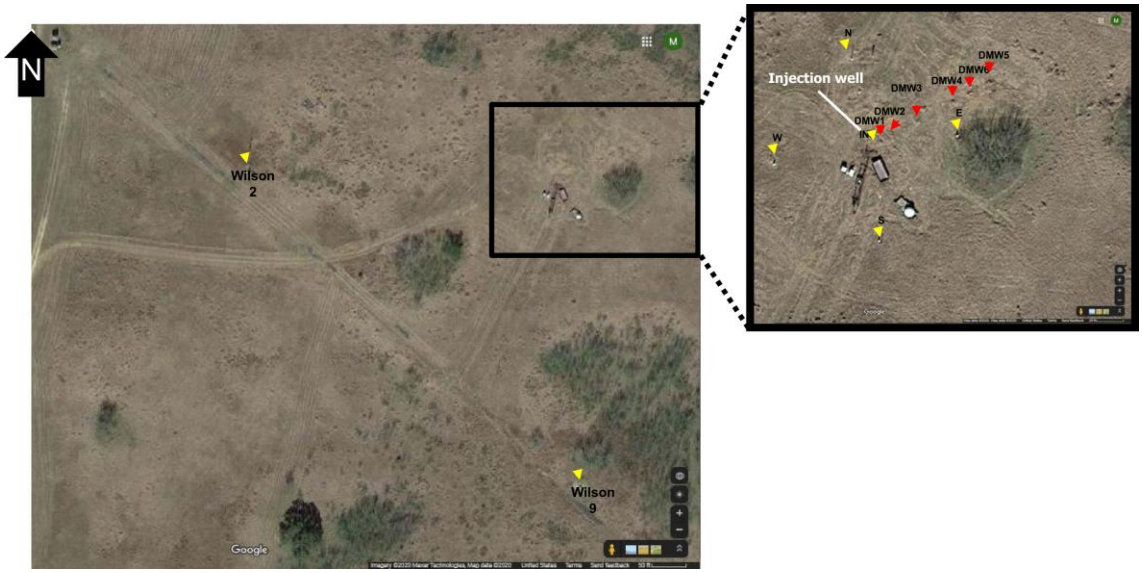

Figure A2-1: Study area showing the location of the cored wells.

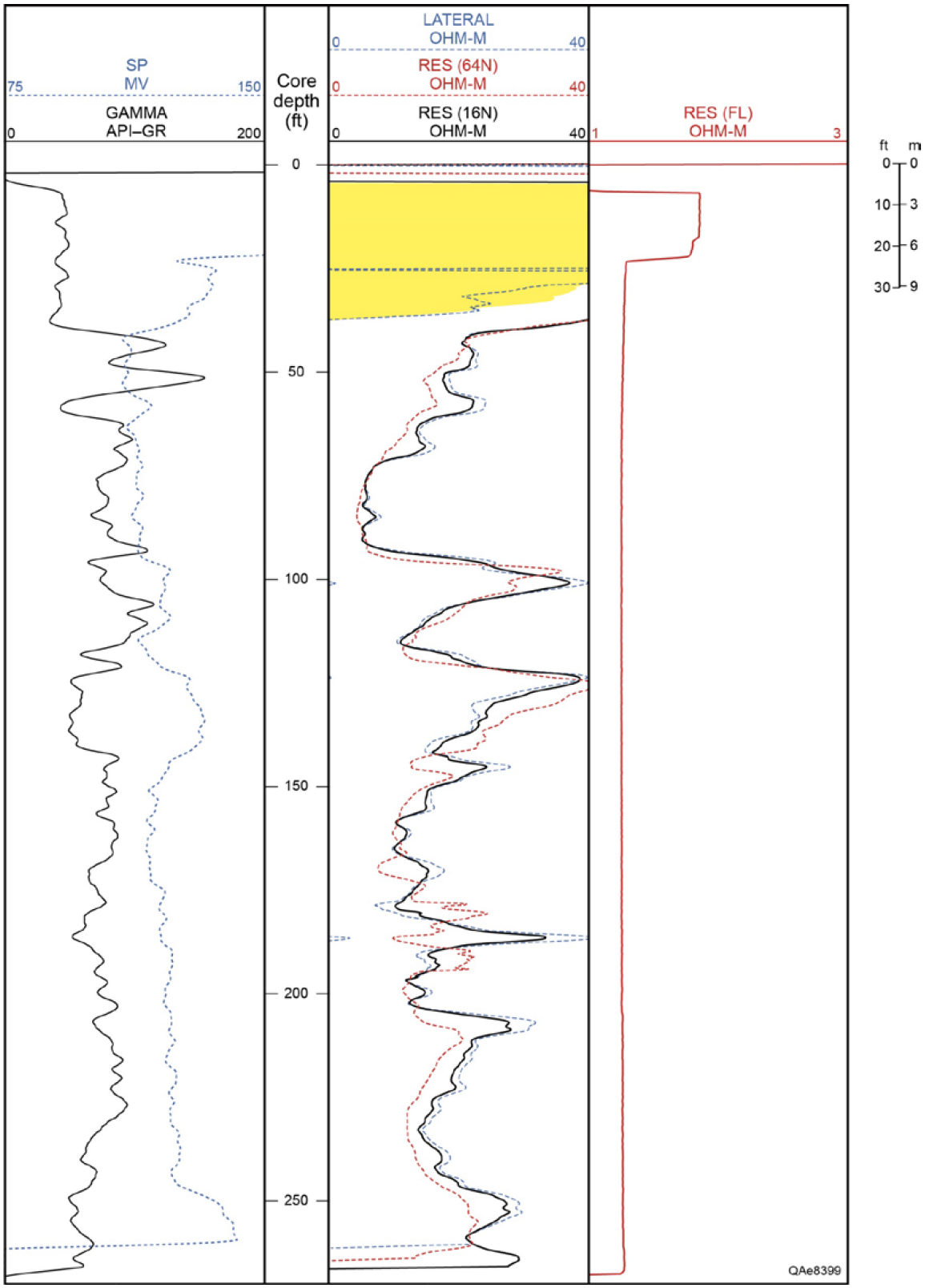

Figure A2-2: Wireline log from the injection well, with location shown in the inset map in Figure A2-1.

The Wilson-9 well is located approximately 250 ft (76.2 m) south of DFPS (Figure A2-1), and the corresponding retrieved core is located at the legacy core collection at the Bureau of Economic Geology. This core is used in this study because strata in this core are not distorted as a result of coring, in contrast to those in DMW-1 and DMW-3 cores. The Wilson-9 core contains approximately 12 ft (3.7 m) of section from the Wilcox Group, ranging from 201.4-to 216.6-ft (61.4- to 66.0-m) depth (Figure A2-3). The DMW-3 core was described from 110- to 190-ft (33.5- to 57.9-m) depth (Figure A2-4), of which the interval from 169- to 180-ft (51.5- to 54.9-m) depth was slabbed. The DMW-3 core is presented in this appendix before the DMW-1 core, because the proposed interval for injection in this study (169 to 180 ft or 51.5 to 54.9 m in the DMW-3 core) is mostly missing in the DMW-1 core. The DMW-1 core was described from 110- to 267-ft (33.5- to 81.4-m) depth (Figures A2-4, A2-5, A2-6). Approximately 35 ft (11 m) of this core was successfully slabbed, allowing for selected inspection of lithology and sedimentary structures. Data recorded in all three cores include grain size, stratification, contacts, as well as accessory features such as soft-sediment deformation, burrows, clay clasts, and organic fragments that are diagnostic of sedimentary processes and facies. These core descriptions were supplemented by photographs that illustrate bedforms, contacts, and important accessory features that aid in the interpretation of facies and depositional systems.

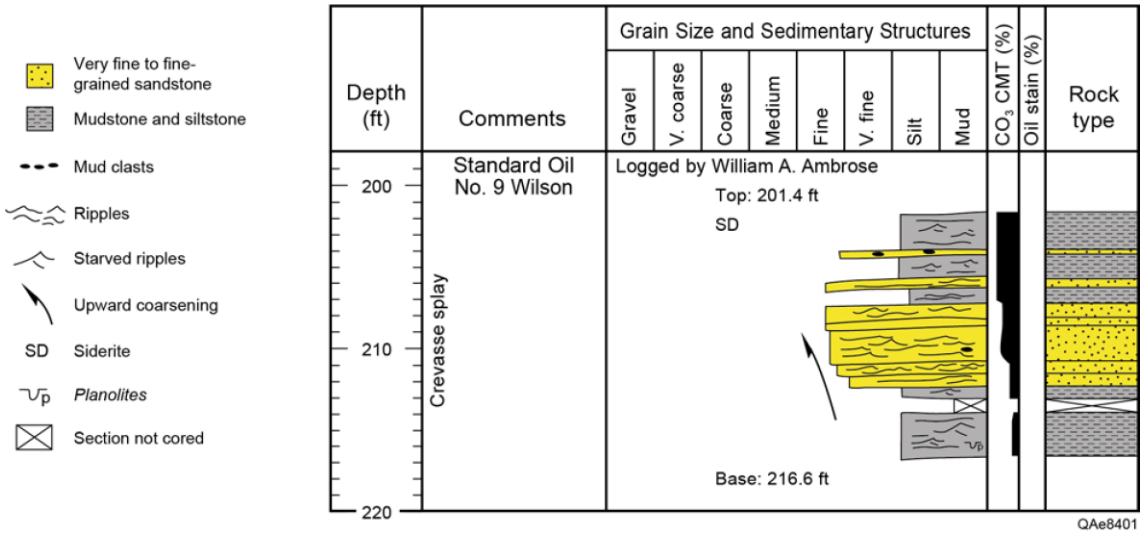

Figure A2-3: Description and interpretation of the Wilson-9 core retrieved from the depth interval of 201.4 to 216.6 ft (61.4 to 66.0 m). Wilson-9 well is shown in Figure A2-1. Several core photographs are shown in Figures A2-7 through A2-9.

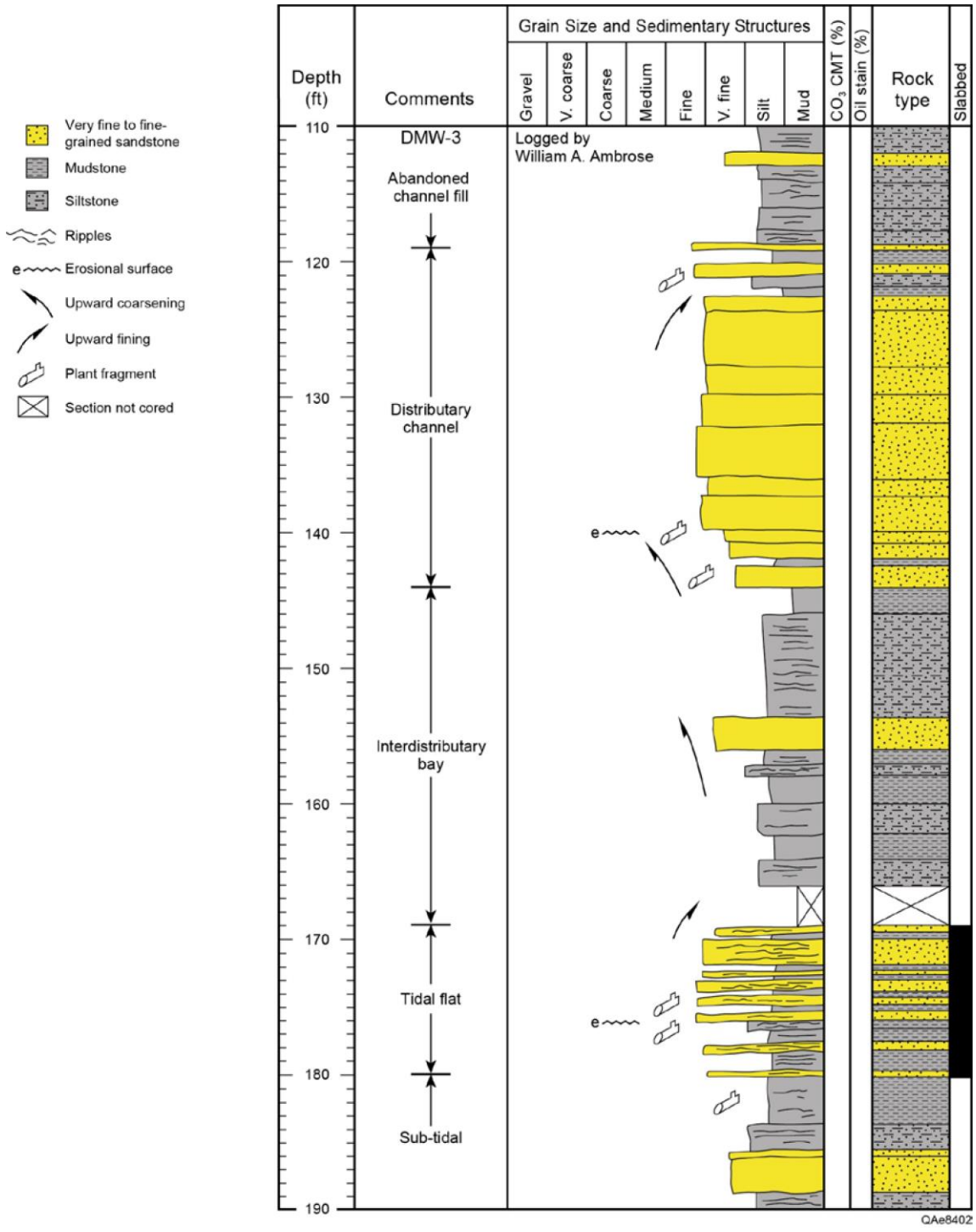

Figure A2-4: Description and interpretation of the DMW-3 core retrieved from the depth interval of 110 to 190 ft (33.5 to 57.9 m). DMW-3 well is shown in Figure A2-1. Several core photographs are shown in Figures A2-12 through A2-16.

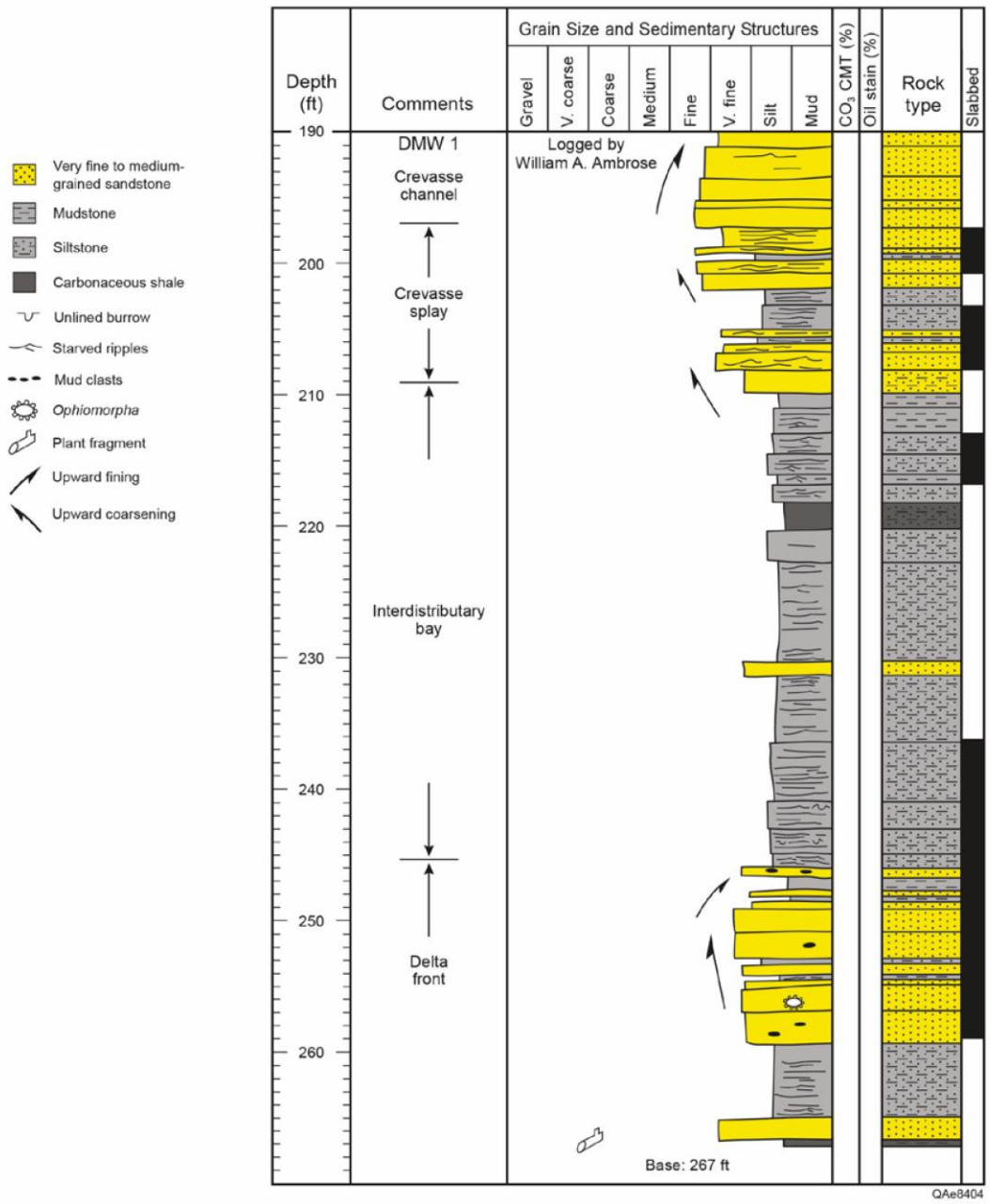

Figure A2-5: Description and interpretation of the DMW-1 core retrieved from the depth interval of 190 to 267 ft (57.9 to 81.4 m). DMW 1 is shown in Figure A2-1. Several core photographs are shown in Figures A2-19 through A2-26.

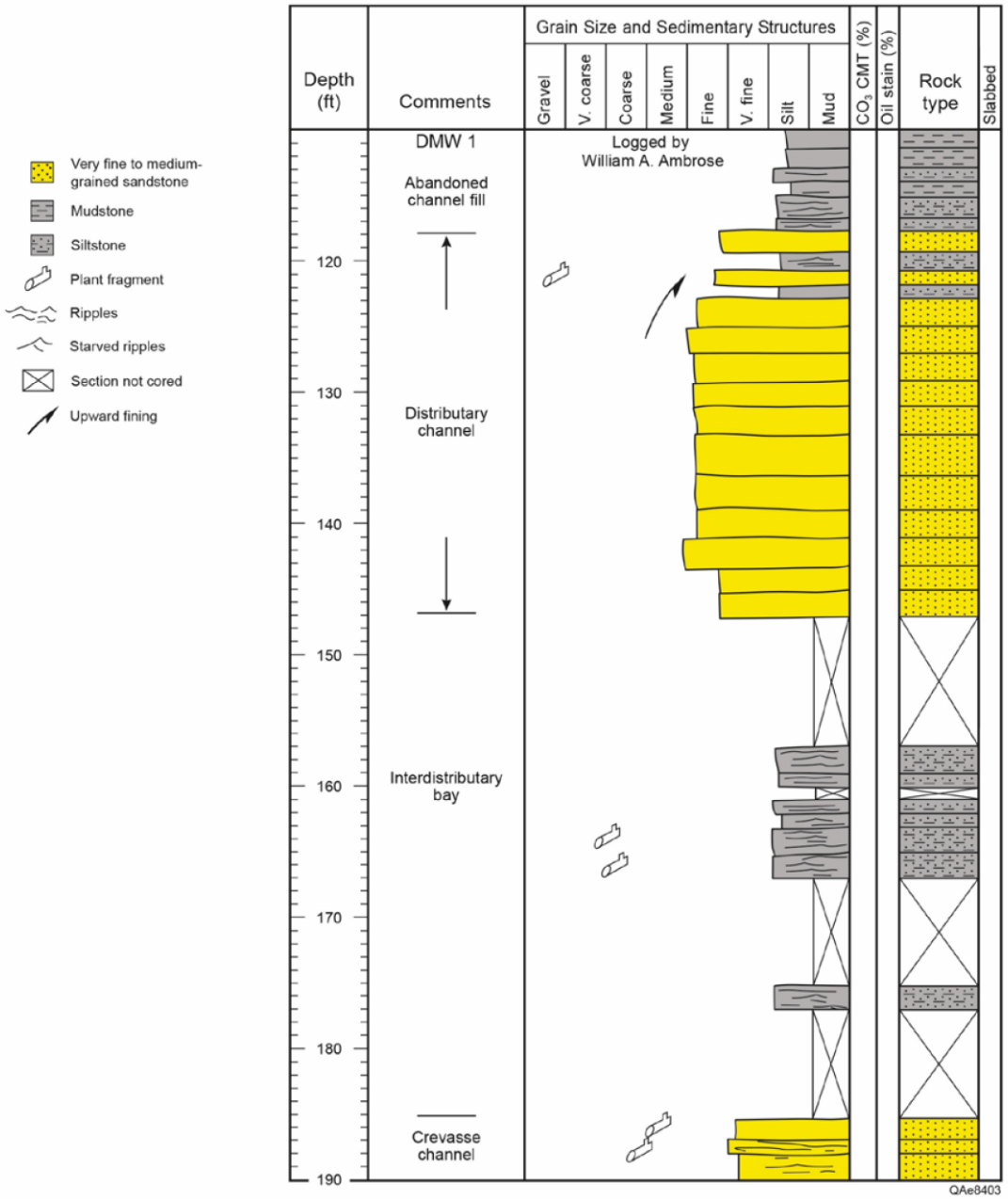

Figure A2-6: Description and interpretation of the DMW-1 core retrieved from the depth interval of 110 to 190 ft (33.5 to 57.9 m). DMW 1 is shown in Figure A2-1. Several core photographs are shown in Figures A2-19 through A2-26.

Wilson-9 core description and interpretation: The Wilson-9 core contains a short, 12.2-ft (3.7-m) section in the Wilcox Group (Figure A2-3). The base of the section, from 213.5- to 216.6-ft (65.1- to 66.0-m) depth consists of an upward-coarsening interval with silty mudstone at the base with thin (millimeter-to-centimeter scale), lenticular beds of very fine-grained sandstone (Figure A2-7). Minor accessory features include microfaults (Figure A2-7a) and oxidized wood fragments (Figure A2-7b). The basal section of very fine-grained sandstone is overlain abruptly by a section of fine-grained sandstone at 212.5-ft (64.8-m) depth (Figures A2-3 and A2-8a). This middle section of fine-grained sandstone is slightly upward-coarsening and extends to 207.5-ft (63.3-m) depth. It is

composed primarily of mud-draped, ripple-stratified sandstone. Many of these mud drapes occur in thin, millimeter-scale couplets (Figures A2-8b, c). The middle, sandy section is overlain by a muddy section to the top of the core at 201.4-ft (61.4-m) depth (Figure A2-3). With the exception of two, thin (<6-inch or 15.2-cm) beds of fine-grained sandstone, this upper section is composed of very fine-grained sandstone and 5- to 10-mm mudstone drapes (Figure A2-9). The relative proportion of mudstone versus sandstone in this upper section increases upward. These mudstone drapes are cyclic, commonly occurring at intervals ranging from 0.3 to 0.43 inches (0.7 to 1.1 cm).

The cored section in the Wilson-9 core consists of a middle, sandy section of crevasse-splay deposits bounded above and below by tidally modified interdistributary deposits (Figure A2-3). A mesotidal interpretation (diurnal tidal range between 6.6 and 13.2 ft or 2 to 4 m) (Davies, 1964) for this section is based on the presence of 1.) flaser bedding, consisting of mud-encased, lenticular sandstone beds that record fluctuating depositional energy (Figures A2-7b, c); 2.) double-mud-draped ripples (Figures A2-8a, b); and 3.) cyclic beds of mud layers that occur at approximately evenly spaced intervals (Figure A2-9).

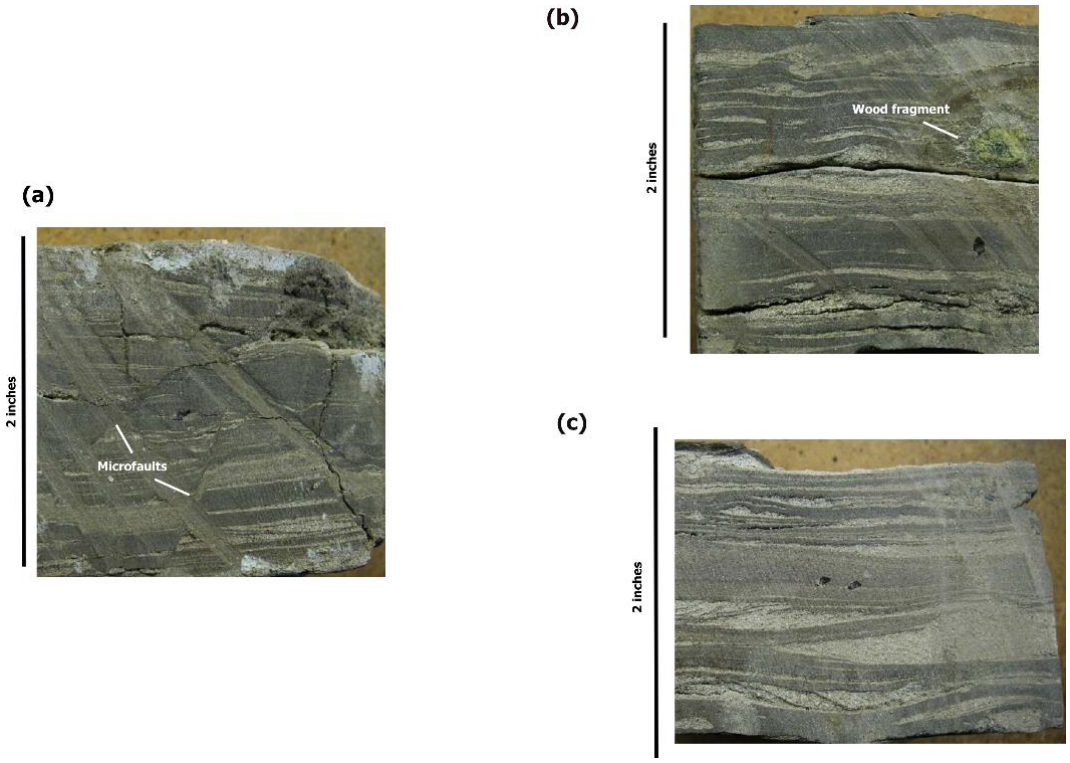

Figure A2-7: Photographs of tidally modified interdistributary facies in the Wilson-9 core. (a) Silty mudstone with thin (<1 cm) beds of very fine-grained sandstone at 214.9-ft (65.5-m) depth, featuring microfaults. (b) Lenticular beds of very fine-grained sandstone with silty mudstone and oxidized wood fragment at 214.5-ft (65.4-m) depth. (c) Flaser bedding, consisting of lenticular beds of very fine-grained sandstone encased in silty mudstone at 213.9-ft (65.2-m) depth. Small black patches in photographs (b) and (c) are ink marks. The corresponding core description is shown in Figure A2-3.

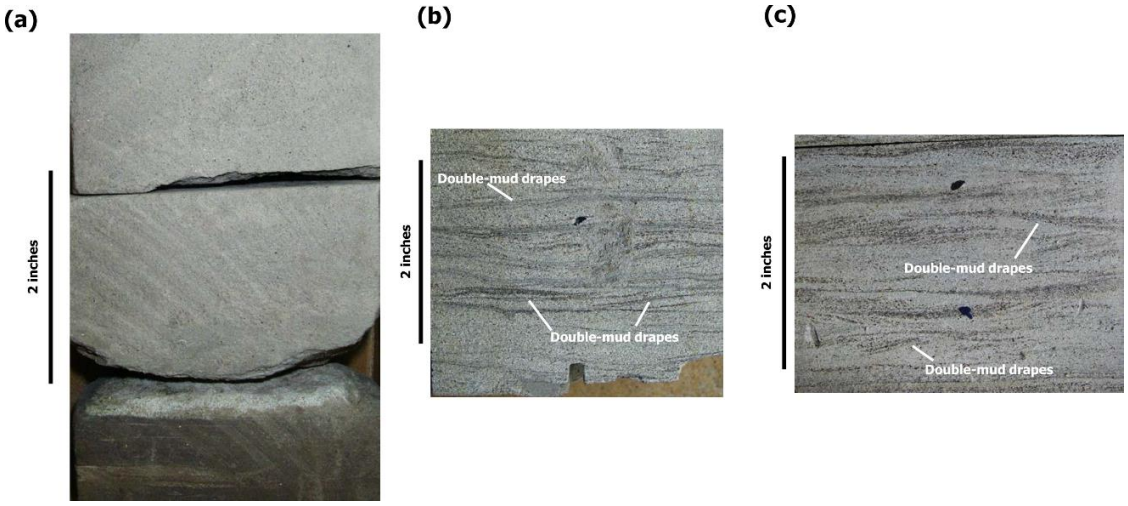

Figure A2-8: Photographs of crevasse-splay facies in the Wilson-9 core. (a) Fine-grained sandstone at the sharp base of crevasse splay at 212.5-ft (64.8-m) depth. (b) Fine-grained, ripple-stratified sandstone with millimeter-scale mud drapes at 210.7-ft (64.2-m) depth. (c) Fine-grained, ripple-stratified sandstone with thin, discontinuous mud drapes at 208.5-ft (63.6-m) depth. Many of these mud drapes occur in couplets. Small black patches in photographs (b) and (c) are ink marks. The corresponding core description is shown in Figure A2-3.

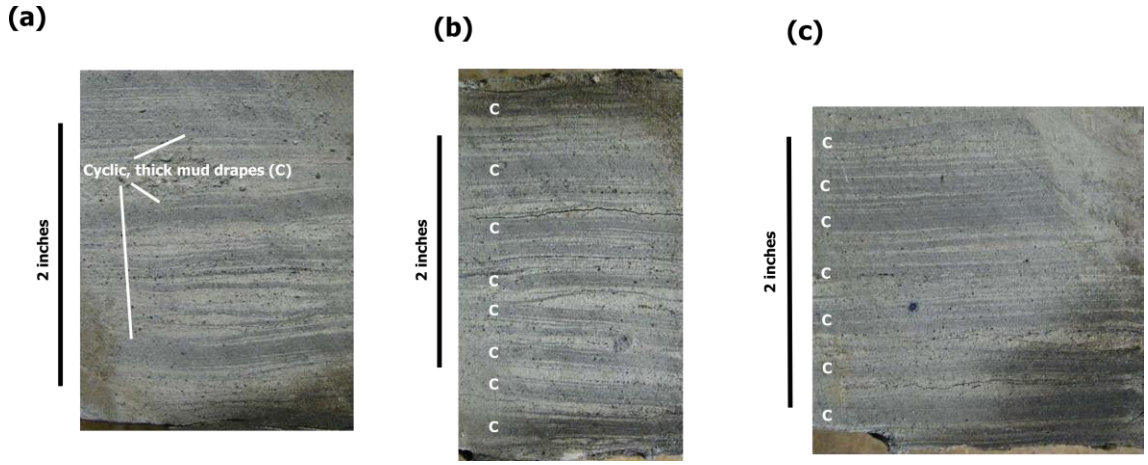

Figure A2-9: Photographs of thick (5 to 10-mm), cyclic mud drapes in the Wilson-9 core in tidally modified interdistributary facies above crevasse-splay deposits depicted in Figure A2-8. These thick mud drapes are denoted with capital letter C in photographs (b) and (c). (a) Sandstone-dominant section at 204.8-ft (62.4-m) depth. (b) Nearly equally thick beds of sandstone and mudstone at 204.5-ft (62.3-m) depth. (c) Mudstone-dominant section at 204.0-ft (62.2-m) depth. The corresponding core description is shown in Figure A2-3.

Flaser bedding is common in tidally modified settings, where alternating flood currents and slack-water, suspension sedimentation produce lenticular, mud-draped ripples (Figure A2-10) (Reineck and Wunderlich, 1968; de Raaf and Boersma, 1971; Reineck and Singh, 1973; Mutti et al., 1985; Dalrymple, 1992; Bellile, 2003). Double-mud-draped ripples record diurnal and/or semi-diurnal tides, in which each mud drape is the result of slack-water conditions between each cycle of flood- and ebb-tides (Visser, 1980; Dalrymple, 1992) (Figure A2-11).

Cyclic beds of muddy layers such as those in Figure A2-9 also record tidal cycles. Thickest mud layers in these types of bedding commonly represent sustained periods of suspension sedimentation

and are associated with relatively weaker neap tides. They are preserved only where reworking fluvial and wave processes are weak. Examples in the rock record include the Pennsylvanian in the Illinois Basin (Kvale et al., 1989; Kvale and Archer, 1990) and the Anadarko Basin (Ambrose et al., 2015).

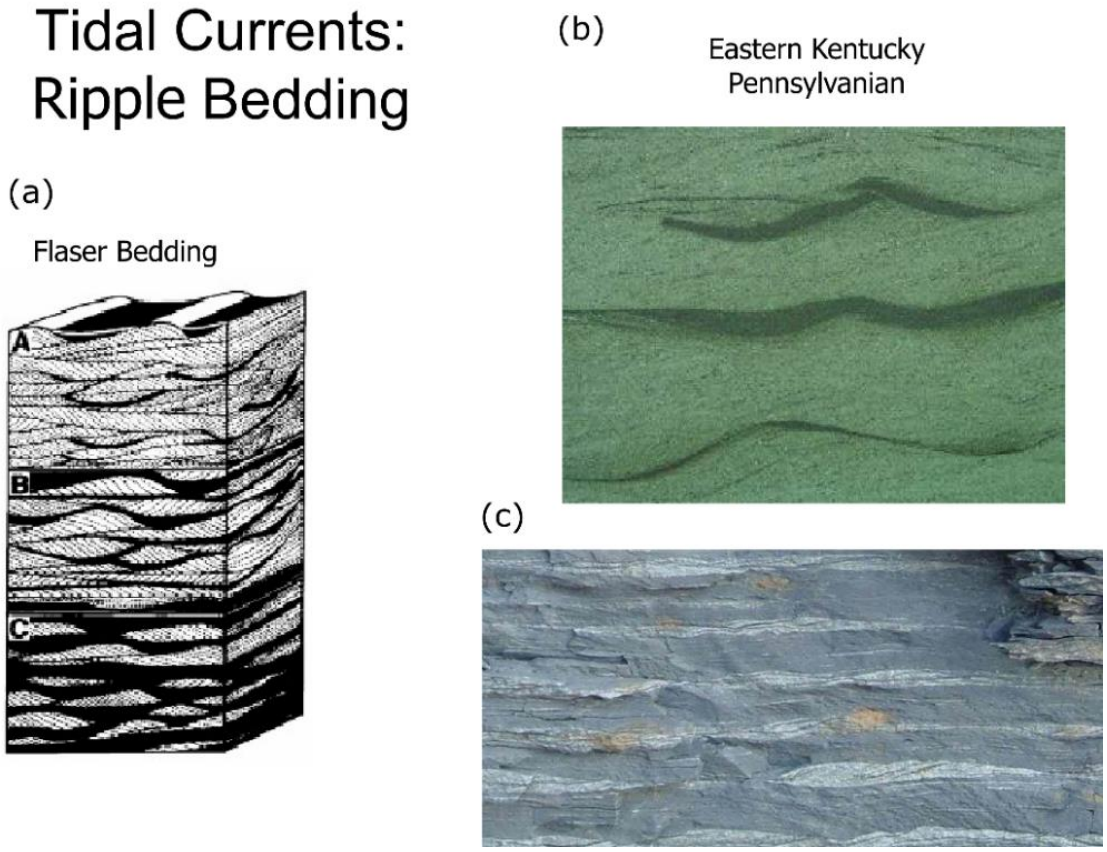

Figure A2-10: (a) Flaser bedding, ranging from A (sandy), to B (intermediate sandy), and to C (muddy). (b, c) Examples of flaser bedding from Pennsylvanian-age outcrops in eastern Kentucky. Modified from Reineck and Singh (1973) and Bellile (2003).

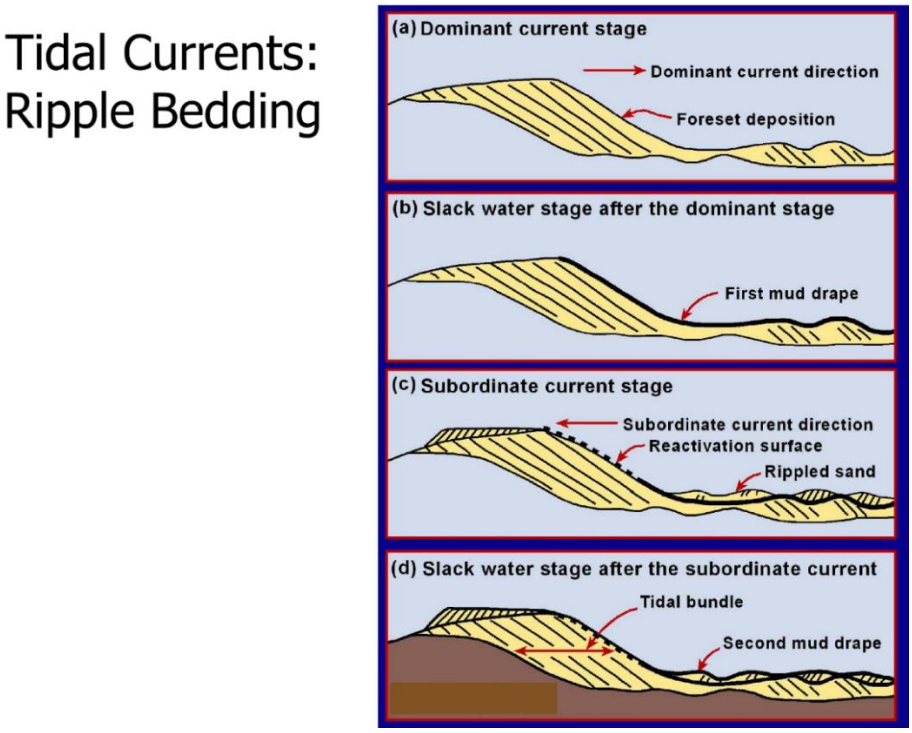

Figure A2-11: Origin of double-mud drapes in tidally modified depositional systems. Modified from Visser (1980) and Dalrymple (1992).

DMW-3 well core description and interpretation: The DMW-3 core, described from 110- to 190-ft (33.5- to 57.9-m) depth, is composed of two main sandy zones, with a lower sandy zone from 169- to 180-ft (51.5- to 54.9-m) depth and an upper sandy zone from 123- to 144-ft (37.5- to 43.9-m) depth (Figure A2-4). The lower sandy zone is composed of very fine to fine-grained, sandstone beds with abundant mud drapes and discontinuous lenses of mudstone (Figures A2-12 and A2-13). Several types of bedding occur within the sandy zone from 169- to 180-ft (51.5- to 54.9-m) depth, including muddy heterolithic, sandy heterolithic, sandy, and muddy beds (Figure A2-12). Muddy heterolithic beds consist of continuous, millimeter-scale mudstone beds with subordinate lenses of sandstone (Figure A2-12a). They are commonly truncated by 1- to 1.5-inch (2.5- to 3.8-cm) sandy beds that consist of very fine to fine-grained sandstone (Figure A2-12a). Sandy heterolithic beds are composed predominantly of fine-grained sandstone with minor amounts of mudstone occurring as discontinuous drapes and lenses (Figures A2-12b, A2-13). Many of these muddy drapes occur as doublets (Figure A2-13b). Muddy beds range in thickness from 2 to 4 inches (5.1 to 10.2 cm) and are composed of mudstone with thin (millimeter-scale) laminae of very fine-grained sandstone (top of Figure A2-12a). The upper 5 ft (1.5 m) in the lower sandy zone from 169- to 174-ft (51.5- to 53.0-m) depth is upward-fining, grading upward from fine-grained sandstone to very fine-grained sandstone interbedded with siltstone and mudstone (Figure A2-4).

The lower sandy zone is overlain by a muddy section that extends from 144- to 169-ft (43.9- to 51.5-m) depth (Figure A2-4). This muddy section is composed of muddy siltstone and thin (<2-ft or 0.6-m) sandy beds with discontinuous, muddy drapes (Figures A2-14a,b, respectively). Sandy components within these muddy siltstone beds occur either as round-shaped *Planolites* (described by Pemberton and Frey, 1982; Frey and Bromley, 1985; Pemberton et al., 1992*)* or discontinuous lenses (Figures A2-15a,b, respectively).

The upper, sandy section that extends from 123- to 144-ft (37.5- to 43.9-m) depth consists of a basal, 4-ft (1.2-m) section of very fine-grained sandstone (Figure A2-4). It is overlain abruptly by fine-grained sandstone at 140-ft (42.7-m) depth (Figure A2-4). Because of the disaggregated nature of the sandstone in this section, no stratification is preserved. The sandstone is moderately well-sorted and ranges in color from orange-brown-yellow to yellowish gray (Figures 16a,b).

The upper 13 ft (4 m) of the core is composed of muddy siltstone with three thin (<1-ft or 0.3-m) beds of very fine and fine-grained sandstone (Figure A2-3). The base of this muddy, upper section is marked by a 1-ft (0.3-m) thick zone of carbonaceous, silty mudstone with streaks and lenticular beds of very fine-grained sandstone (Figure A2-16c).

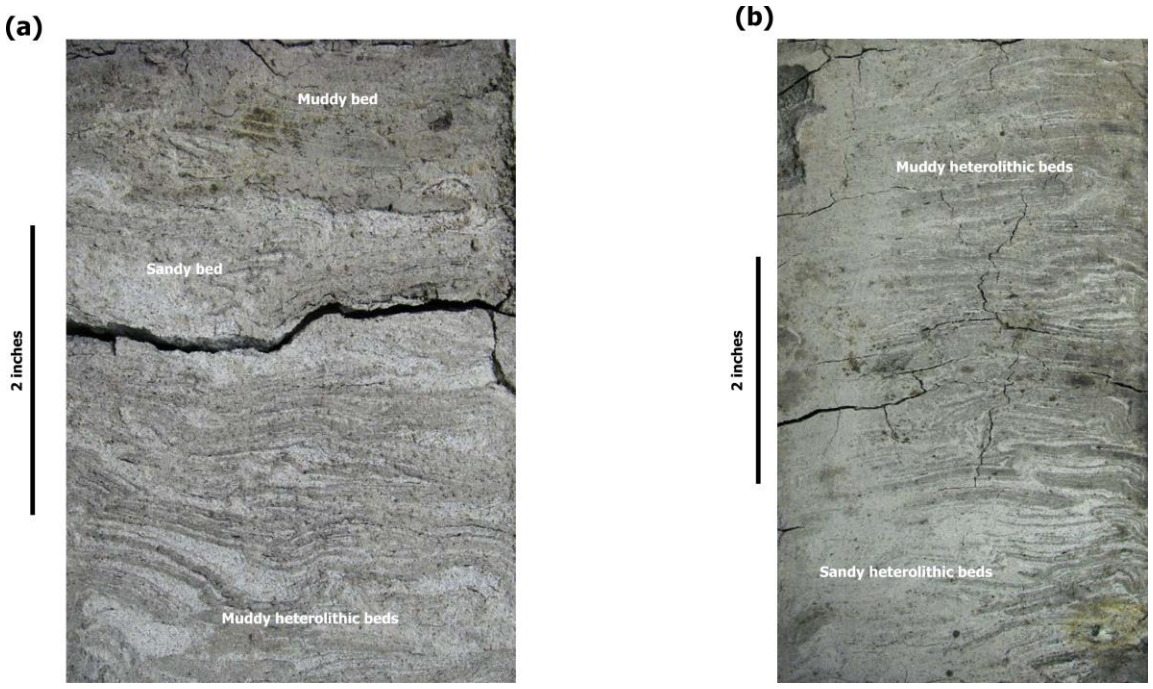

Figure A2-12: Photographs of tidal-flat facies in the DMW-3 core. (a) Basal section of muddy, heterolithic section composed of interbedded, very fine-grained sandstone and mudstone, overlain by sandy and muddy beds at 180.0-ft (54.9-m) depth. (b) Sandy and muddy heterolithic sections at 177.0-ft (54.0-m) depth. The corresponding core description is shown in Figure A2-4.

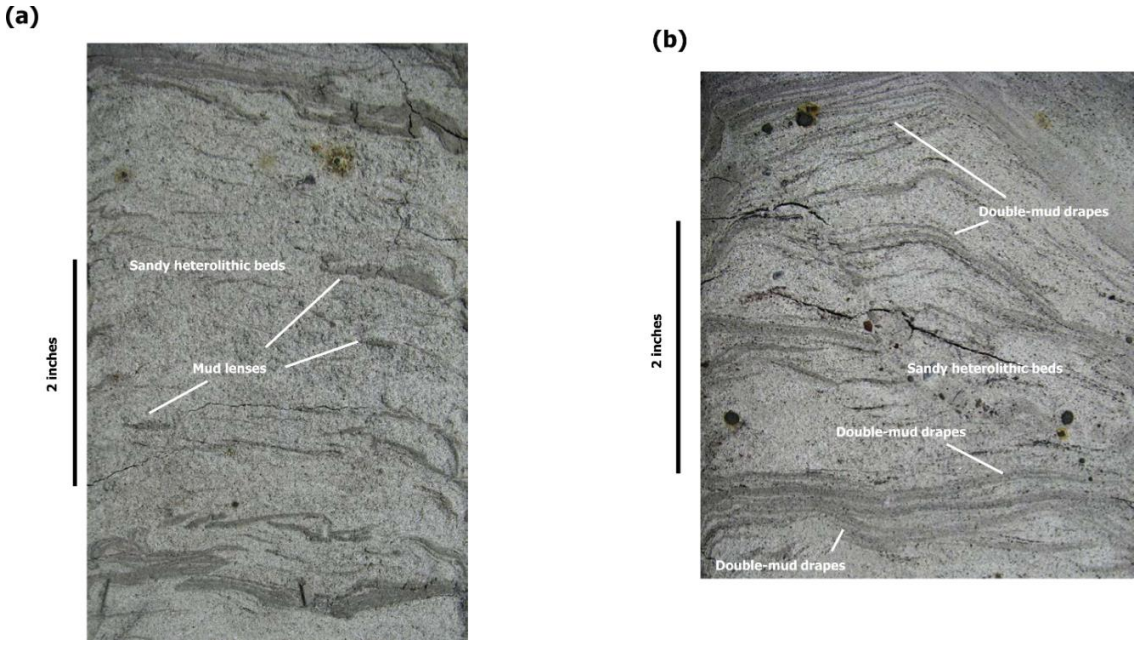

Figure A2-13: Photographs of sandy heterolithic beds in tidal-flat facies in the DMW-3 core. (a) Fine-grained sandstone with discontinuous muddy lenses at 175.0-ft (53.4-m) depth. (b) Very fine-grained sandstone with abundant mud drapes at 172.4-ft (52.6-m) depth. The corresponding core description is shown in Figure A2-4.

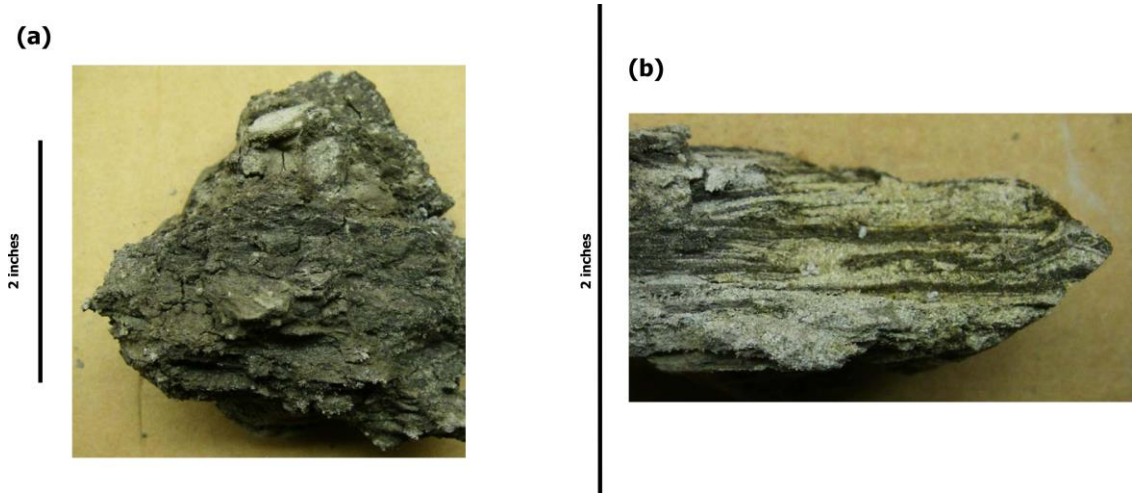

Figure A2-14: Photographs of muddy, non-framework facies in the DMW-3 core. (a) Silty mudstone in tidally modified interdistributary facies at 165.0-ft (50.3-m) depth. (b) Very fine-grained sandstone with thin mud drapes in distal-crevasse-splay facies at 157.5-ft (48.0-m) depth. The corresponding core description is shown in Figure A2-4.

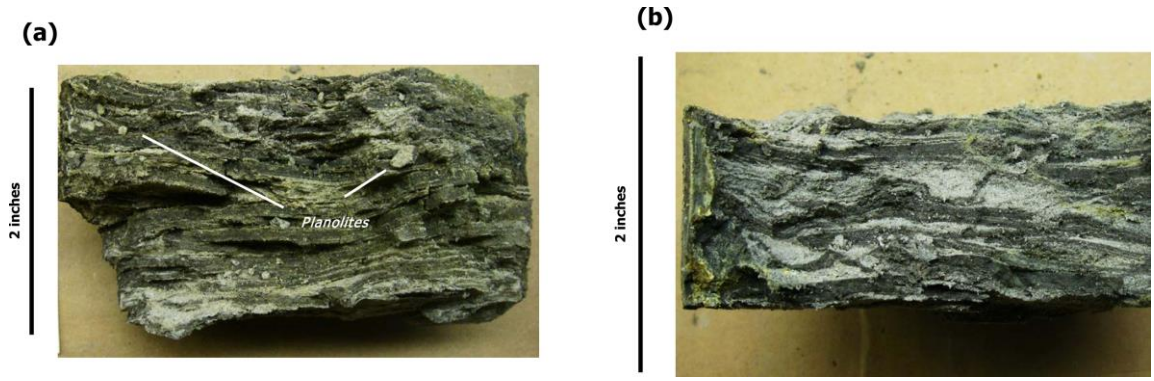

Figure A2-15: Photographs of tidally modified interdistributary facies in the DMW-3 core. (a) Silty mudstone with thin (millimeter-scale) beds of very fine-grained sandstone and minute Planolites at 153.3-ft (46.7-m) depth. (b) Silty mudstone with lenticular beds of very fine-grained sandstone at 147.0-ft (44.8-m) depth. The corresponding core description is shown in Figure A2-4.

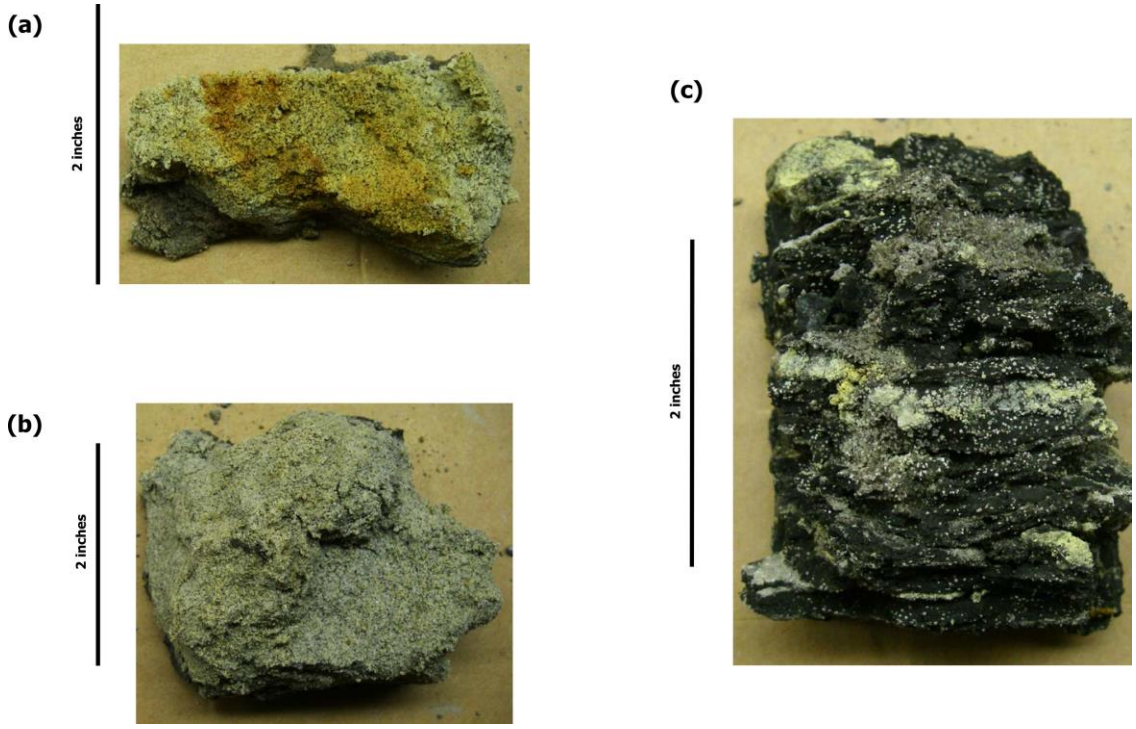

Figure A2-16: Photographs of channel-fill sands and overlying, thin (<1 ft or 30 cm) marsh deposit in the DMW-3 core. (a) Orange-yellow, fine-grained, unconsolidated sand at 131.0-ft (39.9-m) depth. (b) Yellow-gray, very fine to fine-grained, unconsolidated sand at 125.3-ft (38.2-m) depth. (c) Carbonaceous, silty mudstone and minor streaks and lenticular, very fine-grained sand beds in marsh facies at 121.0-ft (36.9-m) depth. The corresponding core description is shown in Figure A2-4.

The lower sandy zone from 169- to 180-ft (51.5- to 54.9-m) depth in the DMW-3 core represents tidal-flat deposits. This interpretation is based on 1.) a heterolithic succession of thin sandy and muddy beds; 2.) the abundance of mud drapes and discontinuous lenses of sandstone and mudstone; 3.) an upward-fining vertical grain-size profile at the top; and 4.) its association with muddy siltstones of shallow-marine origin.

Sediments in the lower sandy zone are tidalites within a tidal-flat succession. Modern depositional analogs include the North Sea coast of northern Netherlands and Germany (Van Stratten and Kuenen, 1958; Klein, 1971; Terwindt, 1971; Roep, 1991) and the southeastern coast of England (Evans, 1965). Examples from the rock record include the Lower Precambrian Pongola Supergroup in South Africa (von Brunn and Hobday, 1976), the Eocene Sabinetown Formation at Bastrop, Texas (Figure A2-17), the Eocene Misoa Formation in the Maracaibo Basin in Venezuela (Maguregui and Tyler, 1991; Ambrose et al., 1995), the Pennsylvanian Douglas and Tonkawa Formations in the Anadarko Basin in the Texas Panhandle (Ambrose et al., 2015), and tidal-flat facies at the Wash, the United Kingdom (Figure A2-18).

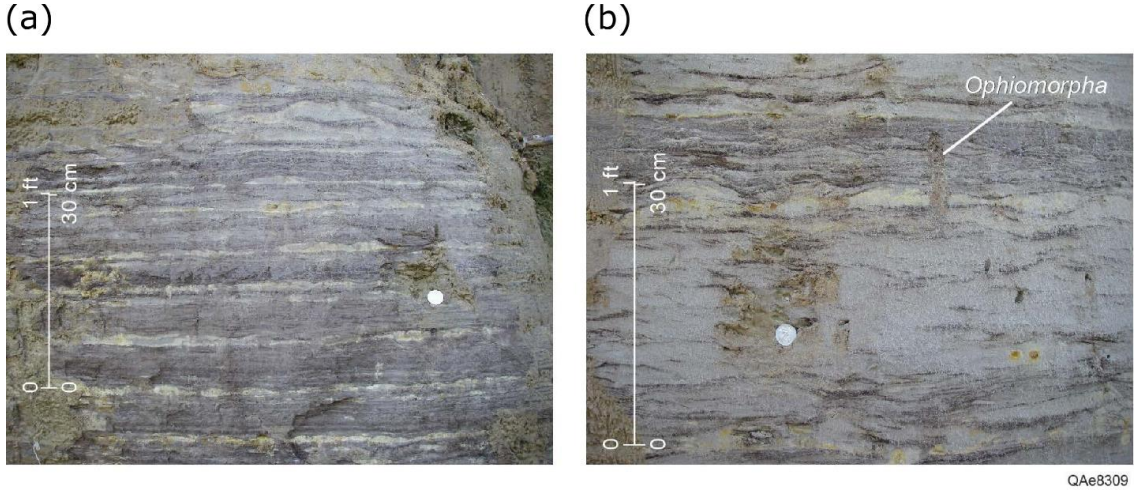

Figure A2-17: (a) Photograph of tidal-flat deposits, consisting of lenticular, ripple-stratified beds of very fine-grained sandstone interbedded with silty mudstone in the upper part of the Eocene Sabinetown Formation at Copperas Creek, southeast of Bastrop, Texas. (b) Closer view of (a), with lenticular beds of very fine-grained sandstone crosscut by Ophiomorpha.

Figure A2-18: Photograph of meandering tidal channel within tidal-flat facies at the Wash in the United Kingdom. Photograph by G. Evans, featured in Weimer et al. (1982).

Tidal flats are commonly upward-fining, grading upward from flaser-bedded sand and silts ("tidal bedding" after Wunderlich, 1970) to mudstone with lenticular beds of very fine-grained sand and silt (Reineck, 1967; Klein, 1971; Weimer et al., 1982). Alternating beds of sand and mud record fluctuating energy as a result of tidal currents followed by periods of slackwater deposition (Roep, 1991). These types of successions occur in embayments with tidal activity (Reineck, 1967), lagoonal tidal flats (Van Straaten and Kuenen, 1958), and along open coastlines with embayed areas (Evans, 1965, 1970).

The muddy section that extends from to 144- to 169-ft (43.9- to 51.5-m) depth represents low-energy, tidally modified interdistributary deposits (Figure A2-4). *Planolites* (Figure A2-15a) indicates a marine origin. It is overlain by a 4-ft (1.2-m) thick section of upward-coarsening sandstones, in turn, abruptly overlain by a 17-ft (5.2-m) thick section of fine-grained sandstone (Figure A2-4). This 4-ft (1.2-m) thick, upward-coarsening section is a crevasse-splay deposit truncated by a distributary-channel sandstone section at 140-ft (42.7-m) depth (Figure A2-4). The top of the distributary-channel deposit is marked by an upward-fining section at 123-ft (37.5-m) depth that represents abandoned-channel-fill facies.

DMW-1 core description and interpretation: The DMW-1 core is described from 110- to 267-ft (33.5- to 57.9-m) depth (Figures A2-5, A2-6). As in the DMW-3 core, it contains several sandy zones separated by muddy sections of mudstone with thin (<2-ft or 0.6-m) beds of siltstone and very fine-grained sandstone. Four main sandy zones occur from 1.) 245- to 259-ft (74.7- to 79.0-m) depth; 2.) 199- to 210-ft (60.7- to 64.0-m) depth; 3.) 186- to 202-ft (56.7- to 61.6-m) depth; and 4.) 117- to 147-ft (35.7- to 44.8-m) depth (Figures A2-5, A2-6).

The basal sandy zone 1 from 245- to 259-ft (74.7- to 79.0-m) depth is slightly upward-coarsening, ranging from very fine-grained sandstone at the base to very fine to fine-grained sandstone at the top. Bedding is indistinct because the core is unconsolidated. The section contains small (millimeter-scale) mud clasts and a possible *Ophiomorpha* burrow (Figure A2-5). This sandy zone is overlain by a heterogeneous and muddy section of finely interbedded mudstone and silty, very fine-grained sandstone beds (Figure A2-19). Stratification in this heterogeneous section is poorly preserved because the bedding has been distorted in the coring process, although the mottled texture at the base of the photograph in Figure A2-19a may record burrowing by marine organisms. The finely interbedded nature of this muddy section is present throughout the section, up to the base of sandy zone 2 at 210-ft (64.0-m) depth. Stratification is indistinct, although thin (<1-cm) ripples are observed locally (Figure A2-20a). The other stratification consists of thin, millimeter-scale, sandy laminae interbedded with mudstone (Figure A2-20b). Mudstone beds occur at regular 0.8- to 1.2-inch (2.0- to 3.0-cm) thick intervals in some sections (indicated by letter M in Figure A2-20b). Microfaults also occur in the section (Figure A2-20b), although they may be coring-induced.

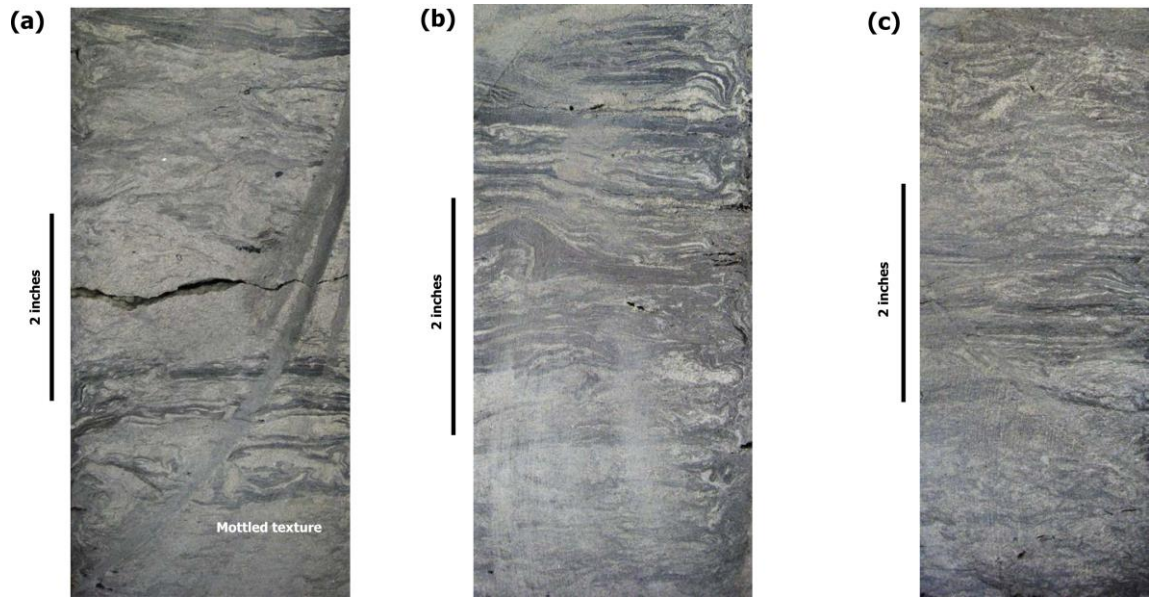

Figure A2-19: Photographs of tidally influenced, interdistributary-bay deposits in the DMW-1 core. (a) Mottled, very fine-grained sandstone interbedded with thin (millimeter-scale) mudstone beds at 245.5-ft (74.8-m) depth. Inclined, dark-gray streaks are saw marks. (b) Two-inch (5.1-cm) zone of very fine-grained sandstone and thin, millimeter-scale beds of mudstone overlain by mud-dominated zone with thin sandstone beds at 244.5-ft (74.5-m) depth. (c) Mottled bedding with 1.5-inch (3.8-cm) zone in the middle of the section composed of continuous beds of mudstone and thin sandy laminae at 243.8-ft (74.3-m) depth. The corresponding core description is shown in Figure A2-5.

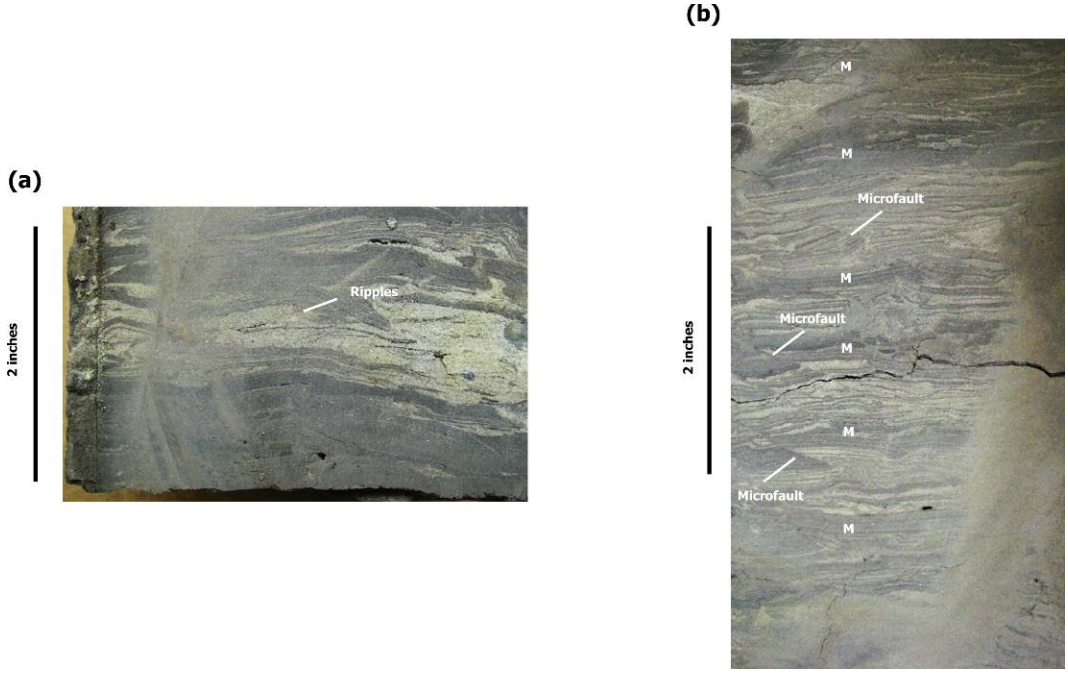

Figure A2-20: Photographs of tidally influenced, interdistributary-bay deposits in the DMW-1 core. (a) Ripple stratification in very fine-grained sandstone beds encased in mudstone at 216.5-ft (66.0-m) depth. (b) Cyclic beds of mudstone (denoted by letter M) and 0.8- to 1.2-inch (2.0- to 3.0-cm) beds of thin sandy laminae at 214.0-ft (65.2-m) depth. Low-angle microfaults are also present. The corresponding core description is shown in Figure A2-5.

Sandy zone (2) extends from 199- to 210-ft (60.7- to 64.0-m) depth (Figure A2-5). It is composed of two upward-coarsening sections, with a lower section that extends from 205- to 210-ft (62.5- to 64.0-m) depth. The upper section ranges from 199- to 202.5-ft (60.7- to 61.7-m) depth. Cyclic mudstone beds also occur in both of these upward-coarsening sections (Figures A2-21, A2-22). These cyclic mudstone beds occur either as discrete, continuous layers that extend across the face of the core, or as irregular beds that merge and encase lenticular sandy beds, as shown in Figures A2-21a and A2-21b, respectively.

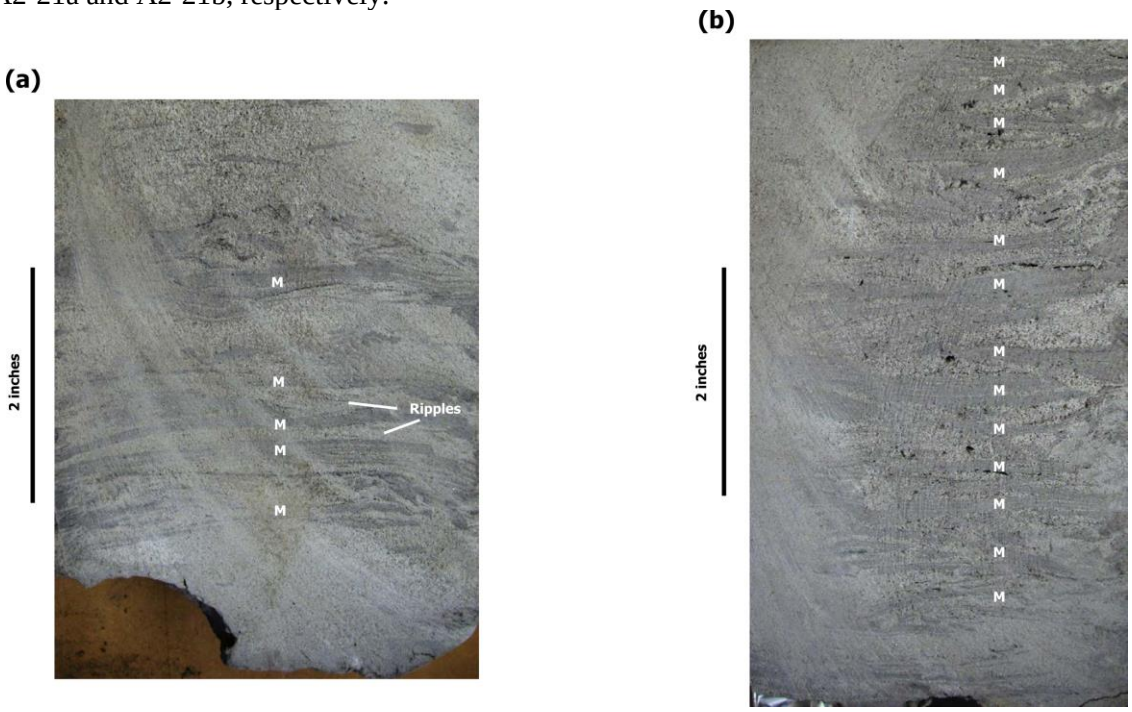

Figure A2-21: Photographs of tidally influenced, crevasse-splay deposits in the DMW-1 core. (a) Cyclic mudstone beds (denoted by letter M) draping ripple-stratified beds of very fine to fine-grained sandstone beds at 207.5-ft (63.3-m) depth. (b) Cyclic beds of mudstone (denoted by letter M) and lenticular beds of very fine-grained sandstone at 205.0-ft (62.5-m) depth. The corresponding core description is shown in Figure A2-5.

Another sandstone-rich zone (3) extends from 186- to 198-ft (56.7- to 60.4 m) depth (Figures A2-5, A2-6). It has an upward-fining grain-size profile, ranging from fine-grained sandstone at the base to very fine to fine-grained sandstone at the top. Stratification in this section consists primarily of migrating ripples with organic-rich, mud drapes (Figure A2-23). Plant fragments occur from 186- to 188-ft (56.7- to 57.3-m) depth (Figure A2-6).

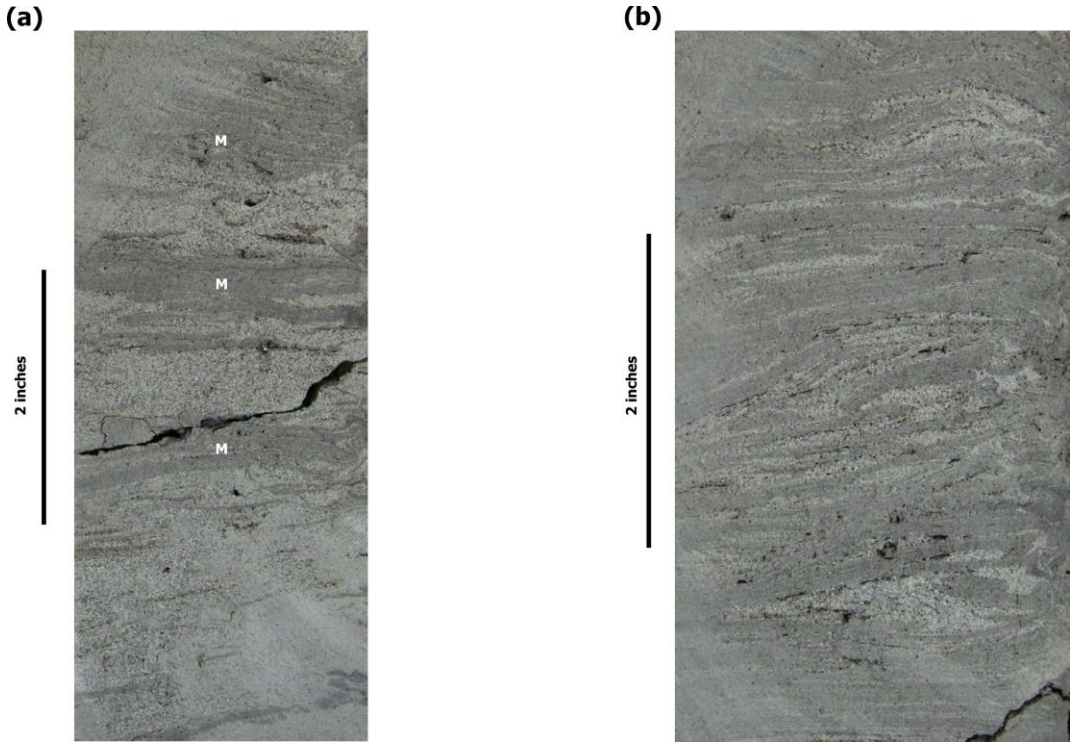

Figure A2-22: Photographs of tidally influenced, crevasse-splay deposits in the DMW-1 core. (a) Cyclic mudstone beds (denoted by letter M) and irregular, poorly stratified beds of fine-grained sandstone beds at 200.0-ft (61.0-m) depth. (b) Mud-dominated section with lenticular beds of fine-grained sandstone at 198.0-ft (60.4-m) depth. The corresponding core description is shown in Figure A2-5.

Figure A2-23: Photograph of ripple-stratified, fine-grained sandstone in crevasse-channel facies in the DMW-1 core at 187.0-ft (57.0-m) depth. The corresponding core description is shown in Figures A2-5 and A2-6.

A poorly recovered, muddy section occurs above sandy zone (3) (Figure A2-6). It is composed of mudstone with thin (millimeter-scale) beds of very fine grained, lenticular sandstone and siltstone (Figure A2-24). This muddy section is overlain by the thickest and most coarse-grained sand in the DMW-1 core (Figure A2-6). Because this sand is unconsolidated, sedimentary structures are not observed. It exhibits several hues that include yellowish-gray, yellow, and gray, a function of the degree of iron-oxide staining (Figure A2-25). This 30-ft (9-m) thick sand grades upward into a muddy section that extends to the top of the core (Figure A2-6). This muddy section consists of gray mudstone with thin (millimeter-scale) beds of very fine grained, lenticular sandstone (Figure A2-26a) and organic-rich, dark mudstone with laminae composed of very fine-grained sandstone (Figure A2-26b).

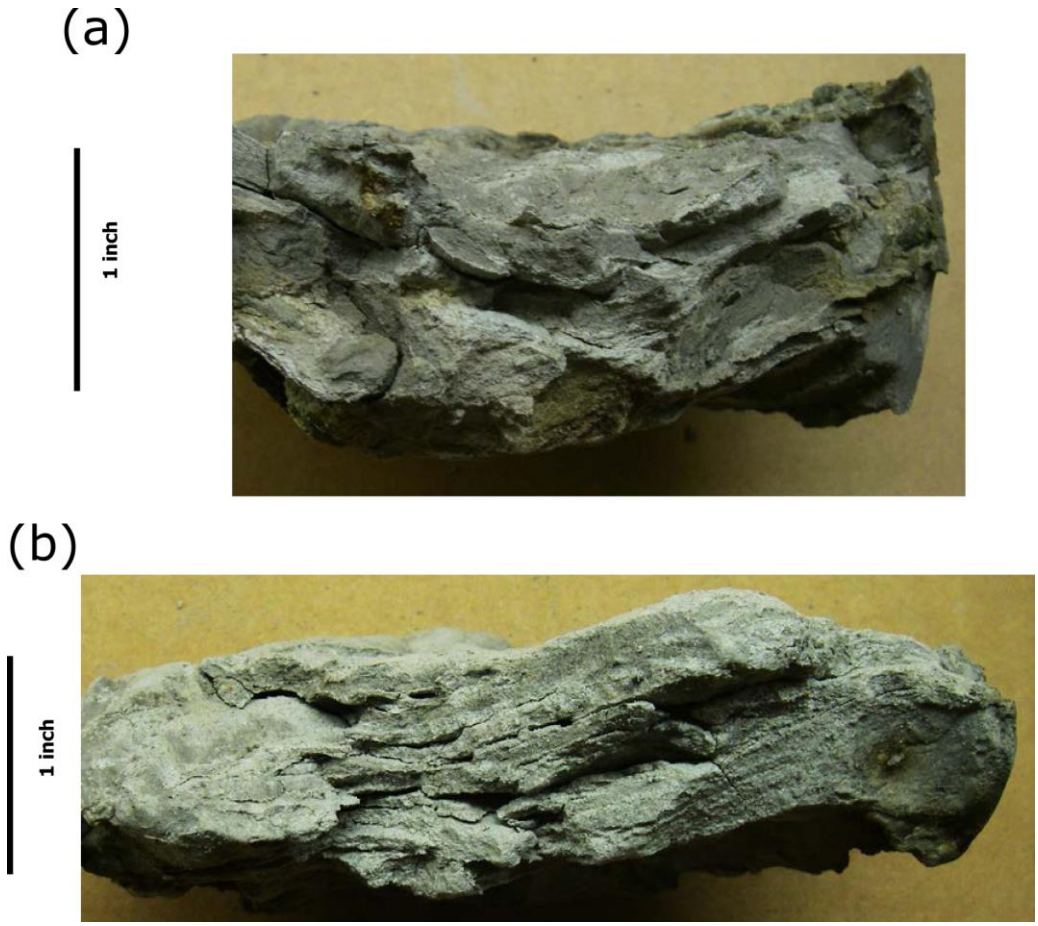

Figure A2-24: Photographs of muddy interdistributary-bay deposits in the DMW-1 core. (a) Mudstone with lenticular beds of siltstones and very fine-grained sandstone at 163.0-ft (49.7-m) depth. (b) Mud-dominated, planar-stratified section at 158.0-ft (48.2-m) depth. The corresponding core description is shown in Figure A2-6.

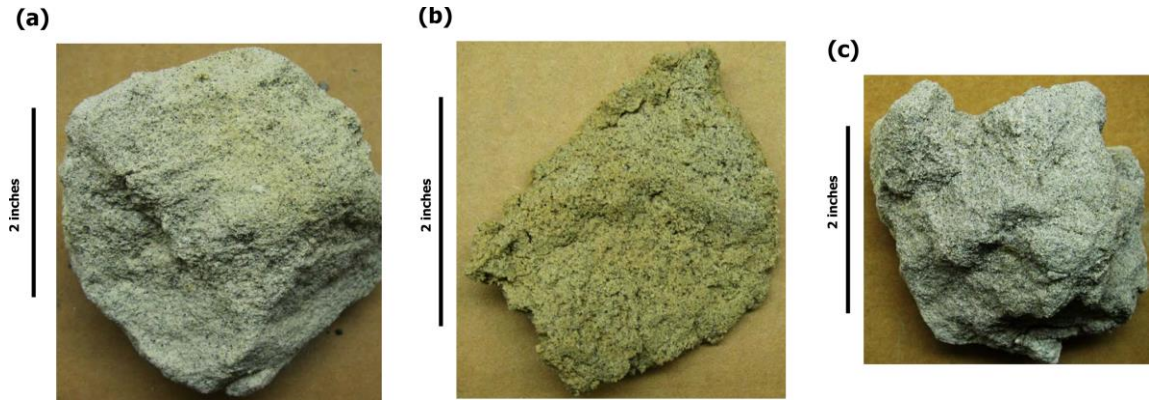

Figure A2-25: Photographs of unconsolidated sandy distributary-channel deposits in the DMW-1 core. (a) Yellowish gray, medium-grained sand at 142.0-ft (43.3-m) depth. (b) Yellow, fine-to-medium-grained sand at 135.0-ft (41.2-m) depth. (c) Gray, medium-grained sand at 126.0-ft (38.4-m) depth. The corresponding core description is shown in Figure A2-6.

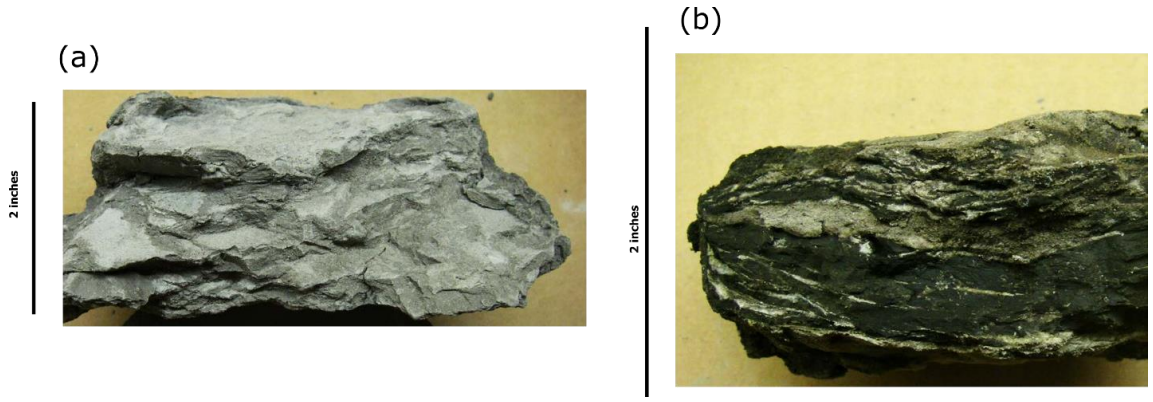

Figure A2-26: Photographs of abandoned-channel-fill deposits in the DMW-1 core. (a) Gray mudstone thin (millimeter-scale) beds of very fine grained, lenticular sandstone at 115.0-ft (35.1-m) depth. (b) Organic-rich, dark mudstone with laminae composed of very fine-grained sandstone at 112.0-ft (34.1-m) depth. The corresponding core description is shown in Figure A2-6.

The DMW-1 core is composed of a succession of tidally modified deltaic facies that include delta-front, interdistributary-bay, crevasse-splay, and distributary-channel (Figures A2-5, A2-6). Delta-front deposits occur in the lower sandy zone from 245- to 259-ft (74.7- to 79.0-m) depth (Figure A2-5). They are characterized by 1.) upward-coarsening grain-size profile from which progradation is inferred; and 2.) presence of marine burring organisms including possible *Ophiomorpha.*

Interdistributary-bay facies, present from 210- to 245-ft (64.0- to 74.7-m) depth, consist of mostly mudstone with thin (<2-ft or 0.6-m) beds of siltstone and very fine-grained sandstone (Figures A2-5, A2-19, A2-20). Their shallow-marine interpretation is in part based on the presence of *Planolites* in the lower part of the section (240- to 245-ft or 73.2- to 74.7-m) depth and stratigraphic position above delta-front facies (Figure A2-5).

Crevasse-splay facies, present from 202- to 210-ft (61.6- to 64.0-m) depth, record progradation of breached-levee deposits into interdistributary-bay areas. Crevasse-splay deposits are well-documented worldwide, including the fluvial-dominated Mississippi Delta (Coleman and Gagliano, 1964) and in tidally modified deltaic systems such as the Mahakam, Ord River, and Mekong Deltas (Allen et al., 1979; Wright et al., 1963; Ta, 2002). They are commonly dominated

by lower-flow-regime traction currents, recorded by ripple stratification (Figure A2-21a), and where present in areas of tidal influence, contain lenticular sand beds and flaser bedding (Figures A2-21b, A2-22b).

The upward-fining section from 186- to 198-ft (56.7- to 60.4-m) depth is genetically related to underlying crevasse-splay deposits and represents erosion-based, crevasse-channel deposits (Figure A2-6). Similar crevasse-channel deposits are documented in fluvial-dominated deltaic systems in the Upper Cretaceous Woodbine Group in Leon County, Texas (Hentz et al., 2014) and in tide-dominated deltaic systems in the Pennsylvanian (Desmoinesian) Spoon Formation in the south part of the Illinois Basin (Ambrose, 1983).

Distributary-channel facies in the upper part of the DMW-1 core from 117- to 147-ft or 35.7- to 44.8-m depth are differentiated from underlying crevasse-channel facies by being 1.) thicker, and 2.) coarser-grained (Figures A2-5, A2-6). These distributary-channel facies are correlative to those in the DMW-3 core, where they occur from 118- to 140-ft (36.0- to 42.7-m) depth as fine-to-medium-grained sandstone beds within a blocky-to-upward-fining succession (Figure A2-4). The scale and grain size of these distributary-channel deposits are comparable to those in the Upper Cretaceous Woodbine Group in East Texas field (Ambrose and Hentz, 2010) and in Leon County (Hentz et al., 2014).

A.3 Vertical Seismic Profiling at the DFPS

In this survey, intelligent Distributed Acoustic Sensing (iDAS^{TM}) system from Silixa, LLC was connected sequentially to the existing permanent fiber optic cables at three wells. Seismic waves were generated by a Big-Bang 750 Accelerated-Weight-Drop (AWD) seismic source from 3Dgeophysics, and the acoustic wave arrival was recorded in multiple wells at the DFPS, which are equipped with DAS fiber cables. The resulting one-dimensional (1D) velocity profile was used as input for ray-tracing modeling to optimize the surface arrangement of the seismic source in subsequent deployments and generate ideas for the type and location of the seismic source.

For each well, the seismic source was placed at a close distance (less than 5 ft) to that well, and 20 shots were initiated by almost five-second spacing. Simultaneously, the acoustic signal was recorded at the optical fiber cable in the same well. Silixa conducted stacking of these 20 recordings to improve the quality of the 1D velocity profile. Subsequently, three nonzero-offset VSP surveys were conducted by placement of the seismic source at the south well and recording the acoustic signal through the optical fiber cable at the west, north, and east wells at the DFPS. Afterwards, the effect of water injection into the fracture zone on the fiber optic signals was assessed. Water was injected at rate of 3-5 gpm and maximum pump pressure of 200 psi and the acoustic signals were passively recorded through the west, north, and east wells in order. As suggested from forward modeling, the results indicated that the passive signals during water injection into a previously placed propped fracture space were relatively weaker than required for tomographic detection of changes in a preexisting fracture. The data gathering and results are detailed below.

DAS operating principle

The iDAS^{TM} makes it possible to create a digital record of acoustic signals along a continuous length of an optical fiber. Figure A3-1 shows the principle of iDAS^{TM} operation where an acoustic field interacts with the backscattered light along a continuous length of optical fiber. By analyzing the backscattered light, and measuring the time between the laser pulse being launched and the signal being received, the iDAS^{TM} can measure the acoustic signal at all points along the fiber with lengths extending into tens of kilometers. The measurements along the entire length of the sensing optical fiber are time synchronized, and the system enables coherent phase and amplitude data for the acoustic signals.

DAS native acoustic output

iDAS^{TM} and Silixa's new Carina® systems natively measure signals proportional to strain rate. This strain rate is computed over a length of fiber equal to the gauge length of the system. In the DFPS deployment, both iDAS^{TM} and Carina® were configured with a gauge length of 2 m. The measurement is a running average along the fiber. This means that in this survey every 1 m spaced receiver channel outputs the strain rate averaged over the 2 m gauge length centered on that channel. A linear conversion was applied to the raw data to convert to strain rate-proportional values. These converted values were written to the SEG-Y files supplied as data deliverables.

Conversion to other physical properties

Conversion from strain rate to strain is possible with an additional processing step involving a time integration. This processing step has the effect of boosting the low frequency energy in the signal, and flattening the noise spectrum. Hence, data which is converted to strain units can provide output which is well suited for seismic processing when applying some commonly used routines. This processing step also has the effect of putting iDAS^{TM} data in phase alignment with geophone data if they were to be deployed simultaneously, although the dimensions of the iDAS^{TM} data are in terms of strain, and not speed ($m.s^{-1}$) as is commonly measured with a geophone. The data can be

further processed to geophone equivalent units (speed, m s^{-1}). Silixa has developed an algorithm to enable this conversion to be made.

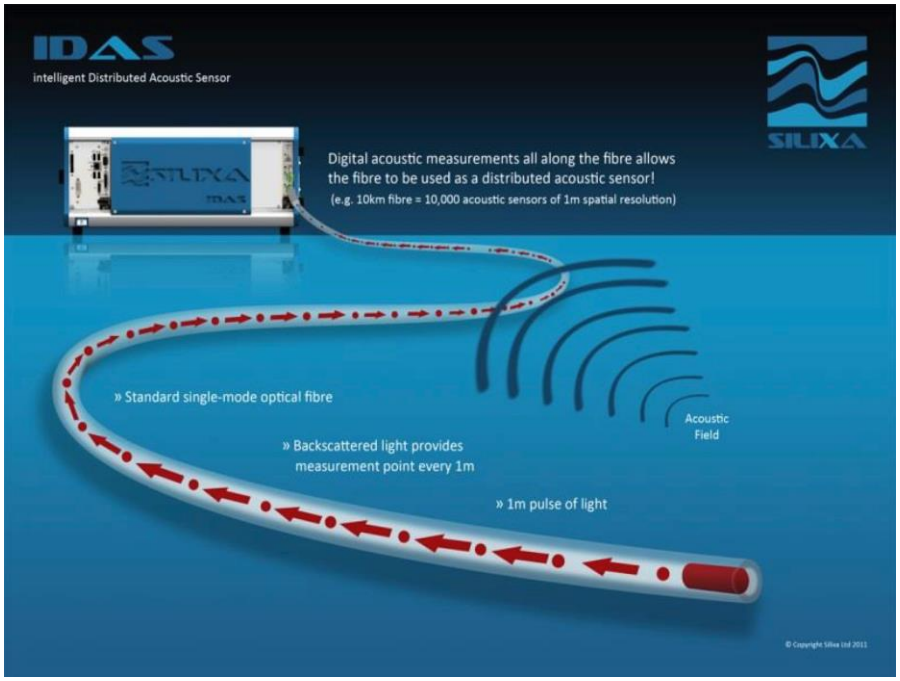

Figure A3-1: iDAS™ operational principle.

DAS directional response

The sensing array used for this survey comprised three separate wells completed with fiber optic cable (single-mode) cemented between casing and pipe. These arrays were terminated down-well and so each well was interrogated individually.

As a result of well-understood characteristics underlying the operation of the system, iDAS™ and Carina® data exhibit sensitivity which is dependent on the angle of incidence of seismic energy with respect to the orientation of the fiber. In general, this is exhibited as enhanced sensitivity to those seismic signals with particle motions directionally aligned with the axial direction of the sensing fiber (Hornman, 2013). Consequently, the system tends to be less sensitive to broadside P-wave arrivals; that is, P-waves that arrive from directions perpendicular to the axial orientation of the sensing fiber. It is important to note that this directionality in sensitivity is dependent on the component of the seismic wave arriving at a certain angle of incidence. By convention, the angle of incidence is 0° for arrivals propagating along the axial dimension of the fiber and 90° for arrivals propagating perpendicular to the fiber. Then this means that the sensitivity to a P-wave arrival is greatest at angles of incidence near 0°. Note that for shear waves, the greatest sensitivity occurs where the deviatoric strain imposes the maximum fiber strain. This means that the sensitivity to shear waves is greatest for angles of incidence close to 45° (or 135°).

Survey outline

iDAS™ data were acquired during multiple surveys: 1.) zero- and nonzero-offset seismic VSPs; 2.) quiet or background acquisition; and 3.) acquisition during pump-loop operation; and 4.) injection-well stimulation. Data were acquired in each of the three observation wells equipped with fiber optic cables.

The zero-offset VSP data were used to create a velocity model of the site and guide a feasibility study examining the utility of a grid or walkaway VSP acquisition program. The pump-loop data were acquired to investigate the acoustics associated with pump operation, and the data were collected during fluid injection into the fracture to evaluate the signal associated with surface and in-well fluid transport as well as the effect of fluid pressurization in the single injection stage.

Equipment information

The fiber-optic cable arrays were individually interrogated by a single iDAS^{TM} instrument. Acquisition timing was controlled by high accuracy GPS clocks. The use of a GPS antenna allows all files to be timestamped. This timestamp is recorded in UTC; local time was UTC -5 hr.

The specification of the iDAS^{TM} system equipment used to record the surveys is given in Table A3-1.

Table A3-1: DFPS equipment list.

Equipment Component	Specification
Interrogator	iDAS^{TM} 17053 10-m gauge length Software version: 2.4.1.111

Fiber optic arrays

There are four wells completed with fiber-optic cabling at the DFPS (Figure A3-2). These are named east, north, west and south observation wells. The cable from each wellhead was buried along a path to a common junction box where connectors were spliced on to the cable ends. The length of surface cable varies for each well, but the depth of all the wells is approximately 100 m.

In the south well, it was determined that the fiber was broken somewhere along the buried run from the junction box to the wellhead. Because the path of the buried cable was not known and there was no spare cabling at either the well or junction box, data was not acquired on the south well.

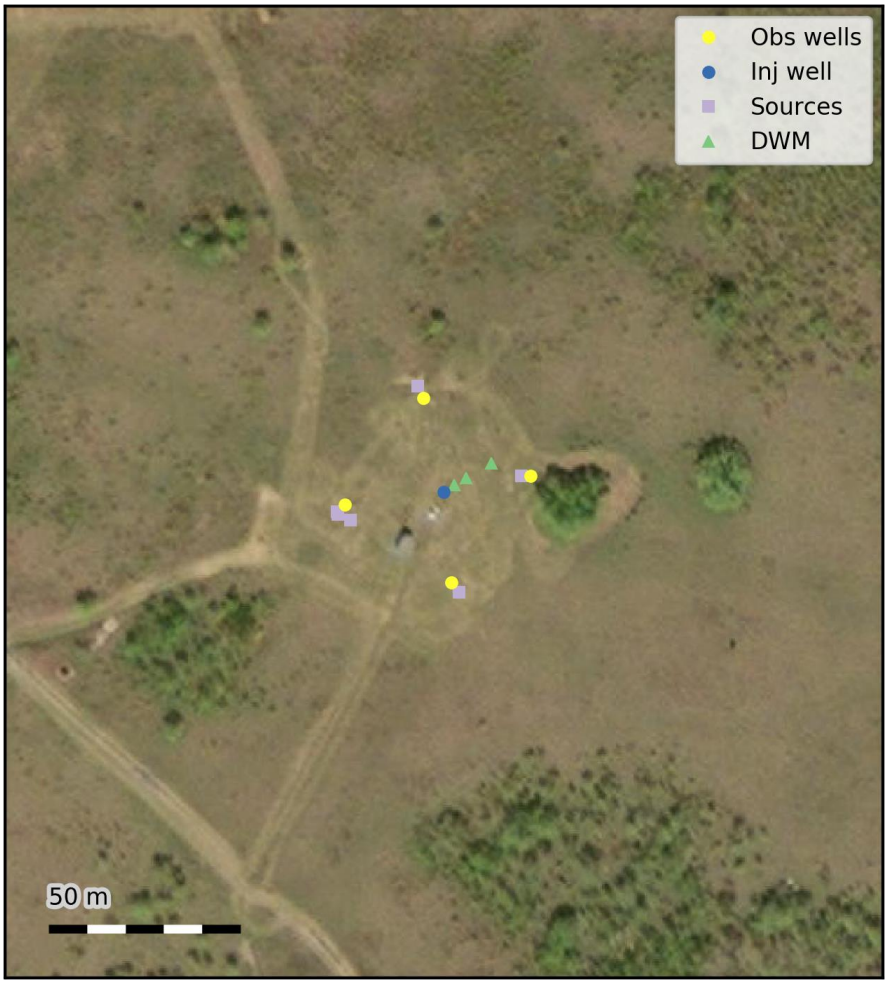

Figure A3-2: Injection and observations wells, along with AWD source locations, at the DFPS. Only DMWs 1-3 are shown (green triangles).

Receiver positions

In order to calibrate the positions of each DAS receiver channel, a series of tap test measurements were made. These tap tests were conducted at the location of each of the observation wellheads.

Tap tests are performed by recording data while the cable is tapped at the desired location. The propagation of the seismic signal is then used to locate the fiber receiver channel closest to the tap location. Once the receiver channel is identified, this channel can be assigned a physical location. Additionally, fiber distance to the lowest point of the fiber run can be inferred from the enhanced backscatter associated with fiber termination. Provided information about the shape and depth of the well, the receiver positions along the rest of the fiber optic cable can be assigned by interpolating along the well path. In the case of this project, the wells were assumed to be completely vertical, so all receivers in a given well share the same horizontal coordinates.

Table A3-2: Fiber locations on the east-well cable. MSL and FD stand for elevation above mean sea level and fiber distance, respectively.

FD (m)	Easting (m)	Northing (m)	MSL(m)
198.47	486116.22	3219927.55	200.28
292.50	486116.22	3219927.55	100.28

Table A3-3: Fiber locations on the north-well cable.

FD (m)	Easting (m)	Northing (m)	MSL(m)
148.64	486091.76	3219945.33	200.60
256.66	486091.76	3219945.33	100.60

Table A3-4: Fiber locations on the west-well cable.

FD (m)	Easting (m)	Northing (m)	MSL(m)
195.58	486073.87	3219921.09	200.82
297.75	486073.87	3219921.09	100.82

Acquisition settings

Acquisition settings were optimized and verified prior to data acquisition. The settings listed in Table A3-5 were used while acquiring data for VSP, quiet operation, and injection/pump loop operation.

Table A3-5: iDAS™ 17053 acquisition settings used for all wells.

Setting	Value	Unit
Sampling frequency	4	kHz
Time Decimation	20	-
Laser launch rate	80	kHz
Spatial sampling	1	m
Measurement length	576	FD
P-value	15	-
Gauge length	10	m
Output decimation	4	-

The instrument dynamic range and noise floor are dictated by the length of the interrogation fiber, quality of spliced and connectorized unions and the acquisition settings. For a given fiber optic cable installation, the expected noise floor can be estimated and the actual noise floor performance can be measured by analyzing data during times when neither high amplitude nor high frequency acoustic signals are anticipated. The expected and measured noise floor performance for the east, north, and west wells are shown in Figure A3-3. The measured noise floors for all three wells exceed expected performance along the length of the downhole receivers.

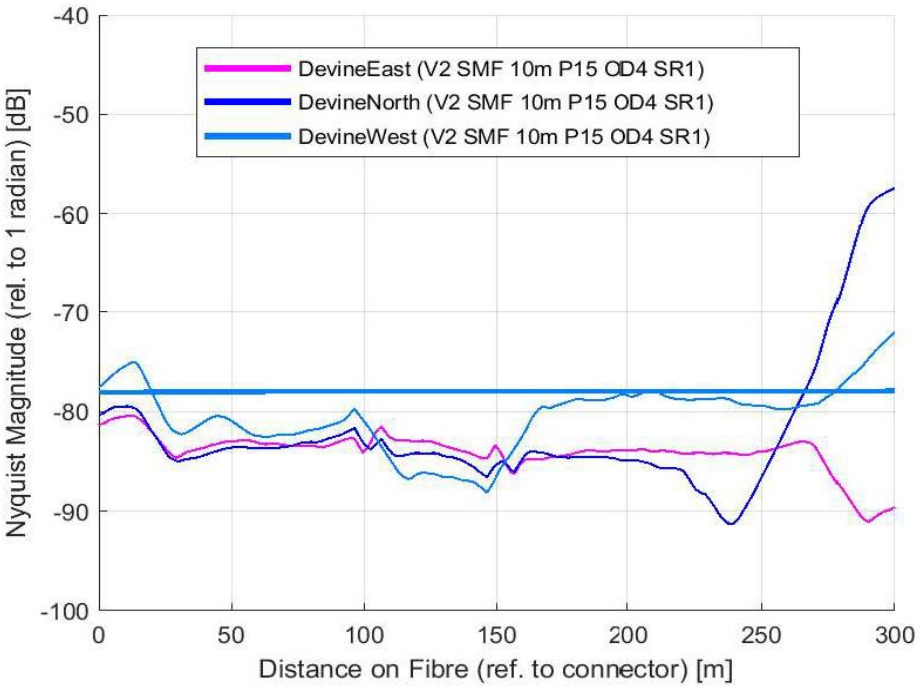

Figure A3-3: Expected (thick lines) and measured (thin lines) noise floors for cables in east, north, and west wells. The junction box is reached at around 150 m. All wells are approximately the same depth, but the surface run from junction box to wellhead is slightly different for each well. The noise past 240 m refers to the extra length of the fiber optic cable at the Silixa's cable spool on the surface.

Experiments

The primary goal of this mobilization was to acquire zero-offset VSP data from the observation wells at the DFPS. Additional iDAS™ data were collected to monitor the effects of water circulation in the pump loop routed from the pump apparatus to the injection well. Data were also acquired concurrent with injection well stimulation. Both the pump loop and injection data were supplemented with data acquired during a period when no fluid pumping or injection well stimulation was taking place. This quiet dataset can be used to evaluate the level of ambient noise at the test site.

Figure A3-4: Accelerated Weight-Drop (AWD) source used at the DFPS.

Accelerated weight-drop shots

VSP data for each observation well comprises a series of repeated active source shots generated by an AWD source. This source is essentially a large hammer plate that is accelerated toward ground impact by springs (Figure A3-4). A series of twenty shots were performed at each source location (once every 5 s). SNR was enhanced by stacking repeated shots performed at the same source locations.

The spectral content of the AWD source was examined for a single iDAS^{TM} receiver located in the east well at a True Vertical Depth (TVD) of 55 m, which is the approximate depth of our preexisting fracture. The FFT power spectrum shows little frequency content above 100 Hz (Figure A3-5). The location of this receiver is annotated with a black arrow in the east well AWD wavefield, shown in Figure A3-6. Analysis of the spectral content at other receivers in the east well—as well as those in the north and west—showed similar frequency content.

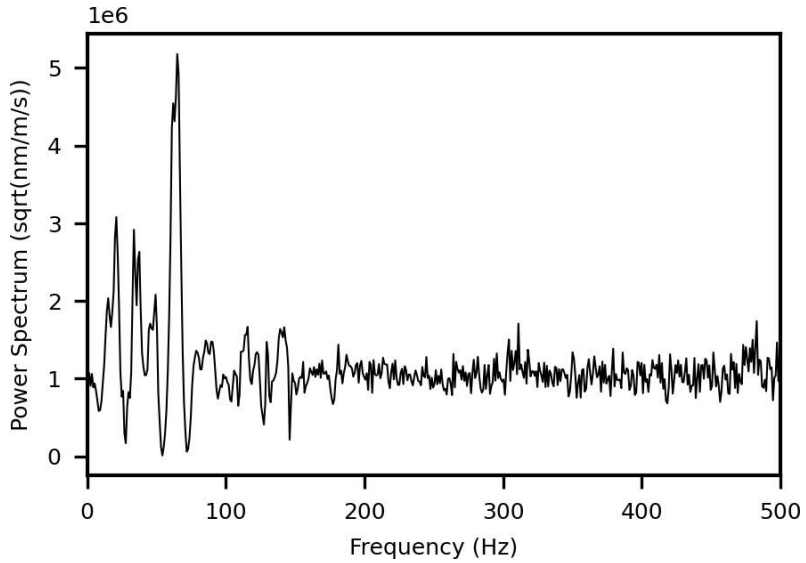

Figure A3-5: Spectral content of the AWD source measured at the TVD of 55 m in the east well.

Stacked shot data were filtered with a 5–100 Hz bandpass filter to improve first arrival picks. By picking the first waveform arrival time from the stacked shots at each receiver location, a two-way travel time (TWT) was measured between each source/receiver pair (Figure A3-6, Figure A3-7, and Figure A3-8).

Since the system gauge length was 10 m, the TWTs were smoothed using a 10-m-trace moving window in order to mute receiver-to-receiver TWT variability prior to further processing.

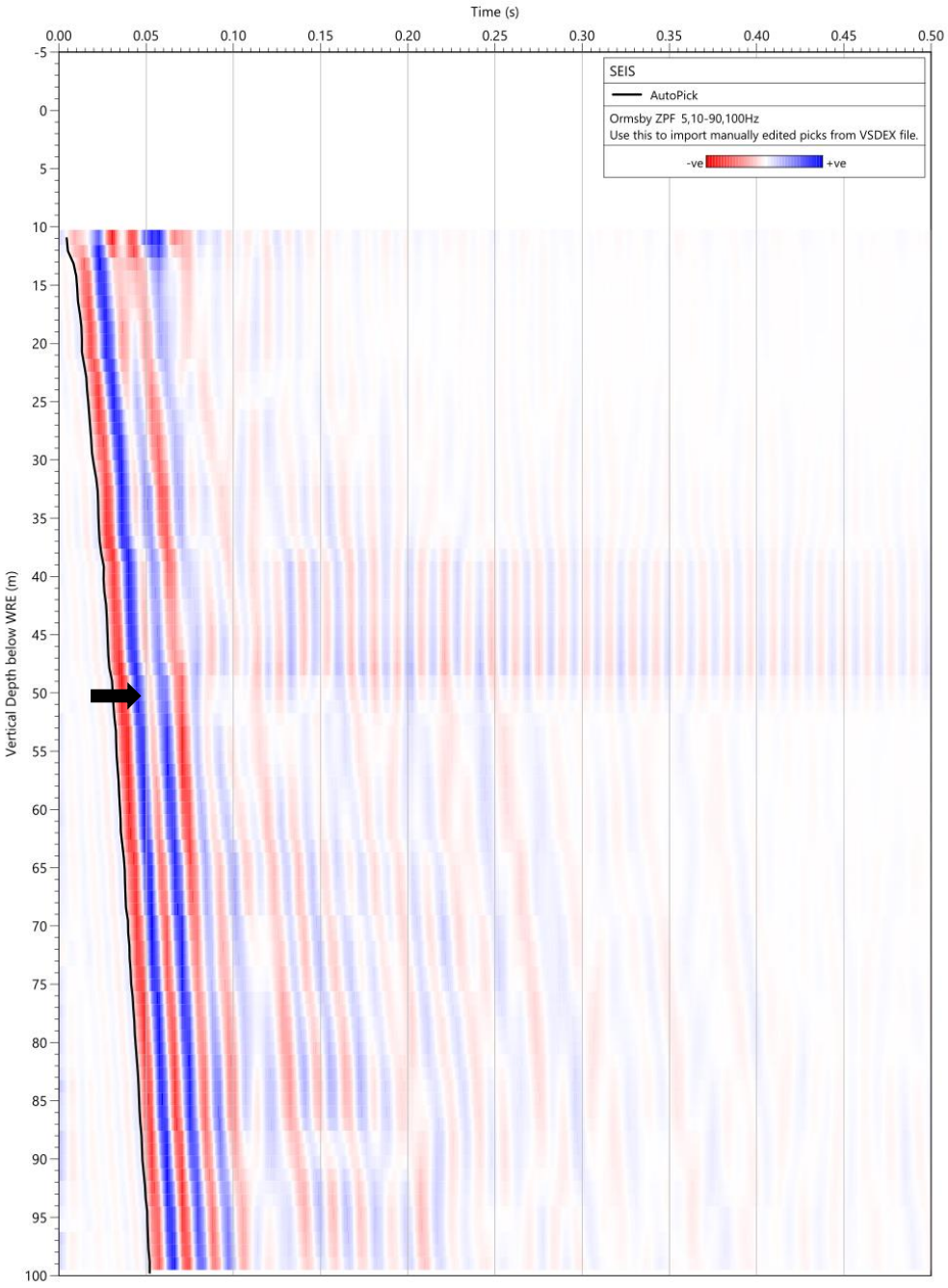

Figure A3-6: First arrival picks from the east-well VSP. The location of receiver for Spectral content of the AWD source measurement in Figure A3-5 was at the TVD of 55 m as shown by a black arrow.

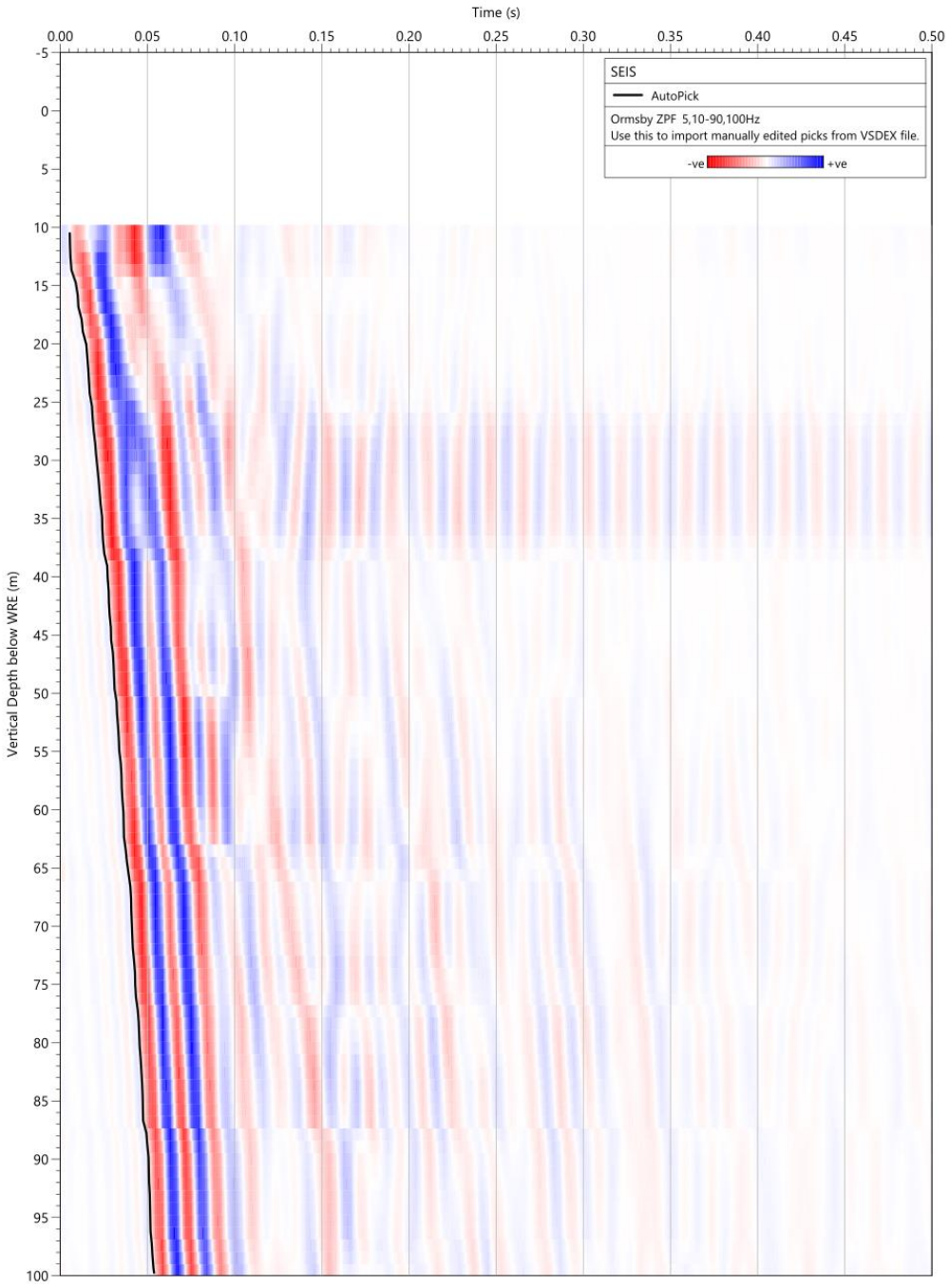

Figure A3-7: First arrival picks from the north-well VSP.

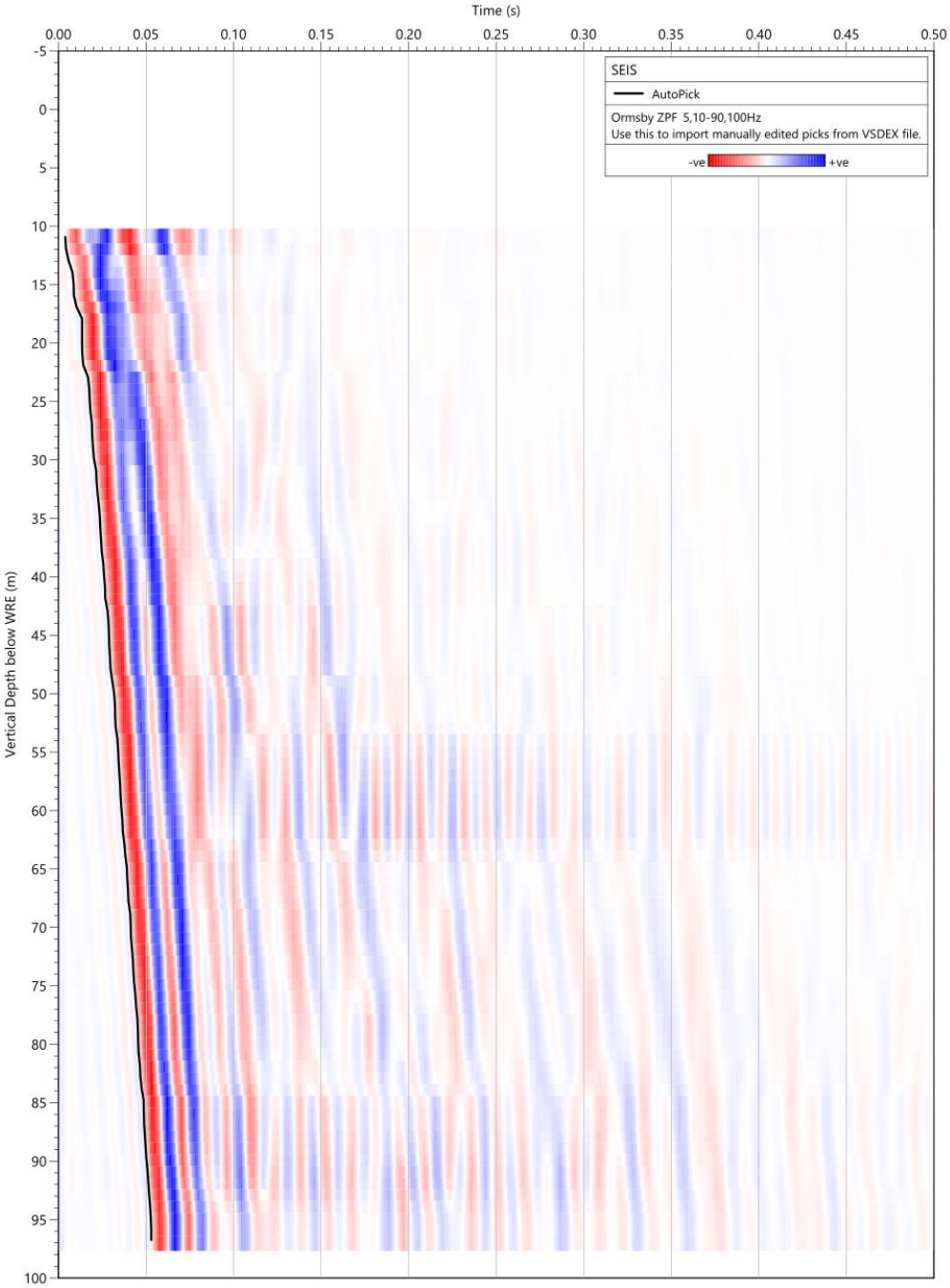

Figure A3-8: First arrival picks from the west-well VSP.

Pump loop monitoring

An attempt was also made to assess the ambient signal due to the pump operation and injection fluid circulation in a loop close to the water tank at 300-ft distance from the monitoring site. iDAS^{TM} acoustic data were acquired on each of the three observation wells during this water circulation.

iDAS™ acquisition settings employed for this experiment were the same as those used for the AWD shots (Table A3-5).

Pumping began shortly after the start of data acquisition on the east well. Pumping activity continued while data were acquired on the north well and finally on the west well. The results indicated that the ambient signal due to the pump operation and the water circulation were relatively weak. This confirmed that the pump and water circulation close to the pump may not impose too much environment noise during recordings.

Injection monitoring

Acoustic data were acquired during active injection and pressurization of the field at the DFPS. Data were recorded in each well (east, north, and west) separately in the time period during startup, displacement, pressurization, and shut-in. Data recording began on the west well, and then pressurization was achieved. The next well to be interrogated was the north well followed by the east well.

Silixa provided an SNR analysis for this dataset. However, we expect that depending on the nature of the acoustic energy generated by fluid injection and the degree of fracture dilation, there is a potential for identifying acoustic signal associated with injection and/or slow strain around the fracture plane.

Quiescent monitoring

To aid in interpreting the pump loop and injection monitoring datasets, acoustic data were also acquired on all three wells during a quiescent period when no pumping, injection, or shots were being performed. This quiet data can be used as the basis for quantifying the noise level of the acquired data as well as identifying any sources of ambient signal such as offsite equipment and vehicle traffic. Acquisition settings used with the injection monitoring and quiet data collection were the same as those used for the AWD shots (Table A3-5).

Data deliverables

TDMS acoustic format

Raw iDAS™ files are recorded during each of the three experiments in TDMS format. These files contain header information describing the data acquisition parameters, but do not contain any source or receiver coordinates. Examples demonstrating the parsing of acoustic data and meta data can be found at https://silixa.com/resources/software-downloads/.

Velocity profiles

Stacked, smoothed TWTs were used along with source and receiver geometries determined from well coordinates, tap tests, and measurements to source locations to compute a velocity profile applicable to each observation well. As expected, measured velocities increase with depth. Below approximately 55 m in depth, the velocity profiles become almost uniform with depth.

Measured velocity profiles derived from the zero-offset VSP data acquired in the east, north, and west wells are shown in Figure A3-9 through Figure A3-11 for the east, north, and west wells, respectively.

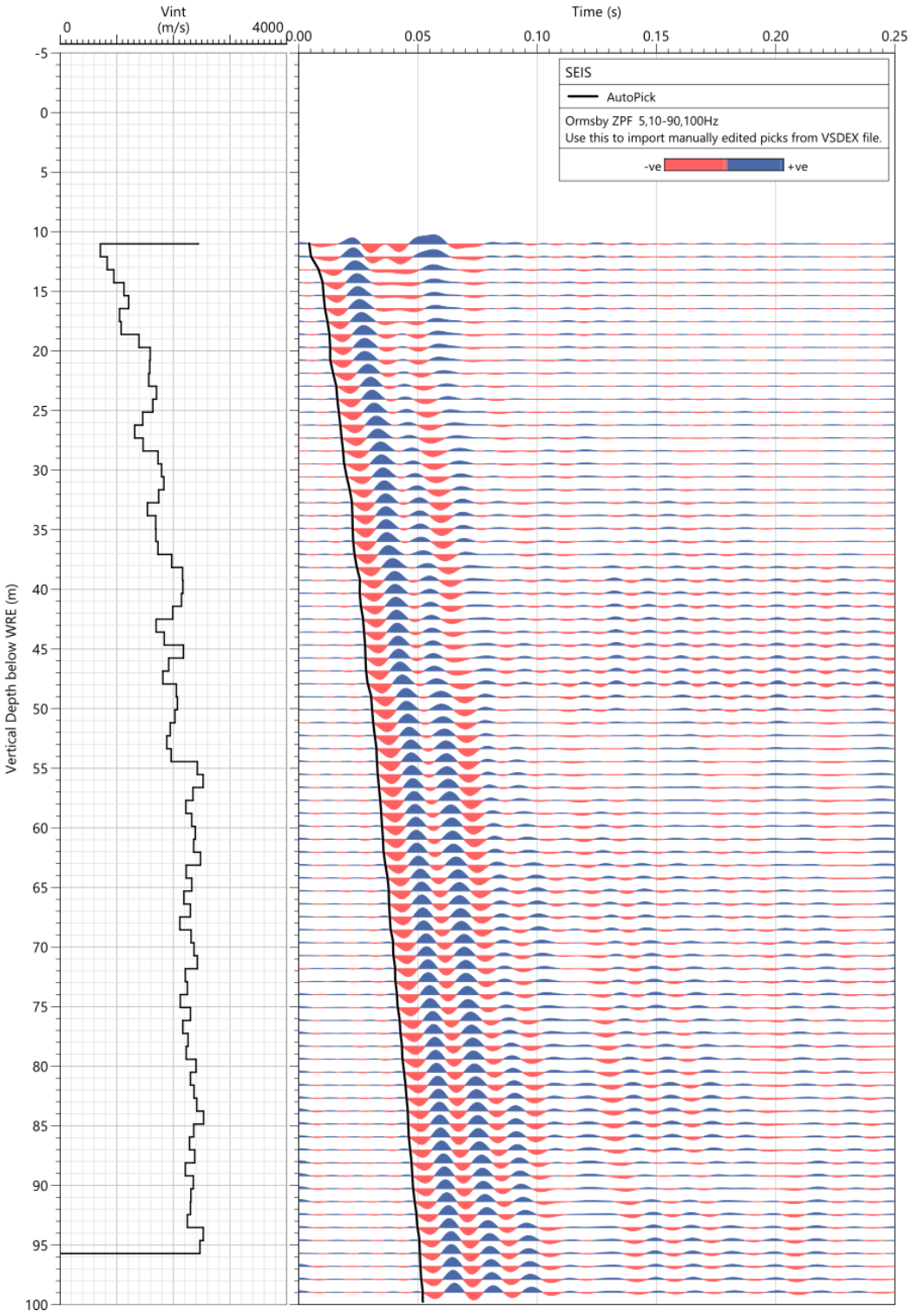

Figure A3-9: Measured VSP velocity profile for the east well.

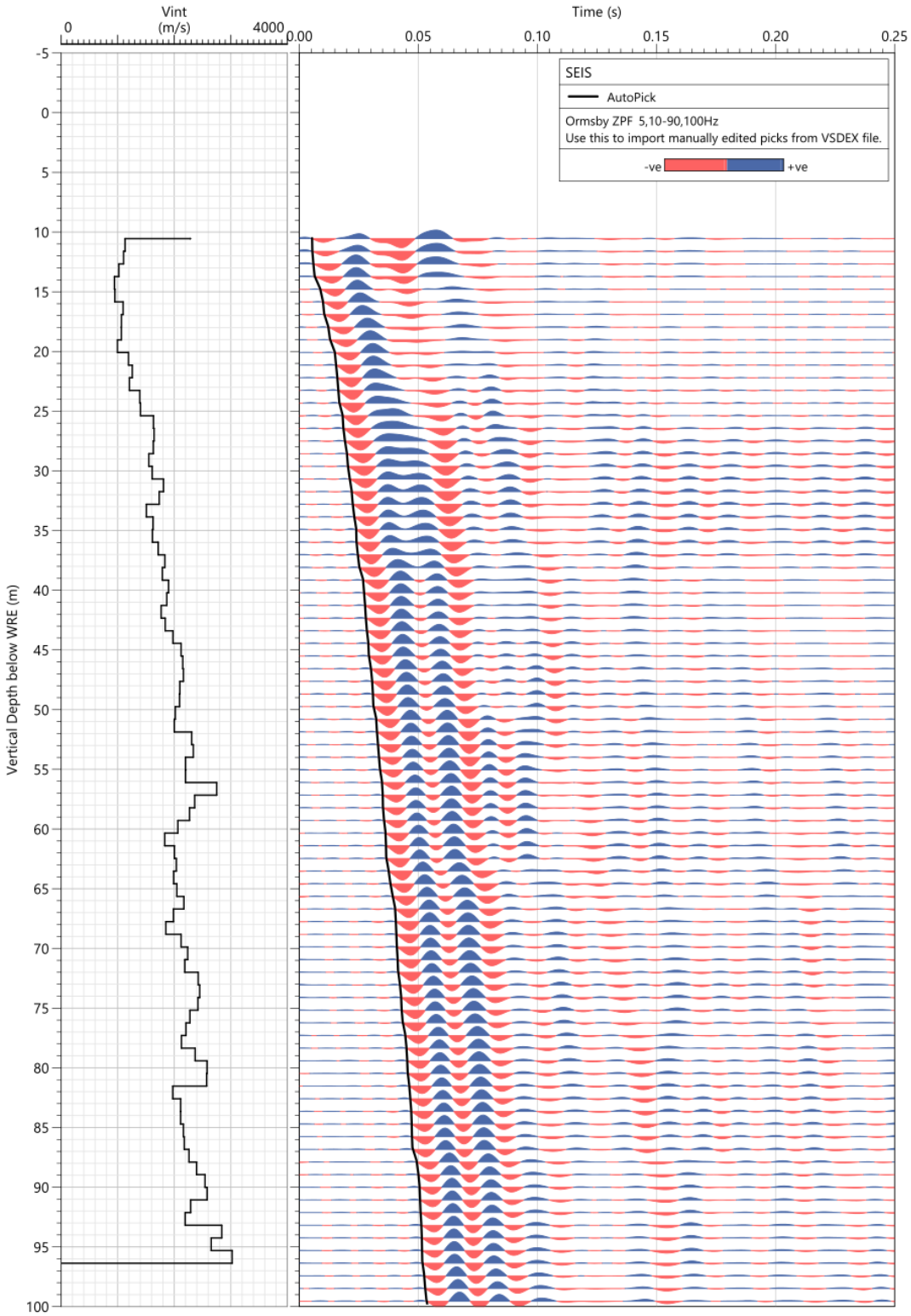

Figure A3-10: Measured VSP velocity profile for the north well.

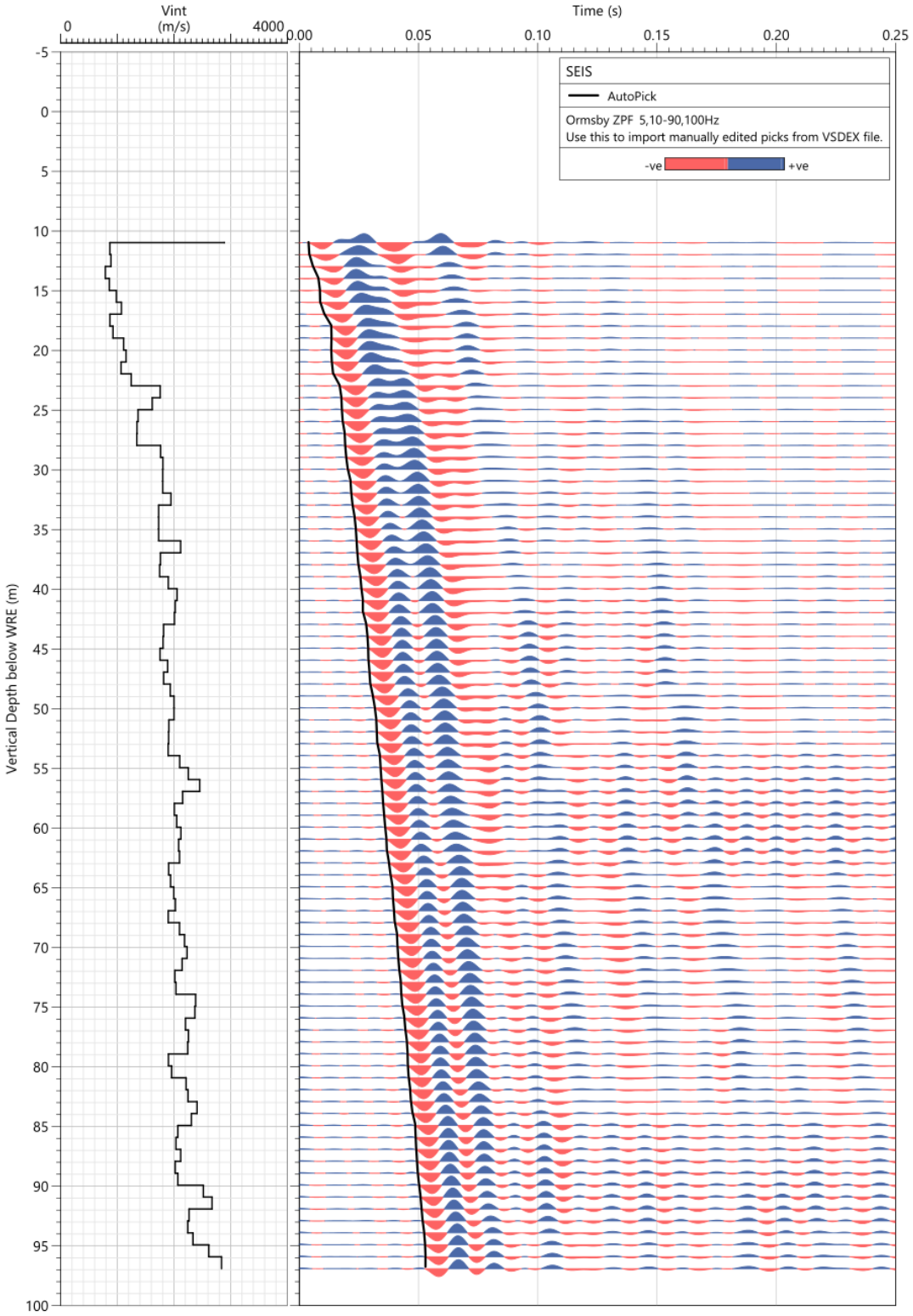

Figure A3-11: Measured VSP velocity profile for the west well.

Velocity model

A velocity model, optimized using the measured velocity profiles as input, was found to have no significant dip and so a flat, layered model was selected to represent the p-wave velocities at the DFPS. The velocity model profile is plotted in Figure A3-12. TWT residuals—as calculated using ray-traced source to receiver distances—are compared with the TWTs picked from each well's VSP stack in Figure A3-13. The agreement between measured and modeled TWTs is within a few of milliseconds for all receivers deeper than 10 m.

The group of receivers recording the top 10 m gauge length (0–10 m TVD) show TWTs unexpected for a weathered layer. It is suspected that the steel well casing is being excited by the AWD source within the top few meters of TVD, thus making velocities appear greater than they should for a sandy, unlithified medium. This is reflected in the velocity model as a region of higher velocities for TVD < 7 m.

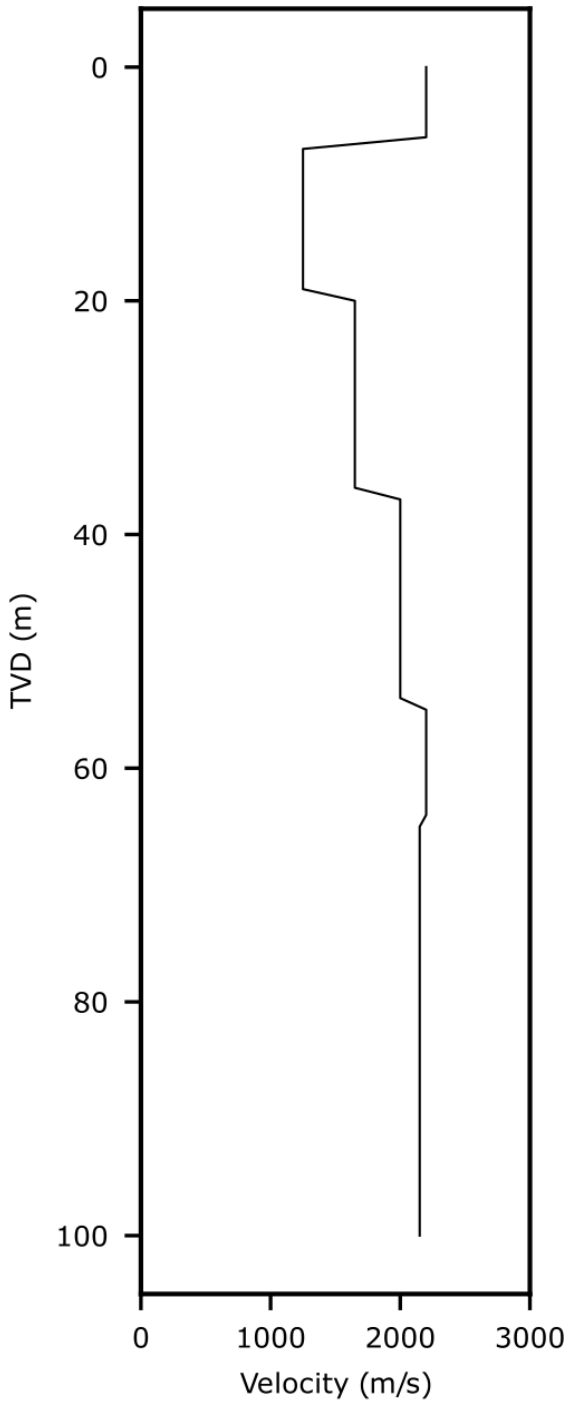

Figure A3-12: The DFPS velocity model optimized from VSP measurements on the east, north, and west wells.

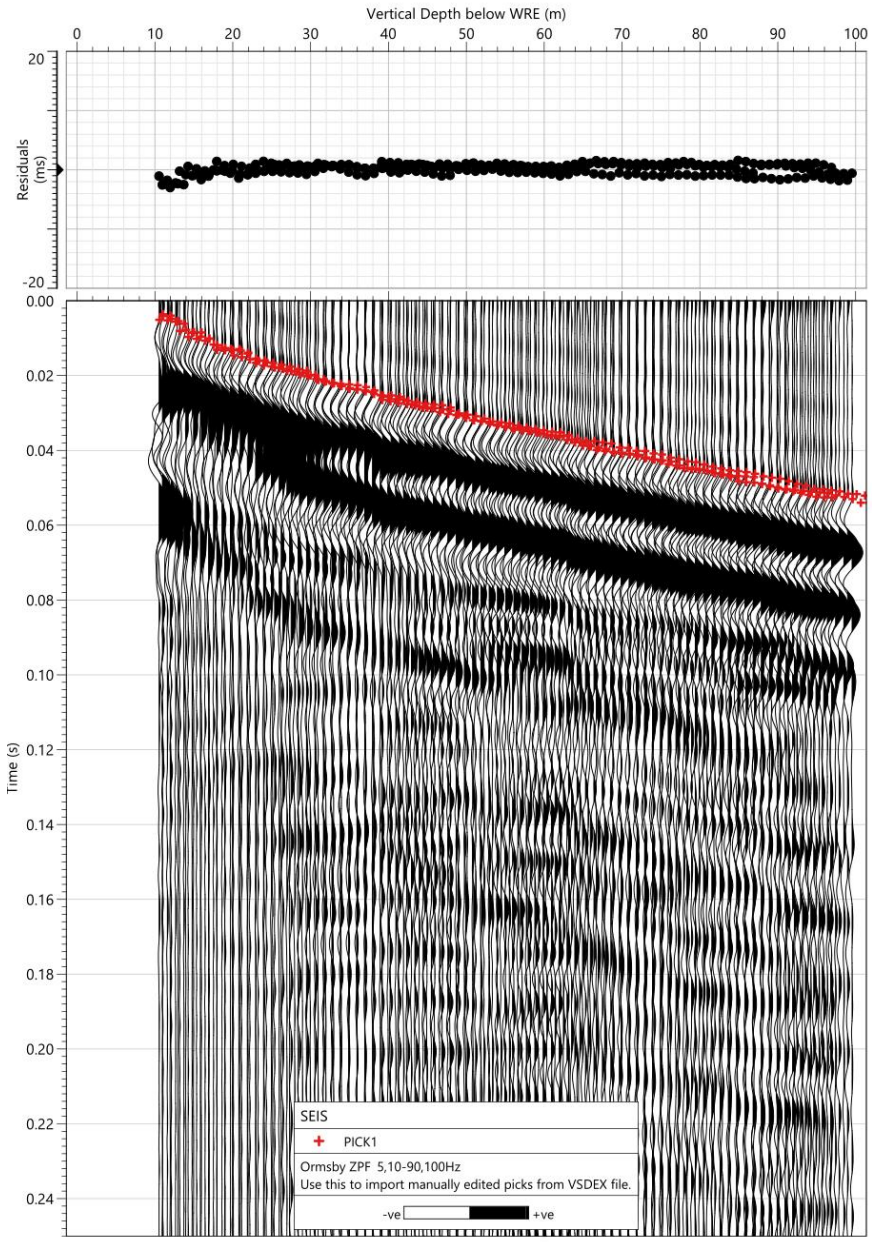

Figure A3-13: TWT residuals between optimized velocity model and velocity profiles measured on the east, north, and west wells.

Time-lapse survey feasibility

The very high SNR and wide frequency content of the survey are positive indications for the feasibility of time-lapse imaging at injection depth. The simple, progressive, non-dipping velocity layers suggest that there would likely be no complications in designing a grid or walkaway VSP source array. Some considerations for obtaining the best possible results from a time-lapse imaging study are listed in the following sections, which include seismic source frequency content, imaging resolution, shot stack SNR, and possible additional receiver installation.

Frequency content

The spatial scale of the DFPS is small relative to other time-lapse imaging project sites. While this is logistically beneficial and alleviates achieving good SNR with smaller sources, it would be important to select a seismic source with a high frequency content in a future project aiming at imaging injection-related features. Higher frequencies than what we achieved with the tested seismic source should provide better vertical resolution for constraining reflector depths. Higher frequencies also translate into smaller waveform wavelengths, which are more sensitive to interactions with features with contrasting P- and/or S-wave velocities.

A small, mobile, vibrating seismic source that can sweep through a range of frequencies is a good candidate for imaging features at the DFPS. The advantage of shallow well and feature depths is that frequency-dependent dispersion effects present less challenge compared with larger scale studies.

Imaging resolution

The horizontal resolution of an imaging inversion is dependent upon the source array grid spacing and spatial extent. As such, this is mostly a trade-off between logistical and resource expense and horizontal resolution of reflections. Logistically, running a walkaway seismic source in an area that overlaps the fracture is not feasible due to the installed CSEM survey surface antennas. In addition, a seismic source that impacts the ground surface normal to the fracture plane may dynamically load the dilated fracture leading to abrupt aperture changes that may impose a tremendous complexity to the interpretation of the collected hydrogeological and EM data. Therefore, acquisition would likely require sources at large offsets to avoid adverse effects on the EM receivers and the fracture aperture.

Signal-to-noise ratio

One way to improve the feasibility of a time-lapse imaging study is to increase SNR of stacked shots by simply stacking a greater number of shots at each source location. The improvement in SNR for multiple shots compared to a single shot scales with the square root of the stack count. This means that SNR improves with stack count in a diminishing fashion. Assuming random noise, one can expect an SNR improvement by 2 folds by stacking four shots, and an improvement by 4 folds by stacking 25 shots; however, only an improvement by 10 folds by a stack count of 100.

For the current VSP measurements, a stack count of 20 was used to ensure good SNR while keeping mobilization and equipment rental costs low. A similar cost-benefit analysis is advisable for a future time-lapse imaging study. If a different seismic source mechanism is selected it would be necessary to reevaluate the optimal stack count to achieve the best possible SNR since each source has a unique combination of frequency content and force-rating per shot. This could be performed in the field by analyzing a series of test shots.

Additional receivers

The potential benefits of constructing new well(s) instrumented by Constellation™ fiber optic cable as part of the Carina® system can also be evaluated and optimized in a ray-trace modeling exercise. Beyond the additional geometric leverage provided by installing new observation wells with Constellation fiber, the large improvement in system noise floor that comes with the Constellation system would provide immediate gains in SNR as well as the ability to directly measure fracture dilation in a future observation well that transects the fracture.

The ability to instrument new well(s) with a 2-m gauge-length Carina® system would be of particular benefit when applied to the small spatial extent and well depths at the DFPS. Since a 2-m gauge-length DAS comprises five times the number of fully independent receiver channels, the ability to resolve features at depth would be greatly improved.

We had requested additional funding from the DOE to install the Constellation fiber at a new observation well that we had planned to construct. However, DOE could not fund this request at this time. We hope to install such a fiber in a new observation well in follow-up studies.

Future elastic seismic imaging

The new velocity model in Figure A3-12 was useful for elastic modeling and elastic seismic imaging to further evaluate VSP sensitivity to fracture dilation, as elaborated in Subtask 5.3.

A.4 Tiltmeter Mapping of Fracture Dilation During 2022 Field Deployment

During the 2022 field deployment, FRx Inc. was contracted to conduct surface tiltmeter monitoring survey to record subtle surface uplift during injections, useful for deducing the dilated fracture geometry. In this appendix, we present the details of the tiltmeter setup at the DFPS and the findings of this survey.

Tiltmeter layout

Tiltmeters were placed in subsurface vaults to attenuate mechanical noise and suppress the impact of weather and diurnal temperature fluctuations upon tiltmeter output. The vaults are constructed of plastic housings used to house lawn irrigation plumbing. We constructed a level concrete floor in each vault (Figure A4-1). Two-inch PVC conduit connects the vaults to three centralized locations where data management equipment can be staged. The fifteen vaults are arranged in three spiraling arms, each arm having five locations symmetrically around the injection well. Vault locations are approximately 10, 13, 17, 20, and 27 m from the injection well, although some variation occurred during placement to accommodate other systems at the site. The positions of locations constructed in 2016 were measured by a total station. Swing-line measurements made the positions of the three newer vaults from previously surveyed landmarks. The layout of tilt locations is shown in Figure A4-2.

The azimuth of each tiltmeter was measured with the Digital_Compass_for_Android tool installed on a Samsung S8 phone with Verizon services. Table A4-1 lists the geography of the tiltmeter layout and quantitatively provides the coordinates used to draw Figure A4-2.

Figure A4-1: Tiltmeter vaults and tiltmeter installation. (left) The tiltmeter is the round can that is placed within the triangular plate. Leveling was performed by turning the black knobs at the corners of the plate. The blue data / power cable is threaded through the 2-inch PVC conduit to the remote Data-Acquisition-System electronics and power supply. (right) A closed tiltmeter vault in the foreground with a brick and a surveying target on top. Two additional vaults are in the background, and the data-acquisition-system *electronics were located beside the stack of yellow shipping containers.*

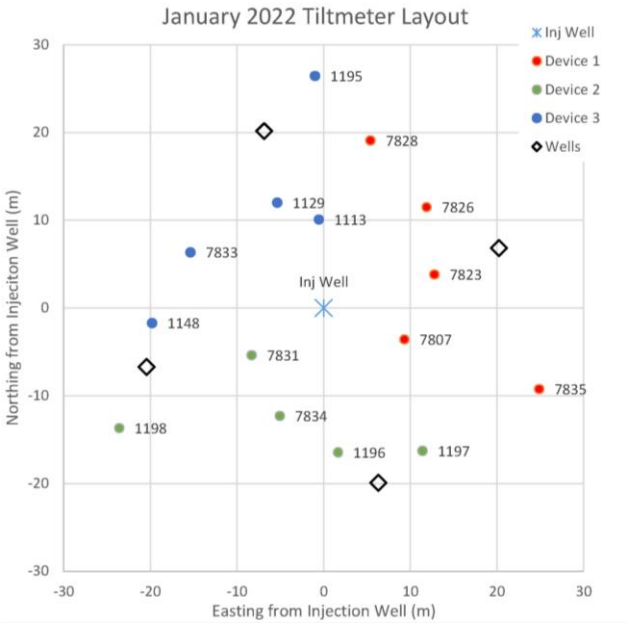

Figure A4-2: Plan view of tiltmeter locations. The axes show distance from the injection well in the north-south and east-west directions. The injection well is shown by "X." The colored dots and the serial number of the deployed tiltmeter by the labels beside the dots indicate the installed tiltmeter vaults. The tiltmeter vaults in each helical branch were spaced from the injection well at average distances of 10, 13.3, 16.6, 19.9, and 26.8 m. Different colors of the dots connote the sets of five tiltmeters connected to each data-acquisition-system *device.*

Table A4-1: Tiltmeter placements and well locations.

Tiltmeter / Location Name	Associated Data-Acquisition-System	Northing (m)	Easting (m)	Distance from Inj. Well (m)	Tiltmeter "Y" Axis Azimuth
TM7807	Dev#1	-3.59	9.30	9.97	330°
TM7823	Dev#1	3.82	12.77	13.33	323°
TM7826	Dev#1	11.49	11.87	16.52	6°
TM7828	Dev#1	19.09	5.40	19.84	333°
TM7835	Dev#1	-9.25	24.85	26.52	330°
TM7831	Dev#2	-5.38	-8.30	9.89	329°
TM7834	Dev#2	-12.30	-5.07	13.31	315°
TM1196	Dev#2	-16.46	1.64	16.55	315°
TM1197	Dev#2	-16.30	11.39	19.88	324°
TM1198	Dev#2	-13.70	-23.58	27.27	322°
TM1113	Dev#3	10.09	-0.55	10.10	336°
TM1129	Dev#3	12.00	-5.35	13.14	319°
TM7833	Dev#3	6.35	-15.37	16.63	327°
TM1148	Dev#3	-1.71	-19.79	19.86	325°
TM1195	Dev#3	26.44	-0.99	26.45	321°
Inj. Well	-	0	0	0	-
West Well	-	-6.73	-20.44	21.52	-
South Well	-	-19.92	6.30	20.89	-
East Well	-	6.83	20.23	21.35	-
North Well	-	20.16	-6.87	21.30	-

Tiltmeters and the data acquisition system

The adopted tiltmeters hold various precisions. Seven tiltmeters are hi-gain versions of the Jewell Instrument Series 700 platform tiltmeter specified to resolve 0.1 microradians. The remaining eight are medium gain versions of the same device rated at 1.75 microradians. Each tiltmeter generates a pair of bipolar analog voltage signals in the range of ±5 volts as measures of tilt angles in two orthogonal vertical planes. Each tiltmeter also generates a 0-1 volt signal proportional to its temperature.

Analog-to-digital conversion is accomplished by National Instruments Series 6200 devices operated at 1000 Hz. Each data-acquisition-system device presents 16 analog data channels, so five tiltmeters can be connected to each of the three Series 6200 devices, identified as Dev#1, Dev#2, and Dev#3. Circular mil-spec connectors mounted on a weather-resistant box connect the tiltmeter cables to the Series 6200 device within the box. For this work, each such unit was located on the ground surface at the centralized location associated with one of the three spiraling arms described above. A U-1 lead-acid battery (approximately 6.5 kg of mass) was positioned beside Dev#1 and Dev#2 to provide power for the tiltmeters and the data-acquisition-system devices. A larger, Group-31 deep-cycle lead-acid battery (approximately 27 kg) powered Dev#3 and associated tiltmeters.

The Series 6200 devices use USB connections to communicate with a computer. A single Panasonic CF-19 Toughbook computer was staged adjacent to Dev#3. A 500W DC to AC inverter connected to the large lead-acid battery powered the computer and an auxiliary USB hub. Dev#3 connected directly to the hub, but two pairs of 20-meter USB extension/repeater cables, routed across the ground surface, connected the hub to Dev#2 and Dev#1. Notably, the Toughbook operated on Eastern Standard Time (EST), because, in the remote field setting of the DFPS, it could not connect to the cloud to synchronize with standard internet clocks. Consequently, the timing of all tilt data in this report differs by one hour from other works documented by the project.

National Instrument drivers installed in the Toughbook support instructions implemented on the Microsoft .Net platform. An application encoded in Visual Basic defines the structure of the data acquisition. Within it, the digital signals from the Series 6200 devices are trend-averaged with a 16 pole Bessel filter, displayed tabularly and graphically, and recorded at 0.5 Hz. All data are recorded as voltages measured by the Series 6200 devices – the application of calibration coefficients to render angles of tilt and degrees of temperature is left to subsequent data processing. The fast acquisition with filtering eliminates electrical and mechanical noise and sharpens the resolution of the system.

Essentially continuous operation over nearly two weeks required batteries to be refreshed every twelve hours. Consequently, the project utilized six batteries with three being recharged while the other three were powering operations. A 15-Ampere charger proved adequate to recharge the large battery, while a small 2-bank, 2-Ampere charger supported the smaller batteries.

Operation and data quality

Tiltmeter vaults were cleaned, and tiltmeters were installed two days before data acquisition. The tiltmeters were installed with a maximum extension of their adjustment legs – about 5 centimeters - as a precaution against water accumulation within their vaults. This setup, while enhancing the reliability of the planned multi-day campaign, also carried the cost of potentially less mechanical or thermal stability. Leveling and electronic startup were performed on the morning of 19 January 2022, and data were collected for the rest of the day and overnight to demonstrate the system's capacity.

Over the course of two weeks, the tiltmeters generated signals that remained within measurable range. The absence of drift beyond the minimum or maximum detectable voltages reflects the mechanical stability imparted by the subsurface deployment in vaults. Still, signal quality proved to be less consistent than usually realized over the course of a few hours, which is the timeframe FRx devoted to monitoring environmental injection work and also was the timeframe for work done during 2016 and 2017 at Devine. Figure A4-3 displays the thirty raw tilt signals from 19 January to 2 February. Annotations on the plot indicate examples of quality issues that required additional manipulations and compensation during data processing. These quality issues are listed in the following.

(1) *Continuous Drift*. While most tiltmeter channels generated signals spanning a range of ±50 mV, one channel –generated by the "Y" axis of TM-1195 – drifted continuously throughout the two-week campaign. Subsequent examination revealed accumulated corrosion at one of the contacts between the tiltmeter and its NI-6200 device. Assuming that the corrosion developed at a consistent rate during the campaign and that the corrosion imparted a consistently severe effect, compensation during data processing consisted of a linearly increasing bias.

(2) *Electronic Settling*. The electrolytic sensors within the tiltmeters measure the electrical impedance established by the position of a proprietary fluid within a carefully constructed vial. The impedance is affected not only by the position of the bulk of the liquid but also by the electrochemical characteristics of the recently wetted surfaces within the vial. More specifically, the electrolyte movement leaves a double-layer film on a formerly wetted surface that slowly drains and equilibrates. As a result, tiltmeters require several hours to settle after being deployed. This behavior necessitates the deployment of the tiltmeters days before the collection of useful data. Accordingly, further presentation and discussion herein omit the data collected on 19 January.

(3) *Diurnal characteristics*. All signals seemed to express a diurnal noise. Similar effects probably occurred but proved insignificant due to shorter timeframes during the previous projects conducted at the DFPS and also probably occurred during tiltmeter work during environmental remediation work, which has been the primary application of this tiltmeter system. Some effects can be attributed to the temperature changes in the tiltmeter electronics and the A2D devices. The electronics manufacturers specify temperature coefficients, but the application of these proved inadequate to suppress all noise. Additional sources of noise may include the thermal expansion/contraction of the tiltmeter legs or topographic variation of the surface soils and vaults due to temperature change and/or moisture. To compensate for all noise sources related to temperature, artificial and ad-hoc temperature compensation coefficients were computed for each data channel as the slope of the plot of the raw tilt signal versus the tiltmeter temperature during late night and early morning hours. These values differed from the manufacturers' specifications by as much as an order of magnitude. We note that the observed diurnal effects are much larger than earth-tide effects. Whether the deeper EM geophysics conducted contemporaneously with the tilt measurements provided an impact was not examined and remains unknown.

(4) *Step upon battery changes*. These unexpected abrupt shifts of a few millivolts presumably reflect electrostatic phenomena involving generation and dissipation of charge resulting from handling batteries and cables at each NI-6200 device. During data processing, these steps were eliminated by applying appropriate bias steps to the signals.

(5) *Step disruptions*. These random, larger step changes occur during every tiltmeter campaign. Although the underlying cause – whether mechanical displacement or electronic disruption – often is not documented, compensation is simply the application of appropriate bias steps to the signals.

Figure A4-4 displays the less noisy tilt signals obtained from applying the compensation processes. Subsequent data processing applied the measured orientation of tiltmeter axes and the calibration coefficients for each tiltmeter to these voltages to determine an angle of deployment (as measured relative to gravity), and changes in the angles are reported as tilt.

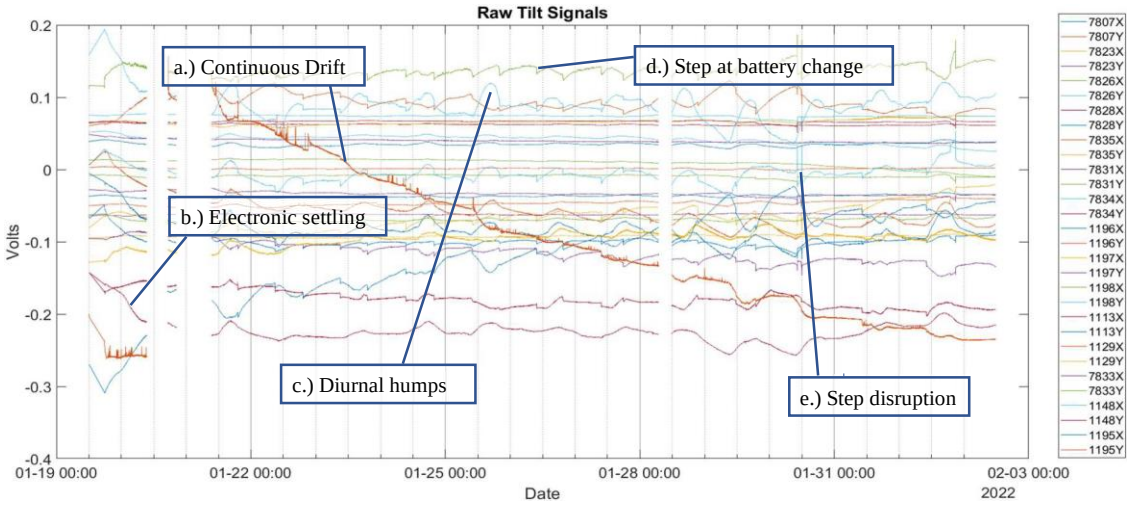

Figure A4-3: Raw tilt signals with annotations of quality issues. Each trace plots one of the thirty tilt signals reported by the NI-6200 data-acquisition-system *packages, the legend bar on the right identifies the tiltmeter number and either "X" or "Y" channel by color. The leveling screws of the tiltmeters were set during the morning of 19 January so that output signals were near the middle of the -5V to +5V range of signal. Departures from the initial signal level are intended to be interpreted as tilt angles, but at least five other phenomena asserted effect that can be treated as quality issues that require remediation during subsequent data processing: a) continuous drift by one channel (1195Y); b) settling behavior, c) diurnal deviations, d) small steps at battery changes, and e) random step disruptions. The data gaps are due to temporary pause of the data collection.*

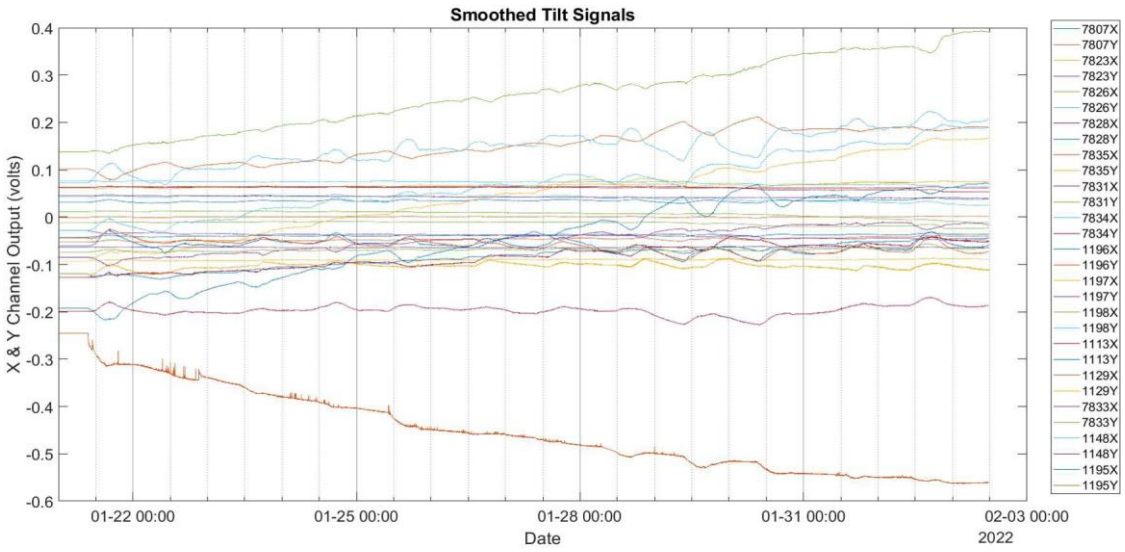

Figure A4-4: Tilt signals during process monitoring after processing for step removals and temperature corrections. Each trace plots one of the thirty tilt signals reported by the NI-6200 data-acquisition-system *packages. Quality issues have been diminished by focusing on the process performance period, applying temperature corrections (which suppressed diurnal and drift effects), manually biasing data after abrupted steps, and linear interpolations across temporal gaps.*

Tilt vector plots

A temporal display of all tilts is as much of a jumble of lines and traces as the plots of voltage (Figure A4-3, Figure A4-4). A plot of tilt vectors at each measurement location provides a more clear and useful perspective of the data. In particular, the tilt vector due to specific acts of injection constitutes information about the in-situ distribution of injected material. Thus, tilt vector plots need to be drawn relative to a baseline interval before the injection event. Selection of the baseline interval tends to be obvious for significant and quick injection events but needs to incorporate specific project timing in the case of prolonged and slow injection. Two approaches for defining baselines are reported herein. Table A4-2 lists the baseline periods that were initially assumed to apply to each day of injection work. The criteria for these selections are time-of-day (early morning) and expectations of signal trends rooted in experience. Table A4-3 lists the baseline times adopted with the consideration of process timing. For 22, 25, and 30 January, the baseline intervals are identical in both tables because no injection operations were reported on those days. Table A4-3 defines a baseline interval for injection work on 2 February, which was not evident using the criteria upon which Table A4-2 was developed. Generally, the selection of the baseline with regard to process timing (Table A4-3) is tending to be at a later time during the day compared to these times in Table A4-2.

Table A4-2: Presumed baseline episodes underlying tilt vector plots. These times were selected on the basis of time-of-day (generally early morning) and expectations of tilt signal development by experience. Operation information regarding injection and shut-in time were not considered in these selections.

Date	Baseline Start Time (EST)	Baseline Stop Time (EST)
21 January 2022	09:27:55	11:37:50
22 January 2022	02:00:00	08:00:00
23 January 2022	02:00:00	08:00:00
24 January 2022	02:00:00	08:00:00
25 January 2022	02:00:00	08:00:00
26 January 2022	03:30:00	09:30:00
27 January 2022	03:00:00	09:00:00
28 January 2022	03:00:00	07:00:00
29 January 2022	02:00:00	08:00:00
30 January 2022	03:00:00	09:00:00
31 January 2022	03:30:00	09:30:00
1 February 2022	03:25:00	09:45:00

Table A4-3: Baseline episodes considering reported injection and shut-in times. These baseline intervals were selected to immediately precede commencement of injection.

Date	Baseline Start Time (EST)	Baseline End Time (EST)	Shut-in Time (EST)
21 January 2022	09:54:55	10:27:00	1/21/2022 16:14
22 January 2022	02:00:00	08:00:00	
23 January 2022	09:15:00	12:31:00	1/23/2022 17:50
24 January 2022	09:26:00	13:00:00	1/24/2022 17:35
25 January 2022	02:00:00	08:00:00	
26 January 2022	10:00:00	13:00:00	1/26/2022 18:56
27 January 2022	10:04:00	13:00:00	1/27/2022 19:06

The tilt vector plots are generated by computing the tilt magnitude and azimuth using vector arithmetic, creating a set of arrows that correspond in length and orientation to the magnitude and azimuth, and drawing the arrows as rooted at the coordinates of the tiltmeter locations listed in Table A4-1. Specifically, using a net dip in the north-south plane, d_y, and net dip in the east-west plane, d_x, tilt magnitude and azimuth can be computed by $\sqrt{d_x^2 + d_y^2}$ and $tan^{-1}(d_x/d_y)$, respectively.

Figure A4-5 contains an example of such a plot. The tilt vectors at shut-in on 27 January are depicted as blue arrows with roots at the tiltmeter locations indicated as red and yellow-filled circles. The baseline period for this plot extended from 3:00 a.m. to 9:00 a.m. EST on 27 January. This figure also shows how components of tilt developed over the course of the day and a list of values at the moment of shut-in. A final feature in Figure A4-5 is the location of the "centrum." This element is drawn at the median of the coordinates of the intersections of lines drawn through the 105 pairs of tilt vectors. For fifteen non-parallel vectors, there are 105 pairs, equal to the permutation of two vectors out of 15 or 15!/(13!×2!). The centrum should not be construed to have any physical meaning but instead provides some sense of the centrality of the tilt pattern and suggests the quality and repeatability of the data. For the injection days other than 27 January, the tilt vector plots at the shut-in times listed in Table A4-3 can be found in Figure A4-6 through Figure A4-9.

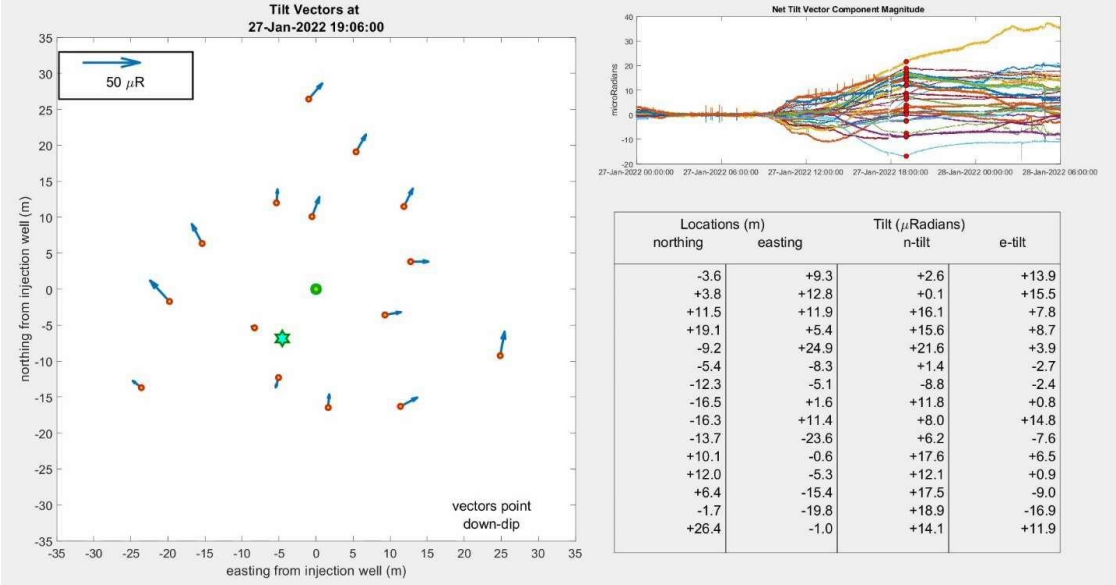

Locations (m)		Tilt (μRadians)	
northing	easting	n-tilt	e-tilt
-3.6	+9.3	+2.6	+13.9
+3.8	+12.8	+0.1	+15.5
+11.5	+11.9	+16.1	+7.8
+19.1	+5.4	+15.6	+8.7
-9.2	+24.9	+21.6	+3.9
-5.4	-8.3	+1.4	-2.7
-12.3	-5.1	-8.8	-2.4
-16.5	+1.6	+11.8	+0.8
-16.3	+11.4	+8.0	+14.8
-13.7	-23.6	+6.2	-7.6
+10.1	-0.6	+17.6	+6.5
+12.0	-5.3	+12.1	+0.9
+6.4	-15.4	+17.5	-9.0
-1.7	-19.8	+18.9	-16.9
+26.4	-1.0	+14.1	+11.9

Figure A4-5: Tilt at shut-in on 27 January 2022 at 19:06 EST. Tilt magnitude relative to the 50 μR scale arrow and the azimuth of the blue arrows plotted in the left frame indicates the tilt vectors at each tiltmeter location (red/yellow circle). Temporal evolution of tilt magnitudes after a baseline period spanning from 3:00 a.m. until 9:00 a.m. are shown in the upper right, with the red dots indicating the moment of shut-in. The table in the lower right tabulates the tilt vector components at shut-in. The injection well is the green circle in the left frame. The median of the intersections of the pairs of extrapolated tilt vectors – the "Centrum" – is the blue star.

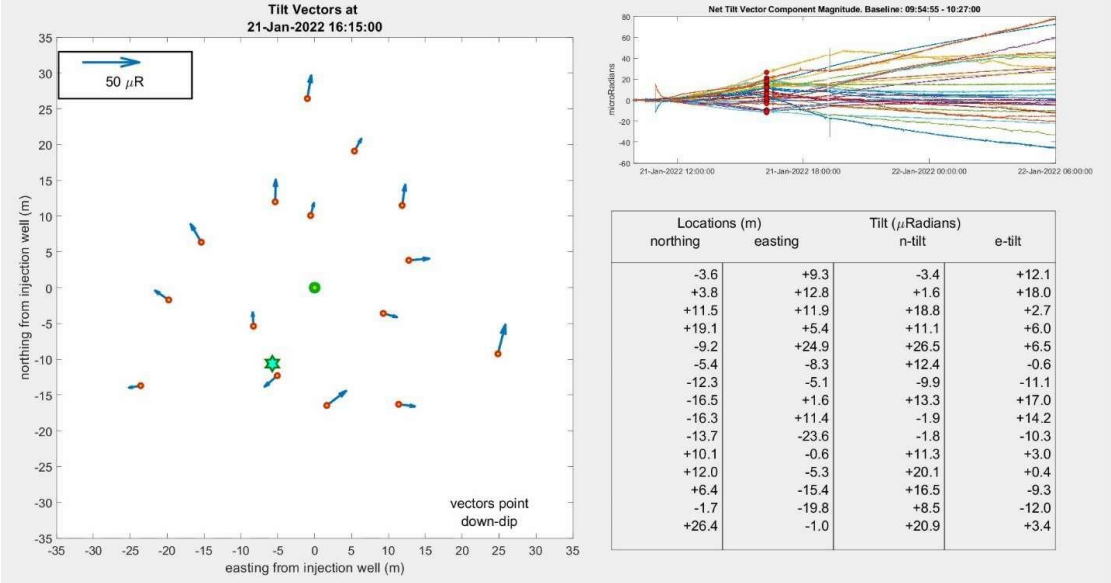

Locations (m)		Tilt (μRadians)	
northing	easting	n-tilt	e-tilt
-3.6	+9.3	-3.4	+12.1
+3.8	+12.8	+1.6	+18.0
+11.5	+11.9	+18.8	+2.7
+19.1	+5.4	+11.1	+6.0
-9.2	+24.9	+26.5	+6.5
-5.4	-8.3	+12.4	-0.6
-12.3	-5.1	-9.9	-11.1
-16.5	+1.6	+13.3	+17.0
-16.3	+11.4	-1.9	+14.2
-13.7	-23.6	-1.8	-10.3
+10.1	-0.6	+11.3	+3.0
+12.0	-5.3	+20.1	+0.4
+6.4	-15.4	+16.5	-9.3
-1.7	-19.8	+8.5	-12.0
+26.4	-1.0	+20.9	+3.4

Figure A4-6: Tilt vector plots within one minute of the listed shut-in time (16:15 EST) on 21 January 2022. Refer to the Figure A4-5 caption for the format of this figure.

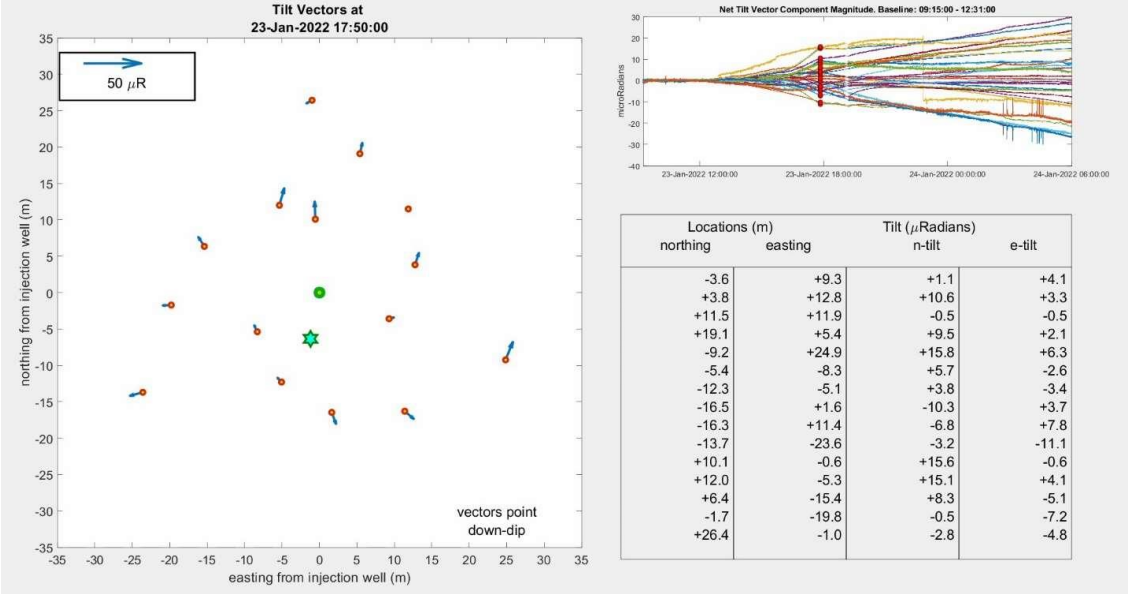

Locations (m)		Tilt (μRadians)	
northing	easting	n-tilt	e-tilt
-3.6	+9.3	+1.1	+4.1
+3.8	+12.8	+10.6	+3.3
+11.5	+11.9	-0.5	-0.5
+19.1	+5.4	+9.5	+2.1
-9.2	+24.9	+15.8	+6.3
-5.4	-8.3	+5.7	-2.6
-12.3	-5.1	+3.8	-3.4
-16.5	+1.6	-10.3	+3.7
-16.3	+11.4	-6.8	+7.8
-13.7	-23.6	-3.2	-11.1
+10.1	-0.6	+15.6	-0.6
+12.0	-5.3	+15.1	+4.1
+6.4	-15.4	+8.3	-5.1
-1.7	-19.8	-0.5	-7.2
+26.4	-1.0	-2.8	-4.8

Figure A4-7: Tilt vector plots within one minute of the listed shut-in time (17:50 EST) on 23 January 2022. Refer to the Figure A4-5 caption for the format of this figure.

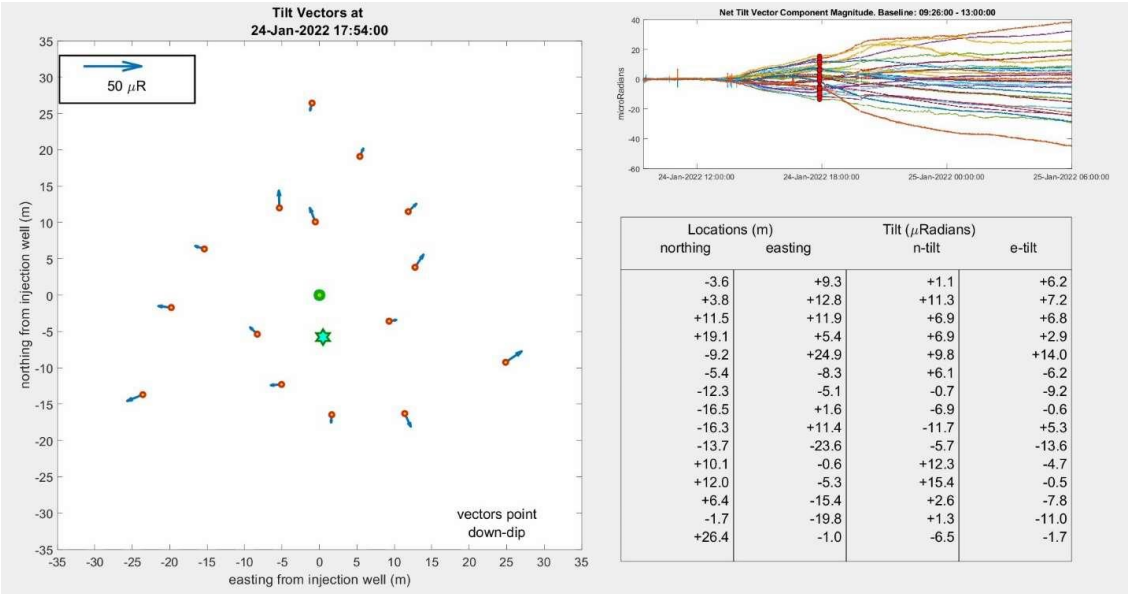

Locations (m)		Tilt (μRadians)	
northing	easting	n-tilt	e-tilt
-3.6	+9.3	+1.1	+6.2
+3.8	+12.8	+11.3	+7.2
+11.5	+11.9	+6.9	+6.8
+19.1	+5.4	+6.9	+2.9
-9.2	+24.9	+9.8	+14.0
-5.4	-8.3	+6.1	-6.2
-12.3	-5.1	-0.7	-9.2
-16.5	+1.6	-6.9	-0.6
-16.3	+11.4	-11.7	+5.3
-13.7	-23.6	-5.7	-13.6
+10.1	-0.6	+12.3	-4.7
+12.0	-5.3	+15.4	-0.5
+6.4	-15.4	+2.6	-7.8
-1.7	-19.8	+1.3	-11.0
+26.4	-1.0	-6.5	-1.7

Figure A4-8: Tilt vector plots within one minute of the listed shut-in time (17:54 EST) on 24 January 2022. Refer to the Figure A4-5 caption for the format of this figure.

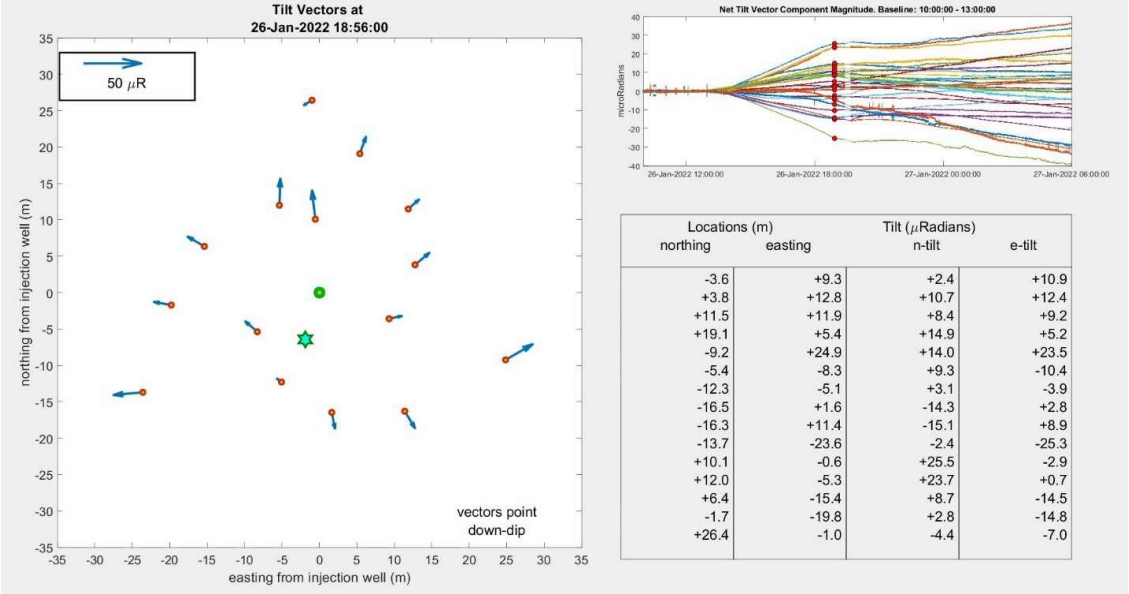

Locations (m)		Tilt (μRadians)	
northing	easting	n-tilt	e-tilt
-3.6	+9.3	+2.4	+10.9
+3.8	+12.8	+10.7	+12.4
+11.5	+11.9	+8.4	+9.2
+19.1	+5.4	+14.9	+5.2
-9.2	+24.9	+14.0	+23.5
-5.4	-8.3	+9.3	-10.4
-12.3	-5.1	+3.1	-3.9
-16.5	+1.6	-14.3	+2.8
-16.3	+11.4	-15.1	+8.9
-13.7	-23.6	-2.4	-25.3
+10.1	-0.6	+25.5	-2.9
+12.0	-5.3	+23.7	+0.7
+6.4	-15.4	+8.7	-14.5
-1.7	-19.8	+2.8	-14.8
+26.4	-1.0	-4.4	-7.0

Figure A4-9: Tilt vector plots within one minute of the listed shut-in time (18:56 EST) on 26 January 2022. Refer to the Figure A4-5 caption for the format of this figure.

Sequences of tilt vector plots can be developed over the course of individual days or injection episodes. These can be assembled into a video file. A review of the video reveals the development of tilt due to the injection. Typically, the tilt vectors grow during injection, and the centrum assumes a consistent trajectory. Upon shut-in, tilt vector growth ceases or reverses as the injected material and force of injection dissipates. Table A4-4 lists links to the video files for the tilt vector plots corresponding to the baseline times tabulated in Table A4-2 and Table A4-3. These videos are "Unlisted", meaning that anyone with the link can view these videos; however, a web search does not find these videos.

Table A4-4: YouTube video addresses for tilt vector plots.

Date	Video URL	Video URL (with timing considerations)
21 January 2022	https://youtu.be/hkFHJiiSTvU	https://youtu.be/b78jSuYCBRg
22 January 2022	https://youtu.be/oe1izmzkGN4	https://youtu.be/qV4O-BoXaIk
23 January 2022	https://youtu.be/LYaU8ZEISgI	https://youtu.be/jzEjQKq9VHc
24 January 2022	https://youtu.be/w0nH0TDHSGM	https://youtu.be/cz05WSXiHCE
25 January 2022	https://youtu.be/D-mlcJrDxeU	https://youtu.be/QELs9QPtAl4
26 January 2022	https://youtu.be/KIMOp_gGv1c	https://youtu.be/1wRg80vTKsk
27 January 2022	https://youtu.be/M6IE3kMaMHU	https://youtu.be/z7MkKnxw650
Explanatory video	https://youtu.be/4v4NlkMvb8c	

Tilt inversion

The tiltmeter system and related data processing capabilities of FRx have been developed and utilized to monitor the creation of shallow, wide-aperture fractures in surface soils as part of efforts to remediate soil or groundwater. The tiltmeter deployment, data gathering, and tilt vector display

aspects can be expected to extend directly and effectively to the challenges of the 2022 project at the DFPS. The FRx interpretation relies upon a double dislocation model of a discrete hydraulic fracture within an unperturbed, although deformed, solid matrix, i.e., FRx data inversion does not anticipate leakoff into the formation or poroelastic effects that would arise during leakoff. In as much as the injection rates used during the present work were slow and the injection pressures incrementally greater than lithostatic, the FRx forward model involving an elliptical, planar hydraulic fracture of constant aperture probably is inappropriate, and descriptive information generated using it best be considered meaningless. Nonetheless, the data were fed to the inversion routines, and parameter estimates were generated.

The forward model – the presumed injection form – is characterized in Figure A4-10. This idealized depiction of a hydraulic fracture involves eight parameters. Three parameters define the size of the feature: 1.) the radius or extent in the dip direction, 2.) the radius or extent in the strike direction, and 3.) the uniform aperture. Two more parameters define the orientation of the fracture: 4.) the dip and 5.) the azimuth of the dip. The final three parameters define the position of the fracture: 6.) the depth, 7.) the lateral displacement from the parent well in the dip direction, and 8.) the lateral displacement in the strike direction. A feature described with these eight parameters manifests in a tilt pattern on the ground surface that can be calculated from the laws of elasticity. The inversion process varies eight parameters while seeking to minimize the "error" between the calculated deformation and the measured tilts. This parameter estimation process is highly nonlinear and subject to issues with local minima. Consequently, the ideal form described by the "best estimated parameters" is subject to substantial uncertainty.

FRx has harnessed non-parametric statistics to characterize the statistical distribution of the estimated parameters. This approach involves considering the projections of subsets of only a few tiltmeters. Since four tiltmeters generate eight signals, each quadruplet of tiltmeters can describe the fracture parameters. There are 1365 unique subsets that can be formed from fifteen tiltmeters (i.e., the combination of 15 things taken four at a time). The 1365 sets of estimated fits define eight probability distributions, which can be examined to determine what values are most likely to occur. This is similar to a Theil-Sen estimator or Kendall-Theil Robust Line Analysis.

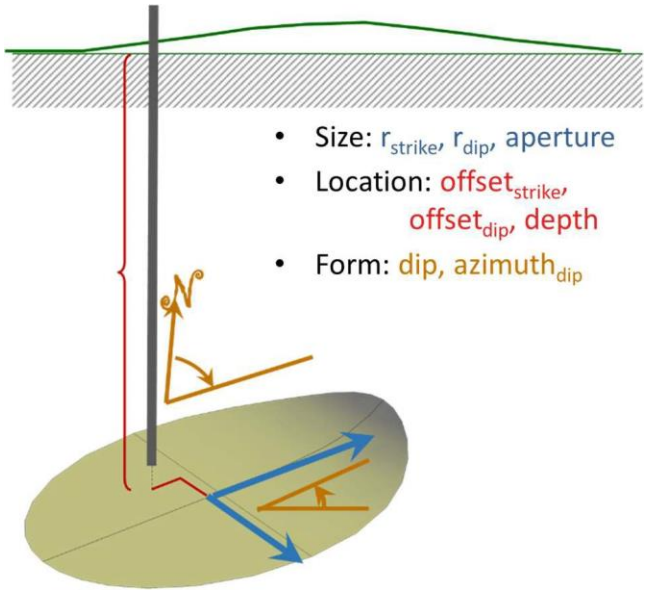

Figure A4-10: Parameters of an idealized fracture. Eight parameters are required to characterize a thin, dipping, an elliptical cylinder that serves as the fracture shape within the forward model for tilt data inversion. Three parameters describe the radii (blue arrows) and thickness (not indicated) of the 3D fracture. Three more dictate its position (red, orthogonal lines). Unless absolutely flat-lying, two angles (orange arcs) are needed to indicate directions. The injection well is indicated by the thick, vertical, gray line. Deformation of the ground surface is indicated, conceptually, as the green profile.